JOSÉ - JUPITER ORBITING SPACECRAFT:

A SYSTEMS STUDY

Volume I

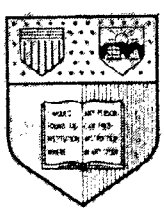

COLLEGE OF ENGINEERING
Cornell University
Ithaca, New York 14850

JOSÉ - JUPITER ORBITING SPACECRAFT:

A SYSTEMS STUDY

Volume I

Prepared Under
Contract No. NGR 33-010-071
NATIONAL AERONAUTICS AND SPACE ADMINISTRATION

by

NASA-Cornell Doctoral Design Trainee Group
(1967-70)

October 1971

College of Engineering
Cornell University
Ithaca, New York

Table of Contents

Volume I

Table of Contents, cont.

Volume II

Appendices

Table of Contents, cont.

Volume II

Appendices

Authors

Charles K. Paul	Chapters I, II, III, IV, VI. Appendices A, B, C1, C2, C3, C4, F, F1, F2, F3, F4, F5.
Thomas R. McDonough	Chapters I, II, VI. Appendices F, F1, F2, F3, F4, F5.
Alan W. Schorr	Chapters II, VIII, IX.
John L. Matilaine	Chapters II, VII. Appendix G
Phillipe L. Lamy	Chapters II, V. Appendices D, E.
Michael H. Redlin	Chapters II, IX.

Preface

The following report is the result of an educational experiment conducted at Cornell with the support of the NASA Office of University Affairs. The intent of the experiment was to determine whether meaningful doctoral design work in a systems engineering context could be conducted in the university environment. In addition to Cornell, Purdue, Georgia Tech, Kansas State, and Stanford were involved in similar programs. The schools named are scattered both regionally and philosophically.

The modes of approach devised by the several schools have differed. At Cornell the mode has involved a central project with the individual students assuming responsibility for a major subsystem. In the majority of cases students have been able to satisfy the thesis requirement for the doctorate by an in-depth study of an aspect of their project responsibility.

Student interest has been high from the outset of the program and in the majority of cases faculty have willingly become involved. Although the number of students in this and following groups is small, sufficient have presented theses to their special committees successfully so that there is little doubt that design oriented or mission directed thesis work is judged acceptable from an academic point of view.

The personnel and faculty have varied with time. As in industry a certain turnover occurs as life goals change. A listing of personnel engaged in the project and areas of concern follow:

Personnel

NASA Supported

Charles K. Paul - Civil Engineering

Faculty Advisor: Professor A. McNair

Thesis: "Attitude Control, Trajectory Analysis, and Science Objectives of a Jupiter Orbiting Spacecraft"

Doctoral Degree Received: June 1970

Presently on Faculty of Division of Basic Studies, Cornell University.

Thomas R. McDonough - Astronomy

Faculty Advisor: Professor N. Brice

Thesis: "The Interaction of the Solar Wind with the Interstellar Medium".

Doctoral Degree Expected: February 1972

Presently a Graduate Student at Cornell University.

Alan W. Schorr - Mechanical Engineering

Faculty Advisor: H. N. McManus, Jr.

Thesis: "The Design, Modeling, and Optimization of a Space-Oriented Radioisotope Thermoelectric Power Supply"

Doctoral Degree Received: September 1971

Robert L. Ryan - Electrical Engineering

Left the program after one year to attend Harvard Business School.

John L. Matilaine - Electrical Engineering

Faculty Advisor: Professor N. Brice

Does not intend to complete doctoral work -- changed objective.

Presently employed by radio station WVBR, Ithaca, N. Y.

Affiliated (Non-NASA Supported)

Charles H. Acton, Jr. - Electrical Engineering

Faculty Advisor: Professor N. Vrana

Project work on Galilean moons of Jupiter.

M.Eng. (Electrical) Degree: February 1970

Presently at NASA-JPL, Pasadena, California

Phillipe L. Lamy - Aeronautical Engineering

Thesis Advisor: Professor H. N. McManus, Jr.

Thesis: "Design Criteria, Investigation and Selection of a Jupiter Orbiter Propulsion System"

M.S. Degree: September 1971

Presently pursuing doctoral work in the Department of Theoretical and Applied Mechanics, Cornell University.

Michael H. Redlin - Mechanical Engineering

Faculty Advisor: Professor R. M. Phelan

Presently on active duty with the United States Navy.

Will complete doctoral studies after service.

From the writer's point of view the experiment has been interesting and instructive. The program at Cornell has answered affirmatively the pedagogical question originally posed.

H. N. McManus, Jr.
Professor of Mechanical Engineering
Program Director

Chapter I: The Planet Jupiter: A Brief Summary

A. Introduction

Jupiter, the largest planet of this solar system, with a mass more than twice the combined masses of all the other planets, is the fifth planet in distance from the sun. Jupiter is the first of the major planets encountered after passing through the asteroid belt from the sun. The remaining major planets are Saturn, Uranus, and Neptune. These major planets are generally classified as such because of their relatively large diameters (50,000 to 140,000 km.); low densities (0.7 to 1.7 gm/cm^3); and extensive, optically thick atmospheres containing hydrogen, helium, methane, and ammonia as well as other gases in lower abundance. In contrast to these major planets are the four terrestrial planets, i.e., Mercury, Venus, Earth, and Mars, having small diameters (5,000 to 13,000 km.); high densities (4.2 to 5.5 gm/cm^3); relatively thin atmospheres with a known planetary solid surface. Thus, the understanding of the origin of the solar system and eventually the universe necessitates the understanding of the differences between major and terrestrial planets; and Jupiter, the major planet closest to Earth, is first in line to be investigated by an interplanetary spacecraft.

Other features unique to Jupiter are of course its famous Red Spot, the South Tropical Disturbance, and other atmospheric phenomena, and twelve associated satellites, four of which possess retrograde orbits. Also, there is a likelihood that there exist zones within Jupiter's atmosphere having physical and chemical properties conducive to the creation and harboring of life forms. It can be argued that, accepting present theories of atmospheric constituents and energy exchanges necessary for the creation of simple life forms, Jupiter's atmosphere may very well be the most ideal location for the creation of life forms in this solar system, including Earth with its present gas abundances.

It should be remarked that much of the information contained in this chapter, i.e., the present Jupiter state-of-knowledge will be improved by the time this report is completed. A very excellent, detailed synopsis of Jupiter, already outdated as far as numerical parameters which are presented, is Handbook of the Physical Properties of the Planet Jupiter, NASA SP-3031, 1967, by C.M. Michaux, with 265 references. The reader interested in the historical accumulation of knowledge of Jupiter and various conflicting theories concerning properties of the planet is referred to this comprehensive account. Also, a more concise, updated description of Jupiter is presented along with the other major planets, in A Brief Survey of the Major Planets: Jupiter, Saturn, Uranus, and Neptune, JPL Technical Memorandum 33-424, April 1, 1969 by R.L. Newburn, Jr. Any understanding of the scientific objectives of a Jupiter mission requires the study of these two works.

B. Definitions

Although standard terms in the astronautical sciences, the following elements are defined below for ready reference:*

1. Aphelion: The point on a heliocentric elliptical orbit farthest from the sun.

2. Apogee: The point on a geocentric elliptical orbit farthest from the Earth.

3. Apojove: The point on a zenocentric elliptical orbit farthest from Jupiter.

4. Ascending Node (of an orbit): That point on an orbit at which a body (planet or satellite) crosses from south to north the reference plane (e.g., the ecliptic for the planets) on the celestial sphere. The opposite point, separated by 180° of longitude is the descending node.

---

* Michaux, C.M., Handbook of the Physical Properties of the Planet Jupiter, NASA SP-3031, 1967.

5. Astronomical Unit (a.u.): A fundamental unit of length used in astronomy. In celestial mechanics, it is defined as the radius of an idealized circular and unperturbed orbit of Earth around the Sun. Radar determinations by Muhleman (1964) yield: 1 a.u. = $1.495989 \times 10^8 \pm 600$ km.

6. Conjunction: The configuration of the Sun, a planet, and Earth when the heliocentric longitudes of the latter two are equal. The three bodies then lie most nearly in a straight line. When the planet is between the Sun and Earth, the planet is said to be in inferior conjunction; when the Sun is between Earth and the planet, the planet is said to be in superior conjunction. Thus, of all the planets, only Mercury and Venus can ever be in inferior conjunction, whereas all of them can be in superior conjunction.

7. Day (ephemeris): Average value of the mean solar day taken over the last three centuries.

8. Day (sidereal): Time interval between two successive transits of the vernal equinox over the same meridian.

9. Day (solar): The time interval between two successive transits of the sun over a meridian. Since this time interval varies with Earth's orbital motion, a mean solar day was chosen, based on a mean annual motion of Earth (assuming an equivalent circular orbit) or a fictitious mean Sun.

10. Declination (of a celestial point): The angle between a point and the celestial equator, measured along the hour circle through the point and counted as north (+) or south (-) of the equator.

11. Direct Sense: Counterclockwise revolution about a body looking down body's north polar axis toward the center.

12. Ecliptic: The annual, apparent path of the Sun's center on the celestial sphere, as seen from Earth, or the intersection of the Earth's orbital plane with the celestial sphere.

13. Ephemeris (fundamental): An astronomical table predicting the positions of celestial bodies at regular intervals of time (also called almanac).

14. Epoch: An arbitrary instant of time at which positions are measured or calculated.

15. Gregorian Date: A date on the official calendar in use throughout the Christian world. The Gregorian calendar was instituted in 1582 by Pope Gregory XIII to correct errors accumulating in the Julian Calendar.

16. Heliocentric: Sun centered; term derived from helios the Greek word for sun.

17. Julian Date: The number of mean solar days that have elapsed since the adopted epoch of Greenwich mean noon on January 1, 4713 B.C.

18. Laplacian plane (or proper plane): A plane that is fixed relative to the planet's equator, and upon which the precessing orbital plane of a satellite maintains a nearly constant inclination. The plane's position is determined by the balance of the orthogonal components of the disturbing forces (e.g., from the planet's oblateness or the Sun's attraction).

19. Libration: Periodic oscillation about a mean position as, for example, caused by perturbations.

20. Limb: Edge of the illuminated part of a disc.

21. Line of apsides: A straight line infinitely extending the major axis of an elliptical orbit. The line passes through those points closest (periapsis) and farthest (apoapsis) from the dynamical center.

22. Line of nodes: A straight line that joins the intersection points (nodes) of the two great celestial circles that determine the orbital plane and the reference plane used to describe the motion of a planet or satellite.

23. North celestial pole: The northern point of intersection of the Earth's rotation axis with the celestial sphere.

24. Occultation: The obscuring of an observed body by a body passing in front of it.

25. Opposition: The configuration of Sun, Earth and planet when the heliocentric longitudes of the latter two are equal. The three bodies, with Earth in the middle, are then most nearly in a straight line. Mercury and Venus can never be in opposition.

26. Osculating orbit: The instantaneous elliptical orbit that a planet or satellite would follow at the date considered (epoch of osculation) if all disturbing forces were removed.

27. Perigee: That point on a geocentric elliptical orbit closest to the Earth.

28. Perihelion: That point on a heliocentric elliptical orbit closest to the Sun.

29. Perijove: That point on a zenocentric elliptical orbit closest to Jupiter.

30. Phase: The fraction illuminated of the disc area.

31. Phase angle: The angle between the Sun and Earth, as observed from a planet whose center is the vertex.

32. Precession: The very slow (long period) motion (26,000 years for Earth) of a planet rotation axis about the north pole of the ecliptic, caused by the action of the Sun and any large satellite upon the planet's equatorial bulge.

33. Retrograde sense: The opposite of direct sense of rotation; i.e., clockwise.

34. Right ascension: The angular arc measured along the celestial equator from the vernal equinox eastward (i.e., counterclockwise) to the intersection of the hour circle of the point (semigreat circle passing through the north celestial pole and the point).

35. Synodic period of revolution (of two planets or satellites): The time interval between consecutive oppositions or conjunctions of two bodies revolving around the same center.

36. Terminator: The line separating the illuminated from the non-illuminated portions of a planet or satellite; one observes a morning or evening terminator on the disc.

37. Vernal equinox: The point at which the Sun, in its annual apparent path around the Earth, appears to cross the celestial equator from south to north at a certain time of the year (presently on March 21), or the ascending node of the ecliptic on the equator.

38. Year, Julian: The mean length of the year on the Julian calendar; it is equal to 365.25 mean solar days, or $365^{\underline{d}}\ 6^{\underline{h}}$ exactly.

39. Year, sidereal: The time interval between two successive returns of the Sun to a fixed celestial point (fixed star); it is equal to the true period of revolution of Earth and is equal to 365.25636 mean solar days, or $365^{\underline{d}}\ 6^{\underline{h}}\ 9^{\underline{m}}\ 10^{\underline{s}}$.

40. Year, tropical: The time interval between two successive returns of the Sun to the vernal equinox. Because of precession, it is shorter than the sidereal or true year. It is equal to 365.24220 mean solar days, or $365^{\underline{d}}\ 5^{\underline{h}}\ 48^{\underline{m}}\ 46^{\underline{s}}$.

41. Zenocentric: Jupiter centered; the prefix "zeno" is derived from the Greek name for the chief of gods, Zeus; the Latin equivalent is Jupiter.

C. Mechanical Properties of the Planet Jupiter

Table I-1 presents a summary of important parameters of the planet Jupiter contrasted with those of Earth. All parameters are standard astronomical elements and should be self-explanatory. The longitude of the perihelion, $\tilde{\omega}$,

Table I-1: Jupiter Mechanical Properties

Parameter	Jupiter	Earth
1. Mean Orbital Elements (Epoch: 1960, Jan. 1.5 ephemeris time)		
Mean Solar Distance, a, (a. u.)	5.202803	1.000000
Mean motion, n, (deg/day)	.083091	.985609
Eccentricity, e	.048435	.016726
Inclination to ecliptic, i, (deg.)	1.30536	0.0
Longitude of ascending node, Ω, (deg.)	100.04444	0.0
Longitude of perihelion, ω, (deg.)	13.67823	102.25253
Mean longitude at epoch, L_o (deg.)	259.83112	100.15815
2. Orbital Constants		
Sidereal year (in Earth Sid. year)	11.86177	1.00000
Tropical year (in Earth trop. year)	11.86223	1.00000
Mean synodic period (in Earth Sid. year)	1.09205	1.09205
Mean synodic period (in Earth trop. year)	1.09210	1.09210
Perihelion distance (a.u.)	4.950805	0.983273
Aphelion distance (a.u.)	5.454801	1.016727
Min. distance from Earth (a.u.)	3.9308	
Max. distance from Earth (a.u.)	6.4363	
Mean orbital velocity (km/sec)	13.06	29.77
3. Planetary Properties		
Mass	317.9	1.0
Gravitational mass GM(km^3/sec^2) ($G = 6.673 \times 10^{-23}$ $km^3/sec^2/gm$)	1.267077×10^8	3.9860115×10^5
Mean density (gm/cm^3)	1.334	5.52
Equatorial radius (km)	71,371.610	6,378.160
Oblateness	1/15.4	1/298.3
Mean surface gravity (cm/sec^2)	2664	983
Period of rotation (h m s)	System I: 95030.003	23 56 4.08
	II: 95540.632	
	III: 95529.37	
Inclination of planet's equator to orbital plane of planet (° ' ") (Jan. 1, 1960)	3 04 10	23 26 36

is measured in two planes, i.e., $\omega = \Omega + \omega$, where Ω is the longitude of the ascending node and ω is the argument of perihelion. The mean longitude at epoch of the planet, L_o, is the constant in the formula $L = L_o + nt$, where L is the mean longitude of the planet at time t after the epoch (t=0), and n is the mean daily motion. The mean anomaly is usually defined as $L - \omega$.

Since there are other planetary perturbations on any planet, the orbit of a planet is not precisely defined by its osculating ellipse corresponding to the instantaneous position and velocity vectors at any epoch. These vectors, expressed as functions of time, contain both secular (progressively changing) and periodic terms. Mean elements presented in Table I-1 cannot therefore be used in precise calculations of a planet's position since they ignore the periodic terms. An outstanding long period perturbation (900 years), commonly termed the Great Inequality, exists in the orbits of Jupiter and Saturn, produced by the near commensurability of their periods of revolution, i.e., in the ratio 2 to 5 (12 years for Jupiter and 30 years for Saturn).

Two general methods which have been used to determine Jupiter's mass are: (1) the measurements of perturbations of the motions of planets or minor planets, and (2) the scaling of the orbits of Jupiter's satellites.

Values of Jupiter's equatorial and polar radii have been determined by extensive astronomical measurements with both the filar micrometer and the heliometer. The difference between the two radii divided by the equatorial radius yields the value termed the optical flattening. The oblateness term presented in Table I-1 is the dynamical flattening, affected by Jupiter's gravitational equipotential surface. The motion of the perijove caused by Jupiter's fifth satellite yielded the value shown in the table.

The three general methods employed for deriving the rotation rate of Jupiter are (1) the optical method on the visible cloud surface, (2) the spectroscopic method for the upper atmosphere (Doppler shift), and (3) the radio emission method. The systems I and II rotation rates, shown in Table I-1,

are both derived by the optical method of averaging rotation rates of many distinct cloud features since 1880. System I is used for all markings and features found in the Equatorial Zone (See Section E of this chapter) or on its boundaries; the adopted longitude of the central meridan for System I is $\omega_{o1} = 47.31^{o}$ at the adopted epoch (this epoch also applies to System II) t_o = Greenwich mean noon, July 14, 1897. System II is used for all features outside of the conventional limits of the "Great Equatorial Stream" (roughly 10^{o} N and S in latitude); the adopted longitude of its central merian is $\omega_{o2} = 96.58^{o}$.

The spectroscopic method of the measurement of the Doppler Shift of Fraunhofer lines of the solar spectrum reflected by Jupiter's clouds of high albedo is seldom used today because of its low accuracy and experimental difficulties.

Statistical analysis of decametric radio bursts from Jupiter defines the radio emission method of determining rotation rate. The radio bursts are small relative to the disc of Jupiter and fixed relative to each other; thus a System III rotation rate was derived wherein the central meridian was taken equal to the central meridian of System II at the epoch 1957, January 1, 0^{h} universal time. Thus, in System III, the period of the radio burst should be constant. Such was the case until 1961, when a change of period of 1.17^{s} was discovered for the radio bursts. This is a significant change when compared to the constancy of the period before 1960, the magnitude of the bursts, and the minute irregularities in the Earth's rate of rotation (in the order of milliseconds). Possible explanations for this apparent gradual shift of the radio source with respect to System III longitude are: (1) if the radio bursts are governed by Jupiter's magnetic field, and if the magnetic field originates within Jupiter's planetary core, then significant changes in Jupiter's core

could certainly influence the decametric radiation; (2) coupling effects between Jupiter's magnetic field and the interplanetary medium, the period drift being a virtual change linked to the variations in the focusing properties of the Jovian ionosphere, magnetosphere, or even the interplanetary medium. An interesting phenomenon with regards to the Great Red Spot occurred at approximately the same time as the decametric period change; its optical period lengthened by $1.01\frac{s}{}$ per year. Thus, the Great Red Spot and the decametric burst might be related.

To the first order in the oblateness, or dynamical flattening (f), Jupiter's equatorial gravity is given by:

$$g_{eq} = \frac{GM_J}{R_{eq}^2} \left(1 + f - \frac{3\omega^2 R_{eq}^3}{2GM_J}\right)$$

where: GM_J = Gravitational mass of Jupiter

R_{eq} = equatorial radius

ω = angular velocity of rotation at the equator

To the same degree of accuracy, the gravity at any latitude (ϕ) is given by:

$$g_\phi = g_{eq}\left[1 + \left(\frac{5\omega^2 R_{eq}^3}{2GM_J} - f\right) \mathrm{Sin}^2\phi\right]$$

The centrifugal force term, $\frac{\omega^2 R_{eq}^3}{GM_J}$, exceeds the oblateness term for the planet Jupiter.

D. Jovian Radiation

The most unique characteristic of Jupiter to the terrestrial radio astronomer is its intense emission of nonthermal, polarized radiation, unlike any other planet of our solar system. The existence of this radiation enables us to deduce the presence of a Jovian magnetic field. Space probes have found

that Mars and Venus both lack substantial magnetic fields, and the absence of Jovian-style radiation from any other planet observed from earth makes us suspect that the only planets in our solar system which have strong magnetic fields are Jupiter and the Earth. That two such utterly dissimilar planets should have fields while the other seven apparently do not, is one of the great mysteries of the solar system, and consequently an excellent reason to devote an orbiting satellite to the exclusive study of Jupiter.

The observed radio radiation is of three distinct types: decametric, decimetric, and thermal. The overall radio spectrum of Jupiter is shown in Figure I-1. The decametric has the longest wavelength and the most erratic behavior. Discovered by accident in 1955 (Burke and Franklin), the decametric radiation consists of sporadic, intense, polarized, broadband ($\sim$1 MHz) noise bursts that drift in frequency. The intensity of the bursts increases with increasing wavelengths, and they have been observed at frequencies as low as can be detected through our ionosphere ($\sim$5 MHz at best), and this type of radiation seems to cut off at about 40 MHz. This latter fact enables us to estimate the Jovian magentic field, for although there is no generally accepted theory of the decametric radiation, most of the proposed theories require that the radiation be generated at the local electron cyclotron frequency, $f_c = eB/2\pi mc$ (B = magnetic field in gauss); e and m are the electron charge and mass; c is the speed of light). The high-frequency cutoff of 40 MHz then implies that the field at the point of generation of the highest frequency must be the order of ten gauss, and less elsewhere. This is a field an order of magnitude larger than the Earth's ($\sim$0.5 gauss), which is all the more remarkable because Jupiter's large size implies that a dipole moment of the order of 10^4 times the earth's is needed to generate such a field at the surface of the planet.

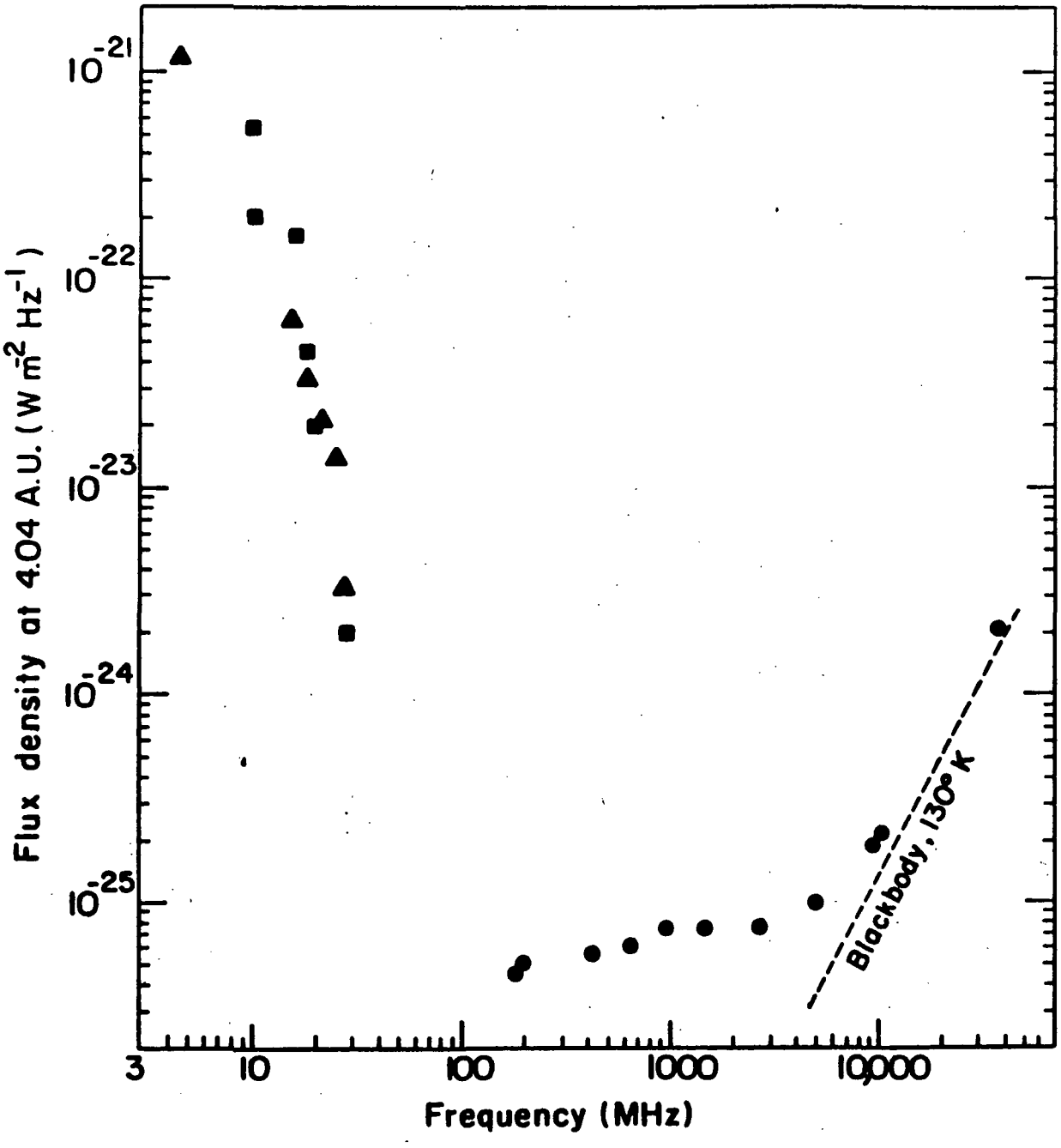

Figure I-1: Average Power Spectrum of Jupiter (from Carr and Gulkis, 1969).

A curious characteristic of this radiation is that it is controlled by the position of the Jovian satellite Io relative to earth. When Io is in either of the two positions shown in Figure I-2, terrestrial observers have the highest probability of receiving the decametric bursts.

The decametric radiation is also remarkable in that it appears to be "tied" to the planet. If the number of bursts detected at a particular frequency is plotted against Jovian longitude, as in Figure I-3, we find that several distinct "sources" emerge. Furthermore, these sources rotate with a rotation period different from, and more constant than, that of any visible feature of the planet, including the Red Spot. The longitude system based on the radio rotation period of $9^h55^m29^s.37$ is called System III, to distinguish it from System I, which is based on the rotation of visible equatorial features, and which is about 5^m faster than System III; and System II, based on visible mid-latitude features, which is about 11^s slower than System III. The sources in Figure I-3, on which System III is based, are most distinct at the highest decametric frequencies. The sources become broader at longer wavelengths, and are indistinguishable at longest wavelengths.

The decimetric radiation is radically different from the decametric. It is steady, not bursty, and has the flat spectrum shown in Figure I-1, with a flux density of about 7×10^{-26} $W.m^{-2}Hz^{-1}$, from around 40 MHz to a few GHz, at which point it becomes overwhelmed by the thermal radiation. It is 30% linearly polarized at 30 cm, and is believed to be synchrotron radiation from relativistic electrons in the trapped radiation ("Van Allen") belts of Jupiter. If the electrons were distributed uniformly throughout a uniform magnetic field, such a flat spectrum would imply an electron number vs. energy spectrum $N(E) \propto 1/E$. However, because the geometry is likely to be far more complex than that, the assumption of such an electron distribution is invalid.

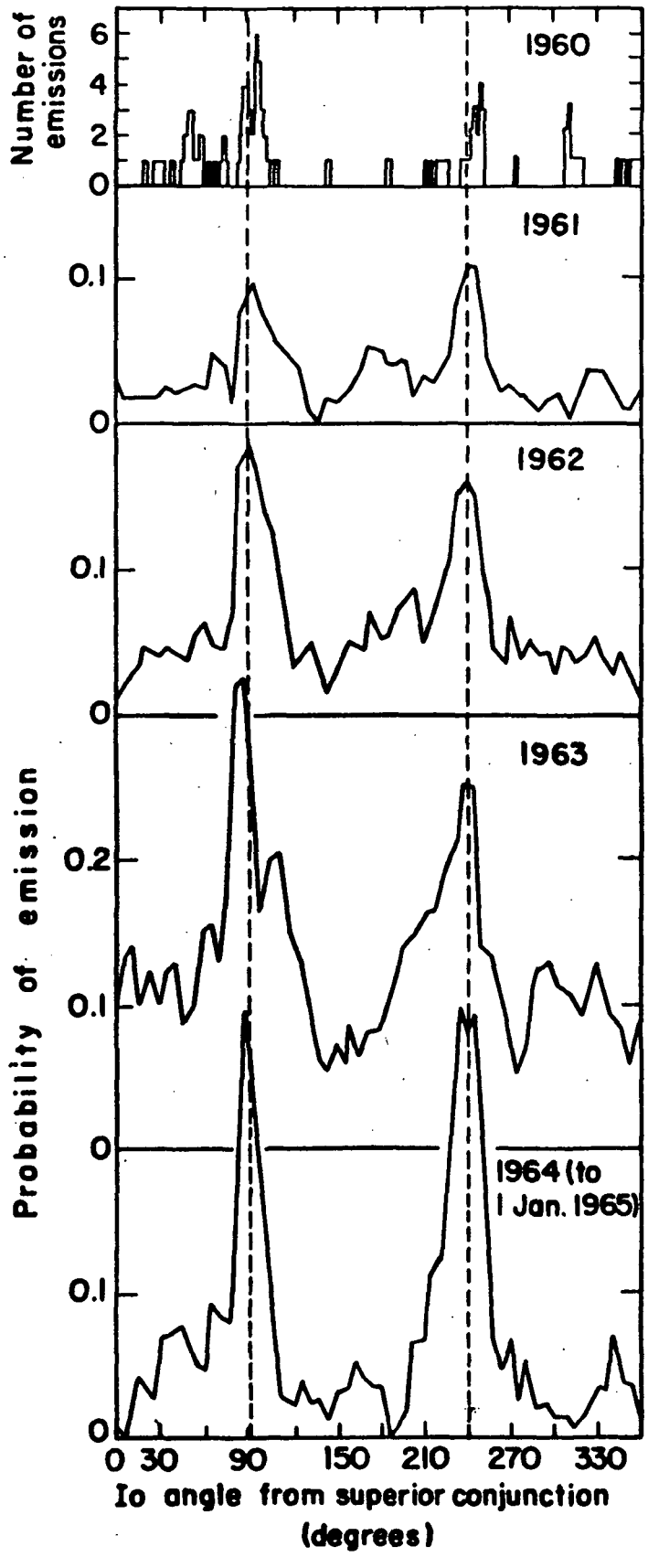

Figure I-2: Io positions for Best Chance of Decameter Reception (from Dulk, 196

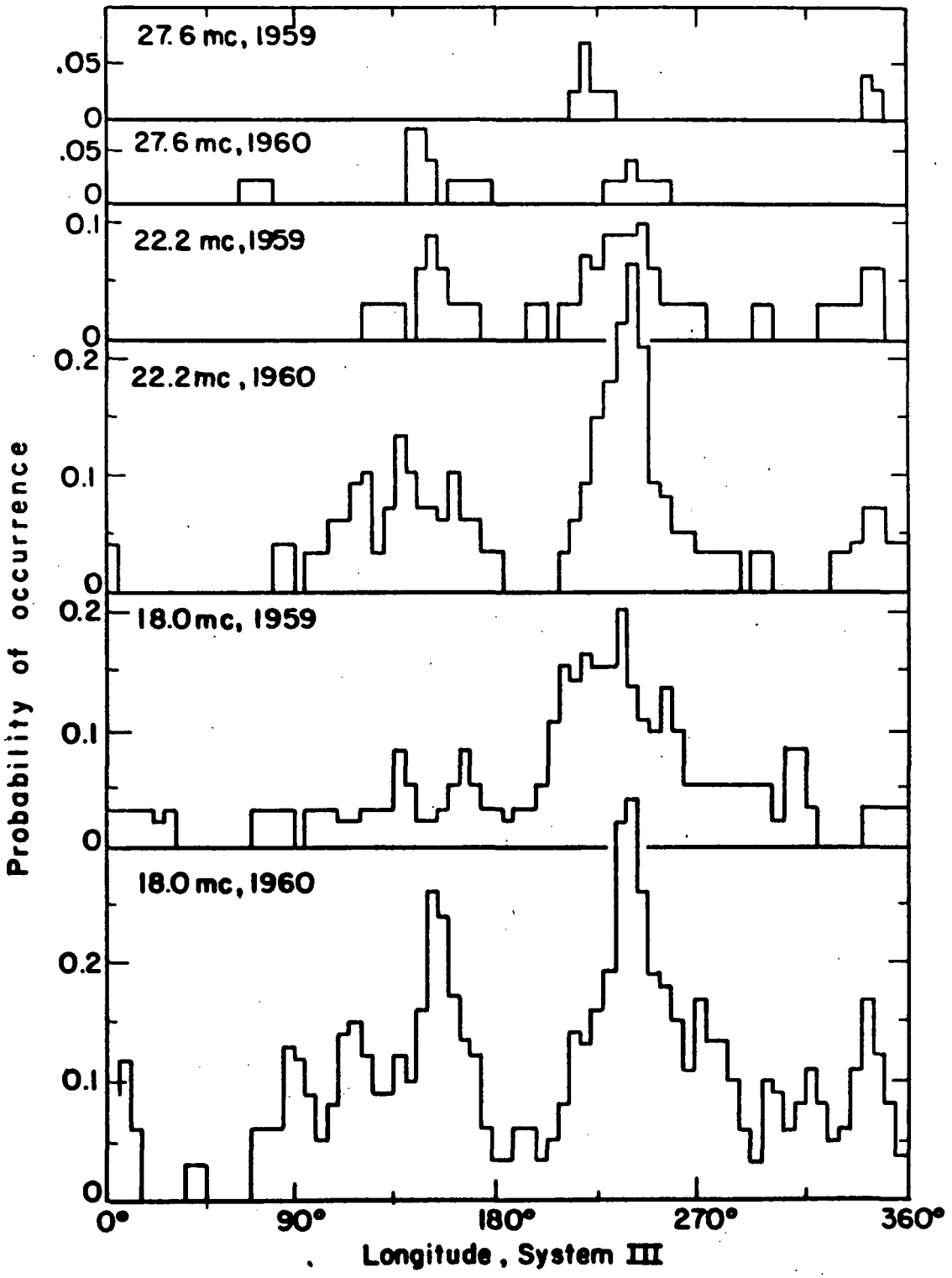

Figure I-3: Probability of Decametric Emission vs. Jovian Longitude (from Carr et al., 1961).

It is not possible to unambiguously determine the magnetic field strength from the decimetric radiation, without knowing the actual electron distribution, but rough estimates which have been made yield a field of $\sim$1 gauss (Carr and Gulkis, 1969) in the belts, which is consistent with a surface field of $\sim$10 gauss.

The radiation has been mapped by Berge (1966) at 10.4 cm, as shown in Figure I-4, and by Branson (1968) at 21 cm. This map indicates that the magnetic dipole axis of Jupiter is tilted by $\sim 10^{\circ}$ from its rotational axis, much like the earth.

E. The Jovian Magnetosphere

The magnetic field of the earth is known from space probes to create a cavity in the solar wind. The magnetic field excludes the impinging charged particles out to the point where the magnetic pressure, $B^2/8\pi$, is comparable to the solar wind particle pressure, nmv^2 ($n \cong 5$ protons/cm^3 at 1 AU; m = proton mass; v = solar wind speed $\approx$ 400 km/sec). We expect the same phenomenon to occur at Jupiter, with the stronger Jovian field carving out a much larger cavity in the weaker solar wind. The size of this cavity in the solar direction should be $\sim$50 Jovian radii (Carr and Gulkis, 1969), whereas the earth's cavity is only $\sim$10 terrestrial radii. The internal structure of the Jovian magnetosphere is expected to differ considerably from that of the earth because of Jupiter's rapid rotation period of $\sim$10 hours which, for a planet an order of magnitude larger than the earth, generates a centrifugal acceleration two orders of magnitude larger at the surface of Jupiter than for earth.

F. The Atmosphere of Jupiter

1. Temperature and Composition:

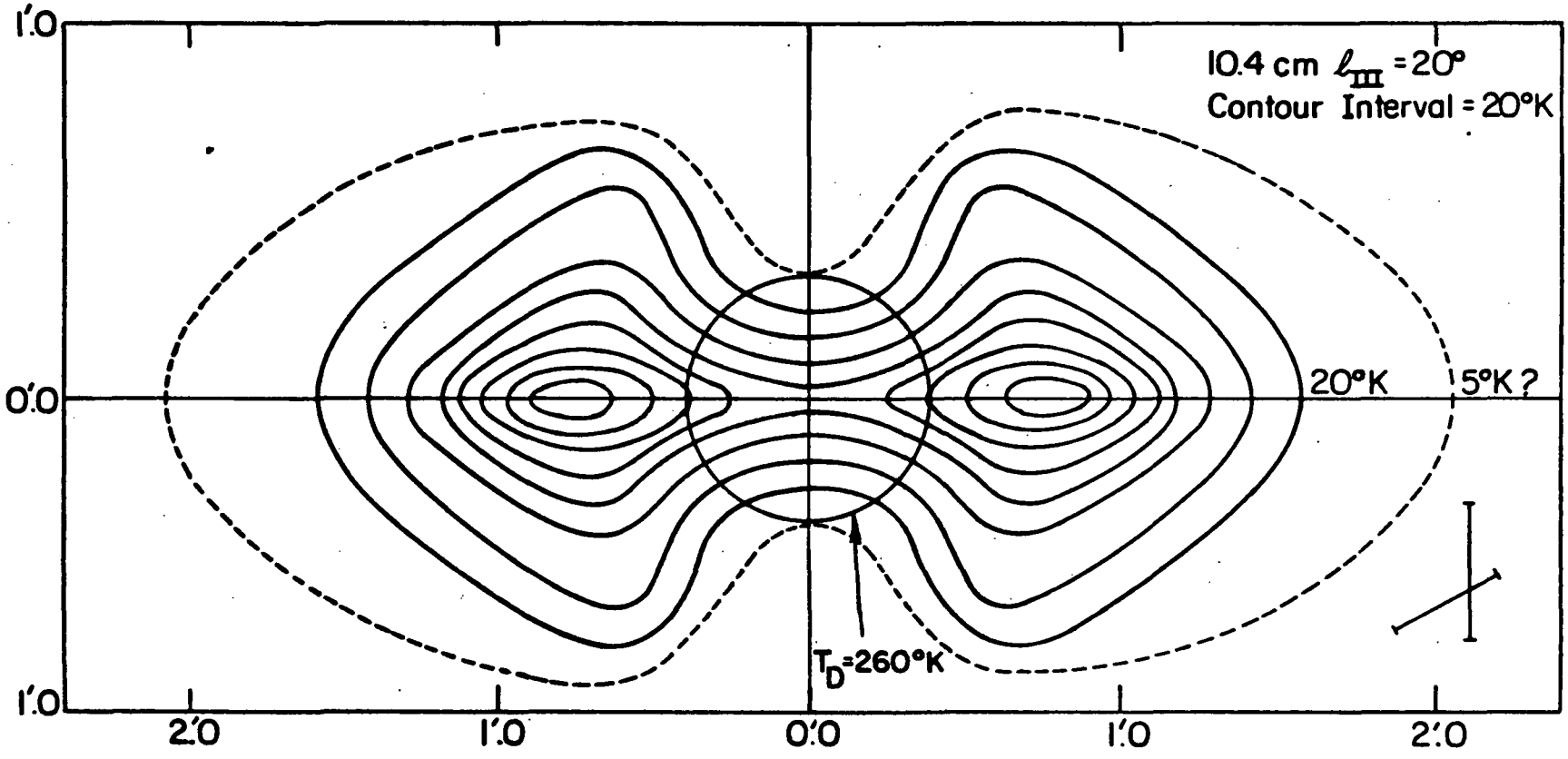

Figure I-4: Map of Jovian Decimetric Emission (from Berge, 1966). The scales are in minutes of arc, and are for a Jupiter distance of 4.04 AU.

The brightness temperature T_b of a body is the temperature of a black body that would give the same energy output per unit wavelength, at a given wavelength, as is actually observed. Thus brightness temperatures for Jupiter are somewhat dependent upon the wavelengths recorded radiometrically. Table I-2 presents the recent measurements of Jupiter's brightness temperature:

Table I-2: Jupiter Brightness Temperatures

(from Newburn, R.L., Jr., 1969)

Wavelength	T_b (°K)	Authority	Date
8-14 μ	128 ± 2.3	Murray and Wildey	1963
8-14 μ	128.5 ± 2.0	Murray, Wildey, and Westphal	1964
818 μ	139	Sinton	1964
17.5-25 μ	150 ± 5 (equator) 130(poles)	Low	1966
1 mm.	155 ± 15	Low and Davidson	1965
3.19 mm.	$111 \pm^{22}_{11}$	Tolbert	1966
3.4 mm.	140 ± 5	Epstein	1968
4.29 mm.	$105 \pm^{18}_{12}$	Tolbert	1966
8.35 mm.	144 ± 23	Thorton and Welch	1963
8.57 mm.	113 ± 11	Tolbert	1966
8.6 mm.	$140 \pm^{18}_{14}$	Kalaghan and Wulfsberg	1967

As mentioned in Section D, the longer wavelength radiation possesses non-thermal components, although the thermal component can be separated by assuming 22 percent polarization of the radiation as also mentioned. Generally, the assumption leads to higher brightness temperatures T_b of from 224 to 260° K, indicating that the longer wavelength radiation probably originates deeper in Jupiter's atmosphere.

Methane and ammonia have been spectroscopically detected in Jupiter's atmosphere; model studies of Jupiter's atmosphere reveal that the bulk of the atmosphere must be of low molecular weight, i.e., it must consist of hydrogen and helium. This conclusion was verified by the photoelectric recording of the occultation of the star σ Arietis by Jupiter in 1952, from which a scale height could be derived of 8.3 km. which corresponds to a mean molecular weight of 3.3 for an assumed stratospheric temperature of 86° K and thus confirming the dominance of hydrogen and helium. Molecular hydrogen, extremely difficult to detect in an optically thick atmosphere, was detected spectroscopically with the identification of lines in its quadrupole rotation-vibration spectrum. There are conflicting views as to whether hydrogen or helium is more abundant; generally most observers seem to favor about a 2:1 ratio of hydrogen over helium, with 70 kilometer-atmospheres for molecular hydrogen. Abundances for methane and ammonia are around 150 and 7 m. atm. respectively. Spectroscopic searches have placed upper limits on the possible abundances of the gases shown in Table I-3, none of which have actually been detected.

Table I-3: Upper Limits of Possible Jupiter Gasses

(from Michaux)

Gas	Upper Limit of Abundance (m. atm.)
C_2H_2 (acetylene)	3
C_2H_4 (ethylene)	2
C_2H_6 (ethane)	4
CH_3NH_2 (methylamine)	3
CH_3D (methyl deuteride)	20
HCN (hydrogen cyanide)	2
SiH_4 (silane)	20
HD (deuterium hydride)	500

Assuming Jupiter's atmosphere to be in thermodynamic equilibrium (the presence of condensables of course negates this assumption but does not invalidate the gross conclusions stated here), most of the carbon would be present in the form of methane, most nitrogen as ammonia, and most oxygen as water. At the cloud surface with temperatures as indicated in Table I-2, the water as well as the ammonia would be frozen, although there may certainly be layers of the atmosphere below the cloud surface where the water and ammonia could exist in liquid and vapor phases.

2. The Visible Surface

Figure I-5 reveals the Jovian belts and zones; Jupiter is displayed in the astronomic convention with South at the top of the page. The visible surface of Jupiter has been observed and described best by Bertrand M. Peek. As the latitudinal limits of the zones and belts, as well as all cloud markings, are continuously changing, no latitudes are designated in Figure I-5. A fine summary of the latitude variations can be found in Michaux's Handbook of the Planet Jupiter mentioned above, pp. 72 and 73.

One of the most famous planetary features in this solar system is Jupiter's Great Red Spot. An elliptical feature some 40,000 km. in length and 13,000 km. in width, the Great Red Spot was discovered in 1665 by Cassini and called the "eye of Jupiter". As shown in Figure I-5, it is located in the South Tropical Zone and extends into the South Equatorial Belt as a bay called the Red Spot Hollow. This hollow is always visible and permits location of the Red Spot when the Spot is very faint, since the color and visibility of the Spot vary - its last prominent darkening was in 1962-63, for example. The Red Spot has been observed and recorded extensively for over 120 years; it has surprisingly wandered randomly through a total of 1200° of longitude in a longitudinal system best fitted to minimize the extent of wandering (for example, the wandering amounts to 3529° in the System II longitudes).

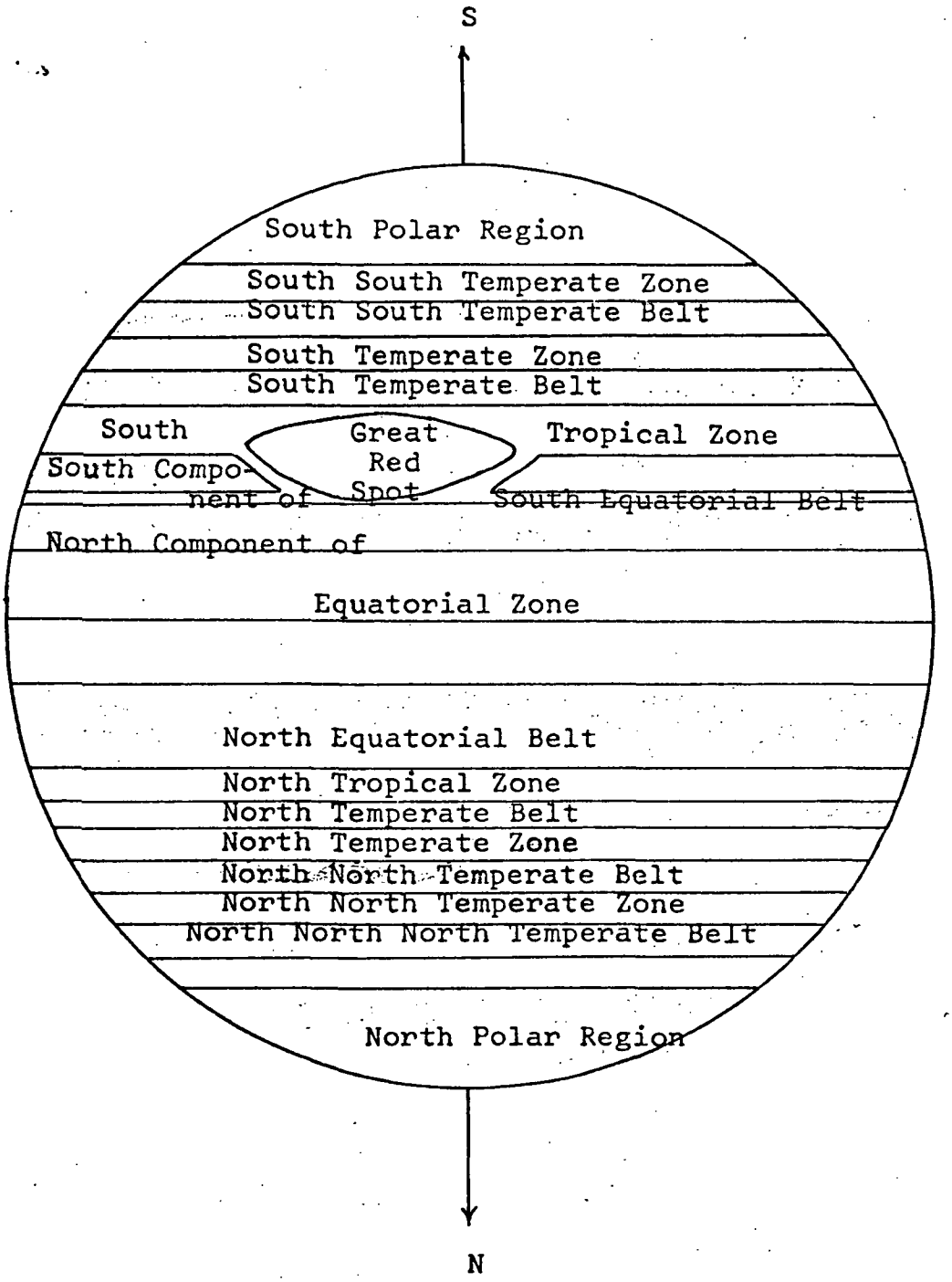

Figure I-5: The Belts and Zones of Jupiter's Visible Surface. (From Michaux, Handbook of the Planet Jupiter.)

Figure I-6 shows the wandering of the Red Spot in the above-mentioned minimizing longitude given by: $\lambda = \lambda_{II} - 264.3^{\circ} + 28.62^{\circ}t$, where λ_{II} = System II longitude and t is time (Peek, Bertrand M.).

Older theories explaining the Red Spot invoking a solid mass floating in Jupiter's atmosphere are now generally discarded for the reasons that: (1) assuming the light density of the upper atmosphere of predominently hydrogen and helium, there is no known solid element having a lighter density, and (2) to minimize the potential energy of the floating body, it should be gradually moving toward the equator; measurements do not indicate a northerly motion of the Red Spot.

The Taylor column explanation for the Red Spot, proposed by Hide, theoretically derived by Proudman, and confirmed experimentally by Taylor (Jupiter Handbook, Michaux) is generally accepted today. This explanation is based on the fact that a rotating, homogeneous , incompressible fluid will tend to move two-dimensionally in planes perpendicular to the axis of rotation. Then, if there exists a topographical feature of even a very small height on Jupiter's solid (?) surface, it will be surmounted by a column of stagnant air of the same horizontal dimensions, extending throughout the depth of the atmosphere, while the remaining air will flow around the column as if the column were solid.

Hide has analytically verified that the Great Red Spot could be a Taylor column if Jupiter's atmosphere is no deeper than 2800 km. He has further shown that a feature on Jupiter's surface only 1 km. in height in a 1000 km.-thick atmosphere could produce a Taylor column. He proposes a Jupiter model consisting of a fluid core with a thin, solid mantle covered by a deep, massive atmosphere. Momentum exchange is possible between the atmosphere and mantle; assuming the Red Spot's rotation to be that of the mantle, differences between atmospheric and mantle (hence Red Spot) rotations are then possible.

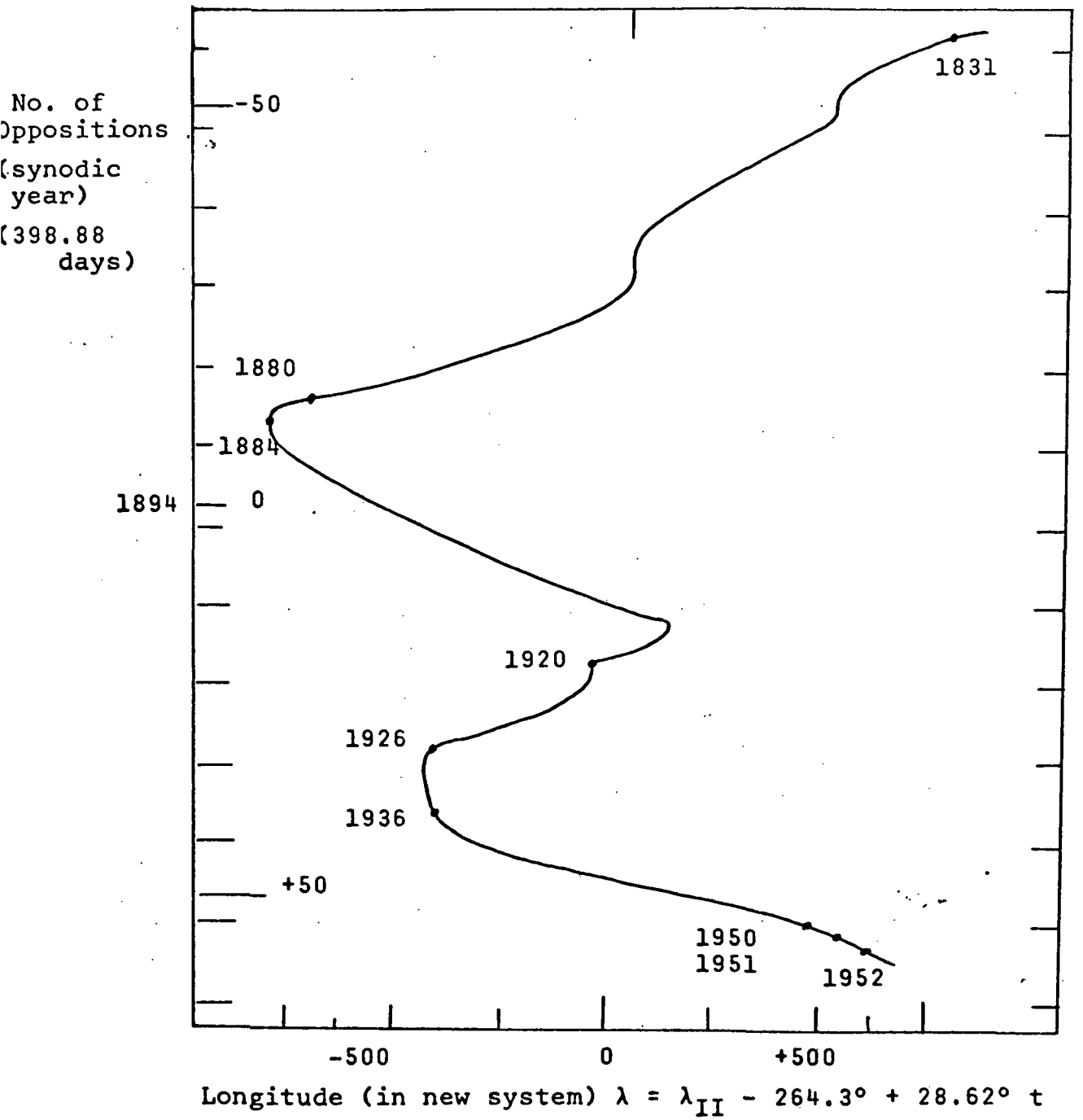

Figure I-6: Longitudinal Wanderings of the Great Red Spot, 1831-1955. (From Michaux, Handbook of the Planet Jupiter.)

Noting that there exists a hollow indentation north of the Red Spot (in the South Equatorial Belt), but not to the South of the Red Spot, and that transitory spots in the atmosphere are swept around the Red Spot Hollow, Hide concludes that this is in accordance with experimental results of laboratory investigations of Taylor columns. Gas within the Taylor column (Great Red Spot) does not freely exchange with gasses surrounding it, thus the color differences.

There are many distinguishing features of Jupiter's atmosphere. Second in importance to the Red Spot is the South Tropical Disturbance from 1901 to 1940. This disturbance, a dark shading of a few degrees of latitude in the South Tropical Zone, rotated at a faster rate than the Red Spot and hence caught up to it in June 1902. It leaped across the Red Spot in a few days instead of the expected six weeks due to the rotation rate difference. Nine such conjunctions between the South Tropical Disturbance and the Red Spot took place before the disturbance disappeared visually in 1940.

There are and have been Dark South Tropical Streaks, Oscillating Spots, and Circulating Currents observed on Jupiter. The Circulating Currents, excellently described by Peek, are so termed because dark spots, having originated in the south part of the South Tropical Zone and eventually reaching the concave edge of the South Tropical Disturbance, were actually seen to be swept back in the opposite direction and continued at the same rate along the northern edge of the South Temperate Belt.

The photometric properties of Jupiter warrant a brief description of corresponding nomenclature. Each passband U (ultraviolet) B (blue) V (visual) R (red) I (infrared) WXYZ (additional long wavelength passbands) is defined by a detector-filter combination and is 1000 $\mathring{A}$ at its half-amplitude points. The effective wavelengths of the various passbands are (from JPL TM 33-424, Newburn):

Passband	U	B	V	R	I	W	X	Y	Z
Effective $\lambda(\mu)$	0.353	0.448	0.554	0.690	0.820	1.06	1.13	1.63	2.21

The magnitude of a celestial body is a reciprical logarithmic measure of its brightness. The visual magnitude of a planet is given by:

$$V = V(1,0) + 5 \log (rd) + \Delta m(\alpha)$$

where: $V(1,0)$ = magnitude at unit distance from Earth and Sun

r = distance from Earth in a.u.

d = distance from Sun in a.u.

$\Delta m(\alpha)$ = correction with phase angle α

Another value often quoted is the mean opposition magnitude V_o given by:

$$V_o = V(1,0) + 5 \log a(a-1)$$

where: a = the planet's semi-major axis in a.u.

Since the phase angle (α) of Jupiter never exceeds 12°, photometric measurements of Jupiter are complicated. A value of V(1,0) equal to -9.25 and a corresponding V_o equal to -2.55 are used here.

Colors are now defined by the difference in magnitudes between adjacent passbands of the detector. Zeros of the system were chosen so that U-B and B-V are 0.00 for a star of spectral Type A0 V and so that passband V agrees with an older "classic" photometric system. The colors of the Sun and Jupiter are (JPL TM 33-424):

Adj. Passb. Diff.	U-B	B-V	V-R	R-I	V-W	V-X	V-Y	V-Z
Sun	0.14	0.63	0.45	0.29	0.64	0.74	1.12	1.17
Jupiter	0.48	0.83	0.50	-0.03	0.36	-0.23	-0.49	-0.66

The brightness of Jupiter in each passband at mean opposition is then (JPL TM 33-424):

Passband	U	B	V	R	I	W	X	Y	Z
Magnitude	-1.24	-1.72	-2.55	-3.05	-3.02	-2.91	-2.32	-2.06	-1.89

Setting V for the Sun and Jupiter equal, the color differences between Jupiter and the Sun (J - S) are (JPL TM 33-424):

Passband	U	B	V	R	I	W	X	Y	Z
J - S	+0.54	+0.20	0	-0.05	+0.27	+0.28	+2.97	+1.61	+1.83

The Bond albedo is that fraction of the total parallel incident flux reflected in all directions by a body. The Bond albedo is the product of (a) the geometric albedo ($p(\lambda)$), the fraction of the total parallel incident flux reflected back in the direction it came, and (b) the phase integral ($q(\lambda)$), a multiplier which averages the variation in reflection with phase angle. As indicated, the albedos are functions of wavelength λ. The geometric albedos (p) for the major planets can be measured directly from Earth; the phase integral (q) cannot be measured since the phase angle never exceeds 12° and hence must be derived by theory. Presently accepted values for the geometric albedos of Jupiter at different passband wavelengths are (JPL TM 33-424)

Passband	p(U)	p(B)	p(V)	p(R)	p(I)	p(W)	p(X)	p(Y)	p(Z)
Value	0.270	0.370	0.445	0.466	0.347	0.33	0.18	0.11	0.08

Values of the phase integral (q) for the U, B, and V passbands are given below. These values can have gross errors associated with them because of the difficulty mentioned above:

Passband	q(U)	q(B)	q(V)
Value	1.55	1.60	1.65

The visual Bond albedo is then (0.445)(1.65) = 0.73, thus seventy-three percent of all light in a passband near 5540 $\mathring{A}$ is reflected back into space, only twenty-seven percent is absorbed.

The bolometric Bond albedo, necessary for energy balance studies, is the Bond albedo integrated over all wavelengths. Values of 0.45 and 0.50 have been quoted (JPL TM 33-424). These values correspond to average temperatures of Jupiter's upper atmosphere of 105° K. and 103° K. respectively. A cursory glance of Table I-1 shows that the albedo-derived temperatures are much less than the radiometrically measured temperature of Table I-1. JPL TM 33-424 even shows that errors in the phase integral, atmospheric cooling due to planetary rotation, and energy sources external to the planet (cosmic debris) cannot account for the fact that the actual atmospheric temperatures of Jupiter are higher than those derived by Bond albedo measurements. There exists then a fundamental cosmogonic problem if the emitted flux from Jupiter is greater than the absorbed solar flux, as the temperature differences indicate.

3. Atmospheric Models of Jupiter (Jupiter Handbook, Michaux)

(a) Kuiper's Models: See Figure I-7. The composition of Model a is, by weight: 63.5 percent hydrogen, 34.9 percent helium, 0.26 percent ammonia, 0.11 percent methane, with the remainder of 0.60 percent neon, 0.34 percent water, and 0.15 percent argon. Model b consists, by weight, of: 37.7 percent hydrogen, 59.5 percent helium and practically the same amounts of ammonia and methane as for Model a. As shown in Figure I-7, the models consist of an isothermal stratosphere at 86° K. overlaying a troposphere in adiabatic equilibrium. The indicated cloudtop boundary is the equilibrium point of vapor and solid phases of ammonia, ammonia crystals supposedly forming the opaque white clouds. Kuiper calculated the pressures at the cloudtop layer to be 24 atm. for Model a and 2.0 atm. for Model b.

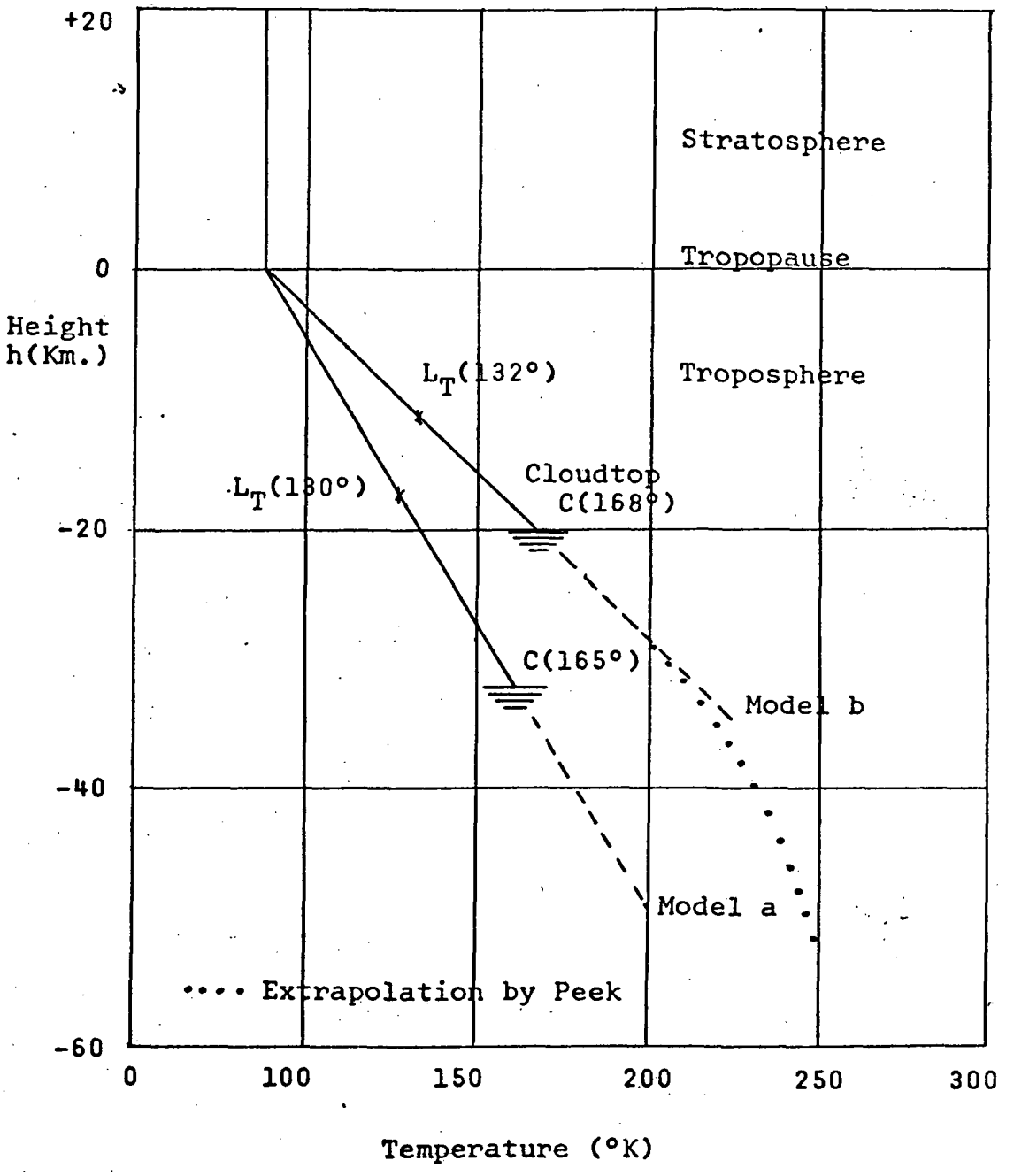

Figure I-7: Kuiper's Jovian Upper Atmospheric Models (from Michaux, Jupiter Handbook).

(b) Öpik's Models: Öpik assumed an atmospheric composition of: 2.3 percent hydrogen, 97.2 percent helium, 0.0029 percent ammonia, and 0.063 percent methane. Assuming a scale height of about 10 km. (instead of 8.3 km. determined as indicated in Section E 1), Öpik derived a saturation temperature for ammonia vapor of 156° K. and a pressure of 11 atm. for the cloudtop layer. He also concludes an ammoniacirrus cloud layer.

(c) Gross and Rasool's Model: See Figure I-8. Two extreme models were adopted; Urey's Model I with a hydrogen to helium ratio (H/He) of 20/1, and Öpik's Model II with a H/He of 0.03/1. The respective mean molecular weights of the two models are 2.2 and 3.95 and the pressure at the cloudtop surface for both is 3 atm. The vertical temperature distribution above the clouds was calculated on the basis of radiative equilibrium and gray atmosphere (atmosphere absorption independent of wavelength).

(d) Trafton's Models: Constructing non-gray radiative models, taking into account the thermal opacities of hydrogen, helium, and ammonia, and using his own computations of absorption coefficients of hydrogen and hydrogen plus helium mixtures, Trafton confirmed the backwarming effect indicated by radiometric measurements by Murray. They predict the existence of a shallow convection zone in the Jovian upper atmosphere at about the cloudtop layer, and a correlation may thus exist between the convection zone and the cloudtop layer as it does on Earth.

G. Internal Structure of Jupiter

There exists much theory and many models regarding Jupiter's structure from the cloudtop layer to the planetary center. Models of Jupiter have been constructed using (1) various ratios of hydrogen to helium as a function of depth, (2) the best available theoretical equation of state for these elements, (3) the equations of hydrostatic equilibrium and conservation of mass,

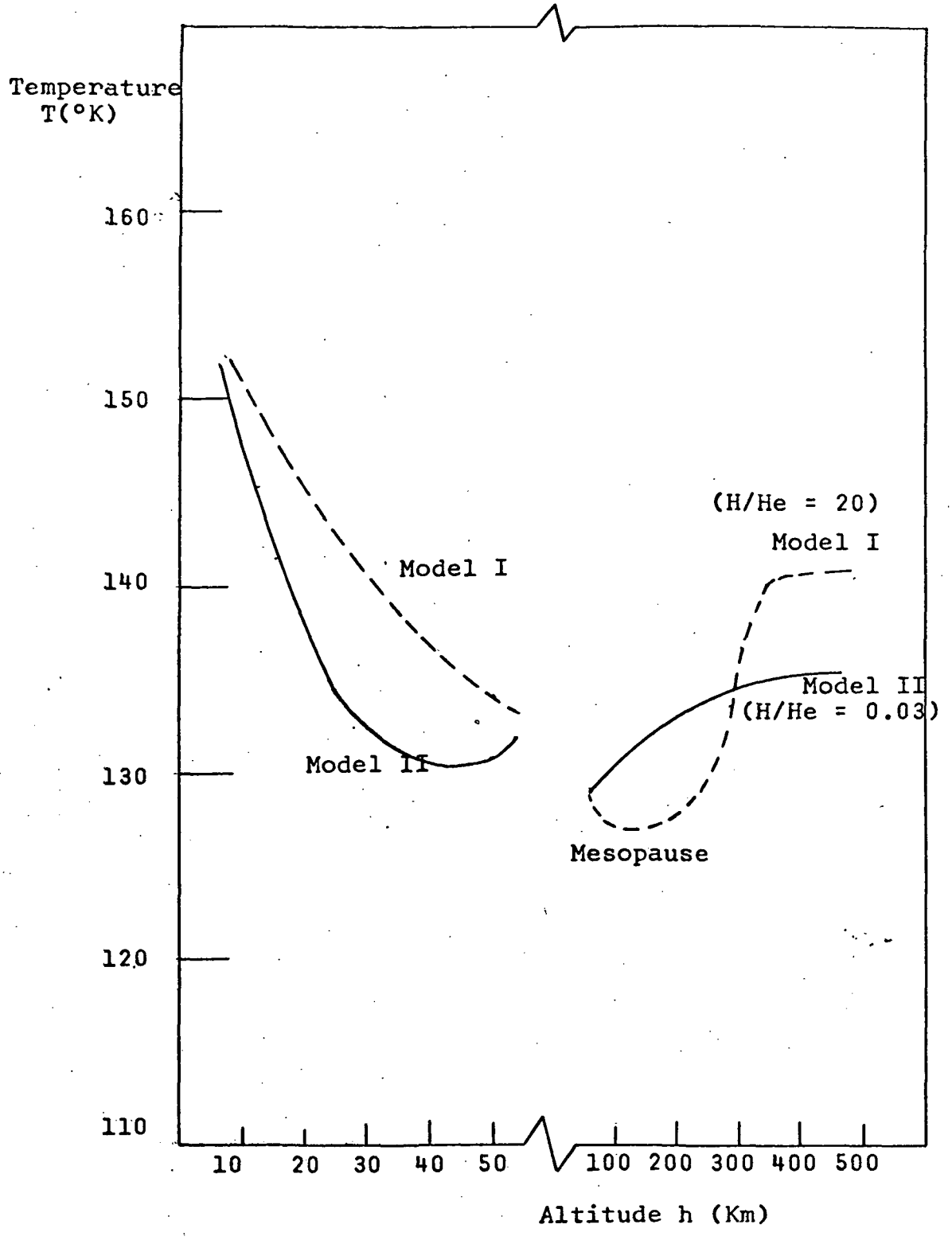

Figure I-8: Gross and Rasool's Jovian Upper Atmospheric Models (from Michaux, Jupiter Handbook).

(4) boundary conditions set by the observed mass, oblateness, and gravitational quadrupole moment determined from the motions of the satellite, and (5) the fact that the mean density of Jupiter is only 1.35 gm/cm^3. One of the main complications to internal structure models is (2) above; i.e., the experimental data for a suitable equation of state for hydrogen at pressures of 2 x 10^4 bars has to be extrapolated to pressures internal to Jupiter of 2 x 10^8 bars. It has been shown theoretically that solid hydrogen should change to a metallic phase at about 10^6 bars. There may be other phase transitions about which nothing is theoretically known today; therefore, assumptions of a gradual transition from gaseous to liquid to a solid phase of hydrogen with increasing depth and an associated transition to an oceanic interface of ammonia and water slush have to remain speculative. There may exist continents or "icebergs" of solidified hydrogen, water ice, ammonia ice, or simple carbon-hydrogen-nitrogen compounds.

Table I-4 presents estimates of the depth of the lower atmosphere; i.e., from the cloudtop layer to some defined planetary surface.

Table I-4: Depth of the Jovian Atmosphere (from Michaux, Jupiter Handbook)

Atmospheric Characteristics	Cloudtop Temperature ($^\circ$K)	Depth (km.)	Reference
Hydrogen (H_2), isothermal temp. grad., perfectly compressible	150	500[a]	Wildt
H_2, adiabatic, variation of C_p/C_v with temperature	150-1000	500	Wildt
H_2, isothermal, partial compressibility, var. of solidif. density with pressure	150	750	DeMarcus
H_2, " " "	100	380[a]	
Neon Molecular Weight (μ) = 4	150-400	100-120[c]	Peek
H_2, N_2, He, O_2, isothermal	120	6000	Jeffreys
H_2, He, adiabatic	150	4250	Peebles

Table I-4 (cont.)

(a) Distance between cloudtop layer and level at which hydrogen solidifies. Pressure at cloudtop layer is 10 atm.

(b) Depth below cloudtop layer at which density reaches 0.09 g/cm^3 (solidification density of H_2 at p = 0). Value of acceleration, g, adopted = 2600 cm/sec^2.

Figure I-9, from Michaux, shows the superposition of Gallet's lower Jovian atmosphere on Peeble's Jovian interior. Table I-5 indicates a model planet for Jupiter based on an equation of state lying midway between an adiabatic atmosphere and an isothermal atmosphere. The model does assume an adiabatic atmosphere, 3 atm. pressure, and 150°K. temperature at the cloudtop layer, and a hydrogen abundance of 0.80 by weight in the material above the core.

A current "best" model for Jupiter incorporating the most likely features of many models might envision (JPL TM 33-424) overall abundances by mass of 76 percent hydrogen, 22 percent helium, and 2 percent heavier elements. A metallic hydrogen lattice (convective) extends out to 80 percent of the radius; over this is a fluid atmosphere of essentially molecular hydrogen. The temperature gradient would be adiabatic throughout the planet, with temperatures of 165 - 225°K. at the cloud deck, 2000-3000° K. at 80 percent of the radius, and 4000-5000°K at the center of the planet. The central density would be about 4 gm/cm^3 and the central pressure about 5×10^7 atm.

H. The Natural Satellites of Jupiter

Table I-6 presents the orbital elements of the twelve Jovian satellites and Table I-7 presents physical data for the four Galilean satellites. Jupiter's satellites can be classified into groups, i.e., satellites J I through J V,

Table I-5: Model Planet for Jupiter

(from Michaux, Jupiter Handbook)

Relative Radius r/R_J	Pressure, p (10^6 atm.)	Density (gm/cm^3)	Relative Mass
1.0	2.94×10^{-6}	5.5×10^{-4}	1.0
0.995	3.64×10^{-4}	0.0164	0.99995
.99	2.75×10^{-3}	.055	.9996
.98	.0197	.147	.997
.96	.0934	.28	.988
.94	.226	.40	.973
.92	.374	.47	.957
.9	.56	.55	.941
.85	1.27	.76	.878
.8	2.16	.96	.815
.75	3.44	1.39	.74
.7	5.10	1.63	.64
.65	7.07	1.84	.55
.6	9.34	2.1	.46
.55	11.7	2.3	.38
.5	14.7	2.5	.30
.4	20.2	2.9	.19
.3	26	3.3	.11
.2	33	3.7	.05

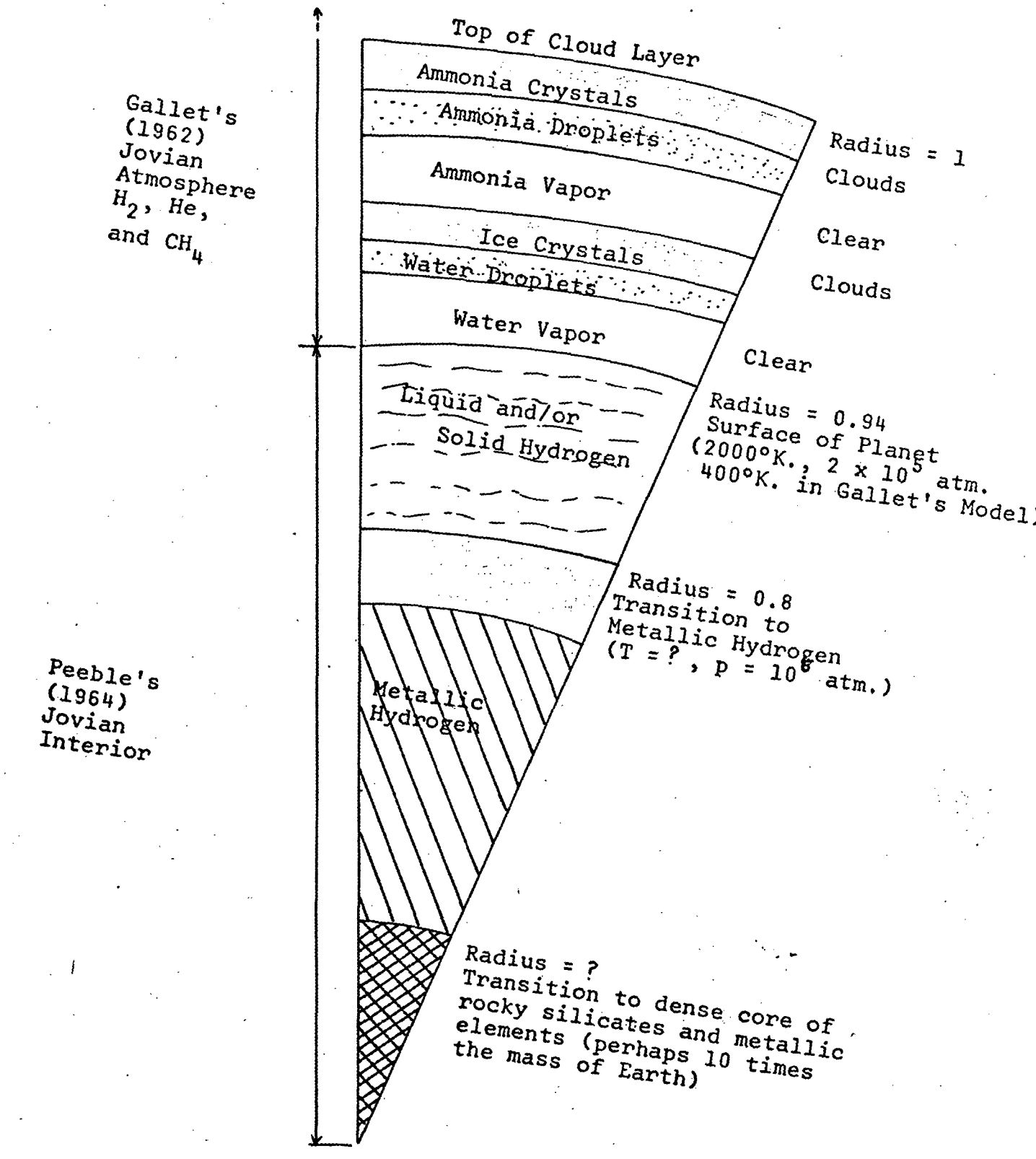

Figure I-9: Jovian Cloud Layers Proposed by Gallet Overlying Jovian Interior by Peebles (from Michaux, Jupiter Handbook).

Table I-6: Orbital Elements of the Jovian Satellites

(from JPL TM-424)

Satellite	Semimajor Axis (km)	Eccentricity	Inclination (to Jupiter's Equator) (° ')	Sidereal Period (d h m s)
J V (Amalthea)	181,500	0.0028	0 27.3	0 11 57 22.7
J I (Io)	422,000	0.0000	0 01.6	1 18 27 33.5
J II (Europa)	671,400	0.0003	0 28.1	3 13 13 42.0
J III (Ganymede)	1,071,000	0.0015	0 11.0	7 03 42 33.3
J IV (Callisto)	1,884,000	0.0075	0 15.2	16 16 32 11.2
J VI	11,487,000	0.158	27 36	250 14
J VII	11,747,000	0.207	24 48	259 16
J X	11,861,000	0.130	29 00	263 13
J XII	21,250,000	0.169	147	631
J XI	22,540,000	0.207	164	692
J VIII	23,510,000	0.378	145	739
J IX	23,670,000	0.275	153	758

Table I-7: Physical Data of the Galilean Satellites

(from JPL TM-424)

Parameter	J I (Io)	J II (Europa)	J III (Ganymede)	J IV (Callisto)
Reciprocal Mass (Jupiter = 1)	26×10^3	40×10^3	123×10^2	20×10^3
Mass (Earth = 1)	0.0122	0.0079	0.0258	0.0159
Mass (Moon = 1)	0.9940	0.6461	2.1011	1.2922
Mean Diameter (Earth = 1)	0.262	0.229	0.400	0.371
Mean Diameter (Moon = 1)	0.961	0.840	1.467	1.358
Mean Diameter (km)	3340	2920	5100	4720
Mean Density (gm/cm^3)	3.73	3.62	2.22	1.71
Magnitude, V (1,0)	-1.90	-1.53	-2.16	-1.20
Magnitude, $\bar{V}_o$	+4.80	+5.17	+4.54	+5.50
Color U - B	1.30	0.52	0.50	0.55
Color B - V	1.17	0.87	0.83	0.86
Color V - R	0.66	0.57	0.59	0.61
Color R - I	0.32	0.31	0.31	0.32
Visual Bond Albedo	0.54	0.49	0.29	0.15
Ultraviolet Geometric Albedo	0.19	0.47	0.29	0.14
Visual Geometric Albedo	0.92	0.83	0.49	0.26
Infrared Geometric Albedo	1.15	0.95	0.57	0.31
Surface Gravity (Earth = 1)	0.17	0.15	0.16	0.11

Table I-7 (cont.)

Parameter	JI (Io)	J II (Europa)	J III (Ganymede)	J IV (Callisto)
Escape Velocity (km/sec)	2.4	2.1	2.8	2.3
Maximum Temperature (^{o}K)	143	146	156	166
Brightness Temperature, 8-13μ (^{o}K)	142 $\pm$ 5	122 $\pm$ 5	144 $\pm$ 5	159 $\pm$ 5

Mass of Earth = 5.9733×10^{27} gm., Mean diameter of Earth = 12,734.94 km.

Mass of Moon = 7.3472×10^{25} gm., Mean diameter of Moon = 3476.18 km.

closest to their primary (Jupiter), are termed regular satellites as they are characterized by direct motion in nearly circular orbits almost in the equatorial plane of their primary. J I through J IV are the Galilean satellites and are named as indicated in Tables I-6 and I-7. There is a group of three direct, irregular satellites at about 11 x 10^6 km. from Jupiter and a group of four retrograde irregular satellites at about 23 x 10^6 km. These distant seven satellites are termed irregular since their orbital elements are extremely variable. The orbit dimension concentrations of the three irregular direct (11 x 10^6 km) and the four irregular retrograde (23 x 10^6km) imply a strong liklihood of a separate origin for each group. Little is known about the seven irregular satellites.

Little is also known about J V (Jupiter V, Amalthea), since it is so close to its bright primary, orbits with very high velocities, and is so extremely small. Estimates from an albedo of 10 to 50 percent places its diameter from 75 to 150 miles.

Surface observations of the four Galilean satellites seem to indicate that their periods of rotation and revolution about Jupiter are synchronous; i.e., they maintain the same face toward the primary. The mean longitudes of the first three Galilean satellites have a fixed mathematical relationship ($\theta_1 - 3\theta_2 + 2\theta_3 = 180^\circ$). "For this reason, considerable caution must be exercised in correlating any physical phenomena (e.g., modulation of decametric radio radiation) with the position of an individual satellite." (JPL TM 33-424).

The Galilean satellites, besides being satellites of Jupiter, are interesting members of the solar system in their own right. It has been mentioned previously that Io modulates the decametric radiation. Io also is distinctly

redder than the other Galilean satellites, is unique among the Galilean satellites by showing large variations in color with orbital phase, and is on the average 0.09 magnitudes brighter than normal for about 15 minutes after reappearing from a solar eclipse by Jupiter. The last unique property may be due to a methane or nitrogen atmosphere which is frozen due to the temperature drop during a solar eclipse. No atmosphere has been spectroscopically detected on Io.

Europa exhibits a total variation in visual magnitude larger than Io. A single photometric search for an eclipse effect similar to that of Io gave negative results. Ganymede, the largest and most massive of the Galilean satellites, a body possibly larger than Mercury although only half as massive, has given no spectroscopic evidence of an atmosphere. Callisto is unusual in that is shows little variation in brightness with orbital phase for solar phase angles less than 1.5°, but shows as much as 0.18 magnitude for a solar phase angle of 10°. There is no spectroscopic evidence of an atmosphere.

I. Why Send an Orbiter to Jupiter?

Jupiter has a multitude of mysteries associated with it. We do not understand the sources of its several types of radiation; we do not know why it emits more energy than it receives from the sun; we are unsure of the reason for the permanence of the Red Spot and the transience of all other visible features; the relationship of the satellite Io to the Jovian decametric radiation is a puzzle; we do not know why Jupiter should share with the earth and no other planet the possession of an intense magnetic field. Jupiter, because of its mass and temperature, has probably retained almost the same abundance of chemical elements that the solar system was formed from, giving us a probe through the five billion years separating us from the origin of the planets. Its atmosphere apparently is very similar to the primordial atmosphere

from which life evolved on earth, and complex organic chemicals similar to those of the early days of earth probably exist there. These are an abundance of reasons to earn the exploration of Jupiter a high priority in the space program, but any space probe to the planet must be justified on the basis that it can do things which cannot be done either from ground-based observatories or from earth orbit.

What cannot be done from near the earth? First, is the observation of the night side of Jupiter. Because Jupiter is five times further from the sun than we are, we can never see much of the night side. This complicates the calculation of the energy of the emissions of Jupiter because we do not know how much energy is emitted away from us. Second, because Jupiter's orbital plane almost coincides with our earth's, we can never know what radiation is emitted at large angles to this plane, e.g., to the north or south. Third, we cannot fully understand the Jovian radio emission until we have mapped its magnetic field and measured the spectra of its energetic charged particles, measurements which can <u>only</u> be made <u>in situ</u>. Our own earth's trapped radiation belts were not discovered until Dr. VanAllen's satellite detected them. Fourth, terrestrial radar has not yet succeeded in detecting a reflection off Jupiter. Because a radar reflection falls off as the inverse fourth power of the target distance, it may be better to have a small transmitter close to Jupiter than a large one at earth. Fifth, the ratio of hydrogen to helium in Jupiter is very difficult to measure from earth, and has not yet been successfully done. The occutation of the space probe's transmitter by the planet should provide this ratio, which is a technique that has provided so much useful data on the atmospheres of Mars and Venus. Professor Brian O'Leary of Cornell has suggested that it may even be used to test for atmospheres

of the Galilean satellites. Sixth, while orbiting telescopes can improve the resolution of optical observations considerably over ground-based observations, a high-resolution TV camera orbited around Jupiter can exceed substantially the resolution of foreseeable orbital telescopes ($\lesssim$ 100"). Also, it can observe Jupiter from angles inaccessible to even orbiting telescopes. Seventh, the interaction of Jupiter with the solar wind cannot be resolved except with a space probe.

These are some of the many reasons why a Jovian orbiter will provide us with answers to profound questions that will remain unanswered unless such a probe is sent to the planet.

Alexander, J.K., "Decameter Wavelength Observations of Jupiter, October, 1966 - March, 1967, " NASA TM-X-55996, Goddard Space Flight Center, Greenbelt, Maryland, October, 1967.

Alexander, J.K,. and Stone, R.G., "Low Intensity Decameter Emissions from Jupiter", NASA X-615-64-149, Goddard Space Flight Center, Greenbelt, Maryland, June 1964.

Berge, G.L., "An Interferometric Study of Jupiter's Decimeter Radio Emission", Astrophysical Journal, Vol. 146, 1966, pp. 767-798.

Branson, N.J.B.A., "High Resolution Radio Observations of the Planet Jupiter", Monthly Notices of the Royal Astronomical Soc., Vol. 139, 1968, p. 155.

Burke, B.F. and Franklin, K.L., "Observations of a Variable Radio Source Associated with the Planet Jupiter,"Journal of Geophysical Research, Vol. 60, 1955, pp. 213-217.

Carr, T.D. and Gulkis, S., "The Magnetosphere of Jupiter", Annual Review of Astronomy and Astrophysics, Vol. 7, 1969, pp. 577-618.

Carr, T.D., Smith, A.G., Bollhagen, M., Six, N.F., Jr., and Chatterton, N.E., "Recent Decameter - Wave-Length Observations of Jupiter, Saturn, and Venus," Astrophysical Journal, Vol. 134, 1961, p. 108.

Dulk, G.A., "Io-Related Radiation from Jupiter", Science, Vol. 148, 1965, p. 1586.

Kiess, C.C., Corliss, C.H., Kiess, Harriet K., "High-Dispersion Spectra of Jupiter", The Astrophysical Journal, Vol. 132, July-November, 1960, pp. 221-232.

Kuiper, Gerard P., The Atmospheres of the Earth and Planets, The University of Chicago Press, Chicago, Illinois, 1952.

Michaux, C.M., Handbook of the Physical Properties of the Planet Jupiter, SP-3031, National Aeronautics and Space Administration, Washington, D.C., 1967.

Moore, Patrick, The Planets, W.W. Norton and Co., Inc., New York, New York, 1962.

Morrow, Denis P., "A Study of Polarization of Decameter Radiation from Jupiter", NASA CR-83974, thesis, Radio Astronomy Observatory, Dept. of Physics, Florida State University, Tallahassee, Florida, 1966.

"
Opik, E.J., "Jupiter: Chemical Composition, Structure, and Origin of a Giant Planet", Icarus, Vol. 1, 1962-1963, pp. 200-258.

Peek, Bertrand M., The Planet Jupiter, Faber and Faber, London, 1958.

References (cont.)

Solberg, H. Gordon, Jr., "Jupiter's Red Spot in 1965-55", TN 701-67-14, prepared by New Mexico State University Observatory, Las Cruces, New Mexico, for NASA Headquarters, Washington, D.C., June 1967.

Spinrad, Hyron, Trafton, Lawrence M., "High Dispersion Spectra of the Outer Planets .1. Jupiter in the Visual and Red", Icarus, Vol. 2, 1963, pp. 19-29.

Weil, Nicholas A., Lunar and Planetary Surface Conditions Advances in Space Science and Technology, Supplement 2, Academic Press, New York, New York, 1965.

Whipple, Fred L., Earth, Moon and Planets, Harvard University Press, Cambridge, Massachusetts, 1963.

Chapter II: The Spacecraft Design and Mission Definition

A. Introduction

The purpose of this chapter is to: (1) present an organizational outline of the entire JOSE study, (2) size up the spacecraft (SC) for a Jupiter orbiter mission, and (3) propose a SC configuration compatible with the mission requirements.

A preliminary design was necessary for realistic analyses in the later chapters dealing with attitude control, trajectories, and science objectives. The preliminary design was then modified to take advantage of the results of various subsystems analyses in this report. Chapter IX presents the final spacecraft design.

B. Organizational Structure and the JOSE Mission

Figure II-1 is a flow diagram of the Cornell NASA Jupiter Orbiting Spacecraft (JOSE) mission. The diagram purports to define the major problem areas of the intended mission, provide a rough time schedule for phases of individual research tasks, and integrate respective research results to a coherent conclusion. With regard to the various subsystems indicated in the diagram, the following basic assumptions of the study were adopted by this study group:

1. Tracking Stations and Operations Facilities: The JOSE mission must conform to present (1968) support capabilities of the Jet Propulsion Laboratory (JPL) Deep Space Instrumentation Facility (DSIF), the JPL Space Flight Operations Facility (SFOF), the Atlantic and Pacific Missile Ranges (AMR and PMR), NASA Research Centers, and other tracking stations. The only exception is that the JPL Deep Space Network (DSN) is assumed to be in the Mark III configuration

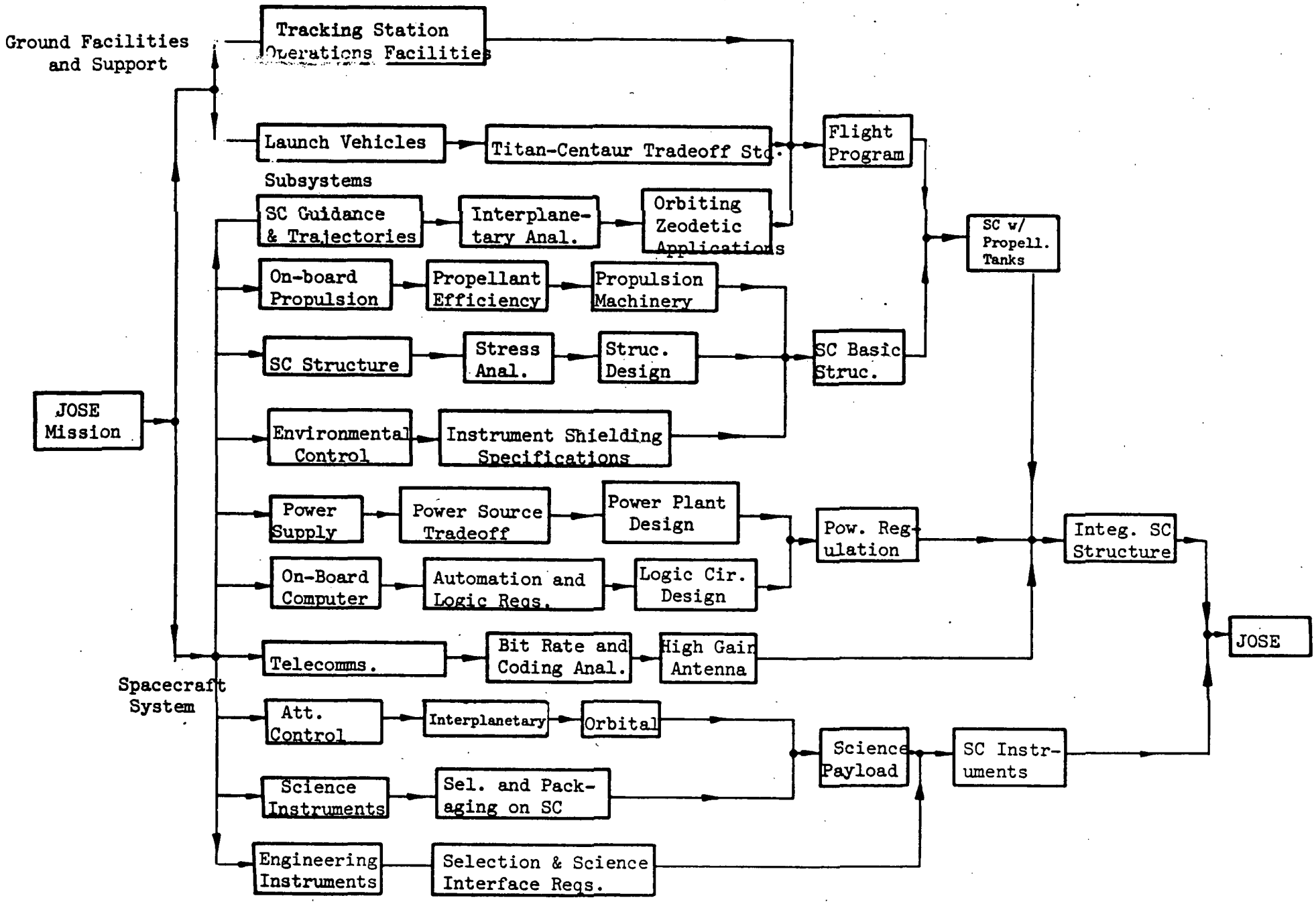

Figure II-1: JOSE Mission Flow Diagram

with three 210-foot antennas by 1975. (The only 210-ft. antenna presently is at Goldstone, California.)

2. Launch Vehicles: The decision regarding the ground rule for a launch vehicle (LV) for JOSE was a difficult one. For the JOSE SC weight arrived at in Section C, only two basic LV's are possible candidates, i.e., (1) a so-called up-dated "intermediary"Titan III D with Centaur E and High Velocity Stage (HVS)-8 stages, and (2) the Saturn I first stage with additional stages such as, for example, the S-IB/Centaur/Burner (B) II, the S-IC/S -IVB/ Centaur/BII, or the S-IC/S-IVB/Centaur.

The Titan III D is proposed for construction in the 1970's; it has far less payload volume capabilities than the Saturn stages, thus implying the required utilization of deployable antennas and Radioisotope Thermoelectric Generator (RTG) booms with the associated risks of unsuccessful deployment.

This Cornell group selected the Saturn class of LV for the following reasons: (1) more payload volume capacity with selective design eliminates the requirement for deployable booms, (2) although launch costs for the Saturn are presumably greater than for the Titan III D, the Saturn stages are existing LV and hence do not require the development necessary for the proposed Titan III D, and (3) with the apparent cutback appearing at the present time (1970) in the Apollo manned lunar missions, the possibilities of the availability of Saturn stages in the late 1970's for a Jupiter mission look promising.

3. Spacecraft Trajectories, Guidance, and Control:

(a) The SC ascent to Earth injection phase is via a 100 n.m. parking orbit with a coast time not to exceed one hour.

(b) Jupiter encounter dates earlier than 30 days after conjunction are excluded in the interest of uninterrupted tracking during the Jupiter approach phase. (This requirement is enforced even more strictly with the three selected trajectories of Chapter III, Conclusions.)

(c) The nominal SC orbit around Jupiter is 1.1 x 100 Jupiter radii (R_J), having a nominal period of 46 days.

(d) The Jupiter ephemeris error is $\pm$ 100 km. by 1980.

(e) The launch opportunities which are accomodated within this study include all years from 1975 through 1985.

4. Attitude Control: Spin stabilization, three axis stabilization, inertia wheels, solar vanes, and gyros are included for consideration.

5. Scientific Instruments: Highest priority instruments from weight, reliability, and scientific return considerations are the magnetometer, geiger counter, solid state detectors, ionization chambers, micrometeoroid detectors, ultra-violet (UV) spectrometer, UV Photometer, Infrared (IR) Interferometer, IR Radiometer, Microwave Radiometer, Television (TV), and others.

6. Power Supply: Must supply 400-600 watts of raw D.C. power while in Jupiter orbit. Solar, chemical and nuclear powered sources are to be investigated along with the possibility of using batteries for handling peak loads.

7. On-board Propulsion: A propulsion subsystem is necessary for course corrections, insertion, and orbital maneuvers.

8. Spacecraft Structure: The SC structure must satisfy low-weight requirements, RTG science instruments interface conditions, and micrometeoroid and radiation protection capability. Gross SC weight at Earth injection is approximately 4400 pounds.

9. On-board Computer: The on-board computer may not be necessary; the Data Automation System (DAS) may suffice for pre-programmed events during Jupiter Orbit.

10. Engineering Instruments: SC engineering parameters such as electronic compartment temperatures and propulsion propellant pressures will be continuously measured and telemetered to Earth on command.

11. Environmental Control: A scientific mission and satisfactory SC performance must have high probabilities of success in interplanetary space and within the Jovian sphere of influence to within 0.1 radius of Jupiter's atmospheric surface.

12. Telecommunications:

(a) The maximum downlink data transmission rate at X-band is 100 kilobits per second (kbps) under ideal Earth weather conditions and when Jupiter is not at aphelion.

(b) Optional flight telemetry system (FTS) data rates are 5, 40, and 60 bps.

(c) Bulk data storage requirements are based on a nominal cycle of 8 hours of recording followed by 4 hours of playback.

(d) Goldstone view is not a constraint on the timing of critical SC events.

(e) One and two way Doppler tracking will be employed for orbit determination (OD), if feasible, when JOSE is near apoapsis.

(f) Antennas to be considered are of the body-fixed type, or single and multiple degree of freedom types.

(g) Sun, Earth, and Canopus are the main pointing sources for the high gain antenna.

(h) Since science recording requirements are so severe during perijove, no data transmission is permitted during one-half solar Earth day on each side of perijove.

C. JOSE Components

Table II-1 is a coarse weight breakdown of the various subsystems for JOSE (see Chapter IX for more details). Many references listed in the Bibliography of this report were consulted in preparing Table II-1. The

basic design philosophy was to (1) first consider the desired science objectives based on information from Chapter I, (2) select appropriate instruments to make meaningful measurements to satisfy those objectives, and (3) to design a spacecraft to successfully accommodate these instruments. This philosophy differs from other, more restricted philosophies, such as selecting a launch vehicle and minimum launch period, which in turn determines the maximum length injection energy and thus the gross spacecraft weight.

D. Proposed Configuration

Figure II-2 shows the spacecraft in the deployed interplanetary configuration. The main equipment compartment is octagonal; two communications antennas on one end and the propulsion engine and thermal louver array on the other. A magnetometer boom and a biaxially articulated scan platform are balanced by two RTG's.

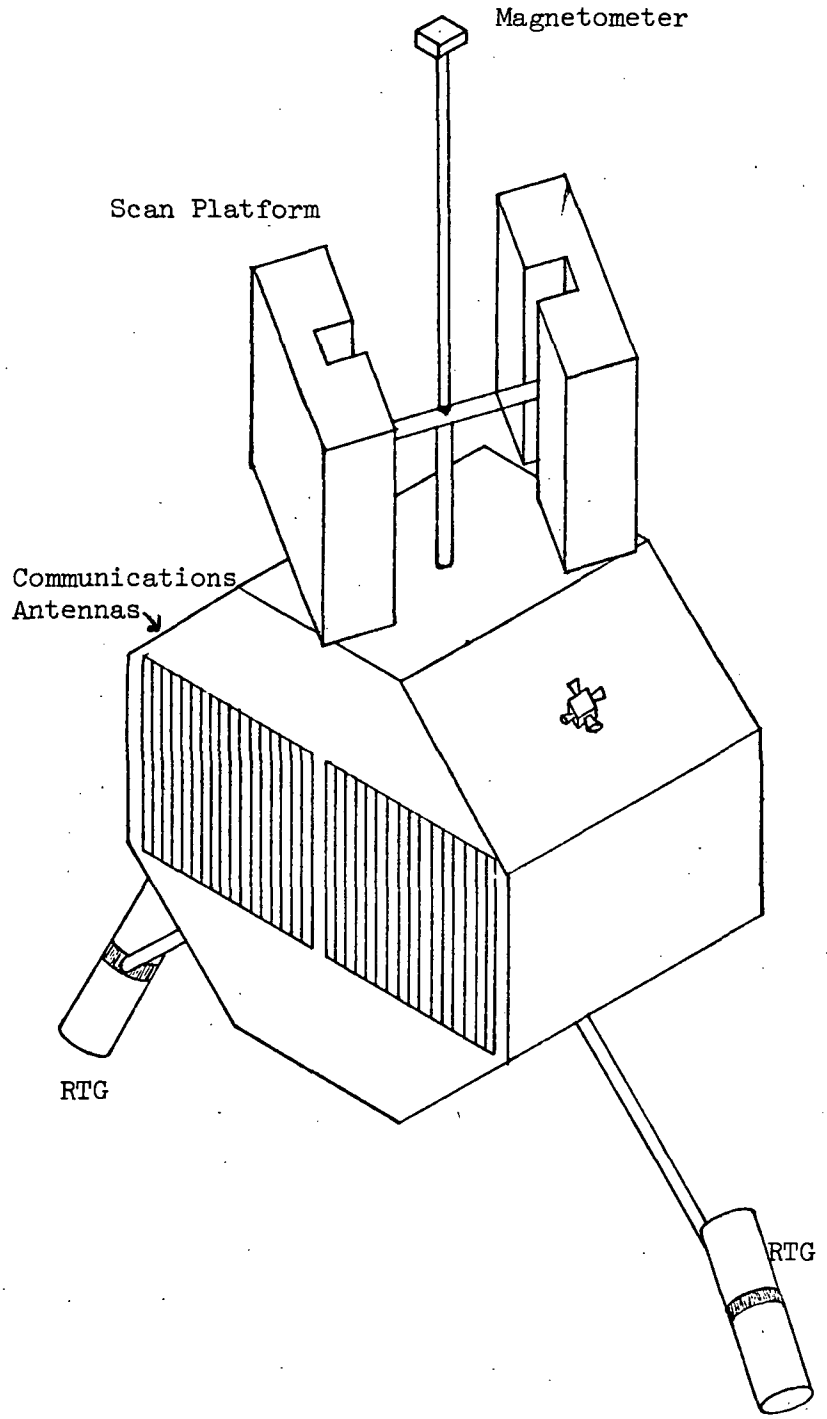

Figure II-2. Spacecraft Configuration

Table II-1

JOSE Component Weight List

Subsystem	Component	Weight (lbs)	Remarks
Science	Fluxgate Magnetometer	4.7	6 watts
	Helium Magnetometer	7.25	7 watts
	Piezoelectric Microphone	2 per	1 watt
	Plasma Probe	6.41	2.6 watts
	Ionization Chambers	2.71	0.5 watts
	Trapped Radiation Counter	2.6	0.4 watts
	Energetic Particle Detector	2.5	0.4 watts
	Cosmic Dust Detector	2.5	0.2 watts
	Cosmic Ray Spectrum Analyzer	18	2 watts
	High Energy Proton Monitor	4	0.6 watts
	Medium Energy Proton Monitor	3	1 watt
	Low Energy Proton Monitor	4	0.2 watts
	Geiger Mueller Counter		used with ion chambe
	Solid State Detectors		" " " "
	Capacitive Film		part of structure
	Faraday Cup Plasma Anal.	5.9	3.1 watts
	Cosmic Ray Telescope	2.6	0.6 watts
	Solar Flare Detector		very small
	Trapped Electron Analyzer	8.3	0.5 watts
	Total Fields & Particles	80	30 watts peak
	Microwave Radiometer	30	10 watts
	Visible Photometer	6	5 watts
	Infrared Radiometer	5	3 watts
	V and UV Spectrometer	20	10 watts
	High Resolution Television	30	20 watts
	Infrared Interferometer	30	5 watts
	Ultraviolet Photometer	3	5 watts
	3 Auroral Photometers	5 ea.	0.5 watts ea.
	VLF Detector	5	1 watt, regular radi
	Null Radio Seeker	5	2 watt, regular radi
	Radar Altmeter	25	10 watts
	Total Planetary	170	75 watts peak
	Total Science	250	105 watts peak
Structure and Thermal Control	Structure	200	
	Planetary Scan Platform	60	10 watts, 70"x48"x20
	Thermal Control	75	
	Meteoroid Protection	100	
	Radiation Protection	115	
	Total	550	
Power Supply	RTG: 2 units (JOSE P-1)	300	use Pu 238, furnish total of 600 watts, 12" dia. x 40" l., lifetime > 5 years
	Power Control Unit	20	
	Shunt Elements	10	
	Shielding	35	around sensitive equipment
	Total: (RTG)	365	

Table II-1 (cont.)

Subsystem	Component	Weight (lbs)	Remarks
Integration	Command Distribution (1)	10	slight power requirement only during launch
	Umbilical (1)	5	
	Pyrotechnic Control Box	10	
	Cabling and Connectors	100	
	Total	125	
Data Handling	Data Handling Unit	50	a few watts at most
	Tape Recorder	25	
	Decoder and Sequencer	20	
	Total	95	
Communication	Receiver (2)	10	100 watts average during transmission.
	Modulator/Exciter (2)	5	
	Traveling Wave Tube (2)	2	
	Circulator Switch (6)	2	
	Diplexer (2)	2	
	Antenna Selector (1)	1	
	Receiver Selector (1)	1	
	Power Amp. Monitor and Selector (1)	1	
	Directional Coupler (1)	1	
	Omni-Antenna Inst. (2)	2	
	Helical-Antenna Inst. (1)	14	
	Total	41	
Attitude Control	Gyro Reference Assembly (1)	10	a few watts at most
	Accelerometer (1)	1	
	Guidance & Control Electronics	20	
	Canopus Tracker (1)	1	
	4 Star and Moon Trackers	40	
	Coarse Sun Sensor (4)	4	
	Fine Sun Sensor (2)	4	
	Gimbal for Fine Sun Sensor (2)	4	
	Sun Sensor Electronics (2)	1	
	Thrust Vector Control (2)	4	
	Regulator Relief Valve (2)	3	
	Solenoid Valves (12)	6	
	Fill Valves (2)	2	
	High Pressure Transd. (2)	2	
	Low Pressure Transd. (2)	3	
	Nozzles (12)	2	
	Lines and Fittings	5	
	Nitrogen	50	
	N_2 Tank & Residual	10	20.65"radius
	Total	172	

Table II-1 (cont.)

Subsystem	Component	Weight (lbs)	Remarks
Propulsion Flox/CH_4	Structure	102	
	Propellant Feed Assembly:		(281)
	tanks	235	
	valves & plumbing	38	
	insulation	8	
	Pressurization System:		(15)
	helium	2	
	tanks	3	
	plumbing	10	
	Engine System	45	
	Total = Dry Inert Weight	443	
	Contingency	44	
	Residuals	43	
	Performance Reserve	17	
	Total = Inert Weight	547	
	Impulsive Propellant	2174	
	Propulsion Module	2721	
Science Experiments		250	
Structure (including meteoroid, radiation and thermal control)			
	Main Compartment	490	
	Scan Platform	60	
Power Supply		365	
Main Propulsion			
	Impulsive Propellant	2174	
	Inert Weight	547	
Communications and Data Handling		136	
Attitude Control		172	
Integration		125	
	Total	4319 lbs.	

1. Auburn - Alabama Engineering Systems Design Summer Faculty Fellows. JOVE: Jupiter Orbiting Vehicle for Exploration, Vol. 1 and II, prepared under contract, NSR 01-003-025 for the National Aeronautics and Space Administration, August, 1967.

2. Canvel, Henry, "Trapped Radiation Detector - Mariner V", Technical Report 32-1197, Jet Propulsion Laboratory, Pasadena, California, November 15, 1967.

3. Clark, J.F., Hymowitz, E.W., Trainor, J.H., "Galactic Jupiter Probes", NASA TM-X-55785, Goddard Space Flight Center, Greenbelt, Maryland, March, 1967.

4. Conrad, A.G., "System Engineering Considerations in Spacecraft Design", Technical Report No. 32-960, Jet Propulsion Laboratory, Pasadena, California, June 15, 1966.

5. Corliss, William R., Harvey, Douglas G., Radioisotopic Power Generation, Prentice-Hall, Inc., Englewood Cliffs, New Jersey, 1964.

6. Corliss, William R., Scientific Satellites, NASA SP-133, National Aeronautics and Space Administration, Washington, D.C., 1967.

7. Davies, W.O., Narin, F., Roberts, D.L., Schmidt, L.A., Scholz, L.C., Stone, C.A., Vickers, R., "Survey of a Jovian Mission", Report No. M-1, prepared by the Astro Sciences Center of IIT Research Institute for the Lunar and Planetary Programs Office, NASA Headquarters, Washington, D.C., Contract No. NAS r-65(06), March 1964.

8. Flandro, G.A., "Utilization of Energy Derived from the Gravitational Field of Jupiter for Reducing Flight Time to the Outer Solar System", Space Programs Summary No. 37-35, Vol. IV, Jet Propulsion Laboratory, Pasadena, California, October 31, 1965, pp. 12-23.

9. General Dynamics, Fort Worth Division, "Mid-Term Technical Report of a Study of Jupiter Flyby Missions", prepared for the Jet Propulsion Laboratory, Pasadena, California, Contract No. 951285, Feb. 17, 1966.

10. General Dynamics, Fort Worth Division, A Study of Jupiter Flyby Missions, Final Technical Report prepared for the Jet Propulsion Laboratory, Pasadena, California, Contract No. 951285, May 17, 1966.

11. Gilligan, J.E., "Thermophysical Aspects and Feasibility of a Jupiter Atmospheric Entry", Report No. S-4, prepared by the Astro Sciences Center of IIT Research Institute for the Lunar and Planetary Programs Office, NASA Headquarters, Washington, D.C., Contract No. NAS r-65(06), January, 1968.

12. Greenspan, J.A., "Asteroid Fly-Through Mission", Report No. S-2, prepared by the Astro Sciences Center of IIT Research Institute for the Lunar and Planetary Programs Office, NASA Headquarters, Washington, D.C., Contract No. NAS r-65(06), April, 1966.

13. IIT Research Institute, "Summary of Flight Missions to Jupiter", Digest Report M-4 by the Astro Sciences Center of IIT Research Institute for the Lunar and Planetary Programs Office, NASA Headquarters, Washington, D.C., Contract No. NAS r-65(06), July 1, 1964.

14. Jet Propulsion Laboratory, "Advanced Planetary Probe - Jupiter Flyby Application", Engineering Planning Document EPD-358, Pasadena, California, August 12, 1966.

15. Jet Propulsion Laboratory, Mariner Mars 1964 Project Report: Mission and Spacecraft Development, Vol. 1, From Project Inception Through Midcourse Maneuver, Technical Report No. 32-740, Pasadena, California, March 1, 1965.

16. Jet Propulsion Laboratory, Mariner Venus 67 Final Project Report: Volume I, Launch Through Midcourse Manuever, Technical Report 32-1203, Pasadena, California, June 15, 1968.

17. Jet Propulsion Laboratory, Ranger VII Part 1, Mission Description and Performance, Technical Report No. 32-700, Pasadena, California, December 15, 1964.

18. Lockheed Missiles and Space Co., Asteroid Belt and Jupiter Flyby Mission Study, Final Report, performed for the Jet Propulsion Laboratory, Pasadena, California, under Contract NAS 7-100, February 28, 1965.

19. Lockheed Missiles and Space Co., Space Flight Handbook, Volume III Planetary Flight Handbook, Part 5, Trajectories to Jupiter, Ceres, and Vesta, prepared under contract to the National Aeronautics and Space Administration, Washington, D.C., 1966.

20. Pedersen, Erik S., Nuclear Energy in Space, Prentice-Hall, Inc., Englewood Cliffs, New Jersey, 1964.

21. Roberts, D.L., "The Requirements of Unmanned Space Missions to Jupiter", Raumfahrtforschung, No. 1, January-March, 1967.

22. Roberts, D.L., "The Scientific Objectives of Deep Space Investigations: Jupiter", Report No. P-1, prepared by the Astro Sciences Center of IIT Research Institute for the Lunar and Planetary Programs Office, NASA Headquarters, Washington, D.C., Contract No. NAS r-65(06), March 9, 1964.

23. Roberts, D.L., "The Scientific Objectives of Deep Space Investigations: The Satellites of Jupiter", NASA CR53736, Report No. P-2, by the Astro Sciences Center of IIT for the Lunar and Planetary Programs Office, NASA Headquarters, Washington, D.C., March 9, 1964.

24. Sloan, R.K., "Mariner Mars 1964 Project Report: Scientific Instruments", Technical Report 32-883, Jet Propulsion Laboratory, Pasadena, California, July 15, 1966.

25. Smoluchowski, R., "Gravitational and Phase Change Sources of Energy in Jupiter", Contract No. NSR-24-005-047, prepared by the University of Minnesota, Minneapolis, Minnesota, for NASA Headquarters, Wash., D.C.

26. Spehalski, R.J. , "Mariner Mars 1964 Mechanical Configuration", Technical Report No. 32-933, Jet Propulsion Laboratory, Pasadena, California, September 1, 1966.

27. TRW Systems, Advanced Planetary Probe Study - Final Technical Report, Volumes I, II, III, NASA CR-79500, 79502, 79501, prepared for the Jet Propulsion Laboratory, Pasadena, California, July 27, 1966.

28. TRW Systems, Voyager Spacecraft, Phase B, Task D, Final Report, Vol.5 , "Science Payload Integration", NASA CR-93538, prepared for the George C.Marshall Space Flight Center, Huntsville, Alabama, October 1967.

29. Volkoff, J.J., Womack, J.R., "Preliminary Investigation to Determine Nuclear Electric Spacecraft Configurations for High Energy Missions", Technial Report No. 32-1085, Jet Propulsion Laboratory, Pasadena, California, June 15, 1967.

30. Witting, J.M., Cann, M.W.P., Owen, T.C. "Critical Measurements on Early Missions to Jupiter", Report No. P-10, prepared by the Astro Sciences Center of IIT Research Institute for the Lunar and Planetary Programs Office, NASA Headquarters, Washington, D.C., Contract No. NAS r-65(06), December, 1965.

31. Witting, J.M. "Scientific Objectives of Deep Space Investigation: Jupiter as an Object of Biological Interest", Report No. P-19, prepared by the Astro Sciences Center of IIT Research Institute for the Lunar and Planetary Programs Office, NASA Headquarters, Washington, D.C., Contract No. NAS r-65(06),May 1967.

Chapter III: Mission Trajectories

A. Interplanetary Trajectory Analysis

1. Introduction and Background

This chapter presents specific important trajectory parameters for the 1975-1985 time period. The supporting analysis represents a combined effort of original analysis and derivations, plus program development of much formulation existing in the Jet Propulsion Laboratory Technical Report No. 32-77. Since the resulting computer program is quite extensive, it is impossible to present here the entire formulation that went into its development. A block diagram of the subprograms and general descriptions will suffice; the interested reader who desires more development of concepts presented herein should consult JPL sources or the author's notes. Jupiter and Earth Ephemeris data for the 1975-85 time period were abstracted from "Trajectories to the Outer Planets via Jupiter Swingby", NASA CR-61186. It should also be remarked that independent derivations by the author have disclosed errors in the above referenced JPL report.

Important trajectory parameters are defined as they appear in this chapter and Appendix B. Appendix A represents the results of this chapter; i.e., for each year 1975-85, seven trajectory parameters are presented as functions of launch and arrival dates (hence flight times). The seven parameters are:

C_3: Twice the energy per unit mass required to inject the SC from Earth orbit onto the Earth-Jupiter transfer ellipse defined by the flight time T_F; units are Km^2/sec^2.

ϕ_L: Declination of the launch asymptote to the Earth's Equator, units are degrees.

ΔV: Required mid-course velocity correction approximately 10 days after launch to null injection errors; units are meters/sec.

VHP: Hyperbolic excess speed at Jupiter; units are km/sec.

σ_1: Semi-major axis of the dispersion ellipse resulting from the mapping of injection and mid-course maneuver errors onto the R-T plane at Jupiter; units are in kilometers.

σ_2 : Semi-minor axis of same ellipse; in kilometers.

θ : Angle of major axis of dispersion ellipse with respect to T-axis; measured CCW in degrees.

Figure III-1 is a block diagram of the trajectory program JOSE. Appendix B briefly describes the various subprograms. Program JOSE is quite general and can accommodate interplanetary trajectories between any two planets of this solar system with only slight modifications. Program JOSE also solves Type I trajectories only (those trajectories having a heliocentric transfer angle between 0 and 180°); however, a very small number of additions to the program would allow it to also solve Type II trajectories (transfer angle between 180° and 360°). Only Type I trajectories are of interest for the Earth-Jupiter trajectories of this study for three main reasons: (1) Type II trajectories are in general characterized by initial heliocentric velocity vectors directed sunward, or inward, of the Earth's orbital velocity vector. This in turn implies that, during the first several days of the mission, the SC is inside the Earth's orbit and SC componets would then have to be designed for high as well as low temperatures. (2) From Appendix A, flight times to Jupiter are seen to be rather long with respect to system hardware reliabilities. To keep the flight time low with Type II trajectories implies high C_3 values and resulting propulsion penalties. A comparison between equal C_3 values for Type I and II trajectories necessarily results in much longer flight times

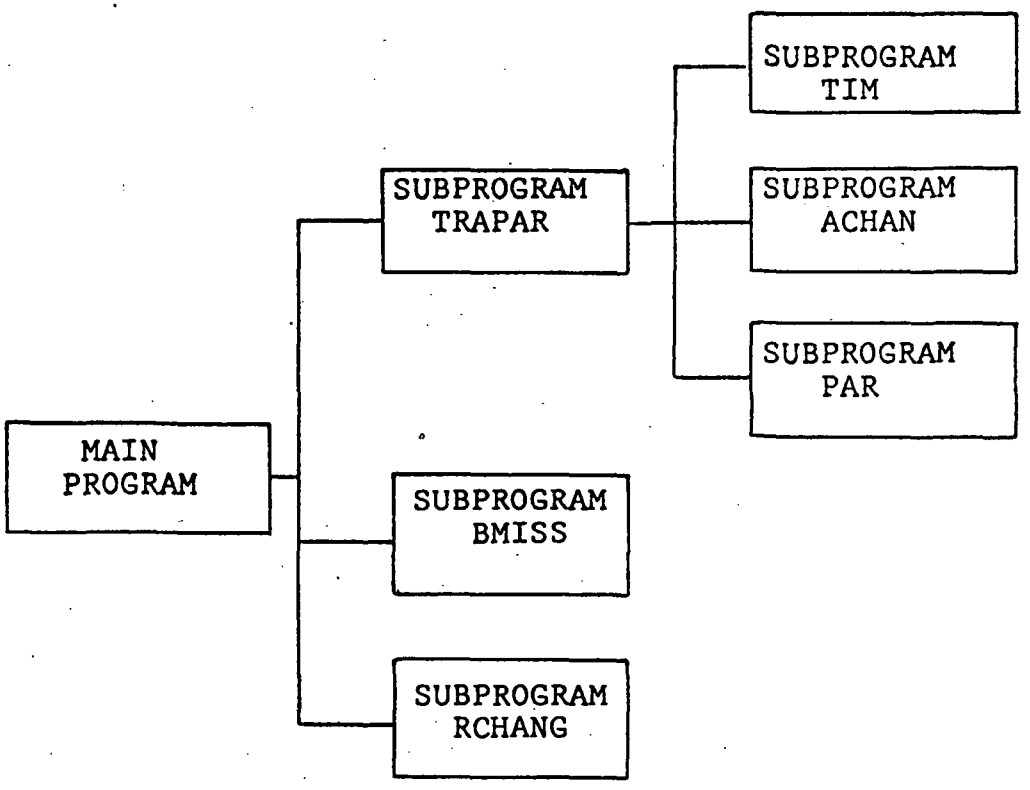

Figure III-1: Block Diagram of JOSE Earth-Jupiter Interplanetary Trajectory Program.

for the Type II trajectories and hence systems reliability degradation.

(3) Type II trajectories generally result in Jupiter approaches having periapsis on Jupiter's dark side. This condition is disadvantageous for closest-approach imaging experiments.

2. Conclusions

From Appendix A, three trajectories were chosen to further analyze their effects on the approach geometry at Jupiter and the later orbits about Jupiter. To cover the time period in question; i.e., 1975-1985, one trajectory each from 1975, 1980, and 1985 launch date was chosen. These trajectory points are indicated in Appendix A. In selecting these three trajectories, an attempt was made to optimize the seven parameters presented. Optimization implies minimizing C_3, ΔV, VHP, σ_1, and σ_2;maintaining θ near 0°; and maintaining ϕ_L near 0°. An eighth factor taken into consideration is C.D., the communication distance at arrival, also shown in Appendix A. It is very important that the Earth is in that portion of its orbit approaching opposition with Jupiter (opposition implies minimum C.D. for the year), rather than approaching conjunction where the Sun will occult communications with the SC during the first few critical orbits about Jupiter.

Listed in Table III-1 are the important parameters for the three selected trajectories as computed by JOSE with the two midcourse maneuvers. Not shown are the following parameters: $\bar{R}_{LA}$ is the Earth position vector at Jupiter arrival at time T in Julian Day Numbers. α and dec. are the right ascension and declination of Canopus at time T. $\bar{R}_P$, $\bar{V}_J$, $\bar{S}_P$, $\bar{R}$, $\bar{T}$, $\bar{R}_{LA}$, α, dec., T, defined in Appendix B, are required as input to Jupiter planetocentric programs which follow in Section B.

It is seen that the three trajectories are quite similar except for the large negative declination in 1985. This could present a real problem for a 1985 launch, since the launch asymptotic declination affects the launch azimuth by:

$\sin \Sigma_L = \cos \phi_L / \cos \phi_{CK}$, where:

Σ_L = launch azimuth from Cape Kennedy Eastern Test Range (ETR)

ϕ_{CK} = latitude of Cape Kennedy (28.3°)

Thus, for $|\phi_L| > 28.3^\circ$, there is a range of azimuths symmetrically distributed around $\Sigma_L = 90^\circ$ (due East) for which the desired declination ϕ_L cannot be achieved without the use of yaw maneuvers during power flight and attendant payload losses. For the 1985 ϕ_L of -37.9°, $\Sigma_L = 64^\circ$ and 116°, hence the launch azimuth must be 26° or more north or south of due East, and ETR safety regulations concerning launching over populated islands prohibit these launch azimuths. Thus the undesirable "dog-legging" yaw maneuvers are required for 1985.

Table III-1

Results of 1975, 1980, and 1985 Selected Trajectories

Parameter*	Year 1975	1980	1985
Launch Date	June 27	Dec. 7	April 15
ϕ_L	-7.1°	21.4°	-37.9°
$C_3 (km^2/sec^2)$	81.8	85.5	84.8
ΔV_1 (m/sec)	30.6	32.6	35.4
$\bar{B} \cdot \bar{T}$ (R_J)	30.16	9.67	10.78
$\bar{B} \cdot \bar{R}$ (R_J)	-55.15	-55.66	-69.78
σ_1 (km)	1966.6	1942.5	1969.8
σ_2 (km)	1834.1	1841.6	1832.7
θ	1.8°	3.0°	$179.8^\circ (-.2^\circ)$
VHP (km/sec)	7.75	8.11	8.40
T_{F1} (days)	793.2	794.1	689.4
T_{F2} (days)	210.5	210.5	210.5
Total T_F (days)	813.7	815	710
Arrival Date	9/18/77	3/2/83	3/26/87

* See Appendix B for parameter definition

B. Jupiter Orbital Considerations

1. Introduction

This section deals with post-interplanetary trajectory phases of the mission and concerns the hyperbolic approach trajectory of JOSE in Jupiter's sphere of influence and the following SC orbits about Jupiter. These phases of the trajectory are uniquely determined by the interplanetary trajectory, hence variations of the orbital trajectory parameters are possible only by the expenditures of large amounts of propellant.

The sections of this chapter briefly describe the various planetocentric programs for JOSE. They are of course applicable for the results of any Earth-Jupiter trajectory. The output of the three selected trajectories tabulated at the close of Section A were used as input for these planetocentric programs to analyze approach and orbital characteristics of the trajectories.

2. Encounter Geometry

This program computes the geometry among JOSE, Jupiter, the Sun, the Earth, and Canopus. The communication distance at arrival R_C is of course:

$$R_C = || \bar{R}_C || = || \bar{R}_P - \bar{R}_{LA} ||$$

The heliocentric position vector of Canopus is given by:

$$\bar{C} = E \begin{pmatrix} \text{Cos dec Cos } \alpha \\ \text{Cos dec Sin } \alpha \\ \text{Sin dec} \end{pmatrix},$$

since dec and α are with respect to the Earth's Equator.

The angles ξ between the planeocentric unit velocity vector of JOSE ($\bar{S}_P$) and each of the Jupiter-Sun vector ($-\bar{R}_P$), the Jupiter-Earth vector

$(-\bar{R}_C)$, and the Canopus vector $(\bar{C})$ are:

$$\text{Cos } \xi_P = -\bar{S}_P \cdot \frac{\bar{R}_P}{R_P}$$

$$\text{Cos } \xi_E = -\bar{S}_P \cdot \frac{\bar{R}_C}{R_C} \qquad (0 \leq \xi \leq \pi)$$

$$\text{Cos } \xi_C = \bar{S}_P \cdot \bar{C}$$

The angles η measured counterclockwise in the $\bar{R}$-$\bar{T}$ plane from the $-\bar{T}$ axis to the projection onto the $\bar{R}$-$\bar{T}$ plane of each of the vectors $-\bar{R}_P$, $-\bar{R}_C$, and $\bar{C}$ are:

$$\text{Cos } \eta_S = \frac{\bar{T} \cdot \bar{R}_P}{R_P \text{Sin}\xi_P} \quad , \qquad \text{Sin } \eta_S = \frac{-\bar{R} \cdot \bar{R}_P}{R_P \text{Sin}\xi_P}$$

$$\text{Cos } \eta_E = \frac{\bar{T} \cdot \bar{R}_C}{R_C \text{Sin}\xi_E} \quad , \qquad \text{Sin } \eta_E = \frac{-\bar{R} \cdot \bar{R}_C}{R_C \text{Sin}\xi_E} \qquad (0 \leq \eta \leq 2\pi)$$

$$\text{Cos } \eta_C = \frac{-\bar{T} \cdot \bar{C}}{\text{Sin}\xi_C} \quad , \qquad \text{Sin } \eta_C = \frac{\bar{R} \cdot \bar{C}}{\text{Sin}\xi_C}$$

These angles are indicated in Figures III-2,3 and 4 for the targeting points of the three selected trajectories.

A unit normal to Jupiter's orbital plane is given by:

$$\bar{W}^T = (\text{Sin } i_J \text{Sin } \Omega_J, \text{ Sin } i_J \text{Cos } \Omega_J, \text{ Cos } i_J) \qquad \text{(III-1)}$$

where i_J = Jupiter's orbital inclination to the ecliptic.

Ω_J = the longitude of the ascending node of Jupiter's orbital plane and ecliptic.

The unit projection of $\bar{S}_P$ onto Jupiter's orbital plane $(\bar{S}_{PR})$ is:

$$\bar{S}_{PR} = \frac{\bar{S}_P - (\bar{S}_P \cdot \bar{W})\bar{W}}{||\bar{S}_P - (\bar{S}_P \cdot \bar{W})\bar{W}||}$$

The angle measured in Jupiter's orbital plane between the Jupiter-Sun vector $(-\bar{R}_P)$ and $\bar{S}_{PR}$ is:

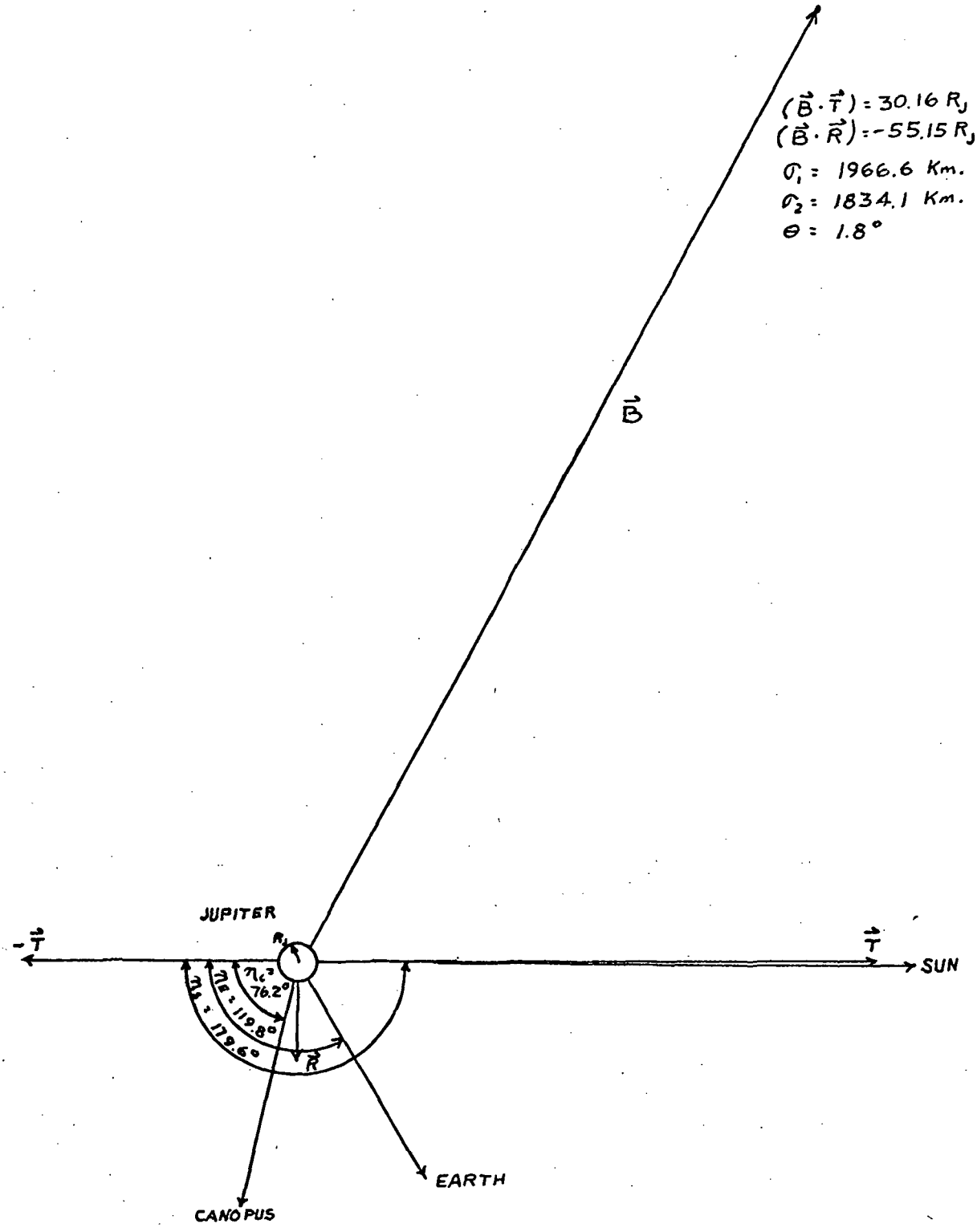

Figure III-2: 1975 R-T Target Plane Plot

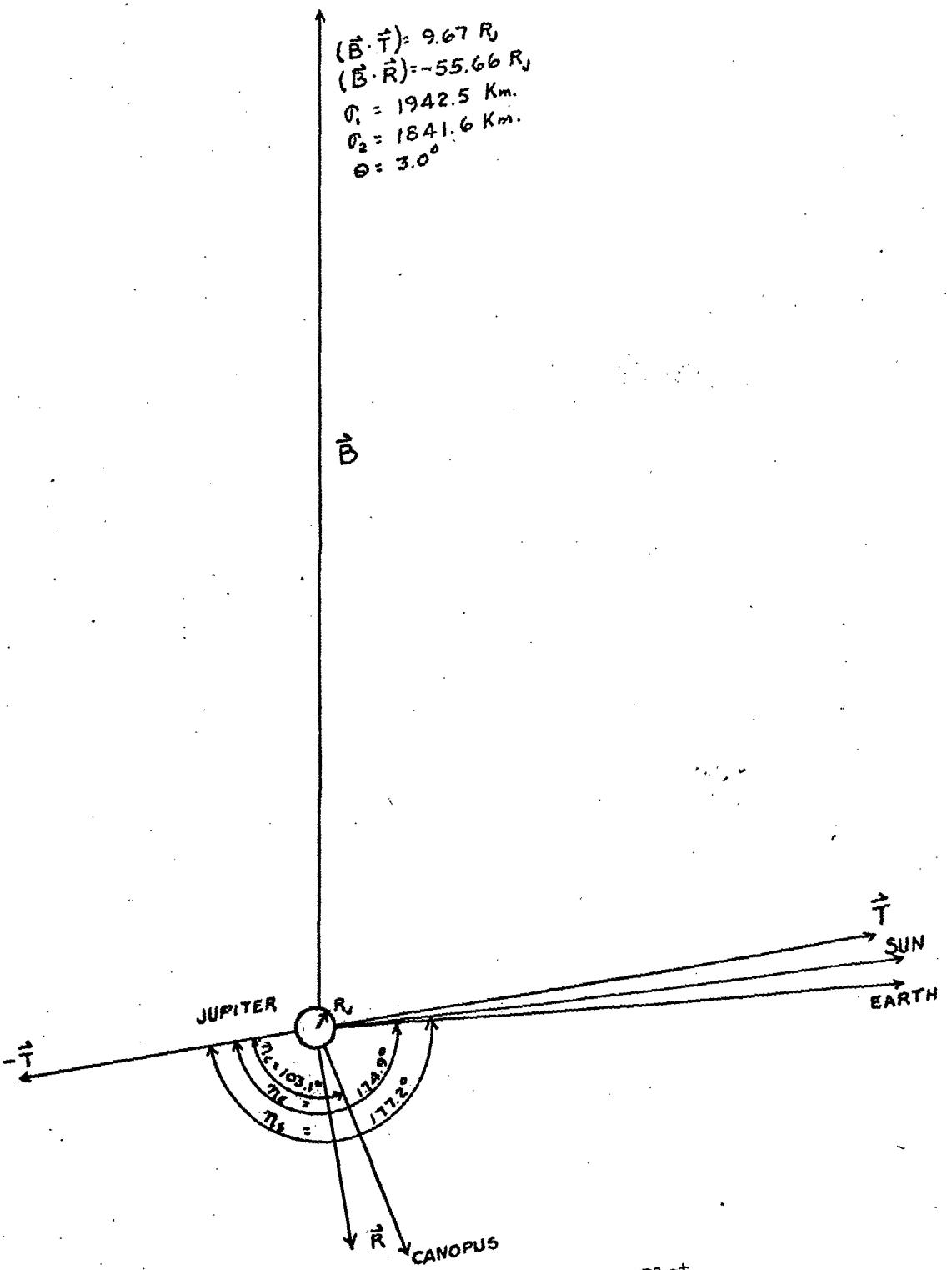

Figure III-3: 1980 R-T Target Plane Plot

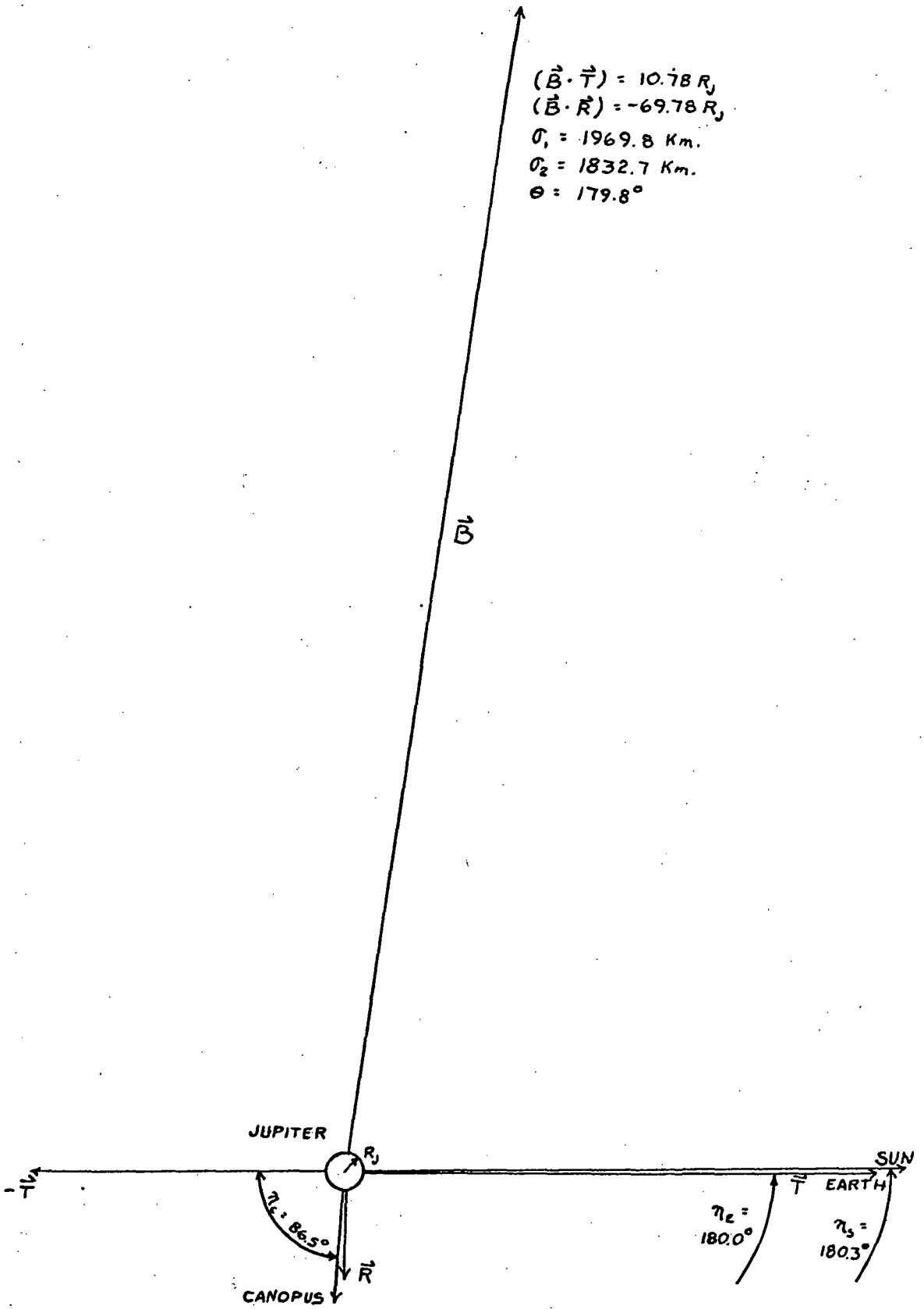

Figure III-4: 1985 R-T Target Plane Plot

$$\text{Cos } \sigma_p = \frac{-\overline{R}_P \cdot \overline{S}_{PR}}{R_P} \text{ , Sin } \sigma_p = \overline{S}_{PR} \cdot \left(\overline{W} \times \frac{\overline{R}_P}{R_P}\right) \quad (0 \leq \sigma_p \leq 2\pi)$$

3. Third Velocity Correction (ΔV_3) at Jupiter

This maneuver is performed when JOSE enters Jupiter's sphere of influence at about 706 R_J from Jupiter's center. At this boundary, Jupiter's gravity field is predominant over the Sun's, and thus the approach hyperbolic trajectory commences. This is an ideal point to apply a third velocity correction to require JOSE to pass at a preselected perijove. A third midcourse maneuver program was written which computes ΔV_3 as a function of perijoves (R_{per}) from 1.1 R_J to 6 R_J. Figure III-5 indicates the maneuver geometry and Figure III-6 presents the results.

ΔV_3 can be applied in such a direction that the SC will arrive at perijove in the equatorial plane. By deboosting at perijove in a direction suitably inclined to the SC velocity vector, JOSE can thus be initially inserted into an equatorial orbit. By attempting to thus null the $\overline{B} \cdot \overline{R}$ component even earlier in the interplanetary phase of the trajectory; i.e., before arrival at Jupiter's sphere of influence, the required ΔV_3 can be reduced significantly. This procedure for placing JOSE initially into an equatorial orbit is quite feasible during real-time mission tracking and data analysis. Since there is no decided advantage in favoring equatorial over highly-inclined orbits, the random configuration of the orbits presented in this chapter will suffice as initial orbits about Jupiter.

4. Approach Configuration of Incoming Hyperbola

As can be seen in Figures III-2, 3 and 4, the large $\overline{B} \cdot \overline{R}$ components result in approach and orbit planes highly inclined to the eliptic and Jupiter's Equator. The unit mass vector $\overline{B}/B$, where $B = ||\overline{B}||$, and the $\overline{S}_P$ vector define the approach and later orbit planes. The angles Δ measured in the orbital plane between $\overline{B}/B$ and vectors to the Sun, Earth, and Canopus were solved from the following formulas, where the vector $\overline{Z}$ represents the

unit vector $-\bar{R}_P/R_P$, $-\bar{R}_C/R_C$, or $\bar{C}$ for the Jupiter-Sun, Jupiter-Earth, or Jupiter-Canopus vector respectively:

$$\text{Cos } \Gamma = \left(\frac{\bar{B}}{||\bar{B}||} \times \bar{S}_P \right) \cdot \bar{Z}$$

$$\bar{R}_{PRO} = \bar{Z} - \text{Cos } \Gamma \left(\frac{\bar{B}}{||\bar{B}||} \times \bar{S}_P \right) = \text{projection of } \bar{Z} \text{ onto JOSE orbital plane.}$$

$$\text{Cos } \Delta = \frac{\bar{R}_{PRO} \cdot \bar{B}}{||\bar{R}_{PRO}|| \; ||\bar{B}||} \quad , \quad \text{Sin } \Delta = \frac{\bar{R}_{PRO} \cdot \bar{S}_P}{||\bar{R}_{PRO}||} \qquad (0 \leq \Delta \leq 2\pi)$$

These angles are shown in Figures III-7, 8 and 9 for the three selected trajectories.

A computer program was developed which calculates the following:

(a) The Approach Hyperbola

Given as input $\bar{B} \cdot \bar{T}$, $\bar{B} \cdot \bar{R}$, VHP, $\bar{S}_P$, $\bar{R}$, $\bar{T}$, $\bar{W}$ (normal to Jupiter's orbital plane), i_J (inclination of Jupiter's Equator to Jupiter's orbital plane), and Ω_J (the longitude measured along Jupiter's Equator from the projection of the Aries vector (X) onto Jupiter's Equator to the ascending node of Jupiter's Equator; i.e., the longitude of the ascending node for Jupiter's Equator), the program computes for $R_{per} = 1.1\ R_J$ and $4\ R_J$ the eccentricity of the approach hyperbola:

$$e = 1 + \frac{R_{per} VHP^2}{GM_J}$$

Where GM_J = the Universal Gravitational Constant times the mass of Jupiter.

The semi-latus rectum (p) of the approach hyperbola is:

$$p = \frac{GM_J}{VHP^2} \left(e^2 - 1 \right)$$

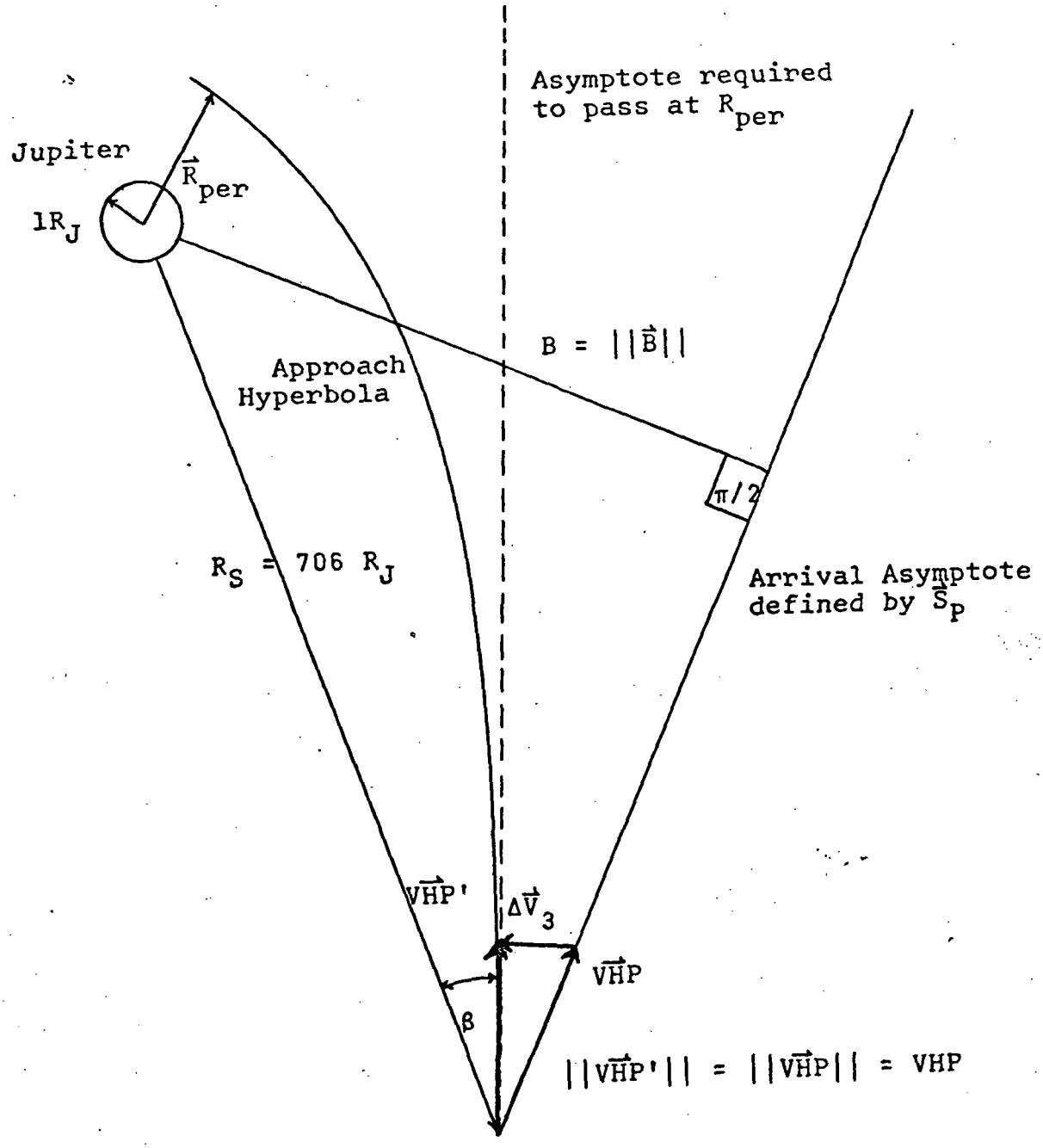

Figure III-5: Geometry of the Third Midcourse Maneuver

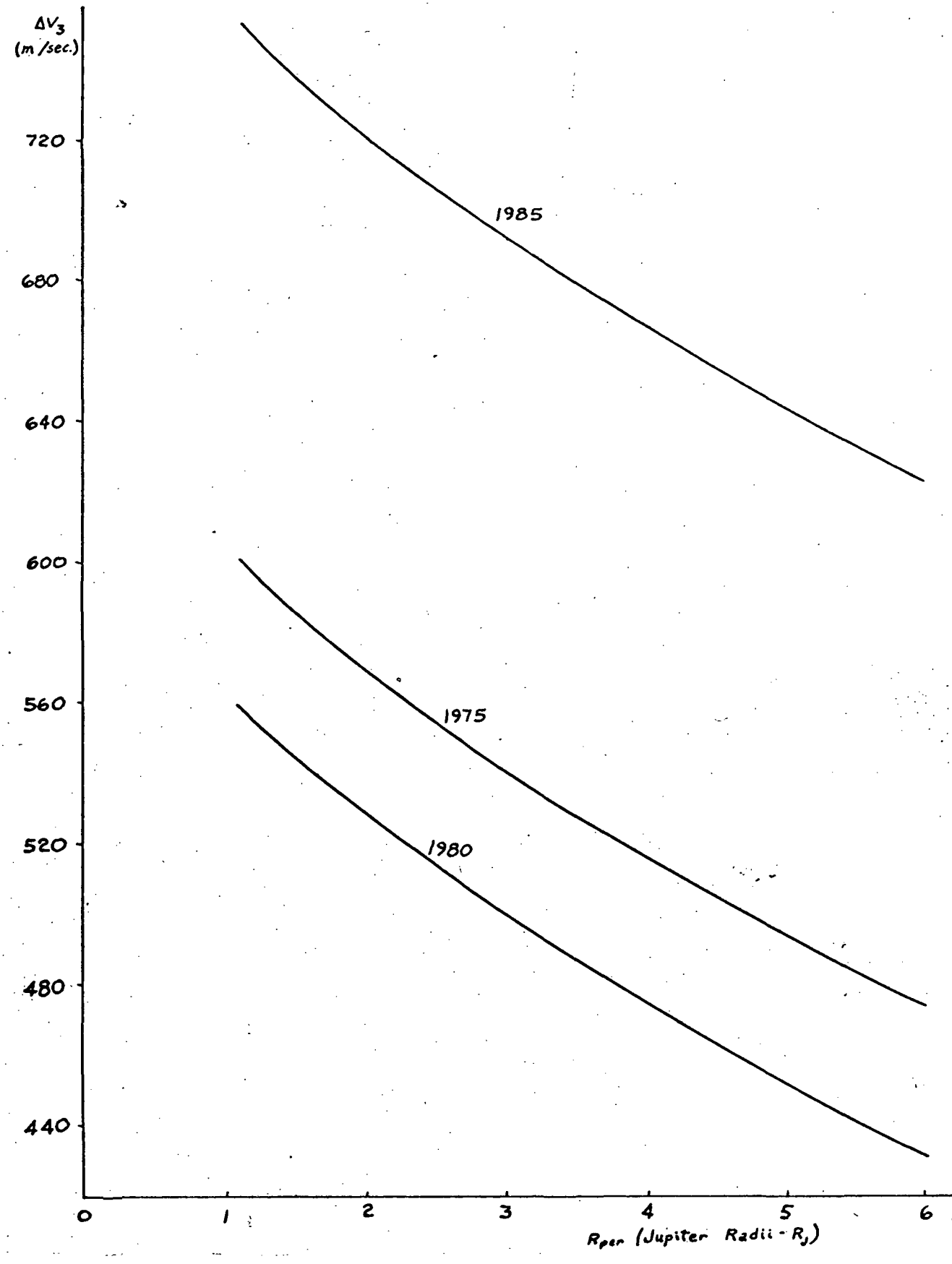

Figure III-6: Third Midcourse Velocity Correction at Jupiter Encounter as a Function of Jupiter Periapsis Distance

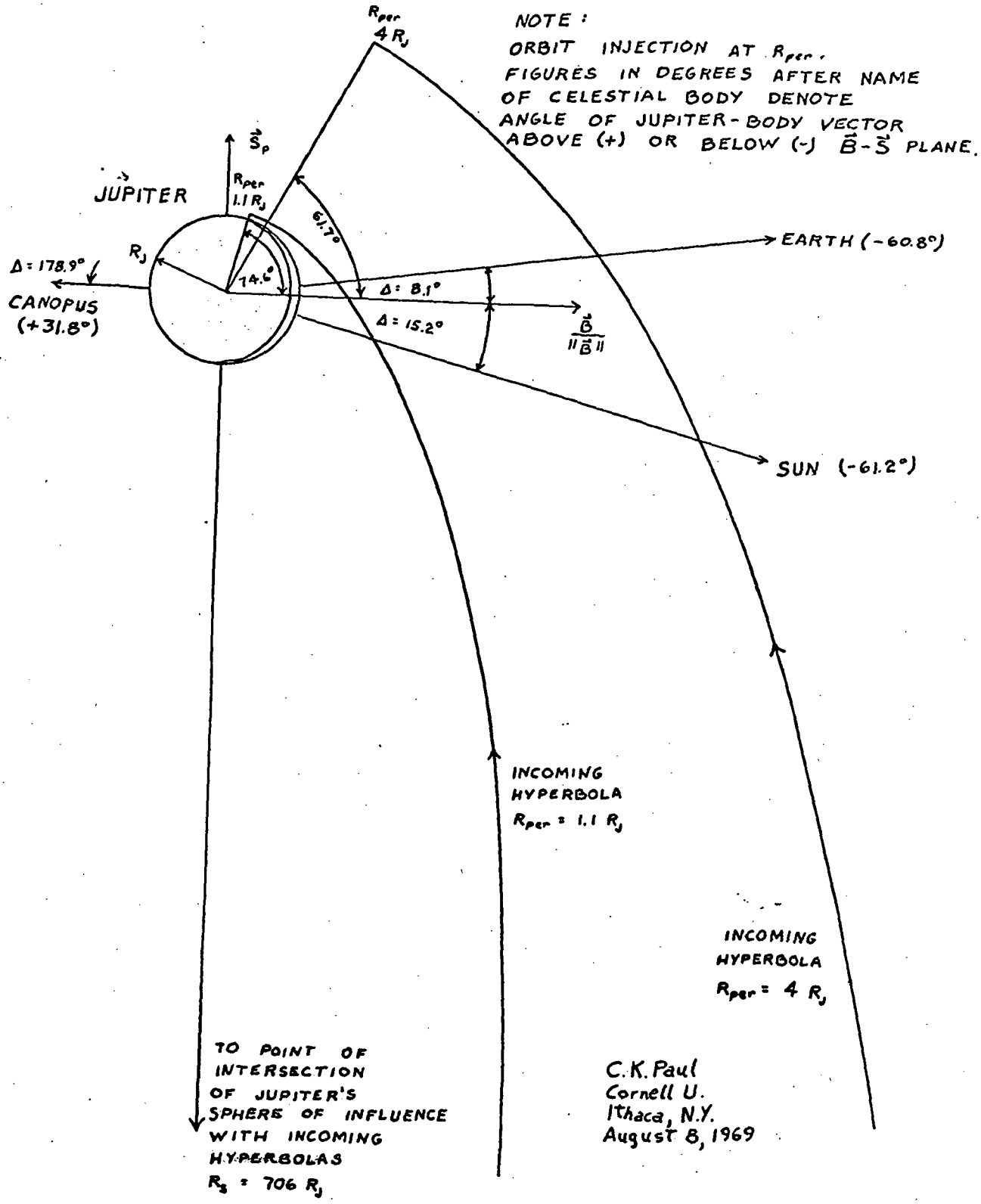

Figure III-7: 1975 B-S Approach Plane Hyperbola Plots for R_{per} = 1.1 and 4.0 R_J

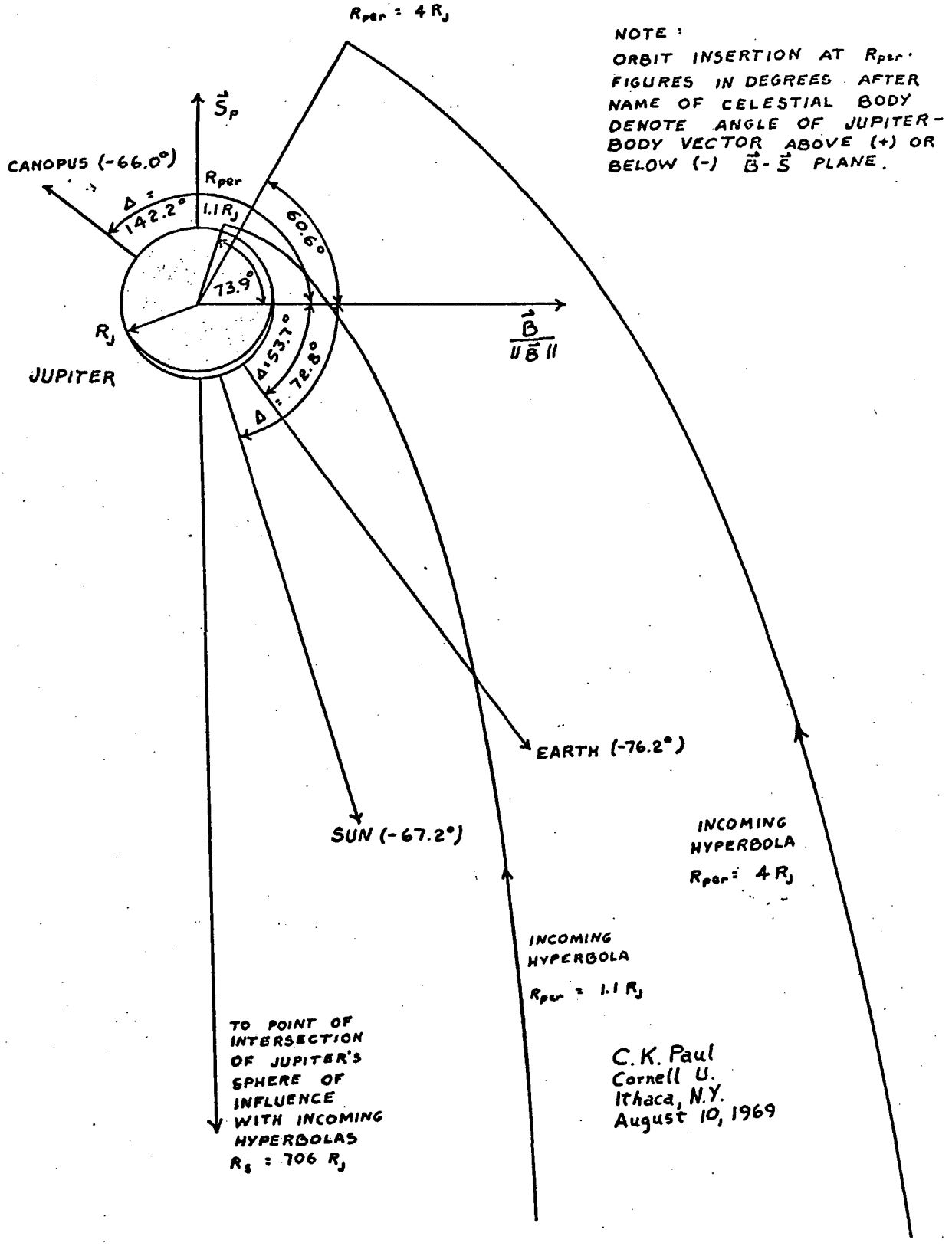

Figure III-8: 1980 B-S Approach Plane Hyperbola Plots for R_{per} = 1.1 and 4.0 R_J

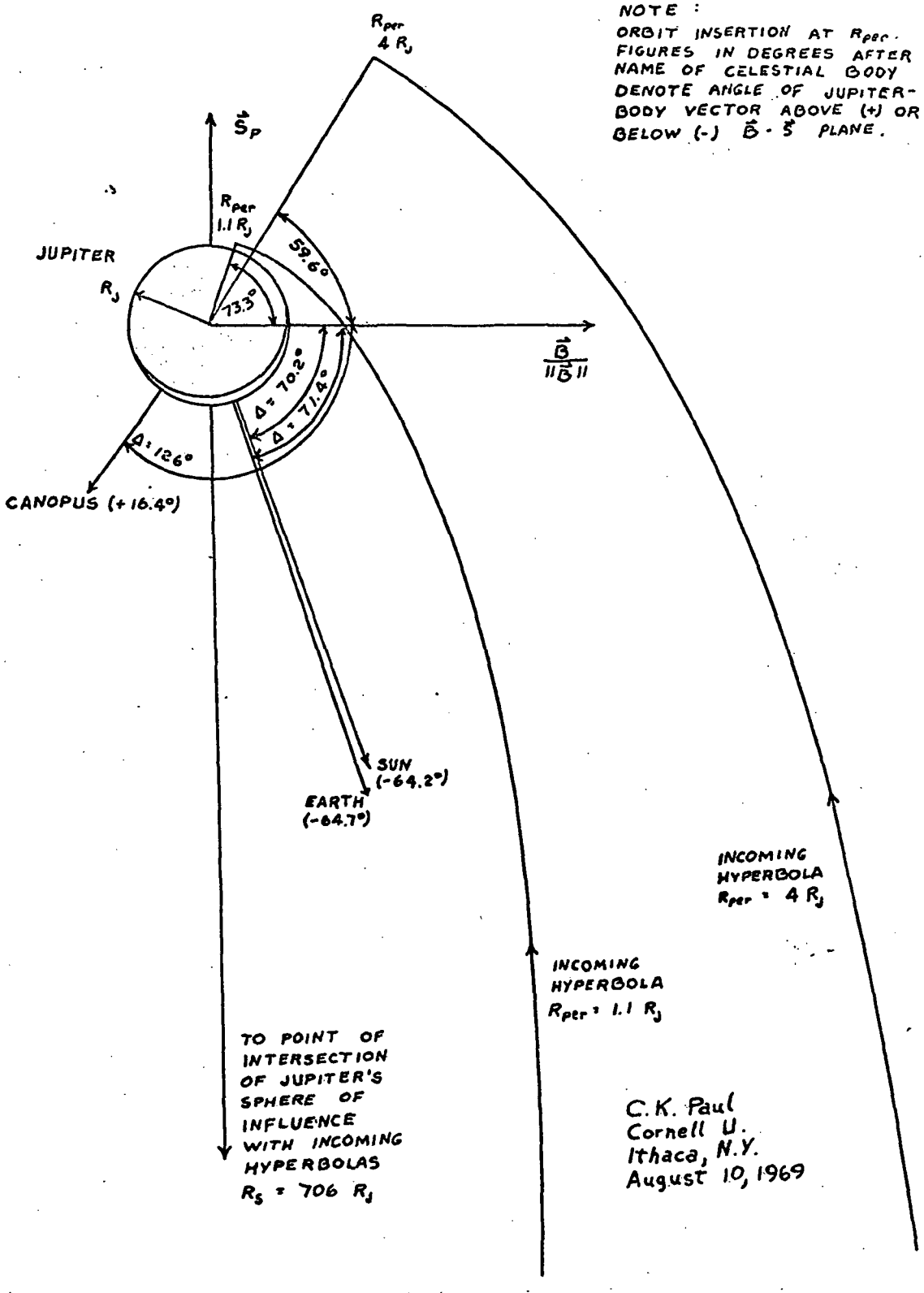

Figure III-9: 1985 B-S Approach Plane Hyperbola Plots for R_{per} = 1.1 and 4.0 R_J

Referring to the sketch below:

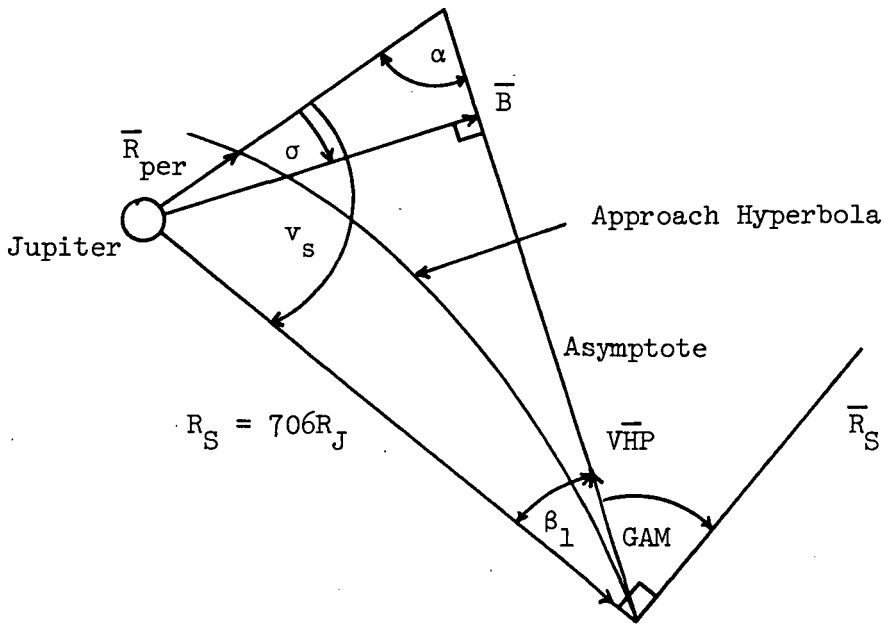

$$\text{Cos GAM} = \frac{\sqrt{p \cdot GM_J}}{VHP \cdot R_S}$$

$$\beta_1 = \frac{\pi}{2} - \text{GAM}$$

$$\text{Cos } v_s = \frac{p - R_S}{eR_S} \qquad (0 \leq v_s \leq \pi)$$

$$\alpha = \pi - (v_s + \beta_1)$$

$$\sigma = \frac{\pi}{2} - \alpha$$

These parameters orient the hyperbola in planetocentric space; various points along the trajectory are computed from:

$$R = \frac{p}{1 + e\text{Cos}v}$$

where v = the angle measured clockwise from R_{per}

R = the radial distance from Jupiter's center.

(b) Deboost Velocity ΔV_4 into Jupiter Orbit

Figure III-10 shows the deboost velocities ΔV_4 as functions of the desired apoapsis distance (R_a) of the orbit about Jupiter for periapsis distances (R_{per}) of 1.1 R_J and 4 R_J. The optimum point along the approach hyperbola to deboost into Jupiter orbit is the periapsis point of the approach hyperbola, and if the perijove of the elliptical orbit about Jupiter is made to coincide with the hyperbola periapsis, this periapsis-to-periapsis transfer requires less ΔV_4 than any other type of transfer. Figure III-10 clearly shows that ΔV_4 can be reduced by lowering R_{per} closer to Jupiter's surface and by flattening the ellipse by increasing R_a. For a periapsis to periapsis transfer then, the velocity V_4 along the hyperbola at periapsis is:

$$V_4 = \sqrt{VHP^2 + \frac{2GM_J}{R_{per}}}$$

The required velocity V_4' at this periapsis for an orbital ellipse of apojove R_a is in the same direction as V_4 and given by:

$$V_4' = \sqrt{2GM_J \left(\frac{1}{R_{per}} - \frac{1}{R_{per} + R_a} \right)}$$

Hence: $\Delta V_4 = V_4 - V_4'$

(c) JOSE Orbital Elements

The orbital elements for JOSE; i (inclination of JOSE's orbital plane with respect to Jupiter's Equator), Ω (longitude of ascending node of orbit), and ω (argument of perijove); are derived with the aid of Figure III-11. A set of orthogonal axes defining the SC orbital plane is readily calculated; since $\bar{B}/||\bar{B}||$, the angle σ between $\bar{B}$ and $\bar{R}_{per}$, and R_{per} are known:

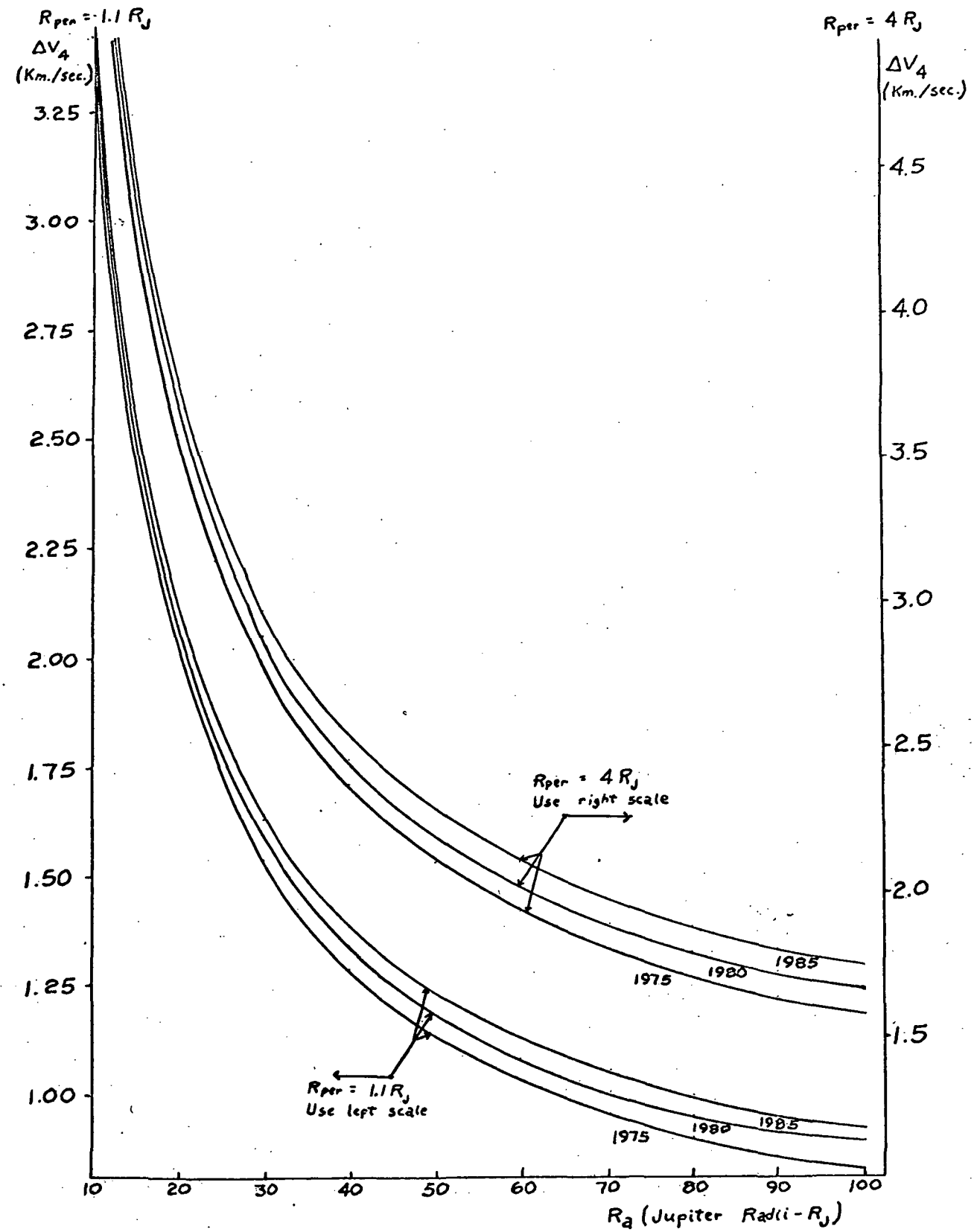

Figure III-10: Periapsis to Periapsis Deboost Velocity as a Function of Apoapsis Distance. Periapsis Distances of 1.1 and 4 R_J

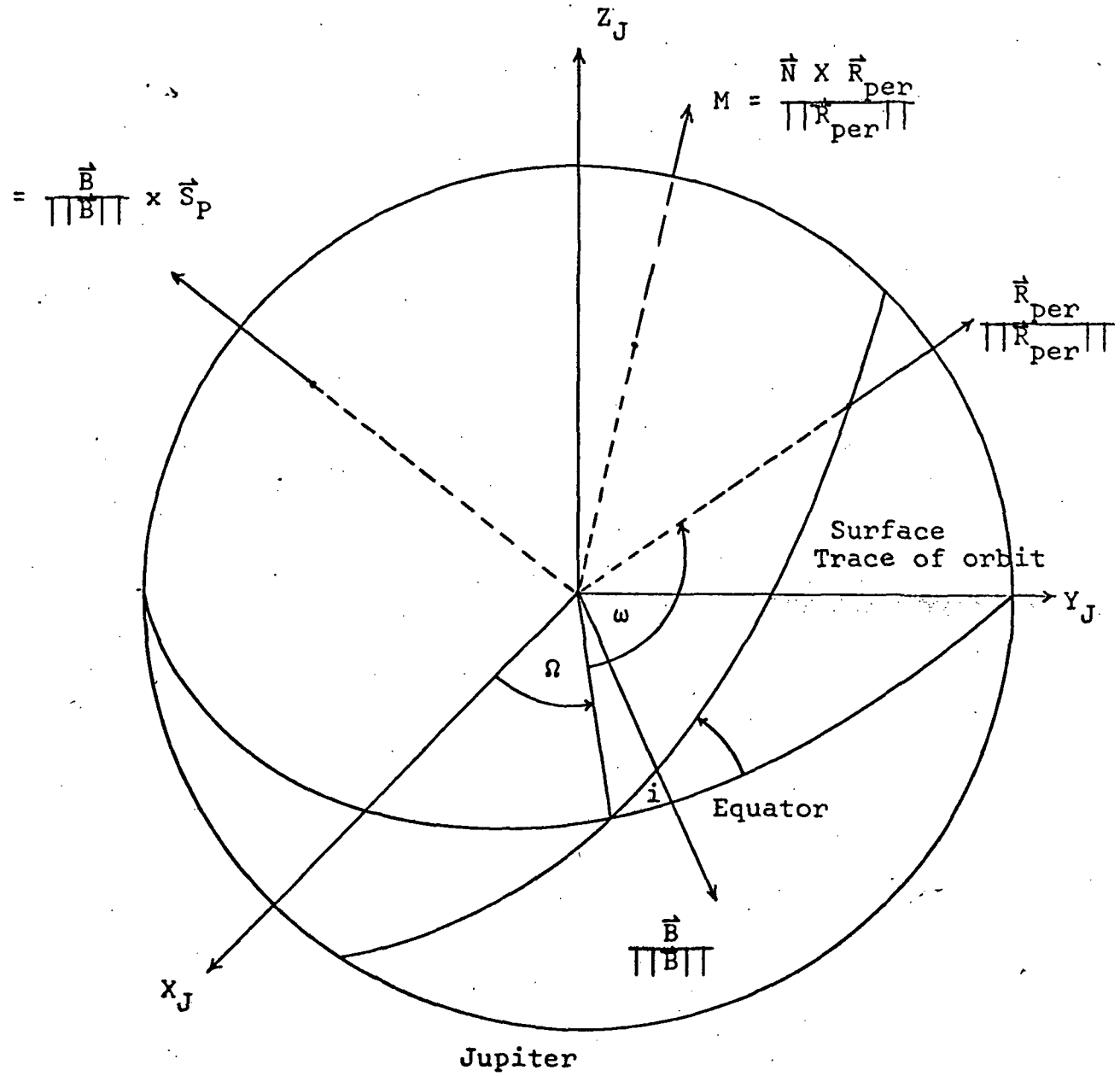

Figure III-11: Geometry for Solution of SC Orbital Elements i, Ω, and ω

$$\bar{R}_{per} = \frac{R_{per}\text{Cos}\sigma\ \bar{B}}{||\bar{B}||} + R_{per}\text{Sin}\sigma\ \bar{S}_P$$

The unit normal ($\bar{N}$) to the orbital plane is simply:

$$\bar{N} = \frac{\bar{B}}{||\bar{B}||} \times \bar{S}_P$$

The unit vector $\bar{M}$ completing this right-handed system is:

$$M = \frac{\bar{N} \times \bar{R}_{per}}{||\bar{R}_{per}||}$$

The next problem is to solve for the $\bar{X}_J$, $\bar{Y}_J$, and $\bar{Z}_J$ axes, where $\bar{X}_J$, $\bar{Y}_J$ define Jupiter's Equator, $\bar{X}_J$ being the projection of the Aries vector onto Jupiter's Equator, and $\bar{Z}_J$ is Jupiter's polar axis.

Equation III-1 defined the normal ($\bar{W}$) to Jupiter's orbital plane, hence, the unit projection ($\bar{X}_o$) of the Aries vector $\bar{X}$ {(1,0,0)} onto Jupiter's orbital plane is given by (see Figure III-12):

$$\bar{X}_o = \frac{\bar{X} - (\bar{X}.\bar{W})\bar{W}}{||\bar{X}-(\bar{X}.\bar{W})\bar{W}||}$$

A unit vector $\bar{Y}_o$ normal to the plane defined by $\bar{X}_o$ and $\bar{W}$ and lying in Jupiter's orbital plane is given by:

$$\bar{Y}_o = \bar{W} \times \bar{X}_o$$

A unit vector ($\bar{X}_1$) in the direction of the descending node of Jupiter's Equator with respect to its orbital plane is given by:

$$\bar{X}_1 = -\text{Cos}\ \Omega'_J\ \bar{X}_o - \text{Sin}\ \Omega'_J\ \bar{Y}_o$$

Since $\bar{X}_1$ lies in Jupiter's orbital plane (as well as its Equatorial plane), a vector $\bar{Y}_1$ given by:

$$\bar{Y}_1 = \bar{W} \times \bar{X}_1$$

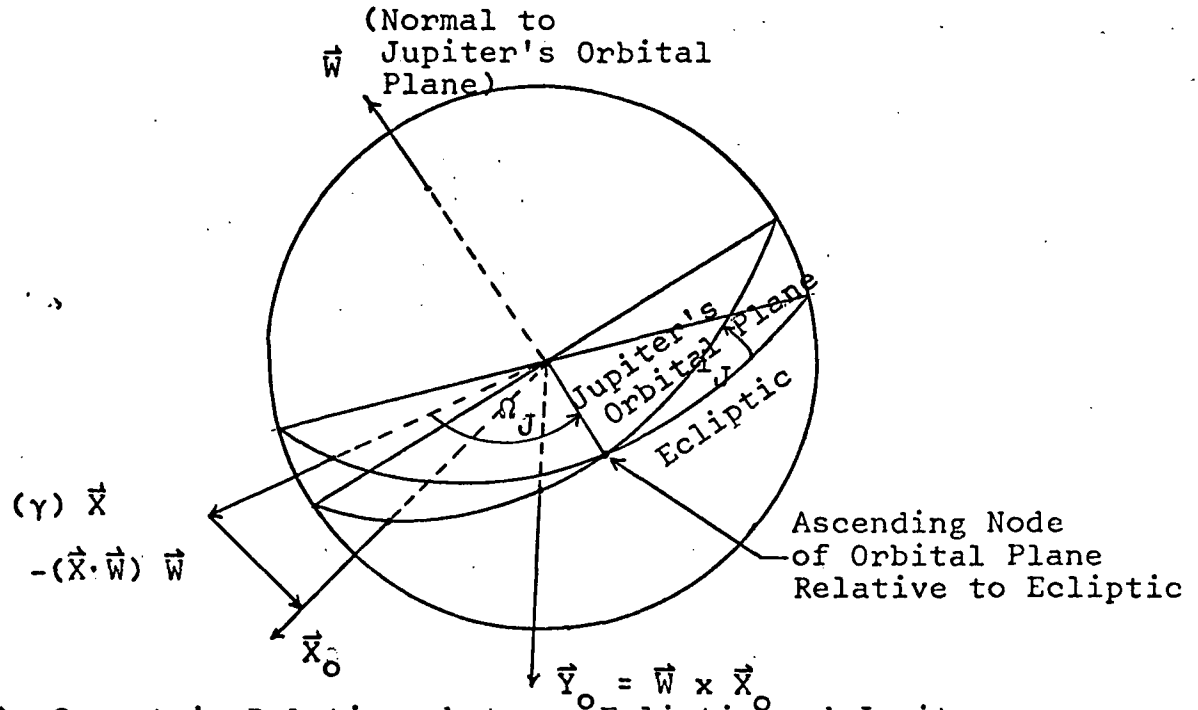

(1) Geometric Relations between Ecliptic and Jupiter Orbital Plane

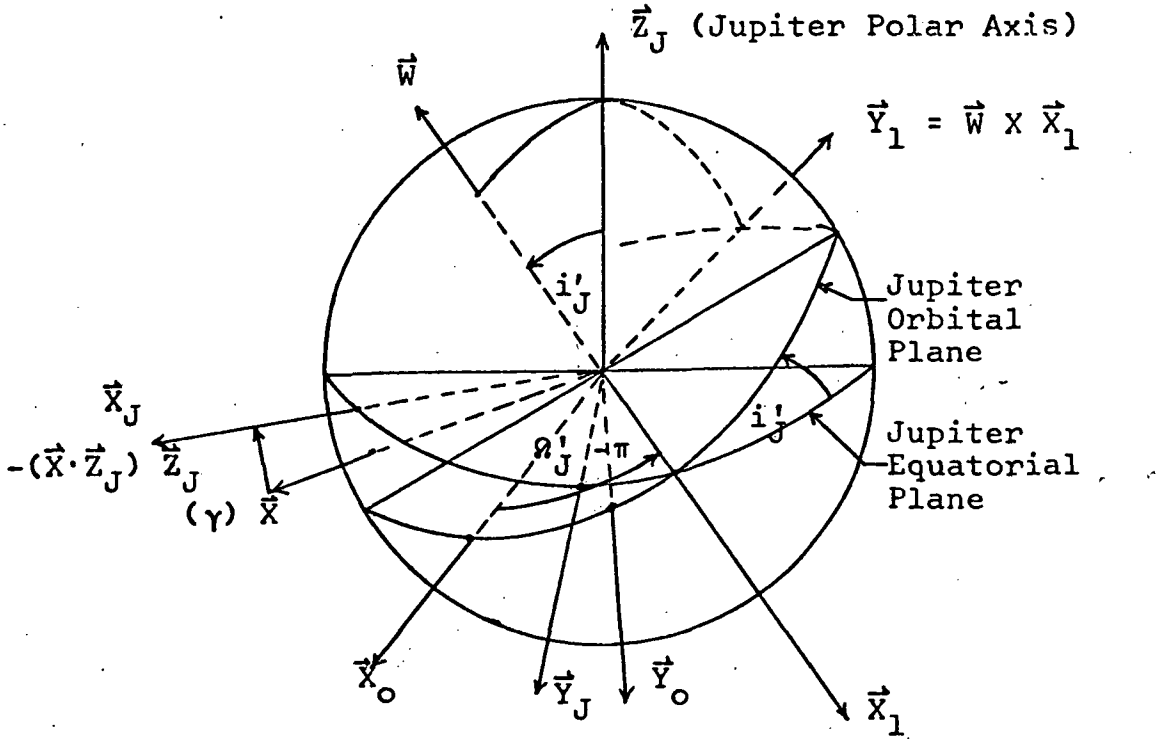

(2) Geometric Relations between Jupiter Orbital and Jupiter Equatorial Planes

Figure III-12: Geometry for Jupiter Equatorial Axes

completes the right handed system and lies in Jupiter's orbital plane. The orthogonal vectors $\overline{W}$ and $\overline{Y}_1$ now define a meridional plane of Jupiter, a plane containing $\overline{Z}_J$, with $\overline{W}$ and $\overline{Z}_J$ inclined to each other by the inclination angle i_J'. Thus, Jupiter's polar axis ($\overline{Z}_J$) is given by:

$$\overline{Z}_J = \text{Sin } i_J' \, \overline{Y}_1 + \text{Cos } i_J' \, \overline{W}$$

$$\overline{X}_J = \frac{\overline{X} - (\overline{X} \cdot \overline{Z}_J)\overline{Z}_J}{||\overline{X} - (\overline{X}.\overline{Z}_J)\, \overline{Z}_J||}$$

$$\overline{Y}_J = \overline{Z}_J \times \overline{X}_J$$

Two transformations can now be developed between the $(\overline{R}_{per}/R_{per}, \overline{M}, \overline{N})$ and $(\overline{X}_J, \overline{Y}_J, \overline{Z}_J)$ coordinate systems, one transformation containing elements which are functions of the desired (i, Ω, ω) angles, the second containing dot-product (direction cosines) of the coordinate system vectors. Thus, the orbital angles can be determined:

$$\text{Cos } i = \overline{N} \cdot \overline{Z}_J \quad (0 \leq i \leq \pi)$$

$$\text{Sin } \Omega = \frac{\overline{N}.\overline{X}_J}{\text{Sin } i} \;, \quad \text{Cos } \Omega = \frac{-\overline{N}.\overline{Y}_J}{\text{Sin } i} \quad (0 \leq \Omega \leq 2\pi)$$

$$\text{Sin } \omega = \frac{\overline{R}_{per}.\overline{Z}_J}{R_{per} \text{Sin } i} \;, \quad \text{Cos } \omega = \frac{\overline{M}.\overline{Z}_J}{\text{Sin } i} \quad (0 \leq \omega < 2\pi)$$

Figures III-13, 14, and 15 show the perspective views of the trajectories near perijoves of 1.1. R_J and 4 R_J.

(d) Orbital Trim Velocities

Orbital trim is defined as any deliberate maneuver of JOSE to vary its orbit about Jupiter. Two types of orbital trim are practical; the first, requiring a velocity change ΔV_5 reduces the inclination i of the SC orbit

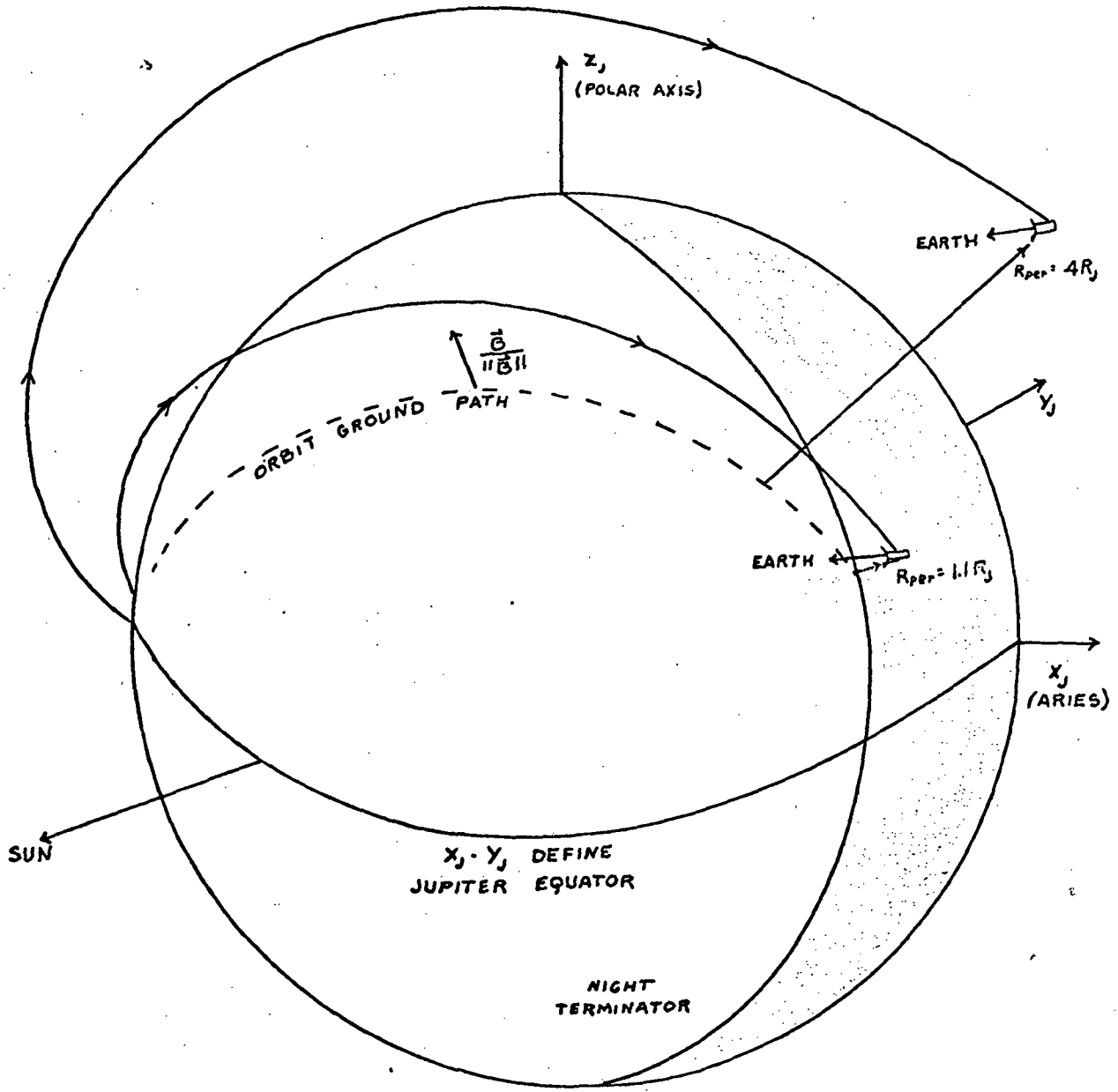

ORBIT PARAMETERS: INCLINATION : $i = 63.8°$
LONGITUDE OF ASCENDING NODE : $\Omega = 177.5°$
ARGUMENTS OF PERIJOVE : $\omega = 171.7°$ for $R_{per} = 1.1 R_J$
$\omega = 158.8°$ for $R_{per} = 4 R_J$

Figure III-13: 1975 Perspective View of Approach Hyperbola JOSE at Perijove - R_{per} = 1.1 and 4 R_J

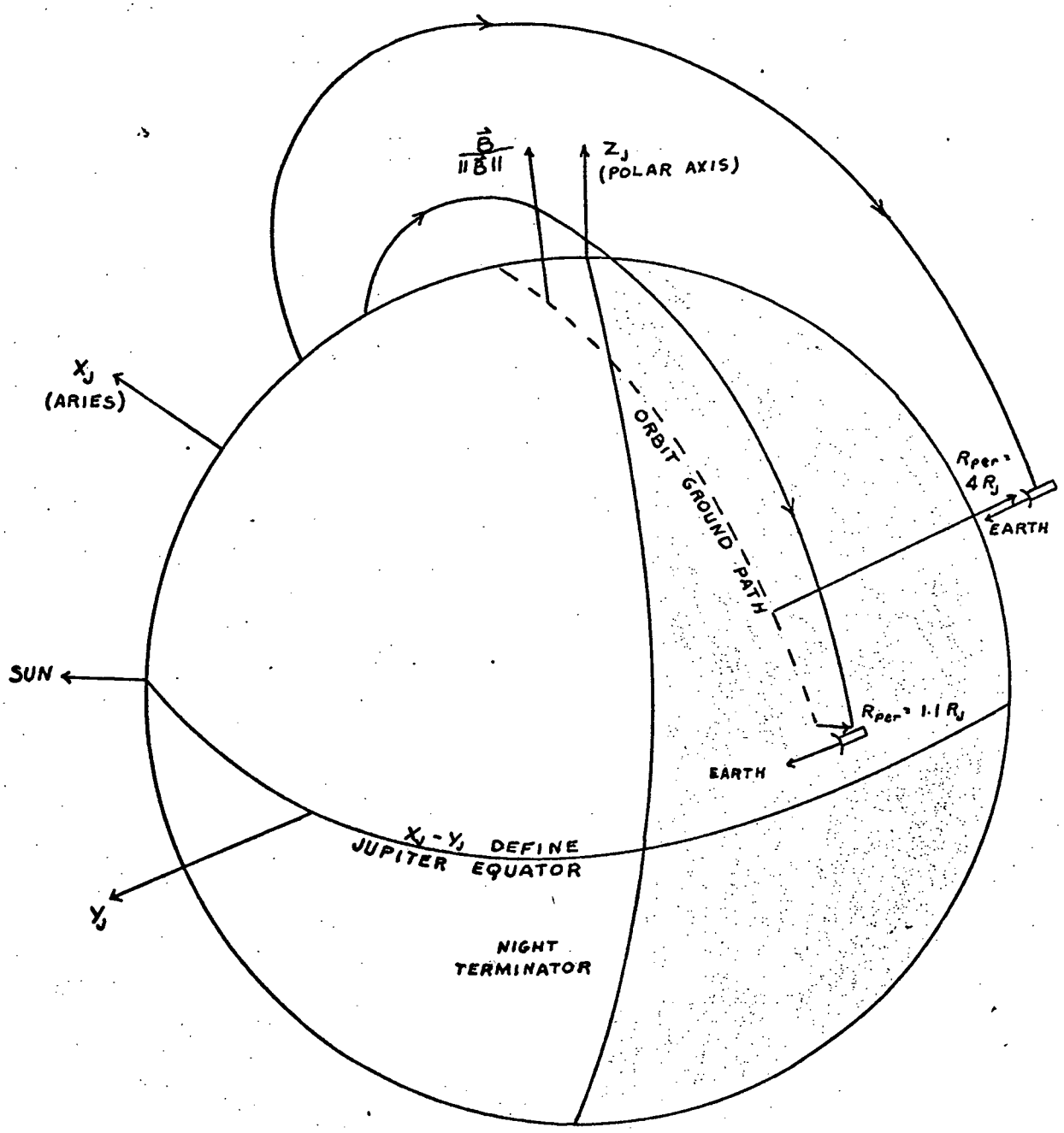

ORBIT PARAMETERS : INCLINATION : i = 77.7°
LONGITUDE OF ASCENDING NODE : Ω = 349.5°
ARGUMENTS OF PERIJOVE : ω = 168.2° for R_{per} = 1.1 R_J
ω = 154.8° for R_{per} = 4 R_J

Figure III-14: 1980 Perspective View of Approach Hyperbolas, JOSE at Perijove - R_{per} = 1.1 and 4 R_J

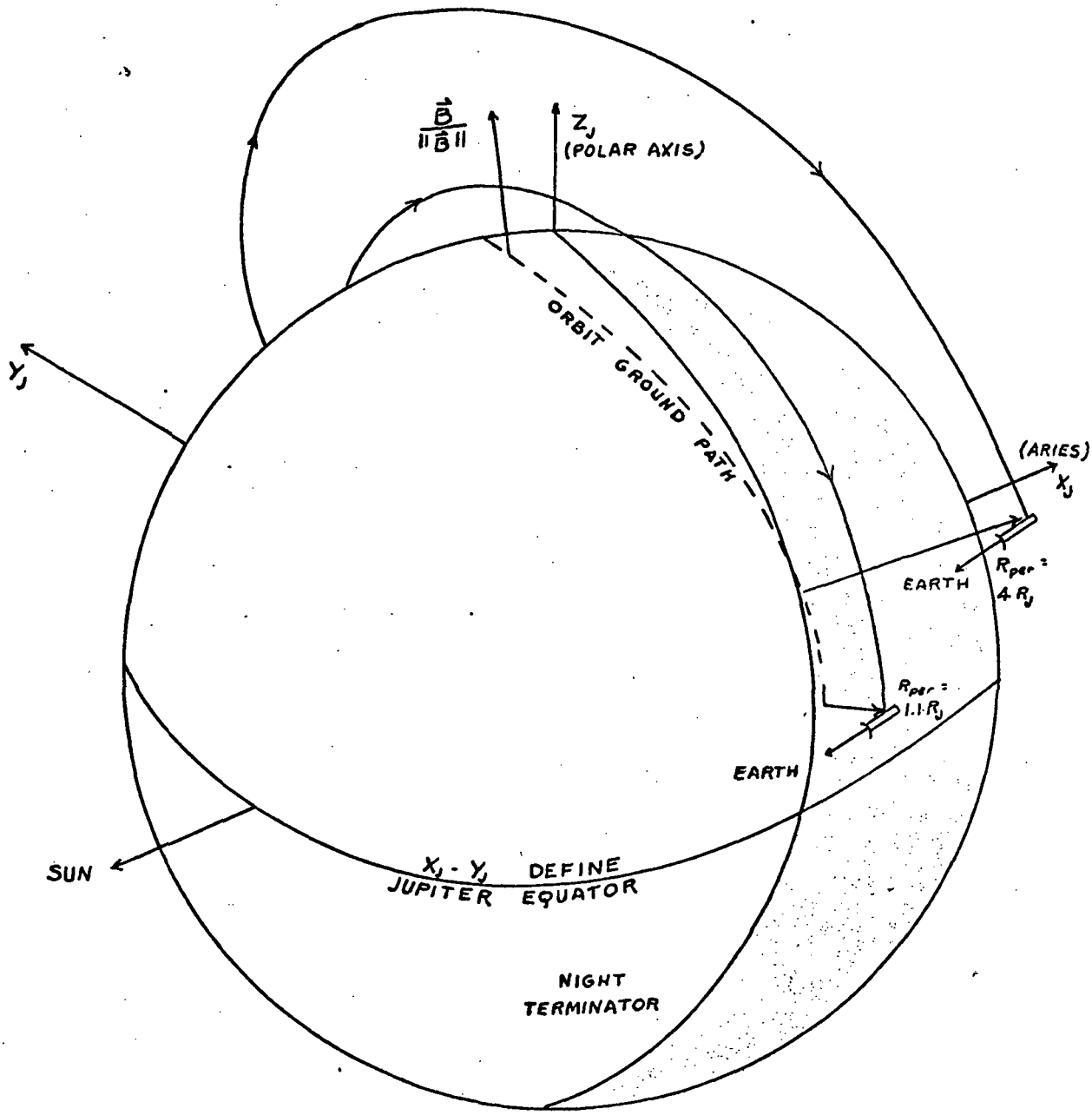

ORBIT PARAMETERS: INCLINATION: $i = 83.2°$
LONGITUDE OF ASCENDING NODE: $\Omega = 118.8°$
ARGUMENTS OF PERIJOVE: $\omega = 164.4°$ for $R_{per} = 1.1\ R_J$
$\omega = 150.7°$ for $R_{per} = 4\ R_J$

Figure III-15: 1985 Perspective Veiw of Approach Hyperbola, JOSE at Perijove - R_{per} = 1.1 and 4 R_J

to 0°; the second, requiring a velocity change ΔV_6, changes the apojove R_a of the orbit.

For the inclined 1975, 1980, and 1985 orbits, ΔV_5 is large since the inclinations are high. For a one-maneuver inclination change, ΔV_5 must be applied at one of the nodes. The ascending node is naturally chosen since the SC velocity V is much smaller there than at the descending node near perijove. The magnitude (R) of the vector from Jupiter to the ascending node is of course:

$$R = \frac{a(1-e^2)}{1+e \cos \omega} \qquad \text{(III-2)}$$

where: a and e are the semi-major axis and eccentricity of the SC orbit about Jupiter.

ω is the argument of perijove.

Noting that:

$$a = \frac{R_a + R_{per}}{2}$$

$$e = \frac{R_a - R_{per}}{R_a + R_{per}} \qquad \text{(III-3)}$$

Thus:

$$R = \frac{2 R_a R_{per}}{R_a + R_{per} + (R_a - R_{per}) \cos \omega}$$

Thus, the SC velocity (V) at R is

$$V = \sqrt{2GM_J \left(\frac{1}{R} - \frac{1}{R_a + R_{per}} \right)} \qquad \text{(III-4)}$$

The ΔV_5 required to rotate $\overline{V}$ by an angle i is:

$$\Delta V_5 = V \sqrt{2(1-\cos i)}$$

Although it is fortunate that the arguments of perijove of all three trajectories are close to 180° (hence, one node is located at a point on the orbit where V is close to a minimum), Figure III-16 indicates that the ΔV_5

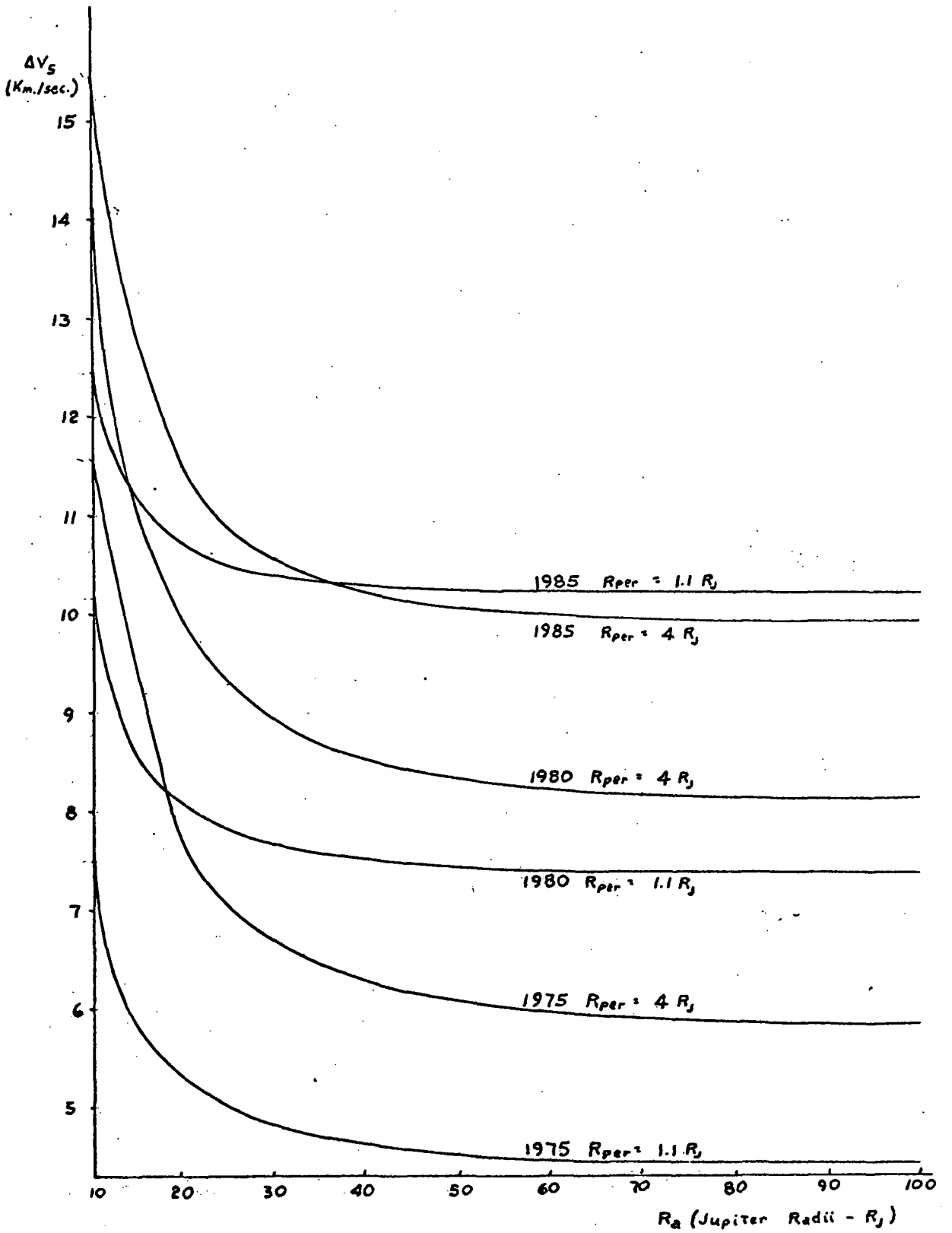

Figure III-16: Orbital Trim Velocity Requirements as a Function of Apoapsis Distance

are still extremely large. For this reason, inclining the orbits all the way into Jupiter's Equatorial plane is probably impractical, hence Figure III-17 indicates the percentage of ΔV_5 from Figure III-16 necessary to incline the original SC orbits any number of degrees. Thus, for example, to incline the 1980-1.1 x 100 R_J orbit into Jupiter's Equator requires 7.34 km/sec. If instead it is desired to reduce the inclination to 30°; i.e., to decrease the 1980 inclination of 77.7° by 47.7°, 65.3% of ΔV_5, or (.653)(7.34) = 4.79 km/sec is required. Inclination changes into Jupiter's Tropical Zones are seen to be very expensive in terms of propellant.

A more optimistic remark is in order at this point. If the mission trajectory engineers do not favor highly inclined orbits such as the three selected here, a small additional boost to ΔV_3 can be made at JOSE's arrival at Jupiter's sphere of influence such that JOSE will be in Jupiter's Equator upon arrival at perijove, as mentioned in Section B-3. Now any inclination changes made later in the mission will be from equatorial to inclined orbits; corresponding ΔV_5 will be much less than those shown in Figure III-16 since ΔV_5 can be made at apojove for the equatorial orbit where SC velocity (V) is a minimum.

Another highly desirable type of orbital trim is the reduction of apoapsis after several orbits. Assuming initial orbits of 1.2 x 100 R_J and 2 x 100 R_J, Figures III-18 and 19 indicate the velocity correction ΔV_6 necessary to reduce the apoapsis R_a = 100 R_J to various R_a' down to 10 R_J. This type of trim is desirable since the propulsion expenditure is relatively small. As seen by the figures, perijove is the ideal point on the orbit to slow down the velocity. The period of the final orbit in days corresponding to R_a' is given at the top of the figures.

In computing ΔV_6 for anomalies (v) other than 0°, the following

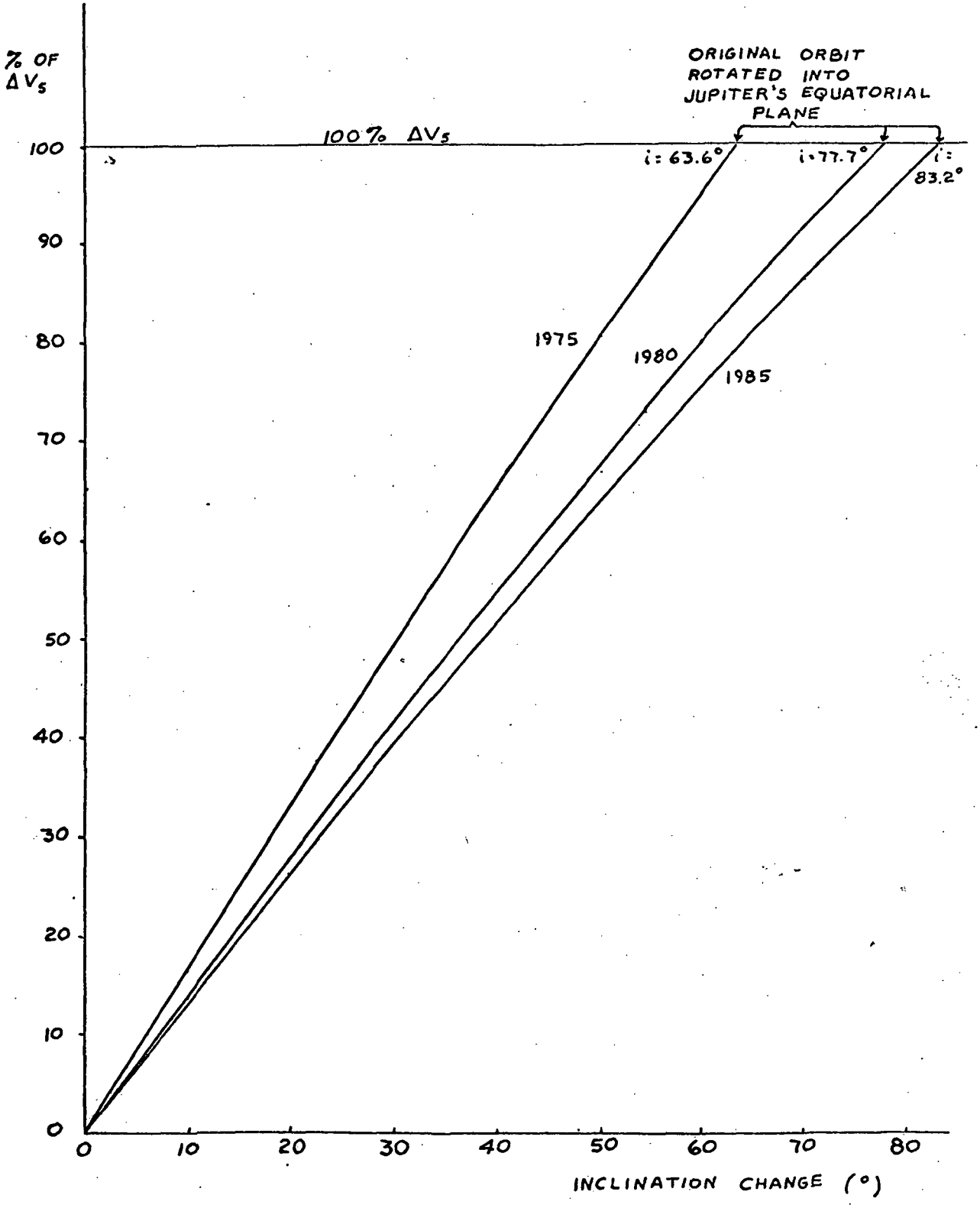

Figure III-17: Percent of Orbital Trim Velocity Required as a Function of Desired Orbit Inclination Change.

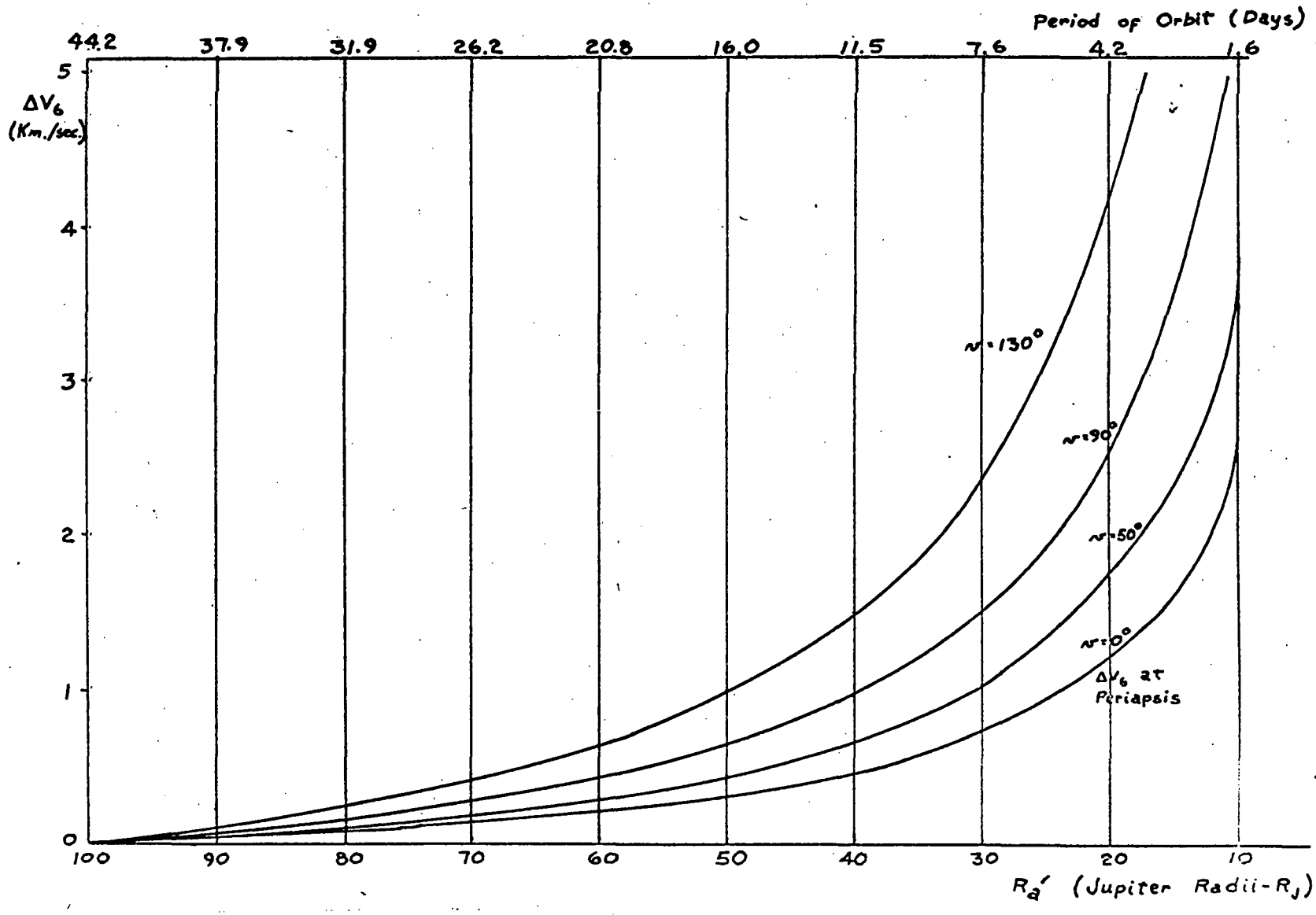

Figure III-18: Velocity Correction to Reduce Apoapsis from 100 R_J to R'_a. v is the True Anomaly of the Maneuver Point. $R_{per} = 1.2\ R_J$

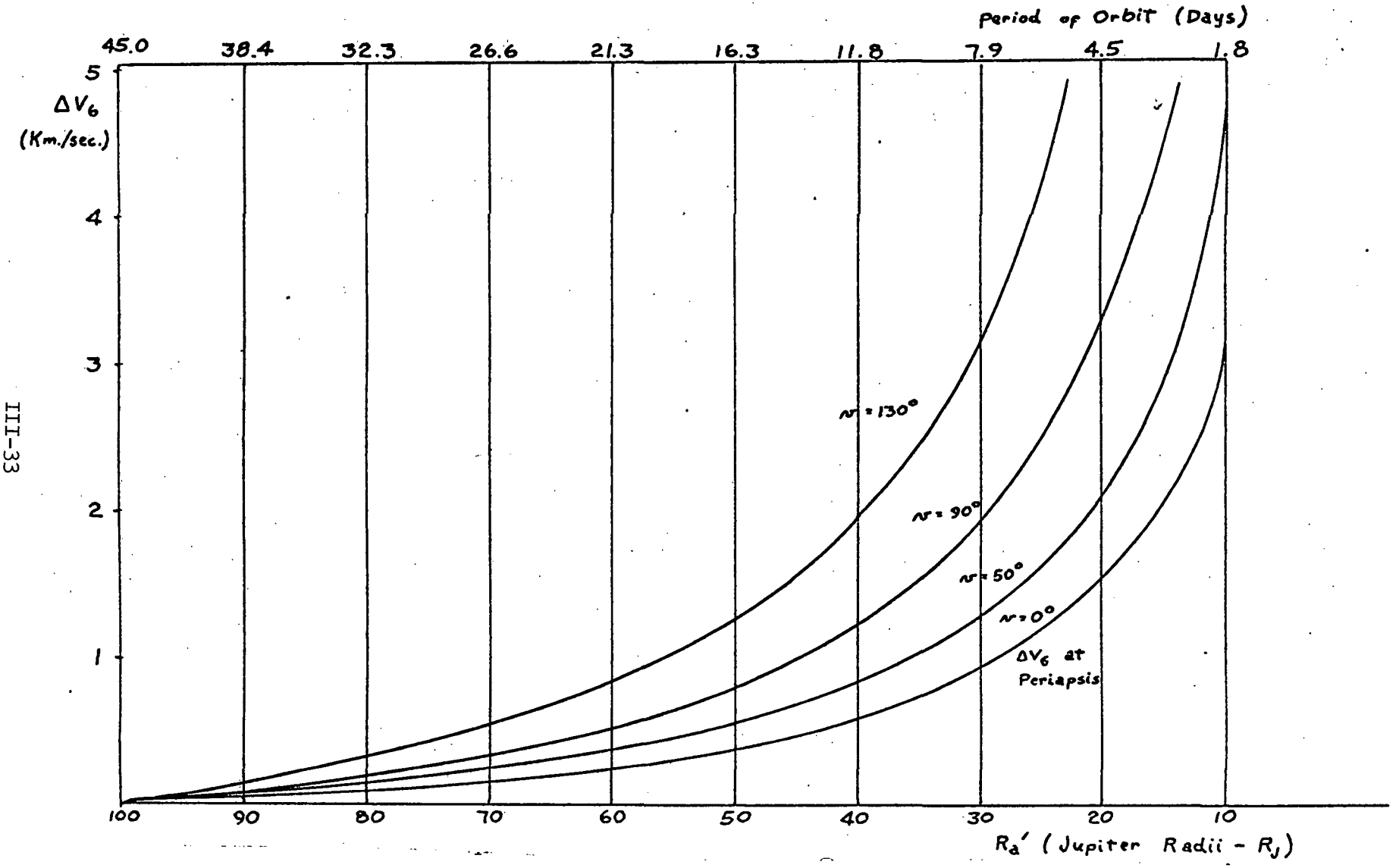

Figure III-19: Velocity Correction to Reduce Apoapsis from 100 R_J to R_a'. v is the True Anomaly of the Maneuver Point. $R_{per} = 2\ R_J$

simplification was employed. A velocity vector $\overline{V}_T$ was computed at the point (v, R) of the initial ellipse, $\overline{V}_T$ defining the transfer ellipse on which JOSE must travel to arrive at the new apojove R_a'. Actually, a directional change in the velocity vector at R_a' is in order since the major axes of the transfer ellipse and the final R_{per} x R_a' ellipse are not completely colinear. This second velocity increment was ignored as it is negligible compared to ΔV_6 applied at (v, R) at the start of the transfer ellipse. This increment at R_a' is very small since all three ellipses; i.e., the intial R_{per} x 100 R_J, the transfer, and the final R_{per} x R_a'; are nearly colinear for anomalies less than or equal to 130° (all the ellipses are extremely flat). Thus the assumption that the major axis of the transfer ellipse is colinear with the major axis of the initial and final ellipses is reasonable and a corresponding velocity rotation at R_a' is ignored. See Figure III-20.

The formulation is as follows: For each orbit and for each selected value of the true anomaly v from 0° to some maximum practical value, equations (III-3) and (III-2) are solved in that order for the initial orbit to obtain a, e, and R . A maximum practical value of v, v_m, implies that, for $v > v_m$, ΔV_6 is excessive since the transfer point of the original ellipse is all ready greater than R_a' from Jupiter and the transfer direction is essentially opposed to the motion of the ellipses.

A good cutoff point for v_m is:

$$\text{Cos } v_m = \frac{-R_a' (R_a + R_{per})}{R_a'(R_a - R_{per}) + 2 R_a R_{per}}$$

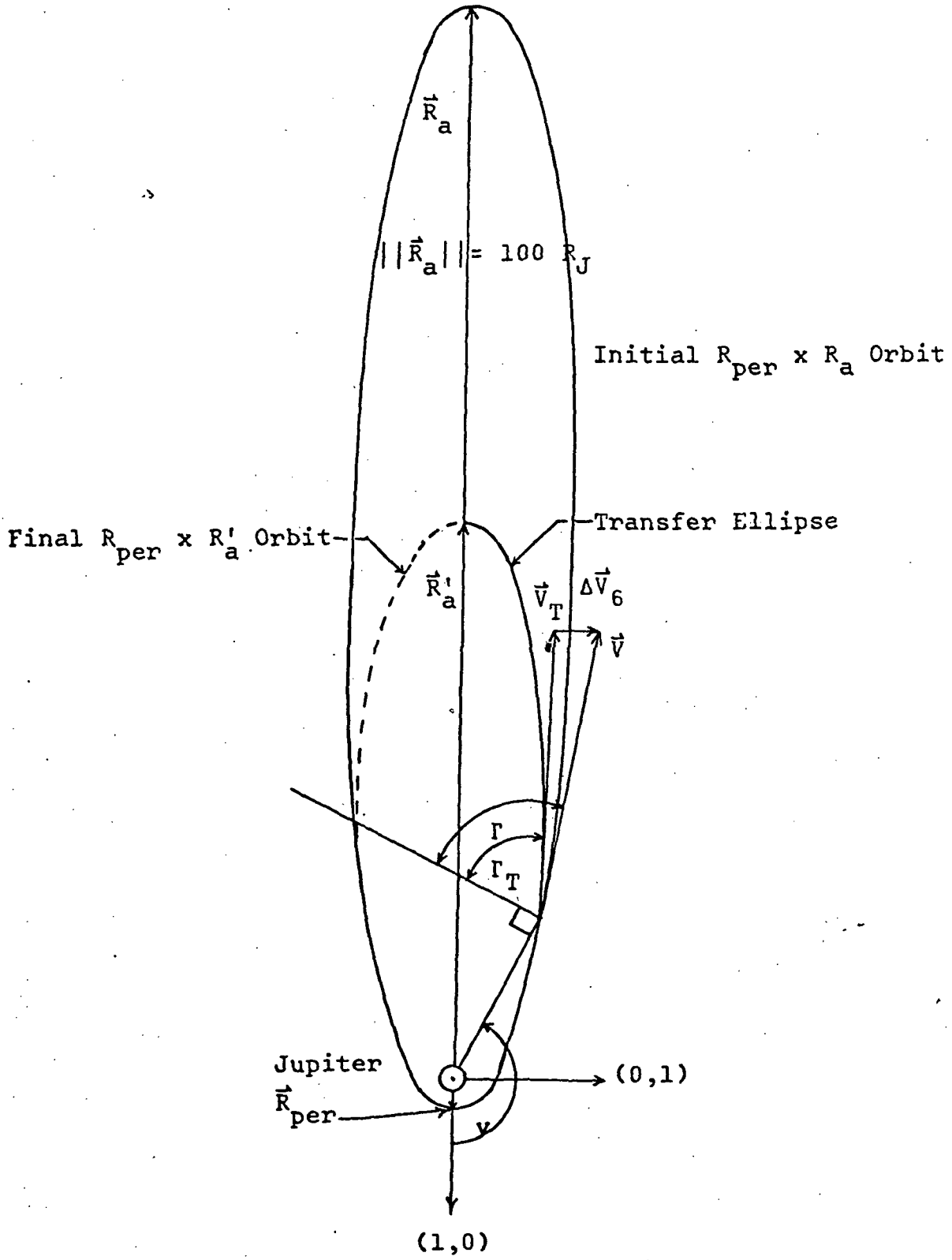

Figure III-20: Geometry of the Apoapsis Trim

The path angle Γ, described and formulated in Section A of this chapter, is:

$$\text{Sin } \Gamma \quad \sqrt{\frac{R}{(1-e^2)(2a-R)}} \quad e \text{ Sin } v \qquad (0 \leq \Gamma \leq \frac{\pi}{2})$$

The velocity(V)at R on the initial ellipse is given by equation (III-4). Since the orbits can all be considered in two-dimensional space, a coordinate system can be defined centered at Jupiter's center, the (1,0) vector pointing along $\overline{R}_{per}$, the (0,1) vector at $v = \frac{\pi}{2}$ from $\overline{R}_{per}$. Then the velocity vector $\overline{V}$ at R on the initial ellipse is given by:

$$\overline{V}^T = V\ (-\text{Cos}\Gamma\text{Sin}v + \text{Sin}\Gamma\text{Cos}v,\ \text{Cos}\Gamma\text{Cos}v + \text{Sin}\Gamma\text{Sin}v)$$

Subsequent derivations with the aforementioned simplifying assumption yields for the transfer ellipse the eccentricity e':

$$e' = \frac{R'_a - R}{R'_a + R \text{ Cos } v}$$

The transfer ellipse semi-major axis is:

$$a' = \frac{R'_a(R'_a + R \text{ Cos } v)}{2R'_a - R(1 - \text{Cos } v)}$$

The magnitude of the velocity ($\overline{V}_T$) is:

$$V_T = \sqrt{GM_J\ (\frac{2}{R} - \frac{1}{a'})}$$

Again, the path angle (Γ_T) at the transfer point relative to the transfer ellipse is given by:

$$\text{Sin } \Gamma_T = \sqrt{\frac{R}{(1-e^2)(2a'-R)}}\ e' \text{ Sin } v \qquad (0 \leq \Gamma_T \leq \frac{\pi}{2})$$

The transfer velocity vector ($\bar{V}_T$) is:

$$\bar{V}_T{}^T = V_T(-\text{Cos}\Gamma_T\text{Sin}v + \text{Sin}\Gamma_T\text{Cos}v,\ \text{Cos}\Gamma_T\text{Cos}v + \text{Sin}\Gamma_T\text{Sin}v)$$

Thus, $\Delta V_6 = ||\bar{V} - \bar{V}_T||$

Finally, the period P is:

$$P = \sqrt{\frac{a^3}{GM_J}}\,2\pi = \sqrt{\frac{\left(\frac{R'_a + R_{per}}{2}\right)^3}{GM_J}}\,2\pi$$

5. Conclusions

After considerable coordination between fields and particles (F & P) objectives and planetary scanning instruments (PSI) objectives, initial orbits having periapsis around 1.1 to 1.25 R_J and apoapsis at 100 R_J seem to be optimum. There are definitely opposing interests between F & P and PSI. F & P objectives require very low periapsis altitudes to measure the maximum planetary radiation flux and extremely high apoapsis distances to ensure that the SC passes through the Solar Plasma Shock Wave. F & P also tend to favor equatorial orbits for resolution of decametric radiation effects of Jupiter's ionosphere. Long periods of time at an apoapsis of 100 R_J is wasteful with respect to planetary imaging, however, and close periapsis in the maximum radiation flux is seriously detrimental to PSI lenses and other components. PSI would prefer orbits with about 6 R_J x 50 R_J parameters; inclination to Jupiter's Equator is not critical for PSI providing a few good passes over the Red Spot are possible. Orbits of a more circular curvature (for example, 5 x 25 R_J) and high inclination are desirable from a celestial mechanics (CM) point of view; i.e., for the determination of Zeodetic mass, size, and gravitational harmonics by measurements of orbit perturbations. Further limiting of Jupiter orbits are performed later when science objectives are described.

Chapter III, Bibliography and References

1. Battin, Richard H., Astronautical Guidance, McGraw-Hill Book Co, New York,New York, 1964.

2. Clarke, V.C., Jr., Bollman, W.E., Feitis, P.H., Roth, R.Y., "Design Parameters for Ballistic Interplanetary Trajectories, Part II. One Way Transfers to Mercury and Jupiter",Technical Report No. 32-77, Jet Propulsion Laboratory, Pasadena, California, January 15, 1966.

3. Crabill, N.L., Mayo, W.L., "Lunar Orbiter Mission Design", paper presented at the Sixth Annual AIAA Aerospace Sciences Meeting Session on Astromechanics, New York, New York, January 22, 1968.

4. Jones, M.F., "Trajectories to the Outer Planets via Jupiter Swingby", NASA CR-61186, prepared by Lockheed Missiles and Space Co. for the George C. Marshall Space Flight Center, January, 1968.

5. Jordan, James F., "The Application of Lambert's Theorem to the Solution of Interplanetary Transfer Problems", Technical Report No. 32-521, Jet Propulsion Laboratory, Pasadena, California, February 1, 1964.

6. Luidens, Roger W., Miller, Brent A., and Kapproff, Jay M., "Jupiter High Thrust Round Trip Trajectories", NASA TN D-3739, Lewis Research Center, Cleveland, Ohio, December, 1966.

7. Miller, B.J., Abbott, A.S., Guidance, Flight Mechanics, and Trajectory Optimization, Vol II - Observation Theory and Sensors, NASA CR-1001, prepared by North American Aviator, Inc., for the George C. Marshall Space Flight Center, March, 1968.

8. Niehoff, J., "An Analysis of Gravity Assisted Trajectories in the Ecliptical Plane", Report No. T-12, prepared by the Astro Sciences Center of IIT Research Institute for the Lunar and Planetary Programs Office, NASA Headquarters, Washington, D.C., Contract No. NAS r-65(06), May 25, 1965.

Chapter IV: Attitude Control

A. Introduction and Summary

The mass and inertial properties of the two JOSE configurations dictate a three-axis stabilized control system. Spin stabilization is briefly investigated in this chapter, but this attitude control is shown to be insufficient for JOSE. Attitude control is then maintained about the three-mutually orthogonal SC X, Y, Z axes, rotations about which are termed pitch, yaw, and roll respectively. Pitch and yaw are referenced to the sun (sun-probe line defined by Z axis) and roll is referenced to the star Canopus. Deviations in the roll axis-sun pointing are sensed by coarse sun sensors and fed to the control electronics. If the deviation in pitch or roll exceeds some specified value (called the "deadband"), the switching amplifier activates a solenoid valve in the gas subsystem allowing cold nitrogen gas to flow through a nozzle, thus applying torque to the spacecraft in a direction to reduce the detected diviation. The spacecraft is said to limit cycle within the deadband.

Possible supplementary methods of attitude control during the interplanetary cruise phase which might feasibly be employed to reduce cold gas consumption in the limit cycle mode are:

(1) Spin stabilization excluded

(2) Gyros

(3) Inertia Wheels

(4) Solar Vanes (or sails)

Spin stabilization was subsequently ruled out for three reasons: (a) The large mass and inertial properties of JOSE result in relatively high propulsion requirements for spinup and despin maneuvers, (b) the approximate equality of X,Y and Z axis moments of inertia result in high precession rates about any spin

axis and (c) sensitive instruments are located on the peripheral areas of the SC thus receiving the maximum radial acceleration forces during spin. Spin stabilization is certainly ruled out during planetary encounter due to the reduction in scanning instrument resolution in the spinning mode.

A gyro control assembly (GCA) is considered an absolute necessity. The GCA is a component of the larger SC Autopilot, which also includes the autopilot electronics assembly, and the thrust vector control assembly (TVCA) composed of four jet vane actuators (JVA) and a mounting ring. The autopilot is only used for control prior to cruise mode acquisition, during mid-course maneuvers, and during Jupiter occultation at encounter. The autopilot electronics processes the three gyro "rate plus position" outputs, transforming these error signals into appropriate deflection commands for the JVA's. Each actuator contro the position of an aerodynamically neutral jet vane in the exhaust stream of the post-injection propulsion system (PIPS) engine. These vanes thus generate, as a function of their position, corrective torques which maintain SC attitude. Prior to cruise mode acquisitions, the gyro control assembly dampens pitch, yaw, and roll motions of the SC and facilitates roll axis sun acquisition and Canopus lock. The gyro system is then shut down for the long cruise period, except for control during mid-course maneuvers and emergency sun or Canopus loss by the sun sensor or Canopus star tracker. The literature is rich with details concerning gyro assemblies, gyrodynamics, coarse and fine sun sensors, star trackers, and planet sensors. They are all state-of-the-art and have been extensively analyzed and employed on Mariners IV, V and Venus 67. This report will not detail this hardware, but will indicate their attitude control interfacing in the conclusion of this chapter.

The implementation and feasibility analysis of supplementing cold gas contro with inertia wheel angular momentum transfer is considered in detail within this

chapter. The advantage of X and Y axis inertia wheels is marginal in this case for the Earth to Jupiter cruise phase; however, the additional attitude control necessary during orbital apojove favors the addition of inertia wheels to the SC.

Solar vanes, although described extensively in the literature, were immediately ruled out for JOSE. The area unbalance about the SC Z axis, caused by expected errors in scan platform and RTG mounting on the SC, is large enough that excessively large solar vanes would have to be installed to counteract this unbalance. Also, the area unbalance relative to the SC center of gravity (CG) might be completely unknown at the time of cruise mode, thus the solar vanes could even be a contributing source to the area unbalance. Rotatable mirrors might be employed to alter the solar photon angle of attack; however, this necessitates the addition of servo drives and other associated machinery at or near the SC periphery.

Appendix C1 describes a typical Earth-Jupiter trajectory to define input requirements to this attitude control study.

B. Expected Disturbance Moments M in Interplanetary Space

The disturbance torques acting on the SC in interplanetary space are caused by three factors:

(1) Solar radiation pressure (photon impingement)

(2) Small meteoroid impacts (treated as a continuous pressure)

(3) Large meteoroid impacts (discrete)

1. Solar Radiation Pressure

Using a value of 13×10^{-8} psf for solar radiation pressure (p) at 1 a.u., and assuming that p varies inversely as the square of the distance from the sun, Figure IV-1 is constructed with: $p = \frac{13 \times 10^{-8}}{r_2^2}$; r_2 is the function of time. The

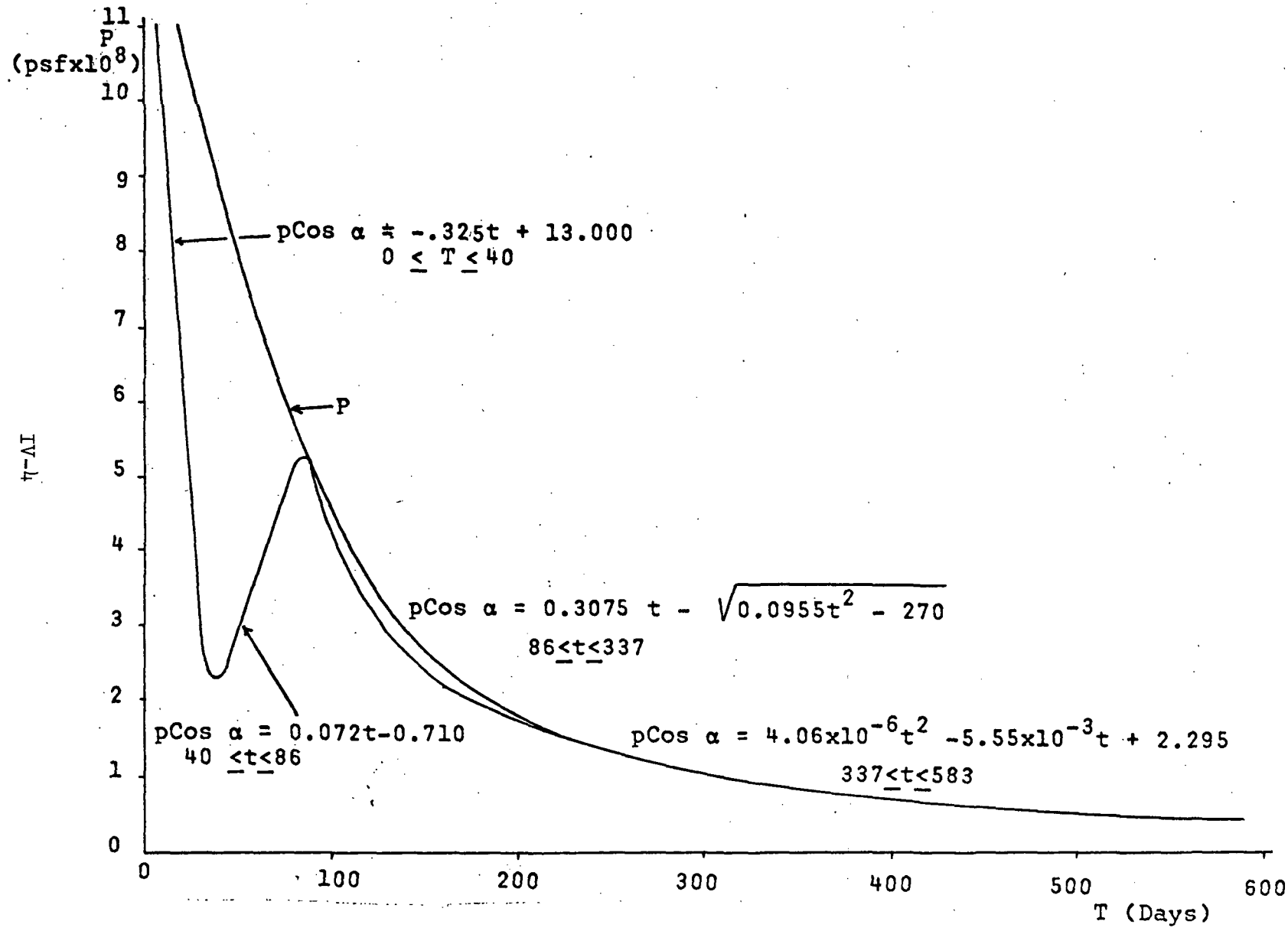

Figure IV-1: Solar Radiation Pressure (P) vs. Time (T)

curve labeled p Cos α is the component of p acting normal to the SC antenna, assuming an Earth-pointing antenna, α the solar aspect angle. p Cos α has been divided into four branches and approximating functions have been deduced for the branches for later analysis.

2. Small Meteoroid Impacts

Meteoroid impacts can be divided into small, fairly continuous colliding particles and larger, discrete meteoroid particles. The smaller meteoroids are dealt with first.

The following meteoroid particle fluxes have been observed, estimated, extrapolated, and discussed in recent years; N is the accumulative number of particles per meter^2/sec having mass greater or equal to M in grams.

Distance from Sun (a.u.)	Type of Particle	Flux N (#/meter^2/sec)	Collision Velocity (km./sec)
1-1.5	comet (10^{-8}g.)	$10^{-13.3_M-1.0}$	40
1.5-5.2	asteroid	$10^{-10_M-0.77}$	$\frac{29.8}{\sqrt{r_2}}$
5.2-5.41	comet	$10^{-14_M-1.7}$	60

It will be noted that roughly 100 lbs. was alloted in Chapter II for meteoroid protection. Noting that meteoroids will generally be approaching JOSE from the side, the projection area (A) for JOSE is measured to be 324.6 ft^2. Assuming that the meteoroid shield is to be aluminum having S.G. = 2.7, aluminum density (ρ_{AL}) is about 168.2 lbs./ft.^{3} The thickness (t) = $\frac{100 \text{ lbs.}}{\rho_{AL} A}$ = $\frac{0.595}{A}$, and t(JOSE) = 0.00183 ft.

The Charter-Sumners equation for meteoroid penetration is:

$$\frac{t}{d} = (2.28)(1.6)\left(\frac{\rho_M}{\rho_{AL}}\right)^{\frac{2}{3}} \left(\frac{V_M}{V_{AL}}\right)^{\frac{2}{3}}$$

where: t = depth of meteoroid penetration into shield

d = diameter of meteoroid particles

ρ_M, ρ_{AL} = density of meteoroid particle and aluminum respectively

V_M = velocity of meteoroid

V_{AL} = velocity of sound in aluminum

Noting the relationship among d, ρ_M, and meteoroid mass M; i.e., $M = \rho_M \frac{4}{3} \pi \frac{d^3}{8}$; and that $V_{AL} = \sqrt{\frac{Eg}{\rho_{AL}}}$, where E = aluminum modulus of elasticity (1.44×10^9 psf), g = gravitational acceleration (32.2 fps^2); the following equation is derived:

$$M = \frac{8.51 \times 10^{10} \, t^3}{\rho_M \, V_M^2}$$

Taking a value of $\rho_M = 0.4$ g/cm^3. = 25 lbs/ft^3;

$$M = \frac{3.404 \times 10^9 \, t^3}{V_M^2} \; ; \; M \text{ in lbs., } V_M \text{ in ft/sec}$$

For complete penetration of JOSE, substitute t, and: $M = \frac{874}{V_M^2}$, with M in grams and V_M in meters/sec.

Substituting V_M = 60 km/sec yields the smallest mass which will penetrate the SC hull: $M = \frac{874}{36 \times 10^8} = 2.425 \times 10^{-7}$ g.

Allowing M' to equal the mass of the smallest particle which will just penetrate 1% of the hull of JOSE, since M varies as t^3:

$$M' = 1 \times 10^{-6} \, M = 2.425 \times 10^{-13} \text{g.}$$

Letting N_M and N_M' denote the flux of particles having mass greater or equal to M and M' respectively, and computed from the flux table shown above, the total number of particles per M^2/sec having mass between M' and M is given by $N_M' - N_M$.

Since this number is relatively large, these smaller size micrometeoroids

are treated as aerodynamic pressure effects. Thus, the maximum mass flow per m^2 per sec. is given by $M (N_M' - N_M)$, and the micrometeoroid density in space is given by:

$$\rho = ATM (N_M' - N_M)/V_M$$

A is the SC area exposed to micrometeoroids and T is the mission duration of 583 days.

The aerodynamic micrometeoroid pressure experienced by the SC is then: $p = \rho V_{M/SC}^2$.

Scaling from the SC configuration the area exposed in the Z direction (solar radiation impingement), and in the XY plane (micrometeoroid impingement), and performing the above calculations, the largest possible moment about the X and Y axis produced by micrometeoroid impact is found to be about 1×10^{-7} ft. lbs. These calculations make use of Figure IV-2, which indicates the square of the micrometeoroid velocity component normal to the SC-Z axis. As a result of the scaling mentioned above, monents produced about the X and Y axes by solar radiation for JOSE are expressed as:

$$M = C\ p\ \text{Cos}\ \alpha \qquad \text{(IV-1)}$$

The C's represent area unbalances and result from expected errors of three inches in establishing area centroid colinear with SC mass C.G.

where: $C_X = 46$ ft.^{3}

$C_Y = 111$ ft.^{3}

Looking at Figure IV-1, it can readily be seen that even at t = 400 days, $M_X \approx 4.6 \times 10^{-7}$ psf, and, for a great part of the mission with t < 400 days, the solar radiation-produced moment is large enough that micrometeoroid-produced moments can be neglected.

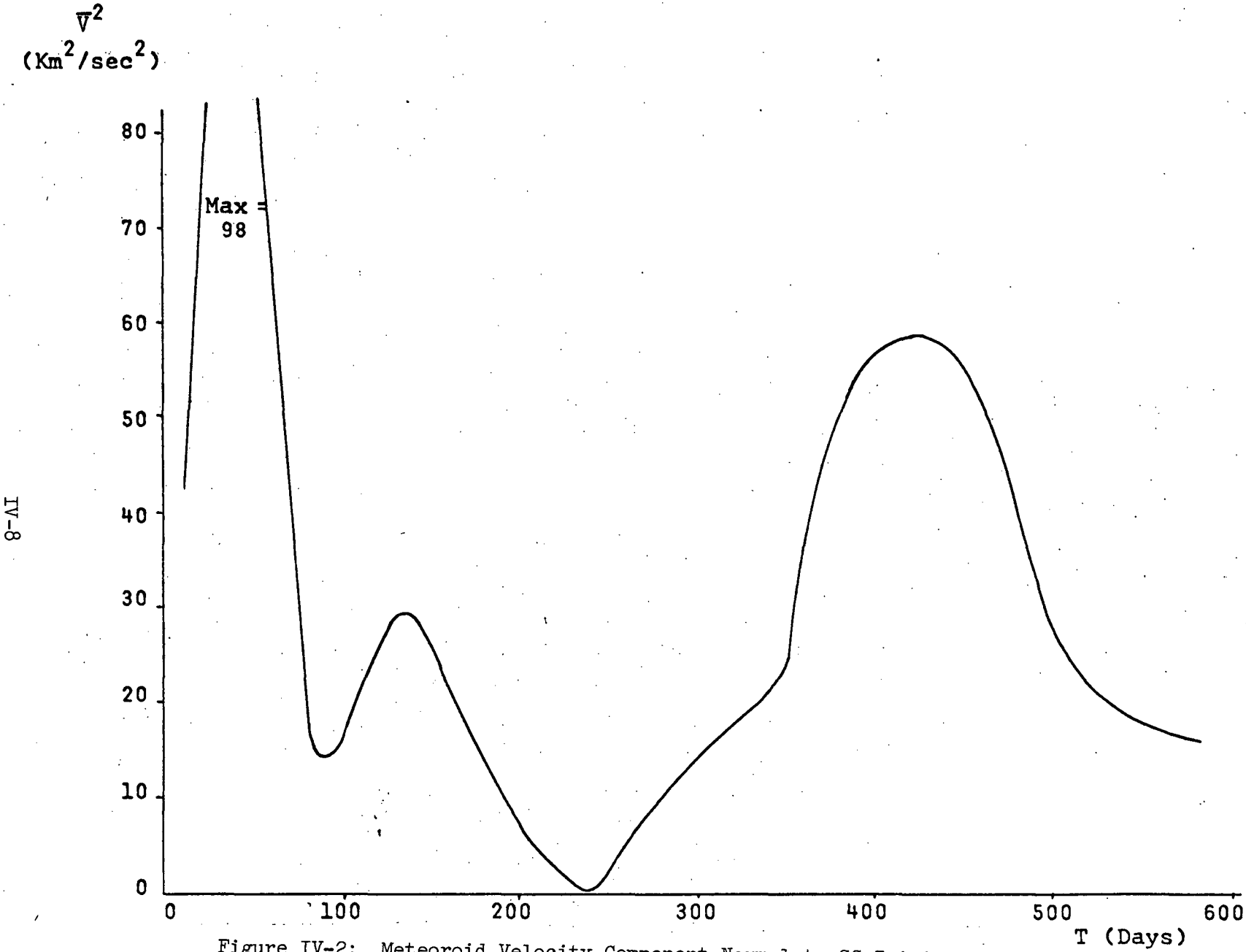

Figure IV-2: Meteoroid Velocity Component Normal to SC-Z Axis ($\overline{V} = V_{M/SC}$ Sin γ_E) Squared vs. Time

3. Large Meteoroid Impacts

The collision of large, discrete meteoroids is a different problem, however. If meteoroid distribution in solar space is assumed to follow a Poisson Distribution (justified somewhat by large population considerations), the probability of k impacts (p(k)) on an area (A) in time (t) is given by:

$$p(k) = \frac{X^k e^{-X}}{p!}$$

where: X = A T N, all terms previously defined. The logical consideration is to determine the largest particle size which the SC might probabilistically collide with during the mission duration T. Thus, with a probability $p(k) \approx 1$, and the number of impacts set at 1 (k=1), an X is desired which determines a particle mass M which is an upper bound to the particle masses with which the SC can expect to collide. It is immediately seen that, with p(1)=1, there exists no X which satisfies the Poisson formula above. Thus, the procedure is to maximize p(k), for a given k impacts, with respect to X. Thus:

$$\frac{dp(k)}{dX} = \frac{1}{k!}\left[-X^k e^{-X} + kX^{k-1}e^{-X}\right]$$

Setting this equal to 0 and solving for X:

$$X = k$$

To insure that X = k is a maximum, differentiate again:

$$\frac{d^2p(k)}{dX^2} = \frac{-k^{k-1}e^{-X}}{k!} < 0 \text{ for all } k = 1, 2, 3 \ldots$$

For k = 1 impact, X = ATN = 1, and N = 1/AT. Since the asteroid region flux is given by: $N = 10^{-10}M^{-.77}$, the upper bound on the mass size M with which the SC would be expected to collide one time is given by:

$$M = \left(\frac{A\,T}{10^{10}}\right)^{\frac{1}{.77}}$$

The exposed side area of the SC is about 180 ft^2 = 16.68 m^2. Since T = 583 days = 5.04 x 10^7 sec., AT = 8.39 x 10^8 m^2 sec. M is thus calculated to be 0.05 gms.

A particle of mass 0.05 grams traveling at a velocity relative and normal to the SC of $V_{M/SC}$ Sin $\gamma_E = \bar{V}$ and striking the SC at the furtherest point from the SC C.G. (distance r) imparts an angular impulse to the SC about the X or Y axis of $H = M\bar{V}r$ and a constant angular acceleration α. Assuming zero initial conditions, the angular velocity after time t is: $\omega = \alpha t$; and the angular position $\theta = \frac{\alpha t^2}{2}$; thus $\alpha = \frac{2\theta}{t^2}$.

In Chapter II it was seen that an angular deviation of $\pm 2^\circ$ was allowed for the Z axis due to SC high gain antenna pointing requirements. Substituting $\theta = \theta_{ALL} = 2^\circ$ above, a maximum $\alpha(\alpha_{max})$ is obtained: $\alpha_{max} = \frac{2\theta_{ALL}}{t^2}$.

The average angular velocity of SC rotation from -2° to $+2^\circ$ is given by:

$$\omega_{AVG} = \frac{d\theta}{dt} = \frac{2\theta_{ALL}}{t}.$$

Equating angular impulse to angular momentum; $H = I \frac{d\theta}{dt}$ (I = SC moment of inertia about appropriate axis of rotation); there results: $H = \frac{2I\theta_{ALL}}{t}$, and thus $t = \frac{2I\theta_{ALL}}{H}$. Placing this expression for t into the above equation for α_{max} yields: $\alpha_{max} = \frac{H^2}{2I^2\theta_{ALL}}$.

Finally, the maximum moment about the X or Y axis due to a discrete meteoroi is given by: $M = I\,\alpha_{max} = \frac{H^2}{2I\theta_{ALL}} = \frac{M^2\bar{V}^2r^2}{2I\theta_{ALL}}$ (IV-2)

For each axis, the meteoroid moment is computed by substituting the appropriate r and I. M = 0.05 grams, $\theta_{ALL} = 2^\circ = 0.0349$ radians, and $\bar{V}^2$ is given as a function of time in Figure IV-2. Scaling the maximum Z distance (r) from the configuration drawing for JOSE gives r = 10 ft. Substituting in the above moment equation and converting all units to the ft-lb-sec system results in the following moments due to discrete meteoroid impacts as function of $\bar{V}^2$.

$M = 1.367 \times 10^{-4} \bar{V}^2$, M in ft. lbs., $\bar{V}^2$ in km^2/sec^2.

4. Summary of Disturbing Moments

Thus, the expected total moment affecting the SC in interplanetary space consists of a continuous solar radiation moment and an intermittent moment produced by high velocity, large, discrete meteoroid - SC impacts.

Summarizing;

$$M = \begin{pmatrix} C_X \\ \text{or} \\ C_Y \end{pmatrix} p \cos \alpha + 1.367 \times 10^{-4} \bar{V}^2$$

5. Consideration and Exclusion of Spin Stabilization

It is interesting to note at this point that spin stabilization is feasible in opposing the continuous solar radiation-produced moments, although a gas jet control system would still have to be incorporated to oppose large discrete meteoroid impacts. The validity of this statement can be shown by the following argument:

Assuming 10 g's (10×32.2 fps^2) as the maximum tolerable acceleration which a SC component on the periphery of the SC (for example, at a distance of eight feet from the Z axis of the SC) can withstand, the allowable spin velocity (ω) of the SC is found to be:

$$\omega = \sqrt{\frac{(10)\ (32.2)}{8}} = 6.35 \text{ rad/sec} \approx 60 \text{ rpm.}$$

The spin angular momentum of JOSE about the Y axis is $H = I_Y \omega = 8190$ ft.lb.sec.

The precession equation (single axis only) of a spinning mass acted upon by a moment is given by: $M_Y = H \dot{\theta}$, $\dot{\theta}$ being the resulting angular velocity about the X axis of JOSE. Since the radiation moment M_Y acts continuously with time, the total angular deviation (θ) of the SC about the X axis can be solved:

$$\theta = \frac{1}{H} \int_0^T M_Y dt = \frac{C_Y}{H} \int_0^T p \cos \alpha dt.$$

ρ Cos α has been determined as a function of t in four branches in Figure IV-1; however, the first branch is sufficient to show that θ will not exceed $\pm 2^{\circ}$ ($\pm$ 0.0349 radians) in time T = 583 days.

For the first forty days;

$$\theta = \frac{111 \times 10^{-8}}{8190} \int_0^{40} (-0.325t + 13)\, dt \; . \; 8.64 \times 10^{4} \text{ sec/day}$$

$$\theta = 0.0030 \text{ radians}$$

By observing Figure IV-1, the remaining area under the p Cos α curve from 40 days to 583 days is clearly not large enough ($\frac{.0349}{.0030}$, or 11.6 times larger than the area between 0 and 40 days) to cause θ to exceed 0.0349 radians. Thus the solar radiation moment can be successfully opposed by spin stabilization.

The unfortunate situation which rules out spin stabilization is the inertial properties of this orbiter spacecraft. The precession equations of a body spinning about more than one axis (the realistic situation) have inertial coupling terms containing $(1 - \frac{I_Z}{I_X})$ in the denominator for θ. For SC with almost equal inertias (which is generally the case with orbiters), the SC becomes extremely unstable about one axis.

C. Radiation-Produced Impulse Results

For the X and Y axis of the SC, the procedure then is to: (1) Determine the average value of solar radiation pressure (pCos α) normal to the SC antenna for each time interval (T_i) indicated by the four branches of Figure IV-1, i.e., T_1 = 40 days, T_2 = 46, T_3 = 251, T_4 = 246 days. (2) Using this average p Cos α and the appropriate C, I, and L for the SC axis, and $\Delta F = 7.48 \times 10^{-4}$ lbs., n and δt were solved. See Appendix C2 for the sizing-up of the gas jets and the limit cycle characteristics. L is the distance between corresponding attitude

jets, δt is the total time required between two successions of n jet pulses. (3) The total attitude impulse (I_{sp}) for the time interval (T_i) was finally computed by:

$$I_{sp} = \frac{2\Delta F \; 0.023n \; T_i}{\delta t}$$

where the first factor of 2 takes into account that two jets on each end of an axis must fire to produce the couple, Δ F 0.0023 n is the impulse required for n pulses of a jet, $T_i/\delta t$ is the number of times in the time period T_i that n pulses of the jets are required (equals the number of limit cycles per period). The results are summarized below in Table IV-1.

Table IV-1: Total X and Y Impulse Requirements Due to Solar Radiation Effects

Time Period (T_i)(days)	X Axis n	X Axis $\frac{T_i}{\delta t}$	X Axis I_{sp}	Y Axis n	Y Axis $\frac{T_i}{\delta t}$	Y Axis I_{sp}
0-40	417	199	2.85	479	378	6.21
40-86	302	166	1.72	347	316	3.76
86-337	215	649	4.80	248	1221	10.04
337-583	117	344	1.39	136	653	3.05
axis sub-totals			10.76			23.06
Total	33.82 Lb. Sec.					

D. Meteoroid-Produced Impulse Results

A reasonable total impulse requirement is now derived for large, discrete meteoroids. Section B3 of this Chapter deduced 0.05 grams as the upper bound of particle mass with which the SC might collide at least one time with maximum probability. The smallest size particle producing a moment just equal or greater to the solar radiation moment is computed to determine the total expected number

of large meteoroids with which JOSE will collide. Equating Eq. IV-1 and IV-2:

$$C\ p\ \mathrm{Cos}\ \alpha = \frac{M^2\ \bar{V}^2 r^2}{2I\theta_{ALL}},$$

all terms previously defined. Thus,

$$m = \frac{\sqrt{2\ C\ p\ \mathrm{Cos}\alpha\ \theta_{ALL} I}}{r\ \bar{V}}$$

where, as before, r is scaled from the Configuration drawings of Chapter II to be ten feet. Consulting Figures IV-1 and IV-2, it is seen that $\frac{p\ \mathrm{Cos}\ \alpha}{\bar{V}^2}$ reaches a minimum at about t = 420 days; p Cos $\alpha = 0.63 \times 10^{-8}$ psf, $\bar{V}^2 = 58\ km^2/sec^2$. C · I is minimum for JOSE's X axis. Thus, the smallest size meteoroid which will be considered is:

$$M = \frac{\sqrt{(2)(46)(0.63)(10^{-8})(0.0349)(1935)}}{(10)\sqrt{58}} \qquad (4.45)$$

(conversion factor)

$M = 3.65 \times 10^{-4}$ grams. Thus, the particles of concern are particles having mass M such that: 3.65×10^{-4} g. $\leq M \leq 0.05$ g.

Using the asteroid region flux formula; i.e., $N = 10^{-10} M^{-.77}$; and the areal-temporal zone (AT) swept out by the SC during the mission of $8.39 \times 10^8 m^2 sec$; the number of particles having mass $\geq 3.65 \times 10^{-4}$ g. $= 10^{-10}(3.65 \times 10^{-4})^{-.77}(8.39 \times 10^8) \approx 40$.

The number of particles having mass ≥ 0.05 g. $= 10^{-10}(0.05)^{-.77}(8.39 \times 10^8) = 1$, of course, since 0.05 grams was computed as an upper bound by flux considerations.

Thus, the total number of particles with which the SC is expected to collide in a corrider AT is 40, and these 40 particles will produce moments larger in magnitude than the continously acting solar radiation moments. These moments must be opposed by gas attitude jets. The interesting results of this probabilistic derivation of expected meteoroid impacts is that the number of impacts (4

is so low that the gas attitude jets will have to be commanded "on" for emergency control only about 40 times. For the remainder of the time in interplanetary space, the attitude jets are merely limit cycling, the period of the cycle being determined primarily by the jet pulses themselves and the solar radiation effects being lost in the limit cycle mode. For this reason, if another attitude control system could be employed during the relatively long interplanetary cruise phase such that the attitude jets could be conserved for emergency conditions and mid-course maneuvers, cold nitrogen weight and literally thousands of pulse firings during limit cycling could be eliminated from the SC. This is the basis for considering inertia wheels in section E.

The total impulse requirements for SC X, Y, and Z axes due to meteoroid collision is conservatively figured by considering 40 impacts per axis, with the point of impact being the furthest point on the SC from the C.G.(r). Estimating about 100 pulses necessary to oppose SC rotation due to meteoroid impact, the total impulse for all three axes is: $I_{sp} = (2)(0.023)(7.48 \times 10^{-4})(100)(40)(3) = 0.360$ lb. sec.

E. Inertia Wheel Analysis

1. Introduction

Inertia wheels on the X and Y axes of the SC are intended to absorb angular momentum produced by solar radiation, therefore eliminating the limit cycling of the gas attitude control jets. If a moment were applied to the SC, and the inertia wheels turned on and accelerated to maintain the SC at a selected attitude, the angular velocities of the wheels would increase until the moment was removed. The angular velocities would remain constant at those velocities existing in the wheels at the time the moment was removed. The solar radiation-

produced moment, however, acts on the SC high-gain antenna continuously with respect to time; thus X and Y axis inertia wheels continue to accelerate and the angular velocites increase without bound until they reach the wheels' tolerable maximum velocities. At this point, the wheels are said to be saturated; they can absorb no additional angular momentum, and the SC begins to lose its attitude reference. If it can be shown that the time required for an inertia wheel to reach saturation is sufficiently larger than the gas jet limit cycle, then a substantial advantage over the gas system alone can be gained by utilizing inertia wheels in conjunction with the gas jet system. The inertia wheel formulation is derived in Appendix C3.

2. Inertia Wheel Velocities

From Figure C4-1 and the tradeoff analysis of Appendix C4, the minimum total impulse occurs at $r = 2 \times 10^{-6}$ rad/sec. Then from Appendix C3, the inertia wheel equations are:

$$\omega_X(t) = -169.3(1-\text{Cos}(2\text{x}10^{-6}t)) - 100.9 \text{ Sin } (2\text{x}10^{-6}t) + 5.22\text{x}10^{-5}t$$

$$\omega_Y(t) = -100.9(1-\text{Cos}(2\text{x}10^{-6}t)) + 169.3 \text{ Sin } (2\text{x}10^{-6}t) + 2.16\text{x}10^{-5}t$$

These inertia wheel equations are conservatively taken for the entire mission, since the solar radiation pressure is maximum at launch. It is found that ω_X reaches 210 rad/sec faster than ω_Y. The former angular velocity terms are plotted in Figure IV-3. The time from inertia wheel turn-on at which the wheel reaches 210 rad/sec is indicated on the curve, the time being 8.41 days for ω_X.

3. Gas Jet With Inertia Wheels Impulse Results

The total gas impulse requirements for the SC with inertia wheels is now calculated. The optimum $r(2\text{x}10^{-6}$ rad/sec) determines the number of roll axis pulses (n_Z) and the time between successive firings (δt_Z). From previous derivations:

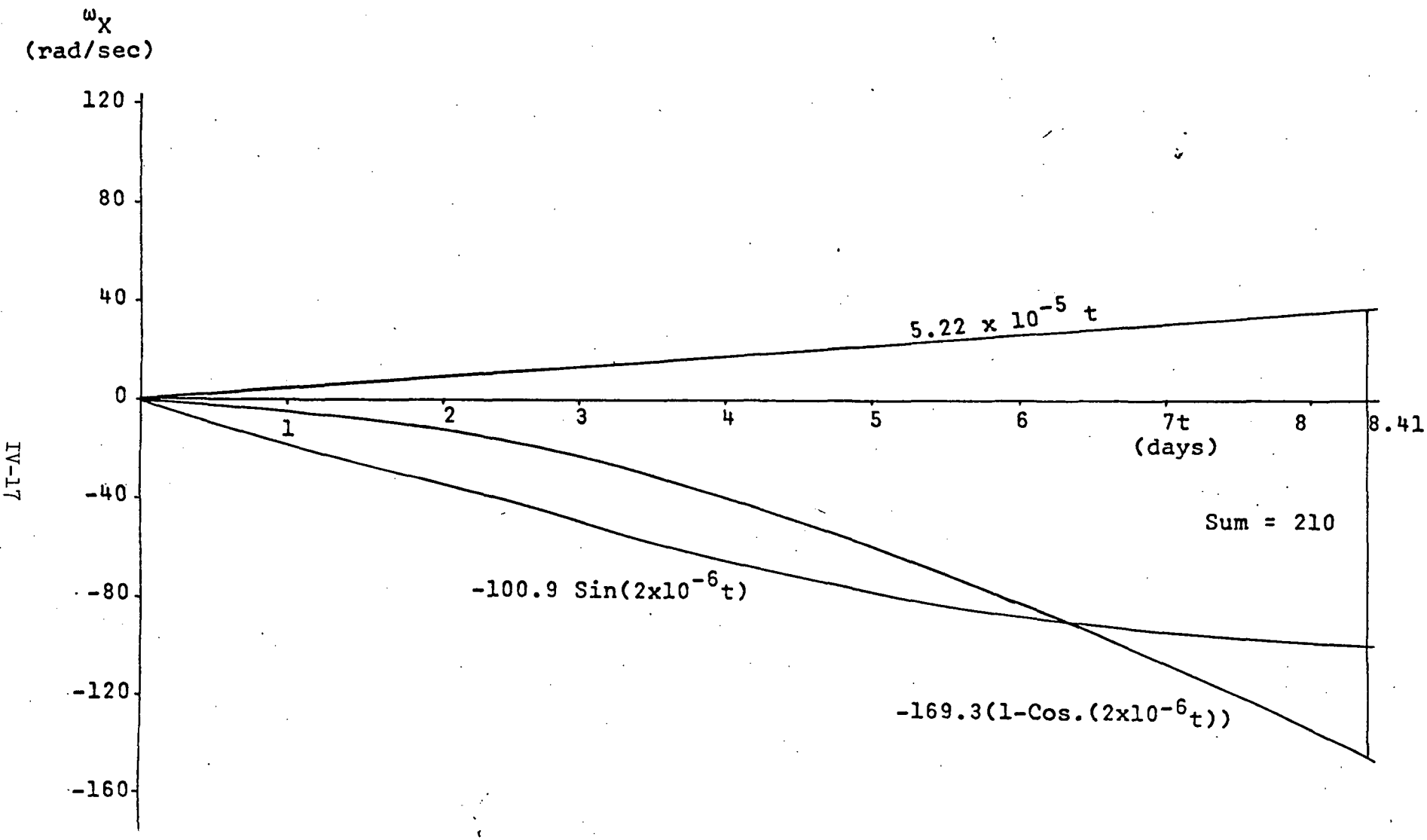

Figure IV-3: JOSE P-1 Inertia Wheel Angular Velocity (ω_X) vs. Time (t)

$$n_Z \approx \frac{r\, I_Z}{0.023\ \Delta F L_Z} = 0.1165\ \left(\frac{I_Z}{L_Z}\right)$$ for fixed ΔF and r;

$$\delta t_Z \approx \frac{0.07 \text{ sec}}{r} = 0.405 \text{ days}$$

$$n_Z \approx 30 \text{ pulses}$$

Noting the n_X and n_Y pulses for the X and Y axes respectively for each of the four time periods (T_i) of Table IV-1, the total impulse for the inertia wheel configuration is seen to be the sum of the impulses for each time period, given as $\frac{2\Delta F \cdot 0.023 n\, T_i}{t_s}$. Thus, for JOSE's X axis:

$$I_{sp} = \frac{(2)(7.48\text{x}10^{-4})(.023)}{8.41}\ \left[(417)(40)+(302)(46)+(215)(251)+(117)(246)\right]$$
$$= 0.464 \text{ lb. sec.}$$

For JOSE's Y axis:

$$I_{sp} = (4.09\text{x}10^{-6})\ \left[(479)(40)+(347)(46)+(248)(251)+(136)(246)\right] = 0.534 \text{ lb.sec}$$

For the Z axis:

$$I_{sp} = \frac{2\Delta F \cdot 0.023 n_Z T}{\delta t_Z} \text{ ; Thus,}$$

$$I_{sp} = \frac{(3.44\text{x}10^{-5})(30)(583)}{0.405} = 1.489 \text{ lb. sec.}$$

Table IV-2 summarizes the inertia wheel-attitude jet impulse requirements and the attitude jet-only system impulse requirements. Also included is the previously derived 3-axis meteoroid impulse requirement of 0.360 lb. sec.

Table IV-2: Total Impulse Requirements

SC Configuration	Cause of Disturbance	Axis	Attitude Control System Limit Cycle Jets Only (lb.sec.)	Limit Cycle Inertia Wheels (lb.sec.)
	Solar	X	10.76	.464
	Radiation	Y	23.06	.534
JOSE	Pressure	Z	1.489	1.489
		Sub-Total	35.309	2.487
	Meteoroid	(3-Axis)	.360	.360
		Total	35.669	2.847

F. Attitude System Tradeoff Analysis

It is immediately seen from Table IV-2 that the limit cycle only attitude system requires 32.822 more lbs. sec. of impulse than the inertia wheel system. The inertia wheel system has weight and power penalties associated with it, however. The penalties associated with each system are derived below.

As a function of required impulse, propellant fuel weight can be determined roughly from:

$$W_F = \frac{I_{sp}(1+\alpha_p)}{\Delta I'(1-\frac{P_f}{P_i})(\frac{T_f}{T_i})} \approx 0.665\ I_{sp}$$

where: α_p = contingency factor for $\Delta I'$ degradation

$\Delta I'$ = specific impulse per pound mass of propellant

P_f = final propellant tank pressure

P_i = initial propellant tank pressure

T_f = final propellant tank temperature

T_i = initial propellant tank temperature, and

typical values are taken for these tank and propellant parameters.

The extra weight required for the attitude jet-only system is then (.665)(32.822) = 21.8 lbs.

Inertia wheel weight is normally given as a function of the wheel's required maximum angular momentum (H_{max}). For saturation at ω = 210 rad/sec, $H_{max} = I_r \omega = (0.04)(210) = 8.4$ ft. lb. sec. Using empirical curves found in the referenced General Dynamics Jupiter Flyby report, JPL #951285, an H_{max} of 8.4 corresponds to an inertia wheel weight of roughly 16 lbs., 2 wheels yield a total of 32 lbs., which is greater than the propulsion fuel weight excess of 21.8 lbs. of the jet-only system. The power requirements of the inertia-wheel system have also not yet been considered.

Before excluding inertia wheels, however, it should be realized that for more than 40 days per SC orbit about Jupiter, the SC will be in radiation monitoring and data transmission modes. During these 40 days, the inertia wheels might feasibly be employed for attitude stabilization, since presumably maneuver requirements will not be excessive at these times. If three year orbital lifetimes are considered, then inertia wheels become very competitive with the jet-only mode.

Also, inertia wheel power requirements are now shown to be negligible. Inertia wheel power is generally a function of maximum torque generated by the wheel. Since the maximum torque $(T_{max}) = I_R \dot{\omega}\ (t)_{max}$, it is simply necessary to differentiate the ω equations with respect to t, thus determining the $\dot{\omega}$ equations for both axes of the SC. Differentiating again to find $\ddot{\omega}$, solving for that time (t) which nulls $\ddot{\omega}$, substituting this value of t into the appropriate equation for $\dot{\omega}$ and this finding the maximum $\dot{\omega}$ for the two equations, eventually results in $\dot{\omega}_{max}$ for the X axis wheel of JOSE as 0.4463×10^{-3} rad/sec.^{2} For two wheels, then, $T_{max} = (2)(0.04)(.4463 \times 10^{-3}) = 3.58 \times 10^{-5}$ ft. lbs.

From curves in the referenced Jupiter flyby report above, this results in an inertia wheel power requirement much less than 1 watt.

G. Conclusion

A loop diagram suffices to indicate the interplanetary control system. The gyro system plays a significant role, hence a slight development is produced here.

The following assumptions are necessary to the development:

(1) The gyro rotors are symmetrical about their spin axes. (X_R axis of drawing below).

(2) The gyro gimbals are symmetric with respect to the gimbals' principal axes. (X_G,Y_G,Z_G).

(3) The angular speeds of the rotors with respect to their corresponding gimbals are constant.

(4) The gimbal plus rotor system moments of inertia with respect to the two symmetric axes of this system are equal. One of these axes is the rotor spin axis (X_R),the second principal axis (Y_R) is orthogonal to the spin axis with the rotor frozen to the gimbal.

(5) In the general situation, the external torques applied about the Z_C (X_C,Y_C,Z_C are the gyro case axes) axis are considered produced by a retarding "spring" force ($-k\ \theta$), a retarding "viscous damping" force ($-c\ \dot{\theta}$), and a disturbance torque (T'_{ZC}); or:

$$T_{ZC} = -k\theta - c\dot{\theta} + T'_{ZC}$$

(6) The angular deflection θ between the X_C and X_G axes, as measured in the X_CY_C plane, is small (in practice, usually less than 1^o); such that $\text{Cos}\ \theta \simeq 1$ and $\text{Sin}\ \theta \simeq \theta$.

(7) $H\phi_x\theta$ is negligible, where: $H = I_{ROT}\Omega$, or the angular momentum of the gyro rotor, I_{ROT} = rotor moment of inertia with respect to the rotor X_R axis, Ω = the angular velocity of the rotor with respect to the gimbal; ϕ_x = angular velocity of the gimbal with respect to the X_C axis; and θ defined in (6).

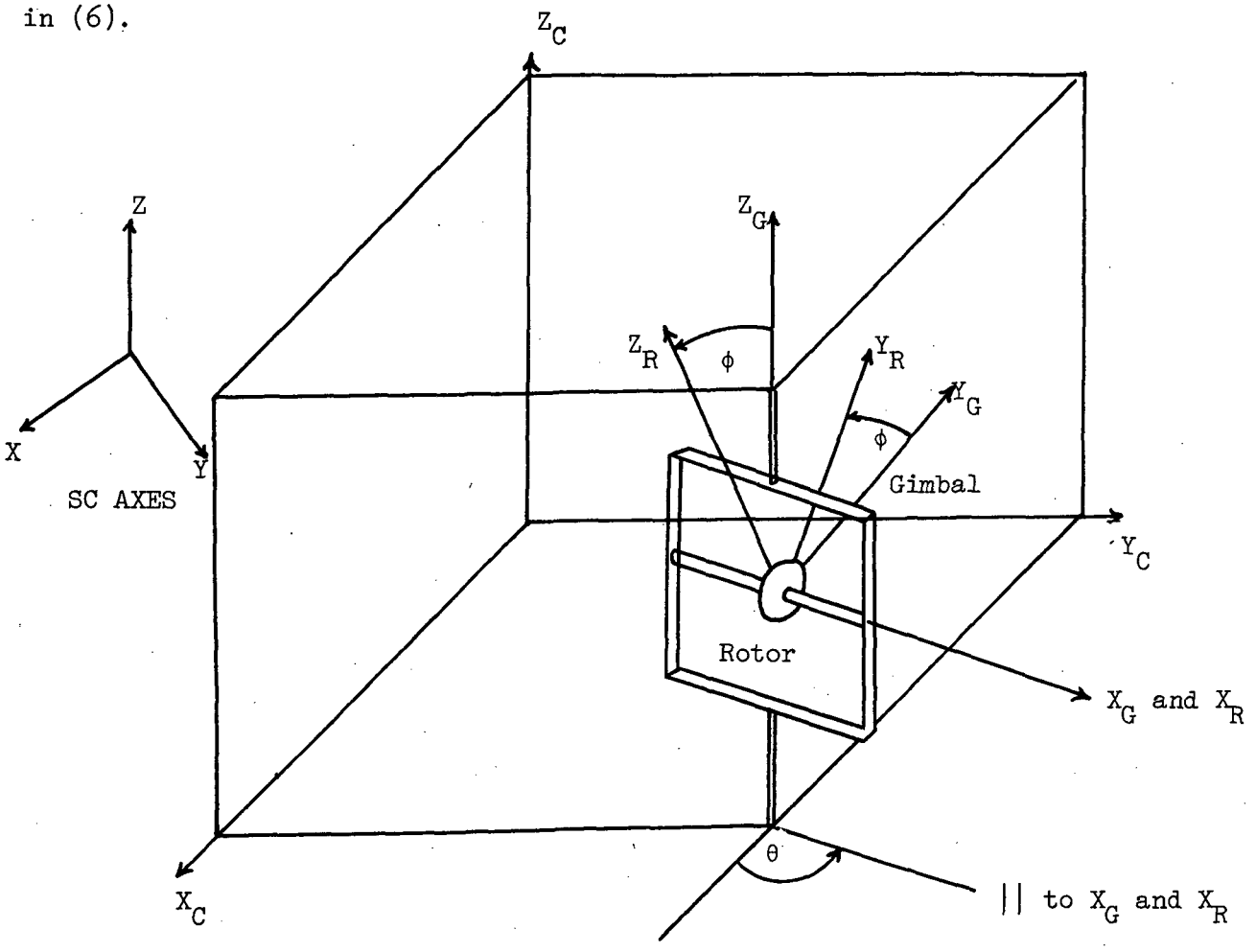

We may thus write, in Laplace Transform notation, assuming zero initial conditions:

$$\theta = \frac{H\phi_y s + T_{zc} - I_3\phi_z s^2}{I_3 s^2 + c_s + k} \qquad \text{(IV-3)}$$

$$\phi_y = \frac{T_{yc} - H(\theta+\phi_z)s}{I_1 s^2} \qquad \text{(IV-4)}$$

where: ϕ_x, ϕ_y, ϕ_z = angular velocities of the gimbal with respect to the X_c, Y_c, and Z_c axes respectively.

s = the free variable obtained through the Laplace Transform

T_{xc}, T_{yc} = analogous to T_{zc} except about the X_c and Y_c axes respectively

I_1, I_2, I_3 = Gimbal plus rotor moments of inertia with respect to the X_R, Y_R, Z_R axis system.

The equations above are of course for a single-axis gyro only; the θ equation is commonly termed the gyro output axis equation, or the gyro transfer function, the ϕ equation is the gyro input equation. It can be immediately seen that the two equations are coupled together and interdependent. There are of course two more pairs of similar θ and ϕ equations which are written for the other two axes gyros.

The following sketch defines the three-gimbal-inertia platform for each axis gyro:

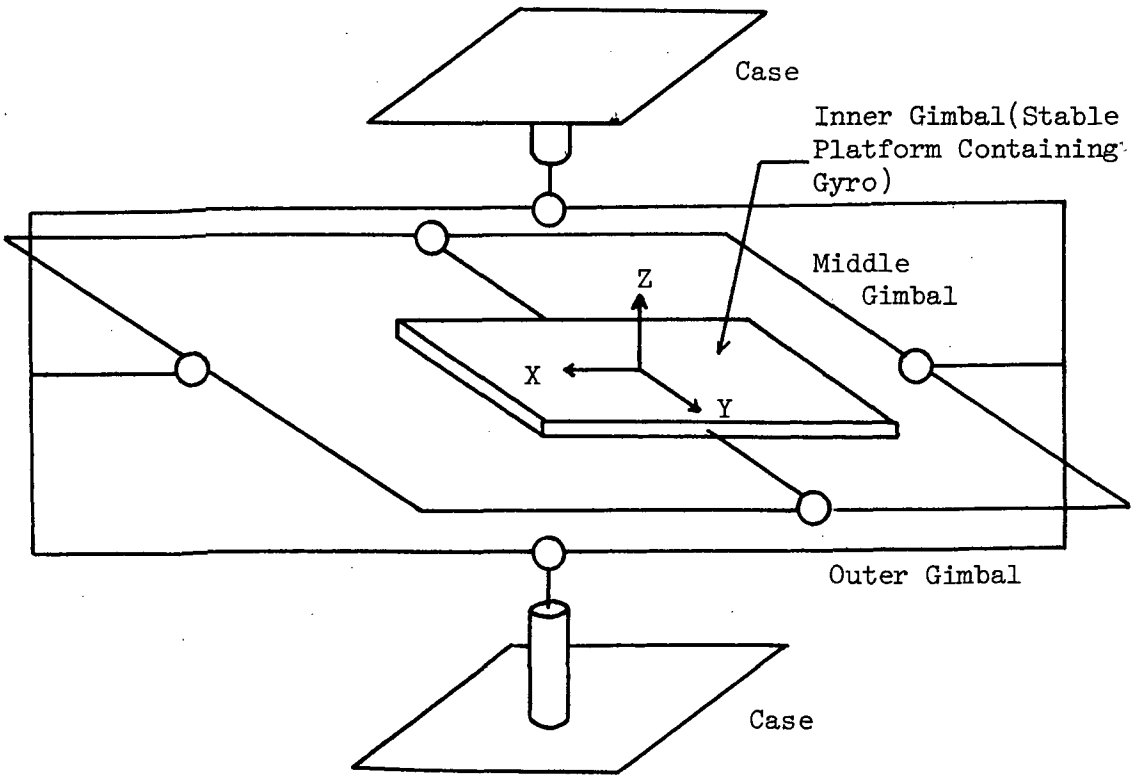

The inner gimbal has an associated platform servo which is used to correct any deviations of the platform by appropriately torquing the platform through torquers mounted along each gimbal. Since the three gimbals are connected orthogonally with swivel connections (the white circles of sketch), note that there is no sense of rotation of the spacecraft and corresponding case which could possibly produce rotational motion of the stable platform. This is of course the purpose of the gimbal system in the GCA. In practice a fourth gimbal is employed to affect gimbal lock between the middle and outer gimbals of the sketch above. Gimbal lock is an orthogonal alignment between the middle and outer gimbals necessary to prevent the outer and inner gimbals becoming aligned in the same plane. This is seen to occur in the above sketch if the middle gimbal rotates through 90° (which is possibly during sun or Canopus acquisition, or midcourse maneuvers). While outer and inner gimbals are aligned, the inner gimbals (thus the platform) can't rotate about its Z axis, thus the platform cannot null attitude errors in this condition and may lose accuracy or tumble, losing the attitude reference altogther.

Thus, the platform servo transfer function may be written about the platform (or case) Y_c axis:

$$-G_{TY}(s) = \frac{T_{SY}}{\theta(s)} \qquad \text{(IV-5)}$$

where T_{SY} = the servo torque about the platform Y_c axis.
Thus, the total external torque (T_{YC}) about the platform Y_c axis is the sum of some disturbance torque (T_{DY}) and the servo torque (T_{SY}); or: $T_{YC}=T_{DY}+T_{SY}$. (IV-

We can thus combine equations (IV-3), (IV-4), (IV-5) and (IV-6) into a single control loop for each axis gyro and combine the three loops. This is shown in Figure IV-4 for the general attitude control system during the interplanetary cruise mode. The figure assumes identical gyros on the three axes, and is self explanatory.

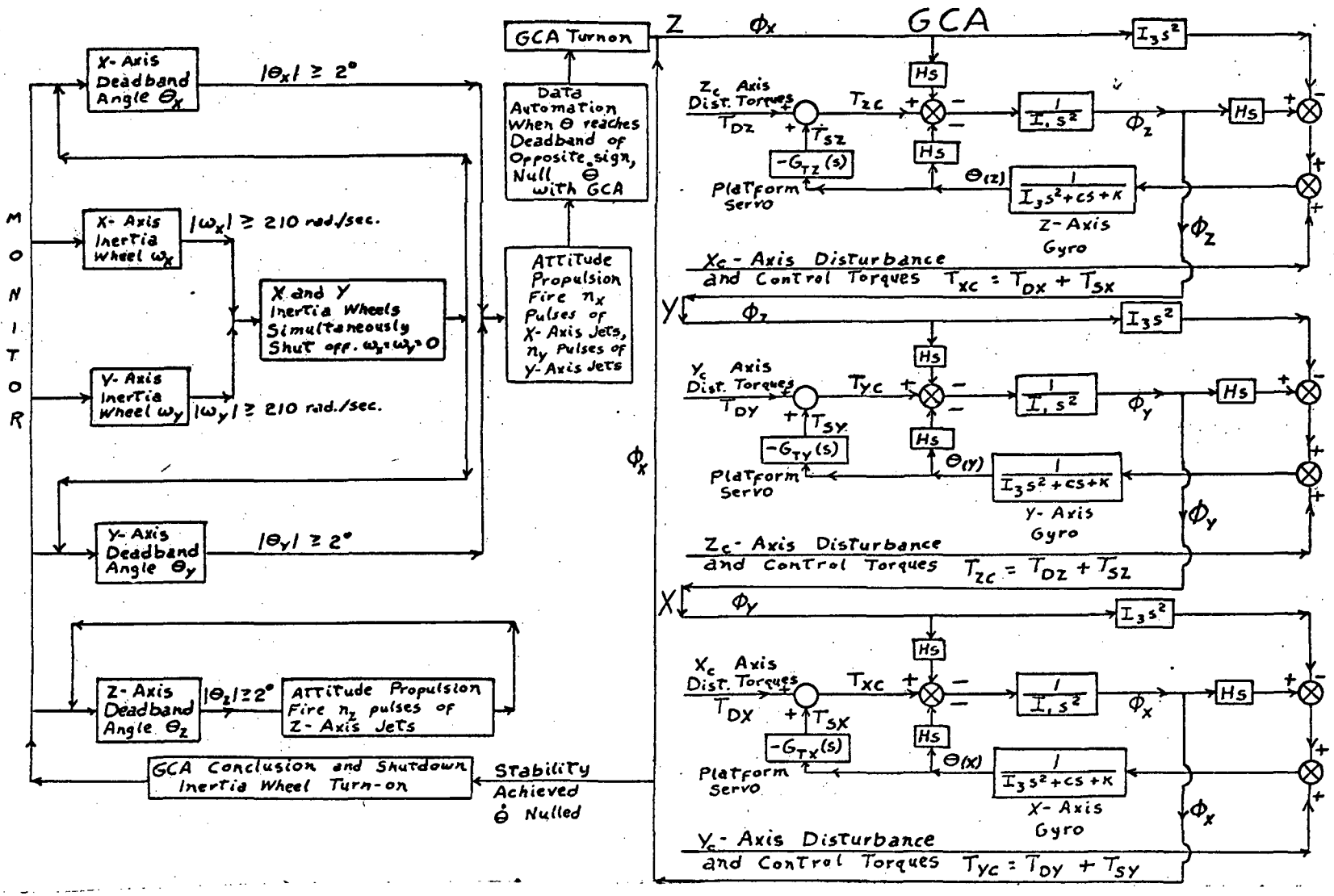

Figure IV-4: Interplanetary Control Loop Diagram for Attitude Control

Chapter IV: References and Bibliography

Adams, James J., and Brissenden, Roy F., "Satellite Attitude Control Using a Combination of Inertia Wheels and a Bar Magnet", NASA TN D-626, National Aeronautics and Space Administration, Washington, D.C., November 1960.

Hatcher, Norman M., "A Survey of Attitude Sensors for Spacecraft", NASA SP-145, Langley Research Center, Hampton, Virginia, 1967.

Leondes, Cornelius, Guidance and Control of Aerospace Vehicles. McGraw-Hill Book Co., Inc. : New York, New York, 1963.

Chapter V: Propulsion Subsystem

A. Mission Requirements

A propulsion subsystem must be provided for the specified spacecraft to meet certain objectives and to achieve the desired mission. It must be designed to satisfy specified requirements defined by the mission under constraints imposed mainly by the spacecraft itself and the environment. It has been found useful to summarize clearly these requirements and these constraints. First, the baseline spacecraft is presented together with the principal characteristics of the selected trajectories. Secondly, the performance needed in terms of velocity increment (ΔV) capability that the propulsion module must provide to the spacecraft to achieve the mission is given. Finally, the mission environment is briefly reviewed. Factors are taken into account when having a direct interaction on the propulsion subsystem, but detailed analysis and constraints on the spacecraft (for instance micrometeroid protection) are presented in other chapters of this report. As indicated, the launch date used in this study is 1980.

1. Spacecraft and Trajectories

The spacecraft baseline has a gross mass at launch of 1955 kg (4300 lb) determined by the capability of the available launch vehicle and the energy level of the transfer from the Earth to Jupiter or an equivalent quantity, the injection velocity (it determines the trip time to Jupiter). The payload, defined as the spacecraft except its propulsion module, was required to be 725 kg (1600 lb), a minimum value to meet the scientific package and the other subsystems mass requirement. It should be pointed out that these values serve as baseline and can

be varied for the purpose of the investigation and to offer alternate configurations.

The transfer trajectory from Earth to Jupiter is an hyperbola characterized by its velocity at infinite V_{HP} = 8 km/sec and its periapsis referred to the center of Jupiter and expressed in Jupiter radii unit of $1.1\,R_J$. The plane of the incoming hyperbola has an inclination of 77.7° with respect to the equatorial plane of Jupiter. The elliptical orbit around Jupiter is achieved by a theoretically perfect periapsis to periapsis transfer. Consequently, the ellipse and the hyperbola have the same periapsis $1.1\,R_J$ and the same inclination 77.7°. The selected apoapsis of the ellipse is chosen to be 100 R_J.

2. ΔV Capability Required

The propulsion subsystem must achieve three course-corrections, orbit insertion and orbital maneuvers. The time origin is the launch date. The first course-correction ΔV_1 = 33 m/sec occurs 16 days after launch. The second course-correction ΔV_2 = 77 m/sec occurs 495 days after launch. The third course-correction requires a velocity increment ΔV_3 which is a function of the launch date and of the periapsis of the elliptical orbit desired after insertion. The parameters selected for the mission give ΔV_3 = 550 m/sec. This correction occurs 742 days after launch, i.e., 73 days prior encounter.

The orbit insertion occurs 815 days after launch and requires a velocity increment which depends on the launch date, the periapsis and the apoapsis of the elliptical orbit. The parameters selected for the mission give ΔV_4 = 900 m/sec. This is the theoretical value for an impulsive maneuver and for a perfect periapsis to periapsis transfer.

The orbital maneuvers are operated successively 1180 days after launch (one year after orbit insertion). First, a change of the orbit plane inclination; for the selected parameters, a ΔV of 7400 m/sec is needed to bring the inclination from its initial value 77.7° to 0° (i.e., equatorial orbit). This value far exceeded the capability of any forseen propulsion system, hence a reasonable alternative was chosen. This was to reduce the inclination by 30° (from 77.7° to 47.7°) using only 41% of the previous ΔV. Therefore, ΔV_5 = 3040 m/sec. Secondly, a reduction of the apoapsis of the initial elliptical orbit. The primary objective was to bring down the apoapsis from $100R_J$ to $50R_J$. The required ΔV depends on the size of the ellipses and the location of the maneuver. The optimal maneuver requires ΔV_6 = 300 m/sec. Later in the study, reaching an apoapsis of 20 R_J appeared necessary for the scientific experiments. The ΔV_6 was subsequently substantially increased to 1230 m/sec to achieve this objective and this was taken into account in the evaluation of the suitability of different propulsion systems.

On the basis of the foregoing, an overall ΔV of 5000 m/sec appears to be the approximate global requirement for the entire mission. This value serves as a primary guideline for the determination of the propulsion subsystem.

3. Mission Environment

a) The primary heating of the propulsion system components is due to the sun; the solar flux density varies inversely with the square of the distance from the sun. It causes a significant heating. This fact is of importance for the propulsion system design, especially liquid propellant systems.

b) The RTG which provides the electrical power for the spacecraft emits both gamma and neutron radiation throughout the mission and presents a hazard for the propellants. The current state of knowledge of the effect of nuclear radiation on propellants is very limited.

c) Micrometeoroids, especially in the Asteroid Belt, are also a potential hazard for the entire spacecraft. Knowledge of their effect is limited at this time but the spacecraft will require some sort of shielding for its protection. No evaluation was done in this study since it has been decided to enshroud the entire spacecraft in a micrometeoroid shield.

d) Planetary radiation of Jupiter consists of Jovian electrons and protons. Their maximum flux rates are predicted to occur at 3 R_J and 9 R_J respectively. This might have an effect especially on solid propellant motors. Jupiter radiation effect needs to be considered only during one year, the time between orbit insertion and the orbital maneuvers.

e) Space radiation exists, too, but it is of less importance in comparison with other sources of radiation.

B. Orbit Insertion Analysis

The success of a Jupiter orbiter mission depends completely on the achievement of the orbit insertion. The importance of this phase of the mission and the problems involved for such a critical operation require accurate analysis.

One of the main objectives of the propulsion system is to provide the deboost capability. An intent of the analysis was to determine the requirements placed on the propulsion unit by the orbit insertion.

A basic consideration, which appears clearly, is the time constraint. When the spacecraft approaches Jupiter, the gravitational attraction keeps increasing and so the velocity of the spacecraft w.r.t. the planet. At the incoming hyperbola periapsis, which is the most efficient location to fire the engine for deboosting, it takes 500 sec. for the spacecraft to rotate by 20°. Comparing this time with the round-trip communication time Earth-Jupiter (roughly 1 hour 40 minutes) shows one of the problems. Even the time available for the maneuver itself appears very small and the question arises, how to initiate the deboost maneuver with a sufficient accuracy so that the firing location will be nearly the periapsis of the hyperbola? Then follows the problem of pointing the engine thrust to the right direction to secure the maximum ΔV offered by the propulsion subsystem.

However, these questions are related to the trajectory analysis and navigation studies and were not investigated in this chapter. Simple assumptions were selected to provide a base for the orbit insertion analysis, which was conducted from a propulsion subsystem point of view. The attention was directed towards:

1) The gravity losses problem

The theoretical ΔV required to transfer the spacecraft from the

incoming specified hyperbola to a specified elliptical orbit is computed assuming an impulsive kick which occurs at the periapsis of the hyperbola. This gives a periapsis-to-periapsis transfer which is optimal because it requires the smallest ΔV when the hyperbola and the ellipse are specified, hence, the minimum fuel consumption. The ΔV required is the difference of the corresponding velocities at periapsis.

But the real system operates in a finite time mode. The spacecraft must compensate the action of the gravity during this finite time of deboost operation. The real ΔV needed to achieve the specified elliptical orbit is greater than the theoretical impulsive ΔV. This increase of ΔV referred as gravity losses was evaluated with the influences of parameters affecting its value.

2) The burning time problem

The time scale of the swing-by at Jupiter as outlined before, brings a constraint upon the time of the deboost operation, i.e., the time the engine must burn to provide the correct ΔV. Roughly, the burning time has to be sufficiently small to assure an efficient maneuver (location at the periapsis of the hyperbola).

The burning time is a function of the specific impulse and the thrust provided by the engine. This second problem bears directly on the size of the propulsion subsystem.

The results of the analysis indicated that no unusual constraints or requirements would be imposed on the propulsion system by the orbital insertion maneuver. However, the gravity losses impose a ΔV penalty of 100 m/sec. For values of burning time of the order of 200 seconds acceptable values of acceleration are experienced. Errors in burning time or thrust level were found to effect the apoapsis of the ellipse. Details of these computations are given in Appendix D.

C. Candidate Propulsion Systems

Two competitive systems, solid propellant and liquid fuel, are possibilities for use on the spacecraft. Solid fuel motors are attractive in that they offer an inherent simplicity. However, little experience with these units exists in several important areas, e.g., controllable thrust, restart, etc. Liquid fuel systems, while requiring more complex hardware, have a considerable backlog of experience.

In deciding on the "best" system the approach was to evaluate the capability of the system within the stated constraints, i.e., weight, mission duration, etc. Fuels which are presently in a development condition but which could be expected to be available at the time of the mission were considered.

D. Solid Propellant Motors Investigation

1. Introduction

The concept which is based on the Surveyor design is the following: one or two large fixed-impulse, high performance solid propellant motors provide the bulk of the mission's required energy (mainly orbit insertion and orbit inclination change) while a liquid propulsion system provides flexibility through a precise control and multiple restart capability for the remaining maneuvers which are mainly mid-course corrections.

The simplicity of solid propellant motors makes this solution very attractive, but the experience in this field is fairly meager especially concerning problems of long term life, restart capability, controllable thrust (magnitude and direction), and influence of the deep space environment on storage.

The evaluation of the system takes into account expected developments of the technology in the near future and considers a beryllium solid motor with a specific impulse I_S = 315 sec. (vacuum, ε = 80). The capability that the liquid vernier subsystem must offer is such that bipropellant combinations are required. Two of them are considered using the pressure fed system:

- N_2O_4/Aerozine - 50 has a low specific impulse (I_S = 305 sec, vac) but benefits from a broad experience (Apollo, Mariner).
- OF_2/B_2H_6 offers a very good specific Impulse (I_S = 416 sec, vac) but has not yet been developed.

2. Baseline Propulsion System

The high burning rate of solid propellant motors yields high accelerations incompatible with the spacecraft configuration, especially

the booms handling the RTG and the scanning platform which would deflect. The problem is to control the acceleration and the acceleration build up of the motor. Subsequently, the solid motor is designed to provide a constant acceleration of 1g and to have a soft-start and shutdown, i.e., to have an acceleration rate, g-dot, equal to or less than 0.2 g/sec. The vernier subsystem operates 6 seconds prior to and 6 seconds after the solid motor operation to diminish transients and establish an autopilot-controlled stable spacecraft.

Problems due to radiation effects have been considered. However, few practical results are currently available in this field.

3. Design Configuration

The requirement on the acceleration leads to use of a regressive end-burning motor geometry, with a charge fully case-bonded throughout the lateral surface. Based on current experience, a favorable propellant envelope with a ratio L/D of nearly one is selected, because it presents better burning conditions for the grain and a compact case easily integrated into the spacecraft.

The liquid vernier subsystem consists of four identical throttleable thrusters, one of which is gimballed to provide roll control and is designed for long-term spacelife, long time operation, and multiple restart capability. Helium is used as pressurant gas, and is stored in two separate tanks. Four propellant tanks plus positive expulsion screen, squib, throttle and shutoff valves are organized in two identical linked arrays to provide capability for uniform propellant consumption from each tank in order to reduce potential center of gravity excursions.

4. Results

It was found impossible to meet the overall ΔV requirement within

the propulsion system mass constraint. The solutions studied have the maximum allowable mass and offer a ΔV below that required for ideal maneuvers.

The first system consists of a single, fixed impulse, burn-to-completion beryllium solid propellant motor (mass = 526 kg) which has a ΔV capability of 1000 m/sec for orbit insertion at a constant acceleration of .75 g and a N_2O_4/Aerozine-50 vernier subsystem (mass = 700 kg) which provides capability for the three course-corrections, for thrust-vector-control, and then has a remaining ΔV of 520 m/sec. This capability may be used to bring down the apoapsis of the orbit from 100 R_J to 38 R_J.

The second solution consists of two fixed-impulse, burn-to-completion beryllium solid propellant motors and an OF_2/B_2H_6 vernier subsystem. The first motor (mass = 526 kg) provides a ΔV of 1000 m/sec for orbit insertion at a constant acceleration of .75 g. The second motor (mass = 323 kg) provides a ΔV of 800 m/sec for orbit trim at a constant acceleration of .55 g. This last capability offers alternatively:

- A reduction of the orbit apoapsis from 100 R_J to 29 R_J.
- A reduction of the orbit inclination by 8°.

The OF_2/B_2H_6 vernier subsystem (mass = 391.6 kg) has the capability for the three course-corrections and thrust vector control during the operation of both solid propellant motors.

Complete details of the "solid propellant motors investigation" are presented in Appendix E.

E. Fluid Propulsion Systems Investigation

1. Introduction

The high performance offered by new bipropellant liquid systems due to their high specific impulse (I_S > 400 sec) make them very attractive for planetary orbital missions where large ΔV's are needed. Their flexibility, precise control and multiple restart capability compensate for the complexity caused by critical components such as valves, pressure regulators, etc.

This evaluation is conducted assuming a propulsion system mass constraint of 1230 kg and calculating the resulting ΔV. A simple calculation using the rocket equation and a mass fraction of .8 shows a maximum ΔV available of 2.85 km/sec for a system I_S = 400 sec. This is well below the ΔV of 5 km/sec needed to satisfy the entire mission.

Propellants considered include earth-storable, space-storable and cryogenic combinations.

2. Characteristics of the Propulsion System

Appendix E presents the overall parameters,conditions, and configurations of possible candidates; the liquid temperature range of the propellants which is a critical parameter for storability capability for long space missions; the specific impulse which has a direct influence on the system performance and depends on the engine feed-system (pump-fed or pressure-fed) and the operating parameters of the engine; finally, handling and safety, thermal stability, material compatibility, mixture ratio and bulk density, and propellant initial conditions are considered. Engine investigation includes configuration (fixed bell nozzle or extendable), cooling technique, sensitivity to thrust, mixture ratio, nozzle expansion, chamber pressure and start modes.

But the critical problem with liquid propellants is the fact that they are very sensitive to thermal environment. For cryogenic and, in a certain measure, space-storable combinations, heat transfer may cause boiloff with its resulting high pressure consequence and weight penalty. In the opposing way, the earth-storable propellants may freeze. Consequently, coatings, insulation, tank pressure, tank dry weight, pressurant gas weight, propellant boiloff are thermally sensitive parameters. Particular attention was given to thermodynamic considerations, assuming a compact propulsion module composed of four spherical tanks, the mission environment based on the solar flux and a payload maintained at $70^{\circ}F$. The spacecraft orientation and thermal insulation of the tanks are the most important parameters for thermal control. For cryogenic and space-storable propellants, the tanks are shaded from the sun by the payload. For earth-storables, the sun-facing tanks configuration is required. Less important parameters are surface finish characteristics, subcooling techniques and shadow shield.

3. Propulsion System Design

A detailed analysis was performed for four combinations representative of the three classes of propellants, two pump-fed systems F_2/H_2 (cryogenic) and Flox/CH_4 (space storable) and two pressure-fed systems, OF/B_2H_6 (space storable) and N_2O_4/Aerozine-50 (earth-storable). The selected constant thrust level is 2000 lbf (8900 N). The pump-fed systems use a regeneratively cooled engine and a nozzle expansion ratio of 100. The pressure-fed systems utilize an ablatively cooled engine and an expansion ratio of 60. Configurations using four spherical propellant tanks were selected for all systems except H_2 which is stored in a single ellipsoidal tank. All tanks are to be formed from 2021 Aluminum. Each tank is individually insulated with multilayer double-aluminized mylar

and tissueglass spacers. The overall propulsion module is assumed protected from meteoroids. Except for H_2 which uses gaseous H_2, the pressurant gas is helium stored inside the propellant tanks for cryogens and space-storable and externally for the N_2O_4/A-50 system. Fluid systems are designed to meet the particular requirements of each propellant combination. The helium pressurant gas is heated by the engine through a heat exchanger. The analysis of the propulsion systems thermal behavior shows that F_2, Flox, CH_4, and B_2H_6 are well suited to the mission. H_2 and OF_2 are heated and reach high pressures. The N_2O_4/A-50 system presents a risk of freezing which can be prevented by a thick insulation (5 in.) a good tank surface finish or, preferably, active thermal control. The weight breakdown gives a propulsion module mass of approximately 1230 kg or a weight of 2700 lb (i.e., a payload of 1600 lb approximately) except for the N_2O_4/A-50 system due mainly to the high insulation weight required. The comparison between the four systems is based on their ΔV performance; the three course-corrections and the orbit insertion are considered. The F_2/H_2 systems offer the best remaining capability of ΔV = 1248 m/sec followed by the Flox/CH_4 with ΔV = 1092 m/sec and the OF_2/B_2H_6 system with ΔV = 999 m/sec. The N_2O_4/A-50 system offers a ΔV of 371 m/sec.

The final selection of a fluid propulsion system requires a trade-off between the ΔV performance and the suitability of the system for the mission (mainly thermal behavior) and shows the superiority of the Flox/CH_4 system assuming its development, testing and qualification prior to 1980. After orbit insertion the orbit time may consist of:

- A change of orbit apoapsis only from 100 R_J to 22.5 R_J.

- A reduction of orbit inclination only by 11°.
- A change of both inclination and apoapsis

  reduction of inclination by 7°

  reduction of apoapsis from 100 R_J to 50 R_J

F. Conclusions and Recommendations

This study shows the impossibility of fulfilling the intended ΔV requirement of 5 km/sec for the proposed mission to Jupiter, within the propulsion system mass constraint of 1230 kg (2700 lb) even with F_2/H_2, the highest performance system available. However, the fundamental operations to guide and orbit the spacecraft can be achieved and a capability is generally available for orbit trim.

The investigation has considered both solid propellant motors associated with a liquid vernier subsystem and a complete fluid propulsion system. The overall comparison between the various solutions has led to the selection of the Flox/CH_4 system for JOSE due to its superiority over the other candidates.

The selected design offers a compact propulsion module based on four spherical propellant tanks close to the engine, and properly insulated and protected from meteoroids. The spacecraft orientation is such that the payload shades the propulsion module from the sun. The Flox/CH_4 is a pump-fed system operating at a mixture ratio of 5 and a chamber pressure of 500 psia. The engine provides a thrust of 2000 lbf with a nozzle expansion ratio of 100, and uses the regenerative cooling process. The NPSP of 4 psia is provided by heated helium pressurant gas stored in two tanks located inside the CH_4 tanks at 4500 psia. Pressure levels are 40 psia for Flox and 35 psia for CH_4 and their temperatures remain perfectly in the range of their liquid state.

After orbit insertion, it is recommended to use the remaining ΔV capability for a single operation, the reduction of the orbit apoapsis from 100 R_J to 22.5 R_J.

All the design parameters are summarized in the tables of Appendix E.

Chapter V: Bibliography and References

1. General Dynamics:
   A Study of Jupiter Flyby Missions, FZM-4625

2. Heitchue, Regis D.: Space Systems Technology

3. Jet Propulsion Laboratory:
   a) Trajectory Selection Considerations for Voyager Missions to Mars During the 1971-1977 Period; Eng. Planning Doc. No. 281.
   b) Mariner Mars 69 Guidance and Control System 605-141.
   c) Outer Planet Orbiter Propulsion, NASA 7-100

4. Lockheed Missiles and Space Company:
   Propellant Selection for Spacecraft Propulsion Systems
   Phase I, Volumes I, II, III, K.19.68.6
   Phase II, Volumes I, II, III

5. NASA Goddard Space Flight Center:
   Phase A, Report Galactic Jupiter Probe, Vol. I and II, X70167566.

6. NASA Lewis Center:
   Analytical Evaluation of Space Storable Propellants for Unmanned Jupiter and Saturn Orbiter Mission, NASA TMX-1793.

7. Pratt and Whitney Aircraft:
   a) Space Storable Propellant Rocket Engine Parametric Data, PDS2686
   b) High Performance Propulsion Systems for Space Missions, GP 68-31
   c) Space Storable Engine Characterization, NASA CR-72552
   d) Oxygen/Hydrogen and Fluorine/Hydrogen Rocket Engine Parametric Data, PDS 2687
   e) Flox/Methane Pump-fed Engine Study, NASA CR-72485

8. Rocketdyne:
   a) Space Storable Propellant Performance Study - Final Report NASA CR-72487
   b) Space Storable Engine Characterization - Final Report NASA CR-72559

9. TRW Systems:
   Advanced Planetary Probe - Final Technical Report
   Volumes I, II, III, IV, NASA 7-100

10. United Technology Center:
    Jupiter Orbiter Propulsion Study UTC 2332-FR; NASA 7-687

11. Yodziz Charles W., Liquid Rockets

Chapter VI: Science Experiments

A. Introduction

It is not feasible nor desirable to describe specifically manufactured instruments for those instruments propsed in Table II-1 and Figures II-2 and II-3 in Chapter II. Specific instruments were used only in sizing up these science packages; here it will suffice to describe in general terms the science objectives which can be satisfied by the various planetary scanning instruments (PSI) and fields and particles (F & P) experiments. An imaging sequence of events is proposed in this chapter, as imaging experiments are generally (1) the major science objectives from a science return qualitative point of view, (2) the most demanding in terms of data storage, and (3) the most complicated to implement because of pointing requirements, photometric considerations, and spacecraft attitude requirements. Appendix F describes the zeodetic celestial mechanics experiment.

B. The Science Payload

1. Ultraviolet, Visual, and Auroral Photometers

Photometers measure electromagnetic flux intensity over one or more broad portions, or a few spectral lines, of the short wavelength region of the spectrum (visible and ultraviolet). Photometers separate the different wavelength regions of interest with filters and employ detectors such as photomultiplier tubes to measure the intensity of the light passed as a function of time and pointing angle. A typical photometer might have a full cone angle field of view of about 10°.

Numerous experiments are possible with these three photometers. For instance, measurement of the extinction of light as JOSE is occulted from the Sun by Jupiter allows the determination of the vertical distribution of that element

filtered by the photometer. Measurement of the transmitted light from the Jupiter surface directly below the SC in the 2550 Å portion of the spectrum allows the determination of Jupiter's ultraviolet albedo.

By employing various filters in the photometer and scanning them with mirrors, a spectrophotometer results capable of measuring electromagnetic radiation in several UV-visual portions of the spectrum.

Photometers can thus be employed to observe such emission phenomena as aurora, permanent airglows, synchrotron radiation, twilight flashes (if existent at Jupiter), fluorescence, and resonance radiation.

These photometers can study atmospheric elemental abundances, composition, structure, color, and dynamics. They are useful in analyzing ionosphere and exospheric structure, composition, and temperature, as well as studying the Red Spot. The ultraviolet photometers can determine the constituents: He (at 584 Å), H (1216), N (1200, 1473), Ne (735, 743), Ar (1048, 1067), O (1304), Kr (1165, 1236), Xe (1295, 1470).

2. Visual-Ultraviolet Spectrometers

The spectrometers differ from the photometers in that the spectrometers disperse the electromagnetic radiation into a spectrum and then scan it with high resolution. Spectrometers are generally utilized in observing absorption phenomena such as extinctions of portions of the solar spectrum with atmospheric depth, absorption spectra of planet-emitted thermal radiation, limb studies, and atmospheric reflection at angles not observable from Earth. From these observations, various atomic, molecular, and ionic species can be determined; the scale height of atmospheric constituents can be measured; Jupiter satellite atmospheric composition, if existent, can be studied; knowledge of the Rayleigh scattering from Jupiter's lower atmosphere and the ultraviolet reflectivity of the planetary surface may possibly be obtained; and detection of atmospheric aurora and nightglow might be achieved. The UV spectrometer is capable of

detecting C (1660 Å), N_2(1300-1500), CO (1500-1800), CO^+(2200, 2300), and CO_2^+(2900).

Ultraviolet spectrometry is emphasized for a Jupiter orbiter since the UV portion of the spectrum of Jupiter's radiation is not available to astronomic observatories on the Earth's surface. Jupiter-wide emission at wavelengths above 1000 Å is available to Earth satellites above the atmosphere, but the emission below 1000 Å requires special optics. JOSE observations about Jupiter can give altitude profiles of UV radiation, are capable of better spatial resolution, and can make night-side observations that avoid confusion of Jupiter emitted radiation with reflected sunlight.

The importance of the UV region of the spectrum is emphasized for the following reasons (Fastie, 1967):

(1) Almost all of the ground-state resonance lines of atomic species are in this region, and resonance reradiation of solar UV flux is an important upper atmospheric reaction.

(2) Almost all of the ions and neutral molecules in the ionosphere absorb and fluoresce in the UV region.

(3) The ionospheric process of dissociation, recombination, and charge exchange produce emission in the UV region.

(4) Collisions between atmospheric species and high-energy particles; such as solar protons, auroral electrons, and photoelectrons produced by extreme UV photoionization; have a high cross section for emission of UV radiation.

A typical spectrometer will have a field of view (FOV) of 2°.

3. Infrared and Microwave Radiometers

Instrumentally the radiometer functions in exactly the same manner as a photometer, the only difference being that the radiometer is sensitive to the higher wavelength infrared and microwave regions of the spectrum. The joint

employment of both the microwave and IR radiometers is an excellent method of obtaining an upper atmosphere temperature map of Jupiter and of settling the "energy balance" problem described in Section F of Chapter I. Temperature maps of Jupiter are excellent methods of studying atmospheric dynamics and physical correlations between the Red Spot and surrounding cloud features. Temperatures of Jupiter's natural satellites can also be measured by JOSE's radiometers. The wavelength region of the radiometers should extend from 5μ to very long wavelengths (50μ) for possible detection of radiation originating deep within Jupiter's atmosphere.

The application of IR radiometers in Tiros and Nimbus Earth satellites for cloud pattern recognition and storm tracking is well known, especially to meteorologists. The idea of applying these radiometers in a similar manner to observe Jupiter cloud spots and currents described in Section F of Chapter I is intriguing. The radiometers might be capable of detecting H_2O, CO_2, and O_3, two of which (H_2O and CO_2) probably exist deep within Jupiter's atmosphere. Although H_2O has strong vibration-rotation bands centered near 1.1, 1.38, 1.87, 2.7, and 6.3 μ which would probably be undetectable by the radiometers because of the dept of the H_2O in the atmosphere, there is an H_2O rotation band starting weakly at 12μ and intensifying out to 65μ which might be detected by the radiometers. Also the 15μ vibration-rotation band of CO_2 might be detected in the same manner.

The radiometers, having a FOV of about 5°, would be required to scan through about 60°.

4. Infrared Spectrometer-Interferometer (Bandeen, 1968)

This Michelson interferometer employs a beamsplitter which divides the incom radiation into two approximately equal components, one directed toward a fixed mirror and the other toward a moving mirror. After reflection from the mirrors,

the two beams interfere with each other with a phase proportional to the optical path difference between the two beams. The two recombined components are then focused on a detector where the intensity is recorded as a function of the path difference. For a continuous spectrum, the superposition of many amplitudes of various frequencies takes place. The resultant, combined signal is the interferogram. The spectrum is reconstructed from the interferogram by applying an inverse Fourier transform.

The interferometer can be used to detect atmospheric polyatomic molecules and to study atmospheric structure, color, temperature, and dynamics. Measurements near the time of solar occultation of JOSE will yield vertical profiles of these features. The interferometer is also applicable in searching for organic molecules, studying the composition of the Red Spot, and analyzing natural satellite atmospheric and surface compositions.

The FOV and the IR interferometer would be about 5^{o}.

5. High Resolution Television

In order to maintain the non-restrictive nature of this science payload, this instrument should more appropriately be termed the imaging system. From preliminary considerations of ruggedness, reliability, lifetime, resistance to radiation exposures, packaging capabilities, versatility, and pointing capabilities, it would appear that the television system is the most attractive. This is not a quantitative conclusion however and a more rigorous tradeoff analysis for a Jupiter orbiter is definitely in order when specific instruments are selected in the future for the mission.

The imaging system, if capable of supporting both wide angle and narrow angle FOV (by zoom lens, for example, or two independent systems), is an extremely versatile instrument. In the wide angle, small focal length mode, it can be used for planetary approach trajectory determination for deboosting into

Jupiter orbit as well as orbit determination for the zeodesy experiment as mentioned in Appendix F. In the narrow angle, long focal length mode, the imaging system is utilized in its science capacity for planetary reconnaissance; observations of atmospheric dynamics, cloud structure, circulation, and color; Red Spot observations; and studies of the topographies and atmospheres of the natural satellites. In comparison to near-Earth capabilities, Earth-based image resolution of Jupiter is presently about 1000 km. Earth orbiters in the late 1970's are expected to improve the resolution at Jupiter to about 300 km. JOSE will improve the resolution to better than 4 km. at perijove, although the advantages of so great a resolution improvement are somewhat dubious when imaging cloud structures rather than a solid planetary surface.

Parameters of the imaging science system selected by the author in conjunction with associated investigators at JPL are a 0.1 second electronic shutter speed (thus eliminating smear characteristics altogether), a 20 mm. format, 100 lines per mm. resolution (thus a 2000 line imaging system), and a 2° FOV in the narrow angle mode. These parameters are slightly "pushing the state of the art", it is felt that they will be attainable in the late 1970's.

6. An Imaging Sequence of Events

As well as the imaging system parameters assumed above in Section 5, numerous discussions with members of the Jupiter Orbiter study group at JPL resulted in the selection of a 10^9 bit tape recorder and a 4½-minute total time to image, record, and transmit a frame (although transmission generally occurs at a later time when transmission visibilities permit). Transmission times are also dependent on the perijove ground rule of Section B 12 (h) of Chapter II; the duration of transmission of course depends on the 100 kbps ground rule of Section B 12 (a) of Chapter II, plus one-way trip time to Jupiter ($\approx$ 40 minutes) plus housekeeping activities (component temperature monitoring, plus others).

Note that with a 2000-line imaging system, or 4×10^6 pixels per frame, and allowing 6 bits per pixel for contrast (or $2^6 = 64$ shades of gray), there are 2.4×10^7 bits per frame. Recording rates for other science instruments are predicted to be approximately:

a) PSI (excluding imaging): probably used most effectively only during one day before to one day after perijove passage. The total number of bits recorded would be approximately equal to that allotted to the imaging system ($.86 \times 10^9$ bits).

b) F & P: From Jupiter radii R_J of from 1.1 to 20 and from 55 to 80, F & P would probably record in a high data rate mode of 2000 bps. From R_J of from 20 to 55 and from 80 to 100, a low data rate mode of 200 bps would suffice. It is to be emphasized that these are continuous recording modes, as opposed to PSI which is intermittent.

The 1.1 R_J x 100 R_J orbit is divided into seven imaging modes as follows:

i. High Resolution Terminators (0-1 day from periapsis)
ii. Intermediate Dark Side (1-5 days)
iii. Radiation Dark Side (5-14 days)
iv. Mapping (14-32 days)
v. Radiation Light Side (32-41 days)
vi. Intermediate Light Side (41-45 days)
vii. High Resolution Light Side (45-46 days)

Brief descriptions of the modes are given below. Table VI-1 tabulates the sequence of events. Figure VI-1 relates the modes to the orbit geometry. Although the imaging system duty cycle appears high, it is important to obtain as much visual data as possible on the first orbit. Imaging can of course be relaxed on subsequent orbits.

i. High Resolution Terminators: This mode allows for the ground rule of no data transmission one-half day on each side of periapsis. This implies one 4-hour period for transmission of a 10^9 bit dump of the tape recorder. Sun and Earth occultations will probably demand a high ratio of other science (excluding imaging) to total science, which accounts for the low ratio (24%) of imaging.

ii. Intermediate Dark Side: Four days or eight data dumps are available. Jupiter's illuminated disc is varying from 130° to 145° of longitude as viewed from the spacecraft for the arrival date of 2 March 1983; the excellent viewing conditions of the morning terminator suggest extensive imaging during this mode (81%).

iii. Radiation Dark Side: Both radiation modes and the mapping mode occur when Jupiter is completely within the field of view of the 2° imaging system. Nine days or 18 dumps are available during this radiation measuring mode; the relatively high "other science" ratio (39%) is due to the fact that it is during this portion of the orbit that the solar plasma shock wave will most likely be crossed. It will thus be desirable to concentrate on fields and particles experiments at this time. An initiation of the mapping mode can be performed at this time, however, since the data bits available for imaging still allow one frame every 17° of Jupiter rotation for a 2° FOV system.

iv. Mapping: The mapping mode clearly emphasizes imaging at 9 days on each side of apoapsis, where it is hoped that the plasma shock wave has already been crossed and low flux properties of Jupiter's radiation fields will not dictate excessive fields and particles experiments. A mapping option is also presented to cover 10° of Jupiter rotation (requiring 15 days and 10 hours of imaging).

v. Radiation Light Side: This mode is similar to the radiation dark side mode, except 90 percent of the total available bits is allotted to imaging. The reduction of bits allotted to radiation measuring from the radiation dark side

is anticipated since the shock wave properties will have been grossly defined on the dark side.

vi. Intermediate Light Side: Jupiter's illuminated disc now covers 170° of longitude for the arrival date shown, hence a high ratio (90%) of imaging is desired.

vii. High Resolution Light Side: The one-half day of non-transmission allows only one data dump before the orbiter reaches periapsis. Other experiments share priority with imaging at this point, and 62 percent of the available bits are allotted to imaging.

7. Vector Helium Magnetometer

The solar wind contains a magnetic field that is $\sim 5\gamma$ ($1\gamma = 10^{-5}$ gauss) at 1 AU from the sun, and which is expected to fall to $\sim 1\gamma$ at the distance of Jupiter. In Chapter I, we noted that Jupiter, however, has most probably an intense magnetic field of $\sim$10 gauss near its surface. Since one of the purposes of our mission is to study the interaction between the Jovian magnetosphere and the solar wind, we would like our instruments to measure fields from 0.1γ to $\sim$100 gauss.

To measure fields from $\sim 0.1\gamma$ to 0.5 gauss, we recommend the use of a vector helium magnetometer similar to that flown on Mariner V. (To increase the range of this instrument to $\sim$100 gauss would considerably increase the weight and power requirements, so we propose using Hall devices, described in the next section, to measure the largest anticipated fields.) The Vector Helium Magnetometer detects the change in infrared absorption of an optically pumped helium-gas cell caused by the presence of a magnetic field. This provides a very sensitive measurement of the three components of the ambient magnetic field, and great care must be taken to insure that the spacecraft is "magnetically clean" so that the spacecraft field detected by the instrument in the absence of an external field is $\leq 0.2\gamma$ and is stable to $\pm 0.07\gamma$ throughout the mission.

Table VI-1: Jupiter Orbiter Imaging Sequence of Events

Mode	Imaging System Capability	Objectives	Sequence	Total No. of Pictures Per Orbit
High Resolution Terminators (0-1 days)	Resolution: 2^{o}FOV: 4-24 km/line	1. Terminator imagery at high resolution. 2. Data at large phase angles. 3. Solar eclipse & occultation data. 4. Satellite data. 5. Aurora studies. 6. Atmosphere studies.	$.24 \times 10^{9}$ bits imagery (24%) $.76 \times 10^{9}$ bits other (76%)	10
Intermediate Dark Side (1-5 days)	Resolution: 2^{o} FOV: 24-70 km/line	1. Atmosphere studies 2. Imagery at large phase angles.	6.48×10^{9} bits imagery (81%) 1.52×10^{9} bits other (19%)	270
Radiation Dark Side (5-14 days)	Resolution: 2^{o} FOV: 70-112 km/line	1. Atmosphere studies. 2. Imagery at large phase angles. 3. Non-imagery.	1.1×10^{10} bits imagery (61%) $.7 \times 10^{10}$ bits other (39%) Initiate mapping-planet coverage every 17^{o} for 2^{o} FOV.	459
Mapping (14-23-32 days)	Resolution: 2^{o} FOV: 112-124-112 km/line	1. Atmospheric circulation studies.	2^{o}FOV 3.32×10^{10} bits imagery (92%) $.28 \times 10^{10}$ bits other (8%) planet coverage every $11\frac{1}{4}^{o}$, 1 frame to cover disc.	1380
Apoapsis Mapping Option (14-23-32 days)	Resolution: 2^{o} FOV: 112-124-112 km/line	1. Atmospheric circulation studies at every 10^{o} of Jupiter rotation.	3.2×10^{10} bits imagery (90%) $.4 \times 10^{10}$ bits other (10%) 2^{o} FOV: 15 days 10 hours of imagery at 10^{o} intervals of Jupiter rotation.	1340

Mode	Imaging System Capability	Objectives	Sequence	Total No. of Pictures Per Orbit
Radiation Light Side (32-41 days)	Resolution: 2° FOV: 112-70 km/line	1. Intermediate resolution of selected features of interest. 2. Data at small phase angles. 3. Cloud structure studies. 4. Non-imagery.	1.62×10^{10} bits imagery (90%) $.18 \times 10^{10}$ bits other (10%) Conclude mapping of uncovered areas, coverage every 12° for 2° FOV.	675
Intermediate Light Side (41-45 days)	Resolution: 2° FOV: 70-24 km/line	1. Intermediate resolution of selected features of interest. 2. Data at small phase angles. 3. Cloud structure studies.	7.2×10^{9} bits imagery (90%) $.8 \times 10^{9}$ bits other (10%)	300
High Resolution Light Side (45-46 days)	Resolution: 2° FOV: 24-4 km/line	1. High resolution of primary features. 2. Zero phase data. 3. Terminator coverage at high resolution.	$.62 \times 10^{9}$ bits imagery (62%) $.38 \times 10^{9}$ bits imagery (38%)	26
		NO. OF FRAMES: TOTAL:	2° FOV: 3120	TOTAL W/ OPTION: 3080

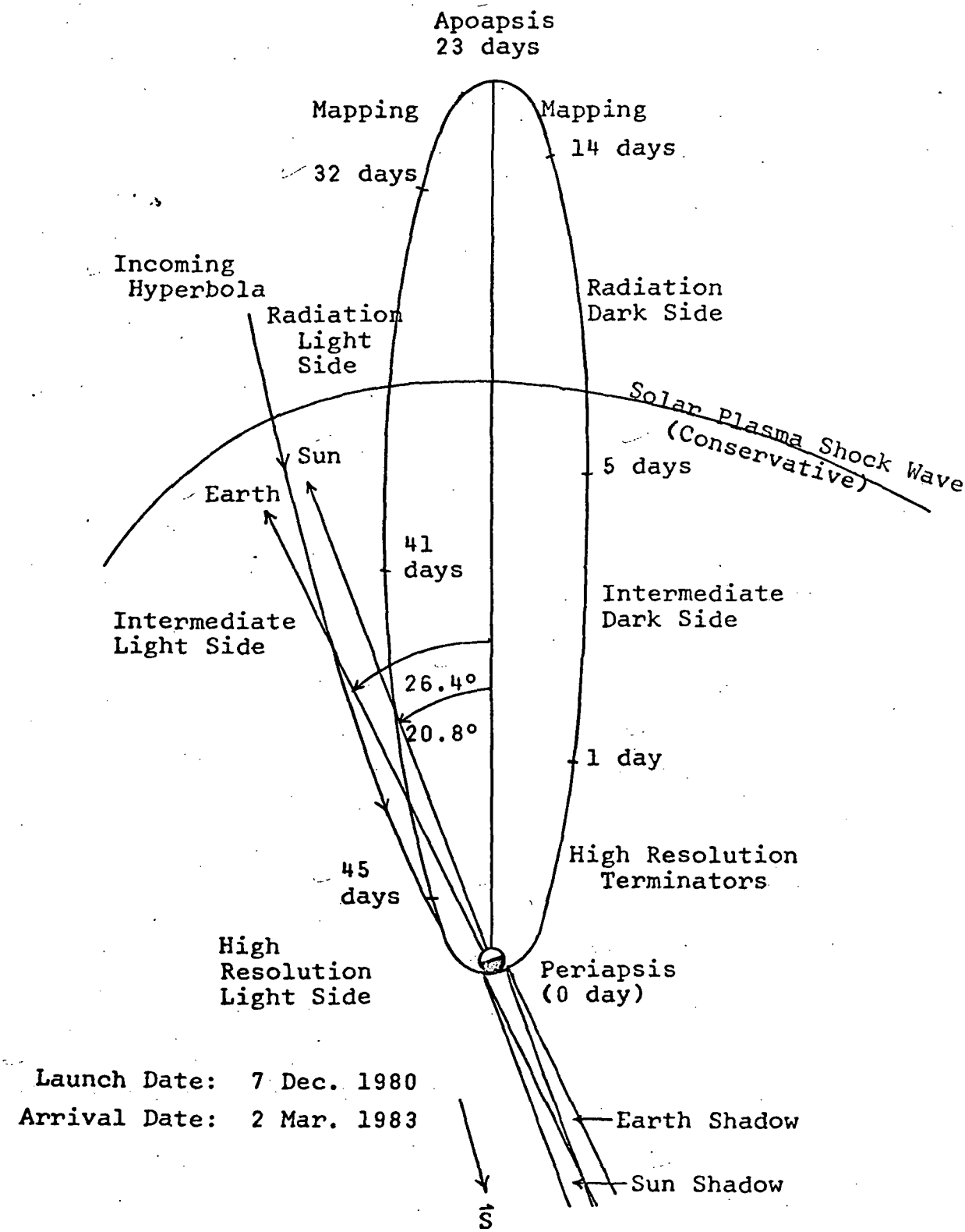

Figure VI-1: Orbit Mode Geometry
1.1 R_J x 100 R_J Orbit

To aid the attainment of this requirement, the sensor is to be placed on a boom. (The boom package temperature is controlled by passive means.)

Dynamic Range: 8 ranges with full-scale values of 2.56, 10.24, 41, 164, 500, 5×10^3, 5×10^4, and 5×10^5 γ. Range may be selected automatically or manually. Minimum resolution is $\leq 0.01\gamma$ in lowest range, all others have resolution of $\leq 2.5\%$ of ambient field.

Sensor (on boom): 1.1 lb.; 0.5 - 1.0 W at 28 VDC; 3"x3"x8"; -40° to $+50^\circ$C (operating); -55° to $+65^\circ$C (storage).

Electronics (in scan platform module): 3.2 lb.; 2W at 28 VDC; 6"x6"x4"; -20°C to $+70^\circ$C (operating); -55° to $+125^\circ$C (storage).

Data: Output is digital, with 9 bits per component. Output response is limited to 10 Hz. To measure the vector magnetic field once per sec., we need a data rate of 27 bits/sec.

8. Hall-Effect Magnetometer

To measure the most intense fields anticipated at Jupiter, $\sim$10 gauss, we prescribe a set of three identical Hall-effect devices, mounted on the scan platform module 2. This will permit the scan platform to be aligned accurately relative to the magnetic field lines, which is desirable from the point of view of observing the high-energy charged particles trapped on the field lines, as in the Van Allen radiation belts of earth.

Dynamic Range: 0.1 to 100 gauss, with a resolution of 1/128 of the ambient field. This allows the scan platform's position relative to the magnetic field to be known to within $\sim 10^{-2}$ radian.

Data rate for one measurement of the magnetic field per sec is 33 bits/sec.

We estimate that this unit would require roughly 1 W. of power, weigh 1 lb., and occupy 50 in^3.

9. Langmuir Probe

This is used to study the density and energy distribution of the low-energy electrons, which, if the distribution is Maxwellian, yields the electron temperature. We suggest using the Dryvestyn modification of the Langmuir probe such as was used on the satellite Ariel I (Bowen et. al., 1964; NASA SP-43, 1963). This permits the energy-distribution function of the plasma to be measured by determining the second derivative of the current vs. voltage characteristic curve of a probe embedded in the plasma.

Energy range: 0 to 10 e V, in 16 steps.

Power: 75 mw, with voltage regulated to $\pm 1\%$.

Size: Approximately 20 in^3, weighing 0.37 lb.

Measurements may be made over times as short as 25 msec. For one complete distribution curve, we need 96 bits/sec.

10. Curved-Plate Electrostatic Analyser

This is an instrument for measuring the energy spectra of electrons and protons from 5 e V to 50 keV. It is essentially a curved capacitor, in which charged particles enter at one end, and only those particles which have just the right velocity such that the electrostatic force on them just balances the centrifugal force of the curved path, survive to exit the "capacitor" and be counted by a Channeltron counter.

The 5 e V to 50 ke V should be divided into 32 logarithmic steps. With 9 bits/measurement and 32 measurements/sec, we need a data rate of 288 bits/sec.

Captive area: 0.5 cm^2; detector dynamic range: 10^{-14} to 10^{-9} amp.

Angular resolution: 12° in θ-plane, 60° in ϕ-plane.

Mechanical: 0.5 kg; 430 cm^3 volume; operating temp., -40° to $+60^\circ C$.

Electrical: 0.65 W max, 0.36 W. min.

11. Plasma Wave Detector

This is designed to detect electric and magnetic plasma waves at essentially audio frequencies, using an electric-dipole antenna and a search-coil magnetic-wave detector. A boom contains the 0.5 m search-coil magnetometer and a 0.5 m long wire-grid electric-field dipole antenna. They are mounted orthogonally, but may be separated by up to 1m.

Boom sensors weight a total of 1.5 lb. (Magnetic sensor is 2" x 2" x 24"; electric one is 1" x 1" x 16", with 4" diameter wire mesh spheres at each end.) Operating temperature, -65 to $\pm$ 40°C; storage, -75 to +40°C. It draws 0.3 W.

Electronics: 6" x 6" x 6", 4.5 lb. (on bus); -40 to +40°C (operating); -50 to +50°C (storage). Draws 1.7 W.

Data rate: -128 bits/sec. This includes a sample of the waveforms of the most energetic waves occuring 2 sec. out of every 300 sec.

Sensitivity: (set by noise power spectrum due to spacecraft): Mag.: $10^{-4}\phi^2$/Hz at 3 Hz, decreasing to 10^{-10} at 3 kHz. Electric: 10^{-14} $V^2/m^2/Hz$ at 3 Hz, decreasing to 10^{-16} at 300 Hz. Flat at $\geq$ 300 Hz.

Frequency response: 3 Hz - 3 kHz (mag.); 3 Hz - 30 kHz (elec.). Frequencies detected are discrete: 4.6, 10, 22, 46, ... Hz.

12. Trapped Radiation Detector

This is a package designed to detect the high-energy electrons and protons trapped in the Jovian magnetic field, forming belts analogous to the terrestrial Van Allen belts. The package we suggest is based on Dr. Van Allen's Pioneer F/G (Jupiter Flyby) proposal, which provides good coverage of the important energy ranges.

The package contains 5 detectors of proven reliability (used, e.g., in Mariners):

Detector A: EON type 6213 end-window GM tube with a window of 1.2 mg/cm^2 mica and 9.4 mg/cm^2 Be, with a 35° half-angle field of view. Dynamic range:

0.5 to 10^6 counts/sec (directional intensities up to 3×10^7 $(cm^2 \text{ sec sterad})^{-1}$). This will detect:

electrons, $E_e > 90$ keV

protons, $E_p > 2.3$ MeV

solar x-rays, $2 < \lambda < 8$ Å

Detector B: Same as A, except without the Be window:

$E_e > 40$ keV; $E_p > 0.5$ MeV

Detector C: Same as A, except with 10 mg/cm^2 Al window instead of Be:

$E_e > 90$ keV; $E_p > 2$ MeV

Detector D: Nuclear Diodes, Inc., totally depleted Si surface barrier diode with 28μ thickness and effective area of 10 mm^2, shielded by Ni foil of 0.15 mg/cm^2 air equivalent thickness. It has four electronically discriminated levels:

D1: $0.2 < E_p < 50$ MeV

D2: $0.3 < E_p < 20$ MeV

D3: $0.5 < E_p < 4$ MeV

D4: $0.8 < E_p < 2$ MeV

insensitive to electrons

Half-angle, 35°. Dynamic range, 0.01 to 10^5 counts/sec (directional intensities up to 1×10^6 $(cm^2 \text{ sec sterad})^{-1}$).

Detector E: Coincidence telescope of 3 miniature GM tubes, each with cylindrical effective volume 2 mm diam x 5 mm length. Outputs are the individual rates E1, E2, E3; double coincidence rate E12; and triple coincidence rate E123. Shielding is $\geq$ 7 gm/cm^2 except at front end of telescope. 30° half-angle. Experimentally selected inter-element shielding sensitive to electrons, $E_e > 2$ MeV through E12, and $E_e > 5$ MeV through E123. Characteristics of detector system will be optimized experimentally to enhance the energy

discrimination and the interpretable significance of the individual rates in terms of assumed electron spectra, and the proton response will also be experimentally determined.

Power: 1.15W continuous at 28 V. $\pm$ 1%.

Mechanical: Volume, 280 in^3. Shape not critical, could be 7"x8"x5" box. Weight, 3.2 lb. Temp: -100 to +30°C (operating); -150 to +40°C (storage).

Data Format: 12 outputs: A, B, C, D1, D2, D3, D4, E1, E2, E3, E12, and E123. Each consists of random pulses at a rate $\leq 10^5$/sec, which is fed into a 9 bit logarithmic accumulator, which must be read by the spacecraft by a freeze, read, and reset-to-zero command.

There are also two temperature and 1 voltage sensors.

Allowing 9 bits/output, and reading the 12 accumulators each sec., we need a data rate of 108 bits/sec.

13. Micrometeoroid Detector

We recommend the use of two micrometeoroid detectors: a piezoelectric type combined with a time-of-flight type. The former is reliable, frequently-flown instrument whose accuracy of calibration will improve as micrometeoroid simulators of higher energies are built, and the latter, currently under development, would provide a measurement of particle velocity that cannot be obtained with the former. Since the former type is momentum- or energy-sensitive, the velocity of the particle must be measured to obtain an accurate value of particle mass, and the time-of-flight detector accomplishes this by measuring the time it takes the micrometeoroid to travel a known distance. Power: 1 W; Size: 5"x5"x5"; Sensitivity: Momenta of 10^{-5} dyne sec and velocities of up to 100 km/sec; Weight: 10 lb; Data rate: 1 bps max.

14. Decimetric Swept Receiver

The Decimetric Swept Receiver is a receiver operating in the range of 50 Mhz to 5,000 Ghz. Since it operates in a noisy environment, 10^9 flux units, its

sensitivity need not be great. It consists of a ten MHz IF strip with about a one MHz bandwidth tacked onto the back end of a double balanced mixer. The input ports of the mixer are coupled to a pair of wideband, low gain antennas, and a swept frequency LO. The two antennas cover the ranges, 50-500 MHz and 500-5000 MHz respectively. The LO sweeps continuously from sixty to 5000 MHz in about fifty seconds. The AGC loop in the IF strip has a time constant of .01 second. This allows a resolution of almost one megacycle in the output data if desired. An A/D converter digitizes the AGC voltage at pre-selected frequencies modifiable by ground command. At maximum data rate, this voltage is sampled every .01 second to provide a reading every megacycle. At this rate there are one hundred six bit words or six hundred bits per second from this experiment. The Decimetric swept receiver is an input on the PSI commutator and is active only when the commutator is active.

A rough estimate for the weight of the electronics other than that contained in the extent telemetry system is $\sim$1 lb., with $\sim$ 0.1 W power required.

15. Decametric Receiver

The decametric radiation is, unlike the decimetric, highly erratic. It is also extremely intense, being $\sim 10^{16}$ f.u. at the order of a Jovian radius from the planet. (1 f.u. = 10^{-26} W m^{-2} Hz^{-1}). This figure represents the most intense signal found at $\sim$ 5 MHz, which falls to $\lesssim 10^{5}$ f.u. at 40 MHz.

We propose a receiver to sample both circular polarizations at 16 frequencie from 1 to 50 MHz. It should measure the intensity averaged over one second at each frequency for each polarization. It should also be possible to occasionally connect the decametric receiver to the video recorder, during times when the loss of a video frame can be afforded. This would permit the recording of the detailed (sub-millisecond) structure of the noise bursts, which could not be otherwise done because of the high data rate required (e.g., to record one second

of this noise with 0.1 msec time - resolution would require $\sim 10^5$ bits).

The antenna may be small, because the signals are about six orders of magnitude stronger at long wavelengths, where a short antenna is least efficient.

Dynamic range desired: 10^4 to 10^{17} f.u.

Data Rate (normal mode): One scan of the spectrum per second for 128 bits/sec.

Electronics: 3 W. average; 3 lb. weight; 100 in^3 volume.

Temperature range: -50 to +40°C (operating); -50 to +75°C (storage).

16. VLF Receiver

The Very Low Frequency (VLF) receiver is modeled on VLF receivers used in earth orbit to detect terrestrial VLF signals.

Frequency response: 0.2 - 100 kHz in 256 equal steps.

Dynamic range: 80 db (using Stanford University log compressor).

Power: 28 ± 5 VDC at 33 ma.

Weight: 0.8 kg (main-body package); 0.13 kg (preamp); 0.32 kg (inflatable loop antenna); 0.5 kg (antenna inflation mechanism).

17. X-Ray and Gamma-Ray Detector

The interaction of the expected Jovian high-energy electrons and protons with the Jovian atmosphere is expected to generate considerable fluxes of X- and γ-rays (Edwards and McCracken, 1967). Following Dr. E.L. Chupp's Pioneer F/G proposal, we suggest using a gamma-ray spectrometer similar to one designed for the OSO-H satellite, and a conventional X-ray detector.

Mechanical: 7 lbs, 370 in^3. Detector requires an area of 49 in^2.

Dynamic range: 10 to 200 keV in six channels (X-ray); 200 keV to 10 MeV in 100 channels (γ-ray).

Counting rate: 500 kHz max. with a dynamic range of 10^4 (X-ray); 150 counts/sec (γ-ray).

Power: 1.8 W.

Data rate: 64 bits/sec normally, increasing in 5 stages to 2048 bits/sec on command.

18. Radio Occultation

This is a zero-weight, zero-power experiment that requires only that the on-board telemetry transmitters be used while the satellite is being occulted by Jupiter or one of its natural satellites. Earth tracking then measures the Doppler shifts caused by both the spacecraft motion and by the apparent path-length change due to the variation in the Jovian outer-atmosphere's index of refraction , which is a function of its constituents. The use of two spacecraft transmitters of different frequencies permits the plasma dispersion to be distinguished from other effects. This type of radio occultation experiment has yielded much useful information on the structure and composition of the Martian and Venusian atmospheres from Mariner flybys, and should, in the case of Jupiter, enable a measurement of the vexing hydrogen-to-helium ratio to be made.

19. Gravitational Red-Shift

It is an experimental fact, as well as a cornerstone of almost all gravitation theories, including General Relativity, that photons lose energy as they rise through a gravitational field, much as any thrown mass does. This energy loss causes a minute reddening of the photon, given by $\Delta f/f = GM/Rc^2$, where $\Delta f/f$ is the fractional frequency shift; G, the universal gravitational constant; M, the planetary mass, c, the speed of light; and R, the distance from the center of mass.

Such a gravitational red-shift experiment has been proposed for earth-orbit, whereas the shift is around thirty times greater for our Jupiter orbiter. (The maser must be on-board to provide the precise timing needed, because earthbound timing signals would be blue-shifted on their way to Jupiter, which would exactly cancel the red-shift we wish to measure.)

This experiment would not only provide a better experimental test of the gravitational red-shift than available near earth, but would additionally map the Jovian gravitational potential.

The maser may be a 21 cm hydrogen maser, for which a stability of the order of 1 part per 10^{14} is plausible within the time-frame of the present project.

We assume a weight of 50 lb and a power requirement of 10 W.

20. On-Board Radar

The on-board radar system has three functions. It is a navigational device, used to place the spacecraft position more accurately than ground based observations ; a scientific instrument, used for celestial mechanics observations ; and an auxiliary data downlink. The downlink aspects of the system are described in the section on telemetry and data processing (Chapter VIII).

a) Navigation:

Ground based navigation is based on long term doppler tracking. This method measures the radius vector and the rate of change of the radius vector from the spacecraft to Earth extremely precisely. At distances of five and six A.U., however, positional errors of tens of thousands of kilometers are likely to result. When an extremely eccentric orbit is planned, as in the case of JOSE, the deboost maneuver and the spacecraft position at the time of the deboost maneuver are extremely critical. Such errors are completely intolerable. Imaging Jupiter and the satellites against star fields help the situation somewhat,

but problems of determination of position still exist. It is necessary to define the center of the body being imaged and to then place that center in the star field, part of which has been occulted by the body being observed. The problem is complicated by the lack of a good measurement of the sizes of Jovian satellites. The radar system herein described is capable of adding another dimension to the measurement. The distance from spacecraft to a Jovian satellite surface can be determined to an accuracy of ten to fifteen kilometers, and the range rate can be determined to an accuracy of ten to twenty meters per second out to a maximum range of eight to nine R_J (7.1×10^5 km = R_J).

As a celestial mechanics instrument, the radar can study the orbits of the spacecraft and the natural satellites of Jupiter by continued observations over a long period. In this way gravitational anomalies possibly caused by Jupiter Mascons or as yet undiscovered Jovian satellites can be studied.

The operating parameters of the radar system are to a great extent determined by convenience. It is convenient to operate at X band because an X band downlink already exists and so the opportunity of making the radar double as a downlink backup is attractive. X band allows the use of an antenna similar in size and construction to the downlink antenna which in addition is highly steerable. Acceptable range capability is obtainable with an RF and power system operating at the same average power as the downlink system. The radar antenna at X band has the same beamwidth as the field of view of the imaging system. This last point, and the fact that the radar antenna must be highly steerable, suggests another possible combination of function. It is convenient on the JOSE spacecraft to make the planetary and imaging instrument scanning platform the mount for the radar antenna. The platform becomes a sandbox, one of the large surfaces of which is the radar antenna. Mounted inside the sandbox and peeking out through small holes in the radar antenna

are the scanning instruments. These instruments are then bore-sighted with the radar beam. Anything in the field of view of the TV camera, for instance, is then also in the radar beam and the distance and range rate can be determined. One important measurement that can be made in this way is the size of the satellite.

b) System Description

The X band antenna is a flat dipole array similar in construction to the two downlink antennas. The main difference is that the radar antenna is circularly polarized, while the downlink antennas are linearly polarized. This is because of the character of reflections from moon-like objects which tend to be rotated in polarization. The physical dimensions of the antenna itself are 1.26 by 1.26 meters.

The transmitting system of the radar consists of a pulsed TWT capable of a peak pulse power of ten kw, average power of 100 watts and maximum pulse width of ten milliseconds. The transmitter is driven from solid state driver stages from the same 8450 Mhz oscillator which drives the downlink transmitter. A phase modulator inserted between the driver and the oscillator impresses a phase code on the transmitted pulse. This phase code is necessary to simulate a very high peak pulse power with a limited peak power system. A controller determines the mode of operation, search, range refine, etc.

The receiving system consists of a front end with a $300^{\circ}K$ noise temperature, a mixer, a variable frequency local oscillator, an IF amplifier, matched filters, timing circuits, and data handling logic. (See figure VI-2).

c) System Operation

Since the relative velocities of the spacecraft and satellites can become rather large (as much as fifty km/sec), the doppler shift in the received signal is given by:

$$\Delta f = 2f_o V/C \qquad 1$$

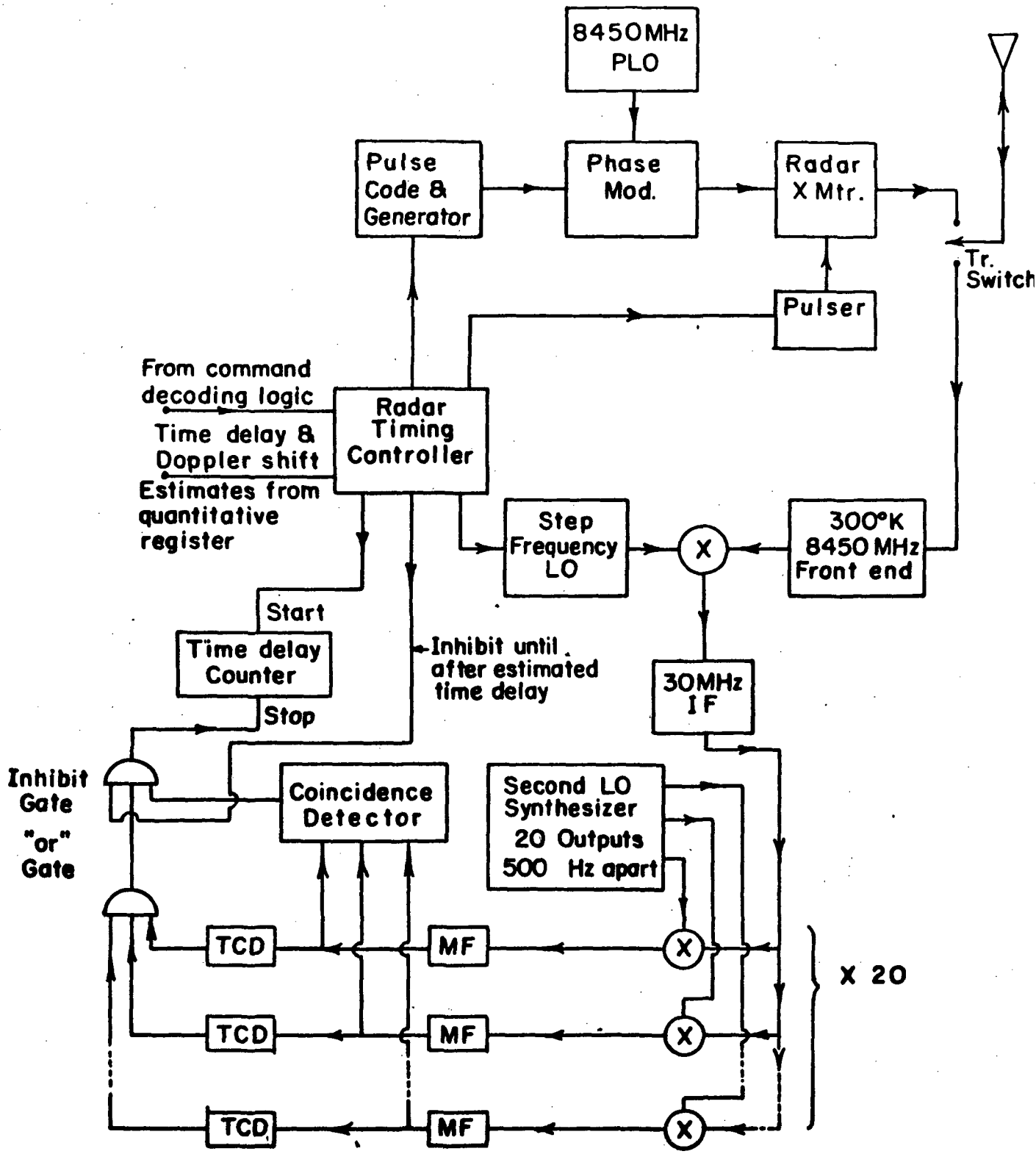

Figure VI-2: Radar System Block Diagram. (PLO = phase-locked oscillator; MF = matched filter, TCD = threshold crossing detector; LO = local oscillator).

where f_o is the transmitted frequency, V is the relative velocity, and C is the speed of light, can be as great as three megahertz. For long range ranging and limited transmitter power, the receiver bandwidth must be small (1-10 Khz) to knock down the noise. There must then be some way to search in the frequency domain for the doppler shifted echoes. In addition the radar is attempting to measure the range to the target by measuring the time delay, so the system must also search in the time domain for an echo. The frequency search is accomplished by switching the local oscillator frequency in steps equal to the bandwidth of the transmitted pulse. These steps are ten kilohertz. The time domain search is accomplished by a threshold device that triggers whenever the input waveform exceeds a preset (set by ground command) level. In addition, since the delay line matched filter method only accomodates doppler shifts that are small compared to the reciprocal of the total pulse length or the echo bandwidth, whichever is larger, there are twenty matched filters spaced in frequency by 500 Hz attached to the output of the IF amp. 500 Hz is chosen because this is the expected bandwidth of the echo returns from Io. Thus twenty frequencies are searched simultaneously, and each ten khz step in the LO frequency brings twenty more frequencies under scrutiny.

The amount of frequency and time domain to be searched depends on the accuracy of ground based measurements and estimates of the parameters to be measured. It is hard to estimate this accuracy, but it appears that the worst case is when the spacecraft is near periapsis. At this time, its velocity is of the order of 50 km/sec and its total doppler shift is about three mhz. Also at this time its distance to the only satellite visible is about six R_J which is near the extreme range of the radar. Under these conditions it seems reasonable to say that the uncertainties in question amount to about .1 second round trip delay time (15 thousand km), and 100 khz doppler shift (2 thousand km/sec).

d) Sequence of Events

The radar sequence is as follows. Upon receipt of a ground command, or at the execution time of a stored command, the LO offset frequency, the detection threshold, and the expected round trip time is determined. A pulse is transmitted. In this, the frequency search mode, the pulse is ten milliseconds long with one hundred phase coded subpulses each one hundred microseconds long. The peak power of this pulse is ten kw. One such pulse transmitted in one second to maintain the average power at ten kw. At the expected time of arrival of the echo, the matched filter banks are enabled and the time of any threshold crossings are recorded. If a pulse is detected in more than three adjacent matched filters simultaneously, it is regarded as a noise pulse, because a signal pulse would be seen in only one filter and perhaps in the adjacent filters, and ignored. A second pulse is then transmitted and the process repeated. Any threshold crossing happening in the same filter output at the same time delay as the first pulse, is regarded as a possible echo. The number of such coincidences is stored. The LO frequency then steps to the second offset frequency and the process repeats. Two pulses are transmitted per LO offset frequency and the number of coincidences stored for each frequency. If the threshold was correctly chosen, there should be only one or two false coincidences per run through the offset frequencies. The frequencies where coincidences showed up are interrogated again, this time with a series of three pulses each. With the threshold set such that the signal to noise ratio must be 3.45 to overcome it, the probability of error, or the probability that a detection is a noise pulse, is less than one in ten to the fifth. If the required signal to noise ratio is set at 4.45 to account for the possibility of a missed echo, the maximum range for the radar is defined by

$$R = 3.11 \left(\frac{P_{av} A^2}{4.45\ N} \right)^{\frac{1}{4}} R_J, \qquad 2$$

where N is the repetition frequency, A is the antenna effective area, P_{av} is the average transmitter power output. This equation holds under the following assumptions:

Rx noise temperature: $300^{\circ}K$

Rx bandwidth always the reciprocal of sub pulse duration

Integration time equals the pulse length resulting in SNR improvement of $\sqrt{TB}$

Satellite radius: 1600 km

Satellite X band albedo: 10%, i.e., most like the moon.

Then with a 1.2 m^2 antenna, 100 watts, and one pulse per second the range is 7.1 R_J. This range is adequate to range from Io consistently when near Jupiter, and the other satellites for varying amounts of time.

After roughly defining the range and doppler coordinates in the search mode, the radar can go to the range refine mode wherein a long series of pulses can be sent and the arrival times averaged. The range definition is approximately given by one half the distance light travels in 100 microseconds, or fifteen km. Repeated measurements, however, reduce the uncertainty by approximately the square root of the number of measurements. In addition, in this mode the output of the receiver is available to be sent back in the time domain via the downlink after A/D conversion. In this way waveform analysis can be formed on the echo waveform and the satellite surfaces can be studied.

Note that the range given is based on a somewhat arbitrary detection scheme. It is nevertheless a valid limit on the range because all of the parameters are well known except, perhaps, the required signal to noise ratio. However, because

this quantity enters the expression for maximum range as a fourth root, large changes in its value have little effect on range. On the other hand, range has an R^4 effect on the required signal to noise ratio. As a result, detection schemes which are only just marginal at the extreme range, rapidly become much more sophisticated than necessary as the range goes down. This implies that search procedures, and coding requirements are much less stringent at short range. Thus provision is made for changing the threshold requirements and the search program format.

21. Ionospheric Topside Sounder

The presence of an ionosphere around Jupiter has been established, and in an effort to provide some information about the detailed structure of it, it is proposed to include a top side sounder on the spacecraft. While the frequency range remains to be worked out, it is clear that the sounder must be a wideband device. It is also clear that the sounder antenna must be compatible with this requirement. It should have a usable range on the order of five Jupiter radii and a height resolution of fifteen km. It remains to calculate the range of the sounder.

a) Sounder Range Determination

The standard radar equation derived from geometrical optics works for spheres only when the range to the sphere is large in comparison to its size. Since the sounder will operate in close proximity to Jupiter, a modification of the radar equation must be made. On the assumption that the reflection layer for a particular frequency is a perfect sphere, Figure VI-3 shows the geometrical optics on which the modification of the radar equation are based. If the sounder antenna is taken as a point source in the transmit mode, which is valid because the ionosphere will never be inside the near field of a short wave dipole, it is clear that A_s is four times as large as A_r modified by the

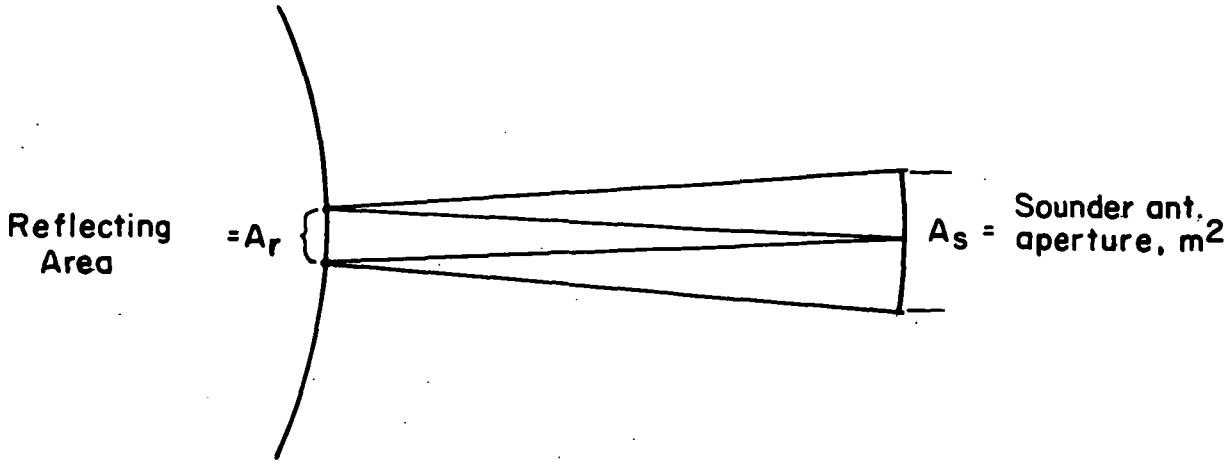

additional factor R^2/r^2, where R is the Jupitercentric distance to the spacecraft and r is the radius of the reflection layer which is about equal to the radius of Jupiter. A_r, the area of the reflection layer which reflects signals back to the sounder antenna, is given by:

$$A_r = A_s r^2/4R^2.$$

Since all the power incident on A_r, and only that power, is reflected back to the sounder antenna, it remains only to calculate the power incident on A_r to get the received echo power. The power received is given by the well known expression:

$$P_r P_t G A_r/4\pi(R-r)^2$$

where R-r is the distance to the reflecting layer.

Or: $$= P_t G A_s r^2/16\pi R^2(R-r)^2$$

Note that in the limit as R gets much larger than r, the expression reduces to the standard form of the radar equation except for the albedo expression sigma (σr^2 = radar cross section) which is here assumed to be one.

If a ten db margin is built into the system to take care of reduction in the value of sigma from one as a result of absorption, and if a galactic noise temperature of 5×10^5 °K, frequency of three mhz, pulse length 100 microseconds and the use of a resonant dipole are assumed, the range is about 5.5 R_J Jupitercentric. These figures are substantially supported in a letter from Dr. Colin Franklin, one of the chief investigators on the Allouette Satellite Project.

The ten db margin should be enough to take care of absorption, but Jupiter noise bursts will most probably wipe out the sounder when they are present.

A considerable problem is presented in the selection of an antenna system for the sounder. The ten db margin does not allow for the kind of losses due to antenna mismatch experienced on the Allouette and ISIS satellite sounders. Losses of the order of thirty to fourty db were reported over some frequency ranges for the antenna system in use on those satellites. They used basically fixed dipoles. There were two on each satellite, one for the low end of the sweep and one for the high end, with some overlap. The behavior of these fixed antennas would preclude any success in the Jupiter sounder because of the narrow margin allowed. Therefore, one dipole with traps, has been settled on. The trap dipole with discrete frequencies appears to be the best idea since it can be optimized at each of the discrete frequencies, and once extended, need not be mechanically adjusted during an ionosonde sweep.

The trap dipole envisioned is a development of the STEM antennas manufactured by Spar Aerospace Products Ltd. The antennas are reeled out of a canister by a motor like a tape measure. The traps are constructed of sandwiched layers of thin film capacitors and inductors molded into the actual tubular element without producing a bump. The total length of the antenna, tip to tip, is some fifteen hundred feet. Such an antenna, without the traps, has already been flown successfully.

The frequencies chosen for the ionosonde and the antenna lengths for each are:

310kHz	1550 ft.	800kHz	587.5 ft.
1800 "	261 "	3000 "	157 "
4500 "	104.4 "	6000 "	78.5 "
18000 "	58.8 "	10000 "	47 "
12000 "	39.2 "	15000 "	31.3 "

The lengths given are the distances between the traps tuned to the appropriate frequency. The length of the 310 kHz antenna is the overal tip to tip length of the whole antenna.

The frequencies given above cover the range of electron density from 1.2×10^9 e/m^3 to 2.8×10^{12} e/m^3.

The sounder consists of a solid state fifty kw peak power pulsed transmitter. Transmitter pulses are 100 microseconds wide and are initiated by realtime or stored ground commands. The receiver consists of a low sensitivity set of front ends switched in sequence to the antenna. TR switching is by mechanical relay because of the long round trip times involved (never less than 40 milliseconds) and the high power levels. The front ends are connected to a mixer whose Local Oscillator frequency is also switched in sequence along with the transmitter frequency. The LO frequencies are derived from the same synthesizer as the transmitter.

Upon transmission of a pulse, a counter starts counting and the receiver is enabled on the appropriate frequency. When the echo is received, the time is noted in the output register along with a frequency code. If no echo is received after the maximum range round trip time (2.8 seconds), a second attempt is made. If no echo is received this time, the sounder steps to the next frequency. If an echo is received, the sounder immediately steps to the next frequency. Each time a pulse is sent and received, the round trip time and the frequency code are noted in the output register. If the output register has not been read out and reset by the time the sounder is ready to load new information into it, further pulses are inhibited. Upon completing two complete sweeps, the sounder stops and waits for another command to begin another sweep, unless the original start command was for a continuous scan in which case the sounder continues to sound until a command to stop is issued.

Since the maximum roundtrip time is 2.8 seconds and the desired resolution capability is 100 microseconds, the time counter must be able to count to 28,000. This requires a twenty five bit ripple through counter. Since the data format calls for output words to be a multiple of six bits, this leaves five bits for a frequency code and any other necessary housekeeping.

The 455 Khz IF strip in the ionosonde is AGC'd so as to allow measurement of the background radio noise in the Jovian vicinity. The AGC voltage is available to the PSI commutator as an input.

22. Plasma Resonance Detector

The Plasma Resonance Detector is a swept frequency, low power oscillator and a receiver operating in the frequency range of ten to one hundred kilohertz. The oscillator operates at a power level of one watt and is coupled into the ionosonde antenna, which it uses during lulls in sounder activity. The oscillator is pulsed at a ten cycle rate with a pulse width of two hundred microseconds. It completes a scan of the frequency range ten to one hundred khz in 6.4 seconds. There are thus sixty-four pulses per scan. Each time a signal above a preset threshold is present at the antenna terminals during the interpulse period, the output of a six bit counter which has been counting the pulse is read out into the output buffer. This buffer is a thirty six bit shift register capable of holding six such numbers. In the event of buffer overflow, the scan is halted until capacity is again available. The output buffer empties, upon interrogation, into the Planetary Science Instrument Commutator.

The Plasma Resonance Detector measures the electron density in the vicinity of the spacecraft.

Chapter VI - References

Anders, R.A., Callahan, D.E., List, W.F., McCann, D.H., Wing, M.E., "100 x 128 - Element Solid State Imaging System", Paper 13/1, WESCON 67 Technical Papers, presented at the Western Electronic Show and Convention, August 22-25, 1967, Session 13, Solid State Imaging, an Evolving Technology.

Ash, J.E., "Analytical Methods and Observational Requirements for Interpretation of Asteroid Distributions", Report No. P-14 by the Astro Sciences Center of IIT Research Institute for the Office of Space Sciences and Applications, NASA Headquarters, Washington, D.C., Contract No. NASr-65(06), December 1965.

Bandeen, William R., "Experimental Approaches to Remote Atmopsheric Probing in the Infrared from Satellites", NASA TM-X-63188, Goddard Space Flight Center, Greenbelt, Maryland, May 1968.

Bowen, P.J., Boyd, R.L.F., Henderson, C.L., and Willmore, A.P., "Measurement of Electron Temperature and Concentration from a Spacecraft", Proc. Royal Soc. (A), Vol. 281, pp. 514-525, 1964.

Brouwer, D., and Clemence, G., Methods of Celestial Mechanics, Academic Press; New York, New York, 1961.

Chupp, E.L., "X-Ray and Gamma Detector for Pioneer F&G Mission", proposal to NASA from Dept. of Physics, University of New Hampshire, Durham, New Hampshire, 1968.

Corliss, W.R., Scientific Satellites, NASA SP-133, 1967.

Edwards, P.J. and McCracken, K.G., "Upper Limits to the Hard X-Ray Flux from the Quiet Sun and Jupiter", Journal of Geophysical Research, Vol. 72, 1967, pp. 1809-1812.

Fastie, William G., "Ultraviolet Measurements in Planetary Atmospheres", Aero-Space Measurement Techniques, Gene G. Mannela, ed., National Aeronautics and Space Administration SP-132, Washington, D.C., 1967.

Gledhill, J.A., "Jupiter's Magnetosphere", NASA TM-X-55704, Goddard Space Flight Center, Greenbelt, Maryland, February 1967.

Gledhill, J.A., "The Structure of Jupiter's Magnetosphere and the Effect of Io on its Decametric Radio Emission", NASA TM-X-55980, Goddard Space Flight Center, Greenbelt, Maryland, June 1967.

Jet Propulsion Laboratory, "Jupiter Advanced Planetary Probe, Science Objectives and Typical Experiments", Engineering Planning Document EPD-280, Pasadena, California, September 15, 1965.

Kaula, William M, Theory of Satellite Geodesy, Blaisdell Publishing Co., Waltham, Massachusetts, 1966.

Leighton, Robert B., Murray, Bruce C., Sharp, Robert P., Allen, J Denton, Sloan, Richard K., "Mariner IV Pictures of Mars", Technical Report 32-884, Jet Propulsion Laboratory, Pasadena, California, December 15, 1967.

References (cont.)

Mannella, Gene G., Aerospace Measurement Techniques, NASA SP-132, National Aeronautics and Space Administration, Washington, D.C., 1967.

NASA, Ariel I, Special Publication, SP-43, 1963.

Paul, Charles K., "Jupiter Orbiter Imaging Sequence of Events", Interoffice Memorandum 3291-69-181, Jet Propulsion Laboratory, Pasadena, California, August 5, 1969.

Paul, Charles K., "Lunar Terrestrial Photogrammetry by Surveyor Spacecraft", a thesis presented to the faculty of the Graduate School of Cornell University for the degree of Master of Science, Ithaca, N.Y., June 1967.

Richter, Dr. Henry L., Instruments and Spacecraft, October 1957 - March 1965, NASA SP-3028, National Aeronautics and Space Administration, Washington, D.C 1966.

Rorden, L.H., Orsak, L.E., Ficklin, B.P., and Stehle, R.H., "Instruments for the Stanford University, Stanford Research Institute VLF Experiment (4917) on the EOGO Satellite," Stanford Research Institute, Menlo Park, Californiz, 1966.

Stewart, R.D., Littebrant, E.L., "A Solid State Image Converter", Paper 13/4, WESCON 67 Technical Papers, presented at the Western Electronic Show and Convention, August 22-25, 1967, Session 13, Solid State Imaging, an Evolving Technology.

Van Allen, J.A., "An Energetic Charged Particle Experiment for the Asteroid/ Jupiter Missions, Pioneers F and G", proposal to NASA from the Dept. of Physics and Astronomy, University of Iowa, Iowa City, Iowa, 1968.

Weckler, Gene P., Dyck, Rudolph H., "Integrated Arrays of Silicon Photodetectors for Image Sensing", Paper 13/2, WESCON 67 Technical Papers, presented at the Western Electronic Show and Convention, August 22-25, 1967, Session 13, Solid State Imaging, an Evolving Technology.

Weimer, P.K., Sadasiv, G., Meyer, J.E., Meray-Horvath, L, Pike, W.S., "A Self-Scanned Solid-State Image Sensor", Paper 13/3, WESCON 67 Technical Papers, presented at the Western Electronics Show and Convention, August 22-25, 1967 Session 13, Solid State Imaging, an Evolving Technology.

Chapter VII: Telecommunications and Data Processing Systems

A. Design Philosophy

The purpose of the telecommunications and data processing systems is to condition data from various sources on the JOSE spacecraft, including science and engineering sensors, in such a way as to facilitate their transmission via radio, back to ground stations. In addition, these systems provide the means by which the spacecraft can be controlled from the ground.

There are many sources of data on the spacecraft, but the most prolific, in terms of data production, is the imaging and planetary science package. Since this package requires more channel capacity in the downlink communications system than all the other systems combined, the channel capacity of the spacecraft as a whole is basically determined by that requirement.

The basic capabilities of the data systems are determined by many factors. The most important are: limitations imposed on the downlink channel capacity by size and weight of downlink transmitting apparatus, and downlink receiving capabilities, and availability of the deep space network facilities. The rate of data acquisition and the duty cycle of the downlink channel, the percentage of time that the DSN is available for JOSE use, determine the maximum bit rate required of the downlink channel. The time between periods of downlink activity determines, then, the storage capacity required of the data systems. The capabilities of the data systems have been specified according to the assumption that the DSN will be available a maximum of eight hours a day. The spacecraft has been designed to tolerate, during cruise mode, lapses of DSN

availability of several days duration without loss of data capability.

The eight hour a day limitation has been placed on the DSN by competition between JOSE and other planetary or deep space missions which most likely will be active during the flight and orbital lifetimes of JOSE. Since DSN operation is expensive, an effort has been made to limit the amount of downlink time necessary even further than the eight hour a day limitation. This has been done by designing for a higher maximum data rate than that necessary to completely dump the spacecraft memory in six hours (the amount of time actually of use out of the eight hours due to acquisition time lag). A data rate of one hundred twenty kbps has been assumed for the high data rate channel. This is sufficient to dump the high volume JOSE memory in about two and a half hours.

The lifetime of the JOSE mission is on the order of five years. Approximately two years are necessary for the original approach to Jupiter, and about three years in Jupiter orbit are a minimum requirement from a scientific standpoint. This presents, of course, a significant reliability problem for a spacecraft with such a multiplicity of functions. The traditional methods of reliability engineering, chiefly redundant systems, have been employed in the JOSE spacecraft, however, instead of duplicating entire functions, an attempt has been made to provide an overlapping of functions between the different downlink and storage devices. For instance, the X band radar, included in the flight primarily as a scientific instrument, can also be used as a back-up high capacity downlink channel. Another example of this is in the data storage tape recorders. There are three such recorders, a 10^9 bit device for storage of video data, a 10^8 bit device for storage of every twelfth

pixel of video information (used to take out the effects of AGC included in the high capacity storage but not the low capacity storage), and a 10^9 bit device for storage of scientific and engineering data. In the event of failure of any of these tape recorders, the other two are able to at least partially take over the job. The chief effect of a failure, then, is not a catastrophic loss of function, but rather an increase in downlink time, or a reduction in the number of video images per data dump.

A very important attribute, versatility, comes to mind. The spacecraft had to be designed such that its systems would be able to swap functions in the event of failure. In this way, the size and weight of merely redundant systems, which would not come into play until the primary systems failed, was saved.

B. System Description

1. Data Automation System (DAS):

The DAS, Fig. VII-1, consists of the commutators necessary to sample and correctly route scientific, engineering, and imaging data, storage tape recorders, and those commands generated by the command subsystem which configure the DAS for the various Data Modes.

There are two main types of data generated in the spacecraft. They are the high bit rate and low bit rate data. The high rate data originates in the imaging and planetary science package. These data are normally stored in a 10^9 bit capacity digital tape recorder which is periodically dumped to the ground station on the high capacity downlink channel. Normally the high rate data sources are inactive during the cruise mode and the high capacity recorder and the high rate

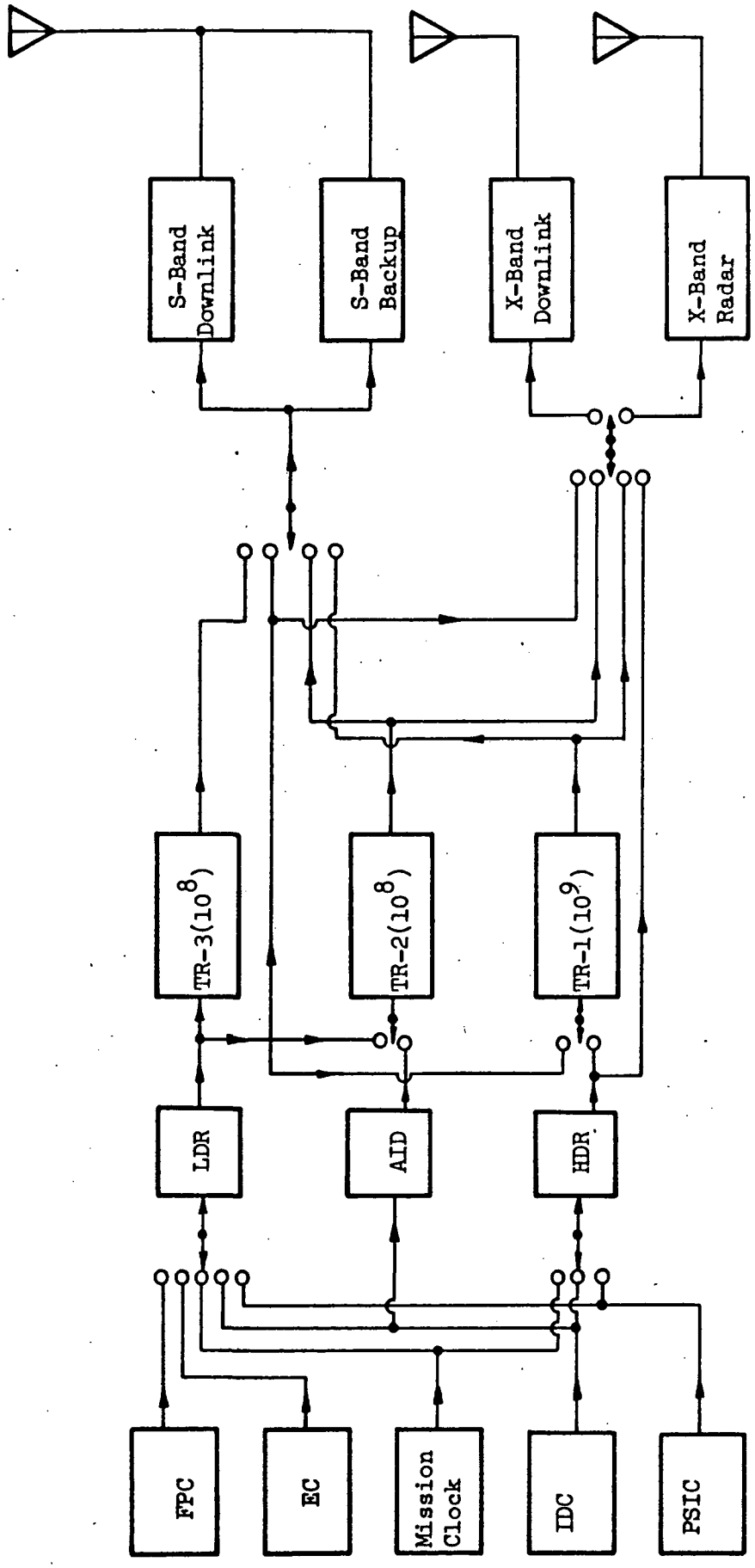

Figure VII-1: DAS Block Diagram

downlink channel are available for the low rate sources.

Low bit rate data originates in the non-planetary (also known as Fields and Particles (F&P))science instruments and engineering sensors. The engineering sensors provide the ground with information concerning the operation of the spacecraft systems, such as temperatures, power supply voltages, and spacecraft attitude. These data are stored in a 10^8 bit capacity (10 kbps) S band downlink channel during periods of high data storage and transmission. Table VII-1 shows the normal allocation of data to storage and downlink channel for different modes of spacecraft operation.

Storage

The DAS has three storage devices for bulk data. TR-1 is a six track tape recorder (digital) with a capacity of 10^9 bits. Its function is to store science and engineering data during the Cruise mode (CRUISE I) and to store video and planetary science information during the ORBIT I mode. TR-1 can be dumped in about two and one half hours through the X band downlink, in about thirty hours through the low capacity S band link, or in about fifteen hours if both S band TWTs are used.

TR-2 and TR-3 are essentially identical six track digital recorders, each with a capacity of 10^8 bits. TR-2 functions as additional low data rate storage during the various cruise modes. During periods of planetary imaging, TR-2 acts as a separate storage device for video information. Every twelfth pixel is encoded into an eight bit binary word (256 levels) at a point before ACG is added to the video signal and stored in TR-2. This performs two functions. First, it allows the effects of AGC to be taken out of the full picture which has been encoded into six bit words

Table VII-1: Storage and Dowlink Allocation

Mode	Stg Allocation	Dwnlink Alloc.	Dump Dur.	Dump Int.
Cruise I	LDR: TR-1(10^9)	TR-1:X(120kbps)	2.32 hr	11.57 day
Cruise II	LDR: TR-1(10^9)	TR-1:X(120kbps)	2.32 hr	5.79 day
Cruise III	LDR: TR-3(10^8)	TR-3:S(20kbps)	1.39 hr	1.16 day
Cruise IV	LDR: TR-3(10^8)	TR-3:S(10kbps)	2.78 hr	1.16 day
Cruise V	LDR: TR-3 and TR-2	TR-3, TR-2:S(20kbps)	2.78 hr	1.16 day
Cruise VI	LDR: TR-3 and TR-2	TR-3, TR-2:S(10kbps)	5.36 hr	1.16 day
Midcourse I	LDR:REALTIME VIDEO:REALTIME	LDR:S (10kbps) VIDEO:X(radar)	--- 3.33 min/pic	--- 3.5 min
Midcourse II	LDR:TR-3 VIDEO:REALTIME	TR-3:S(20kbps) VIDEO:X(radar)	up to 1.4hr 3.33 min/pic	--- 3.5 min
Oribt I	LDR: TR-3 HDR: TR-1 AID: TR-2	TR-3:S(10kbps) TR-1:X(120kbps) TR-2:X(120kbps)	2.78 hr 2.32 hr 13.8 min	1.16 day --- ---
Orbit II	Same as Cruise I			
Orbit III	Same as Cruise II			

Mode Definition:

CRUISE ONE: To be used when continuous DSN monitoring not needed or desired. Assumes 1 kbps constant data output from LDR (Science and engineering data)

CRUISE TWO: Same as Cruise One except assumes constant data output of two kbps

" THREE: Used for both constant monitoring, i.e, once a day. Uses both S band TWTs for 20 kbps. Assumes 1 kbps constant data output.

" FOUR: Same as Three except that only one TWT is used and dump takes twice as long.

" FIVE: Uses both 10^8 bit tape recorders in order to accomodate 2 kbps on a once a day dump schedule. Uses two TWTs.

CRUISE SIX: Same as five, but uses only one TWT.

MIDCRS.ONE: Provides realtime monitoring of spacecraft systems and spacecraft attitude before, during, and after midcourse correction and/or deboost maneuver. X band downlink is via the Radar system because the steerable antenna allows maintaining Earth lock during attitude changes. If maneuver is drastic enough (more than 30^{o} attitude change) S band communication will be lost and engineering data is also routed through the radar system.

MIDCRS TWO: Same as Midcourse One except that LDR Commutator data is stored rather than sent back in realtime.

ORBIT ONE: After orbit is establihsed and planetary (including imaging) science instruments are turned on, both LDR and HDR commutators will be active and need separate downlink facilities.

after AGCing; second, if the 10^9 bit recorder (TR-1) should become inoperative, TR-2 will still be able to store pictures. These pictures would have 200 line vertical resolution, but only 167 line horizontal resolution. Since TR-2 is a six track recorder, a converter is necessary to space the incoming eight bit data so as to fit the six track format. This converter is called the Auxiliary Imaging Data Controller (AID).

TR-3 is the storage repository for the Low Data Rate (LDR) commutator. Six bit words from the science commutator, the engineering commutator, and the mission clock are routed via the LDR commutator to TR-3 for storage. In case of High Data Rate (HDR) commutator, TR-1, or X band downlink failure, the Imaging Data Controller (IDC) and the Planetary Science Instruments (PSI) commutator are also routed via the LDR commutator to TR-3 for storage. TR-3 can be dumped completely in 1.39 hr at 20 kbps, or in 2.78 hr at 10 kbps by the S band downlink system. At a constant rate of 1 kbps, TR-3 can store data for over a day (1.16 day)without overflowing.

Operational Description

Data are routed to the appropriate storage or transmission locations by means of several commutators. These are the Fields and Particles Commutator (FPC), the Engineering Commutator (EC), the Imaging Data Controller (IDC), the Planetary Science Instruments Commutator and Controller (PSIC), the Low Data Rate Commutator (LDR), and the High Data Rate Commutator (HDR). (See Fig. VII -1). The inputs to these commutators are listed in Table VII-2.

In Fig. VI1 -1, note that there are several switches in the data paths. These are to allow different storage and downlink devices to "pinch-hit" for other devices which may have failed.

Table VII-2: Commutator Inputs

Fields and Particles:

- Plasma Probe
- Plasma Wave Detector
- Vector Helium Magnetometer
- Flux Gate Magnetometer
- Trapped Radiation Detector
- Micrometeoroid Detector
- Charged Particle Telescope
- Trapped Radiation Instrument
- Micrometeoroid Detector
- Radio Emission Detector

Engineering:

- Spacecraft Attitude Sensors
- Various Temperature Readings
- Various Power Supply Voltages
- Position of Scan Platform
- Command Confirmation

Imaging Data Controller:

- Video System

Planetary Science Instruments Comm. and Cont.:

- U V Photometer
- I R Spectrometer and Interferometer
- U V and Visual Spectrometer
- I R Radiometer
- Visual Photometer
- Microwave Radiometer
- Ionosonde
- Plasma Resonance Detector
- Decimetric Swept Receiver

Operation

In operation the commutators interrogate their various inputs in turn. Each input is connected to a sensor. Each sensor has its own output format translator, whether it be an A/D converter, a digital accumulator, or a shift register, which translates the output of that sensor into a series of one or more six bit parallel words, plus two status bits. Upon interrogation by the appropriate commutator, the sensor transfers, in parallel, the six bits stored in its output register via the commutator to the appropriate location. The two status bits inform the commutator as to the status of the sensor. The first status bit remains a zero until all of the six bit words are transferred out of the sensor's output translator. When this "no more words" bit is zero, the commutator increment function is inhibited. When all words have been read out, the no more words bit changes to one and the commutator steps to the next input. The second status bit informs the commutator as to whether the sensor is turned on or not, or if the output reading is different from the last time that sensor was interrogated. This last is an elementary attempt at data compression by the elimination of totally redundant data. This second status bit is set to one when the sensor is on and has a new output. Otherwise this bit is set to zero. Upon encountering a zero in this bit, the commutator immediately steps to the first sensor with a one in that bit. It does not skip a timing cycle when it does so step.

The commutators listed in Table VII-2 are themselves inputs to the LDR and HDR commutators. The 28 bit mission clock is an input to these commutators as well. Once each cycle, the last twenty four bits of the mission clock are read into storage so that one second resolution in the

timing of stored data can be achieved. In addition, once each cycle of the FPC, EC, etc. a register is read out that lists the second status bits of the experiments or sensors associated with that commutator. If all the status bits of a particular commutator are zero, a commutator status bit is generated to tell the LDR or HDR commutator to skip that commutator entirely. At the top of each HDR and LDR cycle an eighteen bit start code is generated that tells the telemetry decoder that a new cycle has started. See Fig. VII-2 for a typical LDR bit stream format.

2. Command Subsystem:

The Command Subsystem is that part of the spacecraft that issues commands to the various spacecraft systems and receives and interprets ground commands. Since during the most critical times of the mission, the first approach to Jupiter and the deboost maneuver, the round trip time lag between Jupiter and Earth is of the order of 100 minutes, realtime control of the spacecraft becomes difficult if not impossible. The problem is complicated by the possibility of loss of downlink communication during the deboost and midcourse correction maneuvers. Both up and downlink communication will be lost on the first and subsequent orbits of Jupiter when the spacecraft is occulted from Earth view by Jupiter itself. Therefore the spacecraft must be to some degree automatic. This is best accomplished by a command storage memory updateable by ground command. The memory is loaded with commands in sequence at launch. A binary code which represents the individual command is stored in the memory along with the time of planned execution. A master sequencer clock ticks off the time until the time comes to retrieve the command from the memory and execute it.

There are two main groups of commands and two subgroups in these.

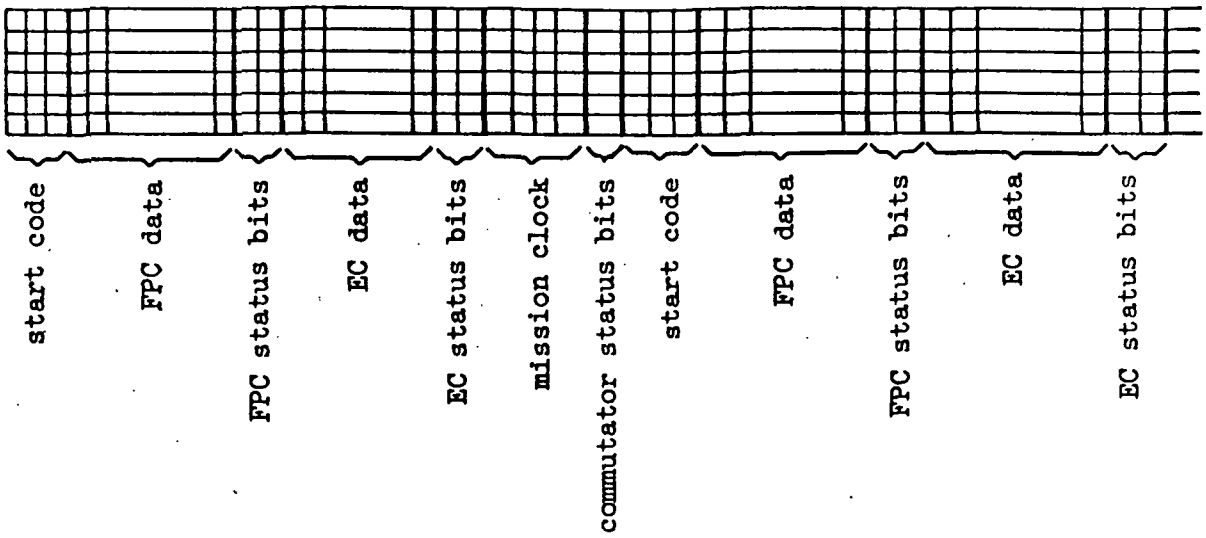

Figure VII-2: LDR Output, Typical Bit Stream Format (Note, IDC and PSIC data not normally included in LDR output)

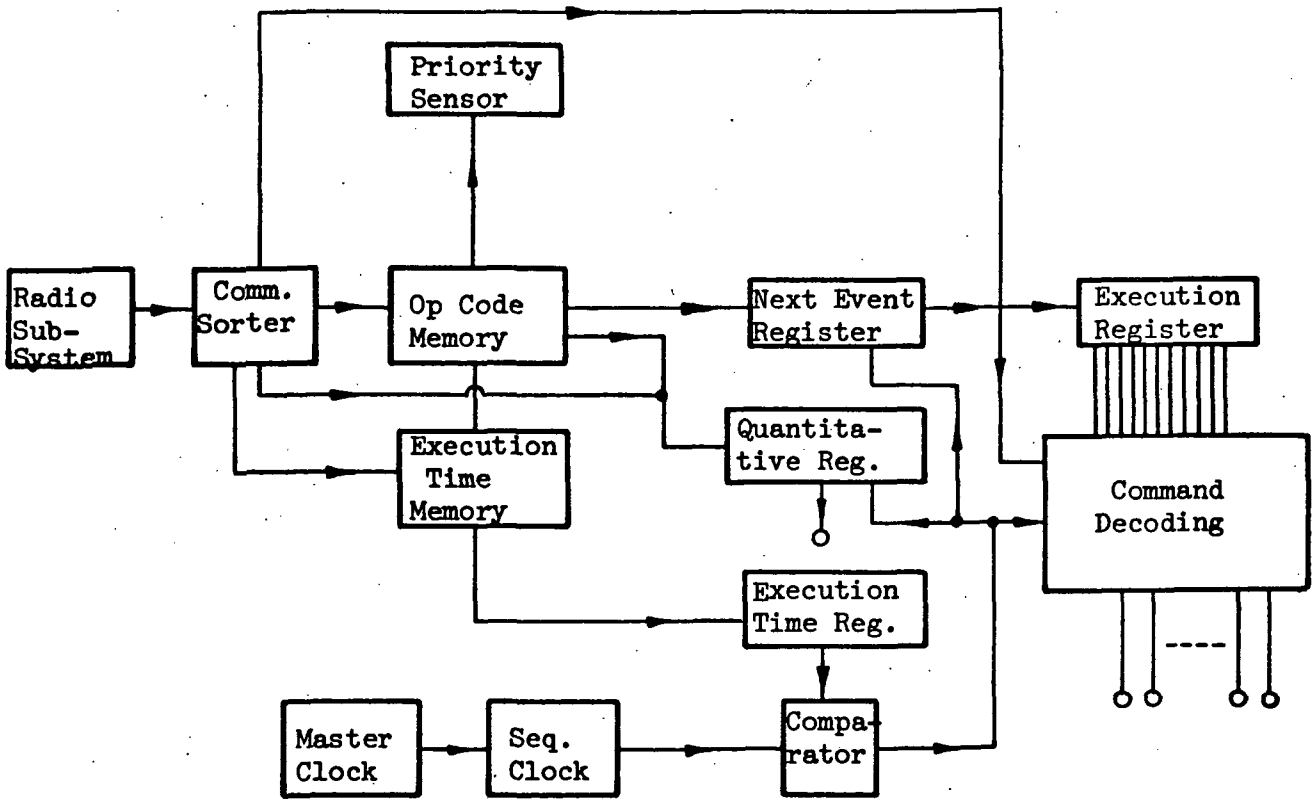

Figure VII-3: Command Subsystem Block Diagram

The main groups are the realtime commands, and the stored commands. The sub-groups within these are the direct commands and the quantitative commands.

Real Time Commands

Real time commands are those which are executed as soon as they are decoded by the command subsystem. As soon as they are received, they are routed directly to the Execution Register (ER) and the decoding logic attached to the register is enabled. For direct real time commands, that is as far as it goes (although an acknowledgement of reception of the command is transmitted to Earth via the downlink channels). A quantitative command carries with it a number which may represent the duration of a midcourse correction burn, a cone angle offset for the Canopus sensor, or a bearing for the scan platform. Immediately upon receipt of such a command, the operational code which specifies what is to be done with the quantity in question is entered into the Quantitative Register (QR). When the decoding logic is enabled, the QR dumps its contents out to the destination of the quantitative command.

Stored Commands

Stored commands may be entered into the memory either before or after launch. Commands that may be entered before launch include those necessary to configure the spacecraft for the cruise mode. As in the case of Real Time commands, stored commands can be either direct or quantitative. Direct commands are loaded sequentially into the memory. The Op code and the time of execution are loaded separately into two separate memories with parallel addressing. A priority sensor interrogates each location in the Execution Time Memory (ETM) each time a new command is added or subtracted from the memory. That location with the

earliest Execution Time (ET), is designated by the priority sensor to be the "Next Event". The Opcode from that location is immediately transferred to the Next Event Register (NER) and the ET from that location is transferred to the Execution Time Register (ETR). A comparator circuit constantly compares the contents of the ETR with the Sequence Clock. When the two times are equivalent, the Opcode is transferred to the ER and the decoding logic is enabled. As soon as the Opcode is executed, the priority sensor again searches the ETM looking for a new Next Event to be inserted in the NER.

A stored quantitative command is similar in operation. The difference is that two adjacent locations in the Opcode Memory are used. The Opcode is stored normally in the Opcode memory as is the Execution time in the ETM, but the memory address is incremented one location to store the actual quantity. From there the process is the same as the direct command except that in addition to the Opcode being routed to the NER and the ET to the ETR, the new quantity is loaded into the QR. When the sequencer gives the green light, the NER dumps into the ER, the ETR is blanked and the QR is dumped to the quantity destination.

In order to reduce the number of bits necessary to describe the Execution Time, the Sequencer Clock is made to run at a variable rate synched to the Master clock. If this were not done, the sequence clock would have to count by seconds for long periods of time. In order to specify execution times to the second, as indeed must be done for delicate maneuvers such as deboost, the execution time code must have enough bits to specify one second out of 150 million, (such a code would repeat about every five years if continuously incremented at a one hertz rate). This requires roughly twenty-eight bits per command so specified. A compromise has been arrived at which requires eighteen

bits to specify the execution time of a command. Eighteen bits is enough to allow the sequencer to run for one full day at one second intervals (to be used during the inital approach and subsequent perijove transits) and for the forty five other days of the Jovian orbit at one minute intervals with days to spare without repeating. During the two year cruise to the Jovian vicinity, the sequencer will be for the most part inactive, or running at a slow rate. No loss of accuracy results from such procedures because the exact start time of the sequencer and its count rate are ground controllable.

At this point it is hard to estimate the number of separate commands necessary to fully control a spacecraft such as JOSE. Based on JPL Mariner experience, and bearing in mind the increased complexity of the JOSE spacecraft, the number 256 was arrived at. The same difficulty applies in deciding what the command capacity of the memory should be. This is not too serious a problem because the entire memory contents are subject to editing via ground command if the number of commands necessary exceeds the memory capacity in a particular circumstance.

All of this, however, introduces reliability problems as well as problems of the availability of the DSN to do such editing on a regular basis. It is then desirable to have as much of the mission as possible already stored in the memory at launch so that an uplink failure at just the wrong moment would not ruin the mission. Without a good idea of the detailed operational characteristics of the mission, it is at this point hard to say where the tradeoff point comes. Once again, based on Mariner experience and extrapolating to a longer and more complex mission, a number was arrived at. The memory will have an unduplicated capability to store one hundred commands. This number is

reduced if some of the commands are quantitative since a quantitative command takes up two locations in the command memory. See Fig. VII-3 for a block diagram of the system, and Fig. VII-4 for a flow chart of its operation. Figure VII-5 illustrates the command word formats.

The system components are as follows:

Opcode Memory:	100 twelve bit words (the first bit is not stored)
Execution Time Memory:	100 eighteen bit words
Next Event Register:	twelve bit shift register
Quantitative Register:	twelve bit shift register
Execution Register:	twelve bit shift register
Execution Time Register:	eighteen bit shift register
Master Clock:	twenty eight bit counter synched by 1 hz
Sequence Clock:	eighteen bit counter synched from variable rate source slaved to master clock.

3. Telemetry Subsystem

In order to provide redundant communications systems and an opportunity to measure the density of electrons in interplanetary space, the JOSE spacecraft will have two separate downlink systems. One will operate at 8450 Ghz (X band) and the other at 2300 Ghz (S band). These frequencies were chosen because they are standard NASA telemetry and tracking frequencies. The X band system will provide the main telemetry channel for imaging and scientific data and consists of two X band TWT transmitters, one capable of one hundred watts of phase modulated CW transmission only, and the other capable of 10 kw peak pulse power (100 w average) for use as a navigational radar. In the event of failure of the CW transmitter, the radar transmitter will also be capable of telemetry transmission in the pulse mode. In addition, the high gain

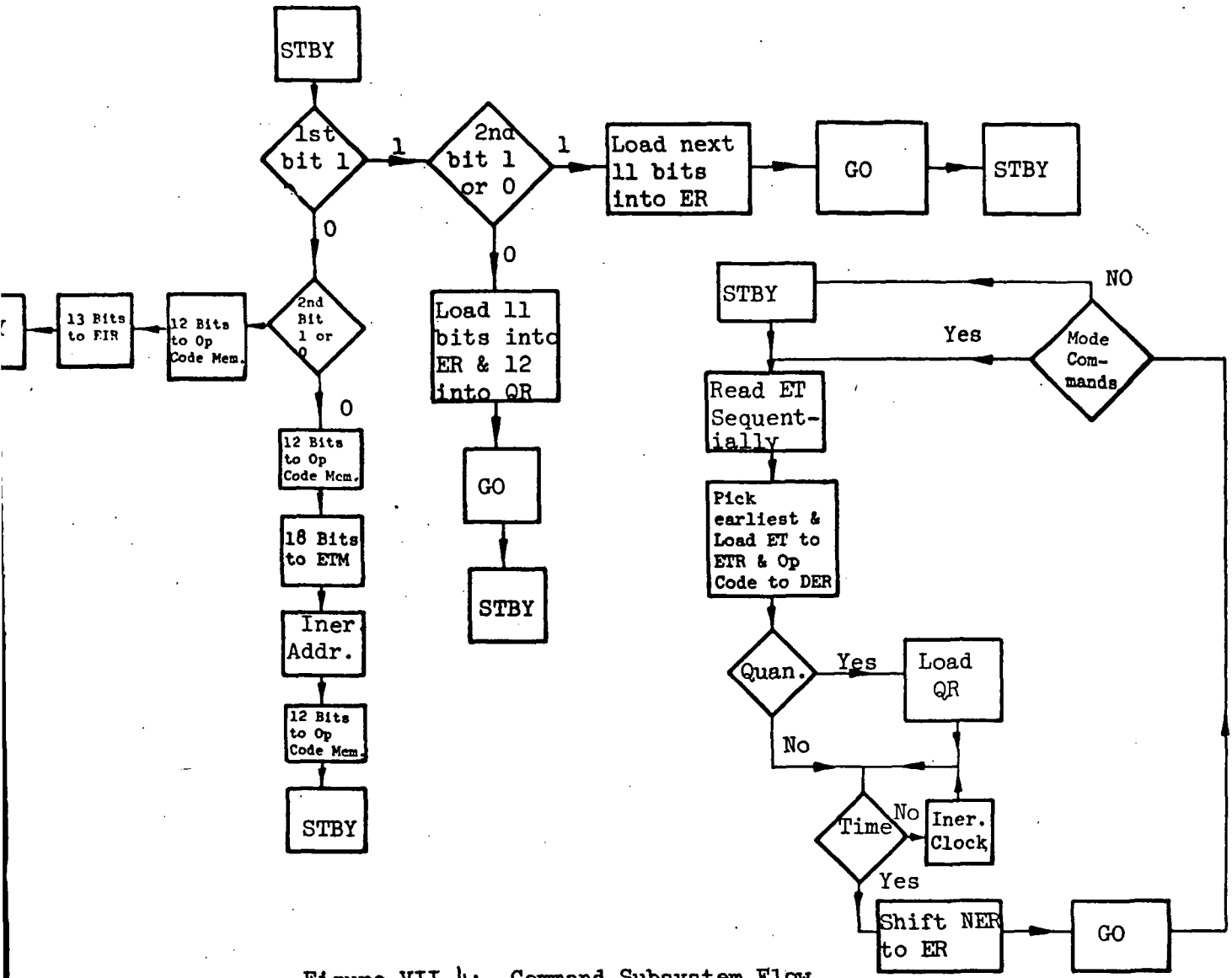

Figure VII-4: Command Subsystem Flow Chart

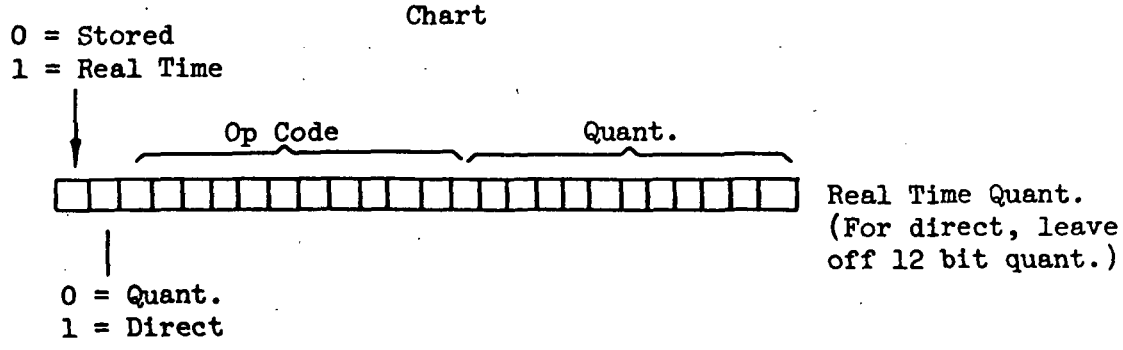

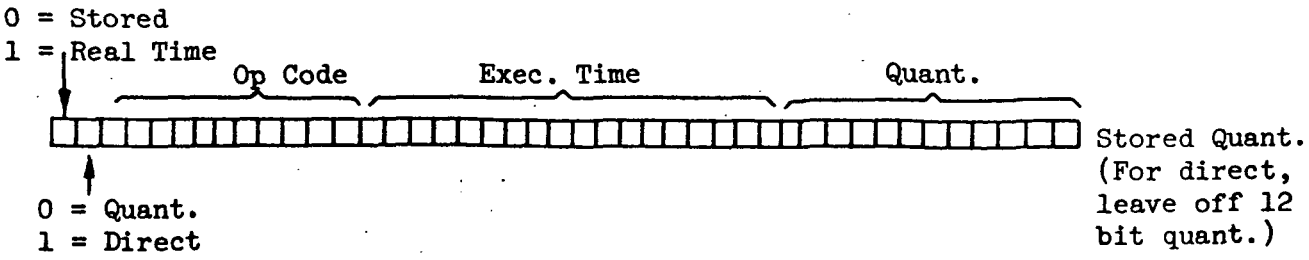

Figure VII-5: Command Word Format

antenna for the radar transmitter is steerable, thus allowing communications with the Earth even when the spacecraft is not properly oriented with respect to the ecliptic and the spacecraft-Earth line.

The S band system consists of two 65 watt phase modulated CW TWTs for redundancy. Its main purpose is the transmission of scientific and housekeeping information. The S band TWTs may be operated in parallel for a total power of 130 watts whenever the X band system is not in use.

The X band system will have a capacity of 117.7 kbps. This capacity is necessary to dump the data stored in the 10^9 bit tape recorder in a reasonable amount of time (2.32 hr). The S band channel has capacity of ten kbps, or if necessary, with parallel operation, twenty kbps. In the event that the S band system must function as an emergency main telemetry transmitter, it will require 14 hours of DSN time to dump the stored data. Since the DSN is available for the most part for only eight hours a day, it could take two days to dump 10^9 bits at twenty kbps.

Following a system suggested in a JPL TOPS in house report, and outlined in Appendix G, the transmitter power antenna gain products for both the X and S band systems were calculated. On the assumption that the 210 ft Goldstone dish or its equivalent is used as the ground tracking antenna, along with a 30° maser front end, the power-gain produce for X band comes to 90.8 dbm. This includes a 5.5 db safety factor to account for adverse tolerances in the system. For a hundred watt transmitter, the antenna gain must then be 90.8-50 = 40.8 db. At 8450 Ghz the required antenna effective aperture is 1.2 m^2.

The power-gain product for the S band link is 77.2 dbm. This includes a 3.6 db allowance for adverse tolerances. Another antenna,

similar in size to the X band antenna, will have a gain of 29.1 db, requiring a transmitter power of 48.1 dbm or 65 watts.

Since the launch constraints seem to be more stringent in regard to physical size of an antenna structure than to the total spacecraft weight, an effort has been made to limit the physical size of the telemetry downlink antennas. This has the additional advantage that the required pointing accuracy is much less demanding, because the antenna beam width is considerably wider. Since parabolas are relatively inefficient (50%), bulky, and require complicated feed structures, it was decided to make the transmitting antennas flat dipole arrays deposited by printed circuit techniques on an insultating substrate, a quarter wavelength thick and backed by a metallic reflecting sheet. Since such an array can be made uniformly illuminated (sidelobes are unimportant) efficiencies can range as high as 80%. On the assumption that the antennas will be 75% efficient, the physical area is 1.6 m^2. The antennas then become squares 1.26 meters on a side and eight mm thick for the X band antenna, and 30 mm thick for the S band antenna. Such antennas can be constructed of very light materials and will weigh less than five pounds. The required surface tolerance of lambda/10 rms error can easily be maintained over an area that size by light and simple supporting structures.

Note that the channel capacities given are under worst case conditions with safety margins of 5.5 and 3.6 db. If for some reason a greater margin appears necessary at some future date, there remains plenty of room to enlarge the antennas. Note that the consequence of an inadequate margin is not a catastrophic failure, but rather a reduction in data rate capability.

The small size of the antennas allow a wider tolerance in their

aiming and thus in spacecraft attitude control. The X band beamwidth is about two degrees as opposed to the $.4^{\circ}$ of an earlier proposed sixteen foot antenna.

Telemetry uplink with present DSN transmitter capabilities presents no difficulty. When used with the 210 ft Goldstone dish, existing 100 kw transmitters when used with waveguide aperture antennas of the type already flown on Mariner'69 and 300° front ends yield channel capacities on the order of tens of kilobits per second. With a spacecraft omni antenna with a gain of three db, the theoretical channel capacity is twenty kbps. Since the required channel capacity is of the order of tens of bits per second it is thus seen that a large margin exists. If the uplink data rate is set at twenty bps, then the signal to noise ratio is thirty db. Since the waveguide antennas are in fact closer to seven db, the SNR then becomes something like 34 db. With this kind of margin, uplink commands can be sent with the requisite error rates (one in 10^5) with simple binary coding.

Since the omni antennas can be used to such advantage, the system complexity is considerably reduced. As already mentioned, a complicated decoder is not necessary. In addition, no TR switching is needed in the X or S band downlink antennas. It is of course still needed in the X band radar antenna.

Uplink redundancy is achieved by the use of four such omni antennas, each with its own separate front end, so situated on the spacecraft that at least one of them can see the Earth at all times.

Downlink Data Encoding

The downlink channels, both S and X band, use essentially identical data encoding systems. An acceptable error rate in the downlink channels

is one in 10^{-3}. The signal energy per bit, noise spectral density ratio has been specified as three db. This requires a fairly sophisticated encoding scheme. The system selected is a convolutional encoding, sequential decoding scheme. It is desirable because its efficiency is such that the channel capacity approaches the maximum given by Shannon and the transmitter implementation is straightforward.

There exists at least one coding scheme, and probably many which has a probability of error given by: (1)

$$P(e) < L/K \; 2^{-N(R_o - R_N)} \qquad \text{VII-1}$$

where L is the length of a block of information to be encoded by the convolutional encoder, K is the number of bits in the "X" register (Fig. VII-6), N is the number of antipodal dimensions in the transmitted waveform, R_o is the error probability exponent parameter which is a function of the energy per dimension/noise spectral density ratio, E_n/N_o, and R_n is the number of input data bits per transmitted dimension.

Reference to Fig. VII-6 will show that the encoder consists of one K-bit X register, V modulo two adders, a commutator, an input buffer, and connections between the X register and the modulo two adders. In operation, an L-bit data word is encoded into an (L+K)V code word. The L-bit word is fed into the X shift register bit by bit. As each new bit is shifted into the register, the commutator sequentially interrogates the V modulo two adders. The process continues until the L data bits have gone completely through the register. Since in order to get the last data bit through the register it must shift through K stages, there are K zeroes on the end of the L-bit data word. Therefore there are L+K shifts and (L+K)V output bits. Since the last KV output bits are due

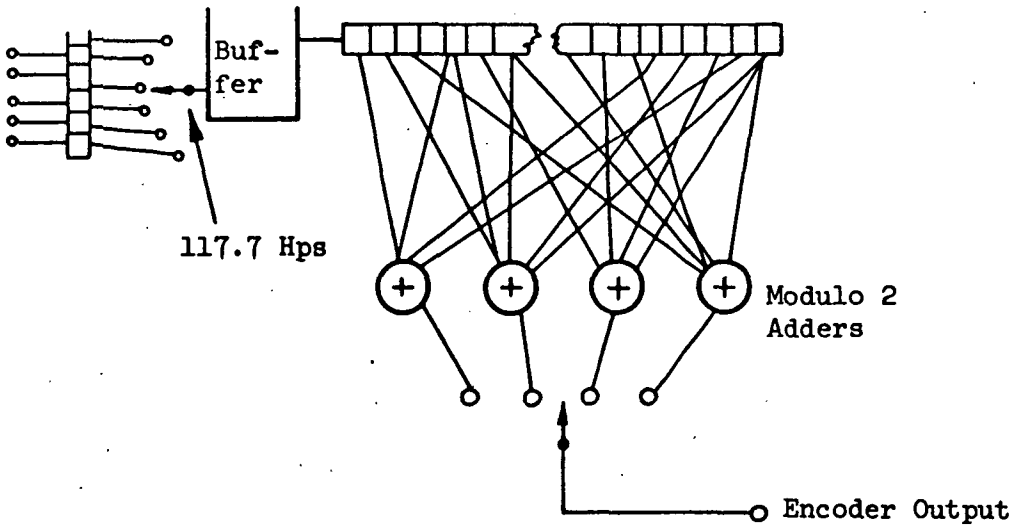

Figure VII-6: Downlink Encoder

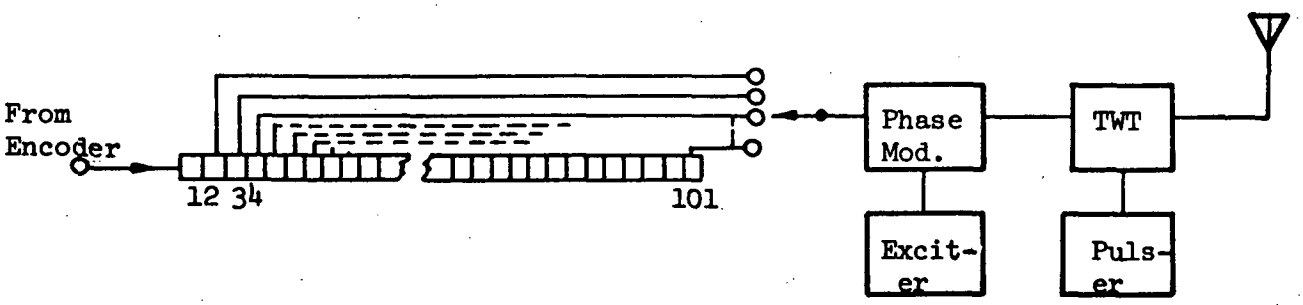

Figure VII-7: Data Compression for Radar Downlink

to no new information, it is desirable to waste as little channel capacity as possible on them. Therefore L should be much greater than K. In this system L/K has been selected as sixteen. The input buffer is necessary to reconcile the difference in rate between the input and the input to the shift register caused by the insertion of the K-bit zero tail.

If the right side of eq. VII-1 is set equal to 10^{-3}, the value of N can be specified given R_o and R_n. R_o is a function of the transmitted energy/dimension, noise spectral density ratio, E_n/N_o. Since the specification has already been made that the energy per data bit, noise spectral density ratio, E_b/N_o shall be three db, the value of E_n/N_o and R_n are determined by the ratio of output bits to input, or data, bits. This ratio is given by:

$$\frac{E_n/N_o}{E_b/N_o} = R_n = L/(L+K)V - 1/V \qquad \text{VII-2}$$

Reference to Fig. 5.9, page 304 of [1] gives R_o as a function of E_n/N_o. It is desirable to maximize the quantity R_o-R_n. This happens when R_n is equal to one fourth. Therefore there are four module two adders.

Setting the right side of Eq. VII-1 equal to 10^{-3}:

$$L/K\ 2^{-N(R_o-R_n)} = 10^{-3} \qquad \text{VII-3}$$

Taking the $\log_2$ of each side:

$$4 - N(R_o-R_n) = -10 \qquad \text{VII-4}$$

For R_n equals one fourth, R_o-R_n equals .08. Therefore N is given by:

$$N = 14/.08 = 175 \qquad \text{VII-5}$$

N, the number of dimensions per codeword block, is not LV as might be suspected at first. Since each output bit depends only on the K bits in the X register at the time it is read out, the real length of the codeword block is K bits and the number of dimensions is then KV. The number of stages in the X register is then specified:

$$K = N/V - 43.75 \text{ or } 44. \qquad \text{VII-6}$$

Also L is specified:

$$L = 16K - 708.$$

Data bits are then transmitted in blocks of 708 at a time and for each such block, 3008 bits are transmitted, the last 176 of which are due to the zero tail.

Both high and low data rate encoders are identical, the difference in their operation due only to the rate at which new bits are loaded into the X registers. For the X band system, the rate is 117.7 kbps. For the S band system, this rate is either 10 kbps or 20 kbps. The transmission bandwidth of the X band system is then about 500 khzs and for the S band system, either 42.5 or 85 Khz.

When the X band radar system functions as a downlink channel, the channel capacity is the same as the main X band downlink channel, 117.7 kbps. The same encoder is used, but a data buffer must be included to store the data output from the encoder during the interpulse periods for transmission during the pulses. The radar TWT is capable of ten kw peak pulse power at a duty cycle of one percent. Thus there must be a hundred to one compression of data during the pulse transmission. The details of the compression depend on the amount of storage deemed practical.

In this system (Fig. VII-7) a 101 bit shift register is used for storage. Code words are fed serially into the shift register at 500 kbps. Every 200 microseconds, a commutator reads out the last one hundred bits of the register into a phase modulator which is modulating the phase of the RF wave. This read out takes two microseconds, the length of the 10 kw transmitter pulse. The first stage of the register stores the bit outputed from the encoder during the pulse.

Power Requirements

The R.F. subsystem (see Fig. VII-8) is the main power consumer. The various TWTs draw power as follows:

S band - 163 watts each

X band - 250 watts each

This is based on the assumption that TWTs will be available by 1975 capable of 40% efficiency at the power levels and frequencies of concern to JOSE.

Of the four TWTs on JOSE any two will be allowed to be on at the same time except that the two X band TWTs may not operate simultaneously. If there is no X band activity, both S band TWTs may be operated for increased S band channel capacity. One S band TWT may be used for a capacity of 10 kbps during periods of X band downlink or X band radar use.

On the assumption that the various driver circuits will dissipate on the order of twenty watts per transmitter and that the encoder systems will draw negligible power compared to the RF subsystem, the power drawn by the downlink systems ranges from a low of 183 watts during transmit to a high of 453 watts during periods of X and S band simultaneous transmit.

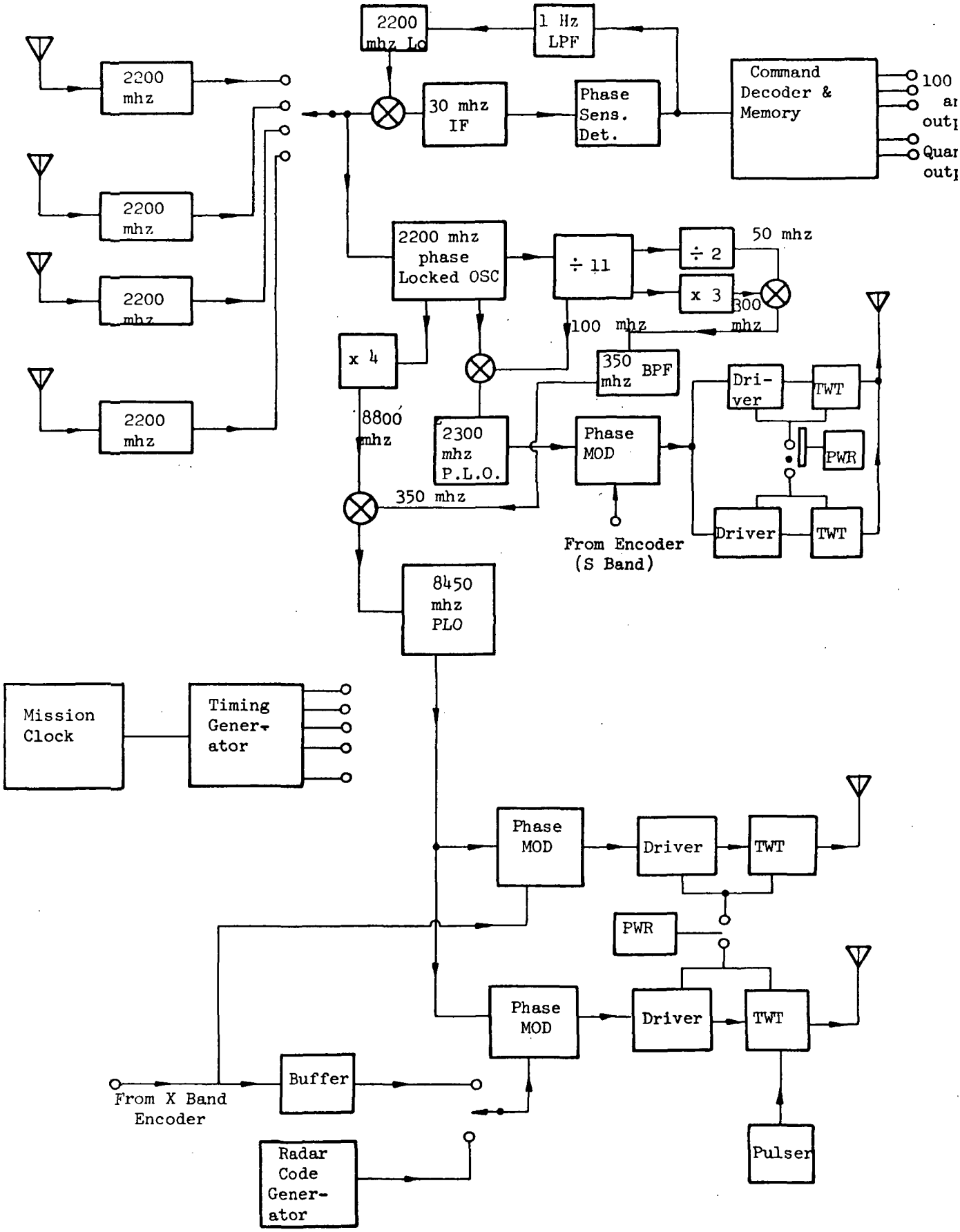

Figure VII-8: R.F. Subsystem

Chapter VII, Bibliography and References

[1] Wozencraft and Jacobs, Principles of Communication Engineering, Chapters five and six, 1965, John Wiley and Sons, New York.

Chapter VIII: On-Board Power Supply

A. Introduction

The power supply for this Jupiter orbiting spacecraft must be designed to operate over a period of 5 years with the maximum power requirements occuring during the last 3 years (i.e., in Jupiter orbit). The maximum raw power required will be in the range of 400-600 watts. The power supply system must be designed to withstand launch conditions, be able to be contained in the launch vehicle shroud, endure interplanetary and Jovian environment, be reliable throughout mission life, and be compatible with mission objectives and other systems.

Three energy sources for the power supply are available:

1) Solar energy
2) Nuclear energy
3) Chemical energy

with basically 2 types of energy converters or generators capable of producing the required electrical power:

1) Static (direct) conversion
2) Dynamic conversion

Stored chemical energy may be converted into electrical power by chemical engines such as turbines or directly by batteries or fuel cells.

Energy storage devices are typically self-contained chemical energy storage and converters in one unit such as

1) Batteries
2) Fuel cells.

B. Space Power Subsystems

1. Solar Cells

Solar radiation intensity, which decreases as the reciprocal of the distance squared from the source, is only 5.1 watts/ft^2 at 5 A.U. Two types of solar cells have been investigated to convert solar energy into electrical power. 1. Silicone solar cells have a conversion efficiency of from 10-15%, weigh about .17 lb/ft^2 and have been proven in near earth space environment. 2. Thin film cells have a lower conversion efficiency (5-8%) but have a specific weight of about 1/3 that of the silicone cells, .06 lbs/ft^2.

Table VIII-1 below summarizes the size and weights for two different 400 W_e solar arrays using the optimistic values of efficiency. This allows for improvements prior to launch date and for the lower space environmental temperature at Jupiter than that at the Earth. A figure of .2 lbs/ft^2 is used for deployment and structure of the array.

Table VIII-1 400 Watt Solar Array

	Type of Solar Cell	
	Thin Film (CdS)	Silicon
Array area	975 ft^2	520 ft^2
Cell weight	59 lbs	89 lbs
Deployment and Structure weight	195 lbs	104 lbs
Total	254 lbs	193 lbs
Specific Power (Watts/lb)	1.57	2.06

Two important considerations must be included in the analysis of a solar cell power supply for the Jupiter mission. The first is the need

for sun-solar panel orientation at all times to maintain maximum power output. This would require continual orientation of the spacecraft or the array requiring additional propellant weight or motors and which may interfere with planetary observations or downlink communications. An energy storage system could be provided but its use would decrease the specific power and the uncertainty of its reliability over a period of many years might jeopardize the mission.

The second and most crucial aspect of employing solar cells to power the Jupiter orbiting spacecraft would be the certain detrimental effect of the intense trapped radiation fields around Jupiter. For the intended orbit of 1.1 x 100 R_J the integrated electron and proton flux over a two-year period is on the order of 10^{12} e/cm^2 and 10^{14} protons/cm^2, in the energy range of 5 Mev < E_e < 100 Mev and .1 Mev < E_{pr} < 4 Mev. Experimental results of proton irradiation of silicon solar cells [VIII-1] indicate that for protons of energies of about 2 Mev a 25% reduction in efficiency can be expected for integrated fluxes greater than 10^{10} pr/cm^2. It is expected that the electron flux will also cause appreciable solar cell damage.

2. Nuclear Systems

Nuclear energy source system may be divided into two broad categories: fission reactors and radioisotopes. At present nuclear reactors have a minimum core weight regardless of conversion system, too large to be considered. The SNAP 10-A reactor ($35KW_{th}$) and shielding for example weighed a total of 495 lbs. [VIII-2].

Radioisotopes provide the most attractive source of power. Orientation is not important and for the properly selected isotope, volume and radiation shielding is small and power level is almost constant throughout the mission life.

The criteria for selecting a radioactive isotope must include items such as half-life, power density, radiation decay spectrum, availability, and maximum temperature capability. References VIII-3 and VIII-6 have comprehensive descriptions of the properties of candidate radioisotopes. Plutonium-238 is the commonly recommended radioactive fuel for deep space missions. Pu-238 is desirable because of its long half life, 89 years, its emission of weak gamma radiation, and the relatively high melting point, 2300°C, of the PuO_2 compound.

Two drawbacks for the use of Plutonium-238 are cost and availability. Projected costs run about $1000 per thermal watt of fuel which in terms of one 400 watt electric space power supply operating at 7% efficiency would require an investment of $5.7 million. Additional fuel is required prior to space flight for life and reliability testing. However, if estimated production of Pu^{238} for the year 1980 is 50,000 thermal watts as predicted [VIII-4] and higher priority use of Pu^{238} is not demanded, availability does not seem to be a major problem.

Since the orbit of the spacecraft of this study passes through the trapped radiation belts of Jupiter adequate shielding of the electronics and equipment must be provided to protect against high energy particles. This then opens the possibility to consider using β-decay radioisotope fuels. Additional handling and safety precautions will have to be exercised prior to launch, but such procedures are certainly within the realm of current technology [VIII-5].

Strontium-90, for example, has a half life of 28 years and in the form SrO has a specific power of 0.79 watts per gram and a melting point of 2430°C, [VIII-6]. This half life means a 12% power source degradation over the 5-year mission life. Availability is high and the cost is less than 1/10 that of Plutonium. A drawback to the use of Sr^{90} is the emission of high

energy gamma radiation (1.7 Mev) from the decay of its daughter nucleus. Additional study is necessary to determine whether the proposed electron and proton shielding will protect components from this radiation. Candidate radioisotopes such as Cesium-137 have too low a melting point (1100°C) and Promethium-147 too short a half-life (2.5 years) to be considered further.

3. Radioisotope Conversion Systems

The thermal energy of radioisotope power sources may be converted into electrical energy by two distinct methods: Dynamic systems represented by Rankine or Brayton cycles and direct (static) conversion systems represented by thermoelectric and thermionic converters.

Brayton gas cycles typical of space flyable models with inlet temperatures around 2000°R have conversion efficiences of 20-35%. Rankine liquid-metal cycles with inlet temperatures of 1700°R and outlet temperatures around 800°R have efficiencies from 15 to 25%. These efficiencies [VIII-7] however, are based on large systems in the kilowatt electric power range and above. As the power level goes below 1 kilowatt, losses become a large fraction and efficiency goes down.

A second drawback of dynamic systems is their limited life. Systems designed and tested in the 1960's have restricted life times. The likelihood of the failure of rotating parts due to corrosion from high temperature gas and liquid metal and from bearing lubrication problems (among others) yield poor system reliability for unattended operations longer than 1 year.

Thermionic devices which convert heat directly into electricity operate at very high temperatures (2000°K) and have efficiencies around 15% [VIII-8]. The specific power for a General Electric designed isotopic thermionic generator with a cathode temperature at 1850°K was 5 watts/pound [VIII-9].

Because of the high temperatures and the use of cesium in many designs, converter life is usually limited to less than 1 year. Heat pipes, an ideal device to transfer heat from a concentrated source to the thermionic converter, also have limited life due to materials interactions problems at high temperatures.

The thermoelectric direct energy converter device while not achieving the high efficiency or power density like that of the thermionic device will provide a space power subsystem which is highly reliable during the 5 year mission lifetime. Thermoelectric systems now operating using lead-telluride (Pb-Te) thermocouples and operating with a hot junction temperature of 1000^{o}F, have efficiencies around 5% and a specific power of 1 watt/lb.

The heat source for this type of converter could be solar, nuclear reactor, or radioisotope. Reactor sources, because of their weight and solar energy, because of their need for orientation and very large collector, are not feasible. As such radioisotope powered thermoelectric generators (RTG's) have been selected as the power supply for this space mission. Besides their high reliability, RTG power output is insensitive to orientation, meteorites, and external radiation.

Indications are that future designs, as well as this study, will use silicon-germanium (Si-Ge) couple material at high temperatures and large temperature differences to achieve efficiencies of 7% and a specific power of 2 watt/lb.

4. Chemical Systems

Electro-chemical storage devices are not feasible as the primary system due to the duration of the mission and the amount of power required. Batteries and fuel cells might be considered for a possible secondary (rechargeable) subsystem, but their attendant reliabilities for a period of 5 years is uncertain.

C. RTG Design Considerations

1. Interactions

The radioisotope fueled generator presents additional interfacing problems with other systems that solar powered converters, for example, would not. The chart below lists the various interactions of the RTG.

RTG - Subsystem Interactions

Radiation damage to electronics

Background radiation noise on sensing instruments

Weight limit set by total allowable payload and other subsystems

Location and volume limitations in launch vehicle shroud

Effect of location of RTG's on moment of inertia and background radiation

Excess RTG heat for thermal control of instruments (temperature excursion limits)

On launch pad cooling

Launch abort safety

Other important tradeoffs concern major RTG system parameters all of which have a direct influence on the power supply weight.

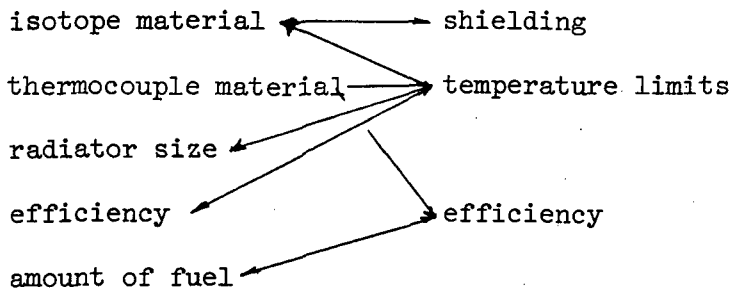

Much work has already been done in the design and improvement aspects of RTG. The General Electric report, Multi-Hundred Watt, Radioisotope Generator Program [VIII-10], in part summarizes the work companies are engaged in concerning the various aspects of RTG design including high

Figure VIII-1. Schematic of an RTG Operating in the Radiation Mode

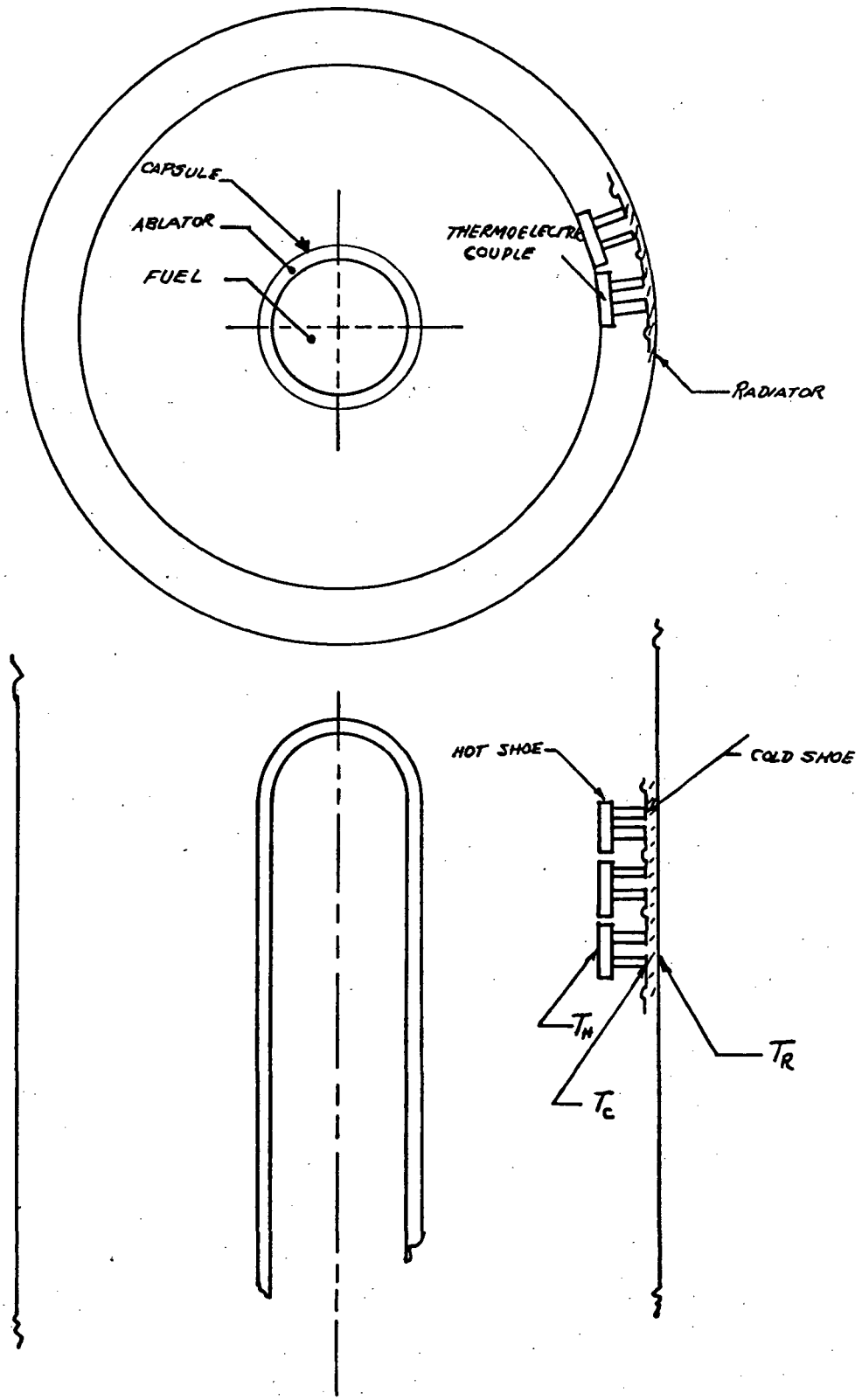

temperature heat source and capsule design and reentry and abort safety. There are, however, aspects of the high temperature, high specific weight RTG design and the integration of the RTG with the spacecraft that are unique for this mission and deserve more detailed discussion.

Figure VIII-1 is a reference schematic drawing of an RTG locating fuel capsule, ablator, thermoelectric elements, radiators and the various temperatures. This RTG is shown operating in a radiation mode - i.e., heat is transferred from the source to the hot side of the thermocouples by radiation alone. The thermoelectric elements are of the Radio Corporation of America Air-Vac Type, Reference VIII-12. The radiation mode in this configuration is advantageous because there is no need for an electrical insulator between or thermal connectors to the hot shoes.

It can be shown [VIII-11] that the maximum efficiency and power at maximum efficiency can be written

$$\eta\Big|_{max} = \left(\frac{T_H - T_C}{T_H}\right) \frac{(1+ZT_M)^{\frac{1}{2}} - 1}{(1+ZT_M)^{\frac{1}{2}} + T_C/T_H} \qquad \text{(VIII-1)}$$

$$W\Big|_{\eta_{max}} = \frac{\alpha^2 (\Delta T)^2}{R_G \frac{(m+1)^2}{m}} \qquad \text{(VIII-2)}$$

where α = Seeback coefficient

$\Delta T = T_H - T_C$

$Z = \alpha^2/RK$

RK = a property parameter of the thermoelectric elements

R_G = internal thermocouple resistance

$m = \frac{R_L}{R_G}$, where R_G = external load resistance

It can be seen from equation VIII-2 that the maximum power is increased by increasing α and ΔT. $\Delta T(T_H - T_C)$ is best increased by increasing T_H rather than decreasing T_C since the radiator size and weight goes as $1/(T_C)^4$. Hence, the desire for high temperature systems.

The expression for maximum efficiency, equation VIII-2, is written in terms of the product of the Carnot efficiency ($\frac{T_H - T_C}{T_H}$) and a thermocouple property factor. Here again it is seen that for a fixed radiator temperature, T_C, the efficiency increases with the hot junction temperature, T_H, and with the property relationship Z.

2. Thermoelectric Material Selection

As previously mentioned, Pb-Te and Si-Ge are the candidate thermocouple material for the RTG converter. Pb-Te has been used extensively because of the vast amount of technology and development with these semiconductors. Pb-Te has a limited useful temperature range because of its low melting point and its long term instability.

Silicon-Germanium has many advantages for high temperature use over Pb-Te. Although having a lower Seebeck coefficient α than Pb-Te, at a comparable temperature, Si-Ge can operate at much higher temperatures resulting in higher values for the factor $Z T_m$ and thus possesses higher efficiencies. Other advantages of Si-Ge and the RCA Air-Vac thermocouple module [VIII-12] and subsequent effects on other aspects of the RTG design and mission are listed below.

Si-Ge has excellent mechanical properties and little vaporization or sublimation over the desired range of operating temperatures.

The mechanical properties allow the thermoelectric elements to be mounted in cantilever fashion from the cold end thus requiring no electrical - or thermal - resistive structure - at the hot end.

The Air-Vac module is made up of entirely non-magnetic materials and lends itself to the construction of an entire converter of non-magnetic material. This is important in that it will reduce the background magnetic field to levels that will not interfere with the sensitive Vector Helium Magnetometer.

The hot shoes of the Air-Vac couples are made of a material similar to that of the couple legs to eliminate thermal expansion mismatches and can be doped to obtain a low electrical resistivity and thus improve performance.

3. Proposed RTG Model

A conceptual design study using the above described Air-Vac Silicon - Germanium couples and radiation mode heat transfer has been performed by the General Electric Co. [VIII-10]. The General Electric reference design RTG will be used as the basic power supply unit for this mission. A summary of the pertinent generator characteristics per RTG unit are given below.

Power per RTG unit	144 Watts B.O.M. (Beginning of Mission)
	128 Watts E.O.M. (End of Mission)
Thermal input power	2000 Watts
Weight (including structure and on-pad cooling)	59.7 lbs.
Hot junction temperature	1100°C.
Cold junction temperature	334°C.
Thermocouple material	80% Si-Ge
Number of series-parallel couples	288

A schematic of two RTG units connected in tandem is presented in Figure VIII-2 giving the outside dimensions. Two such tandem configurations

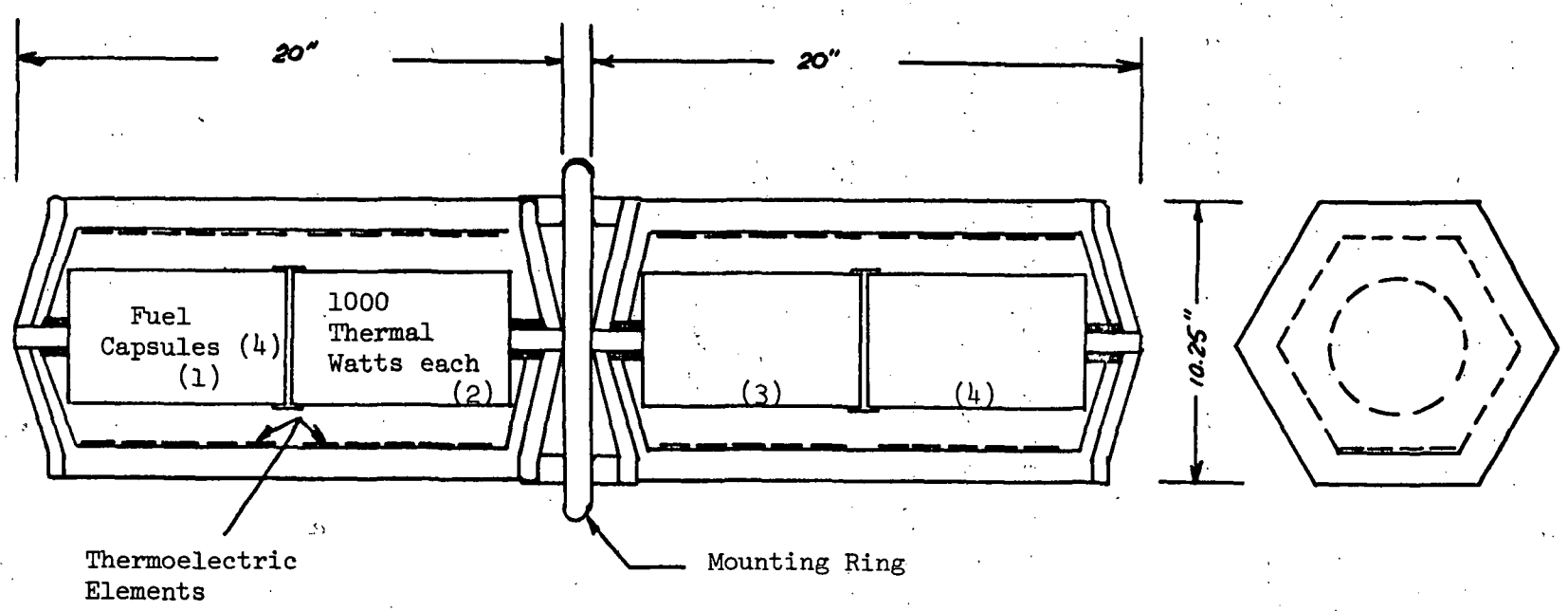

Figure VIII-2. Two G.E. Reference Design RTG Units in Tanden

will be used in the Jupiter orbiting spacecraft to provide a nominal end of mission power equal to 512 watts. A mounting ring weighing about 2½ lbs. is used to attach the units to the spacecraft supports.

D. Power Supply Reliability

The overall reliability of the entire power supply package is dependent upon the reliability of its components: fuel capsule, thermocouple elements and electrical connectors, and batteries and charging circuits if present. Research and development on each of these components will increase the individual reliability while redundant component arrays will increase the overall subsystem reliability. Within the RTG redundancy is most feasible and required only with the thermocouple array.

Thermocouple elements are typically low voltage devices and thus there is the requirement to connect a number of these elements in series to obtain voltages that are easily managed by the power-conditioning equipment. The simplest arrangement to obtain a higher voltage is a single series circuit, but one open circuited element reduces the voltage and power to zero. The need is therefore to have redundant parallel-series networks. A hybrid parallel series circuit is shown in Figure VIII-3.

In the following reliability analysis failure within the circuit is limited to open circuits. The steady degradation over time of the elements is not included in the reliability analysis since the stability has been predicted (about 5% power degradation over the 5 year mission life [VIII-10]).

Assuming that the reliability of each element, R_c, to be equal and constant and that the failures occur independently of one another, the overall array reliability, R_A, may be determined as follows: Referring to Figure VIII-3 the array reliability can be written in terms of the unit reliabilities

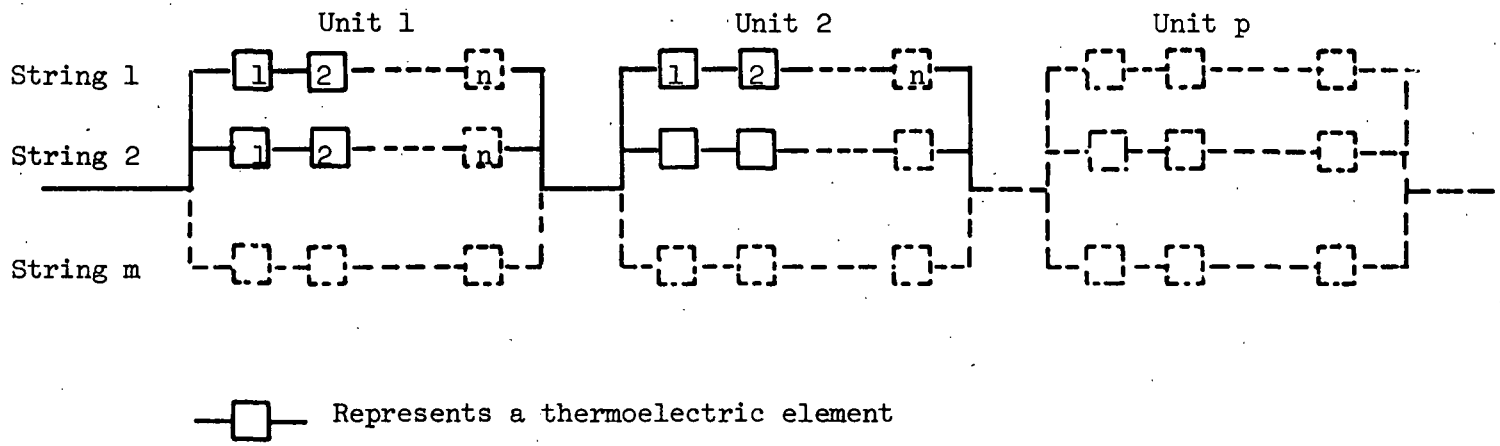

Figure VIII-3. General Hybrid Parallel-Series Array

$$R_A = R_{\text{unit } 1} \cdot R_{\text{unit } 2} \cdots R_{\text{unit } p}$$

The unit reliabilities can be written as

$$R_{\text{unit}} = 1 - P_{\text{fail, unit}}, \text{ where } P_{\text{fail}} \text{ is the probability of failure}$$

$$P_{\text{fail,unit}} = P_{\text{fail,string 1}} \cdot P_{\text{fail,string}} \cdots \cdot P_{\text{fail,string m}} = (P_{\text{fail,string}})^m$$

$$P_{\text{fail, string}} = 1 - R_{\text{string}}$$

$$R_{\text{string}} = R_1 \cdot R_2 \cdots R_n = R_c^n$$

$$\therefore R_{\text{unit}} = 1 - (P_{\text{fail, string}})^m = 1-(1-R_c^n)^m$$

and $$R_A = (1-(1-R_c^n)^m)^p$$

The reliability of specific arrays such as simple series, series-parallel, and parallel-series can be determined by the appropriate selection of m, n and p.

Simple series, m = 1, n = n, p = 1,

Reliability of a series of n couples = R_c^n

Parallel - Series, m = m, n = n, p = 1

$$R_{p-s} = 1 - (1-R_c^n)^m$$

Series - Parallel, m = m, n = 1, p = p,

$$R_{s-p} = (1-(1-R_c)^m)^p$$

The configuration and reliability of the three arrays are compared in Figure VIII-4 for R_c = .98 [VIII-13], for the simple n element series array, the 2 parallel - n series array and the p(n) series - 2 parallel array. From this Figure it can be seen that the reliability of the series - parallel circuit is much greater than either of the two other arrays. In fact, in order to obtain the same reliability between the parallel-series and series-parallel array for R_c = .98 and n = 150 (p_{sp}=150), 100 parallel series strings would be needed.

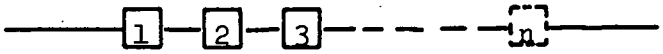

a) Simple series array

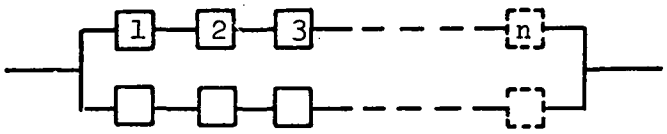

b) 2 parallel - n series array

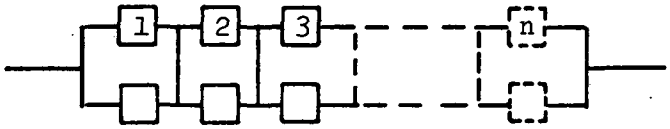

c) p(or n) series - 2 parallel array

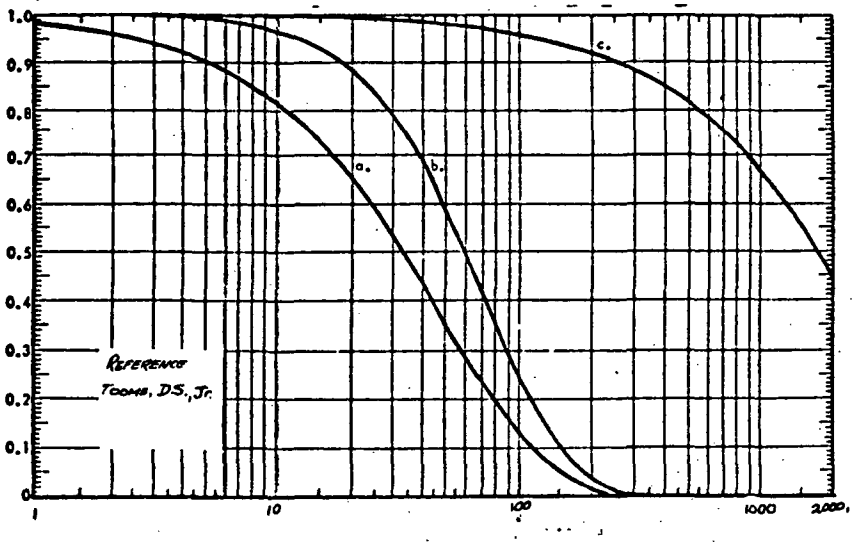

Number of Series Components (n)

Component Reliability R_c = 0.98

Figure VIII-4. Specific Array Configurations and Reliabilities

The above reliability analysis determines the probability that a given array will not fail completely. Of equal importance, along with reliability, is the percent decrease in power and voltage of the system when a few elements within the circuit fail.

E. Power and Voltage Levels

The power and voltage across a given load depends mainly on the internal resistance of the power supply. The closed circuit voltage across the load, V_{closed}, can be written:

$$V_{closed} = \frac{V_{open}}{R_G+R_L} R_L$$

where R_L = load resistance

and R_G = total generator resistance.

The power delivered to the load P_L is:

$$P_L = \left(\frac{V_{open}}{R_G+R_L}\right)^2 R_L$$

For maximum power R_L is made equal to R_G. For maximum efficiency R_L is some fraction m of the internal generator resistance where m depends on the properties and mean temperature of the thermoelectric couples.

For the simple series circuit as mentioned before one open circuit makes R_G infinite and both the voltage and power go to zero.

Parallel Series

For the maximum power generator of the parallel-series circuit, x failed couples (actually the number of failed series strings) decreases the load voltage and power by the following amounts:

$$\frac{V_{closed}\ (x \text{ failed strings})}{V_{closed}\ (x = o)} = \frac{2(m-x)}{(2m-x)} \qquad x \leq m$$

$$\frac{P_L \text{ (x failed)}}{P_L \text{ (x=o)}} = 4 \left(\frac{m-x}{2m-x}\right)^2 \qquad x \leq m$$

For the minimum possible number of strings m = 2 and one failure x = 1,

$$\frac{V_{closed}}{V_{closed\ (x=o)}} = \frac{2}{3} = 67\%$$

$$\frac{P_L(x=1)}{P_L(x=o)} = \frac{4}{9} = 44.5\%$$

and for m = 3

$$\frac{V_{closed}(x=1)}{V_{closed}(x=o)} = \frac{4}{5} = 80\%$$

$$\frac{P_L(x=1)}{P_L(x=o)} = 64\%$$

In order to maintain the power and voltage level above 90% of design with one failure at least 11 parallel strings are needed. Allowing for 2 failed strings, at least 21 strings are needed.

Series-Parallel

The maximum power case ($R_G = R_L$), for the m = 2 series-paralled circuit array will be discussed where x will equal the number of failed elements, no two in one unit.

The voltage and maximum power ratios of the failed circuit to the initial array are given below.

For m = 2,

$$\frac{V_{closed}(x)}{V_{closed}(x=o)} = 2 \left(\frac{p}{2p+x}\right)$$

$$\frac{P_L(x)}{P_L(x=o)} = 4 \left(\frac{p}{2p+x} \right)^2$$

These equations can now be applied to the General Electric RTG design of Reference VIII-10.

The G.E. RTG array is composed of 288 series-parallel thermocouples. With m = 2, p = 144, the circuit can tolerate 32 open circuits (no two in one unit)and maintain 90% voltage and 15 open circuits to maintain 90% of peak power.

When four RTG's are connected in parallel to give the desired power, the reliability of the entire system to complete failure is

$$R_{system} = 1 - (1-R_{RTG})^4$$

Where R_{RTG}, the reliability of one RTG, depends on the internal array.

The voltage and power for the entire system with some failed thermocouples can now be calculated. Assuming the same number of failed couples per RTG unit, the power and voltage in the operating system is determined as before.

Let Δr be the increase in resistance of each RTG and r_u be the initial total resistance per RTG. Then the system closed circuit voltage is

$$V_{closed_{system}} = \frac{V_{open}}{(2 + \frac{\Delta r}{r_u})}$$

and

$$\frac{V_{closed}}{V_{closed,\ initial}} = \frac{2}{2 + \frac{\Delta r}{r_u}}$$

The ratio of the system power with x failed elements P(x) to the initial power, $P_{initial}$, is

$$\left.\frac{P(x)}{P_{initial}}\right|_{system} = \frac{1}{1 + \frac{\Delta r}{r_u} + \frac{1}{4}\left(\frac{\Delta r}{r_u}\right)^2}$$

In order to maintain the closed circuit voltage at greater than 90% of the initial voltage $\Delta r/r_u$ must be less than 0.22. To maintain at least 90% power $\Delta r/r_u$ must be less than 0.11. In terms of the number of failed couples x in the series parallel array $\Delta r/r_u$ can be written

$$\frac{\Delta r}{r_u} = \frac{x}{p}$$

For the case of 150 elements in series, x must be less than 17. The probability of 16 or less failures for a component reliability of .99 is very high (> .99) but total system failure would be expected before this occurred.

The expected voltage and power per RTG and per RTG system may be obtained statistically. For the fail or no-fail independent event, the probability of x and only x occuring where x = number of failed thermocouples is

$$P(x) = \frac{m}{(m-x)!\ x!}\ P_c^{\,x}\ (1-P_c)^{m-x}$$

where $P_c^{\backprime} = 1-R_c$, the probability of failure of a couple over the mission life. m = the total number of elements under consideration (e.g. per string, array, etc.)

The expected voltage E(V) and power E(P) is the voltage and power on the average to be expected at the end of the mission over many mission trials. Mathematically $E(V) = \sum_{i=1}^{m} P(x_i) \cdot V_{closed}(x_i)$

$$E(P) = \sum_{i=1}^{m} P(x_i) \cdot P_L(x_i)$$

The parallel-series and series-parallel arrays were analyzed employing the above technique. For the analysis 150 couples were linked in series for the parallel-series array and 150 - 2 couple units (p = 150, m = 2) were linked in series for the series-parallel array to provide the required design voltage.

Table VIII-2 lists the results obtained for the several parallel-series arrays with increasing number of parallel strings. The reliability of the individual couple was taken to be .99. From the table we can see that the expected voltage and power level is much below 90% initial. Even for the arrays with many parallel strings where the probability of array failure is quite small, the expected voltage and power yields are too small to consider the parallel-series array for the RTG. The reason for such low values of power and voltage is due to the very low reliability of each string, namely 0.221 (see line 1, Table VIII-2).

The series-parallel array is the most straightforward method of improving overall RTG reliability and expected values for voltage and power. Table VIII-3 lists the expected performance of an RTG with a 150-in-series 2-in-parallel array for various couple reliabilities. This table indicates that the individual couple reliability must be greater than .98 in order to have the expected power and voltage levels greater than 90% throughout the mission. In particular, with a couple reliability of .99 we can expect to satisfy minimum voltage and power requirements 98.6% of the time.

Table VIII-4 presents the results obtained for the entire power supply system consisting of 4 RTG's connected in parallel (Figure VIII-4). It can be seen that for the system, the reliability increased as expected.

The expected voltage remains the same as and expected power is near the expected values of the single RTG, Table VIII-3. For the system it is also required that the couple reliability be greater than 0.98

Table VIII-2. Expected Performance of Parallel-Series Thermocouple Arrays, R_c = .99, n = 150

m no. of parallel strings	x no. of failed strings	P(x) probability of x	fraction of initial value with x failed strings		Expected Values fraction of initial	
			V_{closed}	P_{load}	E(V)	E(P)
1	0	.221	1.00	1.00	.221	.221
	1*	.779	0	0	0	0
ΣE(V), ΣE(P)					.221	.221
2	0	.049	1.00	1.00	.049	.049
	1	.345	.67	.445	.23	.15
	2*	.606	0	0	.0	.0
ΣE(V), ΣE(P)					.279	.203
3	0	.0103	1.00	1.00	.01	.01
	1	.114	.80	.64	.09	.07
	2	.402	.50	.25	.20	.10
	3*	.472	0	0	0	0
ΣE(V), ΣE(P)					.30	.18
4	0	.002	1.00	1.00	.002	.002
	1	.034	.86	.74	.029	.025
	2	.177	.67	.45	.119	.079
	3	.418	.40	.16	.167	.067
	4*	.368	0	0	0	0
ΣE(r), ΣE(P)					.317	.173
20	20*	.006				
ΣE(V), ΣE(P)					.352	.139
50	50*	~ 0				
ΣE(V), ΣE(P)					.358	.134

* indicates array failure

Table VIII-3. Expected Performance of a m=2, p=150 Series-Parallel Thermocouple Array For Various Couple Reliabilities

Couple Reliability R_c	Array Reliability	Expected Voltage E(V) Fraction of Initial Value	Expected Power E(P) Fraction of Initial Value
.99	.986	.978	.969
.98	.942	.901	.884
.97	.862	.855	.832
.96	.786	.749	.723

Table VIII-4. System Performance With 4 RTG's Connected in Parallel

Couple Reliability R_c	System Reliability	E(V) fraction of design	E(P) fraction of design
.99	.9998	.978	.965
.98	.997	.901	.877
.97	.981	.855	.840
.96	.954	.749	.746

If long term laboratory life testing of thermoelectric couples at design conditions show that individual reliabilities of at least .99 cannot be obtained, an additional series-parallel string would need to be added or the entire system would have to be designed for an end of mission power level greater than that actually demanded.

The series-parallel array is selected as the preferred array because of its higher reliability and because the voltage and power decrease due to failed elements is less than the other arrays. The parallel-series circuit, to achieve a reliability comparable with the series-parallel array would require many additional parallel elements, but still the expected voltage and power would always be low.

Parallel strings however cannot be added indiscriminately as they would necessitate a change in the thermal power of the heat source or the physical dimensions of the thermocouples. Given that the total length n of a series of thermocouples remains constant in order to provide the required voltage, additional identical parallel circuits would require either larger heat sources or increased thermocouple resistance. With these changes, the RTG would no longer operate at the optimized design maximum efficiency or specific power.

References, Chapter VIII

VIII-1. Kircher, J.F., and Bowman, R.E., "Effects of Radiation on Materials and Components", Reinhold Publishing Corp., New York (1964).

VIII-2. Szego, G.C., and Taylor, J.E., "Space Power Systems Engineering" Progress in Astronautics and Aeronautics, Vol. 16, Academic Press, New York (1966).

VIII-3. Rohrmann, C. A., "Radioisotope Heat Sources", Hanford Laboratories, Hanford Atomic Products Operation, General Electric Co., HW-76323, February 1963.

VIII-4. Streb, A.J., "Radioisotope Power Systems for Manned Space Stations", AIAA Paper No. 64-711, September 1964.

VIII-5. Linde, D.W., 250 Watt Radioisotope Thermoelectric Power Supply System in Advances in Energy Conversion Engineering, IECEC, August 1967, pages 197-206.

VIII-6. Corliss, W.R., and Harvey, D.G., "Radioisotope Power Generation", Prentice-Hall, Inc., Englewood Cliffs, New Jersey (1964).

VIII-7. Stewart, W.L., et. al., "Brayton Cycle Technology", Paper V in Space Power Systems Advanced Technology Conference, Lewis Research Center, Cleveland, Ohio, August 23-24, 1966.

VIII-8. Breitwieser, R., and Schwartz, H., "Thermionics", Paper IV in Space Power Systems Advanced Technology Conference, Lewis Research Center, Cleveland, Ohio, August 23-24, 1966.

VIII-9. Dutram, L.L. and Williams, E.W., "Preliminary Design For a 360 Watt Radioisotope Thermionic Generator", IEEE Trans. on Aerospace, Vol. 2, No. 2, April 1964.

VIII-10. Anonymous, Multi-Hundred Watt, Radioisotope Thermoelectric Generator Program, Phase I Interim Report Doc. No. GESP-7034, General Electric Company, March 1970.

VIII-11. Wright, D.A., "Thermoelectric Generation" in "Direct Generation of Electricity" ed. by K.H. Spring, Academic Press, London, England (1965).

VIII-12. Berlin, R.E., Gnau, L.H., Nelson, R.S., "Silicon-Germanium Air-Vac Technology - A Status Report", Proc. of the 4th IECEC, pp. 386-394, September 1969.

VIII-13. Toomb, Jr., D.S., "Reliability and Circuit Analysis of Thermopiles with Redundant Elements", IEEE Trans. on Nuclear Science, Vol. NS-14, No. 4, August 1967, pp. 17-28.

Chapter IX: Spacecraft Structure and Environmental Design Considerations

A. Factors Affecting General Configuration

The JOSE spacecraft design proposed in this report has been developed to satisfy the many constraints and requirements imposed by the mission, experimental packages, launch vehicle and other subsystems. The spacecraft configuration is governed primarily by major component arrangement, with the final configuration being a compromise based on the various subsystem requirements and incompatibilities. The requirements having the most influence on the spacecraft configuration are:

1) Spacecraft-Earth communications link
2) Radioisotope thermoelectric generators (RTG's)
3) Experiment requirements
4) Trajectory propulsion system
5) Central equipment compartment
6) Launch vehicle constraints

1. Spacecraft-Earth Communications Link Considerations

Because of the great distances involved (4.2 AU to 6.2 AU for a Jupiter orbiter) over which communications must be maintained and the high bit rate (120,000 bits/sec) required by the scanning experiments, television and their respective duty cycles, the antenna must have high gain and be either S-band or X-band. The proposed flat dipole antennas (one X-band for main downlink communications and one S-band used for experiments and as an auxiliary for increased reliability) have a surface area of 17.2 ft^2 apiece and weigh a total of 15 lbs (Chapter VII). This advancement from the large and heavy high gain antennas of past generation spacecraft removes

many of the previously stringent design requirements. However, the high bit rate constraint and the use of two antennas requires that the spacecraft be three axis stabilized rather than have the spin-axis stabilization that was standard on past galatic probes. The advantages and disadvantages of three axis stabilization will be discussed later. Another constraint posed was the desire for a continuously Earth pointing downlink communications system.

2. Radioisotope Thermoelectric Generator Considerations

The RTG power supply and related structure accounts for 405 lbs (25.3%) of the useful payload (Table IX-8). Consequently, they have a major effect on mass distribution and , therefore, on moments of inertia. Because of their low efficiency (7%) and the power requirement on the order of 600 watts, they must have a large, unobstructed solid angle, allowing for thermal radiation for essential cooling. The radiation effects on scientific experiments and the thermal coupling with the spacecraft main compartment must also be considered. All of these items impose stringent design requirements.

3. Experiment Considerations

Experiments that are sensitive to "background" radiation from isotope decay must be located as far as feasibly possible from the RTG's. In addition all experiments sensitive to magnetic fields must be located at a suitable distance from the spacecraft body. Experiments not sensitive to these factors may be mounted in the main equipment compartment. A most influential requirement of the television and spectometer experiments is the desired ability to view the planet Jupiter continuously during any orbit and to scan the planet pole to pole at perijove (1.1 R_J) or at any other position in the orbit.

4. Trajectory Propulsion System Considerations

The propulsion system's size and weight depend upon spacecraft weight and velocity increment required for the mission, and on the type of system chosen. It is desirable that the thrust be produced by a single engine aligned through the center of mass of the spacecraft, and that the propellant tanks be arranged in a manner that eliminates significant mass distribution changes as the propellant is consumed.

5. Central Equipment Considerations

All of the spacecraft components not requiring specific locations are to be located in a central compartment for collective protection against the environment of space. The compartment must provide a stable thermal environment, and protection agains radiation and meteoroid hazards while also providing a sound structure for all equipment and appendages. In the compartment design, major tradeoffs result from the interaction of:

a) The thermal requirement of maximum conservation of heat with a minimum of electrical power dissipation and minimum of insulation.

b) Adequate meteoroid protection with minimum weight and minimum influence on thermal properties.

c) Adequate structural support with minimum heat loss and minimum weight.

6. Launch Vehicle Considerations

In launch configuration the spacecraft must be dimensionally compatible with the launch vehicle payload envelope. The structure must be configured to withstand the dynamic environment of launch and satisfy the cooling requirements of the RTG's.

B. Preliminary Design Decisions

1. Three Axis Stabilization

The choice of stabilization methods was most influential in the subsequent evolution of the final spacecraft configuration. Most of the past flight experience has been with spin stabilized spacecraft and all of the recent studies of deep space probes with small spacecraft have used that method because of weight savings in the attitude control system and its inherent compatibility with large round high gain antennas.

Upon studying the requirements of the proposed downlink communications system with its use of two antennas in parallel for downlink-uplink transmittions and the possibility of a heavy moveable platform, the need for three axis stabilization became quite apparent. In the spin stabilized concept, the antenna must be located on the spin axis to prevent phase modulation of the signal at the spin rate of the spacecraft. The simultaneous location of two earth pointing antennas on the spin axis was deemed practically impossible.

For the three axis configuration the problem of relative spacecraft inertias becomes of only secondary importance. In the spin stabilized concept, not only must the desired spin axis be the principal inertial axis by the recommended proper ratio of between 1.3 to 1.7 (ratio of moment of inertia of spin axis to moment of inertia of the cross axis) but the inertias of the cross axes must be approximately equal and the spacecraft CG must be co-incident with the desired spin axis [IX-8].

However, as a tradeoff for three axis stabilization the attitude control system becomes more complex and heavier.

2. Antennas and Scan Platform - Articulated or Body Fixed?

Simultaneously satisfying the continuous earth pointing requirement of

the communication link and the desired ability of the scan platform necessitates two degrees of freedom between the antennas and scan platform. The scan platform must be capable of 360° of rotation about an axis (line AA) perpendicular to the plane of the orbit and 90° of rotation above and below the orbit plane about an axis (line BB) simultaneously perpendicular to the radius vector and in the plane of the orbit (see Figure IX-1). This capability allows continuous viewing of Jupiter from pole to pole for an orbit of any inclination to the equator.

These objectives can be accomplished by two methods (see Figure IX-2):

a) Antennas and scan platform both articulated with one degree of freedom.

b) Antennas body fixed and scan platform articulated with two degrees of freedom.

The first alternative requires that the spacecraft be continuously reoriented in inertial space as the orbit is traversed. Intuitively, the high reliability of a body fixed communication's antenna more than offsets the loss in reliability of a bi-axially articulated scan platform. For the remainder of the study further investigation will be completed only on configuration b.

3. Communication-Antenna-Scan Platform Configuration

Figure IX-3 shows the communication geometry on March 2, 1983, perijove of the first orbit of the mission. Of interest for the purpose of defining the necessary antenna-scan platform geometry is the angle between the radius vector from Jupiter to the spacecraft and the spacecraft-earth line. Since this analysis is primarily to obtain only an approximation of the geometry, the spacecraft-sun line will be used with the maximum error of $\pm 10.8^{\circ}$. Also neglected is $\Delta\theta$ due to the secular perturbations of Jupiter's

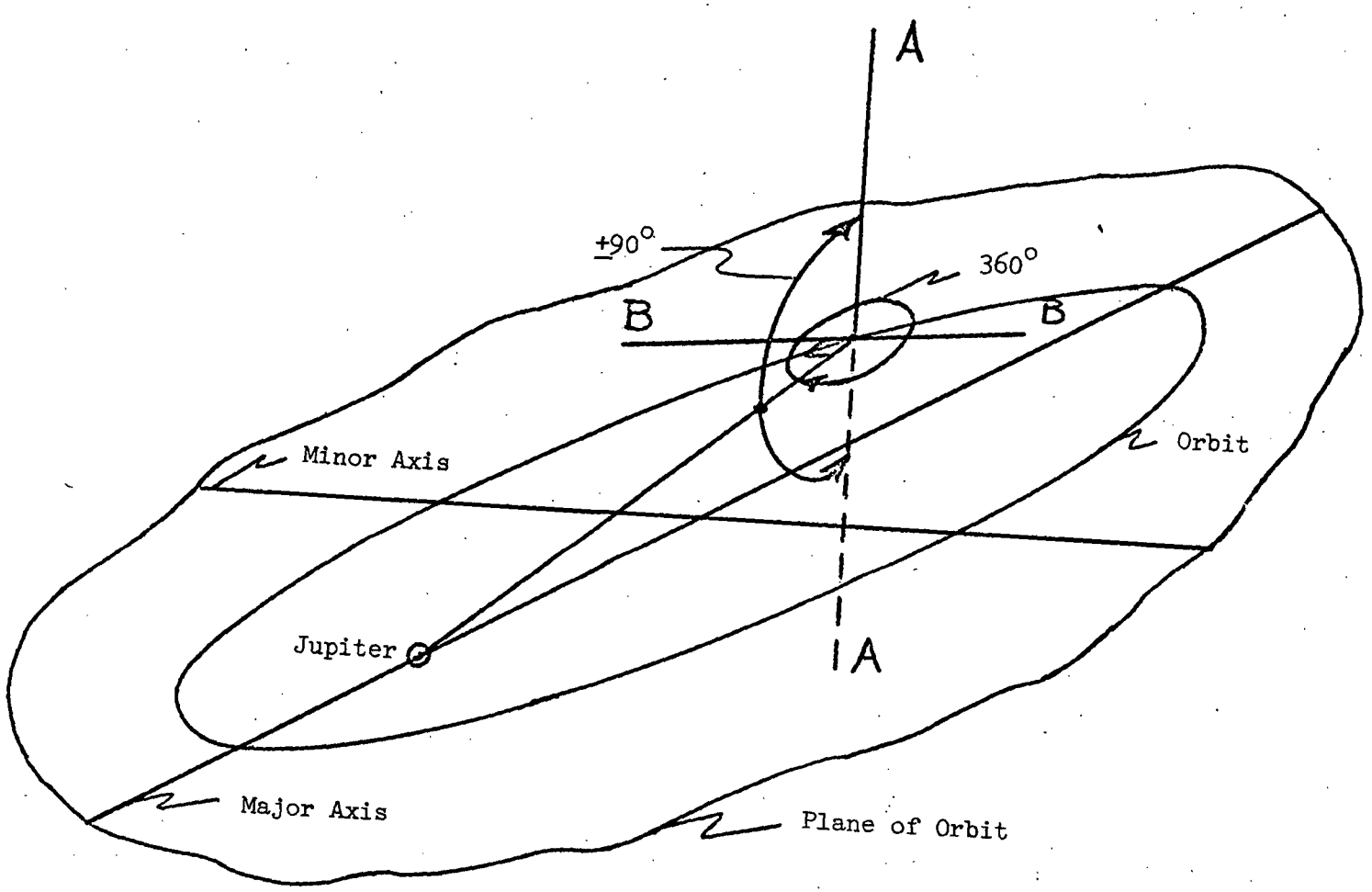

Figure IX-1. Scan Platform Geometry Requirements

Configuration a)

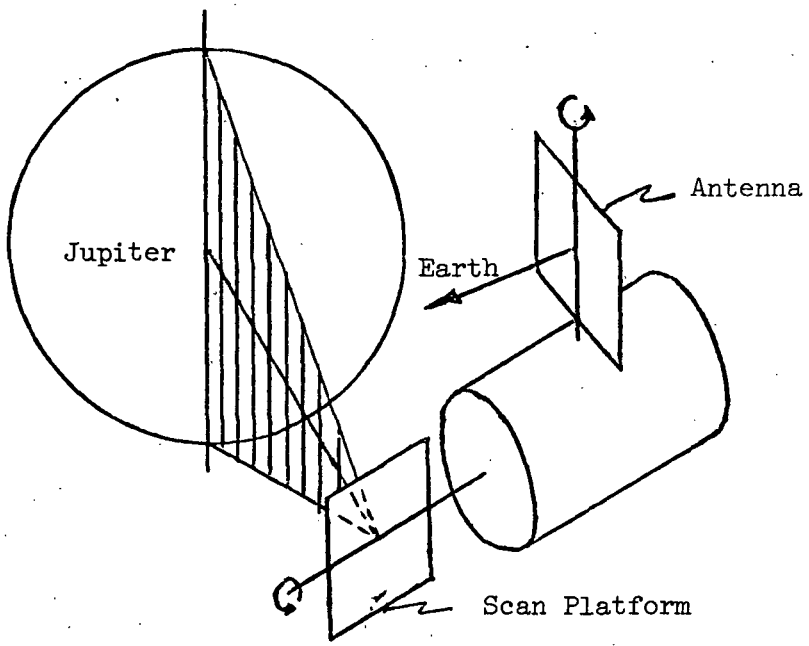

Configuration b)

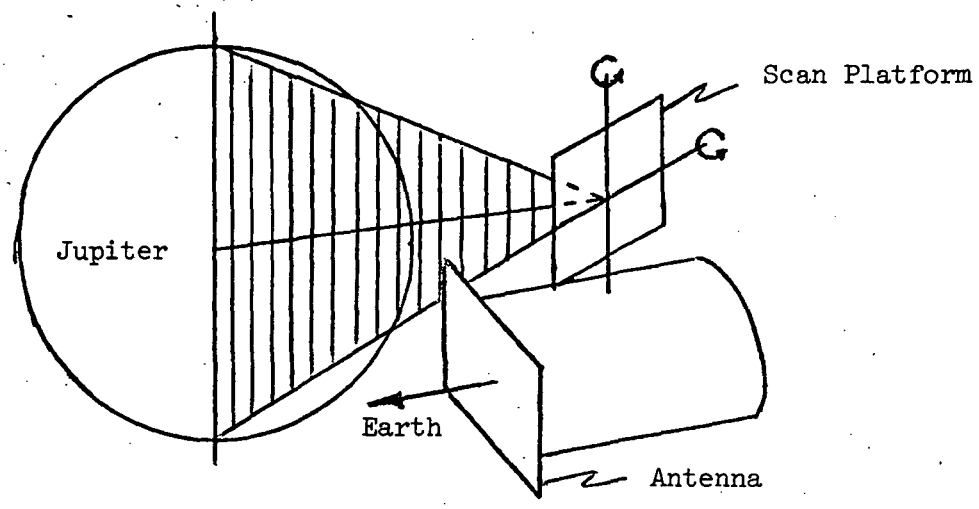

Figure IX-2. Possible Antenna-Scan Platform Configurations

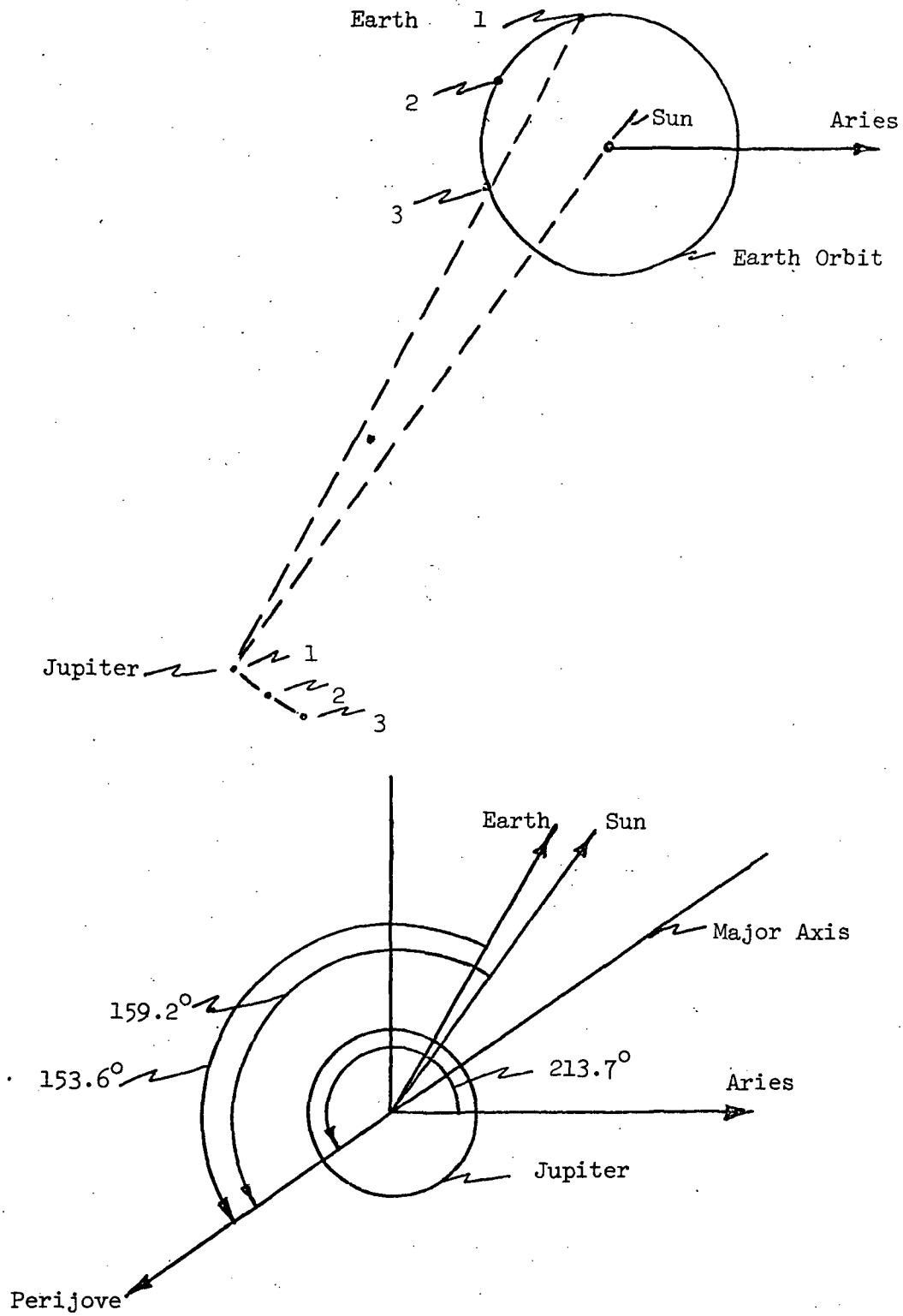

Figure IX-3. Planetary Geometry at Time of First, Second, and Third Orbital Perijove (Projected onto the Ecliptic Plane)

gravity field (+ 1.225°/orbit) and rotation of Jupiter about the sun (+ 3.71°/orbit).

Figure IX-4 shows the physical dimensions of a typical orbit (1.1 R_J x 100 R_J).

The first orbit around Jupiter will be in the equatorial plane which is inclined to the ecliptic by 3°. Subsequent orbits will be inclined to the equatorial plane as the mission requires. Figure IX-5 shows the typical orbital geometry for an inclined orbit and Figure IX-6 shows the variation of angle α for complete orbits of inclination of 0° and 30°. As defined, α is the angle measured counter-clockwise from the spacecraft-sun line to the spacecraft-Jupiter line.

C. Major Subsystem Designs

1. Propulsion System

A preliminary weight allocation study indicated that 1600 lbs. of useful payload (total spacecraft weight less weight of propulsion system) would be necessary to include all the desired scientific experiments and related support apparatus. A propulsion system using a FLOX/CH_4 oxidizer-fuel combination was determined to be most applicable to this mission (see Chapter V).

Figure IX-7 shows the remaining capability in ΔV of the propulsion system after insertion into Jupiter orbit as a function of spacecraft launch weight. The assumptions made in obtaining the results are:

a) Useful payload of 1600 lbs.

b) Mass fraction of .8

c) Specific impulse, I_s, of 400 sec.

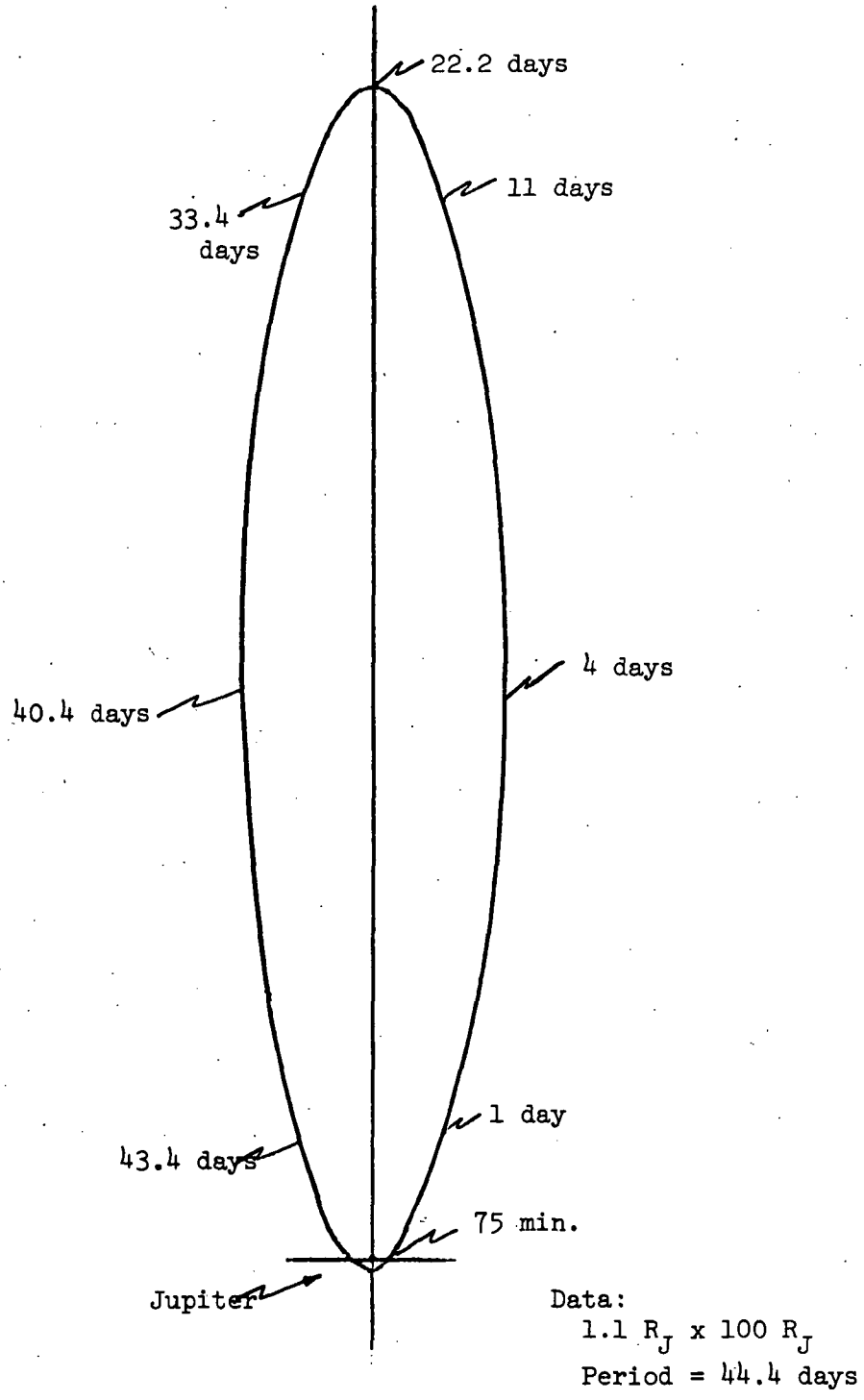

Figure IX-4. Typical Jupiter Orbit

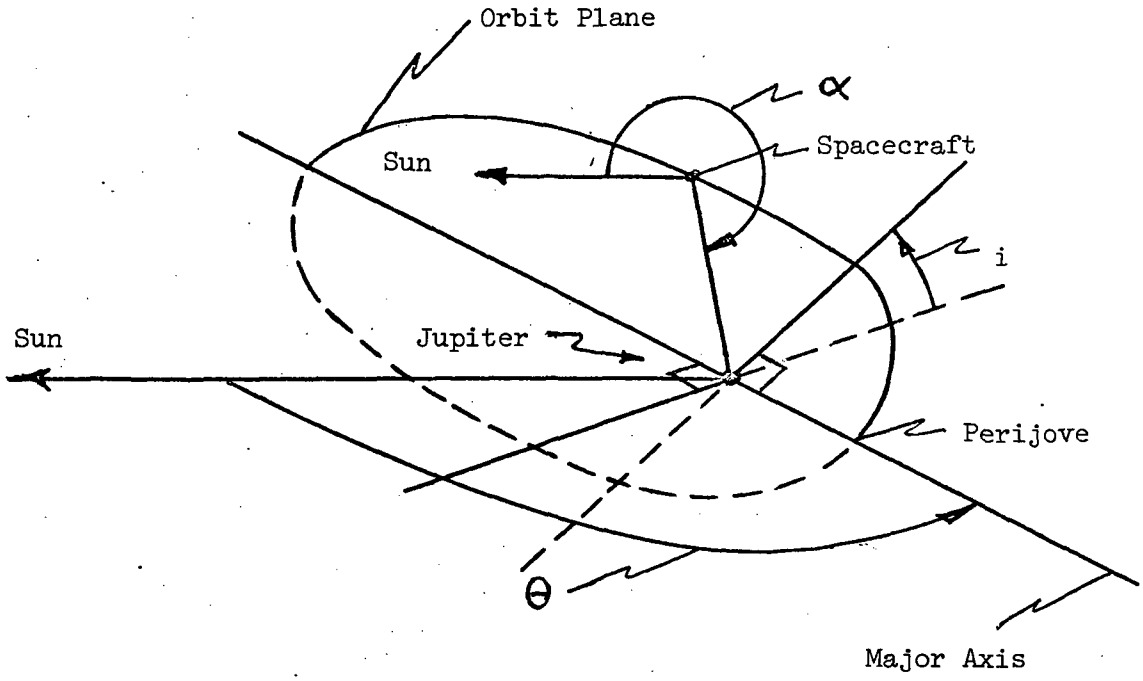

Figure IX-5. Spacecraft-Jupiter-Sun Geometry for an Arbitrary Orbit

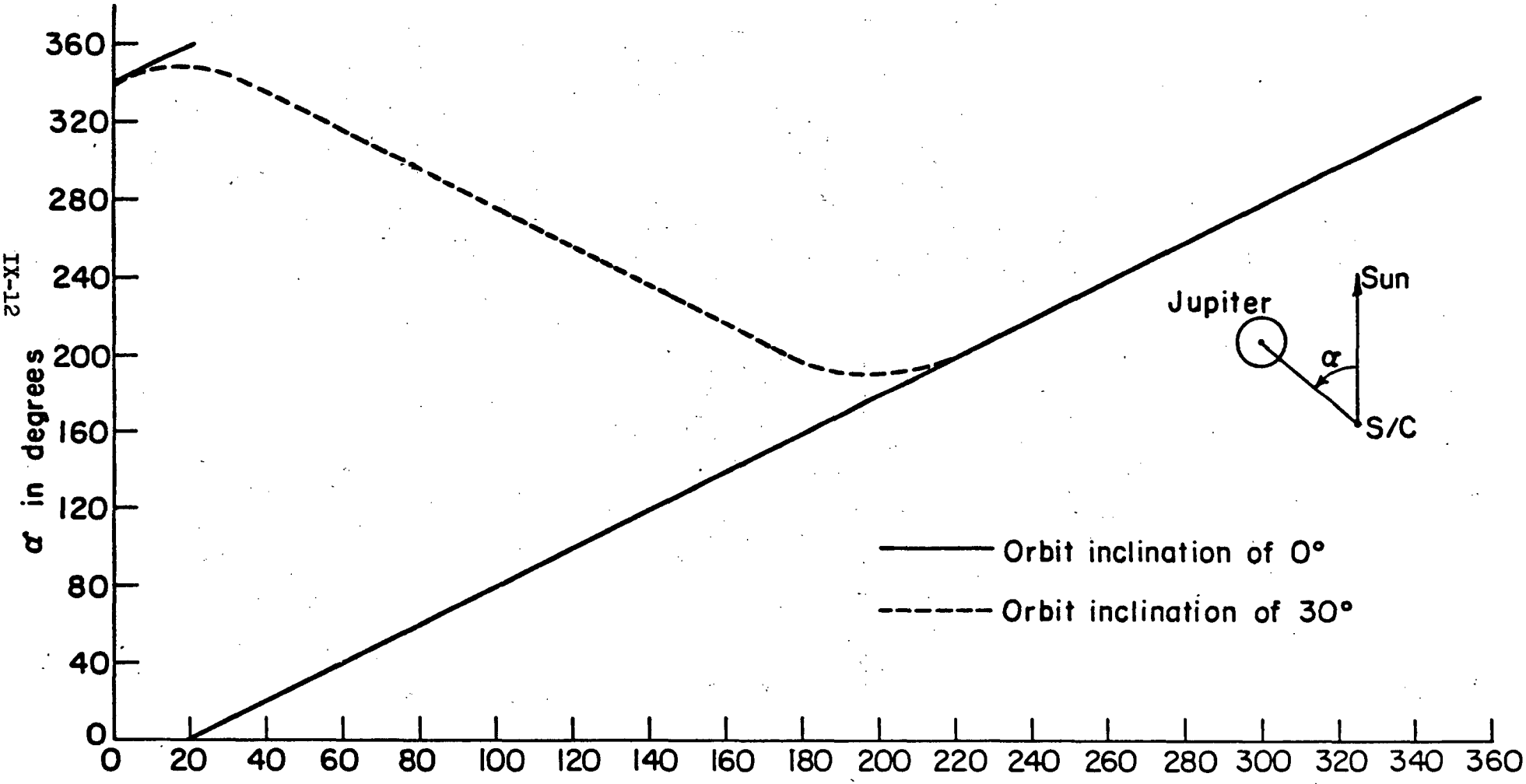

FIGURE IX-6 α VS TRUE ANOMALY FOR ORBIT INCLINATIONS OF 0° AND 30°

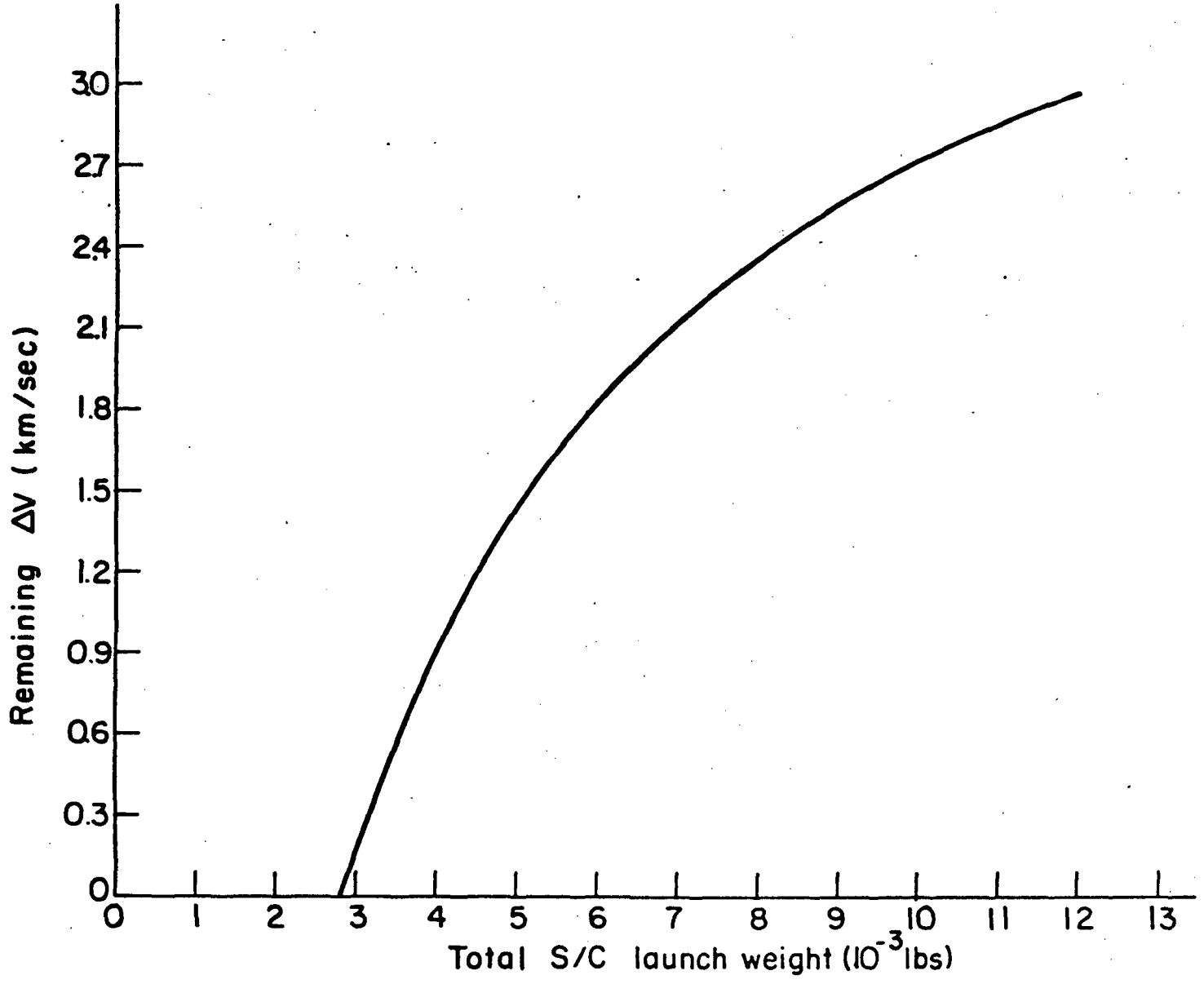

FIGURE IX-7 ΔV CAPABILITY REMAINING AFTER ORBITAL INSERTION VS. TOTAL LAUNCH WEIGHT

d) ΔV required for mid-course trajectory correction of 660 m/sec and ΔV for deboost into orbit of 1 km/sec (Chapter IV).

A survey of present launch vehicle capabilities narrowed the choices of spacecraft launch weight to either less than 4400 lbs for a Saturn S-IB/Centaur/BII or a Titan III-C HKS, or 12,000 lbs for a Saturn S-IC/s-IUB/Centaur/BII. The large increment in total spacecraft (7,600 lbs) to gain only 1.9 km/sec of ΔV is undesirable, thus a decision to specify a spacecraft design weight of 4400 lbs was made.

Table IX-1 is a compilation of the design parameters of the propulsion system illuminated in Chapter V.

The propellant tanks are arranged in a planar formation which will fit inside of a cylindrical body with an outside diameter of 105 inches and a height of 34 inches. The tanks are configured such that the cross axes moment of inertias are equal. The propulsion motor's thrust vector is coincident with the Z axis of the spacecraft. The remaining inert weight (312 lbs) is assumed distributed symmetrically around the Z axis between the tanks and the motor.

2. Meteoroid Protection

A spacecraft traversing the Earth-Jupiter distance will encounter many hypervelocity particles and meteoroids. Interplanetary space can be divided into several zones in which the fluxes of the meteoroids are quite different. Table IX-2 represents the best estimates by JPL of the probably extent of the meteoroid distributions throughout the range of the mission [IX-1]. However, caution must be used when designing for protection of the spacecraft in the outer regions (greater than 1.5 AU) for the estimates of flux are subject to errors in orders of magnitude.

Table IX-1

Propulsion System Specifications

Weight of fuel (lbs)	362
Volume of each fuel tank (ft^3)	7.2
Weight of each fuel tank (lbs)	57.5
Inside diameter of fuel tank (in)	28.8
Weight of oxidizer (lbs)	1812
Volume of each oxidizer tank (ft^3)	10.1
Weight of each oxidizer tank (lbs)	60
Inside diameter of oxidizer tank (in)	32.2
Tank insulation thickness (in)	.5
Total insulation weight (lbs)	31.2
Total weight of pressurant system (lbs)	14.8
Engine nozzle diameter (in)	17
Engine overall length (in)	28
Total propellant weight (lbs)	2174
Inert weight (lbs)	547
Weight of propulsion subsystem (lbs)	2721

Table IX-2

Summary of Meteoroid Zones and Fluxes Involved in Jupiter Mission

Zone	Distance from sun (A.U.)	Type of particles	Collision velocity (KM/SEC)	Flux (No. of particles per M^2-se Mass M in GM)
Earth's dust cloud	1	Cometary	5-15	$10^{-17}M^{-1.70}$
Earth-to-Mars	1 - 1.5	Cometary	40	$10^{-13.3}M^{-1.0}$
Asteroidal Belt	1.5-5.2	Meteoritic	20	$10^{-10}M^{-0.77}$
Jupiter's Dust Cloud	5.2	Cometary	10-60	$10^{-15}M^{-1.7}$ to $10^{-14}M^{-1.7}$

Densities - Cometary .44 GM/CM^3

Meteoritic 3.5 GM/CM^3

For a given flux ϕ of mass M and greater, the probability P of N impacts on area A in time T is given by the Poisson distribution represented as follows:

$$P(N) = \frac{X^N}{N!} \ell^{-x} \quad ; \quad X = A \cdot T \cdot \phi$$

For a known flux, A, a critical mass M_c can be determined as a function of the zero impact probability P(o). This critical mass is the upper bound of possible distructive particles encountered because particles larger than M_c have a probability of impact smaller than the assumed P(o) and thus can be ignored whereas smaller particles will not penetrate a shield designed to resist masses of M_c [IX-4].

The degree of penetration produced by meteoroid velocity impacts is by no means agreed upon, but the Voyager "Advanced Planetary Probe" study by TRW Systems indicates the Summers and Charters equation - corrected for the target finite thickness - gives the greatest penetration depth for a given impact velocity. The thickness L required to provent penetration by particles of diameter d and velocity V_m is:

$$L = 2.28 \; F \; d \left(\frac{P_M}{P_T} \; \frac{V_M}{V_Y} \right)^{2/3}$$

The factor F scales the penetration depth in semi-infinite targets to that in thin sheets; a value of 1.5 is generally assumed. V_T is the sonic velocity of the target material. For a spherical particle the mass can be related to the diameter and all impacts are assumed to be perpendicular to the surface.

Table IX-3 defines the time spent in each zone (Chapter III).

Figures IX-8, IX-9, IX-10 show the required shielding for different probabilities of zero puncture for the various zones. The success of the

Table IX-3

Summary of Distance From Sun and Cumulative Time

Distance	Date	Cumulative Days
1.0	Nov. 25, 1980	0
1.5	Feb. 20, 1981	87
2.0	Apr. 10, 1981	136
3.0	July 20, 1981	237
4.0	Dec. 17, 1981	387
5.0	Apr. 10, 1982	501
5.2	July 1, 1982	582

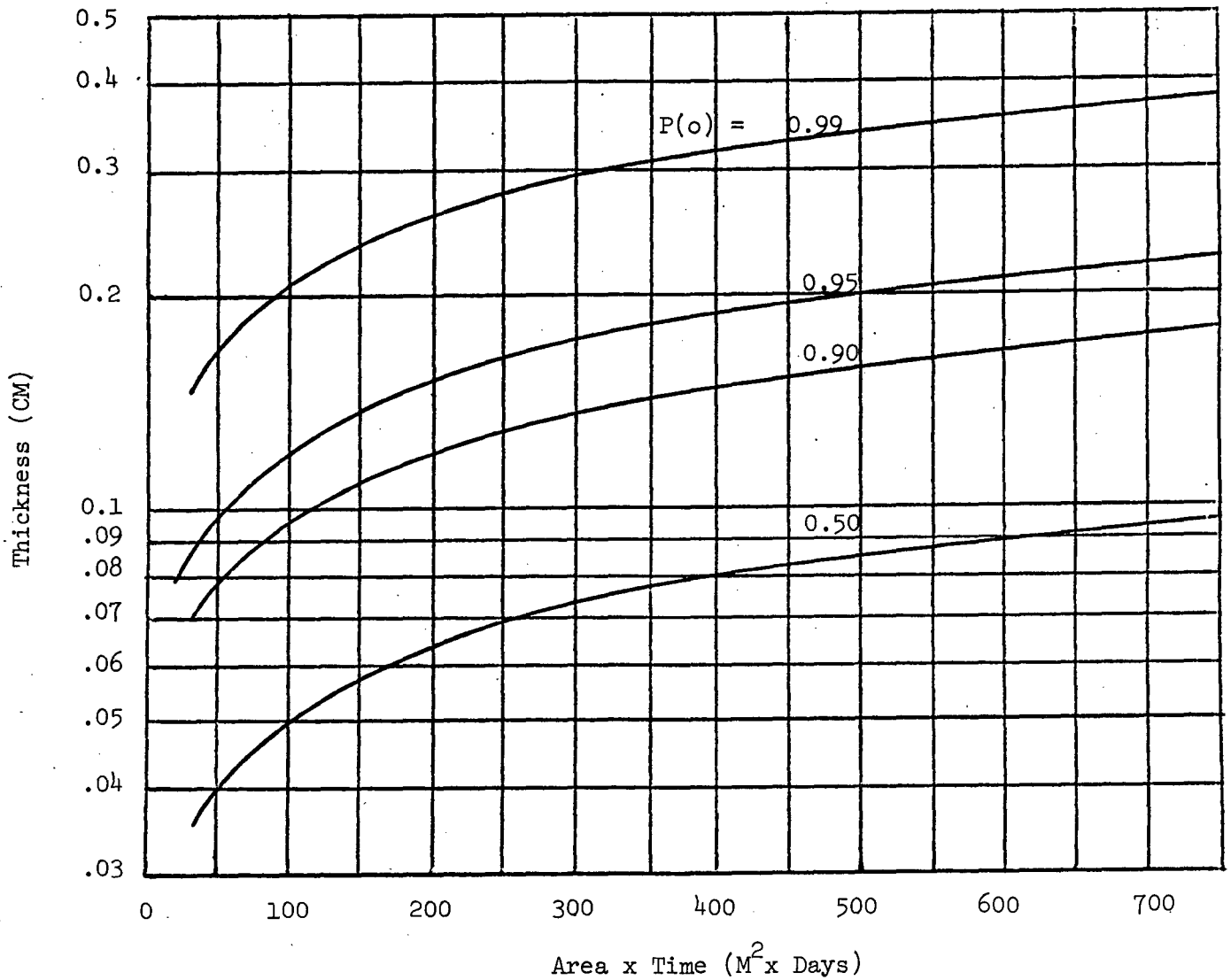

Figure IX-8. Probability of Zero Puncture in Aluminum Sheet Between Earth and Mars (40 KM/Sec)

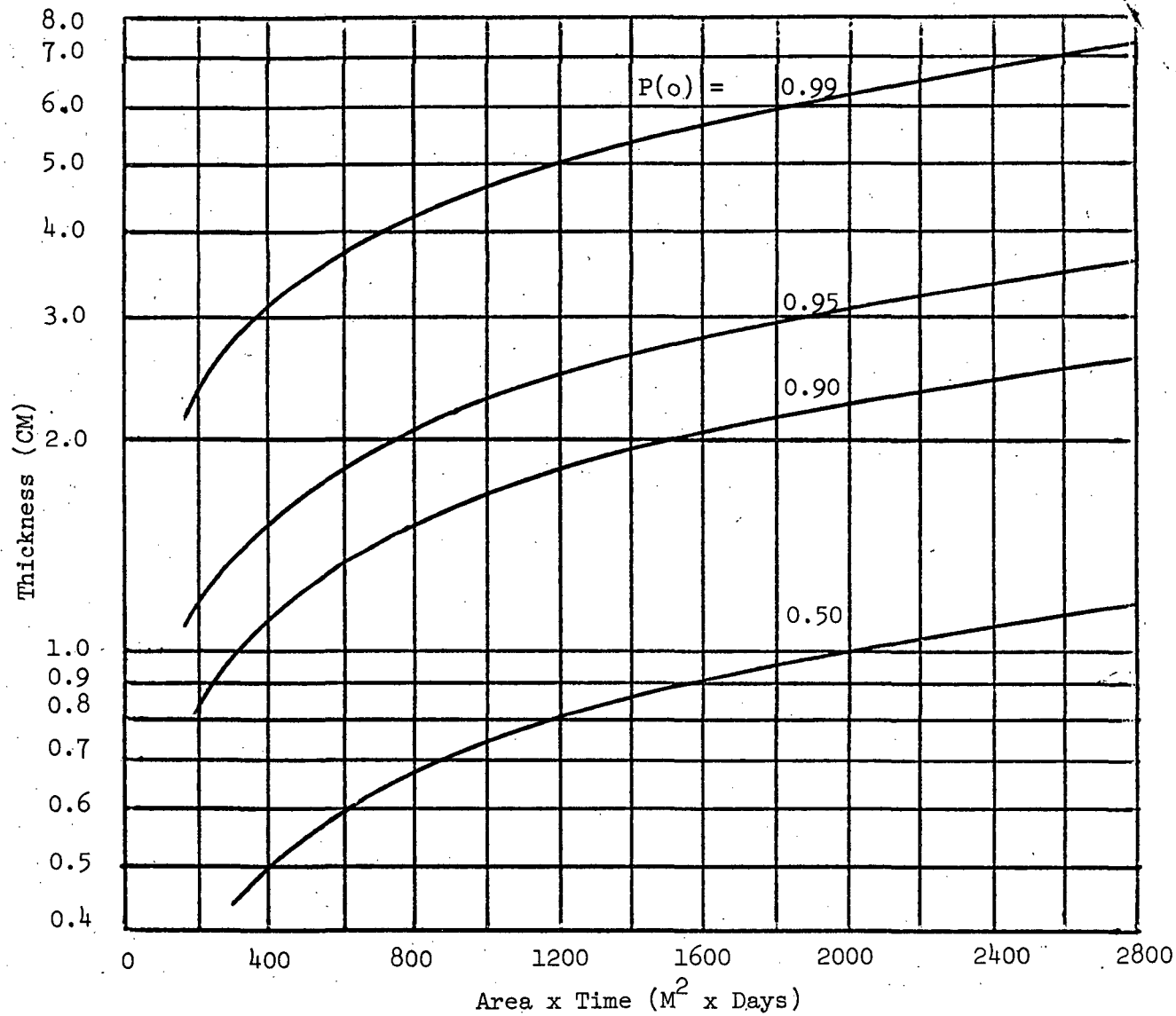

Figure IX-9. Probability of Zero Puncture in Aluminum Sheet From Asteroidal Debris Between Mars and Jupiter (10 KM/Sec)

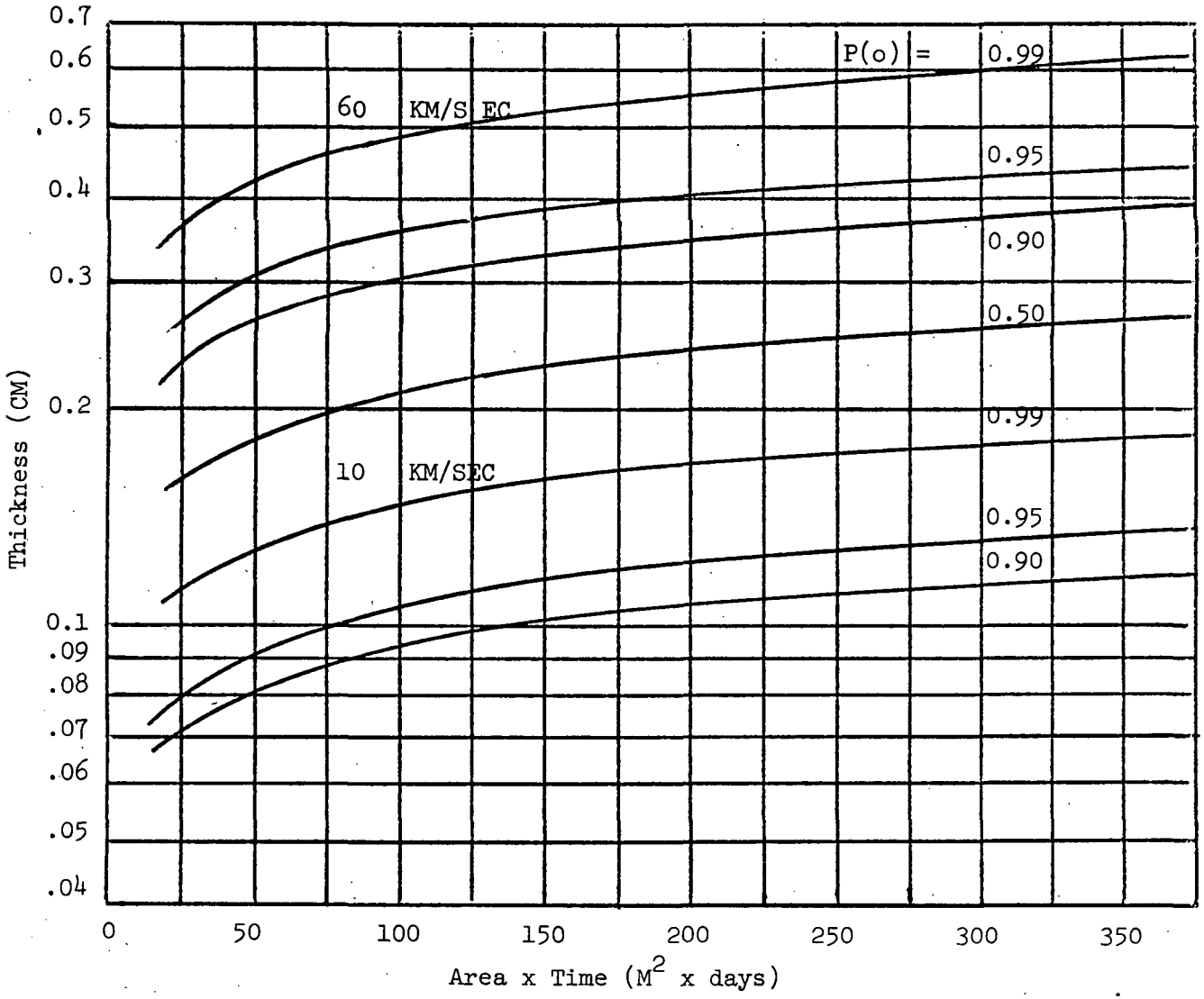

Figure IX-10. Probability of Zero Puncture in Aluminum Sheet From Jupiter's Cloud (Flux = $10^{-15}M^{-1.70}$)

meteoroid protection depends critically on the flux encountered in the asteroid belt between Mars and Jupiter. For this mission a zero impact probability of .9 requires an effective shield thickness of 2.3 cm.

The use of multiple layers of shielding against meteorodis results in tremendous weight savings. The required thickness L in the Summers and Charters penetration equation can be replaced by $\bar{L}$, where

$$\bar{L} = \frac{L_1 + L_2}{K}$$

L_1 is the thickness of the bumper layer, L_2 is the thickness of the base layer and K the factor of effectiveness [IX-8]. The double wall of thickness 1.5 inches, filled with low density (2.3 lbs/ft^3), results in a K factor of .25.

Protection with the above specification requires a panel weight of 2.9 lbs/ft^2. This weight alottment for meteoroid protection is too large and a lower probability of zero impacts must be accepted. The recommended panel has a bumper thickness .025 inches of aluminum alloy 2024-T3, a base thickness of .050 inches of aluminum and 1.425 inches of polyurethane foam; thus a zero probability of .5.

To provide meteoroid shielding over the thermal louvers a panel is designed to maximize radiative heat transfer from thermal louvers to deep space. They consist of curved aluminum vanes stacked on edge and covered on the outside by an aluminum sheet. Total panel thickness is 1.0 inches with a weight of 1.7 lbs/ft^2 [IX-8]. See figure IX-11.

The shielding philosophy here is based on the principle of providing for a small probability of a penetration that can cause a failure. Calculations give a preliminary weight of 150-175 lbs of meteoroid shielding for JOSE. However, this figure can be reduced if the self-shielding properties of the final structure are studied. Several conservative approximations were

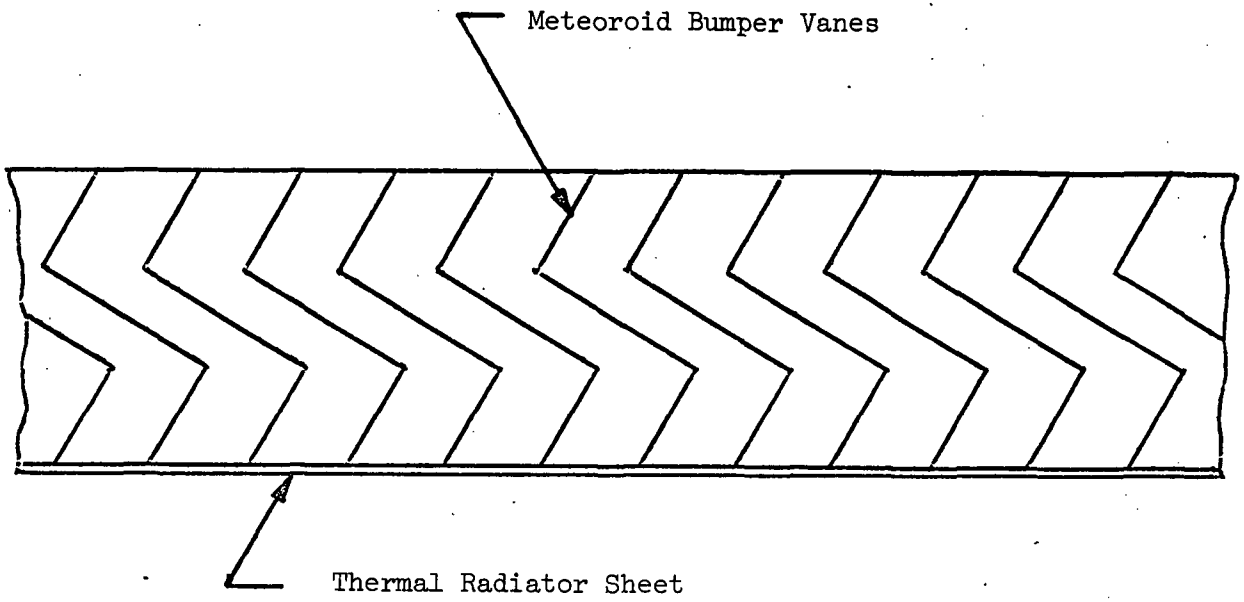

Figure IX-11. Bottom Meteoroid Panel

included in the above analysis, thus it is likely the mission will have a higher probability of success than assumed. If the structural material can be designed to perform the multiple duties of structural support, thermal radiation and meteoroid protection all in one panel, the guidelines of the preliminary weight allocation study can be easily met.

3. Charged Particle and Nuclear Radiation Effects

During the mission life, the Jupiter orbiting spacecraft will be exposed to a radiation environment due to the RTG's, interplanetary radiation, and Jupiter's trapped radiation belts. The RTG's provide a continuous background radiation environment, consisting mainly of neutrons and protons, from the time of launch through the end of the mission. The high energy particle flux of the interplanetary radiation is the dominant radiation source during the transfer phase from the Earth to Jupiter. The intense radiation belts of Jupiter produce an electron and proton radiation field that the spacecraft experiences when in the proximity of the planet.

Radiation is the source of two potential problems on-board the spacecraft: radiation damage to the electronics and background interference which may mask the reading of the radiation measuring instruments. Orientation and location of the RTG's can be used to minimize the neutron and gamma flux on various sensitive parts of the spacecraft. Location of the instruments within the micrometeoroid shielding and in the "shadow" of other nonsensitive components (e.g. fuel tanks) may also reduce the nuclear and particle radiation. Electronic equipment itself may also be designed to have high radiation tolerances.

The following study was undertaken to determine necessity of additional shielding and potential problem areas for the Jupiter orbiting spacecraft.

a. Flux Limits and Damage Tolerances

The upper limit on the background flux from the RTG's is dependent on the sensitivity of the measuring instruments. The very sensitive cosmic ray detector measures down to 2 events/cm^2sec will be mounted on the scan platform, module 2, along with the trapped radiation detector and plasma probe in order to obtain directional sensitivity readings.

Reference IX-1 sets an upper limit of about 10-20 photons/cm^2-sec for the latter instruments.

Radiation damage to the electronic components consists basically of two effects. The first is atom displacement in the lattice which is due mainly to neutron-atom collisions. The second effect is atomic ionization due mainly to the ionizing component of incident radiation. The second effect may be either permanent or transitory in nature depending on the component irradiated and the level of incident radiation while the neutron - atom displacement effect is almost always permanent. The radiation damage threshold doses and dose rates for various components are listed in Table IX-4.

The figures of Table IX-4 indicate that when the integrated component flux and dose rates are kept below 10^6 rads and 10^4 rads/sec respectively, and the integrated neutron flux is below 10^{11} n/cm^2, no appreciable change in the performance of the electronics will occur. However, an upper limit of 10^3 rads/sec must be placed on the optical devices to assure no change in the properties of these devices.

One of the difficulties in establishing radiation damage limits is the inability to correlate radiation damage with all radiations of all energies. The flux-to-rad dose conversion factors for nuclear radiations in materials, since a function of the material is often not well known [IX-6]. Values in Table IX-4 can be used only as a rough criteria to determine critical areas where radiation protection might be necessary.

Table IX-4. Radiation Damage Thresholds for Spacecraft Components

Electronic Equipment or Component	Ionization dose (rads)	Dose Rate rads/sec	Integrated neutron dose n/cm^2 @1 Mev	Integrated proton dose p/cm^2 @10Mev	Integrated Electron dose e^-/cm^2 e^-/1 Mev	5 Mev	Electron Flux rate e^-/cm^2-sec @2Mev
Germanium Transistors	10^6-10^7|1|	10^5 |2|	10^{13} |1|				
Silicon Transistors	10^7 |1|	10^5 |2|	10^{12} |1|				
Microcircuitry Semiconductors		10^4 |2|					
Silicon Dislocations				10^{12} |4|	7.5×10^{14}|4|	2.5×10^{14}|4|	
Communications, Radar, and Guidance	10^7 |1|		10^{13}-10^{14}|1|				
Date Encoder							9×10^8|5|
Canopus Tracker							2×10^9|5|
Optical Devices (ordinary glass)	10^4|3|	10^3|2|		10^{13}|3|			

\|1\| = Reference IX-2
\|2\| = Reference IX-3
\|3\| = Reference IX-9
\|4\| = Reference IX-4
\|5\| = Reference IX-1

b. Radiation Fields Description

i. RTG Field

The isoflux neutron and gamma contours for each of the two-tandem - 4000 thermal watt RTG units is shown in Figures IX-12 and IX-13. The values have been determined from scaled up data of the SNAP-27 generator supplied by Hittman Associates [IX-5]. Even though the currently used G.E. RTG design differs somewhat in dimensions and thermocouple structure and composition from the SNAP-27, the expected radiation fields will be similar. The new neutron flux map can simply be scaled from the SNAP-27 by the ratio of the amounts of radioactive fuel since the RTG can be considered transparent to these energy neutrons. Protons however are absorbed within the fuel source and the RTG, and the simple scaling would have to be modified due to the self-absorbtion along the fuel capsule axis by a factor of about 1.5 to 2.0 for this case [IX-5]. Simple scaling however was used in arriving at the values in Figure IX-13.

ii. RTG Dose and Dose Rates

The RTG-spacecraft orientation in launch (stowed) and mission (extended) configuration is shown in Figures IX-19 and IX-20. The flux and integrated flux and dose rates can now be determined using Figures IX-12 and IX-13 and the following assumptions:

1. An average of 15 days might be spent on the launch pad with fueled RTG's prior to lift off.
2. The flux-to-dose rate for gamma's from the RTG's is

$$1.69 \times 10^{-10} \ \frac{\text{rad-cm}^2}{\text{photon}} \ .^{*}$$

---

* This figure takes into account the weighted average of the various energy level photons, the spectrum having been supplied by Hittman Assoc. [IX-5] and the conversions found in Reference IX-6.

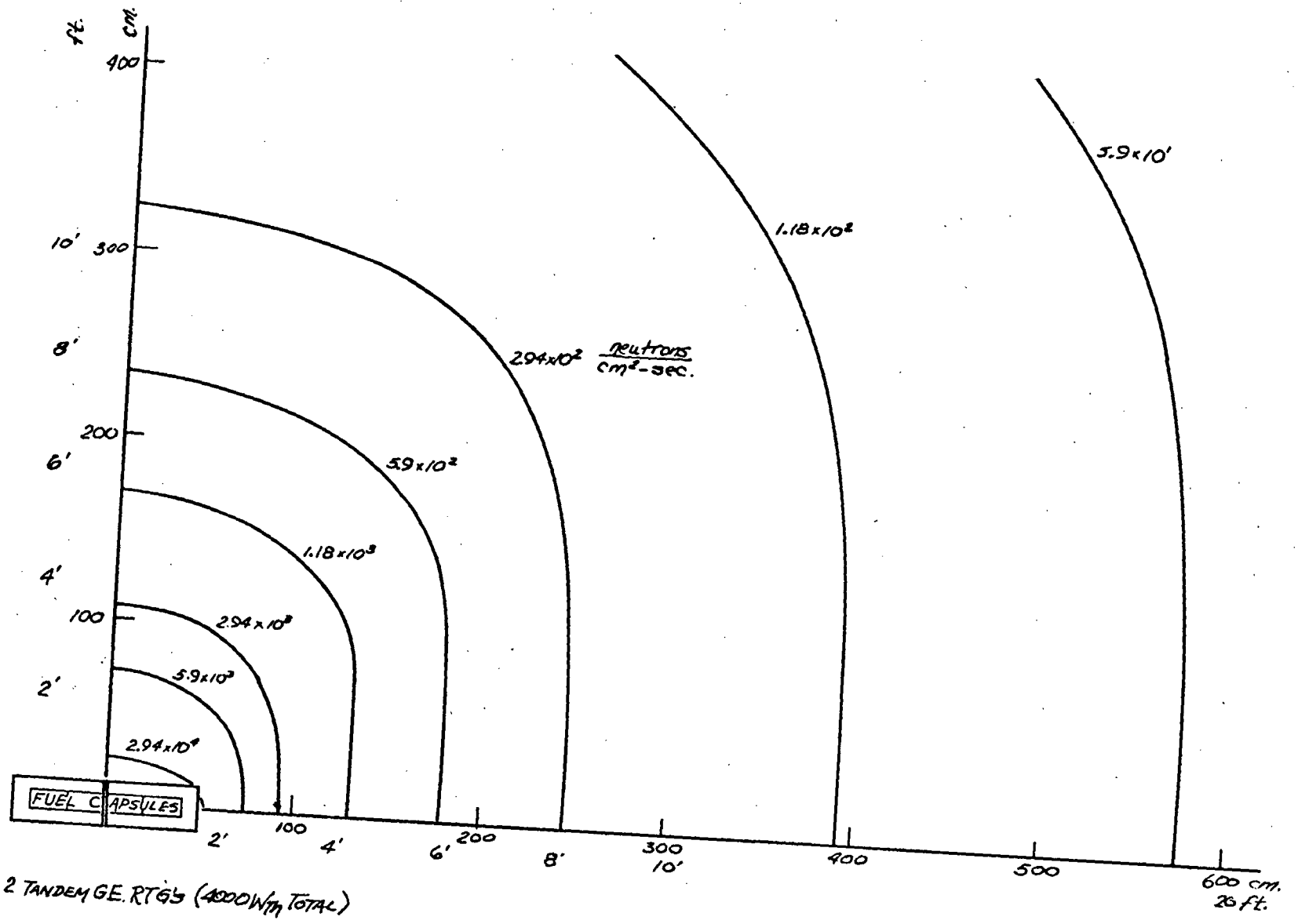

Figure IX-12. Neutron Isoflux Contours

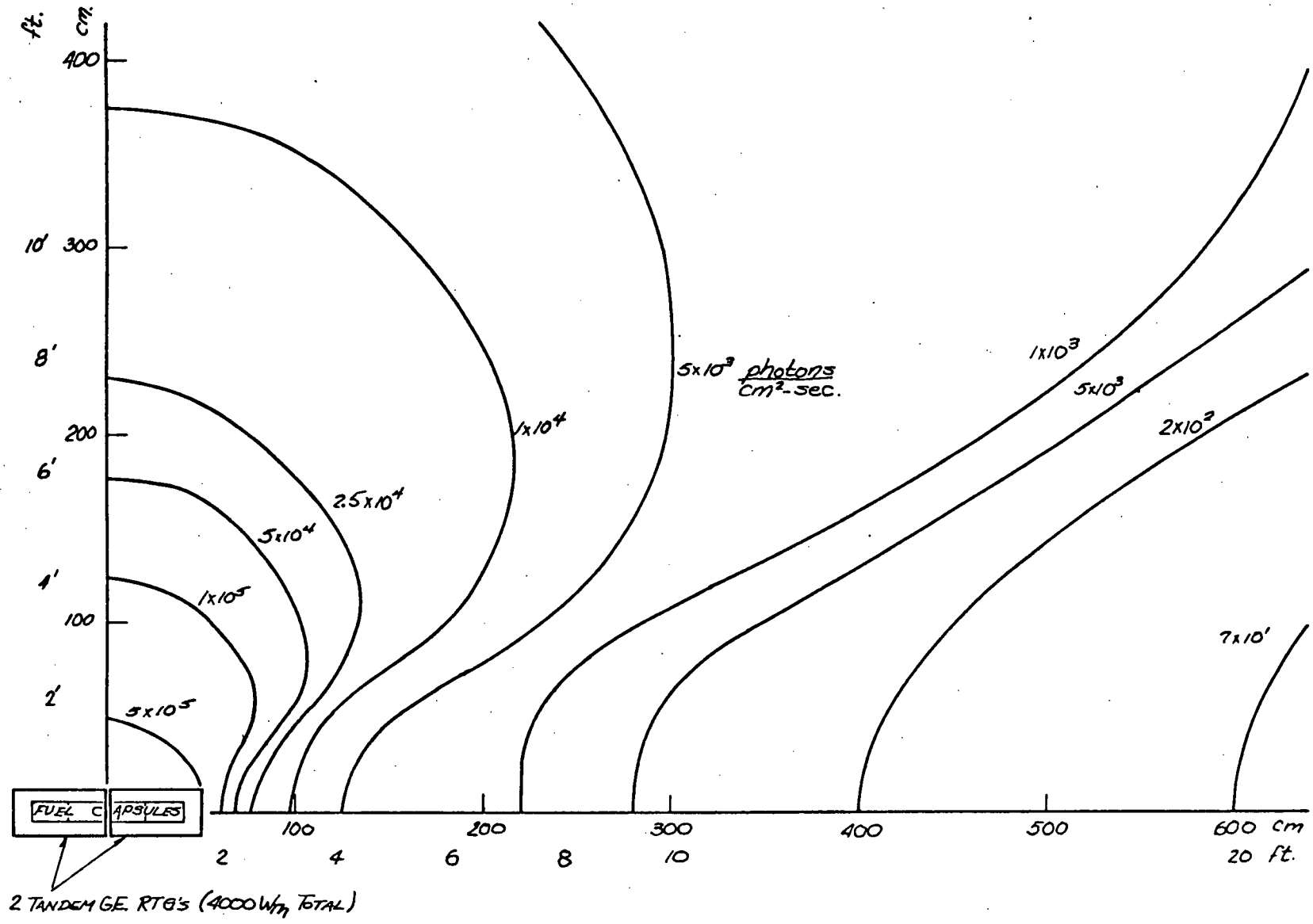

Figure IX-13. Gamma Isoflux Contours

3. There is no radiation interference due to the presence of the spacecraft.

4. For the purpose of determining radiation doses electronics are located at center of either scan platform of spacecraft.

Table IX-5 gives the results obtained for the neutron and gamma flux dose rates and doses that the scan platform and equipment bus will receive during the various aspects of the mission.

iii. Interplanetary Radiation

The high energy interplanetary radiation consists mainly of high energy protons (about 1 Bev) at flux rates of 3 particles/cm^2-sec [IX-4] . Using the conversion of $2 \times 10^{-7} \frac{\text{rad-cm}^2}{\text{particle}}$ [IX-6], the spacecraft receives 52×10^{-3} rads/day or a total of 42.5 rads for the 815 days interplanetary phase, and an integrated flux of 2.34×10^8 protons/cm^2. The contribution due to earth's Van Allen belts calculated from radiation levels given in Reference IX-4 amounts to about 270 rads of 1 Mev electrons.

iv. Jupiter's Trapped Radiation Belts

The electron flux model of Reference IX-7 shown in Figure IX-14, and the proton flux model described in Reference IX-8 were used in determining the radiation absorbed by the spacecraft. These models indicate a maximum electron flux of 2×10^7 e^-/cm^2-sec at about 3 Jupiter radii and a maximum proton flux of 10^9 protons/cm^2-sec at Jupiter radii. The electrons are in the range of 5-100 Mev and the protons in the range of 0.1 to 4 Mev. The time integrated electron and proton flux for a spacecraft in a 1.1 x 100 R_J orbit was computed by a graphical summation method giving the following values of 10^{11} e^-/cm^2 and 10^{13} protons/cm^2 per orbit.

To convert from flux to absorbed dose rate, the values given by Haffner,

Table IX-5. Neutron and Photon Radiation From The RTG's Incident Upon the Scan Platform and Equipment Bus During Mission

Scan Platform	$\frac{n}{cm^2\text{-sec}}$	$\frac{n}{cm^2}$	$\frac{\text{Photons}}{cm^2\text{-sec}}$	$\frac{\text{Rads}}{\text{sec}}$	$\frac{\text{Photons}}{cm^2}$	Rads
Launch[1.]	5.2×10^{2}	6.72×10^{7}	2.4×10^{4}	4×10^{-6}	3.12×10^{9}	5.2×10^{-1}
Cruise[2.]	160	1.12×10^{10}	300	5×10^{-8}	2.1×10^{10}	3.5×10^{0}
$1.1\times100R_J$ Orbit (per orbit)	160	6.2×10^{8}	300	5×10^{-8}	1.2×10^{9}	1.9×10^{-1}
$1.1\times20R_J$ Orbit (per orbit)	160	5.8×10^{7}	300	5×10^{-8}	1.1×10^{8}	1.8×10^{-2}
Equipment Bus						
Launch[1.]	1.2×10^{3}	1.6×10^{8}	5.4×10^{4}	5.2×10^{-6}	7×10^{9}	1.2×10^{0}
Cruise[2.]	300	2.1×10^{10}	800	1.4×10^{-7}	5.6×10^{10}	9.6×10^{0}
$1.1\times100R_J$ Orbit (per orbit)	300	2.1×10^{10}	800	1.4×10^{-7}	3.1×10^{9}	5.2×10^{-1}
$1.1\times20R_J$ Orbit (per orbit)	300	1.1×10^{8}	800	1.4×10^{-7}	2.9×10^{8}	4.8×10^{-2}

1. Launch = 15 days
2. Cruise = 815 days

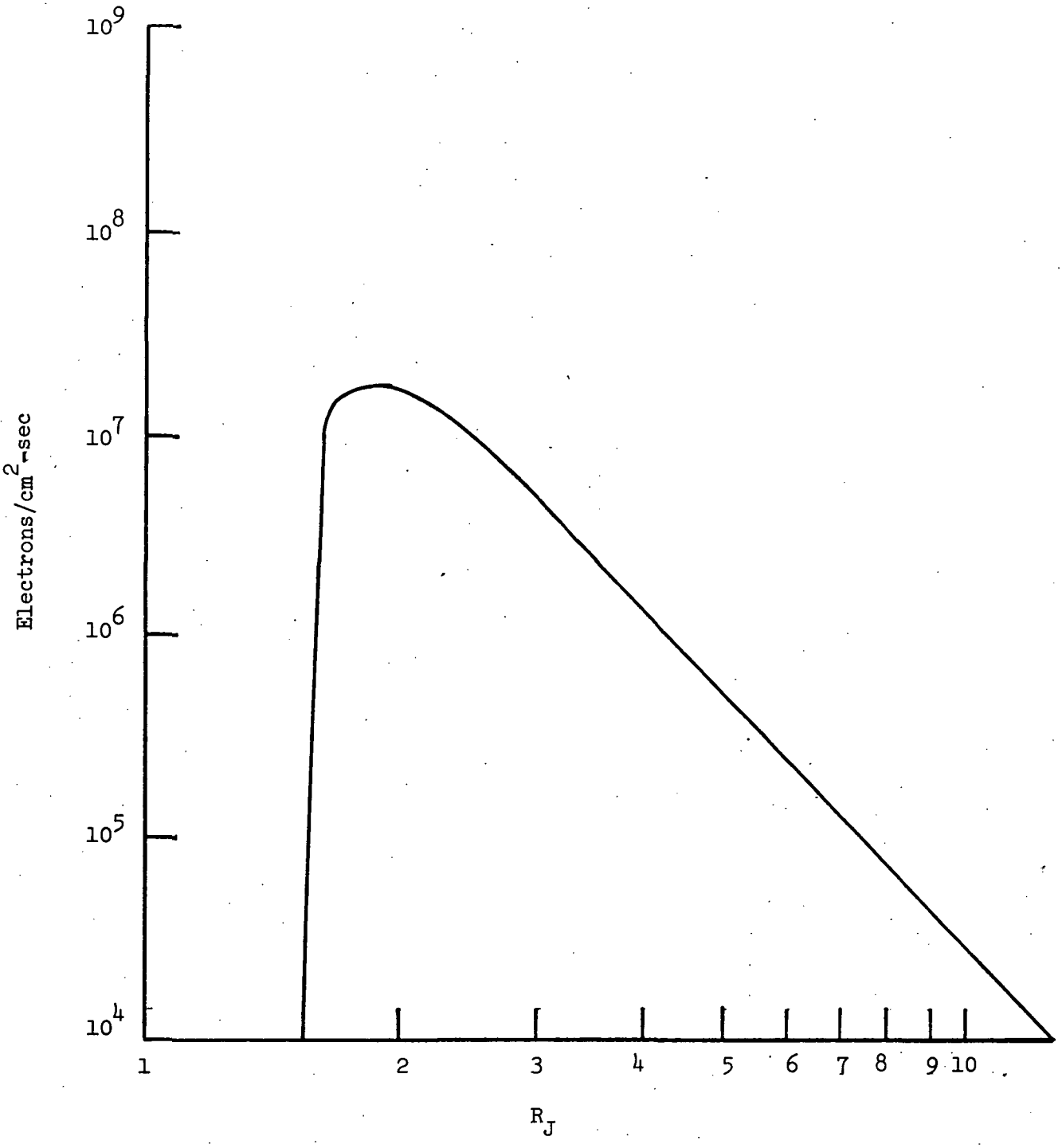

Figure IX-14. Flux of Electrons in Jupiter's Radiation Belt As a Function of Distance From the Dipole in the Plane of the Magnetic Equator Reference IX-7.

Reference IX-6 will be used again. For electrons of energies in the range of 1-100 Mev, the conversion factor is approximately constant and equal to $5 \times 10^{-7} \frac{\text{rad-cm}^2}{\text{electron}}$. For protons between 0.1 and 4 Mev, the flux-to-dose conversion factor averages to about 10^{-5} rad-cm^2/proton. The total dose and dose rate is summarized in the Table IX-6.

The integrated fluxes experienced by the spacecraft when in the $1.1 \times 20 R_J$ orbit are essentially the same as that given above. The integrated dose per year is different and these values are also presented in the table below.

c. Shielding and Problem Areas

i. Damage

All of the above doses have been determined assuming no shielding. The .08 inches of aluminum micrometeoroid shielding however affords some shielding to most equipment and instruments. .08 inches of aluminum will stop all protons of energies less than 17 Mev. This means that except for the parts of the spacecraft which cannot be shielded by the micrometeoroid protector, e.g., sensor optics, the electonics will be protected from the proton component of the trapped radiation belts. The high energy protons of interplanetary space will pass through any shielding but their dose and dose rates are well below accepted tolerance limits.

All electrons however above 1 Mev will pass through the .08 inches of aluminum which means that interplanetary and trapped radiation belts electrons will not be appreciably attenuated. The .08 inches aluminum will reduce the intensity of gamma radiation with energies of .16 Mev by 7% and those with energies of 1 Mev by 3%.

The cummulative neutron and electron (>1 Mev) flux incident on the spacecraft during its mission is presented in Figure X-15. The cummulative ionizing dose radiation, due mainly to the electrons in Jupiter's trapped

Table IX-6. Expected Spacecraft Dose and Dose Rates Due to the Jovian Radiation Belts

Radiation	Maximum Flux Experienced by Spacecraft	Maximum Dose Rate Experienced by Spacecraft	Integrated Flux	Integrated Dose
per orbit:				
Electrons 1-100 Mev	$2 \times 10^{7} e^{-}/cm^{2}$-sec	10 rad/sec	$10^{11} e^{-}/cm^{2}$	5×10^{4} rads
Protons .1-4 Mev	10^{9} pr/cm^{2}-sec	10^{4} rad/sec	10^{13} pr/cm^{2}	10^{8} rads
per year:				
1.1×100 R_J				
Electrons			$8.1 \times 10^{11} e^{-}/cm^{2}$	4×10^{5} rads
Protons			8.1×10^{13} pr/cm^{2}	8.1×10^{8} rads
1.1×20 R_J				
Electrons			$8.7 \times 10^{12} e^{-1} cm^{2}$	4.3×10^{6} rads
Protons			8.7×10^{14} pr/cm^{2}	8.7×10^{9} rads

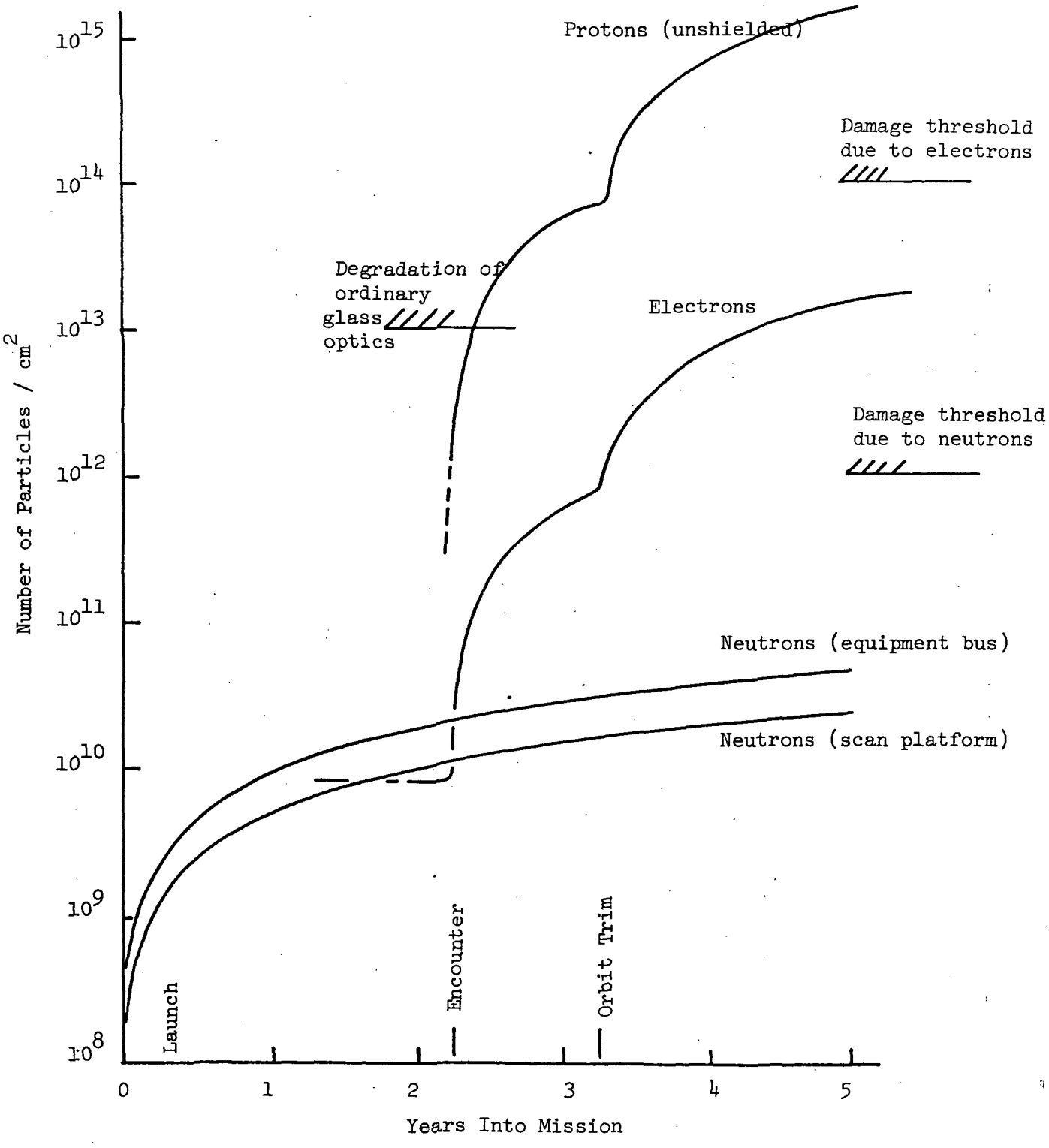

Figure IX-15. Cummulative Fast Neutron, Unshielded Proton, and Electron (>1 Mev) Flux as a Function of Mission Lifetime

radiation belt, is presented in Figure IX-16. In each of these figures the lower limit of threshold damage is shown for each radiation component.

Figure IX-15 indicates that no damage is to be expected from the integrated neutron flux throughout the entire missions life. The cummulative electron flux is also below the threshold level as set in Table IX-4 but only by less than a factor of ten. Due to the uncertainty in the electron flux levels, the actual fluxes may be a factor of 40 higher [IX-1] resulting in electronic components deterioration soon after a year in orbit. The cumulative

The cummulative ionization dose radiation as shown in Figure IX-16 approaches the damage threshold .25 years after the orbit trim maneuver. Again, due to the uncertainty in flux levels, system deterioration may begin during the first year in orbit.

These figures indicate that a potential problem exists with respect to the proper functioning of the electronic components due to the Jovian radiation belts. Shielding of the high energy electrons is not completely straightforward since additional shielding would also be required for the attendant bremsstrahlung radiation. Furthermore, because of the large uncertainty in the predicted flux and energy levels, no definite commitment as to the amount of shielding has been made. Two parallel safety paths though should be pursued; that of shielding and that of using radiation-resistant circuits and components.

Another problem area as far as damage is concerned is that to the optics. The optical elements of instruments which must be used near the planet, where the radiation intensities are the highest (10^4 rad/sec, 10^{13} protons/cm^2-orbit, and 10^8 rads/orbit) cannot be shielded. The optics are then prime targets for radiation damage due to the dose and dose rate from the protons. Highly radiation-resistant or stabilized glass will have to be used and any loss in optical quality due to radiation hardening would have to be compensated for.

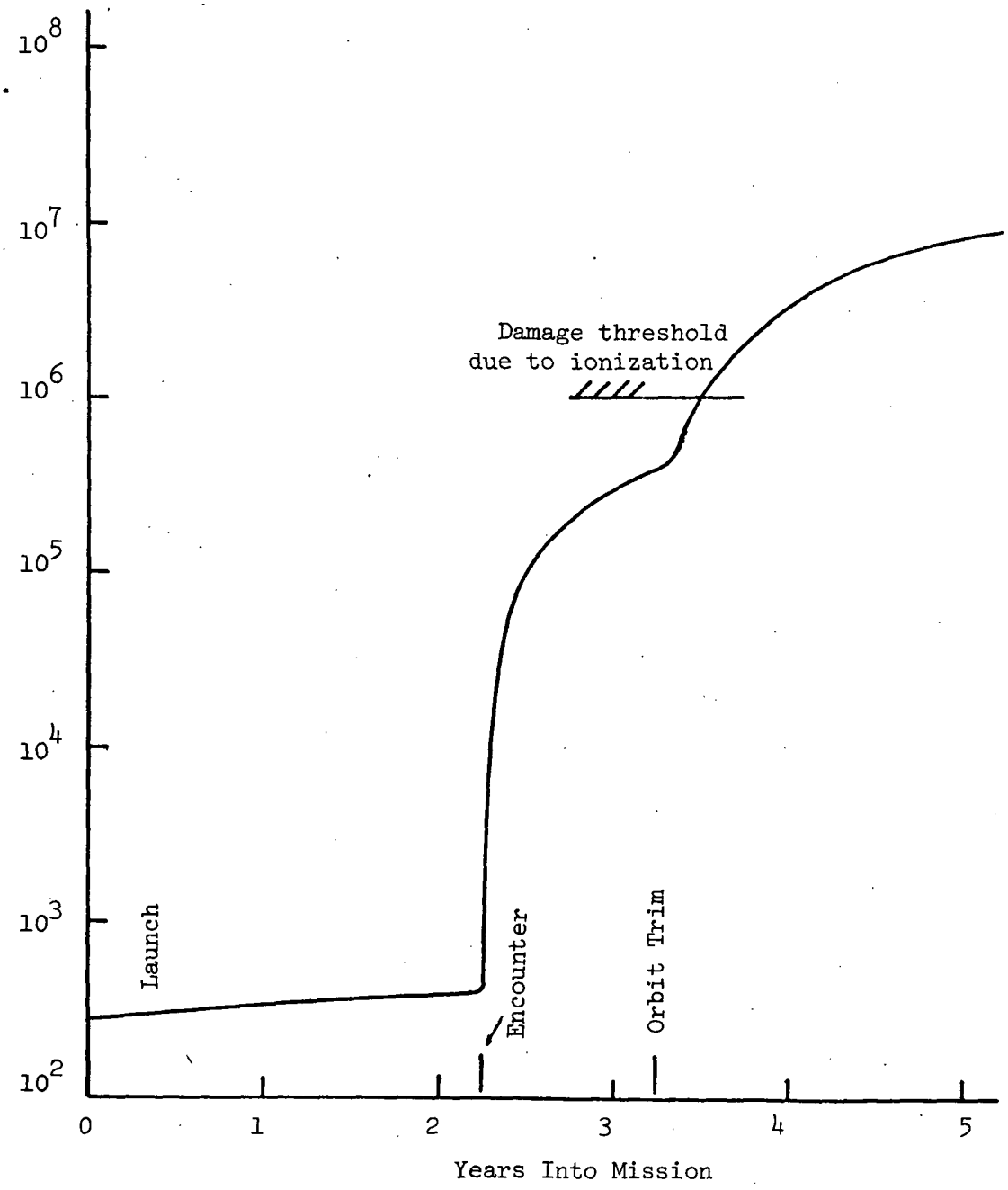

Figure IX-16. Cummulative Ionizing Dose Radiation With 0.08 Inches of Aluminum Shielding as a Function of Mission Lifetime.

ii. Interference

The gamma flux levels incident on the scan platform from the RTG's will interfere with the low level counting of the cosmic ray detector and x- and γ-ray detector. Even though gamma flux rates presented in Table IX-5 do not take into account attenuation or scattering due to the spacecraft, these numbers will be used to determine a conservative amount of shielding.

It is therefore desired to reduce the gamma flux from 300 photons/cm^2-sec by a factor of 20 to 15 photons/cm^2-sec. The thickness and weight for the required amount of shielding to obtain this reduction can be obtained from the following equation:

$$\frac{N}{N_o} = e^{-\mu_m d_m} = \frac{1}{20}$$

where μ_m = mass attenuation factor (cm^2/gm)

and d_m = absorber thickness (gm/cm^2).

From the spectral distribution of photon energies from the RTG, it was determined that to stop 95% of the incident flux, all photons of energies less than or equal to .779 Mev must be attenuated completely. At this energy level μ_m for uranium is about 0.1 giving an absorber thickness d_m of 30 gm/cm^2.

The surface area of the sensitive equipment mentioned above has been estimated to be 500 square inches resulting in a shielding weight of 24 pounds. This is surely an upper limit since the presence of the spacecraft will reduce the flux incident on the instruments.

Minimizing gamma radiation in the direction along the axis of the RTG is cylindrical fuel capsule by making the capsule longer might be an interesting design consideration for future RTG design work. The question is then if the radiation shielding weight saved would more than compensate for the possible increase in RTG weight by going to longer configuration.

4. Preliminary Thermal Analysis

The basic objective of a thermal design is to contribute to maximum life and reliability of all components by providing an optimum temperature environment. The thermal energy for temperature control will be available as electrical power dissipated by the electronic equipment and heat removed from the RTG's.

There are three spacecraft volumes that are essentially thermally independent:

a) Main equipment compartment

b) Isolated scientific packages

c) RTG's

The thermal design of the main equipment compartment is based on having good thermal exchange among the internal components to provide an isothermal volume. A minimum variation in internal temperature is achieved by use of thermostatically controlled variable emittance louvers which are thermally coupled to the main equipment bus.

The design approach for the scientific packages is to insulate and isolate them. Electric heaters will be used to heat these isolated areas if additional sources of power are required.

The design philosophy for the RTG's will be to thermally decouple them from the spacecraft body.

Because of the large variation of solar energy over the trip to Jupiter (see Table IX-7), [IX-10] the main compartment (with the exception of the thermal control surfaces) must be thermally isolated from the external environment. The radiation heat loss can be minimized by a superinsulated blanket consisting of numerous layers of aluminized mylar. The foam used in the meteoroid shielding also serves as an excellent insulator. For an ideal temperature of 25°C the radiated heat loss can be reduced to 10.8 watts/m^2 [IX-8].

Table IX-7

Variation of Solar Constant

With Solar Distance

Solar Distance (Astronomical Units)	Solar Constant (Watts/ft^2)
1.0	130.0
1.5	58.0
2.0	32.5
2.5	21.0
3.0	14.3
3.5	10.6
4.0	8.1
4.5	5.9
5.0	5.2
5.2	4.8

The heat sources available to offset this radiated loss are thermal energy dissipated by internal electrical equipment and heat rejected by the RTG's. The most desirable source is, of course, the electrical energy. Both TRW and JPL recommend use of this thermal energy. Using a portion of the RTG heat dissipation will be considered only if the electrical power is insufficient. Because the RTG's are boom mounted and deployed, heat transfer by conduction will be impractical because of the path length and discontinuities at joints and/or hinges. To use radiated heat the RTG-spacecraft distance should be less than 2 ft; a very undesirable condition from the radiation standpoint.

Another method of obtaining heat transfer from the RTG's is by heat pipes. The reliability of this type of system is high because it contains no moving parts. The pipe, an efficient method of transferring heat, consists of a closed shell, a porous wick, and a fluid. However, the system has other drawbacks:

a) Heat pipes have not been flight tested.

b) Deployable RTG's require deployable heat pipes.

c) A system leak would cause an entire loss of heat transfer.

Without an active temperature control switch, a minimum temperature variation of $40^{\circ}C$ can be expected during the mission lifetime. An active control system would regulate the energy balance and properly decrease temperature variation over the entire mission, by compensating for the following:

a) variation in solar energy

b) difficulty in predicting heat loss to structure

c) variation in heat loss to structure

d) reduction in power due to component failure

Experience with louver systems on the Mariners, Nimbus, and Pioneers have shown them to be reliable variable emittance devices. Figure IX-17 shows the variation in emittance as a function of louver angle for a typical system [IX-8]. A variation of heat rejected from 4 watts/ft^2 for the closed position to 30 watts/ft^2 for the full open position can be realized.

The louvers must be located on the "shady" side of the spacecraft. This will be no problem as the communications antennas are always earth pointing. An annular ring centered around the deboost rocket engine is suggested.

An energy balance on the main compartment is as follows:

Surface area of compartment	324 ft^2
Surface area viewing the Sun	67 ft^2
Internal thermal energy	400 watts
Heat radiated into space (not including louvers)	324 watts
Variation in solar load	435-16 watts
Variation in louver radiation	511-92 watts

With a capacity of 30 watts/ft^2 reduced by 50% due to the effect of the meteoroid shield (see section C-2) an area of 40 ft^2 gives the required capacity with an overload factor of 10%.

The danger of overheating the spacecraft exists before and during the launch, because of the high heat rejection of the RTG's. While operating 15,000 watts of heat must be handled by the proposed forced-air cooling system provided on the pad. During the assent phase the heat capacity of the RTG's is considered sufficient to prevent an excessive temperature rise in the spacecraft.

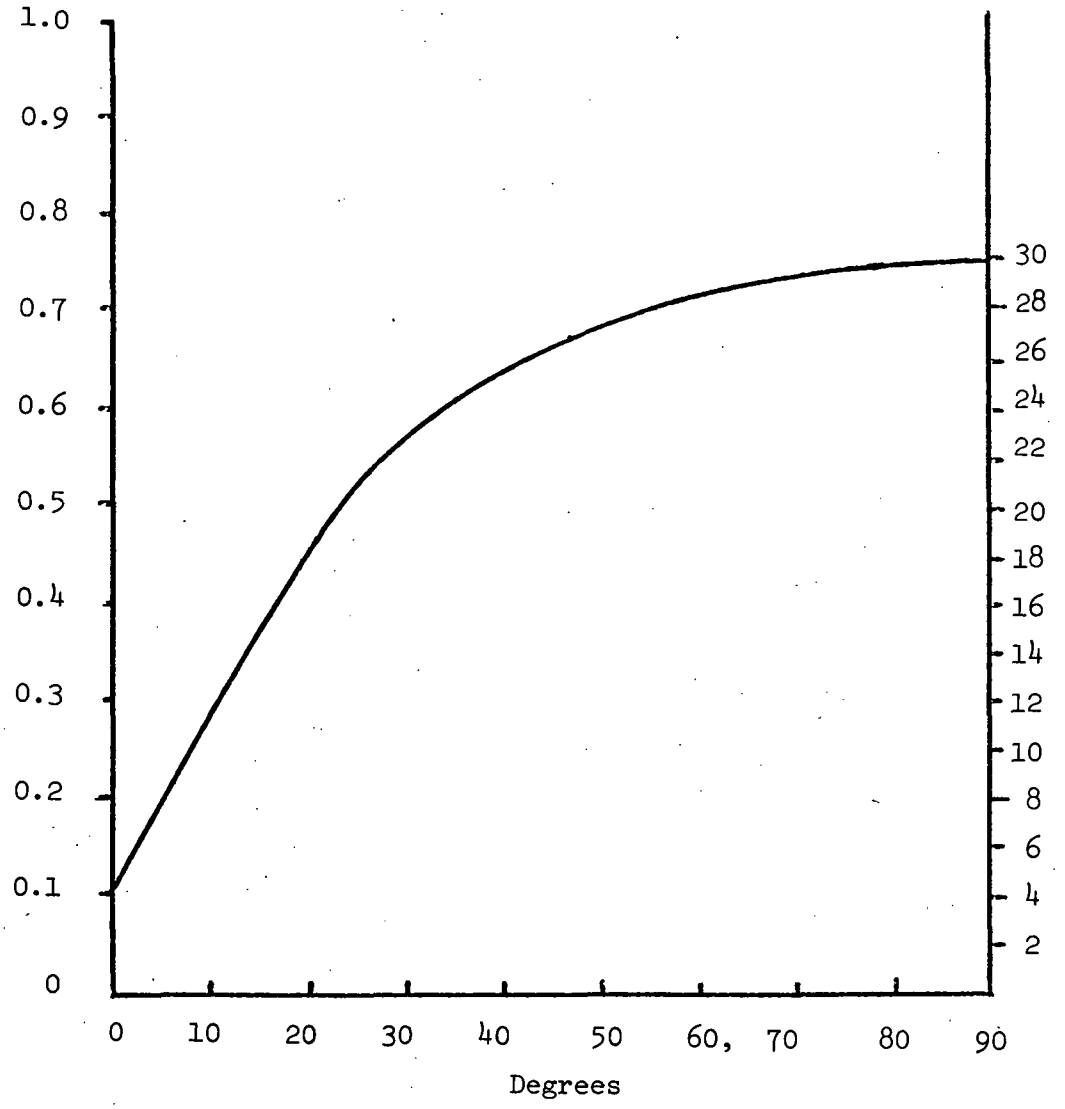

Figure IX-17. Variation in Emittance as a Function of Louver Angle.

5. Dynamic Considerations

From a space dynamics viewpoint, the JOSE design reflects a somewhat conservative approach based on the emphasis on overall reliability. As a result the dynamical feasibility of the mission is not really in question. However, detailed analytical work will be required to design and size the spacecraft components.

Areas of investigation should include the following:

a) Ascent. Response of the folded spacecraft to the shock, vibration and acceleration environment imposed by the launch vehicle. Suggested design values of axial acceleration and cross axial acceleration for a Saturn 1 B are 6 g and 1 g respectively [IX-10].

b) Separation. Tip-off torques and resulting disturbances.

c) Spinup and RTG Boom Deployment. The torque levels employed in imparting spin to the spacecraft for the purpose of deploying the RTG's. The study of the motion, dynamic loads, and energy dissipation will determine the need for shock absorbers and/or damping mechanism.

d) Trajectory Thrusting, Deboost, and Orbital Trim. Response of the deployed spacecraft to the shock, vibration and acceleration accompanying thrust motor operation. A deceleration of 1 g at deboost is proposed.

e) Other Disturbances. In addition to the various disturbances mentioned above, consideration must be given to the more subtle effects of:

   i) Solar pressure forces

   ii) Meteoroid collisions (non-fatal)

   iii) Interaction with the Jovian magnetic field.

The most interesting questions of spacecraft dynamics arise in the area of flexible body attitude control, especially the behavior of the system near a null point.

No major analyses were made in this study to establish mission feasibility. However, the areas mentioned above offer important areas for further study.

6. Spacecraft Structure and Weights

To fulfill the spacecraft requirements described in previous sections, the following structural arrangement has evolved. The main equipment bus is an octagon with its axis coincident with the spacecraft Z axis, designed to contain the propulsion system tanks and electronic equipment. Two flat antennas are mounted side by side on the "sunny" end of the main bus and an annular array of thermal louvers centered around the propulsion motors are mounted on the opposite end. The trajectory propulsion tanks are located in the center of the bus to prevent imbalance due to propellant consumption, and to be protected from meteoroids.

Two RTG's and the scan platform are arranged in a planar manner, the plane being perpendicular to the spacecraft Z axis and coincident with the center of gravity of the main bus. The length of the RTG booms were designed to maintain the required separation for radiation protection and to keep the spacecraft CG coincident with the Z axis. The RTG's are canted toward the radiation-sensitive instruments in the scan platform and on the boom to minimize the radiation coupling. The magnetic field-sensitive experiments are mounted on an extendable body to minimize background fields at the sensors.

Scientific experiments are located in either the scan platform, if they require articulation or scan abilities, or the main bus with unobstructed view angles out of the sides of the spacecraft. Attitude thrusters having roll,

pitch and yaw capabilities are mounted on the circumference of the octagon in a plane perpendicular to the Z axis and passing through the deployed spacecraft CG.

Figures IX-20 through IX-23 show the deployed spacecraft and configuration and basic component positions. Figures IX-18 and IX-19 show the spacecraft mounted within the launch vehicle payload envelope.

The base of the spacecraft, which is designed to fit the Saturn 1 B support ring, consists of an aluminum ring attached to a central structural tube. The tube acts as a compression and torsion member, and provides support for the propulsion tank configuration. Eight ribs attached to the central tube radiate out towards the corners of the octagon providing support for the equipment bays. This skeleton provides the frame to which all other parts of the spacecraft body are attached.

Tables IX-8 and IX-9 give the estimated weight distribution of the spacecraft. These weights were determined by either preliminary calculations of individual subsystems or appropriate scaling of actual systems on other spacecraft designs.

The inertias for the spacecraft are as follows:

	I_x	I_y	I_z	(slug-ft^2)
Interplanetary Configuration	1,935	1,283	2,760	
Orbital Configuration (Ionosonne Deployed)	3,280	1,283	4,105	

7. Scan Platform

The purpose of the scan platform is to allow the necessary scientific instruments to scan all Jupiter's surface at any time. Two degrees of freedom of motion are required for complete scanning, with 360° degrees of motion around an axis perpendicular to the orbit plane and 66° degrees above and below the orbit plane for a pole to pole scan at 1.1 R_J.

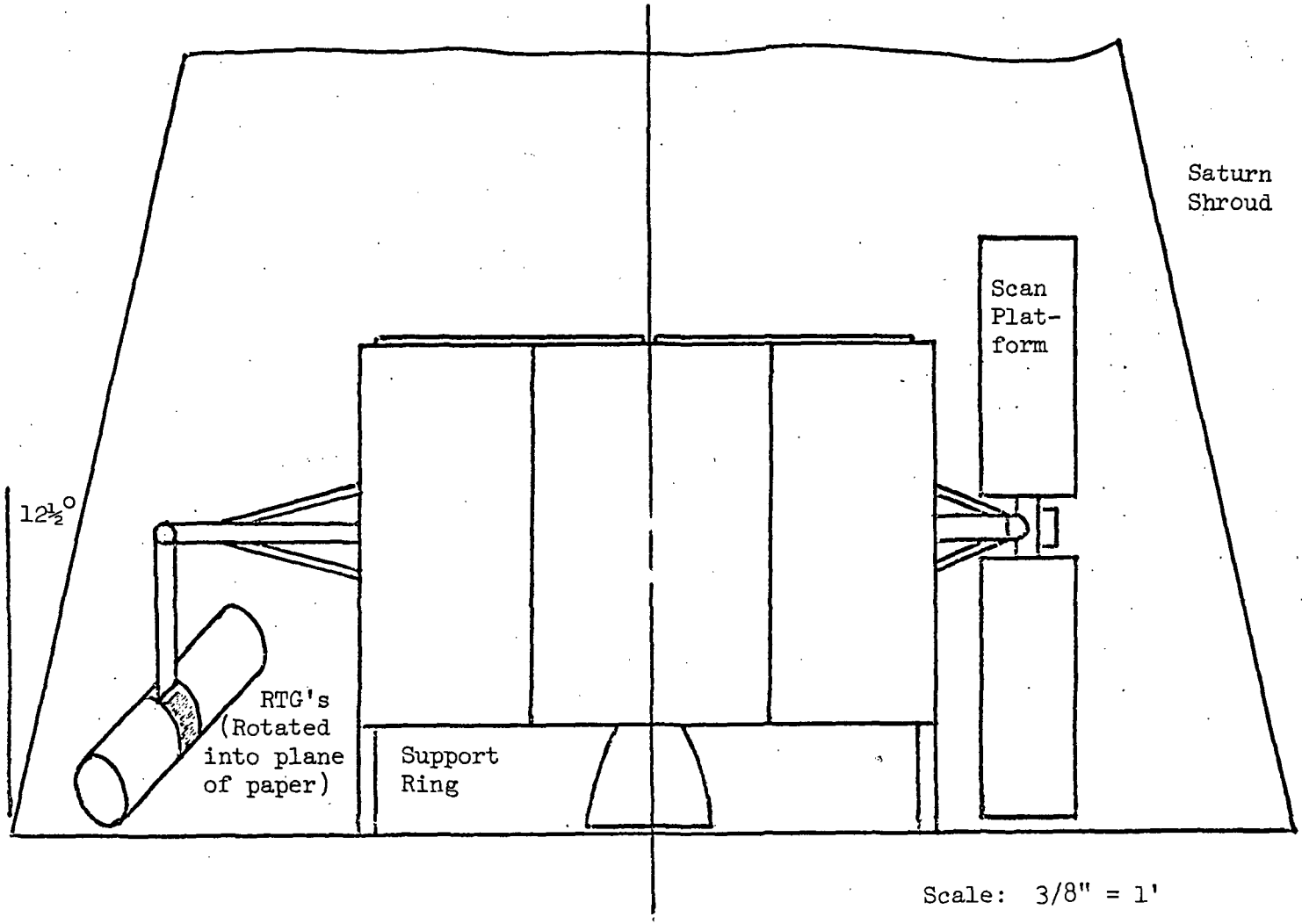

Figure IX-18. JOSE Spacecraft Launch Configurations (Side View)

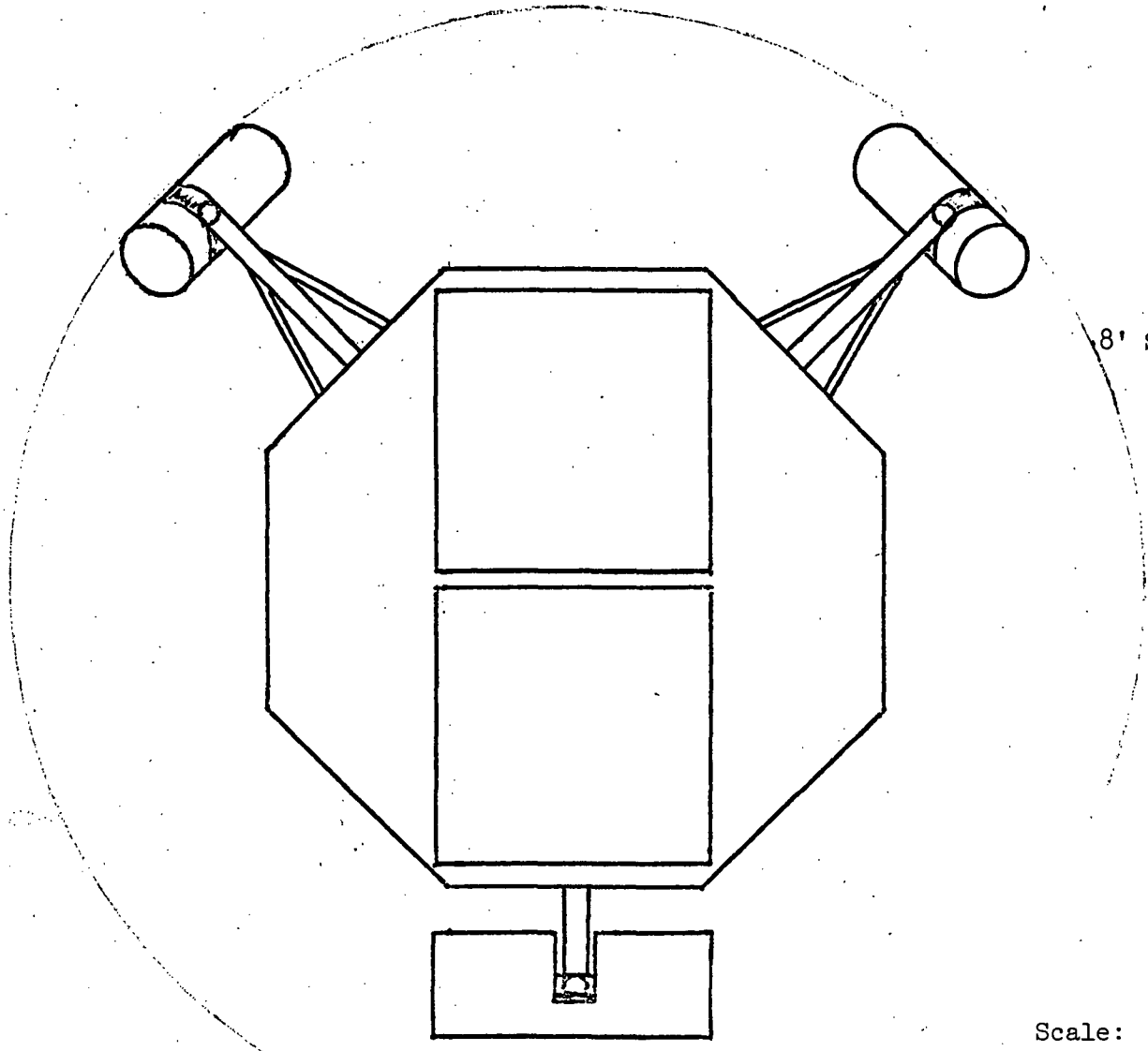

8' Shroud Diameter

Scale: 3/8" = 1'

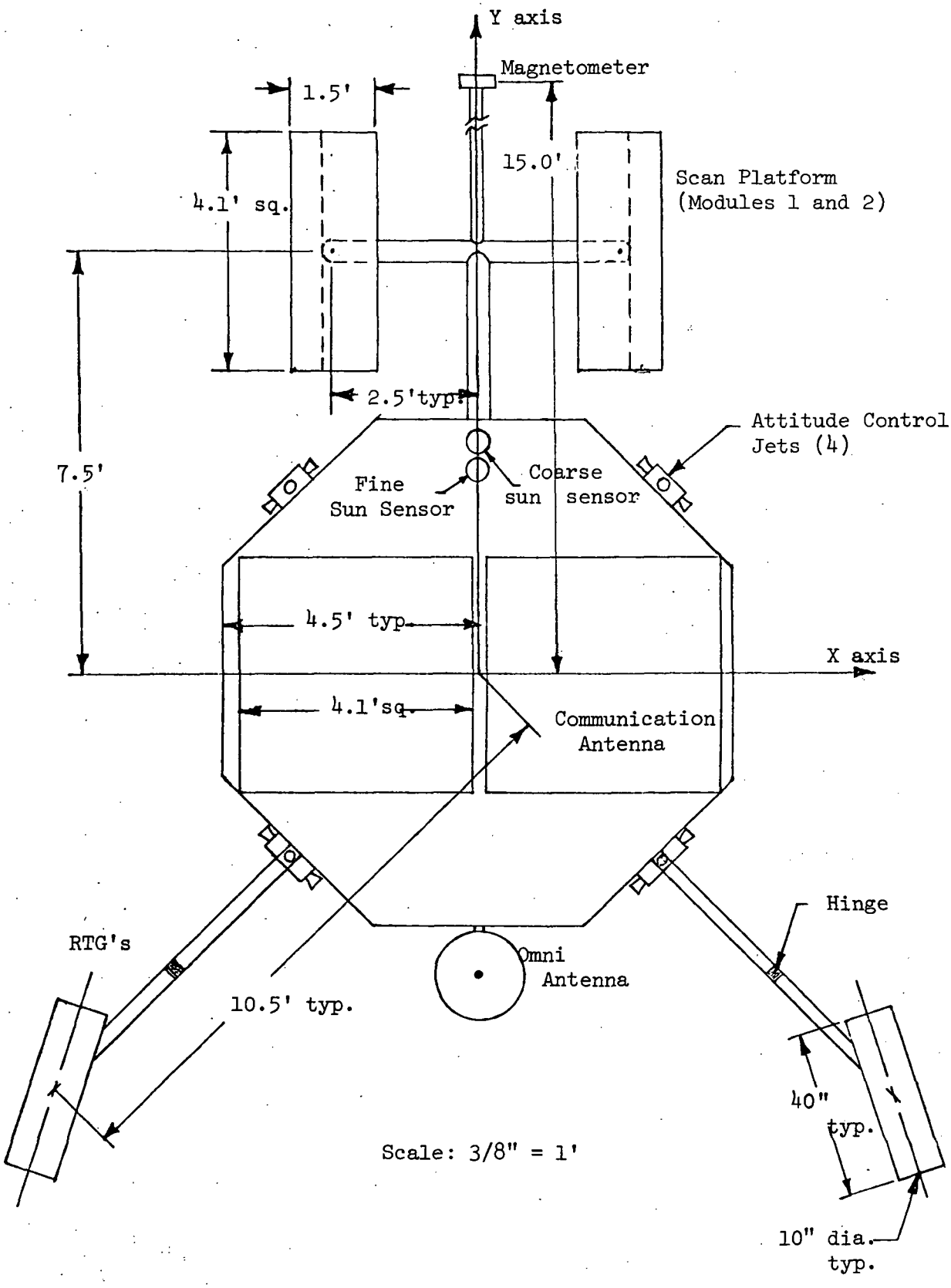

Figure IX-20. JOSE Spacecraft Flight Configuration (Top View)

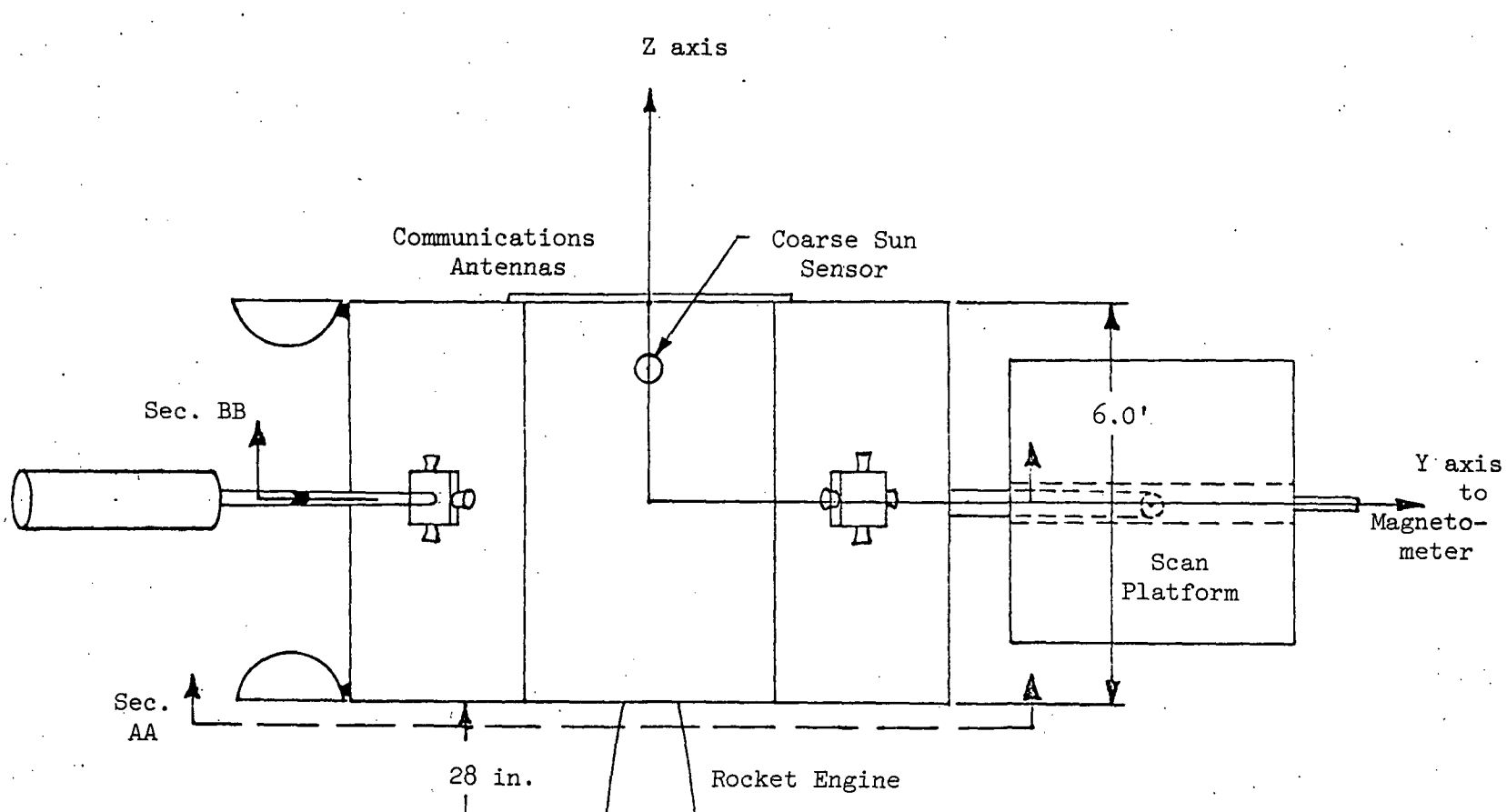

Figure IX-21. JOSE Spacecraft Flight Configuration (Side View)

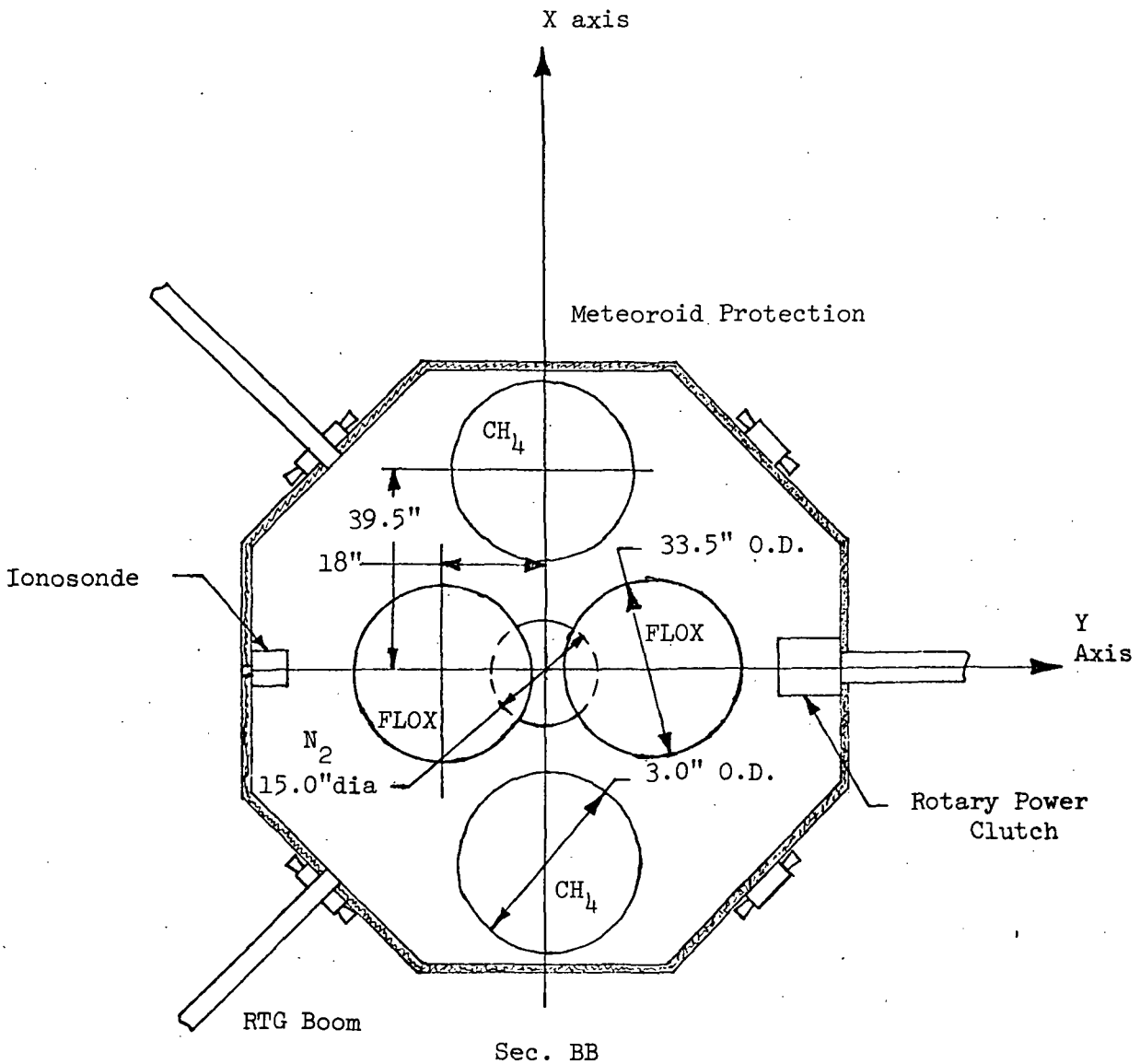

Figure IX-22. JOSE Spacecraft Flight Configuration (Sec. BB)

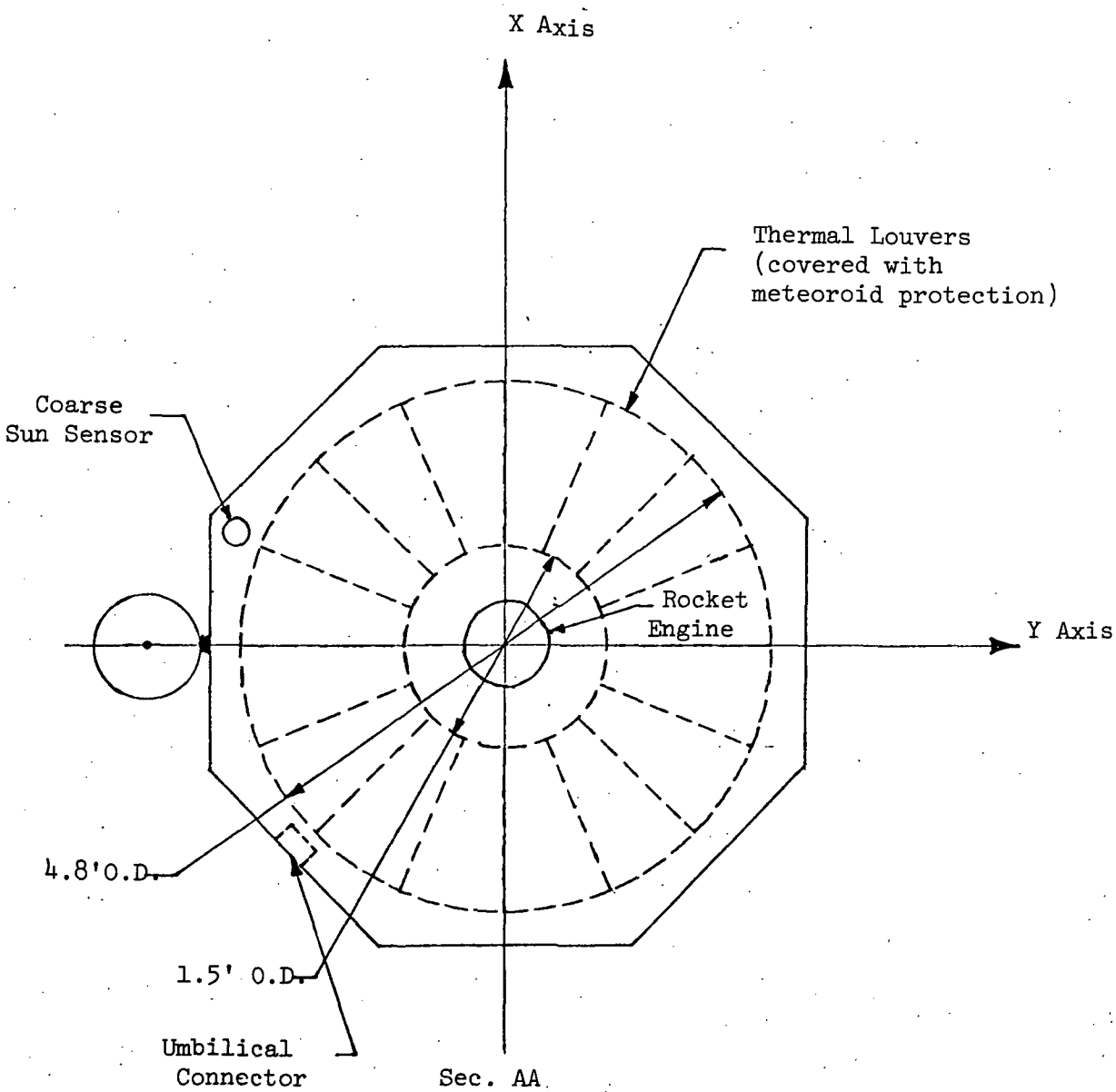

Figure IX-23. JOSE Spacecraft Flight Configuration (Sec. AA)

Table IX-8

Spacecraft Weight Distribution

Power	
RTG's (2) including Shielding	350 lbs.
Booms (2)	40
Other	15
Main Propulsion	
Propellant	2174
Motor	45
All other (see Chapter V)	502
Structure	200
Meteoroid and Radiation Protection	175
Thermal Protection (Active and Passive)	75
Scan Platform (see Table IX-9)	350
Support	10
Communications	
Data Handling	95
High Gain Antennas	15
Omni-Antennas (2)	6
Other	20
Integration	
Command Distribution	10
Umbilical Connector	5
Pyro-Technic Box	10
Cabling and Connectors	100
Attitude Control	
Control Box	32
Canopus Tracker	1
Coarse Sun Sensors (4)	4
Fine Sun Sensor	1
N_2 and Tank	60
Control Jets	8
Star and Moon Trackers	40
Miscellaneous Valves, Lines, Etc.	26
Science other than in Scan Platform	
Helium Magnetometer	1
Magnetometer Boom	10
Ionosonde	14
Total Spacecraft Weight	4,394 lbs.

Table IX-9

Scan Platform Components and Weights

Scan Module 1

Radar Antenna	1.0 lbs
T.V. Camera	30.0
Ultraviolet Photometer	3.0
Infrared Radiometer	6.0
Visual and UV Spectrometer	20.0
Visual Photometer	6.0
Auroral Photometers (3)	15.0
Microwave Radiometer	30.0
Infrared Interferometer	30.0
Horizon Sensor	2.0
Electrostatic Analyser	4.8
VLF Receiver	3.0
Structure	12.5
Thermal and Meteoroid Protection	12.5
Total	175.8 lbs.

Scan Module 2

Radar Traveling Wave Tube	15.0
Radar Power Supply	75.0
Helium Magnetometer Electronics	3.2
Hall Effect Magnetometer	1.0
Plasma Wave Detector and Electronics	6.0
Radiation Detector	3.2
Micrometeoroid Detectors (2)	26.1
Plasma Probe and Electronics	7.0
Radio Emission Detector	6.0
X-ray and γ-ray Detector	7.0
Structure	12.5
Thermal and Meteoroid Protection	12.5
Total	174.5 lbs

The physical dimensions of the platform are defined by the dimensions of the included experiments: the high resolution T.V. is 1.4 ft long and the area of the square radar antenna is 17.2 ft^2 (4.14 ft on a side).

To accomplish the necessary 66° depression requirement the scan platform must be cantilever from the rotational mast to view past the spacecraft bus. For this reason the scan platform was divided into two distinct modules, arranged to counterbalance one another such that the entire system is pivoted about its CG. To rotate the platform about a point other than the CG would cause long term secular perturbations of the spacecraft due to the rotating imbalance force.

Each separate module is supported at its own CG, a cantilever distance of 2.5 ft from the rotor mast. The rotor mast is 3.0 ft long and is terminated by the mechanism required to deploy a stem type magnetometer boom 7.5 ft.

The rotary position of the platform relative to the planet is sensed by the horizon scanner and any commanded angular positions for viewing particular features are automatically maintained. The drive mechanism is a stepping motor capable of $.10^\circ$ steps. For the maximum angular rate of change of 2°/min of time this motor would require steps every 3 sec.

The depression angle of the modules is controlled in the same manner, both modules being coupled to depress simultaneously to avoid any unnecessary reaction forces on the spacecraft bus.

An important area for concern is the rotary coupling at the base of the scan platform mast. This coupling must transfer to the mast all of the necessary forces and torques during all spacecraft maneuvers, 175 watts of peak power for the radar and return to the spacecraft bus all data collected by the instruments.

In the past, electrical power transferred to rotating appendages has passed through a flexible umbilical cable that requires recycling each

orbit by counter-rotation of the mast. For our application this is totally unsatisfactory due to consumption of excess attitude control fuel.

Several solutions to the problem have been proposed: slipring and brush assembly, liquid brushes, rotary transformers and a power clutch. The second and third are currently being investigated but are not present technology, and the first is subject to wear, friction and radio noise.

Boeing has proposed a power clutch that consists of a spring loaded axial stack of rotor and stator elements. During power conduction the elements stay in constant contact for one entire rotation. To recycle, an axial plunger is actuated which unloads the stack and only the rotor elements are forced to counter-rotate by a clock spring [IX-11].

The passive stability of this spacecraft configuration needs to be investigated. It is known that the improper location of energy dissipation devices in a dual spin spacecraft can cause unstable motion [IX-13, IX-14]. Inherent instability would not be fatal because the attitude control system could keep the spacecraft under control but is undesirable because of fuel consumption. A TRW report by M.P. Scher has demonstrated that the non-infinite compliance of the bearing assembly can cause instability [IX-12]. Because of the slow rotation speeds of the scan platform, the threshold of instability is $K < 10^{-6}$ ft-lb/rad. Thus no problems are apparent.

The specific locations of each experiment in the modules has not been defined in this study. However, they have been separated into the two modules according to the need to be scanned. All scanning equipment has been located in module 1, the other equipment located in module 2 for counterbalance.

References, Chapter IX (Environment)

IX-1. Advanced Planetary Probe, Jupiter Fly-By Application, EPD-358, Jet Propulsion Laborabory, California Institute of Technology, Pasadena, California, August 1966.

IX-2. Corliss, W.R. and Harvey, D.G., Radioisotope Power Generation, Prentice Hall, Inc., New Jersey, 1964.

IX-3. Pedersen, E.S., Nuclear Energy in Space, Prentice Hall, Inc., New Jersey, 1964.

IX-4. Survey of a Jovian Mission, Report No. M-1, Astro Sciences Center of Illinois Institute of Technology, Research Institute, Chicago, Illinois, March, 1964.

IX-5. Personnal Communications and Correspondence, Dr. K. Campe, Hittman Assoc., Inc., Columbia, Maryland, May, 1970.

IX-6. Haffner, J.W., Radiation and Shielding in Space, Academic Press, New York, 1967.

IX-7. The Planet Jupiter (1970), NASA Space Vehicle Design Criteria (Environment).

IX-8. Phase A Report Galactic Jupiter Probe, Volumes I and II, X-701-67-566, Goddard Space Flight Center, Greenbelt, Maryland, November 1967.

IX-9. A Study of Jupiter Fly-by Missions, FZM-4625, General Dynamics, Fort Worth Division, Texas, May 1966.

IX-10. Jupiter Orbiting Vehicle for Exploration, Auburn University, Volumes I and II, NASA CR-61180, August, 1967.

IX-11. H. Theron Haynie, "Rotary Relay for Space Power Transfer", Pre-print presented at 5th Aerospace Symposium, Goddard Space Flight Center, June 1970.

IX-12. M.P. Scher, TRW Systems Group, "Effects of Energy Dissipation in the Bear Assembly of Dual-Spin Spacecraft," Pre-print presented at 5th Aerospace Symposium, Goddard Space Flight Center, June 1970.

IX-13. Mingori, D.L., "Effects of Energy Dissipation on the Attitude Stability of Dual Spin Satellites", AIAA Journal, 7 (No. 1): 20-27, 1969.

IX-14. Pringle, R., "Stability of the Force-Free Motions of a Dual-Spin Spacecraft," AIAA Journal, 7 (No. 6): 1054-1063, 1969.

JOSÉ - JUPITER ORBITING SPACECRAFT:

A SYSTEMS STUDY

Volume II

Appendix A

1975-1985 Interplanteary Trajectory Parameters

Parameters:

C_3: Twice the injection energy for unit mass (km^2/sec^2)

ϕ_L: Declination of the launch asymptote (degrees)

ΔV: First mid-course velocity correction (meters/sec)

VHP: Hyperbolic excess speed at Jupiter (km/sec)

σ_1: Semi-major axis of the dispersion ellipsoid at Jupiter (km)

σ_2: Semi-minor axis of the dispersion ellipsoid at Jupiter (km)

θ: Orientation angle of the dispersion ellipsoid at Jupiter (degrees)

C.D.: Communication distance at Jupiter arrival (a.u.)

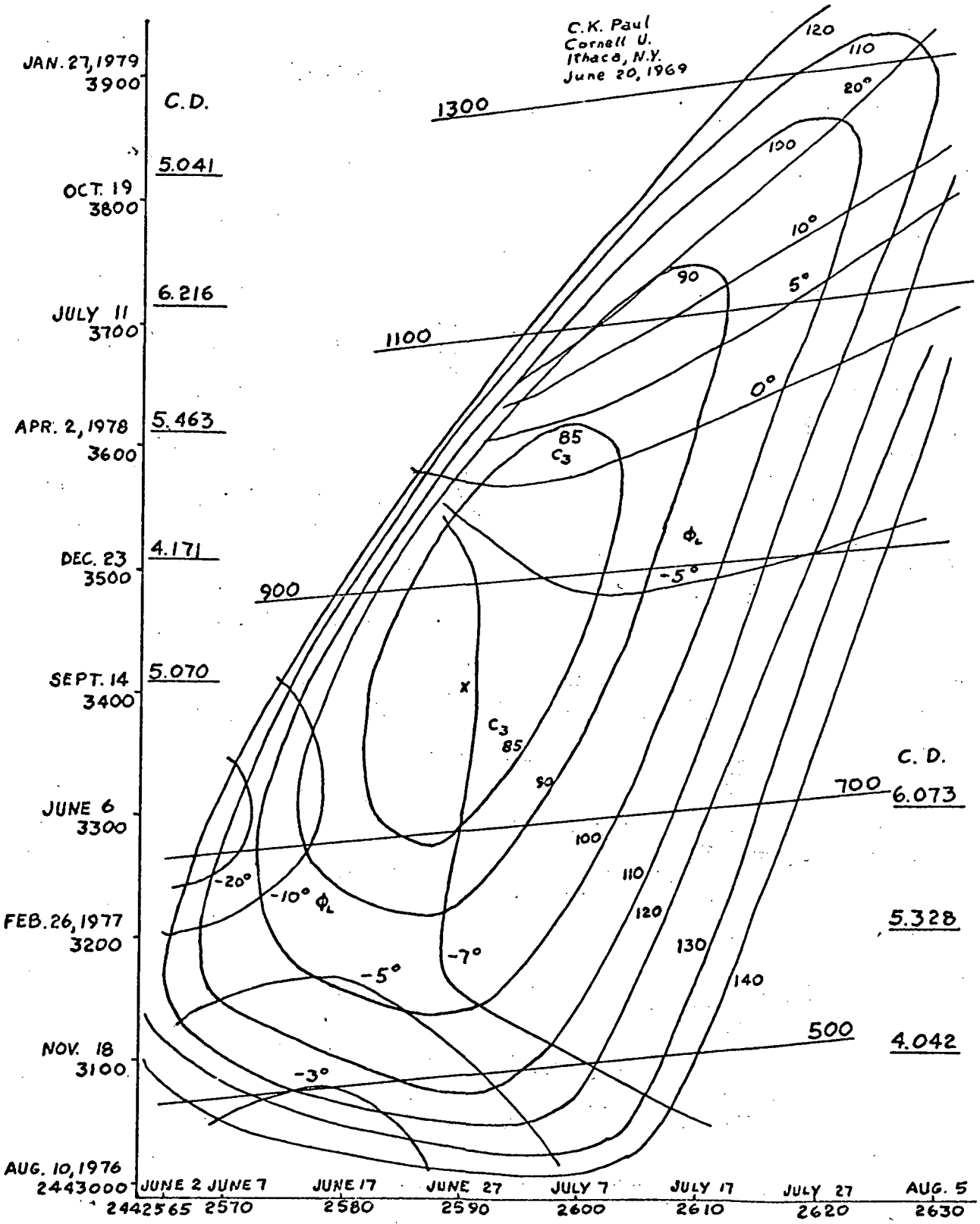

Launch Energy ($km.^2/sec.^2$) and Launch Declination Parameters

1975 C_3 & ϕ_L Parameters

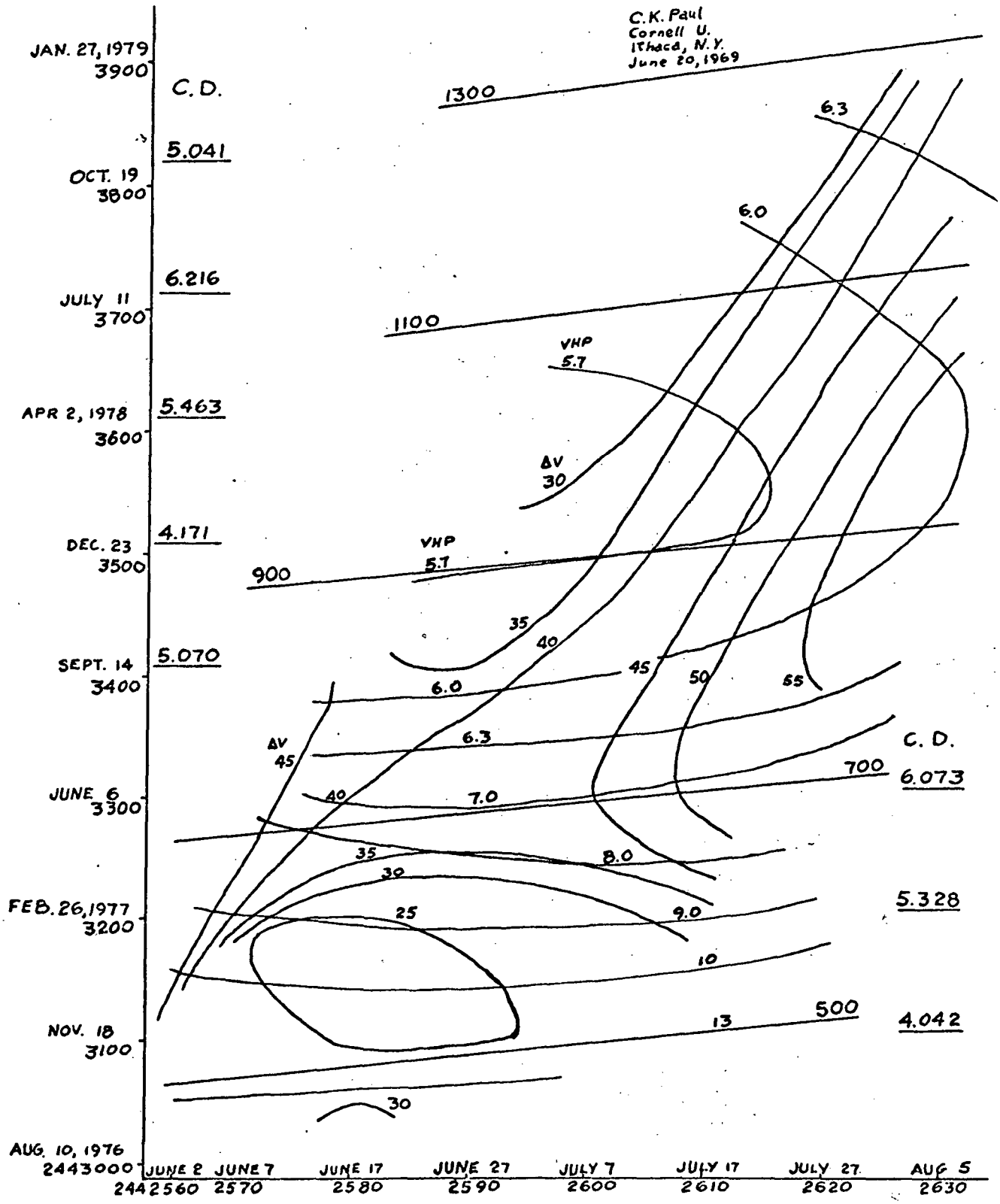

Mid-course Velocity Correction (m./sec.) and Jupiter Hyperbolic Speed

1975 ΔV and VHP Parameters

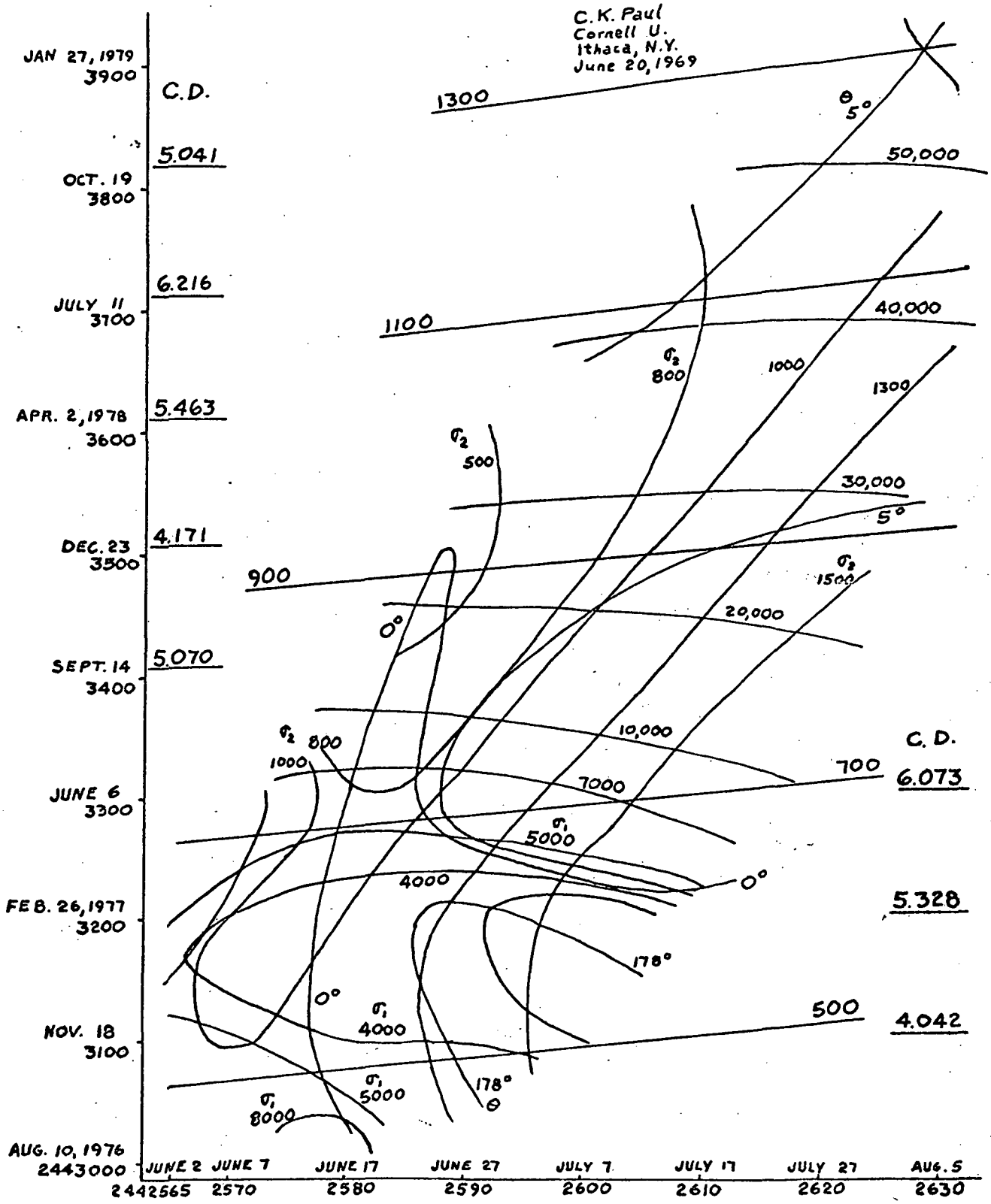

Semi-major and Minor Axes (km.) and Angle of Jupiter Miss Ellipse

1975 σ_1, σ_2 + θ Parameters

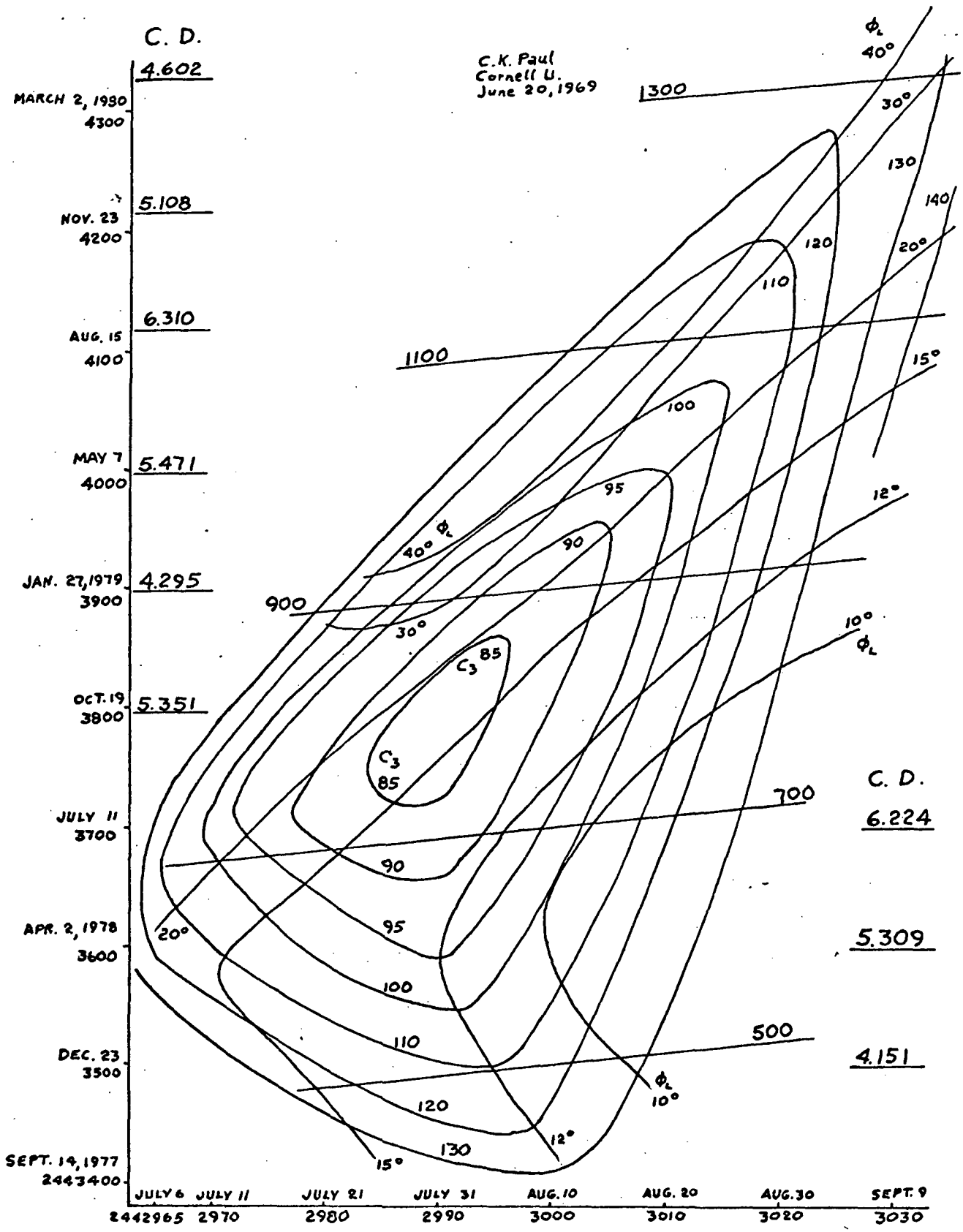

1976 C_3 + ϕ_L Parameters

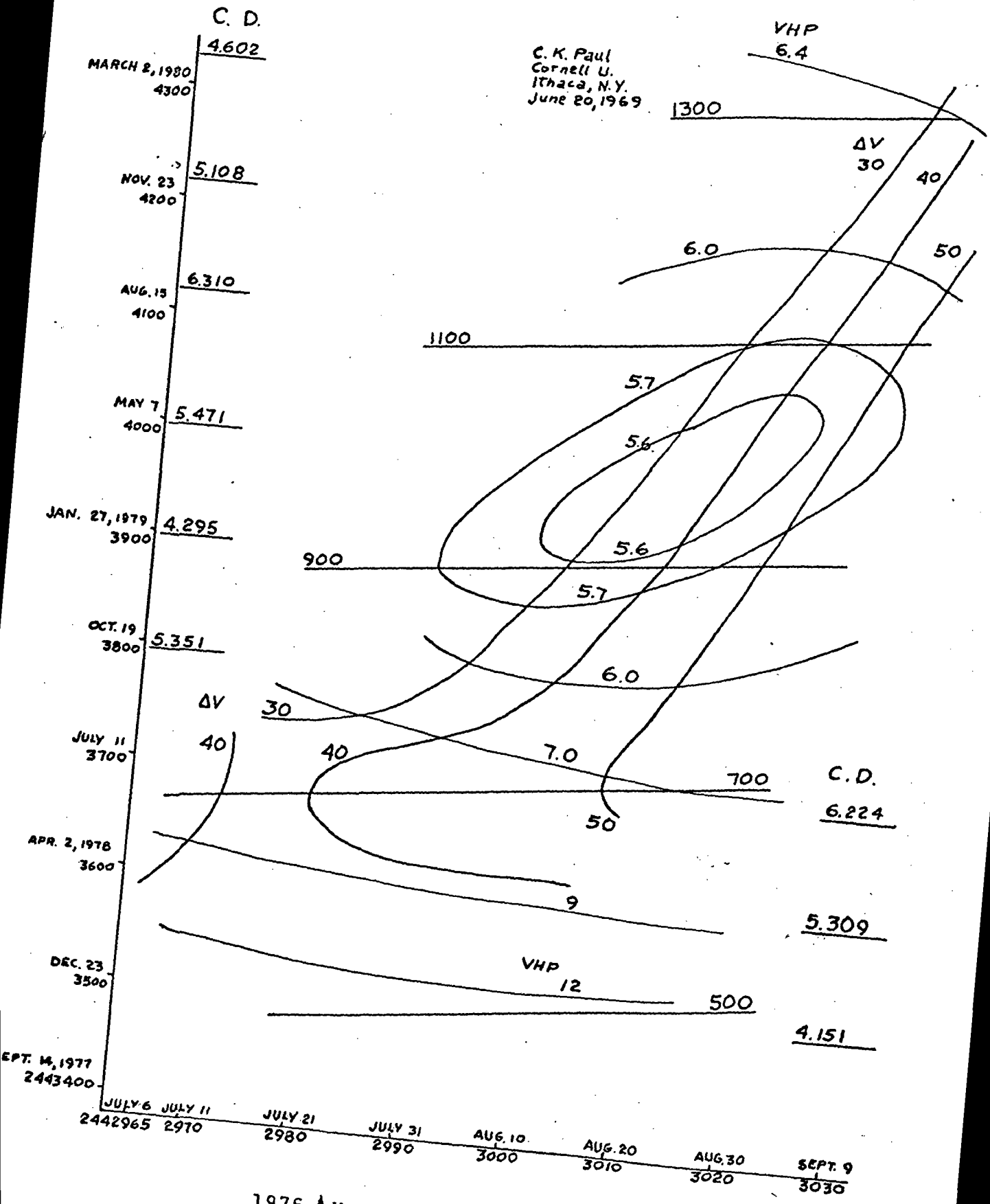

1976 ΔV + VHP Parameters

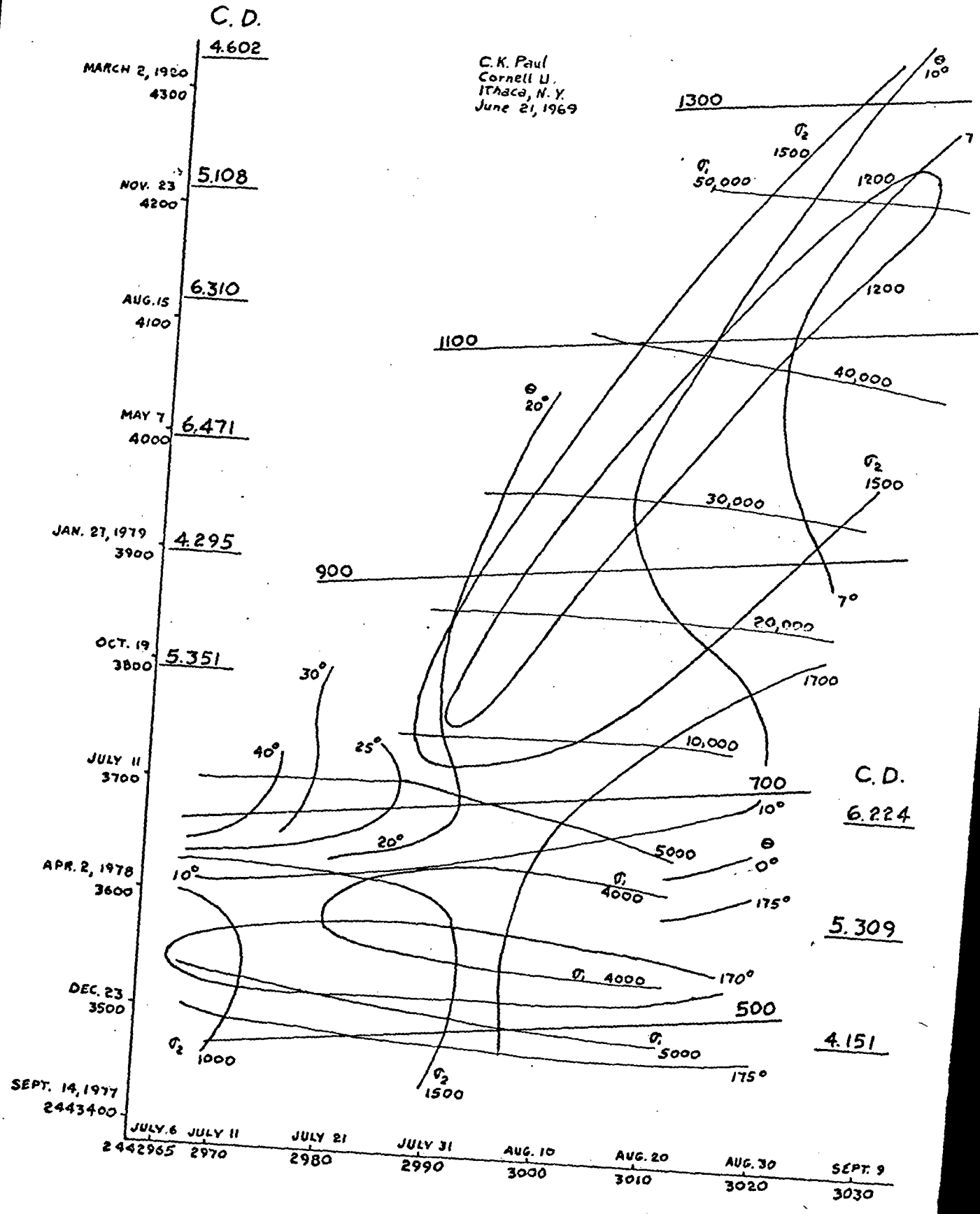

1976 σ_1, σ_2 + θ Parameters

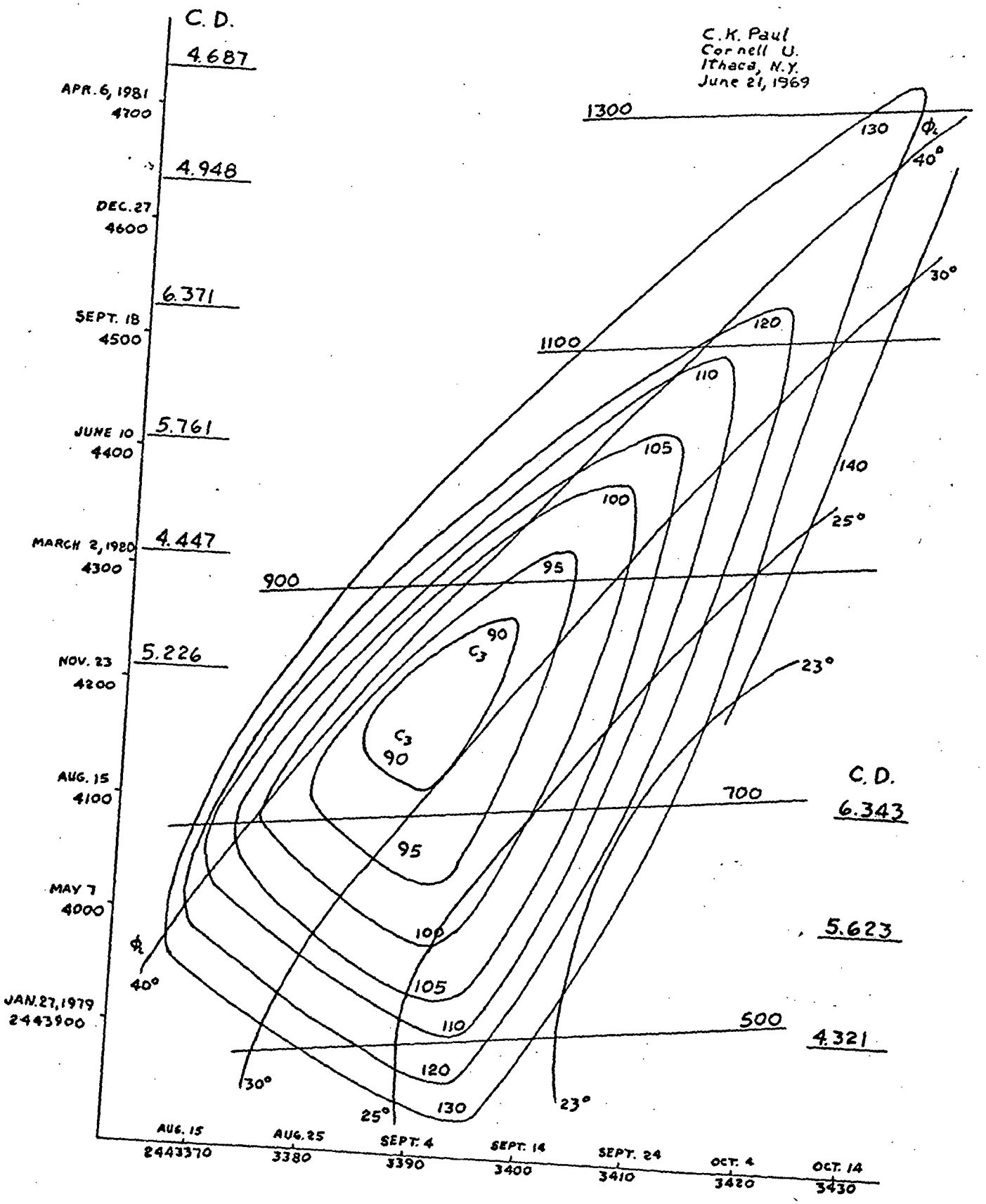

1977 C_3 + ϕ_L Parameters

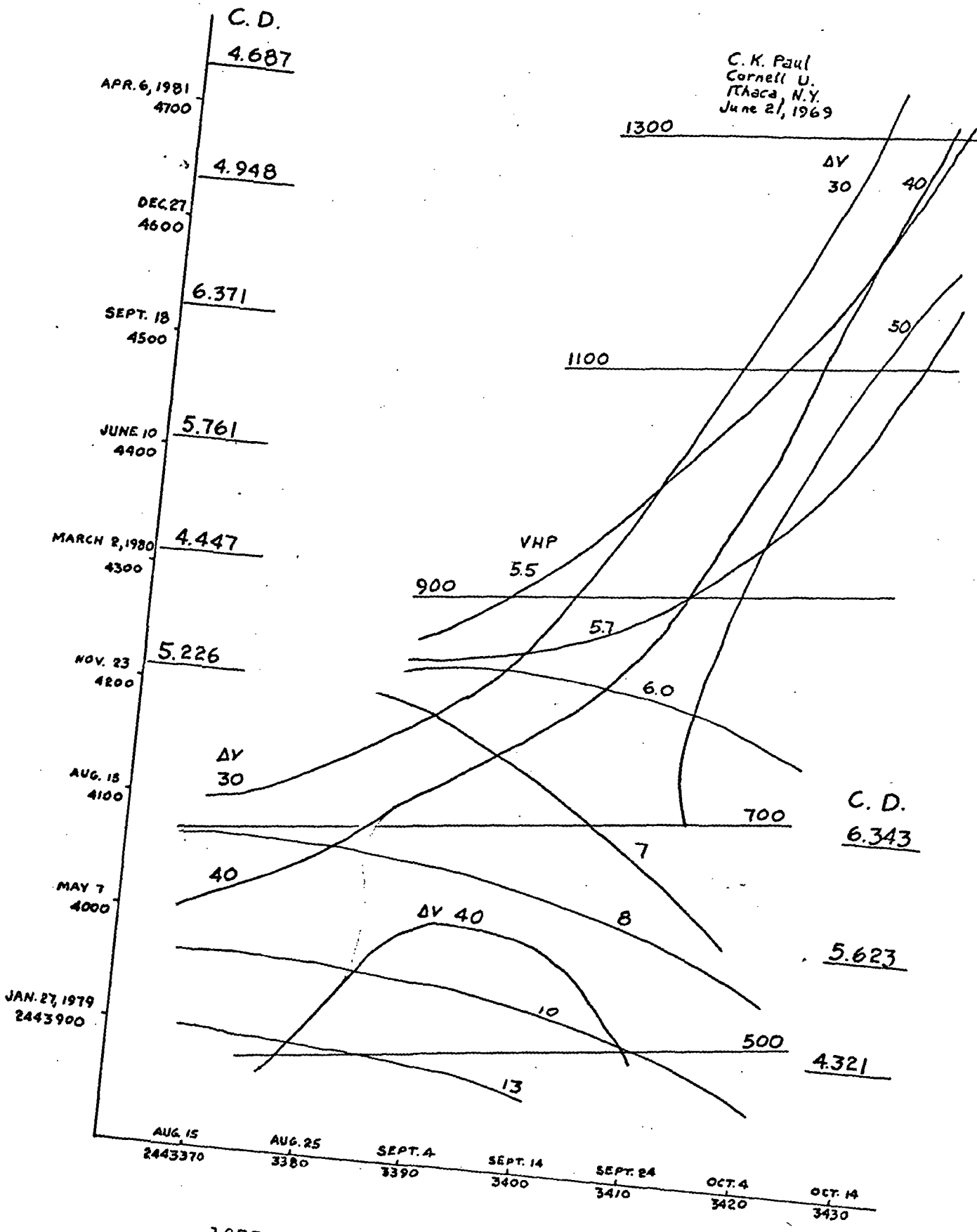

1977 ΔV + VHP Parameters

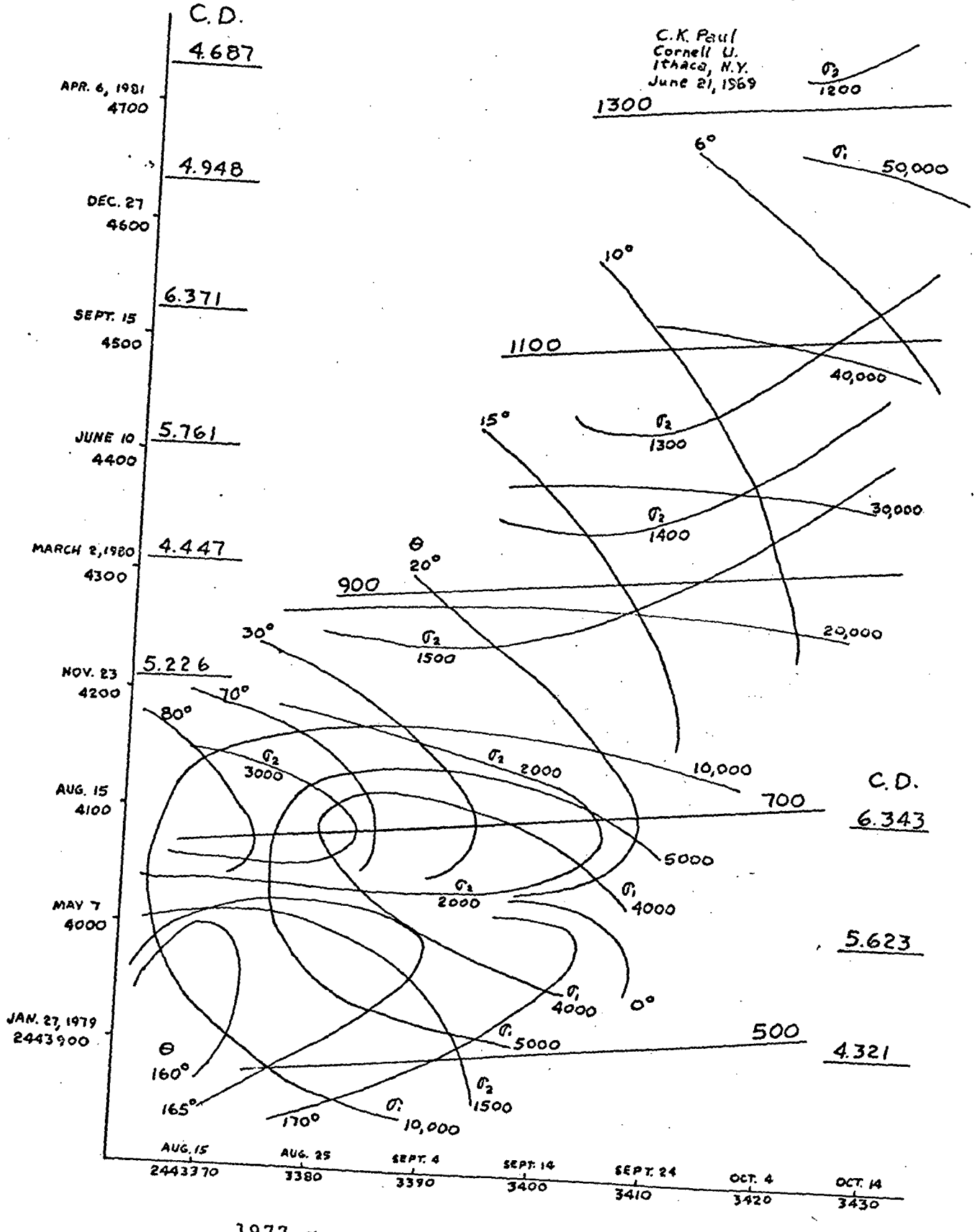

1977 σ_1, σ_2, + θ Parameters

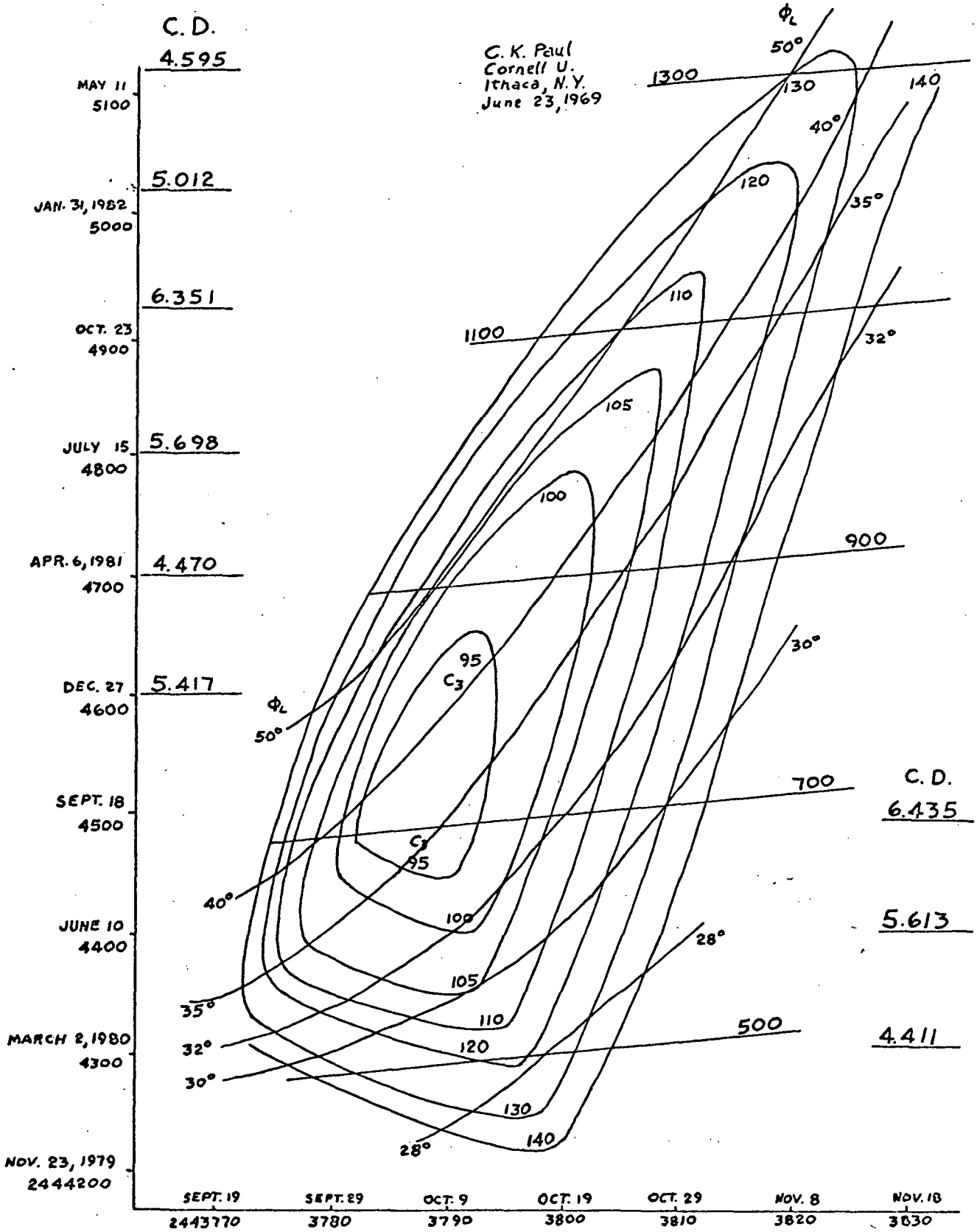

1978 C_3 + ϕ_L Parameters

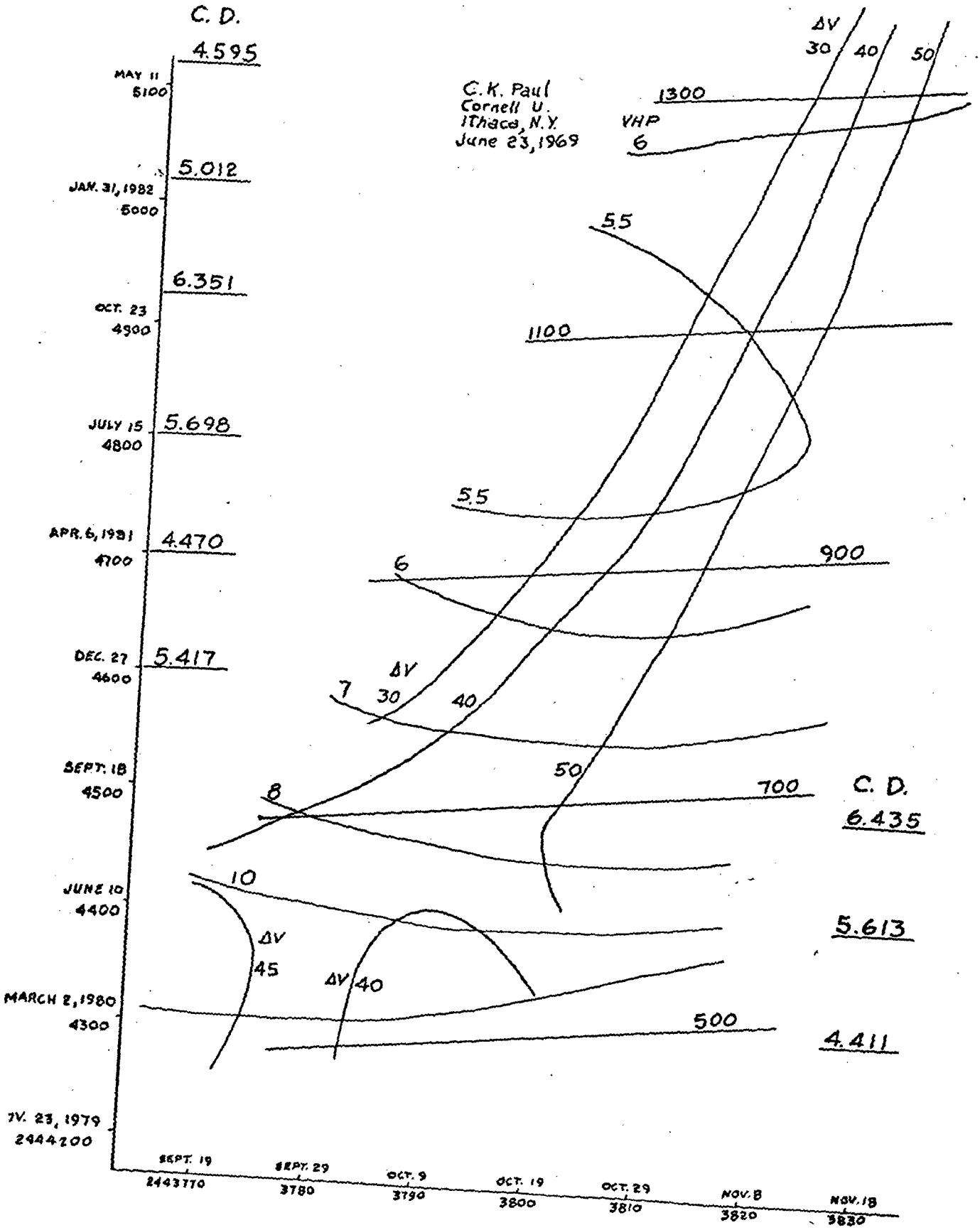

1978 ΔV + VHP Parameters

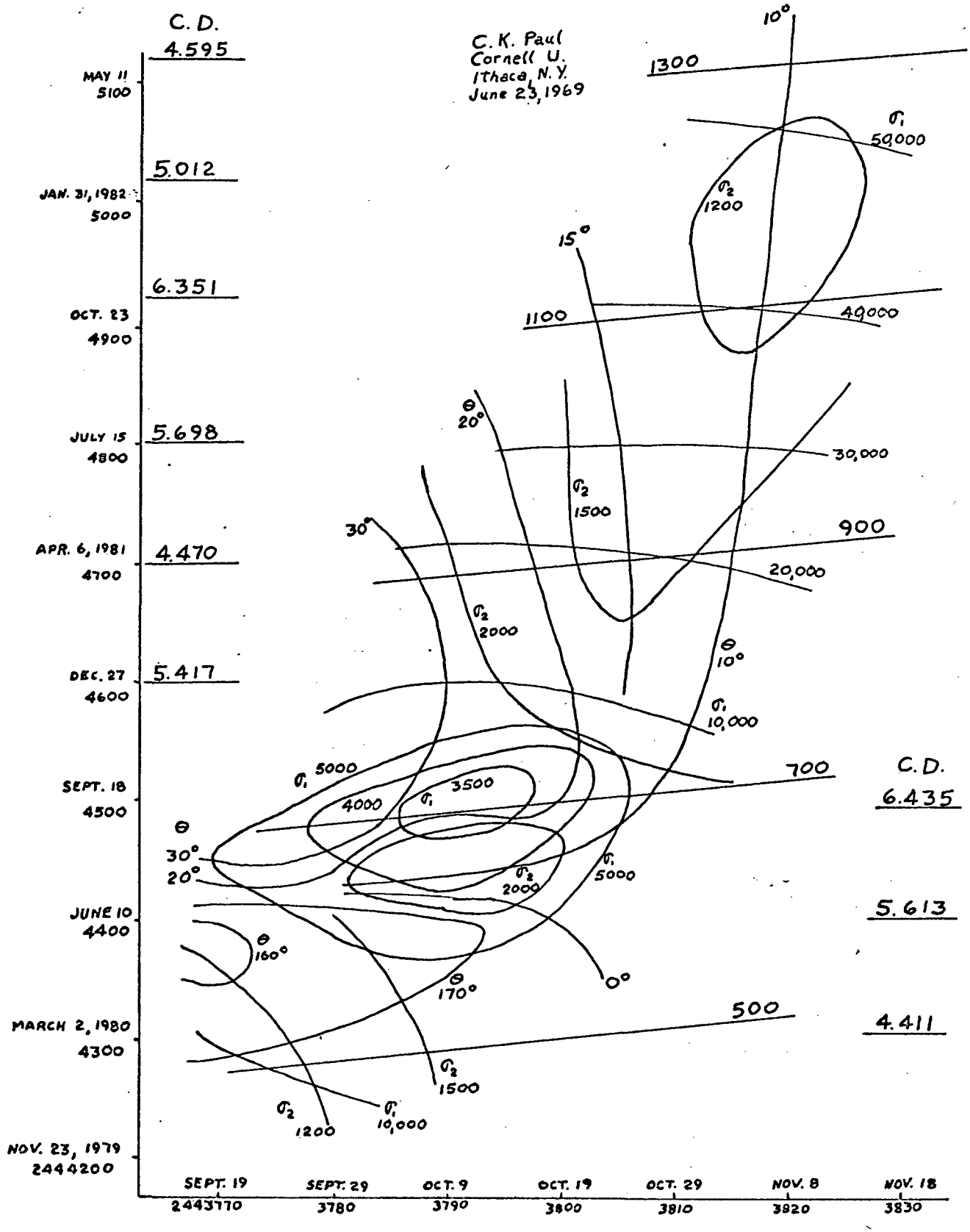

1978 σ_1, σ_2, + θ Parameters

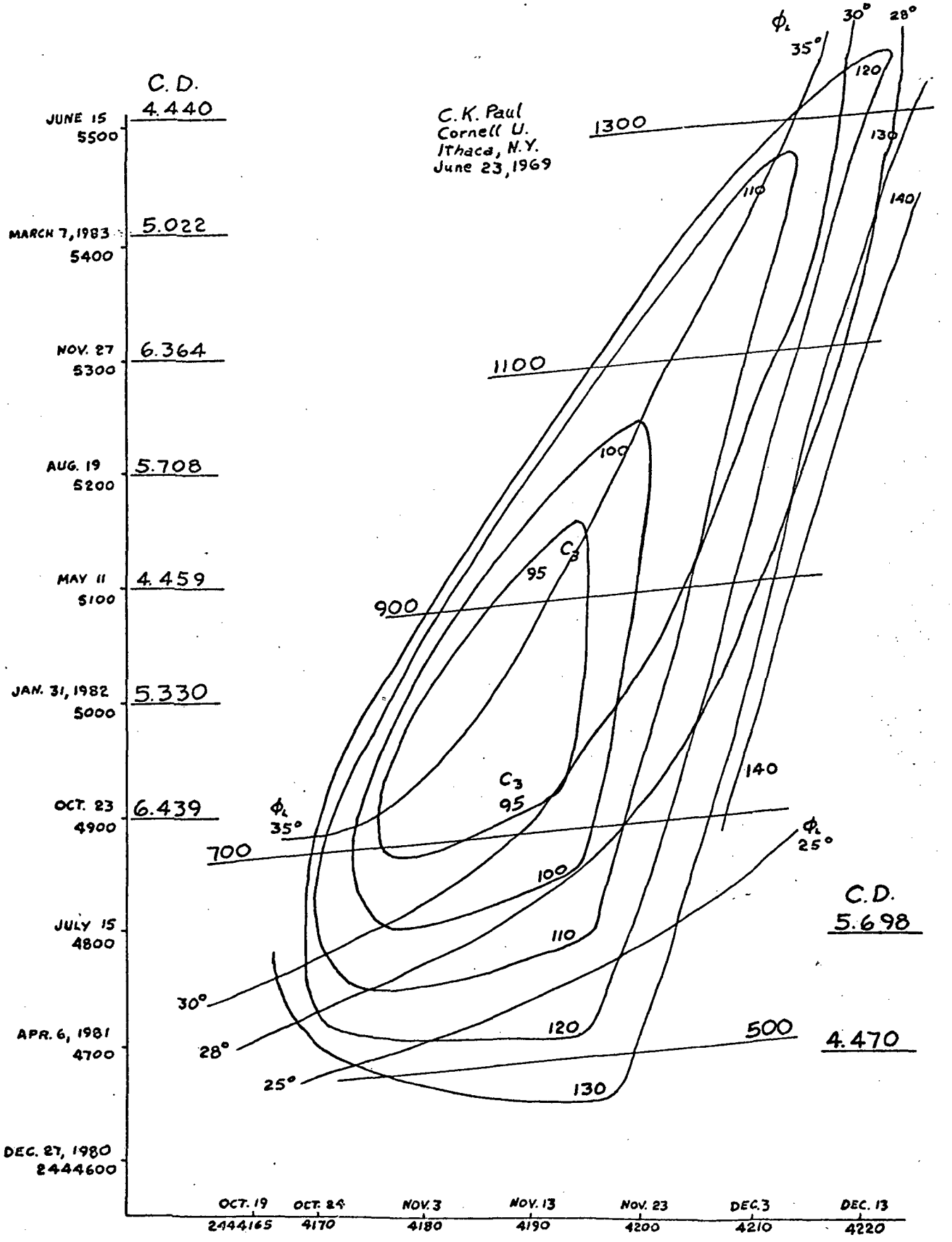

1979 C_3 + ϕ_L Parameters

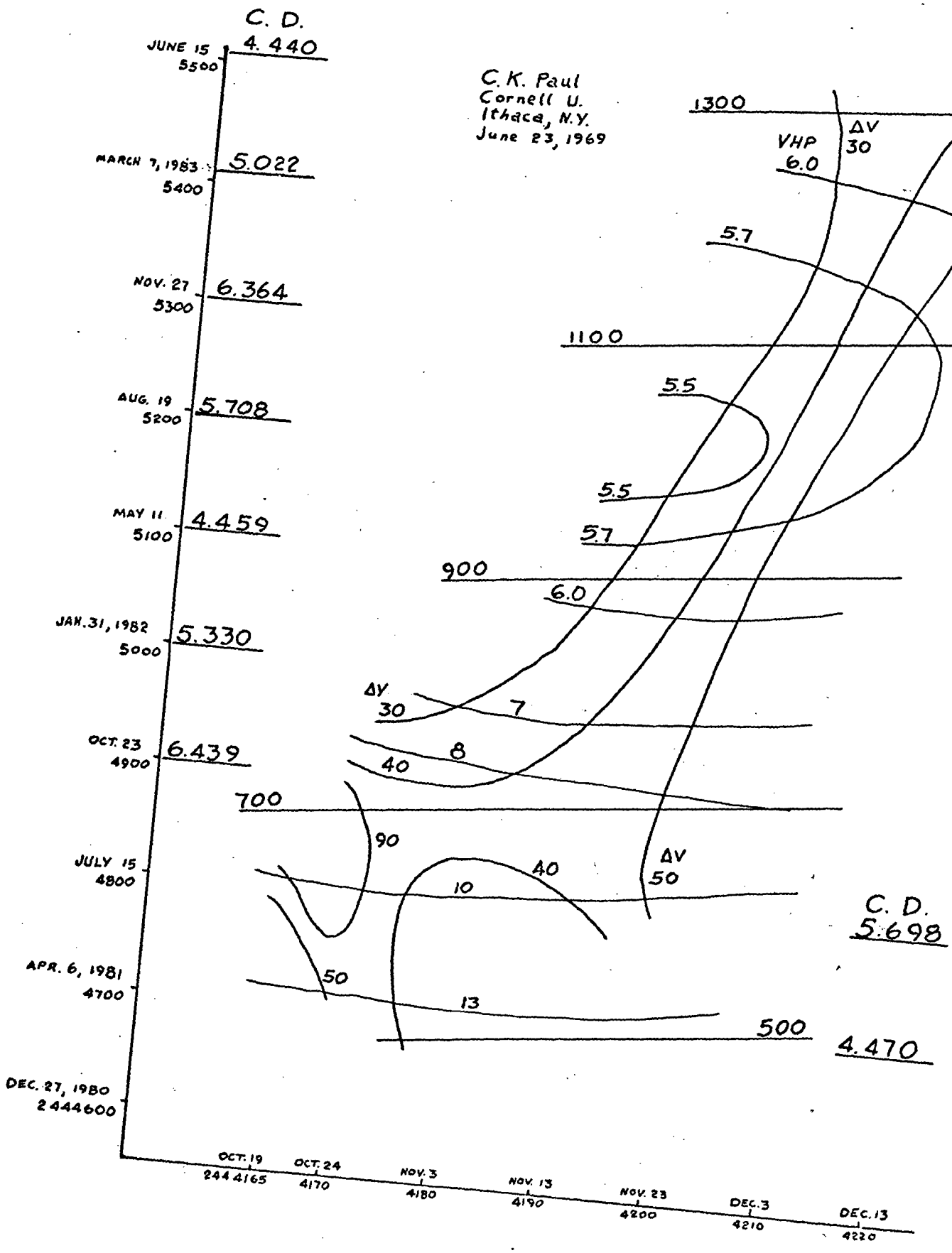

1979 ΔV + VHP Parameters

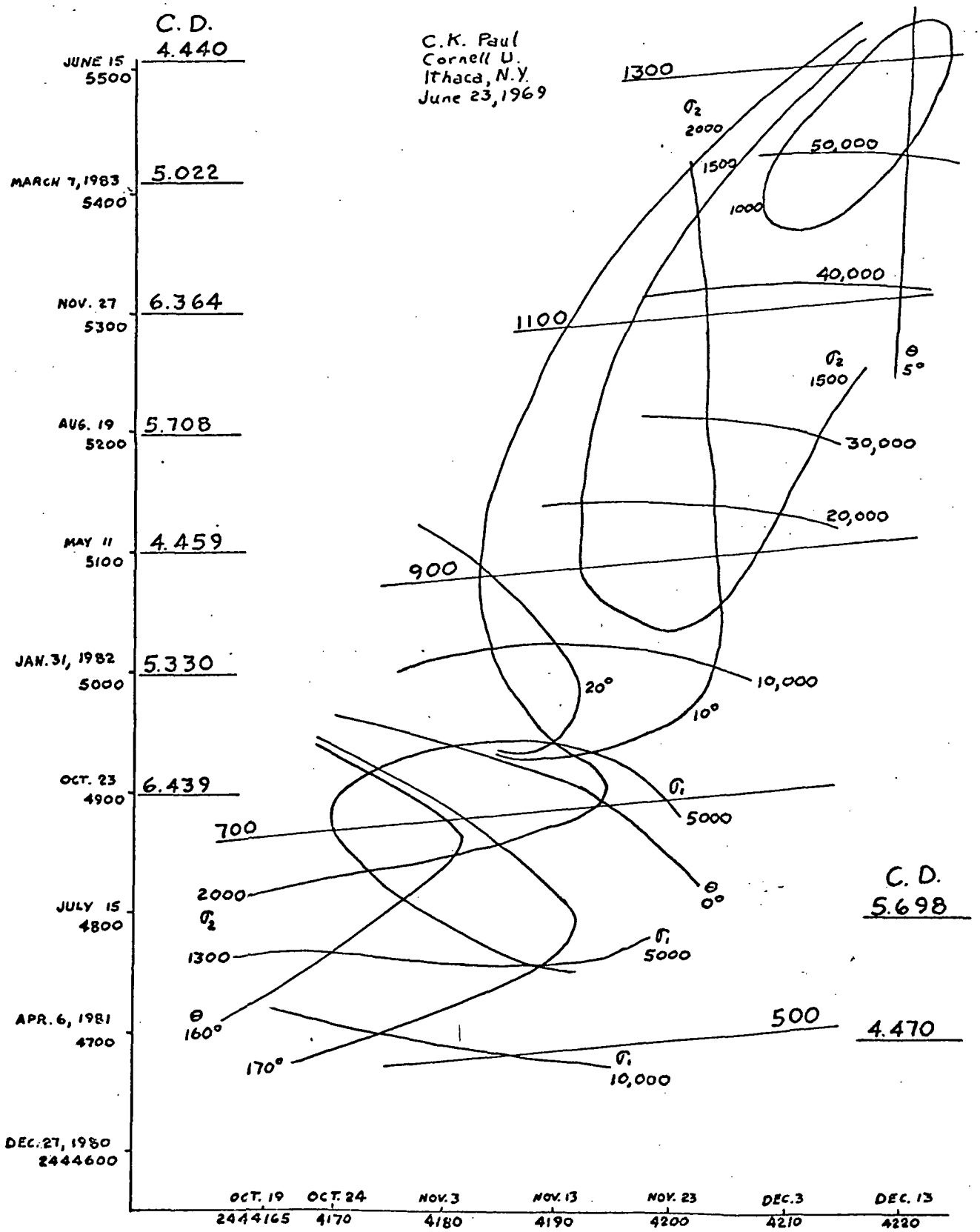

1979 σ_1, σ_2, + θ Parameters

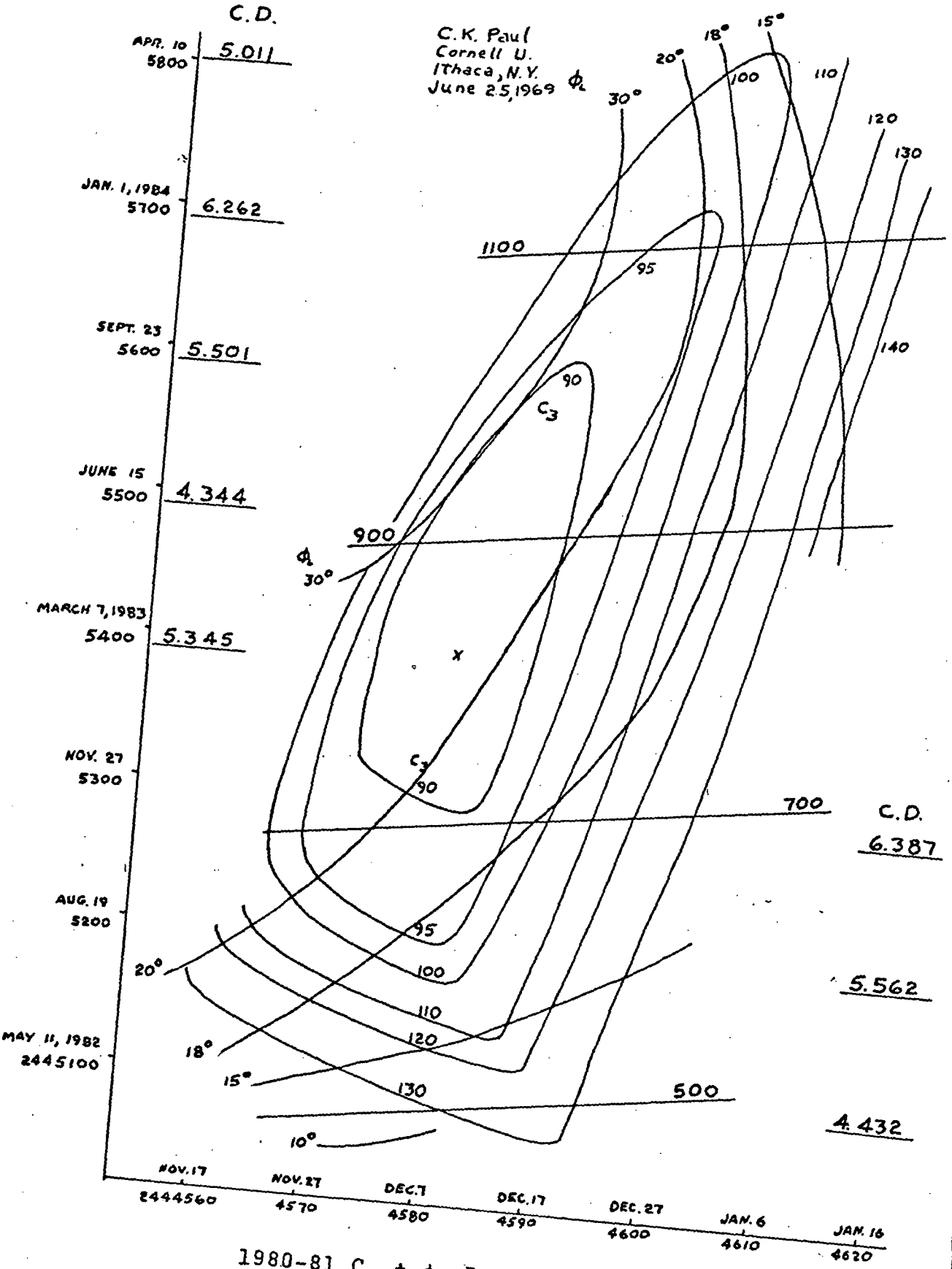

1980-81 C_3 + ϕ_L Parameters

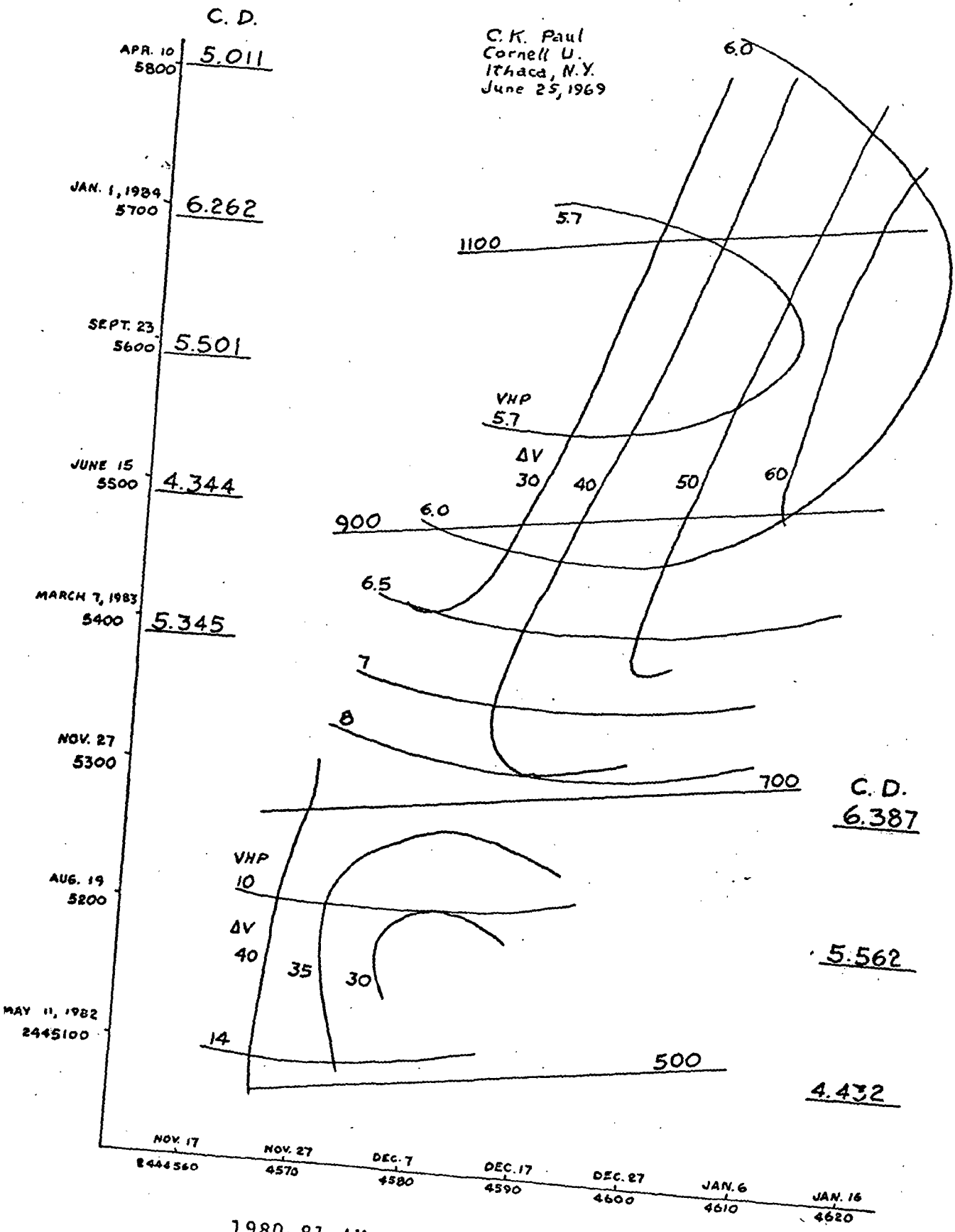

1980-81 ΔV + VHP Parameters

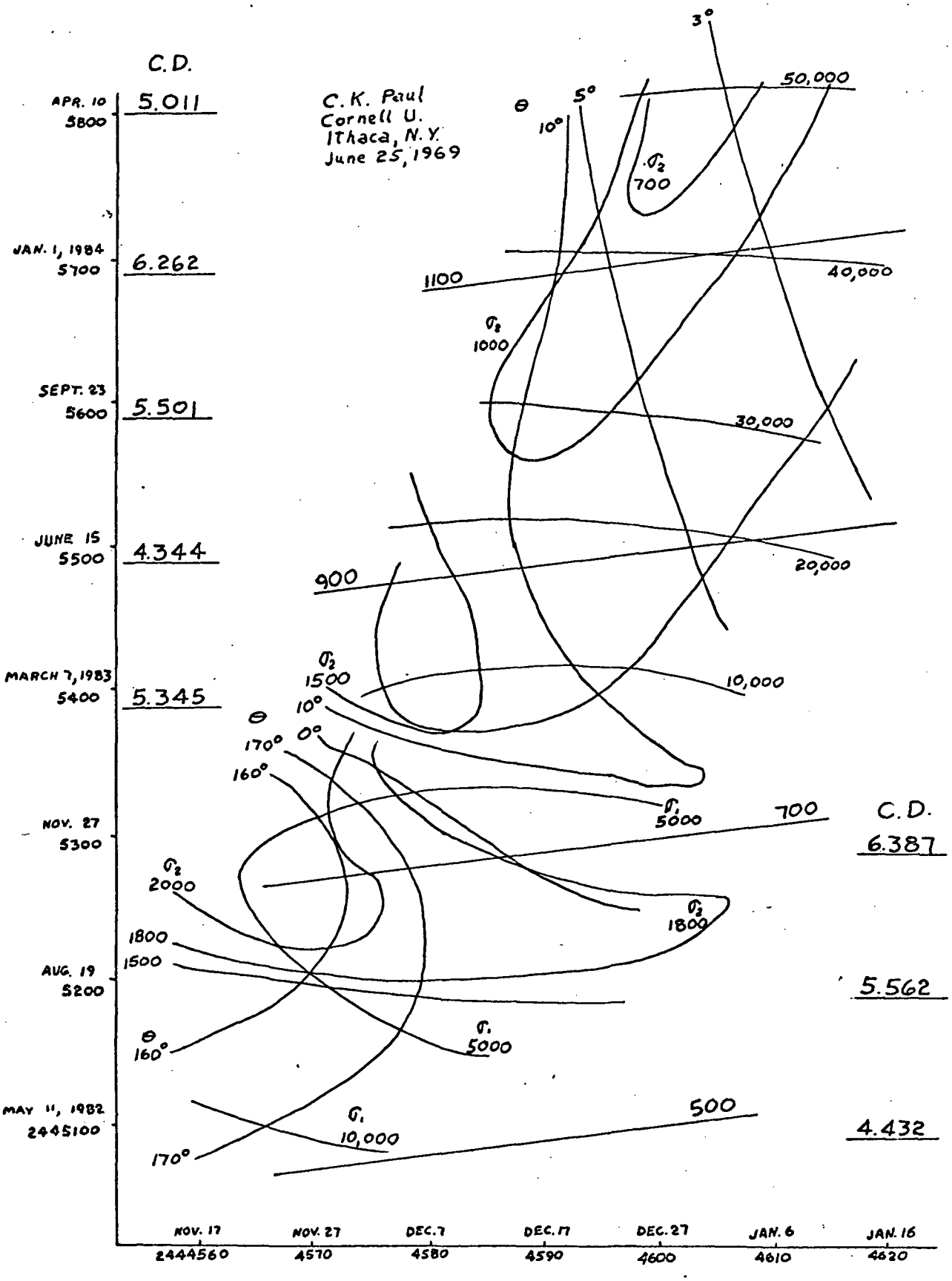

1980-81 σ_1, σ_2 + θ Parameters

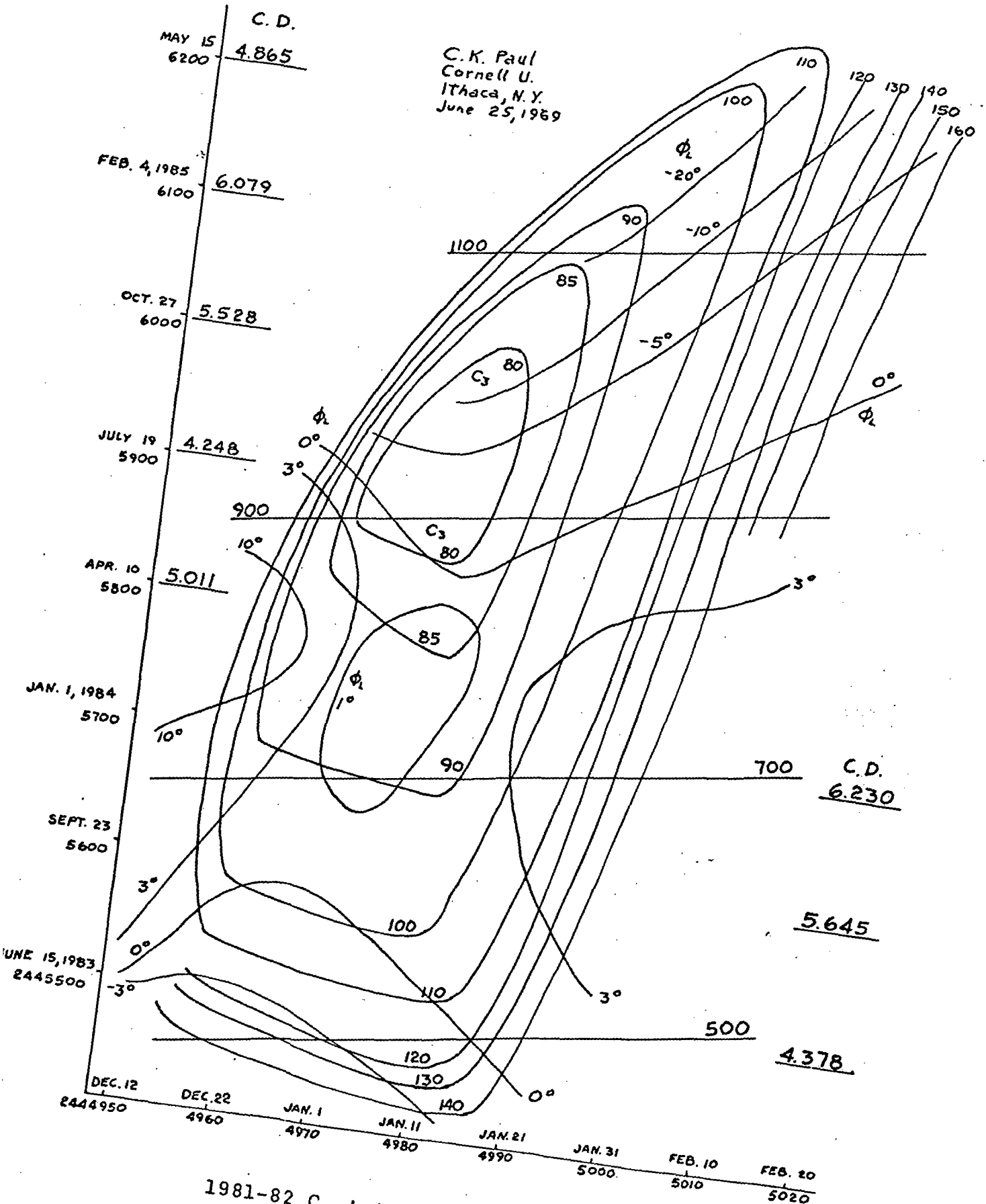

1981-82 C_3 + ϕ_L Parameters

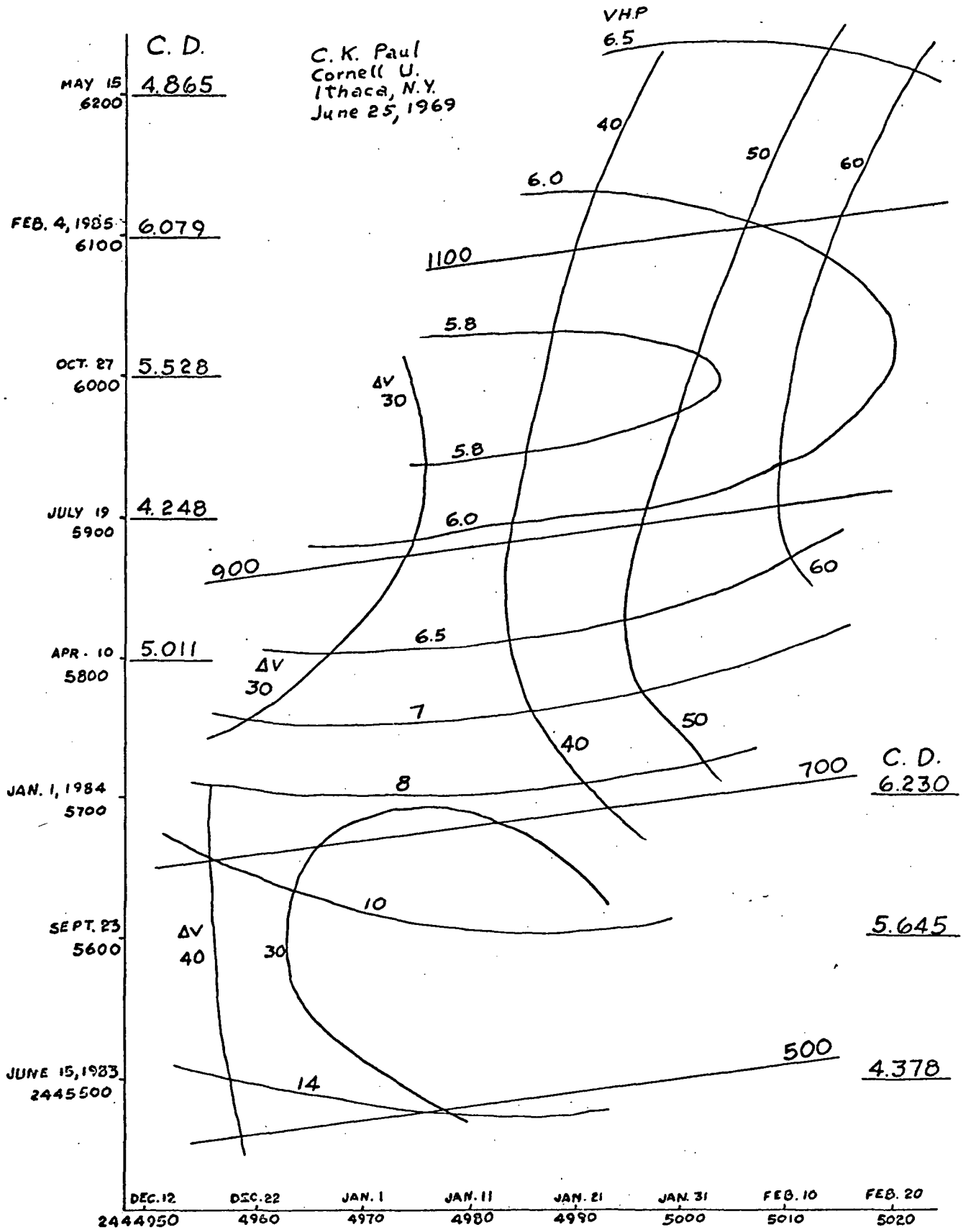

1981-82 ΔV + VHP Parameters

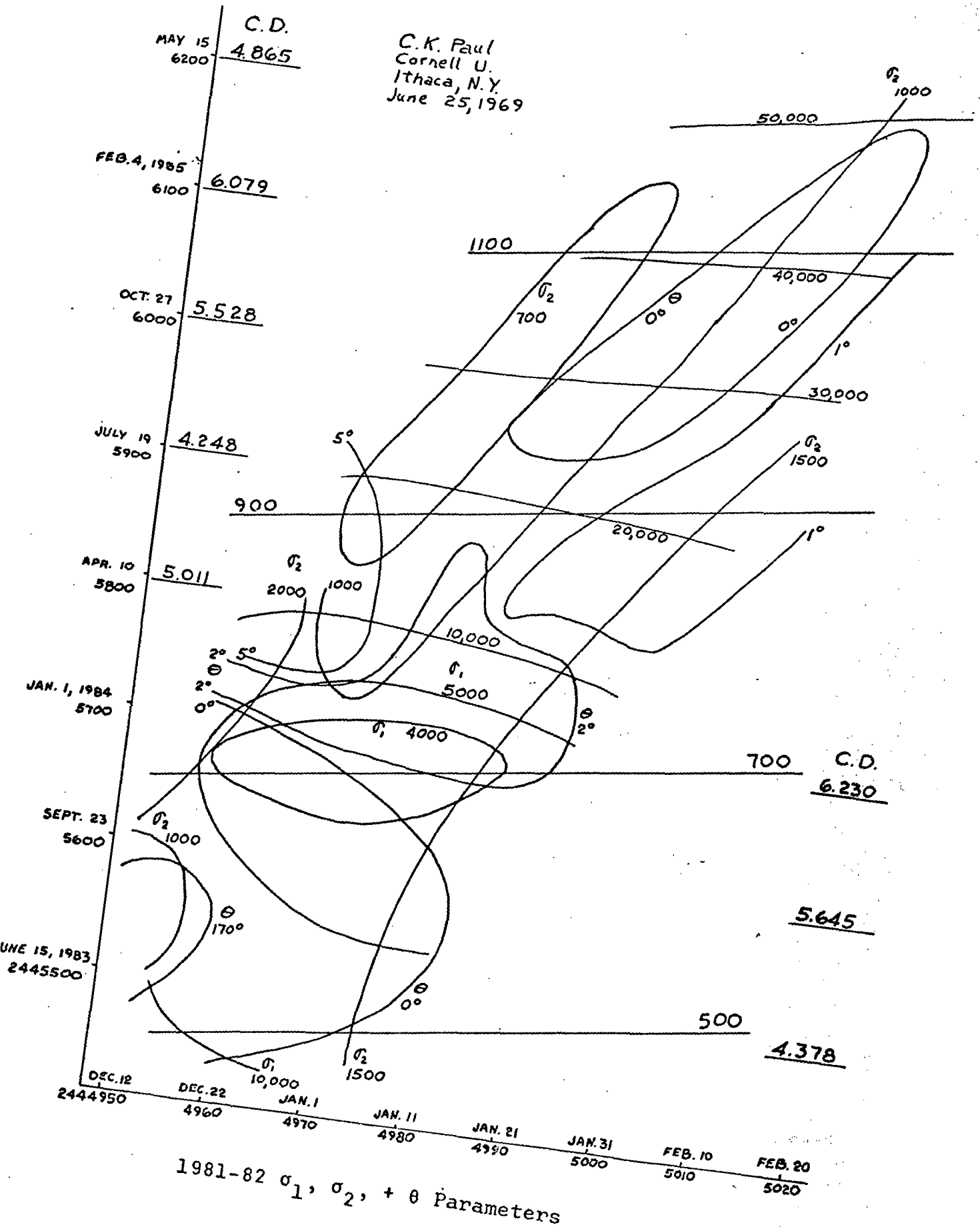

1981-82 σ_1, σ_2, + θ Parameters

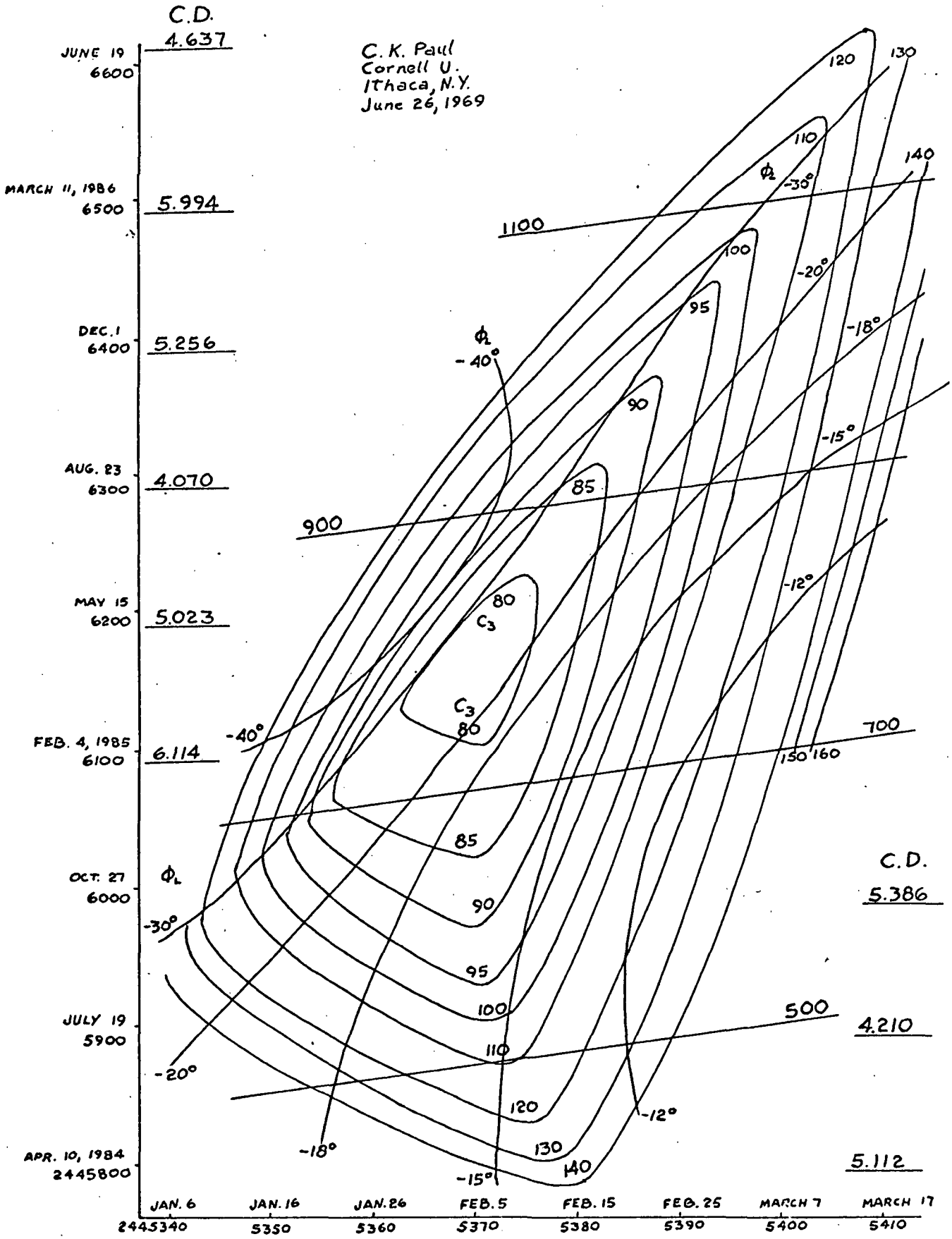

1983 C_3 + ϕ_L Parameters

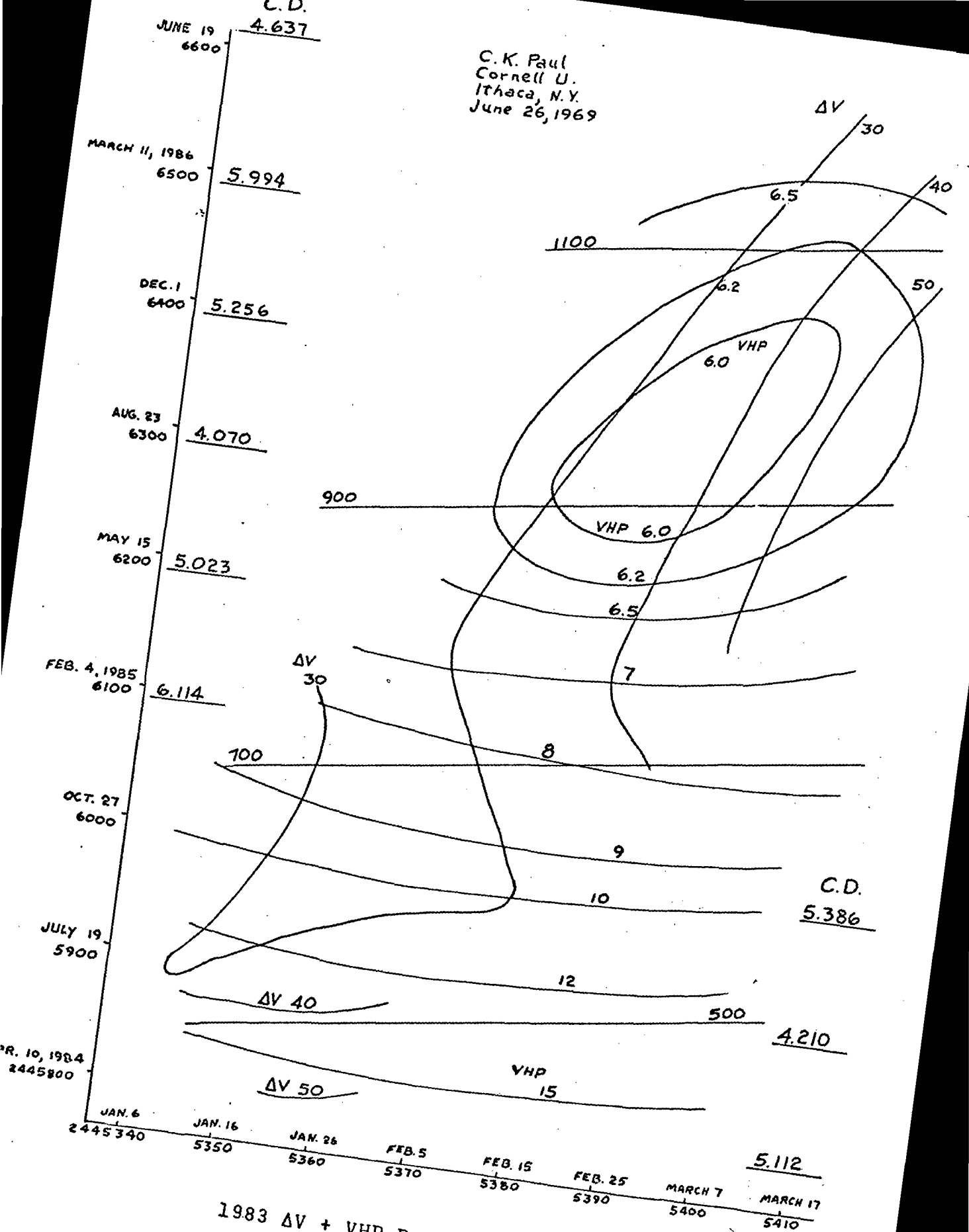

1983 ΔV + VHP Parameters

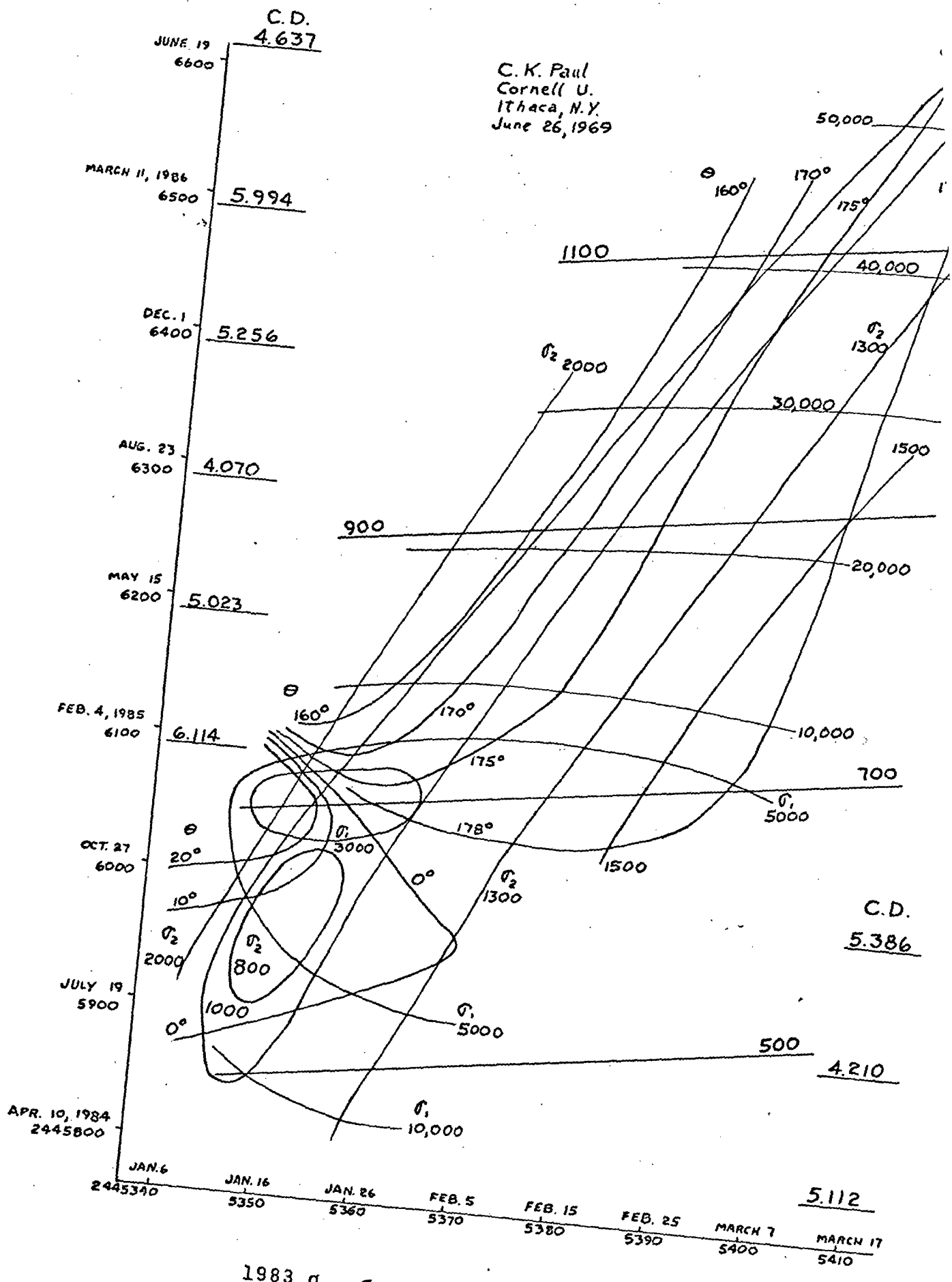

1983 σ_1, σ_2, + θ Parameters

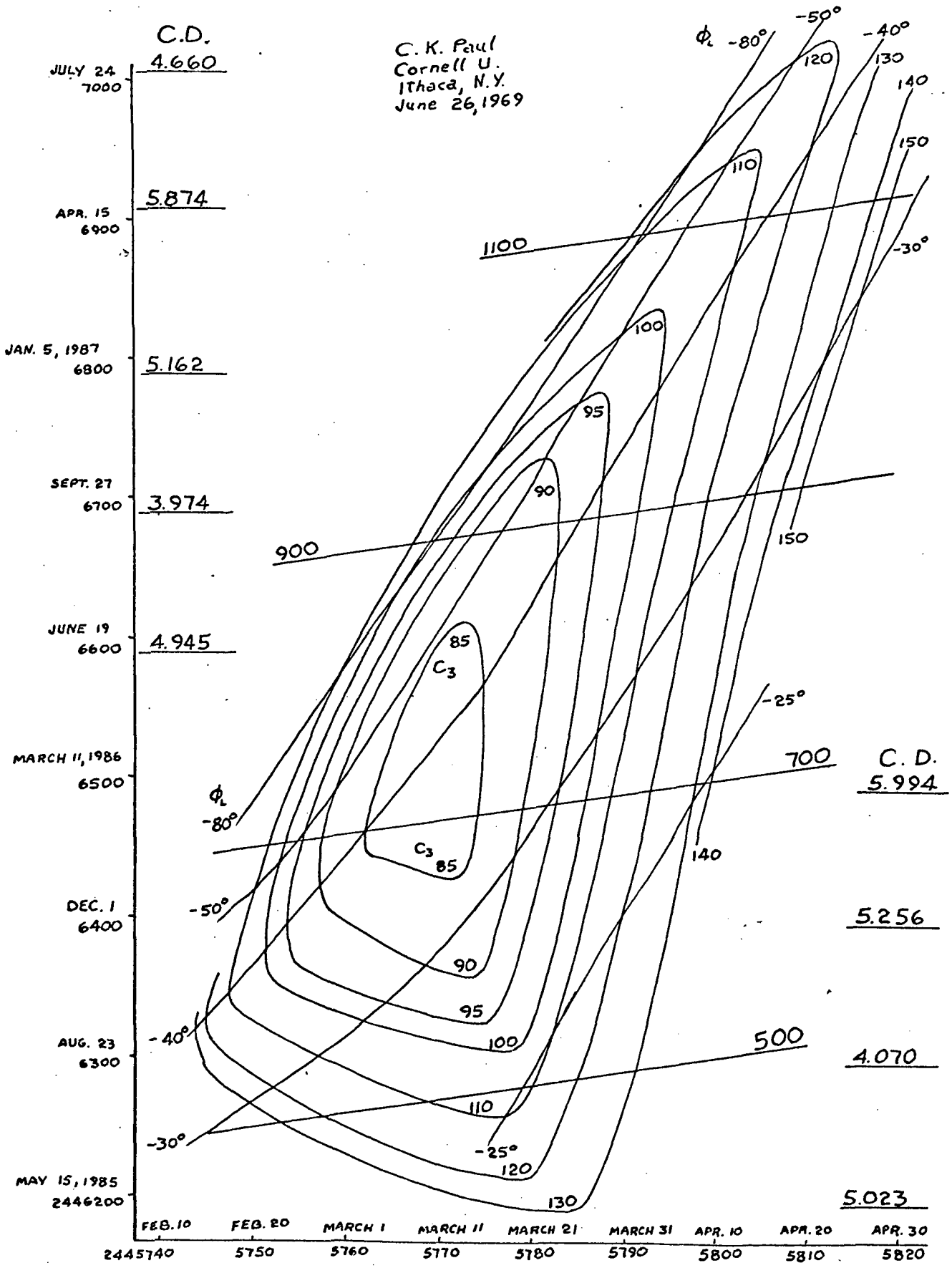

1984 C_3 + ϕ_L Parameters

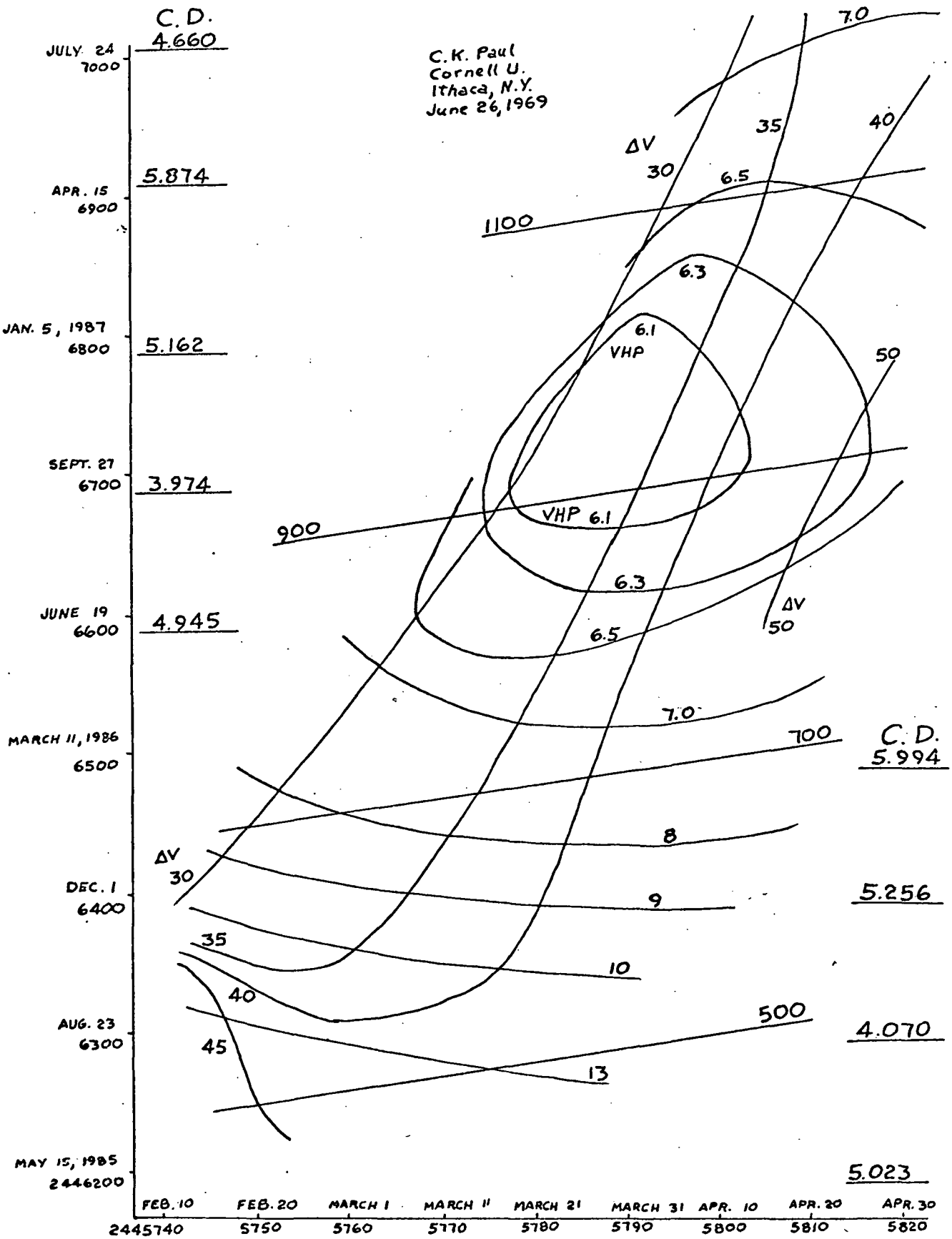

1984 ΔV + VHP Parameters

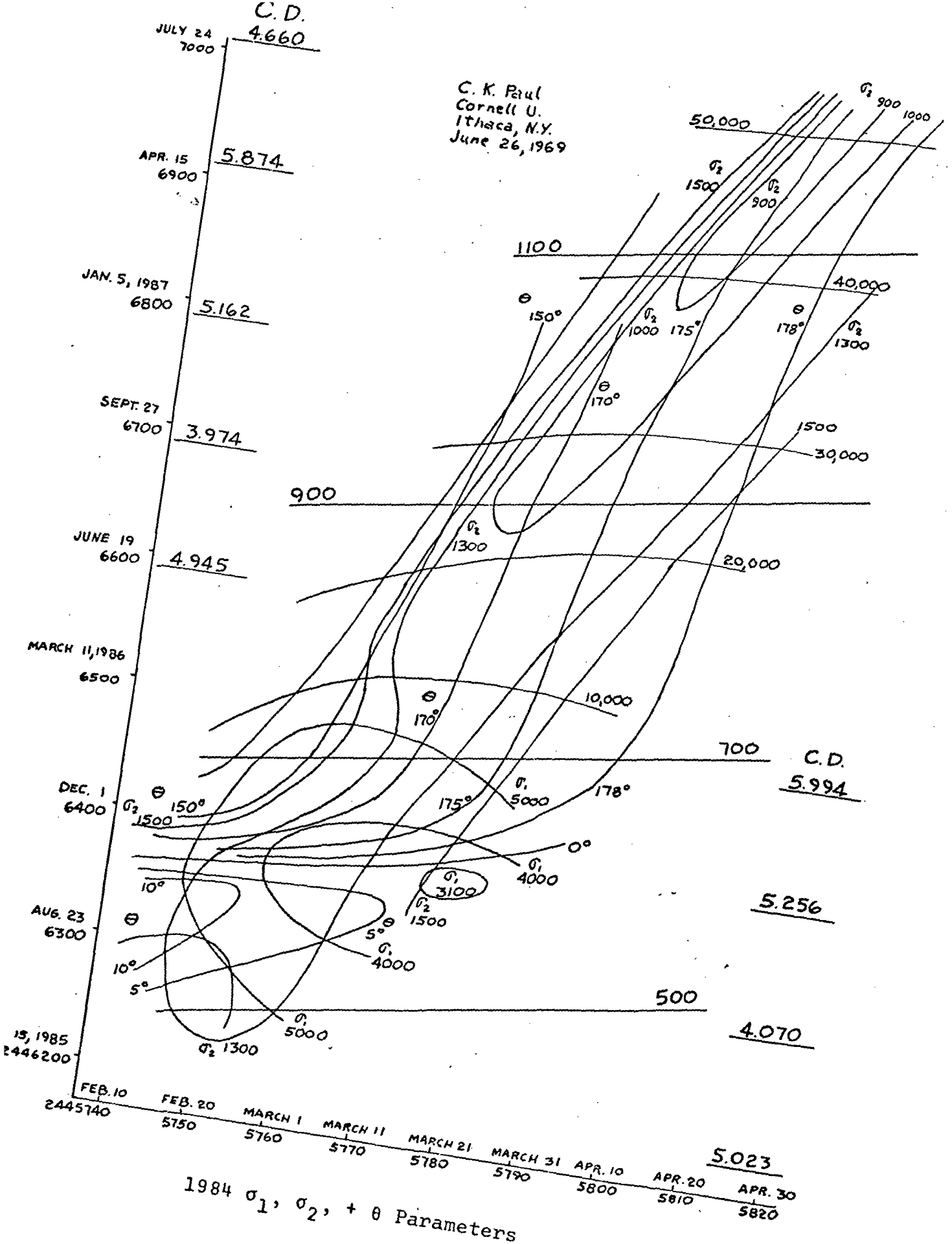

1984 σ_1, σ_2, + θ Parameters

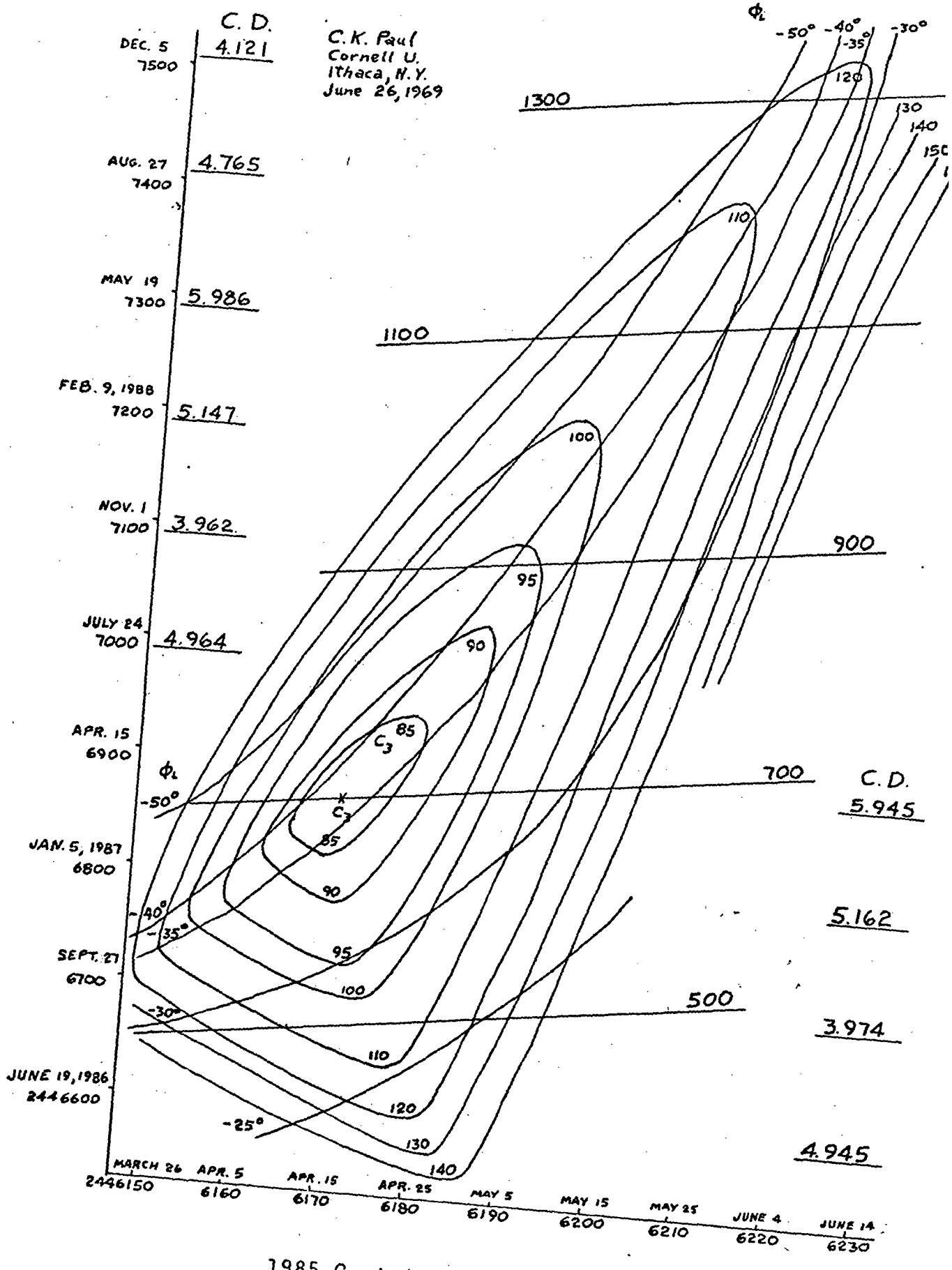

1985 C_3 + ϕ_L Parameters

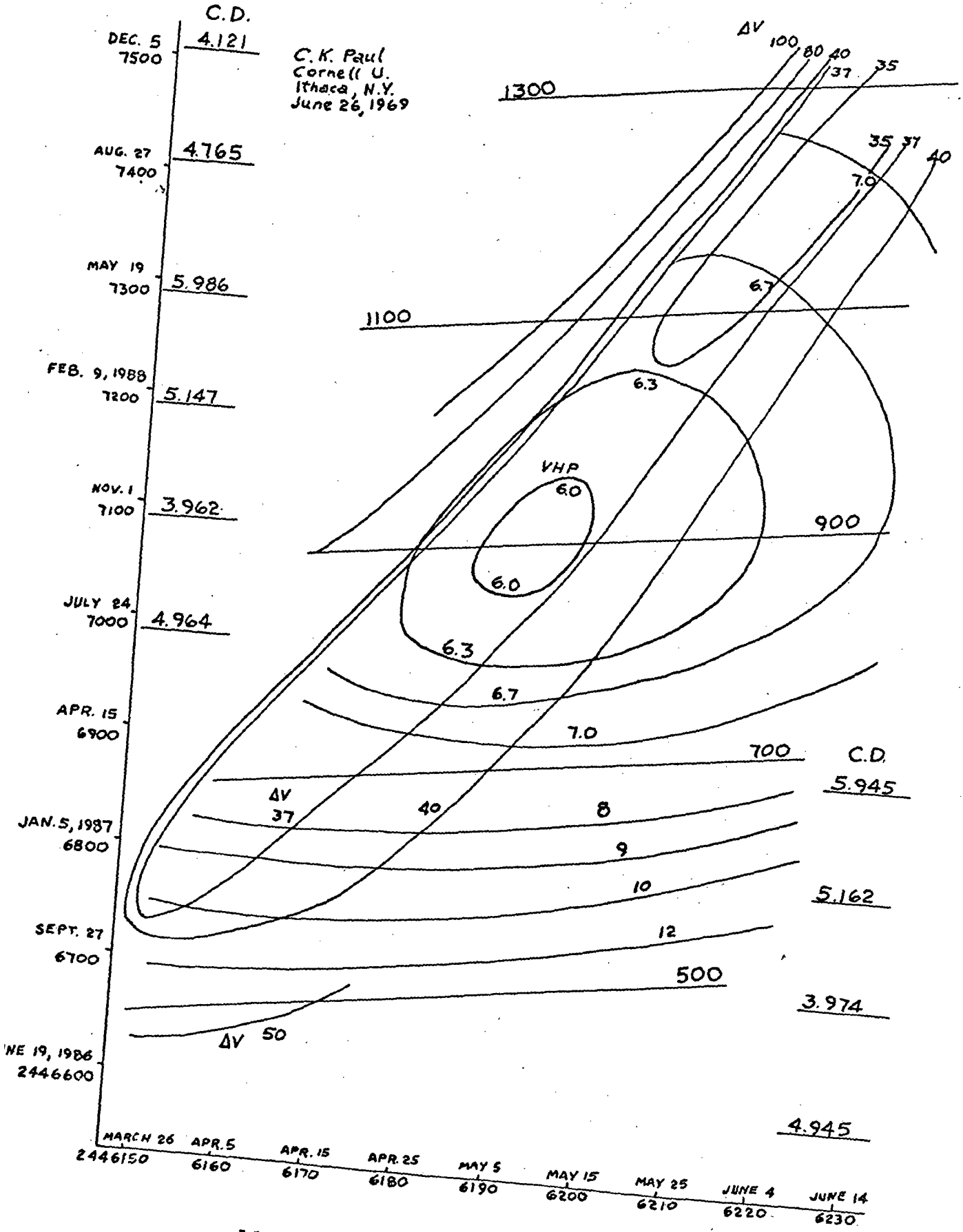

1985 ΔV + VHP Parameters

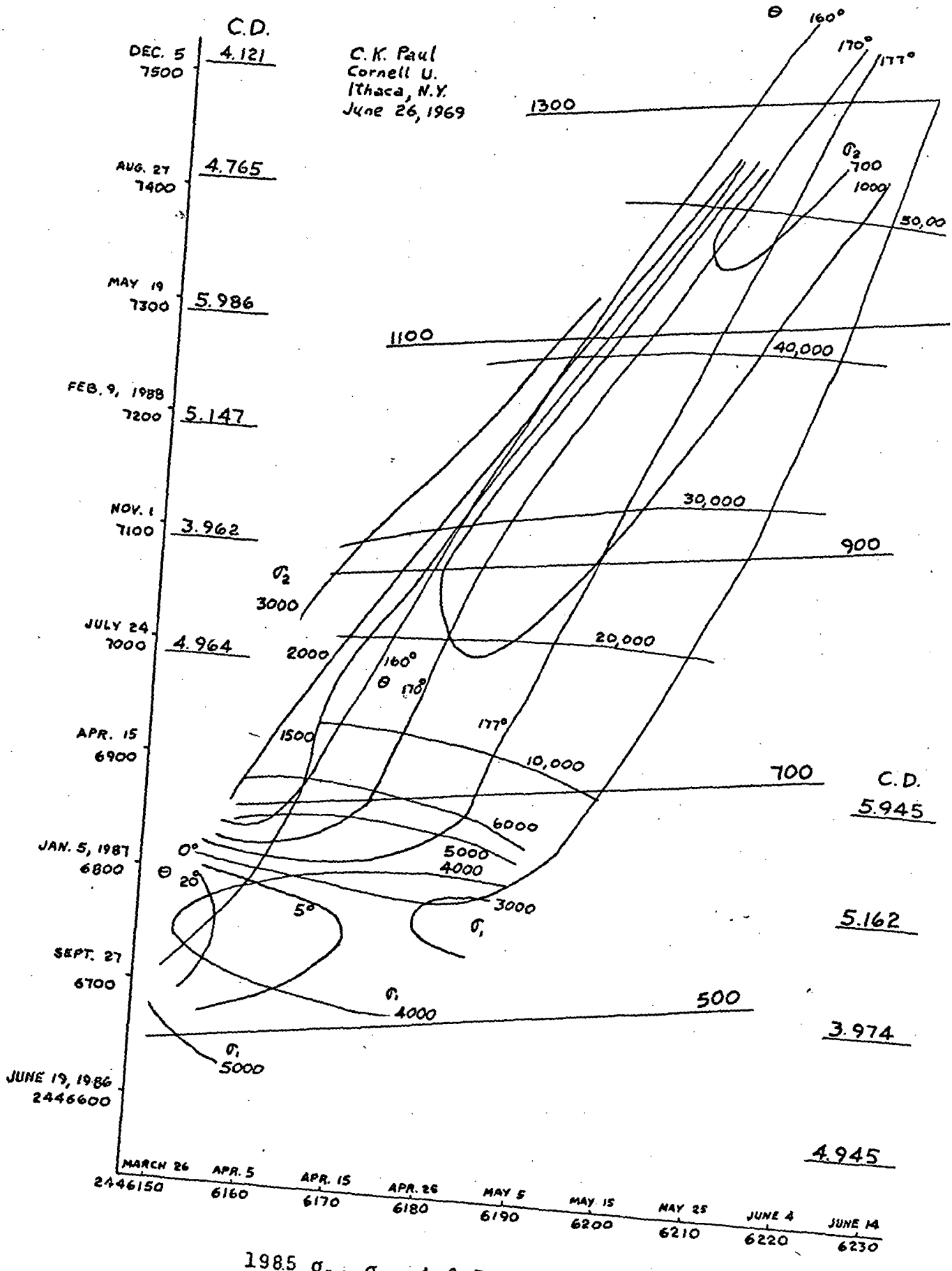

1985 σ_1, σ_2, + θ Parameters

Appendix B: JOSE Subprograms Descriptions

1. Subprogram TIM

Subroutine TIM is the heart of the JOSE program. TIM solves Lamberts' Theorem for the time of flight T between the two planets given as input the following previously computed parameters: (See Figure B-1).

e = the eccentricity of the heliocentric transfer ellipse

v_L, v_P = the true anomalies of the SC (or Earth) at launch and the SC (or Jupiter) at arrival.

a = the semi-major axis of the transfer ellipse.

GM_S; the universal gravitational constant times the mass of the sun, is another necessary input parameter for TIM. In solving for T, TIM first solves the eccentric anomalies at launch and arrival (E_L and E_P), the mean anomalies at launch and arrival (M_L and M_P), the difference in the mean anomalies ($\Delta M = M_P - M_L$), and finally the flight time T.

2. Subprogram ACHAN

Subroutine ACHAN takes as input the following variables:

T_F: the desired time of flight between Earth and Jupiter; in this program the independent variable and the time shown on the curves in Appendix A.

T: the time of flight as computed from Subprogram TIM.

$\overline{R}_L$: the Earth (or SC) heliocentric position vector at launch

a_m: the smallest semi-major axis possible for an elliptical trajectory between Earth and Jupiter.

For each possible Earth-Jupiter trajectory, ACHAN simply tabulates the times (T) required to travel the ellipse for various multiples of the minimum semi-major axis (a_m, $2a_m$, $3a_m$, ...). If the input multiple of a_m is ia_m, i = 1,2 ... , then ACHAN increments ia_m by another multiple of a_m, or $(i + 1)\, a_m$. The new

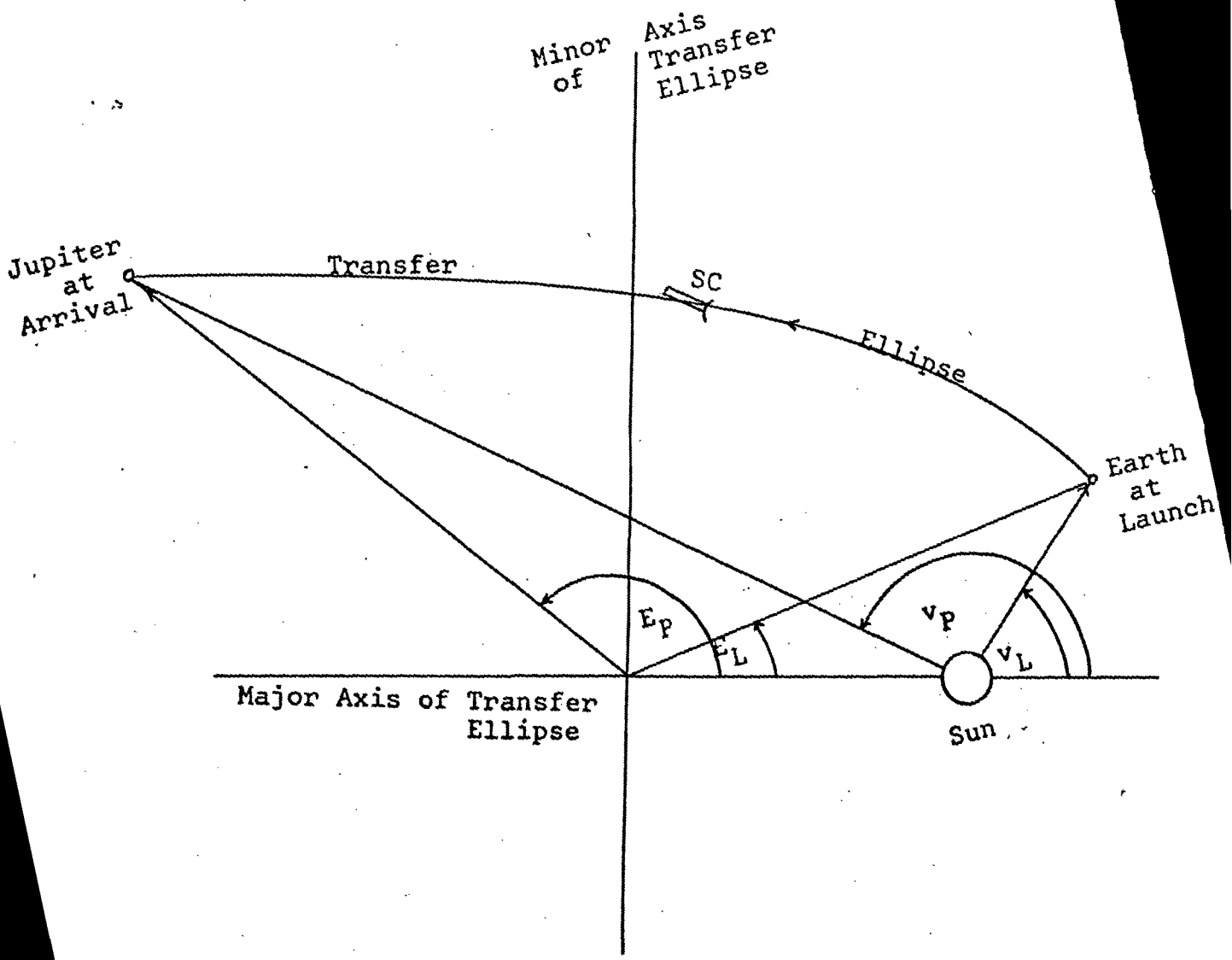

Figure B-1: Interplanetary Trajectory Time of Flight

semi-major axis (a) is set equal to $(i + 1)a_m$; (a) is tabulated and becomes the computed output of ACHAN.

3. Subprogram PAR

Subroutine PAR is the rather complex ellipse solver. It is complex in the sense that it must solve the elliptical trajectory parameters and the ellipse orientation in heliocentric space, given as input parameters (see Figure B-2):

R_L : magnitude of the Earth heliocentric position vector at launch.

R_P : magnitude of the Jupiter heliocentric position vector at arrival.

C : magnitude of the vector difference between Jupiter at arrival ($\bar{R}_P$) and Earth at launch ($\bar{R}_L$), or $C = ||\bar{R}_P - \bar{R}_L||$.

a : defined under TIM

Ψ : heliocentric transfer angle, $\Psi = \text{Cos}^{-1}\left(\frac{\bar{R}_L \cdot \bar{R}_P}{R_L R_P}\right)$ (B-1)

T_F,T : defined under ACHAN.

T_m : computed time of flight for the minimum semi-major axis (a_m) transfer ellipse, computed by TIM. (T_m is not generally the minimum flight time between Earth and Jupiter).

PAR solves, in the following order, the angles β and α, then the distance between foci X, then the angle γ, and the semi-major axis limit a_P. This limit a_P is the semi-major axis of the ellipse between Earth and Jupiter having a flight time of T_F and such that the major axis of the ellipse coincides with the launch vector $\bar{R}_L$. a_P is a necessary variable for comparison with the semi-major axis (a) to determine ellipse orientation as indicated in Figure B-2. According to the variable comparisons; a_P and a, T_F and T_m; v_L is solved ($v_L = \pi \pm \gamma$); then $v_P = v_L + \Psi$, and finally the ellipse eccentricity e is computed. v_L, v_P, and e are the outputs of PAR.

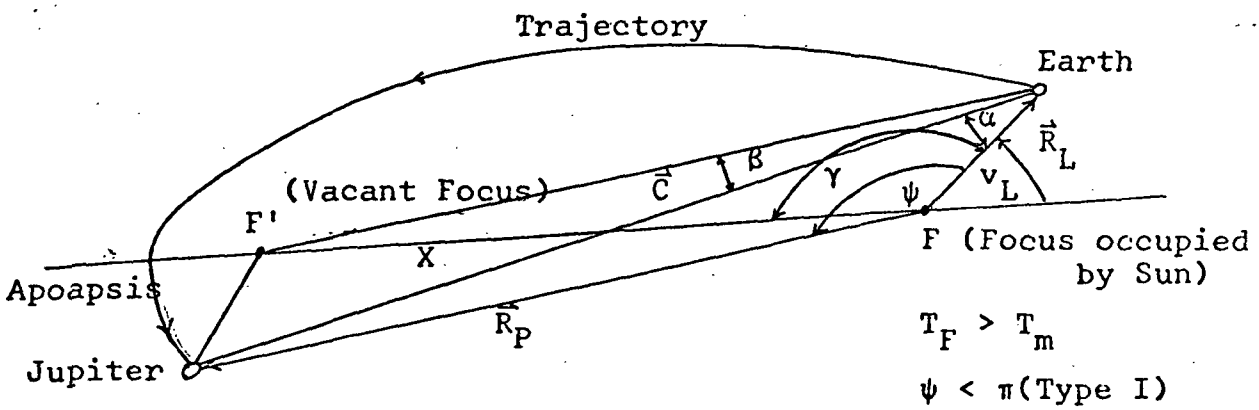

Configuration 1: Trajectory Passing Through Apoapsis

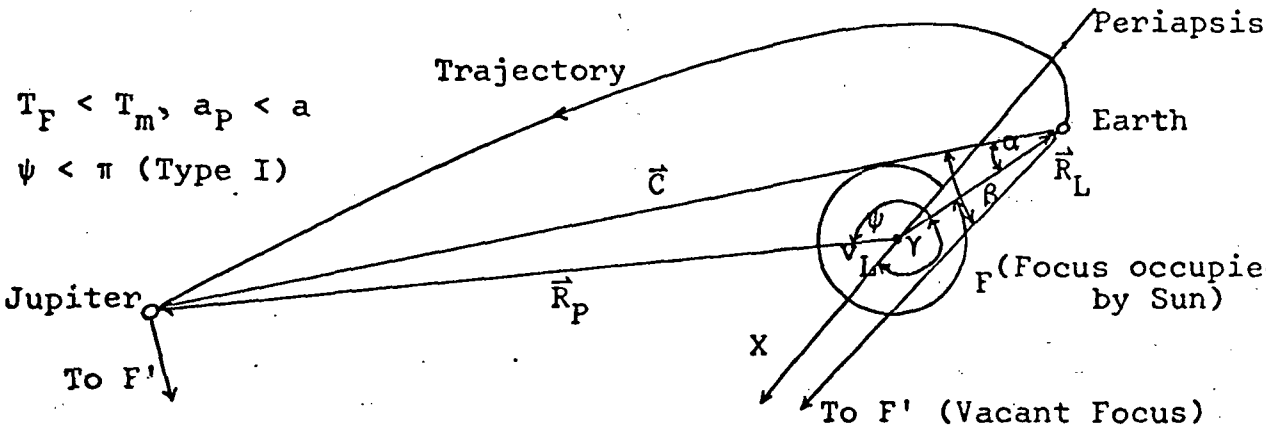

Configuration 2: Trajectory Passing Through Periapsis

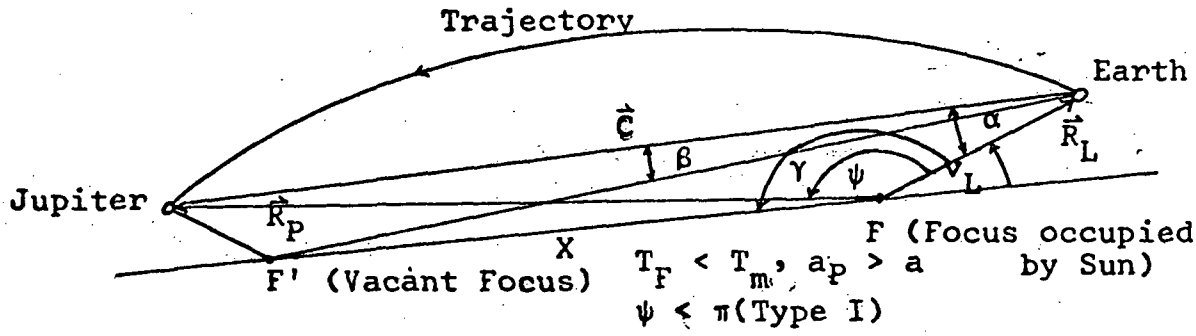

Configuration 3: Trajectory Passing Through Neither Apsis

Figure B-2: Interplanetary Trajectory Elliptical Parameters. Three Possible Configurations for Type I Trajectories

4. Subprogram TRAPAR

Subroutine TRAPAR, calling on subroutines TIM, ACHAN, PAR, basically solves the inverse of Lambert's Equation. Lambert's Theorem states: "The transfer time between any two points on an ellipse is a function of the sum of the distances of each point from the focus, the distance between the points, and the semi-major axis of the ellipse". (Reference - JPL TR 32-77). Functionally, $T_F = T_F(R_L + R_P, C, a)$. In this study, launch opportunities have been selected for each year 1975-1985 at various dates (hence $\overline{R}_L$ is determined), and for each launch date, various flight times T_F are selected (hence $\overline{R}_P$ and thus $\overline{C}$ are determined). The problem then is to solve the inverse of the functional equation above for the semi-major axis (a) by successive iterations for each pair of launch-arrival dates.

More specifically, TRAPAR reads in as input the position vectors $\overline{R}_L$ and $\overline{R}_P$ as well as $\overline{V}_E$ (Earth heliocentric orbital velcoity vector). It immediately computes R_L, R_P, Ψ, $\overline{W}$, C, a_m, p_m, e_m, v_{Lm}, and v_{Pm}; where:

$\overline{W}$ = vector unit normal to heliocentric transfer plane, or:

$$\overline{W} = \overline{R}_L \times \overline{R}_P / R_L R_P \sin \Psi \qquad \text{(B-2)}$$

p = semi-latus rectum of transfer ellipse, and a_m, p_m, e_m, v_{Lm}, and v_{Pm} pertain to the minimum semi-major axis (a_m) ellipse.

The significance of the minimum semi-major axis (a_m) is illustrated in Figure B-3. In the upper sketch, the loci of all points of distance ℓ_1 to Earth is of course a circle of radius ℓ_1 about the Earth, and the locus of all points of distance ℓ_2 to Jupiter is a circle of radius ℓ_2 about Jupiter. The intersection of these circles, i.e., F_1' and F_2', would represent vacant foci of possible ellipses between Earth and Jupiter. Note that the major axis defined by $F\text{-}F_1'$ requires the elliptical trajectory to pass through the apoapsis point (aphelion) between Earth and Jupiter, while the major axis defined by $F\text{-}F_2'$

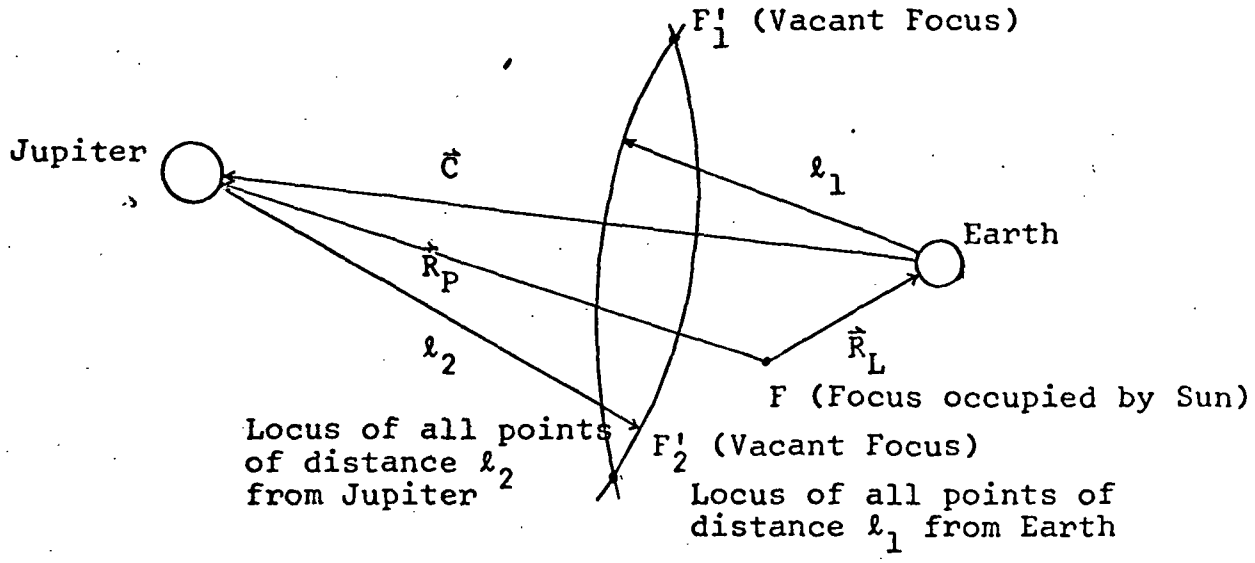

Location of Vacant Focus for Various ℓ_1 and ℓ_2

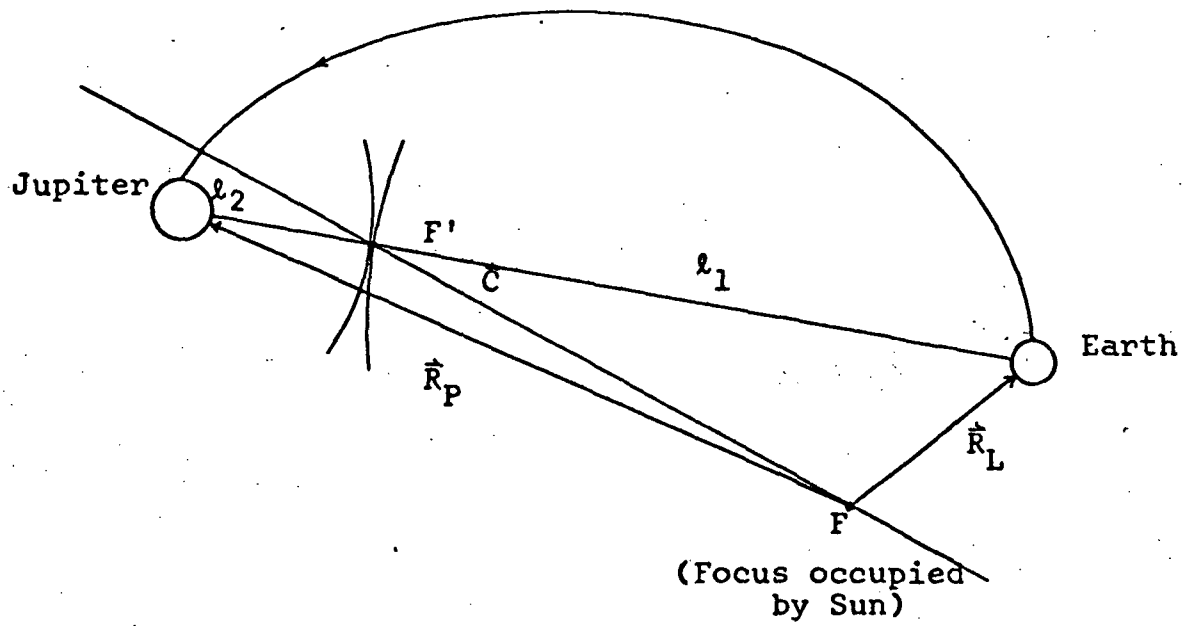

Transfer Ellipse of Minimum Semi-major Axis (a_m)

Figure B-3: Geometry of the Transfer Ellipse Vacant Focus and the Transfer Ellipse of Minimum Semi-major Axis (a_m)

requires the trajectory to pass through perihelion. These two ellipses then are the possible trajectories between Earth and Jupiter for a vacant focus-Earth distance of ℓ_1 and a vacant focus-Jupiter distance of ℓ_2. Since Earth and Jupiter necessarily lie on the ellipse;

$$R_L + \ell_1 = 2a \quad ; \quad \ell_1 = 2a - R_L$$
$$R_P + \ell_2 = 2a \quad ; \quad \ell_2 = 2a - R_P$$

Varying ℓ_1 and ℓ_2 generate all possible transfer ellipses between the two planets. However, note in the bottom sketch of Figure B-3 that, for a given ℓ_1, there is a minimum ℓ_2 for which only one intersection of the circles takes place. This vacant focus (F') generates the transfer ellipse of minimum semi-major axis (a_m) since F' defines the focus where $\ell_1+\ell_2$ is a minimum. Thus:

$$\text{Min } (\ell_1+\ell_2) = \text{Min } (4a - R_L - R_P) = 4a_m - R_L - R_P$$

However, since F' lies on the line segment between the two planets, $\ell_1+\ell_2 = C$; thus:

$$4a_m - R_L - R_P = C, \quad \text{or } a_m = (R_L + R_P + C)/4$$

p_m, e_m, v_{Lm}, and v_{Pm} are then solved by the appropriate elliptical formulas.

Subroutine TIM is then called, assigning to the variables e, v_L, v_P, and a of TIM the values of e_m, v_{Lm}, v_{Pm}, and a_m respectively. TIM thus computes T and assigns it the variable T_m. T_m is then the time required to traverse the ellipse of minimum semi-major axis (a_m) between Earth and Jupiter. Note from the lower sketch of Figure B-3 that, for the planet configuration shown, T_m is certainly not the minimum time for all ellipses possible between Earth and Jupiter. This becomes even more evident as F' is moved closer to Earth (as ℓ_1 is decreased).

T_m is then compared with T_F, the selected time of flight. If $T_m < T_F$, ACHAN is called to increment a_m by a multiple of itself, thus $aa_1 = 2\ a_m$;

the variable a is now assigned the value of aa_1 and subroutine PAR is called to solve for new values of v_L, v_P, and e based on the semi-major axis a now being equal to aa_1 (or $2a_m$). TIM is again called, and a new value of T is computed corresponding to aa_1. This T is compared with T_F; if T is still $< T_F$, the procedure is repeated. The repetitions continue until $T > T_F$, at which point $aa_{i+1} = (i + 2)\, a_m$. The aa_i, i = 1, 2 ..., have been tabulated during the procedure, as well as the times tt_i corresponding to them.

If intially $T_m > T_F$, exactly the same procedure is followed until $T_m < T_F$, since aa_i must always increment a_m as a_m is the minimum semi-major axis possible.

After this procedure, it is now obvious that T_F, the selected flight time, corresponds to a semi-major axis a_{T_F} lying in value between aa_{i+1}, and aa_i, or:

$$aa_i \leq a_{T_F} \leq aa_{i+1}$$

In the domain $[aa_i, aa_{i+1}]$, T may of course be increasing or decreasing; i.e., $tt_i \overset{<}{>} tt_{i+1}$.

The goal now is to determine a_{T_F} by numerical procedures. a_{T_F} is initially approximated by the variable aaa_1. See sketch below:

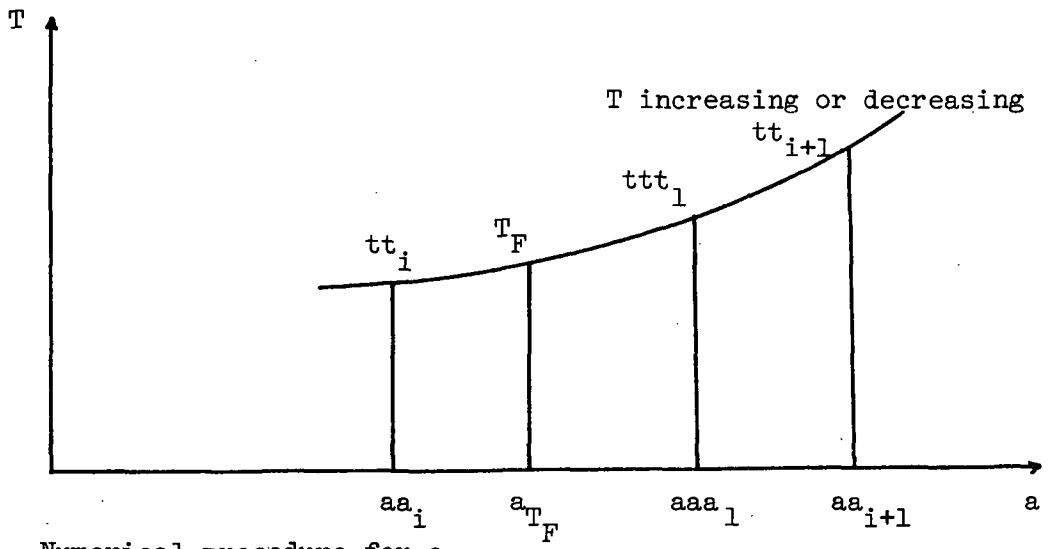

Numerical procedure for a_{T_F}

T as a function of a is of course not explicitly known. The functional dependence involves a large number of equations. a_{T_F} is not known and is the value that is being sought. T can also be increasing or decreasing at the point of interest, namely at a_{T_F}, as indicated in the procedures above. Equating slopes in this small domain of interest $[aa_i, aa_{i+1}]$, the initial approximation aaa_1 is determined:

$$\frac{tt_{i+1} - tt_i}{aa_{i+1} - aa_i} = \frac{tt_{i+1} - T_F}{aaa_{i+1} - aaa_1} \text{ ; whence}$$

$$aaa_1 = aa_{i+1} - (aa_{i+1} - aa_i)\left(\frac{tt_{i+1} - T_F}{tt_{i+1} - tt_i}\right)$$

Then, as before, a takes the value of aaa_1, PAR and TIM are called, from which a new value of T is computed corresponding to aaa_1. This T is tabulated as ttt_1. A new value, aaa_2, is used to approximate a_{T_F} according to:

$$aaa_2 = aaa_1 - (aaa_1 - aa_i)\left(\frac{ttt_1 - T_F}{ttt_1 - tt_i}\right)$$

by the same reasoning used above. (a) again takes the value aaa_2, PAR and TIM are called, T is computed and ttt_2 takes this value of T. ttt_3, in general, will closer approximate T_F than ttt_2 or any of the tt_i, i = 1,2 ... . This procedure is repeated, a new (a) each time being approximated accoring to:

$$aaa_k = aaa_{k-1} - (aaa_{k-1} - aa_i)\left(\frac{ttt_{k-1} - T_F}{ttt_{k-1} - tt_i}\right)$$

The procedure terminates when the T output of TIM is such that $|T_F - T| <$ some preassigned value, in this program the value is taken as one-tenth of a day. The last computed $a(=aaa_k)$ is taken to be equal to the desired a_{T_F}, and is the semi-major axis of the ellipse corresponding to the time of flight T_F.

During the last iteration of PAR and TIM in solving for T, all parameters of the transfer ellipse have thus been computed, including a, e, v_L, and v_P, as well as the orientation of the ellipse in heliocentric space. Figure B-4 indicates the remaining parameters computed by TRAPAR. Noting that $\bar{R}$ and $\bar{V}$ are the instantaneous position and velocity vectors of JOSE at any point along the trajectory, Γ is the acute angle between $\bar{V}$ and the normal to $\bar{R}$, and that the subscripts L and P on $\bar{R}$, $\bar{V}$, and Γ indicate Earth launch and Jupiter arrival points respectively; Γ_L, V_L, and $\bar{V}_L$ are solved in that order. $\bar{V}_L$ is also a function of $\bar{W}$, the unit normal to the trajectory plane and computed previously. Specifically;

$$\text{Sin } \Gamma_L = \sqrt{\frac{R_L}{(1-e^2)(2a-R_L)}}\ e \text{ Sin } v_L \quad \begin{pmatrix} 0 \leq \Gamma_L \leq \frac{\pi}{2} \text{ if } 0 \leq v_L \leq \pi \\ -\frac{\pi}{2} \leq \Gamma_L \leq 0 \text{ if } \pi \leq v_L \leq 2\pi \end{pmatrix} \tag{B-3}$$

$$V_L = \sqrt{GM_S\left(\frac{2}{R_L} - \frac{1}{a}\right)}$$

$$\bar{V}_L = \frac{V_L}{R_L}\left[(\bar{W} \times \bar{R}_L) \text{ Cos } \Gamma_L + \bar{R}_L \text{ Sin } \Gamma_L\right]$$

The important energy parameter C_3 is then:

$$C_3 = ||\bar{V}_L - \bar{V}_E||^2$$

$\bar{S}_L$ is the unit velocity vector relative to Earth's center, then:

$$\bar{S}_L = E^T \frac{\bar{V}_L - \bar{V}_E}{\sqrt{C_3}}$$

and is shown in the lower portion of Figure B-4. E^T is a matrix of rotation from ecliptic coordinates to Earth Equatorial coordinates. Then, ϕ_L and θ_L, the launch asymptote declination and right ascension respectively, are solved by:

$$\text{Sin } \phi_L = (\bar{S}_L)_Z \quad \left(-\frac{\pi}{2} \leq \phi_L \leq \frac{\pi}{2}\right)$$

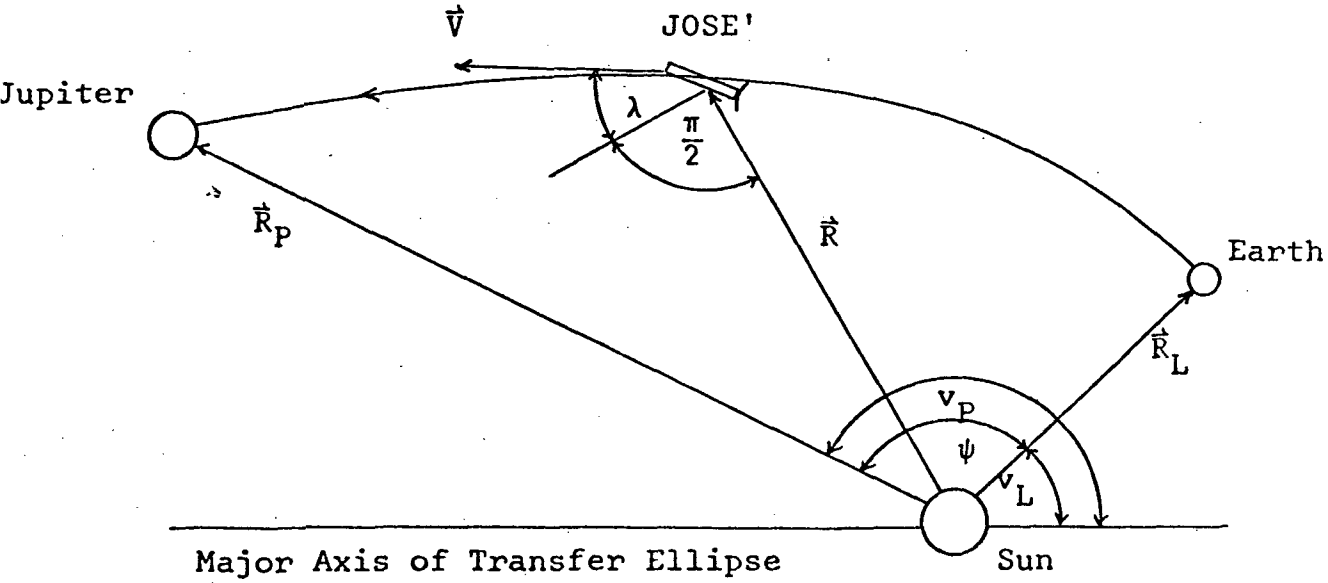

Heliocentric Space

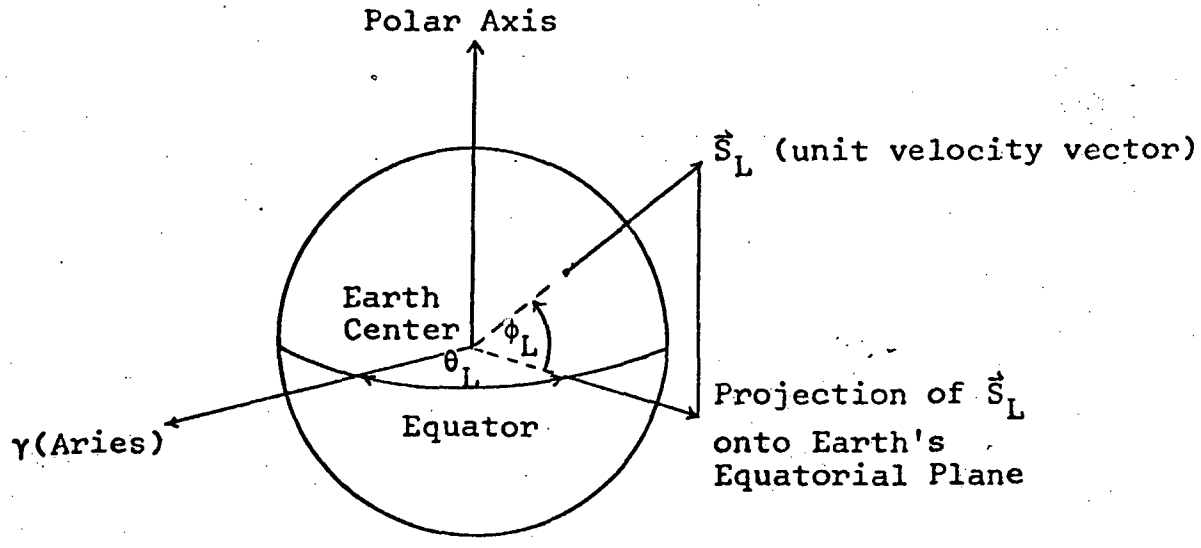

Earth Planetocentric Space

Figure B-4: Launch Velocity Parameters of the Earth-Jupiter Trajectory

$$\text{Cos } \theta_L = (\bar{S}_L)_X \Big/ \sqrt{(\bar{S}_L)^2_X + (\bar{S}_L)^2_Y}$$

$$(0 \leq \theta \leq 2\pi)$$

$$\text{Sin } \theta_L = (\bar{S}_L)_Y \Big/ \sqrt{(\bar{S}_L)^2_X + (\bar{S}_L)^2_Y}$$

where the X, Y, Z subscripts denote the respective Earth equatorial components of $\bar{S}_L$.

The origin of ecliptic coordinates for this program is the Sun; the X axis points toward Aries in the plane of the ecliptic, the Z axis is normal to the ecliptic, and the Y axis lies in the ecliptic normal to the plane defined by the X and Z axes. Z points to the Northern Celestial Hemisphere.

TRAPAR generates as output the variables, R_L, R_P, Ψ, $\bar{W}$, a, e, v_L, v_P, E_L, E_P, M_L, M_P, ΔM, T, $\bar{V}_L$, C_3, $\bar{S}_L$, ϕ_L, and θ_L.

5. Subprogram BMISS

Subroutine BMISS aids in computing the "miss" vector between any selected point on the reference trajectory and that point on the actual tracjectory. The miss vector $\bar{B}$ lies in the plane normal to the SC velocity vector $\bar{V}$. The reference trajectory is the selected trajectory from TRAPAR for a given flight time T_F. The actual, or true, trajectory is the SC trajectory resulting from probabilistically random errors in launch and midcourse maneuvers. If the point on the reference trajectory is the planet Jupiter itself; the miss vector $\bar{B}$ is considered the vector between Jupiter and the SC unit velocity vector relative to Jupiter ($\bar{S}_P$). $\bar{B}$ lies in the plane normal to $\bar{S}_P$; i.e., in the $\bar{R}$-$\bar{T}$ plane. See Figure B-5.

Although Jupiter encounter is examined in Section B of Chapter III, an introductory description is in order. With the variable designation adopted under TRAPAR, $\bar{V}_P$ is the heliocentric velocity vector of JOSE at Jupiter's sphere of influence. If $\bar{V}_J$ is Jupiter's oribtal velocity, then:

$$\bar{S}_P = \frac{\bar{V}_P - \bar{V}_J}{||\bar{V}_P - \bar{V}_J||}$$

$\bar{T}$ is a unit vector normal to $\bar{S}_P$ lying in the plane of the ecliptic ($\bar{S}_P$ in general will not lie in the ecliptic), and $\bar{R}$ is a unit normal to the $\bar{S}_P$-$\bar{T}$ plane. $\bar{B}$, shown in Figure B-5, is the miss vector of the hyperbolic asymptote; the SC approach hyperbola approaches the planet at a closer distance than $\bar{B}$ due to Jupiter's gravitational field. The $\bar{B}$ vector is merely a convenient parameter for evaluating the effects of mapping launch and midcourse errors into miss distance in the $\bar{R}$-$\bar{T}$ plane.

BMISS accepts as input the parameters ϕ_L, θ_L, C_3, $\bar{V}_L$, R_L, e, T_F, a, and T from TRAPAR. From the main program it accepts $\Delta\phi_L$, $\Delta\theta_L$, ΔC_3, $\bar{R}_L$, and $\tilde{T}$; where: (see Figure B-6)

$\Delta\phi_L$ = angular error in declination of velocity asymptote

$\Delta\theta_L$ = angular error in right ascension of velocity asmyptote. At launch injection, $\Delta\phi_L$ and $\Delta\theta_L$ are each assumed = 0.2°. At midcourse manuever, $\Delta\phi_L$ and $\Delta\theta_L$ are assumed = 1.61°.

ΔC_3 = error in energy, or velocity asymptote squared error. At launch injection, ΔC_3 assumed = 0.005 C_3. At midcourse maneuver, ΔC_3 assumed = 0.0005 C_3.

$R_L = ||\bar{R}_L||$

$\tilde{T}$ = the time of flight between the time of launch or midcourse maneuver and the time at which $\bar{B}$ is desired.

The launch hyperbolic excess velocity vector $\bar{V}_{hL}$, where $||\bar{V}_{hL}|| = \sqrt{C_3}$, is clearly given by:

$$\bar{V}_{hL}^{\,T} = \sqrt{C_3}\,(\text{Cos}\ \phi_L\ \text{Cos}\ \theta_L,\ \text{Cos}\ \phi_L\ \text{Sin}\ \theta_L,\ \text{Sin}\ \phi_L)$$

The incremental change in $\bar{V}_{hL}$, or $\Delta\bar{V}_{hL}$, is computed by:

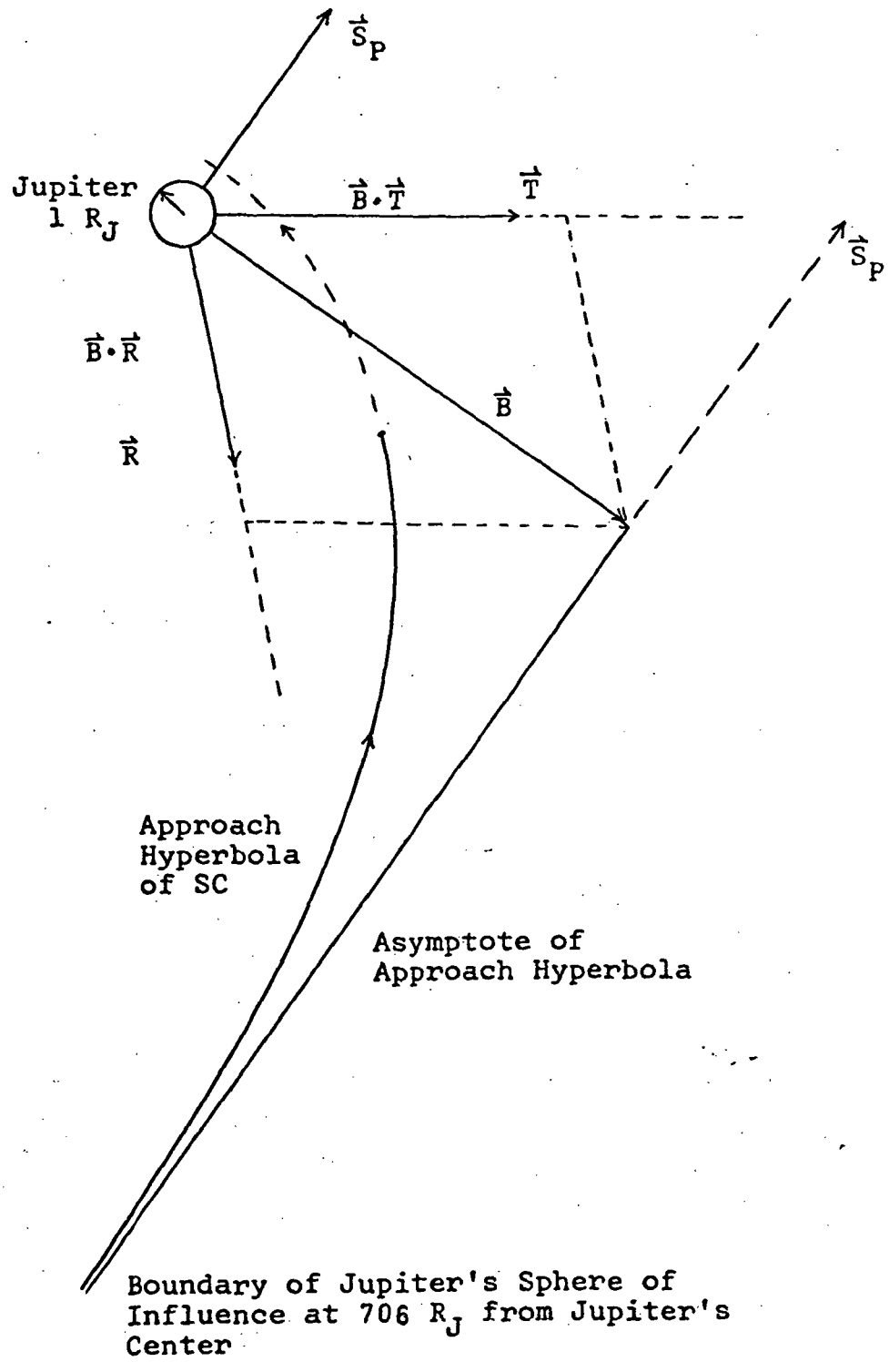

Figure B-5: Miss Vector $\overline{B}$ at Jupiter

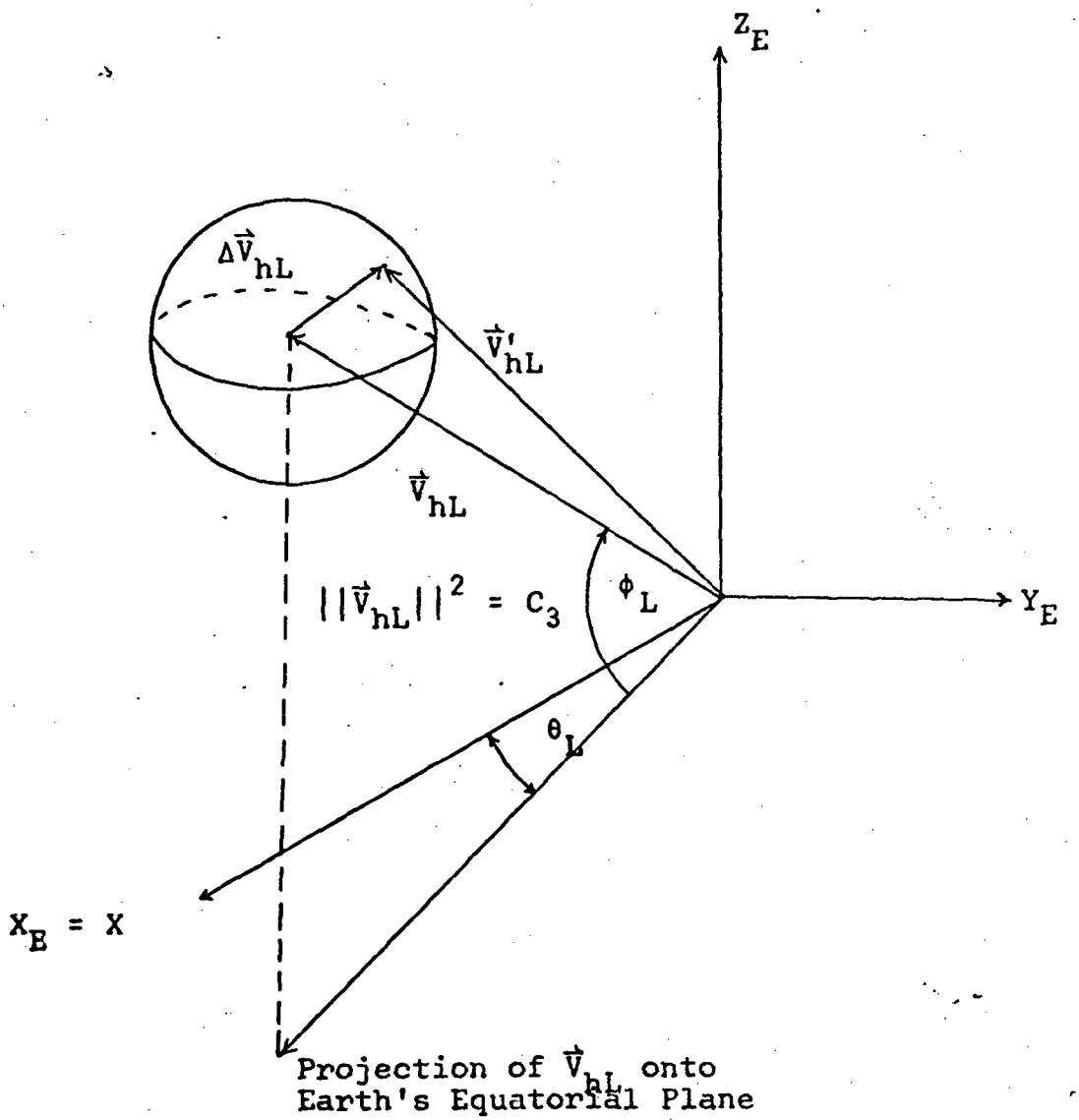

Figure B-6: Spherically Distributed Velocity Error

$$\Delta\bar{V}_{hL} = \frac{\partial\bar{V}_{hL}}{\partial\phi_L}\,\Delta\phi_L + \frac{\partial\bar{V}_{hL}}{\partial\theta_L}\,\Delta\theta_L + \frac{\partial\bar{V}_{hL}}{\partial C_3}\,\Delta C_3, \text{ or:}$$

$$\Delta\bar{V}_{hL} = \begin{pmatrix} -\sqrt{C_3}\,(\text{Sin}\,\phi_L \text{Cos}\,\theta_L\,\Delta\phi_L + \text{Cos}\,\phi_L\,\text{Sin}\,\theta_L\,\Delta\theta_L) + \dfrac{\text{Cos}\phi_L\,\text{Cos}\theta_L\,\Delta C_3}{2\sqrt{C_3}} \\ -\sqrt{C_3}\,(\text{Sin}\,\phi_L\,\text{Sin}\,\theta_L\,\Delta\phi_L - \text{Cos}\,\phi_L\,\text{Cos}\,\theta_L\,\Delta\theta_L) + \dfrac{\text{Cos}\phi_L\,\text{Sin}\theta_L\,\Delta C_3}{2\sqrt{C_3}} \\ \sqrt{C_3}\,\text{Cos}\,\phi_L\,\Delta\phi_L + \dfrac{\text{Sin}\phi_L\,\Delta C_3}{2\sqrt{C_3}} \end{pmatrix}$$

Since $\Delta\bar{V}_{hL}$ is quite small relative to $\bar{V}_{hL}$, the transformation from Earth Equatorial to Ecliptic coordinates can be neglected for $\Delta\bar{V}_{hL}$; hence, the actual heliocentric velocity vector at Earth injection is given by:

$$\bar{V}_L' = \bar{V}_L + \Delta\bar{V}_{hL}$$

Using $\bar{V}_L'$ as the launch velocity, a series of elliptical formulas are solved determining the perturbed trajectory to the point in question. BMISS eventually solves (see Figure B-7):

$$R_P' = a'\,(1-e'\,\text{Cos}\,E_P')$$

where: $R_P' = ||\bar{R}_P'||$ = the magnitude of $\bar{R}_P'$, the true position of the spacecraft on the perturbed trajectory at a time from launch equal to $\tilde{T}$. The reference trajectory position at this time is of course $\bar{R}_P$. If the point of interest is Jupiter, $\bar{R}_P$ is of course Jupiter's heliocentric position vector.

a', e', p', and E_P'=the semi-major axis, the eccentricity, the semi-latus rectum, and the eccentric arrival anomaly respectively of the perturbed trajectory.

The angular momentum vector ($\bar{h}'$) of the heliocentric perturbed trajectory is given by:

$$\bar{h}' = \bar{R}_L \times \bar{V}_L', \; h' = ||\bar{h}'||$$

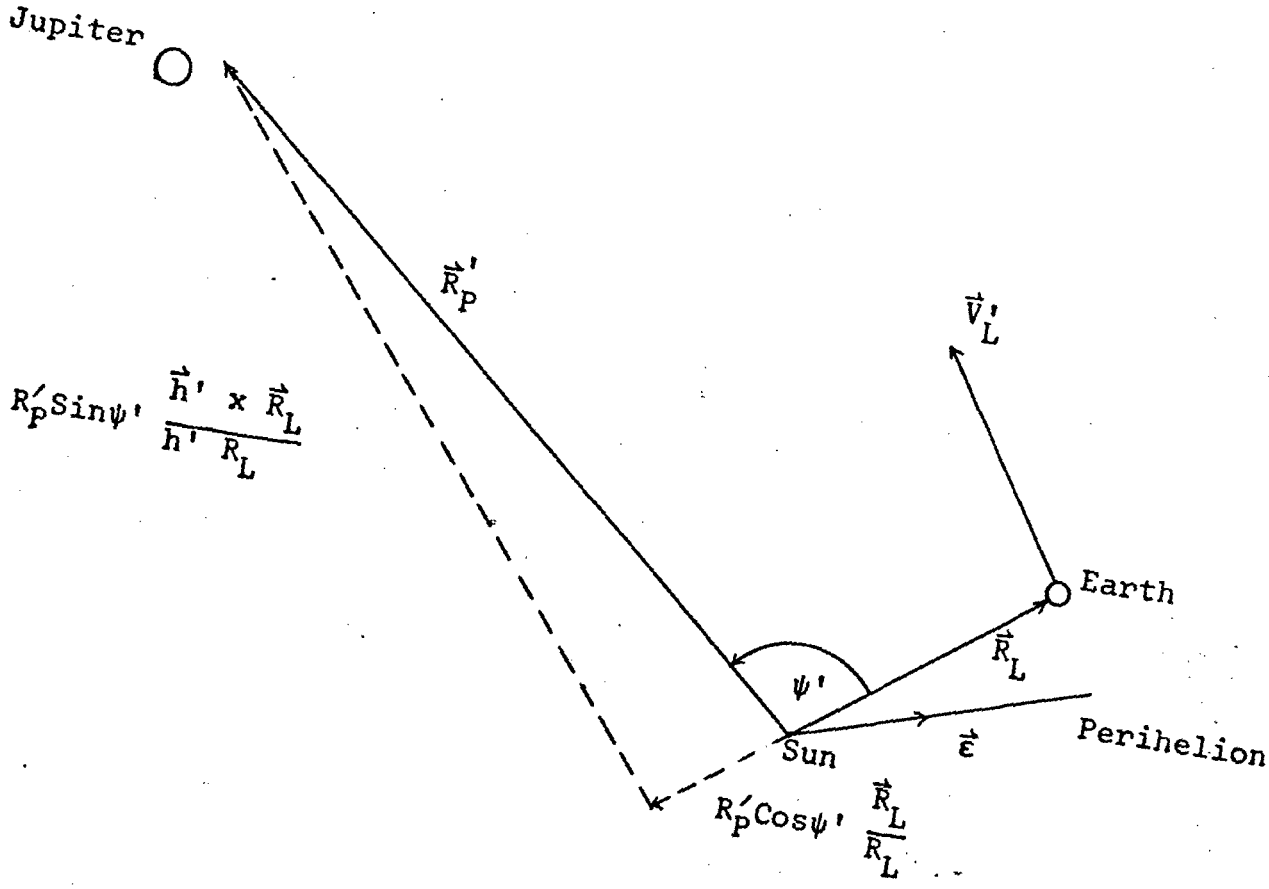

Figure B-7: Geometry Related to $\vec{R}_p'$

The vector $\bar{R}'_P$ is then determined from:

$$\bar{R}'_P = R'_P \left(\frac{\bar{R}_L}{R_L} \text{Cos } \Psi' + \frac{\bar{h}' \times \bar{R}_L}{h' R_L} \text{ Sin } \Psi' \right)$$

where: Ψ' = heliocentric transfer angle of the perturbed trajectory.

A vector $(\bar{\varepsilon})$ of magnitude e' in the direction of perihelion of the perturbed trajectory is given as:

$$\bar{\varepsilon} = \frac{\bar{V}'_L \times \bar{h}'}{GM_s} - \frac{\bar{R}_L}{R_L}$$

The heliocentric velocity at $\bar{R}'_P$ of the perturbed trajectory is:

$$\bar{V}'_P = \frac{\bar{h}'}{p'} \times \left(\frac{\bar{R}'_P}{R'_P} + \bar{\varepsilon} \right)$$

This is the farthest that BMISS proceeds in solving for $\bar{B}$, as $\bar{B}$ is solved in the main program for encounter with Jupiter only. As a final step, for the launch to the first mid-course maneuver, or the first to the second mid-course maneuver, BMISS sets $\bar{R}_L = \bar{R}'_P$ for reasons to be explained below.

6. Subprogram RCHANG

Subroutine RCHANG merely varies the heliocentric position of Jupiter by:

$$\bar{R}_P = \bar{R}_P + t \, \bar{V}_J,$$

where t is a small time interval ($|t| \leq 10.5$ days).

7. Main Program JOSE

JOSE, calling all subprograms, completely solves the Earth-Jupiter trajectories including one or two midcourse maneuvers and miss parameters. Figure B-8 is the flow diagram of JOSE.

JOSE commences by reading in the input for a selected trajectory; i.e., T_F, $\bar{R}_L$, $\bar{V}_E$, $\bar{R}_P$, $\bar{V}_J$. TRAPAR is immediately called and solves the trajectory.

TRAPAR will incidentally determine whether a trajectory is possible or not before solving, given the above input. JOSE then prints as output the values T_F, $\bar{R}_L$, ϕ_L, and C_3.

The first midcourse maneuver to null injection errors is taken to be 10 days ($\tilde{T}$) after launch. BMISS is then called, which solves for the actual position ($\bar{R}_P'$) of the spacecraft after $\tilde{T}$ = 10 days. BMISS now sets $\bar{R}_L = \bar{R}_P'$; thus the actual position of the spacecraft after 10 days from launch becomes a new launch vector $\bar{R}_L$ for determining the trajectory between $\bar{R}_P'$ and Jupiter. The trajectory time left from the first midcourse maneuver ($\bar{R}_P'$) to Jupiter is of course $T_F-\tilde{T}$. Thus, if T_F is now set equal to $T_F-\tilde{T}$ and TRAPAR is again called, a new trajectory is determined from the first mid-course maneuver to Jupiter. $\bar{V}_L$, solved by TRAPAR, is now the velocity vector necessary at the first mid-course maneuver to arrive at Jupiter in T_F-10 days. However, the actual velocity vector ($\bar{V}_P'$) at this position has been solved by BMISS. Thus, the first mid-course velocity correction ($\Delta\bar{V}_1$) must be $\bar{V}_L - \bar{V}_P$. Although the trajectory from the first mid-course maneuver to Jupiter will nearly coincide with the original reference trajectory from Earth to Jupiter, the difference is significant in the fact that $\Delta V_1 = ||\Delta\bar{V}_1||$ may be extremely large. Since this ΔV_1 must be supplied by the spacecraft (implying propellant weight), a solution must be sought to reduce this ΔV_1 to practical limits. This is accomplished by simply relaxing the constraint on the remaining time of flight (T_F-10 days). By allowing the SC to arrive sooner or later than the original selected arrival time, various trajectories from the first mid-course to Jupiter can be computed, the corresponding ΔV_1 compared, and a minimum ΔV_1 selected. This is the reason for Subprogram RCHANG; as the arrival time is varied, Jupiter's position must be varied.

Explicitly then, with T_F-10 days remaining on the trajectory, T_F of TRAPAR is set successively equal to $(T_F-10)-5.5$ up to $T_F=(T_F-10)+5.5$ in steps of .1

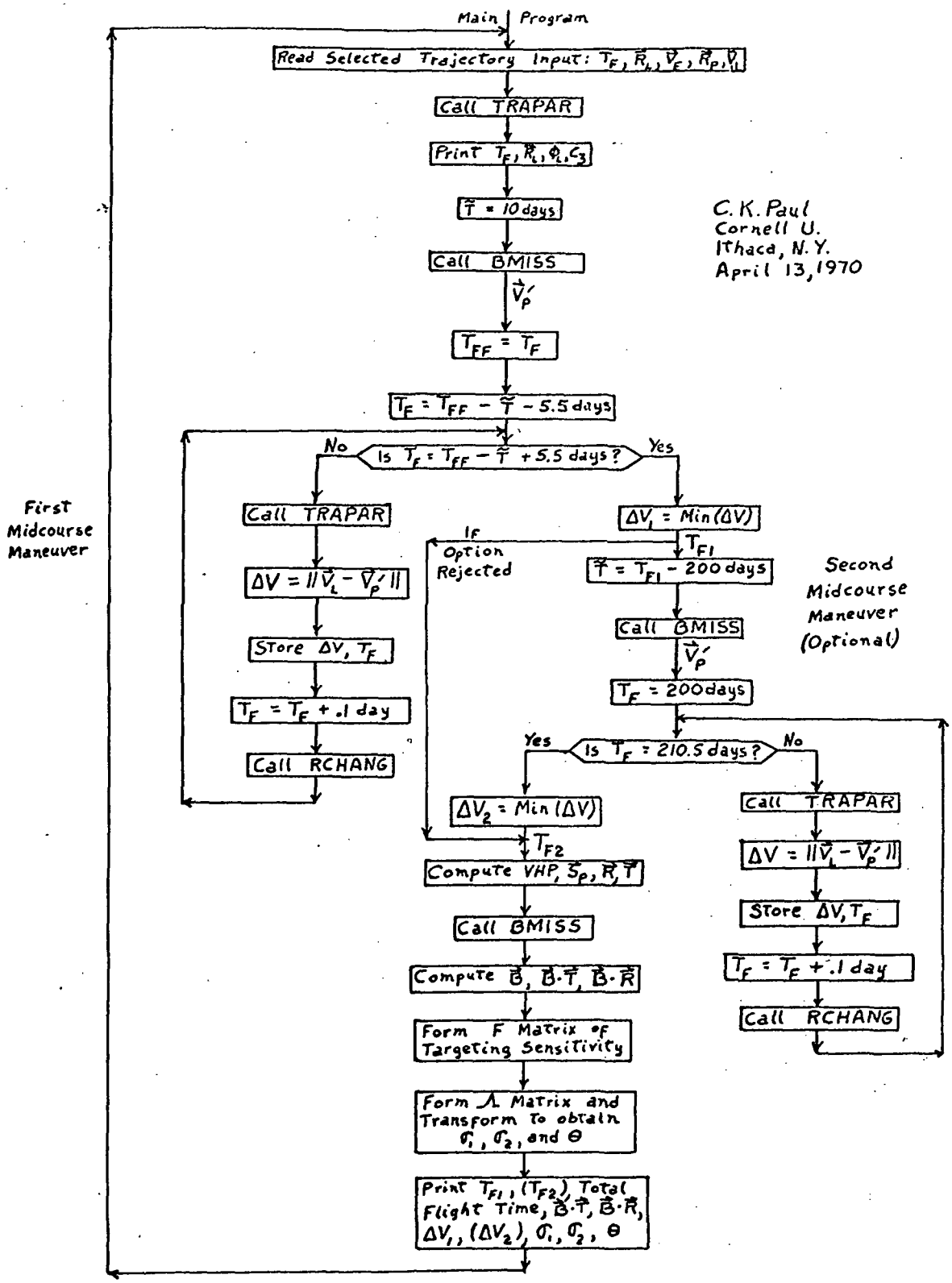

C. K. Paul
Cornell U.
Ithaca, N. Y.
April 13, 1970

Figure B–8: JOSE Flow Diagram

day, and TRAPAR called for each of these values T_F yielding a value ΔV_1. The minimum ΔV_1 and the corresponding trajectory are then selected as the new reference trajectory from the first midcourse to Jupiter. The T_F corresponding to ΔV_1 is termed T_{F1} and is the actual time from the first midcourse to Jupiter encounter. RCHANG has changed Jupiter's position to:

$$\bar{R}_P = \bar{R}_P + \bar{V}_J \, (T_{F1} + 10 - T_{FF})$$

where: T_{FF} = originally selected time of flight.

For the graphs presented in Appendix A, only this one midcourse maneuver is considered since (1) except for ΔV, the other six parameters; i.e., C_3, ϕ_L, VHP, σ_1, σ_2, and θ are hardly affected at all by additional midcourse maneuvers, and (2) at this phase of the analysis, only relative comparisons of the ΔV for different trajectories are desired, and one ΔV_1 for each trajectory suffices for this purpose.

For the three trajectories chosen later for more detailed analysis, however, a second midcourse maneuver is performed at 200 days before Jupiter encounter, hence this maneuver will now be described. The second midcourse maneuver (ΔV_2) is necessary to null propulsion velocity errors associated with the first midcourse maneuver, and hence reduce the magnitude of the miss vector $\bar{B}$ at Jupiter.

In initiating the second midcourse maneuver, JOSE again calls BMISS, this time with $\tilde{T} = T_{F1}$-200 days. Thus BMISS returns $\bar{R}'_P$, the true perturbed position of the SC at the second midcourse maneuver as well as $\bar{V}'_P$. BMISS now sets $\bar{R}_L = \bar{R}'_P$, hence the second midcourse point becomes the new launch position for a new trajectory to Jupiter. As with the first midcourse, JOSE now calls on TRAPAR, with T_F = 200 days, to solve the last elliptical segment between $\bar{R}'_P$ and Jupiter. TRAPAR then returns $\bar{V}_L$, the velocity vector at the second midcourse point, and $\Delta V_2 = ||\bar{V}_L - \bar{V}'_P||$. As may be expected, ΔV_2 will turn out to be

extremely large, hence T_F= 200 days must be relaxed and allowed to vary.

For all three selected trajectories, it resulted that the minimum ΔV_2 occurred for a T_{F2} = 210.5 days, which was the maximum amount T_F was allowed to vary. By increasing T_F to values greater than 210.5 days, further significant reductions in ΔV_2 could have been brought about. This was not performed for the following reasons:

(1) T_{F2} > 210.5 days implies a trajectory lasting more than 10 days longer than the original selected T_{FF} trajectory. Since RCHANG is changing Jupiter's position with instantaneous values of position ($\bar{R}_P$) and orbital velocity ($\bar{V}_J$), a time lag over 10 days results in RCHANG losing accuracy in computing Jupiter's position. This problem could be remedied by simply tabulating later Jupiter state vectors from the ephemerides, but it was decided that it was not meaningful to devote this time in reducing ΔV_2 because of (2) below.

(2) At a slightly later time; i.e., at about two to four months after the second maneuver, JOSE will be entering Jupiter's sphere of influence where a third midcourse maneuver (ΔV_3) is performed to pass at a desired periapsis distance from Jupiter's center. Thus it is not necessary to apply the entire ΔV_2 at the second midcourse maneuver (ΔV_2 turns out to be around 2.3 km/sec for the three trajectories, far too excessive to be considered a midcourse maneuver).

(3) In a real-time Jupiter mission, of course, JOSE is continuously tracked by DSN, hence trajectory perturbations can be compensated by numerous incremental corrections rather than allowing the first midcourse maneuver errors to propagate to the second maneuver point, where these errors are now quite large.

(4) In defense of the second midcourse maneuver in this program, ΔV_2

functions to reduce the $\overline{B}$ vector significantly at Jupiter for meaningful comparisons of the three trajectories. In conclusion, then, ΔV_2 from program JOSE is rather meaningless in itself; the miss vector $\overline{B}$ is significant for comparison purposes. It might also be remarked that the SC will not follow the asymptote of the approach hyperbola in Jupiter's gravity field anyway, hence $\overline{B}$ represents a fictitious SC position.

In the case of the three selected trajectories with the second midcourse maneuver, the values e, a, and v_P of the trajectory corresponding to the minimum ΔV_2 were determined by TRAPAR for the corresponding T_{F2}(= 210.5 days). $\overline{R}_P$ is now the position vector of Jupiter for the date equal to the actual total number of days of flight after Earth launch date; i.e., 10 + T_{F1} - 200 +T_{F2}) or T_{F1} + T_{F2} - 190 days past launch. Eq. (B-1) of section 3 gives Ψ for the last small elliptical segment, the eq. (B-2) of section 4 yields $\overline{W}$, and equations (B-3) of section 4, with the subscripts L replaced by P, determine Γ_P and $\overline{V}_P$. For all the one-midcourse trajectories of Appendix A, e, a, and v_P are determined by TRAPAR for the trajectory corresponding to the minimum ΔV_1 and T_{F1}. $\overline{R}_P$ is the position vector of Jupiter at a date equal to 10+T_{F1} days after Earth launch date.

The important hyperbolic excess velocity at Jupiter is now determined:

$$VHP = ||\overline{V}_P - \overline{V}_J||, \quad \overline{VHP} = \overline{V}_P - \overline{V}_J$$

The $\overline{S}_P$, $\overline{R}$, $\overline{T}$ vectors are then formed by:

$$\overline{S}_P = \overline{VHP}/VHP, \ \overline{S}_P = \text{unit vector in direction of } \overline{VHP}$$

$\overline{T}$ is defined as a vector normal to $\overline{S}_P$ and lying in the ecliptic plane.

$$\overline{T} = \overline{S}_P \times \overline{N}$$

where N = unit normal to ecliptic.

$\overline{R}$ determines the right handed $\overline{S}_P$, $\overline{T}$, $\overline{R}$ system:

$$\overline{R} = \overline{S}_P \times \overline{T}$$

BMISS is called once more, requiring of course the input ΔC_3, $\Delta\phi_L$, and $\Delta\theta_L$ corresponding to either the second or first mid-course maneuver, depending on whether two maneuvers or one maneuver is performed. BMISS now computes $\bar{R}'_P$, the actual position of the SC at time of encounter, and $\bar{V}'_P$, the actual velocity vector at encounter.

Figure B-9 describes the geometry of the miss vector $\bar{B}$ at Jupiter. The perturbed planetocentric velocity is then:

$$\bar{V}'_{hP} = \bar{V}'_P - \bar{V}_J$$

Noting from Figure B-9 that $\Delta\bar{R}'_P = \bar{R}'_P - \bar{R}_P$, the expected error ($\Delta T_F$) in the time of arrival at the closest point of approach P at Jupiter is given by:

$$\Delta T_F = \frac{\Delta\bar{R}'_P \cdot \bar{V}'_{hP}}{V'^2_{hP}}, \quad \text{where} \quad V'_{hP} = ||\bar{V}'_{hP}||$$

The important miss vector $\bar{B}$ is given as:

$$\bar{B} = \Delta\bar{R}'_P - \Delta T_F \bar{V}'_{hP}$$

$\bar{B}$ is of course in the $\bar{R}$-$\bar{T}$ plane, and the R and T components of $\bar{B}$ are computed as $\bar{B}\cdot\bar{R}$ and $\bar{B}\cdot\bar{T}$ respectively.

The last portion of Program JOSE maps injection or midcourse errors into the dispersion ellipsoid at Jupiter. The reader is referred to JPL ballistic transfer trajectories to Venus for background development; however the following remarks should suffice for the developmental procedure. (See also Figure B-10).

Figure B-10 illustrates the mapping from Earth injection to Jupiter encounter; however, in this program, the mapping of interest is the mapping of the last midcourse maneuver to Jupiter encounter. Program JOSE accounts for this by taking $\bar{V}_{hL}$ as the heliocentric velocity vector at the last midcourse man

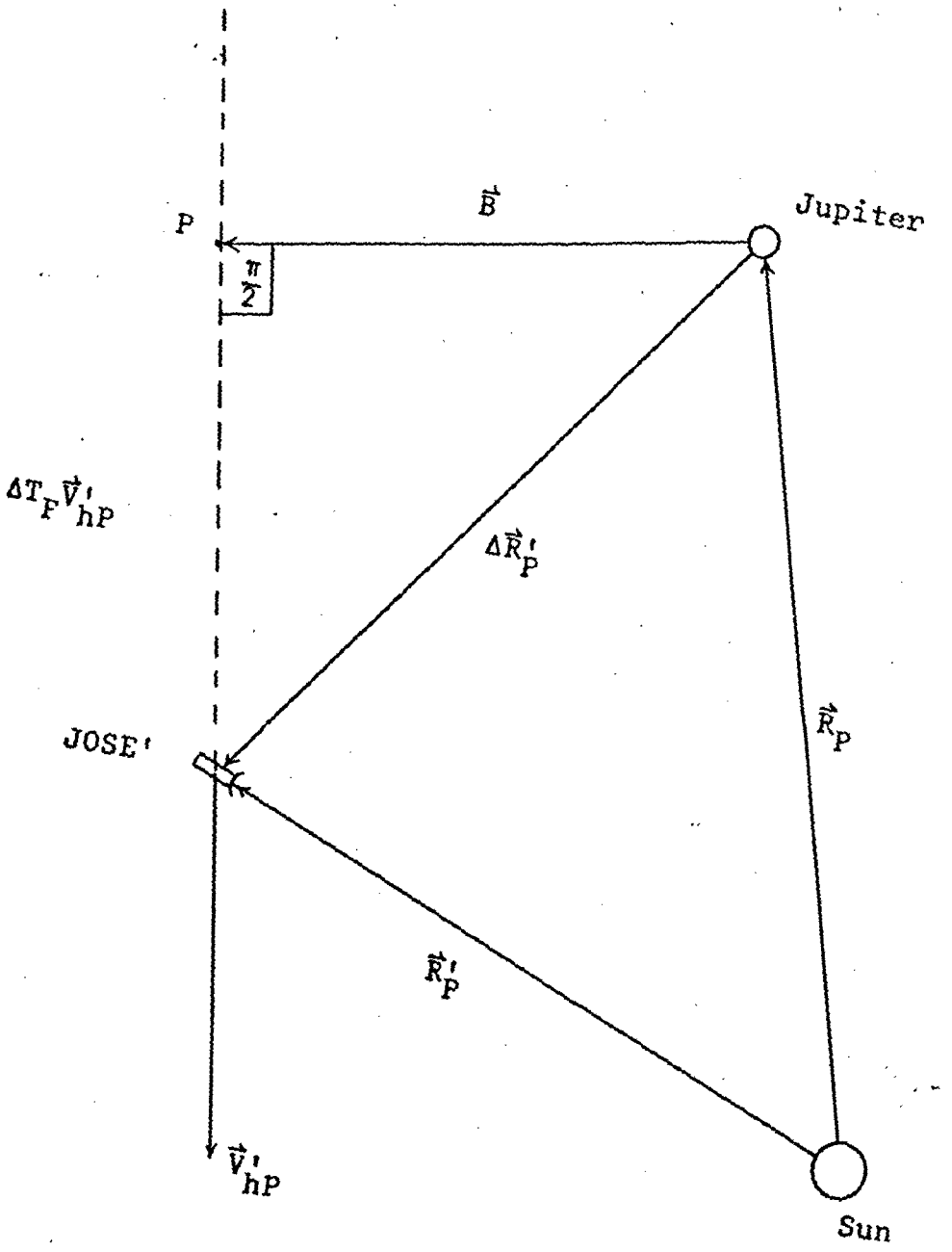

Figure B-9: Geometry Related to $\vec{B}$

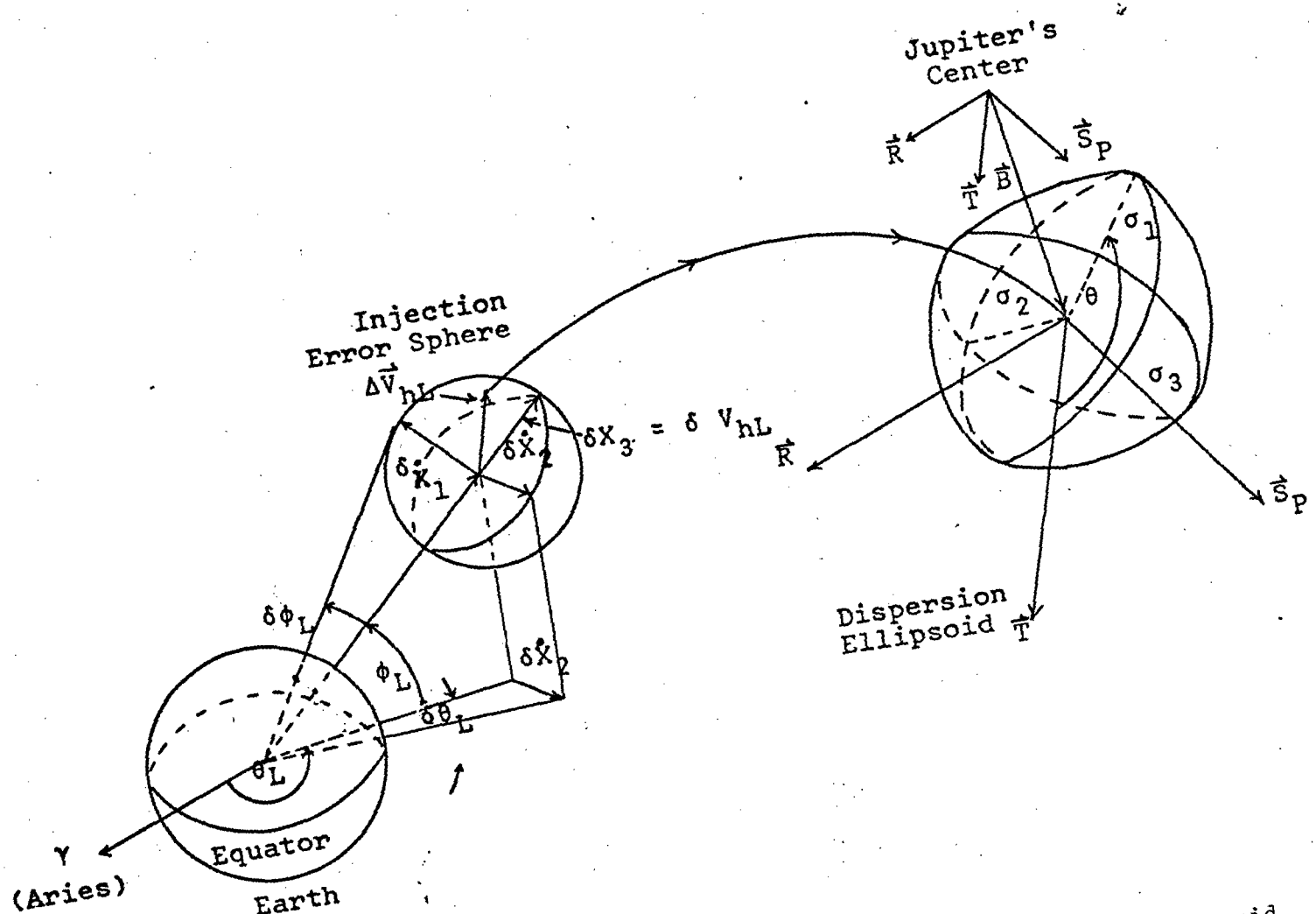

Figure B-10: Mapping of Velocity Errors into the Dispersion Ellipsoid at Jupiter. Injection Error Sphere and Dispersion Ellipsoid Sizes Exaggerated for Clarity.

and ϕ_L and θ_L are referred to the ecliptic rather than Earth's equator (since $\overline{V}_{hL}$ is referred to the X, Y, Z coordinate system, X-Y defining the ecliptic).

The mapping proceeds as follows. A convenient coordinate system ($\delta\dot{X}_1$, $\delta\dot{X}_2$, $\delta\dot{X}_3$) is introduced such that $\delta\dot{X}_3$ is in the direction of $\overline{V}_{hL}$, $\delta\dot{X}_1$ is normal to $\delta\dot{X}_3$ in the direction of increasing declination (plane in which ϕ_L is measured), and $\delta\dot{X}_2$ is in the direction of decreasing right ascension (plane in which θ_L is measured). A matrix F of partial derivatives must now be formed, where:

$$F = \begin{pmatrix} \frac{\partial(\overline{B}\cdot\overline{T})}{\partial\dot{X}_1} & \frac{\partial(\overline{B}\cdot\overline{T})}{\partial\dot{X}_2} & \frac{\partial(\overline{B}\cdot\overline{T})}{\partial\dot{X}_3} \\ \frac{\partial(\overline{B}\cdot\overline{R})}{\partial\dot{X}_1} & \frac{\partial(\overline{B}\cdot\overline{R})}{\partial\dot{X}_2} & \frac{\partial(\overline{B}\cdot\overline{R})}{\partial\dot{X}_3} \\ \frac{\partial\Delta T_F}{\partial\dot{X}_1} & \frac{\partial\Delta T_F}{\partial\dot{X}_2} & \frac{\partial\Delta T_F}{\partial\dot{X}_3} \end{pmatrix}$$

For the parameters $\overline{B}\cdot\overline{T}$, $\overline{B}\cdot\overline{R}$, and ΔT_F; the elements of the matrix F indicate the sensitivity of these parameters with respect to changes in $\delta\dot{X}_1$, $\delta\dot{X}_2$, and $\delta\dot{X}_3$. These partial derivatives can be formed by the chain rule and noting from Figure B-10 that:

$$\delta\dot{X}_1 = V_{hL}\,\delta\phi_L$$

$$\delta\dot{X}_2 = -V_{hL}\,\text{Cos}\,\phi_L\,\delta\theta_L$$

$$\delta\dot{X}_3 = \delta V_{hL} = \frac{\delta C_3}{2V_{hL}}\text{, since } C_3 = V_{hL}^2$$

Thus, for example, the first element of the F matrix is formed by:

$$\frac{\partial(\overline{B}\cdot\overline{T})}{\partial\dot{X}_1} = \frac{\delta\phi_L}{\partial\dot{X}_1} \cdot \frac{\partial(\overline{B}\cdot\overline{T})}{\partial\phi_L}\text{, hence, the elements of F become:}$$

$$\frac{\partial(\bar{B}\cdot\bar{T})}{\partial\dot{X}_1} = \frac{1}{V_{hL}} \frac{\partial(\bar{B}\cdot\bar{T})}{\partial\phi_L}$$

$$\frac{\partial(\bar{B}\cdot\bar{T})}{\partial\dot{X}_2} = \frac{-1}{V_{hL}\text{Cos}\phi_L} \frac{\partial(\bar{B}\cdot\bar{T})}{\partial\theta_L}$$

$$\frac{\partial(\bar{B}\cdot\bar{T})}{\partial\dot{X}_3} = 2\, V_{hL} \frac{\partial(\bar{B}\cdot\bar{T})}{\partial C_3}$$

$$\frac{\partial(\bar{B}\cdot\bar{R})}{\partial\dot{X}_1} = \frac{1}{V_{hL}} \frac{\partial(\bar{B}\cdot\bar{R})}{\partial\phi_L}$$

$$\frac{\partial(\bar{B}\cdot\bar{R})}{\partial\dot{X}_2} = \frac{-1}{V_{hL}\text{Cos}\phi_L} \frac{\partial(\bar{B}\cdot\bar{R})}{\partial\theta_L}$$

$$\frac{\partial(\bar{B}\cdot\bar{R})}{\partial\dot{X}_3} = 2\, V_{hL} \frac{\partial(\bar{B}\cdot\bar{R})}{\partial C_3}$$

$$\frac{\partial\Delta T_F}{\partial\dot{X}_1} = \frac{1}{V_{hL}} \frac{\partial\Delta T_F}{\partial\phi_L}$$

$$\frac{\partial\Delta T_F}{\partial\dot{X}_2} = \frac{-1}{V_{hL}\text{Cos}\phi_L} \frac{\partial\Delta T_F}{\partial\theta_L}$$

$$\frac{\partial\Delta T_F}{\partial\dot{X}_3} = 2\, V_{hL} \frac{\partial\Delta T_F}{\partial C_3}$$

The next problem is to determine the partial differentials of $\bar{B}\cdot\bar{T}$, $\bar{B}\cdot\bar{R}$, and ΔT_F with respect to each of ϕ_L, θ_L, and C_3. A numerical differentiation is the only feasible solution, hence $\Delta\phi_L$, $\Delta\theta_L$, and ΔC_3, applied as midcourse velocity errors at the last midcourse maneuver before encounter, are allowed

to vary be small amounts, each in turn, and the changes produced in $\overline{B}\cdot\overline{T}$, $\overline{B}\cdot\overline{R}$, and ΔT_F as a result of each of these variations is computed by BMISS. Thus BMISS is called nine times in succession, and the numerical division of the change in, for example, $\overline{B}\cdot\overline{T}$ by the selected change in $\Delta\phi_L$, for example, becomes $\delta(\overline{B}\cdot\overline{T})/\delta\phi_L$. Thus the F matrix of targeting sensitivity is formed.

The mapping of velocity errors at midcourse into a dispersion ellipse at Jupiter is given by the quadratic form: $v^T \Lambda\, v = 1$, which defines an ellipsoid about the target point in the $\overline{R}$-$\overline{T}$ plane, where:

v = any vector from an orgin at the target point to the surface of the ellipsoid.

$\Lambda = \sigma_v^2\, F\, F^T$, a symmetric matrix

σ_v = the 1-sigma variance in the propulsion motor velocity, assumed as 0.1 meter/sec.

For convenience, the elements of Λ are written:

$$\Lambda = \begin{pmatrix} \sigma_T^2 & \rho_{RT}\sigma_R\sigma_T & \rho_{TF}\sigma_F\sigma_T \\ & \sigma_R^2 & \rho_{RF}\sigma_F\sigma_R \\ \text{symmetric} & & \sigma_F^2 \end{pmatrix}$$

By setting: $\text{Tan } 2 = \dfrac{2\rho_{RT}}{\sigma_T/\sigma_R - \sigma_R/\sigma_T}$ (if $\rho_{RT} \geq 0$, $0 \leq \theta \leq \frac{\pi}{2}$) (if $\rho_{RT} < 0$, $\frac{\pi}{2} \leq \theta \leq \pi$)

solving for θ, forming a matrix L of eigenvectors of Λ by:

$$L = \begin{pmatrix} \text{Cos}\theta & \text{Sin}\theta & 0 \\ -\text{Sin}\theta & \text{Cos}\theta & 0 \\ 0 & 0 & 1 \end{pmatrix}$$

and then pre- and post-multiplying Λ by L and L^T respectively, the basis for v is rotated such that the upper left 2x2 partition of $L\,\Lambda\,L^T$ is diagonalized,

and the eigenvalues squared of Λ are the diagonal elements. The eigenvalues are the semi-major axis and semi-minor axis of the dispersion ellipsoid in the $\overline{R}$-$\overline{T}$ plane, and the second semi-minor axis in the direction of $\overline{S}_P$ represented in units of days. Thus:

$$L\Lambda L^T = \begin{pmatrix} \sigma_1^2 & 0 & \rho_{13}\sigma_1\sigma_3 \\ & \sigma_2^2 & \rho_{23}\sigma_2\sigma_3 \\ \text{symmetric} & & \sigma_3^2 \end{pmatrix}$$

where: $\sigma_1 = \sqrt{\sigma_T^2 \cos^2\theta + \sigma_R^2 \sin^2\theta + 2\rho_{RT}\sigma_R\sigma_T \sin\theta \cos\theta}$

$$\sigma_2 = \sqrt{\sigma_T^2 \sin^2\theta + \sigma_R^2 \cos^2\theta - 2\rho_{RT}\sigma_R\sigma_T \sin\theta \cos\theta}$$

and, although of no special interest to Program JOSE,

$$\sigma_3 = \sigma_F$$

$$\rho_{13}\sigma_1\sigma_3 = \rho_{TF}\sigma_F\sigma_T \cos\theta + \rho_{RF}\sigma_R\sigma_F \sin\theta$$

$$\rho_{23}\sigma_2\sigma_3 = -\rho_{TF}\sigma_F\sigma_T \sin\theta + \rho_{RF}\sigma_R\sigma_F \cos\theta$$

JOSE finally prints out the computed values of T_{F1}, T_{F2}, total flight time, $\overline{B}\cdot\overline{T}$, $\overline{B}\cdot\overline{R}$, ΔV_1, ΔV_2, σ_1, σ_2, and θ.

Appendix C 1

Selected Typical Trajectory Characteristics for the Attitude Control Study

Figure C1-1 describes a typical trajectory selected for the attitude control analysis performed in Chapter IV. Basic elements of this trajectory are:

1) Launch Date and Period: Nov. 25-Dec. 14, 1980 - 20 days.

2) Arrival Date: July 1, 1982

3) Time of Flight: 583 days

4) Injection Energy at Earth (C_3): 110 km^2/sec^2

The trajectory was also selected to minimize Earth-Jupiter communications distance at encounter.

Figure C1-1 was constructed with the aid of Section 5, Planetary Position Data, of "Trajectories to the Outer Planets Via Jupiter Swingby", NASA CR-61186, and numerous equations and a procedural summary found in JPL Technical Reports 32-521 and 32-77. The X-Y axis system defines the ecliptic of 1960.0, X is in the direction of the mean vernal equinox of 1960.0, and Y orthogonal to X. All three bodies; Earth, Jupiter, and JOSE, are nearly coplanar; as an example, at time of launch, Jupiter is roughly .1 a.u. below the ecliptic and steadily approaching it during the mission.

Figure C1-2 is a plot of the trajectory transfer angle as a function of time. The trajectory transfer angle (θ) is the angle measured counterclockwise from the Sun-Earth vector at launch to the Sun-probe vector. The total transfer angle is 152.8°.

Figure C1-3 shows the change in magnitude of the Sun-probe vector (r_2) with respect to time.

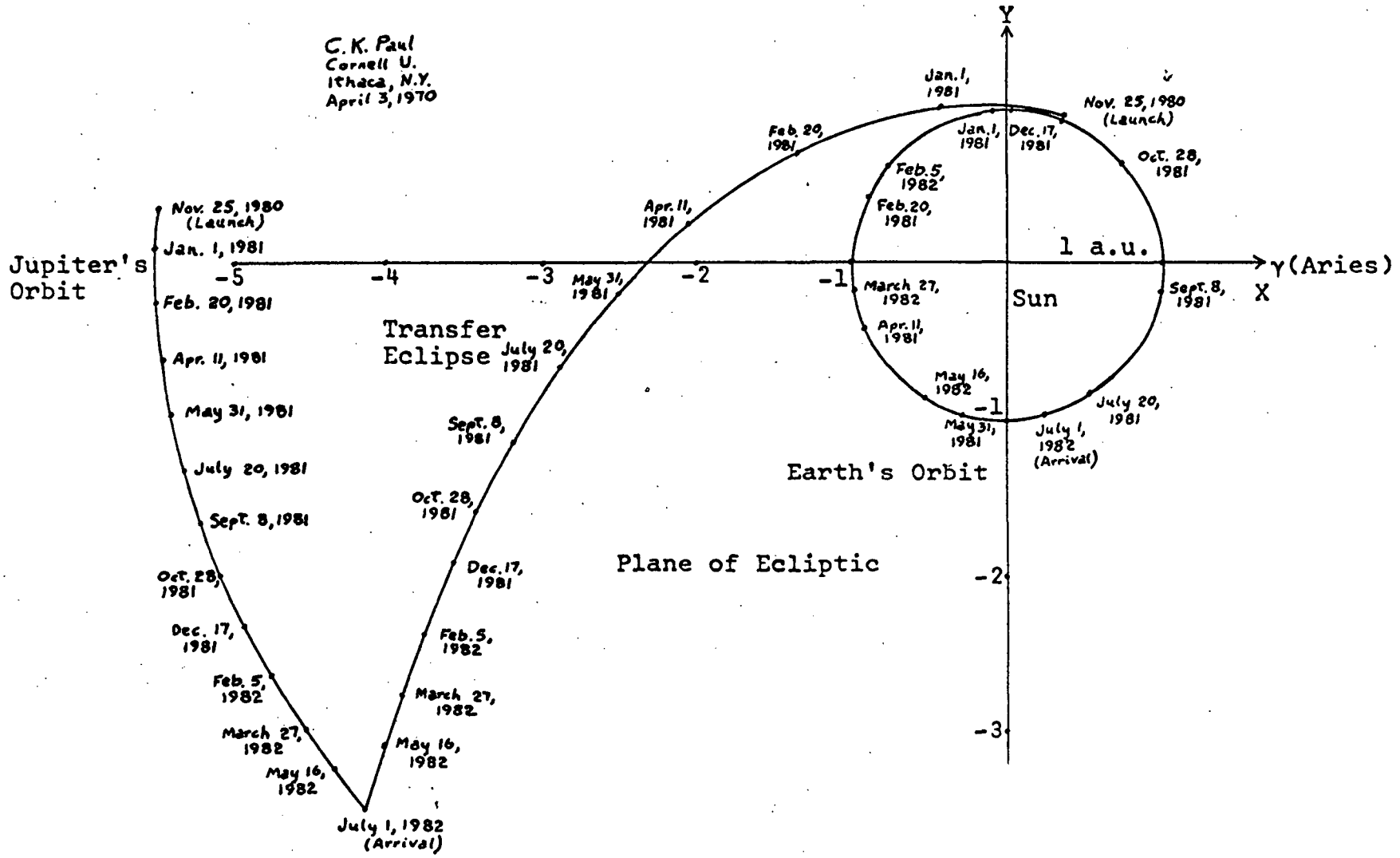

Figure C1-1: Heliocentric Transfer Ellipse, Earth-Jupiter, Nov. 25, 1980 - July 1, 1982

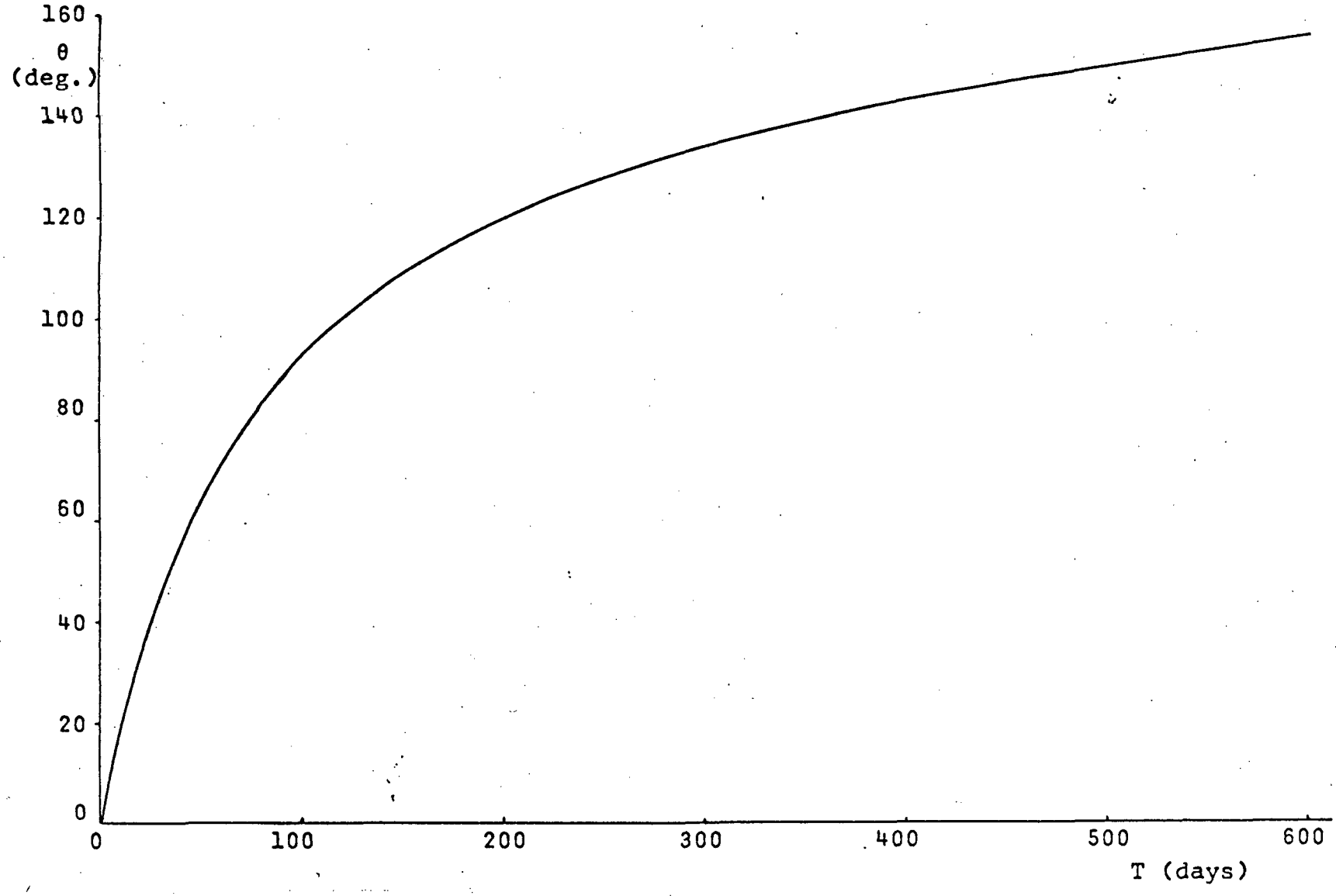

Figure C1-2: Heliocentric Transfer Angle (θ) vs. Time (T)

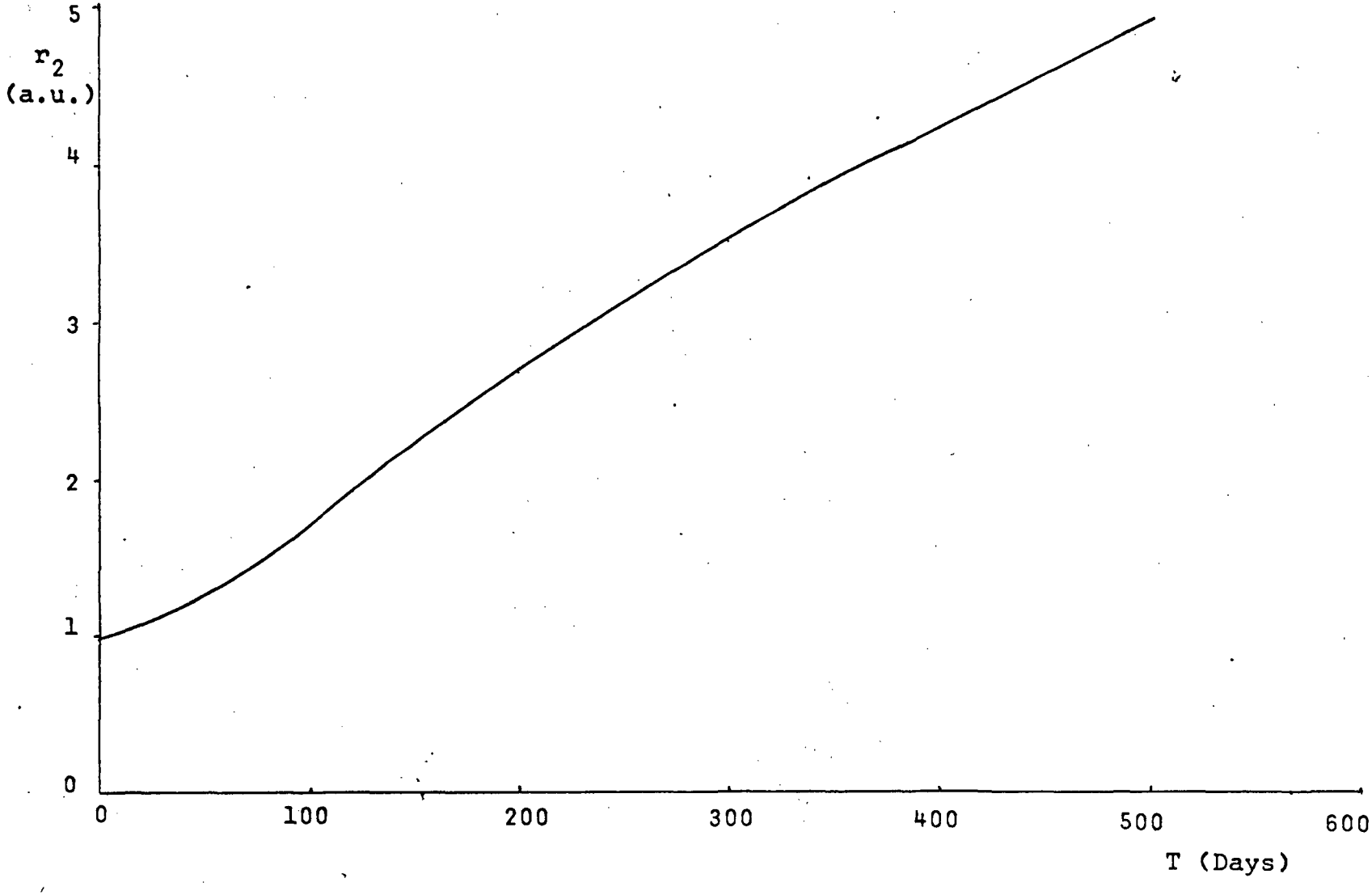

Figure C1-3: Probe-Sun Distance (r_2) vs. Time (T)

Figure C1-4 plots solar aspect angle (α) as a function of mission time. α is the Sun-SC-Earth angle, and can be seen to fluctuate with decreasing amplitude about 0° as a function of time. Mathematically,

$$\text{Cos } \alpha = \frac{\bar{r}_2 \cdot \bar{r}_E}{||\bar{r}_2||\ ||\bar{r}_E||}$$, where $\bar{r}_E$ = SC-Earth vector.

Figure C1-5 indicates the meteoroid relative approach angle (γ), with respect to the SC, as a function of time during interplanetary flight. γ_E measures the angle from the meteoroid velocity vector relative to the SC ($\bar{V}_{M/SC}$) to the SC-Earth vector; γ_S to the SC-sun vector. Figure C1-6 indicates $V_{M/SC}$ (magnitude of $\bar{V}_{M/SC}$) during the flight. See sketch below:

$\bar{V}_M$ = absolute velocity vector of meteoroid

$\bar{V}_{SC}$ = absolute velocity vector of JOSE

$\bar{V}_{M/SC} = \bar{V}_M - \bar{V}_{SC}$

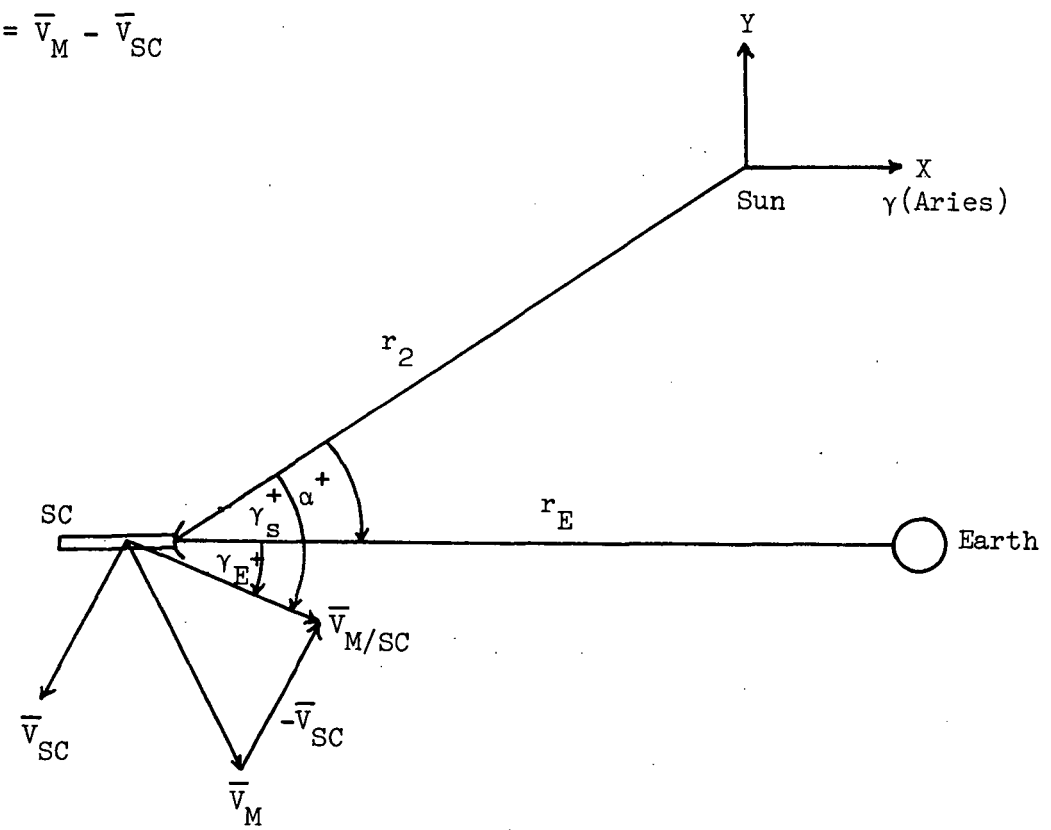

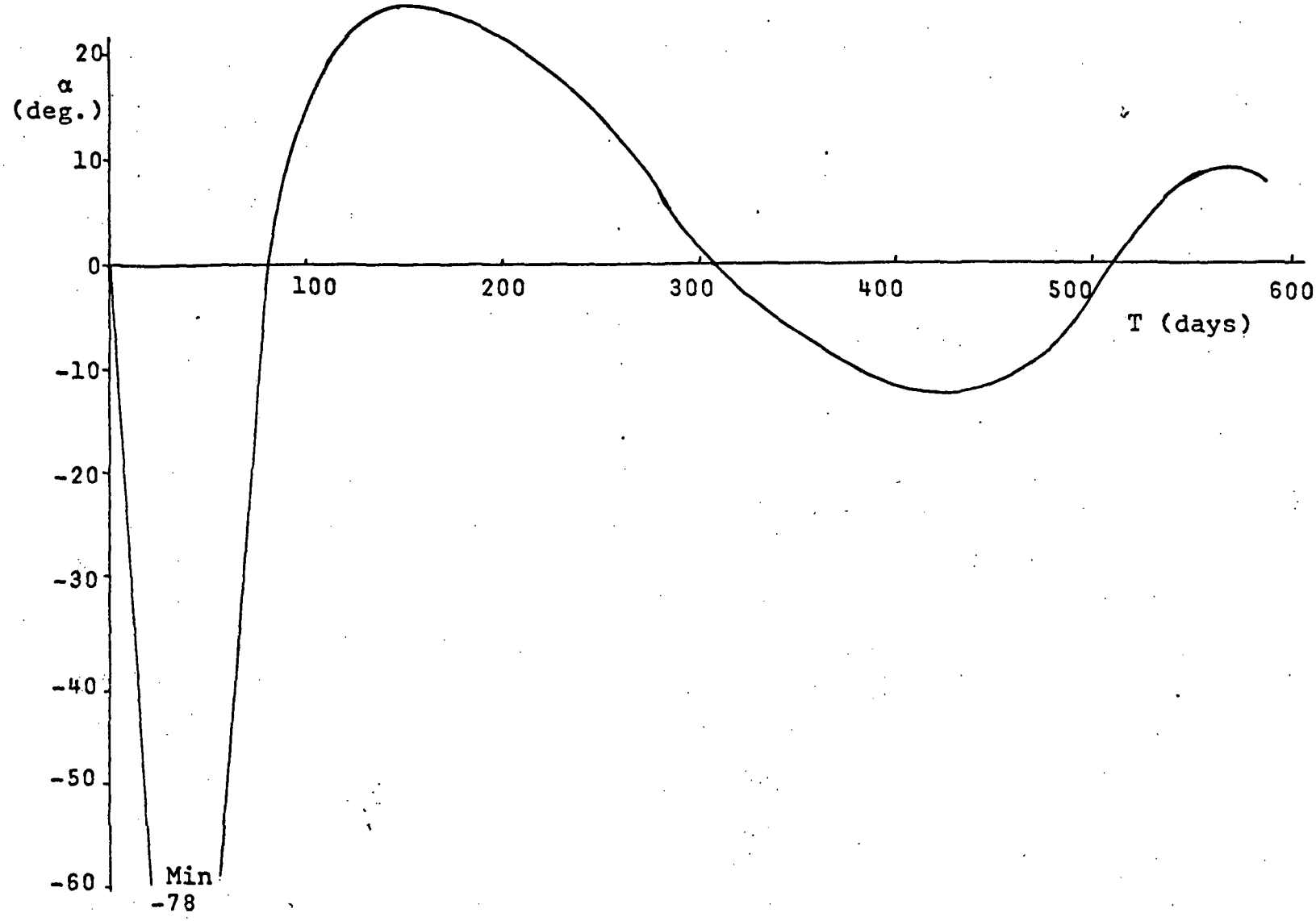

Figure C1-4: Solar Aspect Angle (α) vs. Time (T)

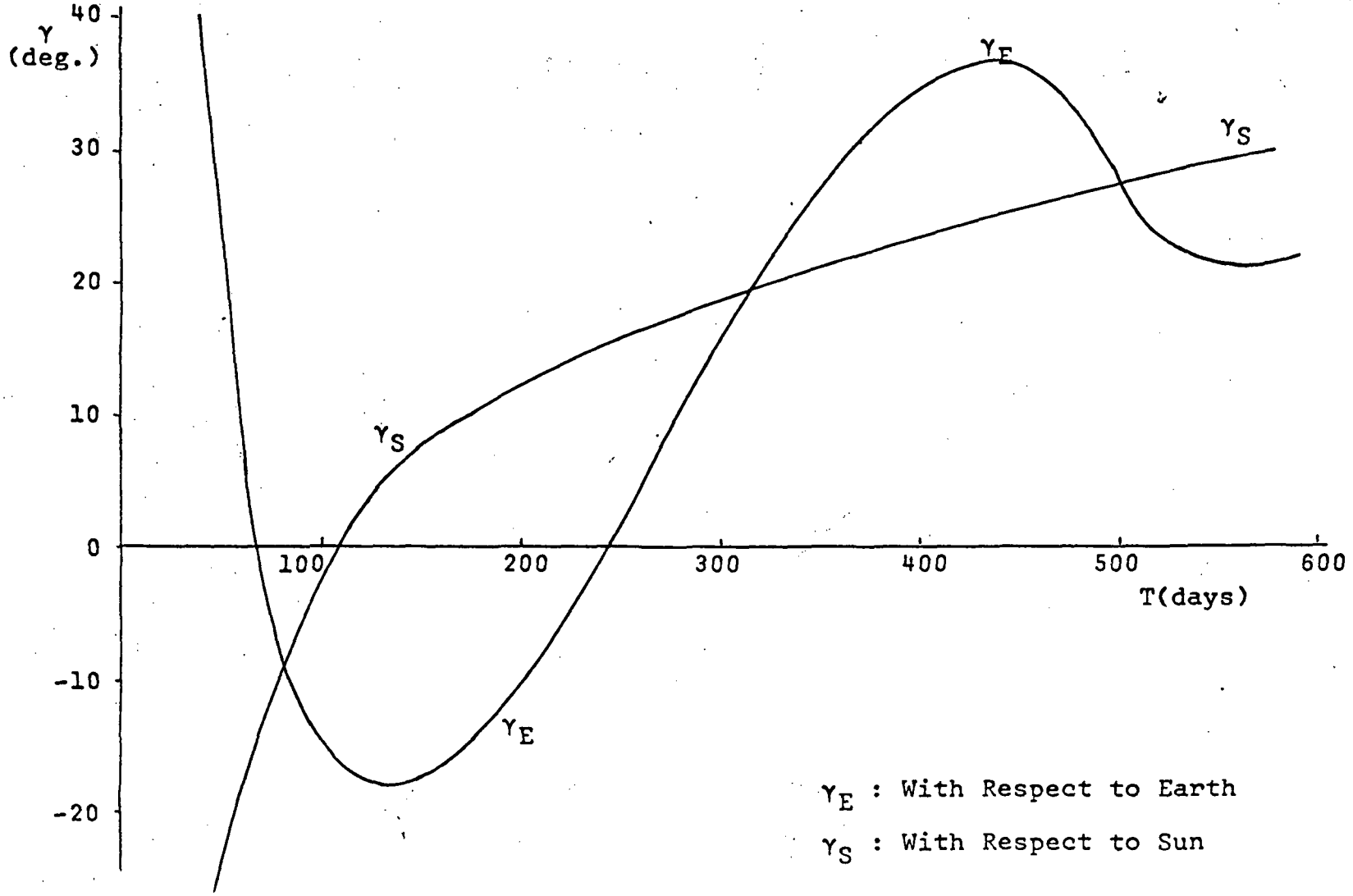

Figure C1-5: Meteoroid Relative Approach Angle (γ) vs. Time (T)

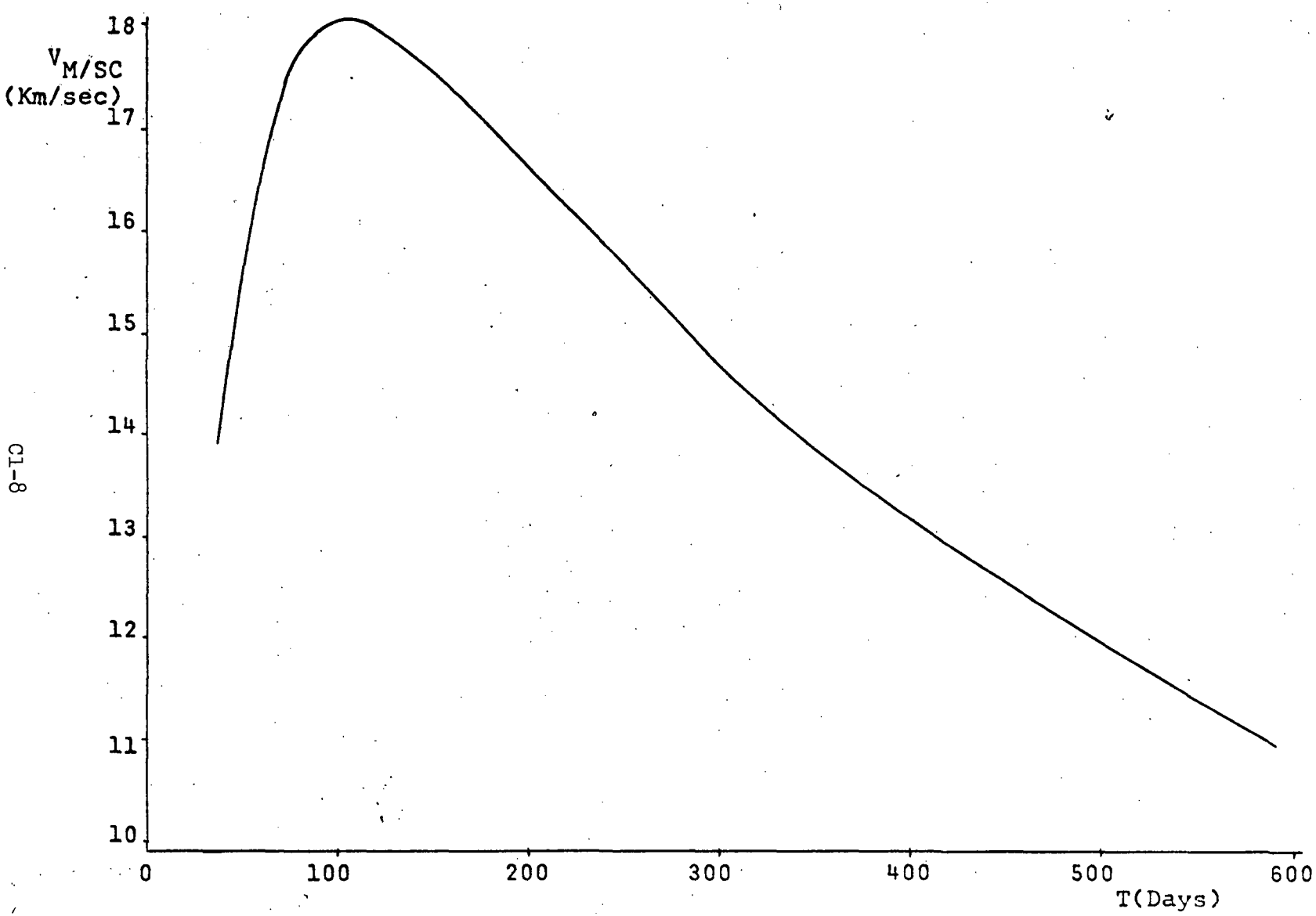

Figure C1-6: Meteoroid Relative Approach Velocity ($V_{M/SC}$) vs. Time (T)

Noting that a meteoroid mass is insignificant relative to the sun's mass (M_S), and noting that G is the Universal Gravitational Constant, the following equation is valid:

$$||\bar{V}_M|| = \sqrt{\frac{GM_S}{r_2}} = \frac{0.01721}{\sqrt{r_2}}$$ in units of a.u. per day, assuming a value of $GM_S = 2.96 \times 10^{-4}$ a.u.^{3}/day^2.

Meteoroid orbits about the sun are assumed circular. To verify the validity of this assumption, Vesta's average velocity is given as 0.0112 a.u./day, and average distance from the sun as 2.361 a.u. Assuming Vesta's orbit to be circlar, the orbital circumference is computed as:

$$2\pi \times 2.361 = 14.8 \text{ a.u.}$$

$$\text{Orbital period} = \frac{14.8}{0.0112} = 1320 \text{ days} \approx 3.62 \text{ years.}$$

3.63 years is usually given as Vesta's orbital period. The magnitude of the SC velocity vector $||\bar{V}_{SC}||$ is computed from:

$$||\bar{V}_{SC}|| = \sqrt{GM_S \left(\frac{2}{r_2} - \frac{1}{a}\right)}$$

where a is the semi-major axis of the transfer ellipse = 4.8 a.u.

Then, since all the parameters of the transfer ellipse had been computed in the construction of Figure C1-1 (such as the eccentricity e = .796, the location of the ellipse foci, the orientation of the major axis),

$$||\bar{V}_{M/SC}|| = \sqrt{||\bar{V}_M||^2 + ||\bar{V}_{SC}||^2 - 2\,||\bar{V}_M||\,||\bar{V}_{SC}|| \cos \Gamma}$$

where: $\sin \Gamma = e \sin v \sqrt{\frac{r_2}{(1-e^2)(2a-r_2)}}$, $0 \leq \Gamma \leq \frac{\pi}{2}$

$$v = \theta - 4.8^\circ$$

$$\cos \gamma_S = \left(\frac{V_{SC}}{V_{M/SC}}\right) \sin \Gamma, \quad V = ||\bar{V}||$$

$$\gamma_E = \gamma_S - \alpha$$

Thus, since $||\overline{V}_{M/SC}||$, γ_E and γ_S are all functions of r_2, which is itself a function of travel time t, Figures C1-5 and C1-6 result.

Appendix C2

Interplanetary Impulse Requirements - Gas Jet System Design

1. Unit Impulse Design

The 12 gas jets are shown in the sketch below. Two jets at each end of an axis are fired simultaneously. The pair produces a couple opposing the SC rotation when the axis reaches the deadband. The other two jets for each axis are redundant.

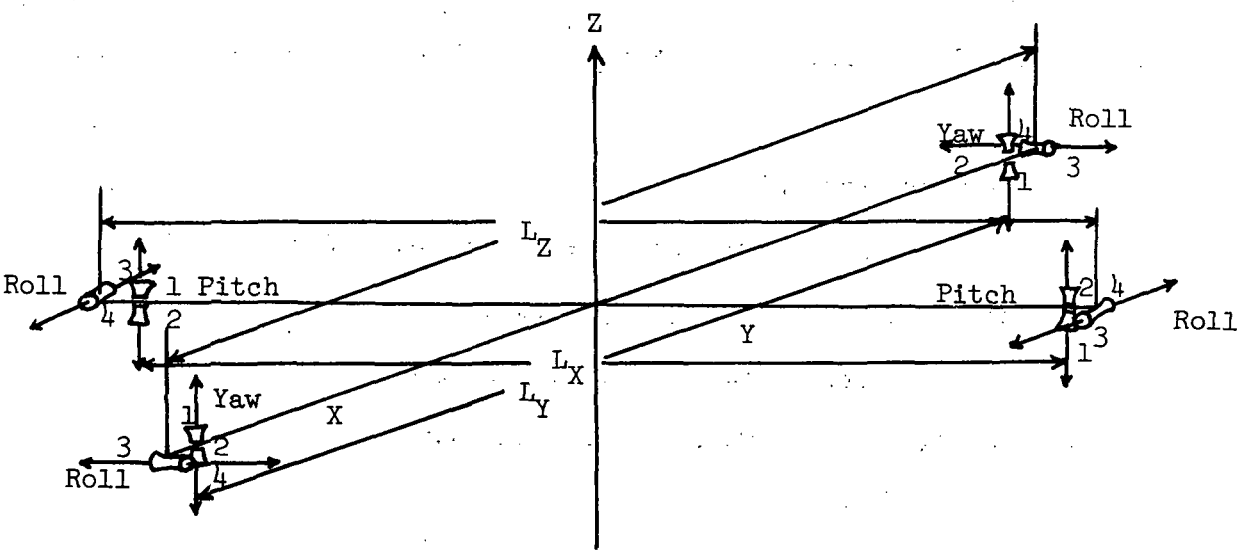

Tabulated below are the scaled distances for the JOSE configuration between the corresponding jets producing a couple.

$$L_Y = L_X = 10 \text{ ft.}$$

$$L_Z = 10.7 \text{ ft.}$$

To design an upper limit to the unit impulse of each jet, the following criteria is considered. A large meteoroid moment also can be produced about the SC-Z axis by the collision of a particle with the extreme outer edge of the SC; r = 11 feet, hence the Z axis moments are given by:

$M_Z = \frac{M^2 r^2 \bar{V}^2}{2 I_Z \theta_{ALL}}$, and: $M_Z = 8.0 \times 10^{-5} \bar{V}^2$, with M_Z in ft. lbs., $\bar{V}^2$ in km^2/sec^2 (from Fig. IV-2).

It is readily seen that, for any value $\overline{V}^2$, the Z axis moment due to discrete meteoroids are larger than the X and Y axis meteoroid moments. Thus, to establish the gas jet force necessary to oppose the maximum Z axis moment, simply let:

$\Delta F = \frac{M_Z}{L_Z} = 7.48 \times 10^{-6} \overline{V}^2 = 7.48 \times 10^{-4}$ lbs. since, from Figure IV-2, $\overline{V}^2 < 100$ km^2/sec^2.

The gas jet unit impulse $\Delta I = \Delta F \cdot \Delta t$, and is taken to be the same for all jets on the SC. Using a pulse width Δt of 0.023 sec., $\Delta I = 1.718 \times 10^{-5}$ lb. sec.

2. Limit Cycle Characteristics

The limit cycle elements will now be determined. When any SC axis reaches the deadband, a number (n) of jet pulses are produced to stop the axis angular velocity and produce a velocity in the opposite direction to null the axis deviation. The following sketch indicates the SC axis motion.

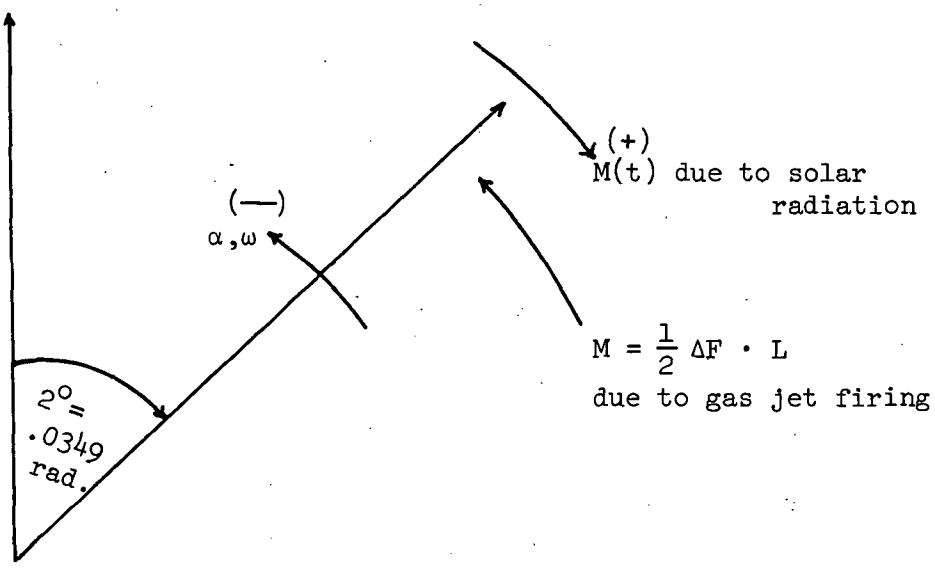

A realistic plot of gas jet-developed force versus time is sketched below:

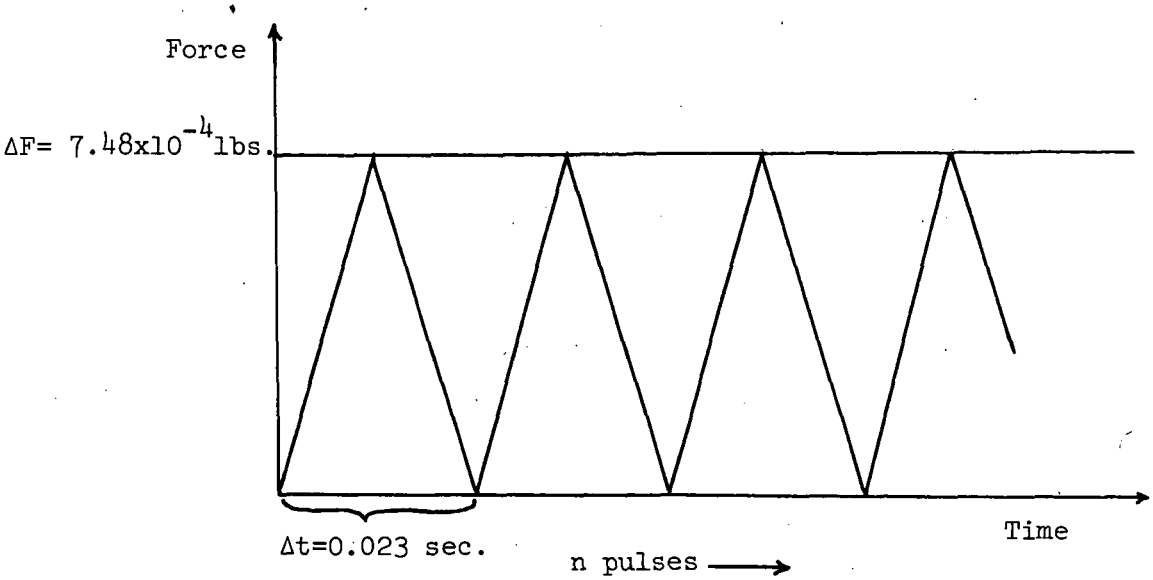

The average linear impulse for each pulse width for each pair of jets is thus 1/2 $\Delta F \cdot \Delta t$. If the pair of jets are fired n times in succession, the total impulse at jet shut-off is 1/2 n $\Delta F \cdot \Delta t$, considered as an average force 1/2 ΔF acting for a period of time $n\Delta t$. Thus, the moment generated by the gas jets ($1/2\Delta F \cdot L$), about the X or Y axis, is roughly 4×10^{-3} ft. lbs. and is far greater than the maximum solar radiation moment (at injection), which is $(13\times10^{-8})(111) = 1.442 \times 10^{-5}$ ft. lbs. Thus for the time period that the attitude jets are firing (=0.023 n sec.), only the gas jet moment is considered as acting on the SC. Thus, the angular acceleration $\alpha = \frac{\Delta F \cdot L}{2I}$. After 0.023 n seconds, the angular velocity of the Z axis is given by: $\omega = \frac{0.012\ \Delta\ F\ L\ n}{I}$. At t = 0.023 n second, the attitude jets are turned off, and the solar radiation pressure begins to take effect and inhibit ω. Thus, initializing t to 0 at 0.023 n seconds, the angular acceleration of the Z axis at time t is:

$$\alpha(t) = \frac{M(t)}{I},$$

and tha angular velocity $\omega(t)$ of the Z axis is given by:

$$\omega(t) = \frac{1}{I}\left[\int_o^t M(t')dt' - 0.012\ \Delta\ F\ L\ n\right]$$

Letting $N(t) = \int_o^t M(t')dt' = -1.666 \times 10^{-12}t^2 + 1.445 \times 10^{-5}t$, using p Cos α for the first forty days since this gives the maximum solar radiation moment, noting that p Cos $\alpha = -.325t + 13$ (t in days) = $-3 \times 10^{-6}t + 13$ (t in seconds), and using JOSE's Y axis in solving for N(t); $\omega(t) = \frac{1}{I_Y}[N(t) - 0.012\ \Delta\ F\ L_Y n]$. The angular position $\theta(0)$ at t = 0 (after firing time = 0.023 n) is equal to $2^o - \frac{\alpha t^2}{2} = 0.0349 - \frac{\Delta F \cdot L_Y}{4I}(0.023n)^2$. Thus, the angular position $\theta(t)$ after time t is given as:

$$\theta(t) = \frac{1}{I_Y}\left[\int_o^t N(t')\ dt' - 0.012\ \Delta FL_Y n\ t\right] + 0.0349 - \frac{\Delta FL_Y 10^{-4} n^2}{I_Y}$$

The optimum limit cycle is obtained by letting $\theta(t)$ become 0 at the same time that $\theta(t)$ reaches -2^o. Thus, solving:

$$N(t) = 0.012\ \Delta FL_Y n, \text{ and}$$

$$\int_o^t N(t')dt' - 0.012\ \Delta FL_Y\ nt - \Delta FL_Y\ 10^{-4} n^2 = -.0698\ I_Y$$

simultaneously for n and t, and noting that

$$\int_o^t N(t')dt' = \int_o^t (-1.666 \times 10^{-12}t'^2 + 1.445 \times 10^{-5}t')dt' = -0.555 \times 10^{-12}t^3 + 0.722 \times 10^{-5}t^2$$

eventually it results that: t = 3450 seconds and n = 580 pulses. The total time from 2^o to -2^o is of course 3450 sec. + (0.023)(580) = 3463 seconds = 0.964 hrs. The above result is interesting in that it is seen that the limit cycle is at most a few hours due to the magnitude of the attitude jet thrust vector. Thus, for this relatively small duration of limit cycle, the solar radiation moment can be considered constant and the preceding equations can be simplified to determine average limit cycles for various phases of the mission.

Proceeding as before, the average solar radiation moment during limit cycle is M = C p Cos α ft. lbs. The angular acceleration resulting from this moment of the SC is $\dot{\omega}$ = Cp Cos α, and this acceleration opposes the angular velocity, derived above caused by n firings of the attitude jets, or $\frac{0.012\Delta FLn}{I}$.

Thus, initializing time t at 0.023 n seconds (jet shut-off), the SC angular velocity is given by: $\omega(t) = \frac{1}{I}[CpCos\ \alpha \cdot t - 0.012\Delta FLn]$.

Noting the angular position of θ at time of jet shut-off ($\theta(0)$) as given above;

$$\theta\ (t) = \frac{1}{I}\left[\frac{CpCos\ \alpha \cdot t^2}{2} - 0.012\Delta FLnt\right] + 0.0349 - \frac{\Delta FL\ 10^{-4}\ n^2}{I}$$

Optimizing limit cycle condition again, it is desired that ω become zero at the same time that θ reaches -2°. Thus:

$$CpCos\ \alpha \cdot t = 0.01\ 2\Delta FLn, \text{ and } 1/2\ CpCos\ \alpha t^2 - 0.01\Delta FLnt - \Delta FL10^{-4}n^2 = -0.0698\ I$$

must be solved simultaneously for n and t. Eventually, the following expression is obtained:

$$t^2 CpCos\ \alpha\ [1/2x10^{-8} + \frac{CpCos\ \alpha}{\Delta FL} \times 10^{-16}] = 0.0698\ I$$

Noting that the maximum value that $\frac{CpCos\alpha\ 10^{-16}}{\Delta FL}$ can take = $\frac{(111)(13)(10^{-16})}{(7.48x10^{-4})(10)} \approx$ $2 \times 10^{-11} << 1/2 \times 10^{-8}$, the second term in the brackets is neglected, and: $t = 10^4 \sqrt{\frac{0.1396I}{CpCos\ \alpha}}$; $n = \frac{10^{-6} CpCos\ \alpha\ t}{\Delta FL}$

The time required for the SC Z axis to return from -2° to $+2^{\circ}$ is now required. Initializing t at $\theta = -2^{\circ}$; $\theta(t) = \frac{CpCos\ \alpha\ t^2}{2I} - 2^{\circ}$, since the angular acceleration is now due to solar radiation moments only. Solving

for t: $t = 10^4 \sqrt{\frac{0.1396\ I}{Cp\ Cos\ \alpha}}$, the same time derived above, required for the Z axis to rotate from $+2^\circ$ to -2°. This fact results because the time of attitude jet firing (0.023 n) is negligible compared to t, as mentioned previously. Thus, the total time required between two successions of n jet pulses is given by:

$$\delta t = 2t + 0.023\ n = 2 \times 10^4 \sqrt{\frac{0.1396\ I}{Cp\ Cos\ \alpha}} + 0.023\ n,$$

$$\text{where, } n = \frac{10^{-6} CpCos\ \alpha \cdot t}{\Delta FL} = \frac{10^{-2}}{\Delta FL} \sqrt{0.1396\ I\ CpCos\ \alpha}$$

This δt and n apply only to JOSE's X and Y axis rotations, since solar radiation moment produces rotations about these two axes only.

Z axis rotation can be produced by discrete meteoroid impacts only, hence Z axis motion is simply limit cycle. Although Z axis impulse requirements will not be computed at this point, since there exists an interesting trade-off later, expressions for Z axis δt_Z and n_Z are derived here for later reference. Equating Z axis angular impulse to angular momentum, letting r equal Z axis angular velocity; $0.023\ n_Z\ \Delta FL_Z = I_Z r$, or

$$r = \frac{0.023\ n_Z \Delta FL_Z}{I_Z}$$

$$\text{Angular position } \theta(t) = \frac{0.023 n_Z \Delta FL_Z \delta t}{I_Z} - 2^\circ.$$

Thus, computing the time necessary to travel from -2° to $+2^\circ$;

$$\delta t_Z = \frac{0.0698\ I_Z}{0.023 \Delta FL_Z n_Z} = \frac{3.04\ I_Z}{\Delta FL_Z n_Z} = \text{a constant throughout the entire mission.}$$

For each SC configuration, n_Z is a free parameter; however, as mentioned, there is later developed an analysis by which an optimum n_Z can be determined.

Appendix C3

Inertia Wheel Formulation

The sketch below suffices to show the dynamic elements involved in the SC axes and the two inertia wheels on the X and Y axes.

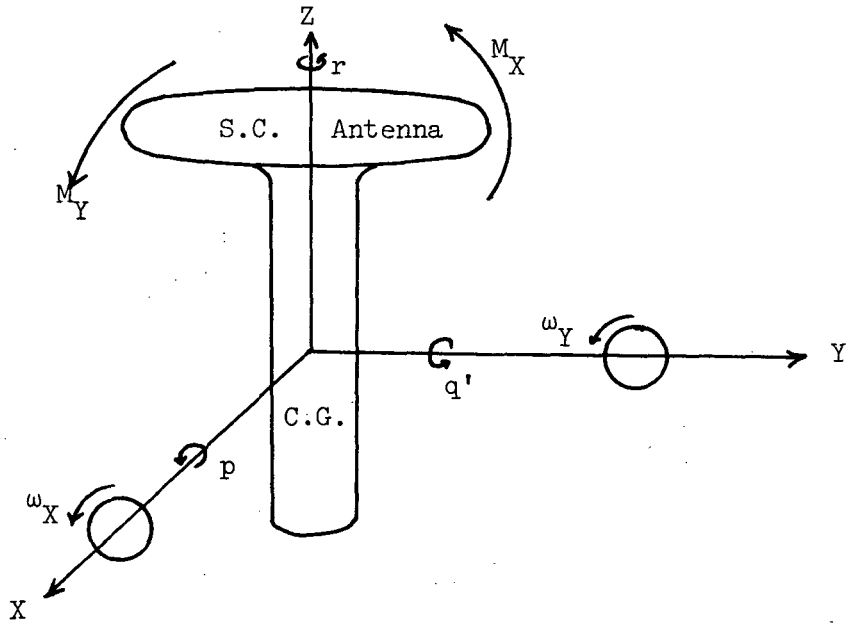

where: ω_X, ω_Y = X-axis and Y-axis inertia wheel angular velocities respectively.

p, q, r = SC angular velocity components about X, Y, Z axes respectively

M_X, M_Y = Solar Radiation-produced moments about X and Y axes respectively.

$M_Z = 0$

Equating the external moments acting on the SC to the total time rate of change of SC angular momentum with respect to inertial space, a basic vector equation is obtained for the system: $\overline{M} = (\dot{\overline{H}})_i + \overline{\Omega}_i \times \overline{H}$

where: $\overline{M}$ = applied moment on SC = $\begin{pmatrix} M_X \\ M_Y \\ 0 \end{pmatrix}$

$(\dot{\overline{H}})_i$ = time rate of change of the angular momentum vector $\overline{H}$ with respect to the coordinate (XYZ) reference frame = $\begin{pmatrix} -I_R \dot{\omega}_X \\ -I_R \omega_Y \\ 0 \end{pmatrix}$

$\overline{\Omega}_i$ = angular velocity of the reference frame (XYZ) with resepct to inertial space = $\begin{pmatrix} p \\ q \\ r \end{pmatrix}$

$$\overline{H} = \begin{pmatrix} H_X \\ H_Y \\ H_Z \end{pmatrix} = \begin{pmatrix} -I_R & \omega_X \\ -I_{R_O} & \omega_Y \end{pmatrix}$$

I_R = inertial wheel moment of inertia about spin axis taken to be equal for both X and Y wheels.

The basic equation yields the following three equations involving functions of time t:

$$\begin{aligned} \dot{\omega}_X(t) - \omega_Y(t)\, r &= \frac{-M_X(t)}{I_R} \\ \dot{\omega}_Y(t) + \omega_X(t)\, r &= \frac{-M_Y(t)}{I_R} \\ \omega_X(t)q(t) - \omega_Y(t)p(t) &= 0 \end{aligned} \qquad \text{(C3-1)}$$

p and q are certainly functions of time; however, r can be considered constant since Z axis rotation is limit cycle only and is not affected by solar radiation moments. An analysis is later performed whereby an optimum r can be selected. M_X and M_Y are shown as functions of time.

Equations like these are normally handled by Laplace transforms, and this is performed here assuming, as is customary, zero initial conditions. The Laplace transform , as a function of s, of a function f(t) is, by definition; $\hat{f}(s) = \int_o^\infty e^{-st} f(t)\, dt$.

Noting that $\hat{\dot{\omega}}(t) = \int_o^\infty e^{-st} \frac{d}{dt} \omega(t)\, dt$ = (integrating by parts, zero initial conditions) $s\, \hat{\omega}(t)$, and also noting that the third equation of Eq. C3-1 is not necessary in solving for ω_X and ω_Y, the following Laplace notation is obtained:

$$\hat{\omega}_X(s) - \frac{r}{s}\hat{\omega}_Y(s) = \frac{-\hat{M}_X(s)}{s\,I_R}$$

$$\hat{\omega}_Y(s) + \frac{r}{s}\hat{\omega}_X(s) = \frac{-\hat{M}_Y(s)}{s\,I_R}$$

Solving these equations simultaneously for $\hat{\omega}_X$ and $\hat{\omega}_Y$, and noting that $\hat{M}(s) = C\,\widehat{p\,\mathrm{Cos}\,\alpha}\,(s)$, and designating p Cos α as p, one obtains:

$$\hat{\omega}_X(s) = \frac{\frac{\hat{p}(s)}{I_R}\left[C_X s + C_Y r\right]}{r^2 + s^2}$$

$$\hat{\omega}_Y(s) = \frac{\frac{\hat{p}(s)}{I_R}\left[-C_Y s + C_X r\right]}{r^2 + s^2}$$

Again, the largest solar radiation pressure (p) is found at launch, hence $p(t) = 10^{-8}(-3.77 \times 10^{-6}t + 13)$, where t is in seconds since $\omega_X(t)$ and $\omega_Y(t)$ are desired in units of rad/sec. This is p(t) for the first branch of Figure IV-1 = p Cos α = $(-0.325t + 13)10^{-8}$, t in days. Then, noting that

$$\int_0^\infty te^{-st}dt = \frac{1}{s^2}\ ;$$

$$\hat{p}(s) = 10^{-8}\left[\frac{-3.77\times10^{-6}}{s^2} + \frac{13}{s}\right]\ ,\ \text{and:}$$

$$\hat{\omega}_X(s) = \frac{10^{-8}}{I_R}\left[\frac{-3.77\times10^{-6}C_Y r}{s^2(r^2+s^2)} + \frac{-3.77\times10^{-6}C_X + 13C_Y r}{s(r^2+s^2)} + \frac{13C_X}{r^2+s^2}\right]$$

$$\hat{\omega}_Y(s) = \frac{10^{-8}}{I_R}\left[\frac{-3.77\times10^{-6}C_X r}{s^2(r^2+s^2)} + \frac{3.77\times10^{-6}C_Y + 13\,C_X r}{s(r^2+s^2)} - \frac{13C_Y}{r^2+s^2}\right]$$

Noting that, for some constant, A, $\frac{A}{s^2(r^2+s^2)}$ can be broken up into: $\frac{A/r^2}{s^2} - \frac{A/r^2}{r^2+s^2}$, and $\frac{A}{s(r^2+s^2)}$ can be broken up into $\frac{A/r^2}{s} - \frac{(A/r^2)s}{r^2+s^2}$

$\hat{\omega}_X$ and $\hat{\omega}_y$ can be written as:

$$\hat{\omega}_X(s) = \frac{10^{-8}}{I_R}\left[\left(\frac{-3.77\times10^{-6}C_X}{r^2} + \frac{13C_Y}{r}\right)\left(\frac{-s}{r^2+s^2} + \frac{1}{s}\right) + \frac{\frac{3.77\times10^{-6}C_Y}{r} + 13C_X}{r^2+s^2} - \frac{3.77\times10^{-6}(}{\frac{r}{s^2}}\right.$$

$$\hat{\omega}_Y(s) = \frac{10^{-8}}{I_R}\left[\left(\frac{3.77\times10^{-6}C_Y}{r^2} + \frac{13C_X}{r}\right)\left(\frac{-s}{r^2+s^2} + \frac{1}{s}\right) + \frac{\frac{3.77\times10^{-6}C_X}{r} - 13C_Y}{r^2+s^2} - \frac{3.77\times10^{-6}(}{\frac{r}{s^2}}\right.$$

The reason for writing $\hat{\omega}_X$ and $\hat{\omega}_Y$ in this rather cumbersome form is obvious when one notes that: $\hat{\text{Cos}}\,rt\ (s) = \frac{s}{r^2+s^2}$, and $\hat{\text{Sin}}\,rt\ (s) = \frac{r}{r^2+s^2}$.

Thus, the inverse Laplace transform of $\hat{\omega}_X$ and $\hat{\omega}_Y$ can readily be written:

$$\omega_X(t) = \frac{-10^{-8}}{I_R}\left[\left(\frac{-3.77\times10^{-6}C_X}{r^2} + \frac{13C_Y}{r}\right)(1-\text{Cos } rt) + \left(\frac{3.77\times10^{-6}C_Y}{r^2} + \frac{13C_X}{r}\right)\text{Sin } rt - \frac{-3.77\times10^{-6}C_Y t}{r}\right]$$

$$\omega_Y(t) = \frac{-10^{-8}}{I_R}\left[\left(\frac{3.77\times10^{-6}C_Y}{r^2} + \frac{13C_X}{r}\right)(1-\text{Cos } rt) + \left(\frac{3.77\times10^{-6}C_X}{r^2} - \frac{13C_Y}{r}\right)\text{Sin } rt - \frac{-3.77\times10^{-6}C_X t}{r}\right]$$

where t must be in seconds.

It is obvious that ω_X and ω_Y increase without bound since there exists a linear term in t for each ω. If the moment were applied and then removed, only sine and cosine terms would be present, with a bound determined by the phases and amplitudes of the trigonometric terms.

Appendix C4

Z-axis Angular Velocity Tradeoff Analysis

In Appendix C2-2, an expression for Z axis angular velocity (r) in terms of the number of roll axis jet thrusts was derived; i.e., $r = \frac{0.023\ n_Z \Delta F L_Z}{I_Z}$, where ΔF = thrusting force (7.48×10^{-4} lbs.), L_Z = roll jet separation distance, and I_Z the SC-Z axis moment of inertia. The time (δt_Z) required to travel from -2° to $+2^\circ$, or the time between n_Z firings of the roll jets, was determined to be:

$$\delta t_Z = \frac{3.04\ I_z}{\Delta F L_z\ n_z} = \frac{(3.04)(0.023)}{r} = \frac{0.067}{r}$$

The interesting r-velocity tradeoff is now evident by observing the ω equations of Appendix C3 and the one-half Z axis period δt_Z. For a fixed wheel saturation limit ω, it is obvious, considering the linear term, that larger r values result in longer times t until the inertia wheel becomes saturated. This means fewer X and Y axis jet firings and hence a propulsion savings. However, increasing r values result in a small δt_Z period about the Z axis, hence more firings of the roll jets are required, with a corresponding propulsion increase. There exists some r at which the total required impulse is minimized; the following describes the determination of the optimum r:

A range of values of practical r was first considered (1.589×10^{-7} rad/sec $\leq r \leq 1.589 \times 10^{-5}$ rad/sec). The optimum r was found to lie within this range. Using various values of r in this range, the time for ω_X and ω_Y to reach an assumed saturation velocity of 2000 rpm ($\approx$ 210 rad/sec) was computed from the ω equations assuming $I_R = 0.04$ slug.ft.^{2}. The results are shown in Table C4-1. A preliminary SC configuration was used in preparing this table rather than the final JOSE of Chapter II. The two SC's are similar

and the result here is valid. For each value of r, the corresponding pulses (n_Z) are indicated; t_s is the time to saturation of an inertia wheel, the X and Y designation after the t_s value indicates whether the X or Y axis wheel respectively is the first to become saturated (thus determining t_s); and the δt_Z value is shown. The other two entries are as follows: The total average impulse consists roughly of two basic requirements; X and Y axis impulse requirements, and Z axis impulse requirements. The Z axis requirements, noting that two jets are fired for each pulse, can be formulated as before: $I_{sp} = \frac{2\Delta F \cdot 0.023 n_Z T}{\delta t_Z}$, where T = the mission duration of 583 days. The X and Y axis requirements can be expressed as: $I_{sp} = \frac{(2)2\Delta F \cdot 0.023 n_{AVG} T}{t_s \; n_X + n_Y}$, where n_{AVG} is the average number of X and Y axis jet pulses $(\frac{n_X+n_Y}{2})$ necessary to oppose SC rotation after inertia wheel saturation, and is given by Table IV-1, for the appropriate time period (T_i) at which wheel saturation takes place. Denoting $2\Delta F \; 0.023T=K$, the sum of the I_{sp} are to be minimized, or the total impulse =

$$K\left[\frac{n_Z}{\delta t_Z} + \frac{2n_{AVG}}{t_s}\right]$$

is to be minimized. Note that $K>0$, and Table C4-1 also indicates $\frac{n_Z}{\delta t_Z}$ and $\frac{2n_{AVG}}{t_s}$. These two parameters, and their sum (the total impulse) are shown in Figure C4-1. The optimum r is seen to be about 2×10^{-6} rad/sec.

Table C4-1

Time for Inertia Wheel Saturation (t_s), Z Axis Limit Cycle Period (δt_Z), and Impulse Requirements For Various Values of Z-Axis Angular Velocity r

r (rad/sec)	n_Z (pulses)	δt_Z (days)	$\frac{n_Z}{\delta t_Z}$	n_{AVG} (pulses)	t_s (days)	$\frac{2n_{AVG}}{t_s}$
1.589×10^{-7}	1	5.01	.2	455	1.208 (Y)	755
5×10^{-7}	4	1.59	2.52	455	10.19 (X)	92
8×10^{-7}	6	.995	6.03	455	12.92 (X)	76.4
1×10^{-6}	7	.795	8.8	455	13.72 (X)	74.9
3×10^{-6}	19	.265	71.7	235	145.5 (Y)	74.9
5×10^{-6}	32	.1598	200	235	243 (X)	201.9
7×10^{-6}	44	.1139	387	129	340 (X)	387.8
9×10^{-6}	57	.0882	646	129	436 (Y)	646.6
1.589×10^{-5}	100	.0501	1995	129	772 (X)	1995.3

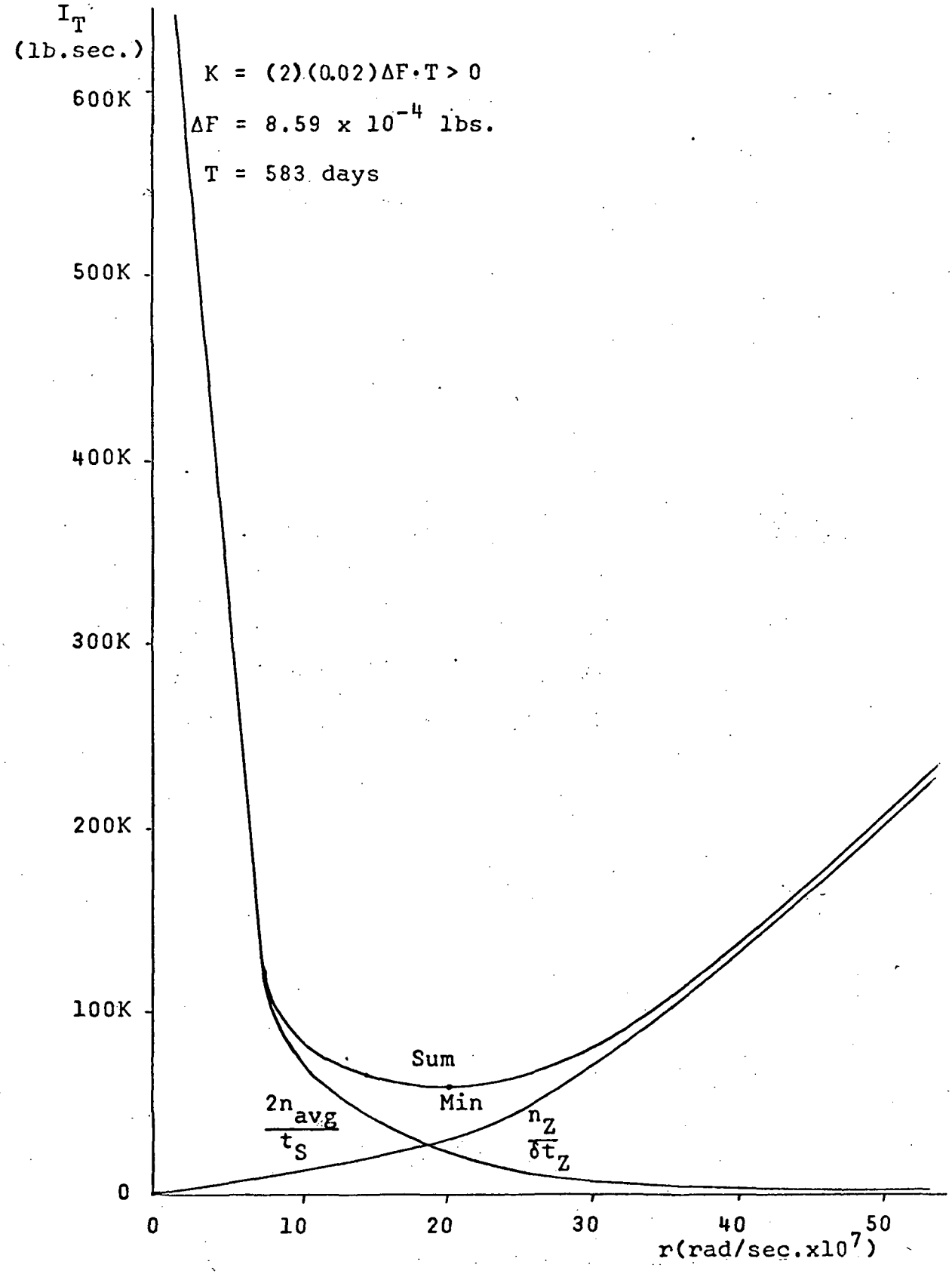

Figure C4-1 : Total Impulse Contributions ($\frac{2n_{avg}}{t_s}$, $\frac{n_Z}{\delta t_Z}$) vs. Z-Axis Angular Velocity (r)

Appendix D: Trajectory Analysis

A. Trajectory Analysis in the Vicinity of Jupiter

1. Definition of Problem

This first investigation was aimed to provide a deep analysis of the trajectories around the encounter point. The basic theoretical configuration is the following:

- an incoming hyperbola defined by its velocity at infinity V_{HP} = 8 km/sec and its periapsis equal to 1.1 R_J (Jupiter radii unit).
- An elliptical orbit defined by its periapsis (1.1 R_J) and its apoapsis (100 R_J).

Both trajectories are in the same plane and have the same periapsis, therefore, they have the same main axis which joins the center of Jupiter to the common periapsis.

A computer program was written to give the polar coordinates of both trajectories and their distribution of velocities.

Jupiter was assumed spherical and the basic equations of the mechanics of planets were used.

The origin is at the center of Jupiter and the axis of reference is the main axis of the trajectories (Fig. D-1).

G = constant of gravitation

M_J= mass of Jupiter

$\mu = GM_J = 0.35 \times 10^{-6}\ R_J{}^3/\text{sec}^2$

R_J is the radius of Jupiter: 71, 372 km

- For the hyperbola:

$$r_h = \frac{a_h(e_h^2 - 1)}{1 + e_h \cos f}$$

$$V_h{}^2 = V_{HP}{}^2 + \frac{2\mu}{\eta_h}$$

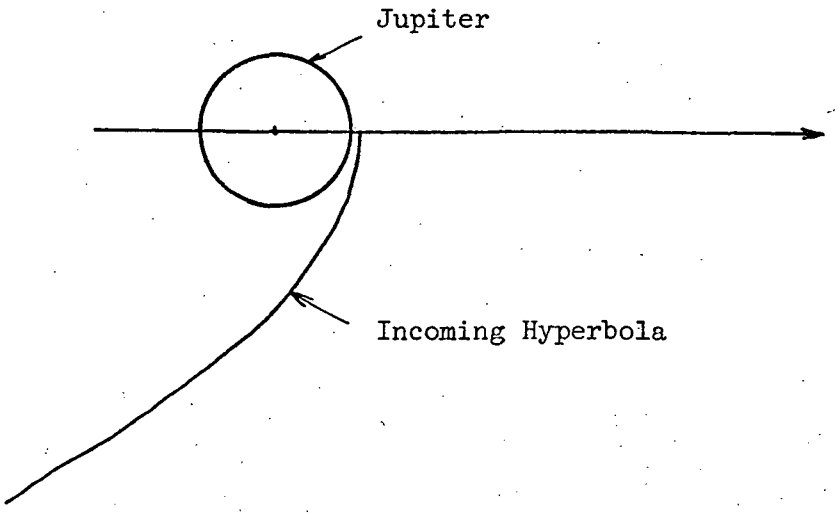

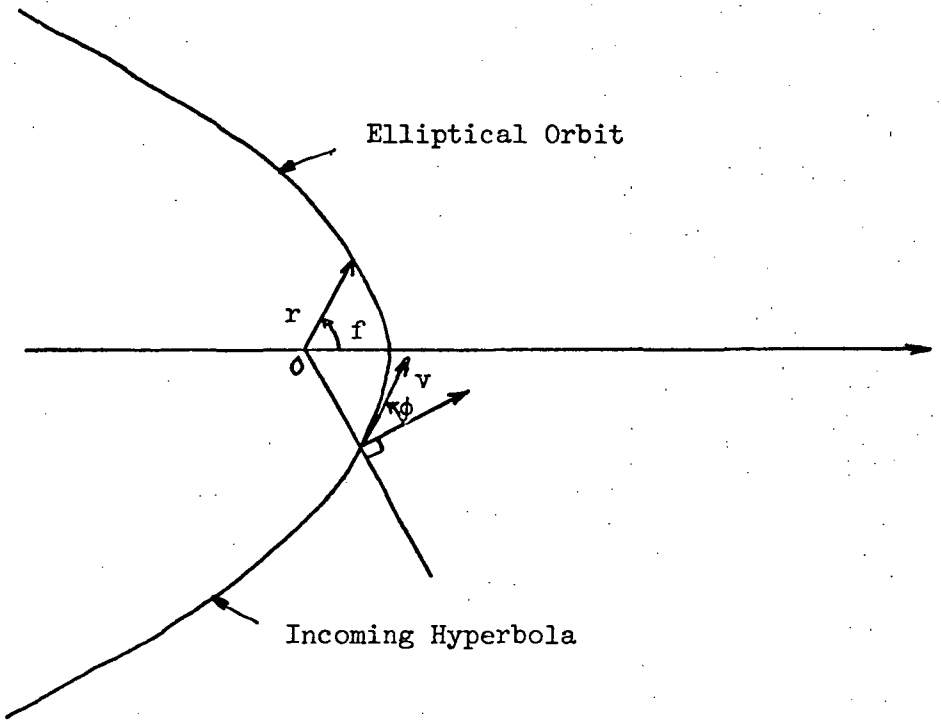

Fig. D.1 Geometry of Insertion

where f is the true anomaly and $a_h = \frac{\mu}{V_{HP}^2}$

• For the ellipse:

$$r_e = \frac{a_e(1 - e_e^2)}{1 + e_e \cos f}$$

$$V_e^2 = \mu\left(\frac{2}{r_e} - \frac{1}{a_e}\right)$$

a_e is the semi-major axis $\quad a_e = \frac{100 + 1.1}{2}(R_J)$

e_e is the eccentricity $\quad e_e = \frac{100 - 1.1}{100 + 1.1}$

For increasing values of the true anomaly, the output gives the corresponding values of the radius, the velocity on both trajectories, and the difference between both velocities $(V_h - V_e)$. Because the trajectories are symmetrical w.r.t. the main axis, the true anomaly is kept positive and varies from 0 to 90 degrees.

2. Conclusions

• The specified hyperbola and ellipse are very close to each other in a broad range around their common periapsis. For instance, at a true anomaly of 10.5° the difference between the two radius is only 10^{-4} R_J that is 7.1 km. At 20°, the difference is 3.8×10^{-4} R_J that is 27 km. This remark implies that both trajectories velocity vectors can be considered having the same support with a very good approximation in a broad region around the periapsis $(-20^\circ \leq f \leq 20^\circ)$. The difference between the velocity on the hyperbola and the velocity on the ellipse for the same true anomaly is therefore a vector having the same alignment and of magnitude equal to $V_h - V_e$.

• Furthermore, this difference $V_h - V_e$ appears very constant in similar conditions. At $f = 0^\circ$, it represents the impulsive ΔV needed for a perfect periapsis to periapsis transfer from the incoming hyperbola to the specified ellipse and has the value 870.1 m/sec. At $f = 10^\circ$, its value is 871 m/sec, i.e., an increase of .9 m/sec and at $f = 20^\circ$, 873.8 m/sec, i.e., an increase of 3.7 m/sec.

• The overall conclusion is the impulsive ΔV needed for the transfer is quite insensitive to the location when the kick is given, in a broad region around the common periapsis which can be taken up to $-20^\circ \leq f \leq 20^\circ$.

For a non-impulsive maneuver, assuming that the direction of the thrust can be kept exactly in the opposite direction of the spacecraft's velocity during the burning time (i.e., the direction of the thrust must rotate), a similar conclusion can be drawn.

From the fuel consumption viewpoint, the location of firing for orbit insertion is not a sensitive parameter and can be chosen in a broad region around the incoming hyperbola's periapsis, up to $-20^\circ \leq f \leq 20^\circ$ without a substantial loss in the efficiency of the maneuver.

B. Orbit Insertion Simulation

The second investigation was directed to provide a full simulation of real orbit insertion maneuver (finite burning time) using a computer program.

1. Definition of the Problem

The spacecraft is assumed to travel on the incoming hyperbola previously specified. At a certain point of the trajectory (longitude of firing) a constant thrust is applied during a certain time and then stopped. The parameters of the resulting elliptical orbit are deduced from the conditions at the end of the thrust period.

2. The Equations

The gravitational field of Jupiter is assumed to be central and of the form μ/r^2. The equations describing the thrust operation are simply the Newton's equations written in polar coordinates r and f.

Two sets of equations were derived for two different cases:

- a fixed direction of thrust (defined by α):

$$\ddot{r} - r\dot{f}^2 = -\frac{\mu}{r^2} + a_o \cos(\alpha + f)$$

$$r\ddot{f} + 2\dot{r}\dot{f} = -a_o \sin(\alpha + f)$$

- a thrust direction maintained in the opposite direction of the velocity vector:

$$\ddot{r} - r\dot{f}^2 = -\frac{\mu}{r^2} - a_o \sin\phi$$

$$r\ddot{f} + 2\dot{r}\dot{f} = -a_o \cos\phi$$

where ϕ is defined by

$$\tan\phi = \frac{r}{\dot{r}\dot{f}}$$

The quantity a_o is homogeneous to an acceleration

$$a_o = g\frac{I_s}{t_b}\left(1 - e^{-\frac{\Delta V}{gI_s}}\right)$$

I_s = specific impulse of the propellant

t_b = burning time

ΔV = velocity increment provided for the maneuver

g = acceleration of gravity (9.81 m/sec)

For a selected longitude of firing on the hyperbola, the initial conditions (radius, velocity) are computed using the equations given in the "trajectory analysis" study. Then the equations of motion simulating the thrust operation are integrated using the Runge-Kutta method (4th order) with an appropriate time increment. At the end of the thrust operation, the final conditions, radius and velocity, are known and they determine one ellipse whose parameters are consequently evaluated.

3. Computer Inputs and Outputs

The program was written for a general investigation and the incoming hyperbola must be specified (values given earlier)

a) Inputs:

V_{HP}

Periapsis of incoming hyperbola

Specific impulse of selected propellant

ΔV available for maneuver

Burning time

Thrust direction characterization (sub-program)

Longitude at firing

b) Outputs:

Periapsis of ellipse

Apoapsis of ellipse

Longitude of the periapsis

Eccentricity of ellipse

Angular momentum of ellipse

Thrust required to achieve the maneuver

Acceleration taken by the spacecraft

The two last parameters are computed for the baseline spacecraft which has a mass at launch of 1955 kg (4300 lb).

4. Results

For this investigation, the specific impulse of the propellant was not varied and assumed to be 400 sec which corresponds to the Flox/CH_4 combination.

a) Influence of the Thrust Direction

The first case considers a fixed direction which was assumed to be in the plane of the trajectories and perpendicular to their (common) main axis.

The difference between the two modes are almost negligible for burning times up to 200 sec. For 500 sec, the efficiency of the second mode appears and brings the apoapsis down by 2.4 R_J with respect to the first mode. However, based on the currently available information, it seems that the second mode (thrust kept in the opposite direction of the spacecraft's velocity or almost) is feasible. It was subsequently decided to use this assumption on the following investigations. However, the previous conclusion is still right and may be useful.

b) Influence of ΔV - Gravity Losses

A ΔV of 900 m/sec which is approximately the theoretical value for an impulsive maneuver never achieves the proposed elliptical orbit of 1.1 x 100 R_J. The resulting orbit turns out to have the same periapsis, 1.1 R_J, but a greater apoapsis of 127 R_J approximately in all the cases. At this point the ΔV was increased in order to reduce the apoapsis to the intended value. Finally a ΔV of 1000 m/sec was found to yield an apoapsis of 96 R_J. Due to possible degradation of performances this

ΔV capability of 1000 m/sec was selected as the baseline value for the whole study of the propulsion subsystem.

In conclusion, the gravity losses represent a non-negligible penalty of 100 m/sec approximately.

c) Influence of the Burning Time

The burning time has practically no effect except on the apoapsis. However, it is very small and negligible for the values up to 300 sec. At 500 sec, it causes the apoapsis to increase by 2 R_J.

For a ΔV of 1000 m/sec the change in apoapsis between 100 sec and 230 sec is only .06 R_J. However, as the burning time increases, the thrust and the acceleration taken by the spacecraft increases too. For instance, for a burning time of 90 sec, the acceleration is approximately 1 g, for 10 sec, it is approximately 10 g. The burning time is not a constraint for the insertion maneuver, but for the thrust (i.e., the weight of the propulsion module) and the acceleration the spacecraft can take.

d) Influence of the Longitude at Firing

The longitude at firing affects both the apoapsis and the longitude of periapsis of the resulting ellipse. Obviously the most efficient way for deboosting is to have a longitude of firing almost opposite to the longitude of shut down of the engine. In this case the longitude of periapsis is nearly 0° and both periapsis (hyperbola and ellipse) are at the same point.

As it was pointed out in the previous part, the longitude of firing does not affect very much the parameters of ellipse. The longitude of periapsis reaches the extremum value of $\pm 0.4^\circ$, but anyway is not a

critical parameter. The following tables summarize the influence on the apoapsis.

Burning time = 100 sec

longitude at firing	apoapsis
optimal	96.01 R_J
-15°	97.76 R_J
$+10^\circ$	97.52 R_J

Burning time = 230 sec

longitude at firing	apoapsis
optimal	96.08 R_J
-15°	97.17 R_J
$+10^\circ$	98.33 R_J

e) Error on the Burning Time

In this case, the thrust is assumed to operate for a longer or shorter time than the proposed burning time therefore showing the resulting effect of errors inherent to propulsion systems.

For a burning time of 100 sec, an error of ± 2 sec (i.e., 2%) causes the apoapsis of the ellipse to change by ± 5 R_J. For a burning time of 230 sec, the same error (i.e., 0.87%) leads to a change of $\pm$ 2.3 R_J. Therefore, depending on the accuracy of operating time offered by a real propulsion system, this may require further attention. An error on the thrust level can be considered equivalent to an error on the burning time and would have an influence on the final orbit.

An alternate approach would possibly consider an accelerometer measuring the acceleration produced by the thrust. An integration would provide directly the velocity increment to be compared to a specified value. This threshold would initiate the shut down of the engine. However, there would still be some error.

f) Error on the Periapsis of the Incoming Hyperbola

For a ΔV of 1000 m/sec, the periapsis of the hyperbola was increased to 1.2 R_J to represent an error on the trajectory. The resulting ellipse has a periapsis of 1.2 R_J and an apoapsis of 108 R_J for an optimal firing. These values are almost independent of the burning time.

5. Conclusion

Two parameters of the resulting elliptical orbit characterize clearly the influence of the various factors. Its periapsis is completely determined by the periapsis of the incoming hyperbola and is insensitive to other factors.

Its apoapsis is slightly affected by each factor considered separately, but errors on the burning time or on the periapsis of the hyperbola might produce a substantial effect. Morever, if several perturbing factors are combined the resulting effect might become very important.

Further study is necessary to investigate these two last points together with practical values and ranges of errors based on the current experience in trajectory, course correction, propulsion system operation (Mariner) and expected values for the future.

The insertion maneuver imposes no constraint on the propulsion subsystem since the resulting elliptical orbit is insensitive to the burning time, provided it doesn't become too large. A practical range appears to be 100 sec to 300 sec which is highly satisfactory for both the thrust level and the acceleration level.

Appendix E: Motor Investigation

A. Solid Propellant Motors

The simplicity of solid propellant motors, the easy way in which they work and the experience that result from the Surveyor's success led to consideration of such a device for a Jupiter orbiter. The basic concept is the following: one or two large fixed-impulse, high performance solid propellant motors provide the bulk of the mission's required energy (orbit insertion and orbit inclination change) while a liquid propulsion system provides flexibility through precise control and multiple restart capability and the remaining maneuvers, mainly mid-course corrections.

It should be pointed out that except for the Surveyor mission, the experience in this field is fairly meager. The problem of long life motors restartable solid motors, controllable thrust (magnitude and direction), influence of the deep-space environment are not solved but are presently under study at various NASA facilities. Reports on these questions are to be published under NASA contracts but are not yet available. The present information is rather limited. Future investigations will take advantage of real life tests and will show the real performance of possible systems.

1. Specific Constraints of Solid Propellant Motors

Before proceeding with any investigations, it is necessary to review briefly what are the specific problems generally encountered with solid propellant motors and to which particular attention will be given later.

Thrust profile: the acceleration due to engine operation is an important parameter especially for solid motors. They generally offer

high accelerations that may have severe effects on the spacecraft: booms which handle the RTG or the scan platform could deflect. Morever, their brutal onset and decay of thrust are also important problems since they contribute to "flapping" of the booms. On the other hand, if the acceleration can be lowered, other problems arise: the burning time increases thus additional requirement for long life-time nozzles and long time vertical stabilization. For the orbit insertion maneuver, the gravity losses due to Jupiter increases when the spacecraft acceleration decreases. However, this is not a problem for an acceleration greater than 0.1 g. The choice of an acceptable thrust/weight ratio is based on the fact that spacecrafts are tested at 1 g on the ground. This value is consequently retained as guideline for the design of the propulsion system.

Environmental considerations: throughout the mission, the propulsion system is exposed to vacuum storage and operation. The question arises as to whether or not solid propellant motor designs should include a nozzle enclosure. It is necessary that the motor be capable of ignition and operation in vacuum. Other considerations refer to the radiations as stated previously, and temperatures experienced by the spacecraft; allowable storage temperatures range from $50^{\circ}F$ to $90^{\circ}F$ for solid propellants.

2. Choosing an acceptable Solution

Configurations using a single controllable solid propellant motor without supplementary vernier liquid motors were eliminated for the following reasons: the large difference in ΔV required for successive maneuvers would compel the controllable solid motor to operate in a transient mode for small ΔV expenditure maneuvers (e.g., course-correction);

the motor must be shut down before it reaches steady-state operation because the impulse generated has satisfied the ΔV requirement. This is particularly a problem near the end of the mission where a large motor case volume will be filled with combustion products. This transient mode of operation is unacceptable from a repeatability viewpoint. The study was then narrowed to solid/liquid combinations.

Configurations using a controllable solid motor for orbit insertion and orbit inclination change and a liquid propulsion system to perform all other maneuvers and provide thrust vector control (TVC) during solid motor operation were also eliminated. They offer no real advantages as compared to fixed-impulse motors and require additional systems for control of the thrust. These systems are far from being operational, they add complexity and their reliability is uncertain.

The study was then narrowed to configurations using one or two large fixed-impulse, high performance, solid propellant motors which provide the bulk of the mission's required energy (orbit insertion and orbit inclination change) while a liquid propulsion system provides TVC during solid motor operation and capability for the other maneuvers through precise control and multiple restart capability.

3. Baseline Propulsion Systems

Description: due to uncertainty in the future development of solid motors, two different approaches were defined and studied. The first approach uses a single two-burn motor for insertion and inclination change maneuvers. The two-burn motor would be equipped with a water-quench system to provide shutdown control and would employ a multiple start igniter. This configuration will show great advantages both for

mass and design (short and compact system) but presents the problems of

- reliable shutdown
- behavior of a half-burnt propellant grain during one year in Jupiter environment
- reliable restart after one year

The current technology leaves these problems unanswered. Therefore, a second approach more "conservative" and of lower performance was considered also. It uses two fixed-impulse, burn-to-completion solid motors in a staged configuration; the first one for orbit insertion, the second one for orbit inclination change. The first motor would be kept after insertion in order to protect the second one from radiation during one year. Then it would be staged off prior to the firing of the second engine. This system presents a certain complexity and lacks the advantages of the previous one. However, it avoids the three unanswered problems and offers also the following advantage: if the first motor fails to work, it can be jettisonned and the second motor will be used for the orbit insertion. The orbit will be different than the one planned but the purpose of orbiting the spacecraft will have been achieved.

In both approaches, the liquid vernier propulsion subsystem provides TVC during the solid motor(s) operation and capability for the three course-corrections and the change of periapsis through four throtteable engines. This requires a total impulse much greater than 50,000 lb.sec., the usual upper limit for monopropellant systems. Thus a bipropellant system should be used. An advantage of a separate liquid vernier propulsion subsystem is that a degraded mode mission could be accomplished in the unlikely event of malfunctions of the solid propellant motor(s), i.e., the orbiter that could degrade to a flyby.

Characteristics: The current technology of solid propellants is based on aluminum. A logical improvement will consist of using beryllium. This seems reasonably attainable by the 1980's. The beryllium propellant will offer a vacuum, specific impulse I_s = 315 sec at a nozzle expansion ratio of ε = 80. An effective motor mass fraction of 0.90 was assumed for the evaluation. The performance characteristics of a beryllium propellant system is summarized in Table E-1.

Although different combinations can be considered, the study was limited to two pressure-fed bipropellant liquid systems highly characteristic of two classes.

N_2O_4/(50% N_2H_4 + 50% UDMH)* benefits from a broad experience (Apollo, Mariner) but has a small specific impulse I_s = 305 sec in vacuum.

OF_2/B_2H_6 is a new, highly promising system but not yet qualified, which offers a very good specific impulse I_s = 414 sec. It is currently under investigation and testing.

An effective mass fraction of 0.80 was assumed for the evaluation of liquid systems; other parameters are summarized in Table E-1. Data come mostly from reference 3c. The basic configuration selected uses four identical throttleable thrusters one of which is gimballed to provide roll control.

4. Analysis of Solid Motors

a) Solid Motor Operation Thrust-Time Profile

The solid motor is designed to provide a constant acceleration (reference value of 1 g) therefore a constantly decreasing thrust. The vernier subsystem should be turned on 6 sec prior to solid motor operation

---

* This combination is usually called Aerozine-50 or simply A-50.

in order to allow vernier motor start-up transients to diminish and to establish an autopilot-controlled stable spacecraft prior to firing the solid motor. The vernier engines throttle during solid motor burn, thereby maintaining TVC. The solid motor is also designed to have a soft start and shutdown, i.e., provide a start and shutdown spacecraft acceleration rate, g-dot, equal to or less than 0.2 g/sec. Start-up and shutdown times are 3.75 sec each, based on current test. The total vernier thrust requirement for TVC decreases because the solid motor thrust decreases. Verniers will continue to operate for a minimum of +6 sec after solid motor thrust decay in order to allow induced transients from the decay to diminish. Fig. E-1 gives the idealized thrust-time profile during a solid motor operation. Taking into account the constant acceleration requirement, the motor geometry becomes a regressive end-burning configuration (Fig. E-2).

b. Propulsion Cutoff Impulse

Propulsion cutoff impulse variability after solid motor operation is determined by the vernier subsystem. Therefore the impulse variability of the vernier subsystem determines velocity variability for all cases. Based on Mariner 69 type of engine technology, the 3σ cutoff impulse variation imparted to the spacecraft is 2 lb.sec for a four vernier configuration. Resultant spacecraft velocity variability after each maneuver is less than 0.01 m/sec (worse value obtained for the last maneuver).

c. Governing Equations

For a constant acceleration a, the mass of the spacecraft decreases with the time as

$$m = \frac{m_0}{I + \frac{at}{gI_s}}$$

where m_0 is the initial mass of the spacecraft. The mass of propellant m_p is given by

$$m_p = \frac{\Delta V}{gI_s + \Delta V}$$

The mass of a solid motor is $m_m = 1.1\ m$, the burning time $t_b = a/v$. The propellant burning rate is a function of P_c the chamber pressure:

$$\eta = 0.2\ (P_c/300)^{0.3}$$

(η in inches/sec, P_c in psia). P_c is related to the thrust F and the nozzle throat area A_t by the rocket equation

$$C_F = \frac{F}{P_c A_t}$$

where C_F, the thrust coefficient is know.

The maximum thrust is $F_{max} = m_0 a$, and the minimum thrust is $F_{min} = (m_o - m_p)a$

d. Computer Optimization

A computer program was developed to characterize the various solutions. The thrust coefficient a/g was the variable and the outputs were:

the mass of propellant

the mass of the solid motor

the burning time

the maximum and minimum thrusts

the maximum and minimum chamber pressures

the length and the two diameters of the propellant case (Fig. E-2).

The selection of the final design was directed to obtain a favorable propellant envelope, i.e., a ratio L/D of nearly one (compatible with the acceleration level) for the following reasons:

Current experience has demonstrated the successful operation of solid motors with an L/D of one (e.g., Surveyor). There has been no demonstration fired at other values of L/D.

The resulting propellant case is highly compact and can be easily integrated into the spacecraft.

e. Results

In order to have some flexibility in the evaluation, two cases were investigated in details. The first case is simply the "full" mission as defined previously; the second case called "alternate" missions, for reasons which will be clear later, deal with smaller ΔV requirements. In brief summary, in terms of ΔV requirement:

For the single two-burn solid motor:

- full mission ΔV = 4000 m/sec
- alternate mission ΔV = 2450 m/sec

For the two solid motors in a staged configuration:

- the first engine provides a ΔV = 1000 m/sec for orbit insertion in any cases
- the second engine provides for the
  - full mission ΔV = 3000 m/sec
  - alternate mission ΔV = 1450 m/sec, 800 m/sec

Recalling that the baseline spacecraft has a fixed mass at launch of 1955 kg with a mass of 1230 kg reserved for the propulsion system, the following conclusions can be drawn.

The maximum acceleration is reached in the case of the single motor which has the capability ΔV = 4000 m/sec and is 1.95 g. This appears

quite acceptable for the overall spacecraft.

For a total capability ΔV = 4000 m/sec, the single motor (m_m=1213.4 kg) has an advantage of 86.6 kg over the two motors configuration (m_m=1300 kg). For a total capability ΔV = 2450 m/sec, this last advantage is 77 kg (951 kg against 1028 kg). This net advantage will be decreased if the mass of the necessary shutdown and restart system is taken into account. No order of magnitude was found for the mass of such a system.

In some cases, the chamber pressure is unusually low for solid propellants (e.g., 400 psia) in order to help limit the spacecraft acceleration. As a result, some difficulty with the combustion of beryllium and/or reduced specific impulse may be encountered (degradation of performances). However, only tests can answer these questions.

Table E-2 summarizes computer results for all cases. In order to get more flexibility, masses of the different motors were evaluated for other values of ΔV. Two curves illustrate these results; Fig. E-3 shows the relationship of the mass of the second motor with increasing ΔV, Fig. E-4 shows the same relation but for the complete system, one-motor configuration, two-motors configuration. As said before, the first one presents a mass saving with respect to the second one.

5. Analysis of Vernier Subsystems

a. Mode of Operation and Equations

TVC operation: TVC starts up 6 sec. before solid motor start up to provide auto-pilot control and reduce transient, and it shuts down 6 sec after the solid motor shutdown for the same reason. Thus TVC operates during a time t_b + 12 where t_b is the burning time of the solid motor controlled, and at a thrust equal to 5% of the solid motor thrust. Assuming a constant decreasing thrust F for the solid motor, the mass of liquid propellant needed during TVC operation is

$$m_p = 0.05 \frac{(t_b + 12)}{gI_s} \frac{(F_{max} + F_{min})}{2}$$

I_s being the vacuum specific impulse of the bipropellant system.

The other maneuvers consist of:

- three course-corrections requiring

$$\Delta V_1 + \Delta V_2 + \Delta V_3 = 660 \text{ m/sec}$$

- the change of apoapsis maneuver requiring

$$\Delta V_6 = 300 \text{ m/sec}$$

In the "alternate mission", this last maneuver is not considered. In all these maneuvers, the vernier subsystem operates at constant thrust, and the mass of propellant consumed is given by the rocket equation:

$$m_p = m_o(I - e^{-\frac{\Delta V}{gI_s}})$$

For $\Delta V_{1,2,3}$

$$m_{p1,2,3,} = 1955(I - e^{-\frac{660}{gI_s}})$$

For ΔV_6

$$m_{p6} = (1955 - m_o^*)(I - e^{-\frac{330}{gI_s}})$$

The mass m_o^* is equal to the mass of all propellant burnt prior to the change of apoapsis maneuver plus the mass of the first solid motor case (which is staged off) for the two solid motor configuration.

b. Results

Preliminary estimates had shown high consumption for TVC and consequently, high values for the mass of the vernier subsystem, for

instance 720 kg for the single motor configuration with a ΔV = 4000 m/sec. Adding the mass of the motor itself, 1213 kg, this gives a total of 1933 kg far beyond the allowed mass of 1230 kg for the overall propulsion system. Necessity of realistic values and systems led to consideration of systems having much less capability. Consequently, detailed investigations were carried out for the following configurations:

- one solid propellant motor configuration offering a ΔV = 1000 m/sec
- two solid propellant motor configuration offering a capability

$$\Delta V_1 = 1000 \text{ m/sec} \qquad \Delta V_2 = 1450 \text{ m/sec}$$

Table E-3 presents the results in terms of mass of propellant, mass of vernier subsystem, mass of propulsion system in all cases. Fig. E-5 shows the mass of the total propulsion system as a function of the total ΔV capability of the vernier subsystem (both course-corrections and orbit trim).

6. Trade-off and Design

The bound limit of 1230 kg for the overall propulsion system drawn in Fig. E-2 shows the range in which workable systems are restricted. In particular, the even low capability configuration using two solid motors ΔV = 1000 + 1450 m/sec is not acceptable. Needless to say, it is impossible to meet both requirements of propulsion system mass constraint and ΔV capability for a "full" mission.

However, assuming now the mass of the spacecraft and the payload specified, a trade-off remains possible between alternate missions. Thus, two solutions were completely defined along the scope of the study. The first one, very classical, can be achieved by the current and near future technology but offers a poor capability. The second one presents

better performance but is based on OF_2/B_2H_6 and will require a deep investigation in the future for development, test and qualification for space.

The first solution consists in a single, fixed-impulse, burn-to-completion beryllium solid propellant motor (mass = 526 kg) which has a capability of delivering a ΔV = 1000 m/sec for orbit insertion at a constant acceleration 0.75 g and a N_2O_4/A-50 vernier subsystem. This bipropellant system or a similar one has been extensively used for space missions (Apollo, Mariner) and benefits from a long experience and strong technology. Further information is expected to be received on its long-range behavior from the Mariner orbiter and Viking. The vernier subsystem had a maximum allowable mass of 700 kg and provides capability for the three course-corrections, for TVC of the solid propellant motor and then has a remaining ΔV = 520 m/sec. This capability may be used in two different ways:

- for a change of apoapsis only, from 100 R_J to 38 R_J
- for a change of orbit inclination only, it will decrease the inclination by 5^o

The total mass of propellant is 587.5 kg

mass of oxidizer = 361.5 kg (800 lb)

mass of fuel = 226 kg (500 lb)

The total mass of helium pressurant gas is 1.45 kg (3.2 lb). The four propellant tanks are identical and are described in table E-4 together with the two identical helium tanks based on information from Ref. 9. The maximum thrust provided by the vernier subsystem is equal to 5% of the solid propellant motor maximum thrust, i.e., 160 lbf. Each of

the four engines has a maximum operating thrust of 40 lbf except during TVC operation where they are throttled. The burning time is a function of the mass of propellant used during a maneuver:

	Propellant Mass Burnt	Burning Time
course maneuvers:	386 kg	1620 sec
orbit trim:	170 kg	715 sec
TVC operation:	31.5 kg	148 sec

The second solution consists in two fixed-impulse, burn-to-completion, beryllium solid propellant motors and an OF_2/B_2H_6 vernier subsystem. The first solid propellant motor has a mass of 526 kg (478 kg of propellant) and provides a ΔV = 1000 m/sec for orbit insertion at a constant acceleration 0.75 g. The second solid motor has a mass of 323 kg (294 kg of propellant) and provides a ΔV = 800 m/sec for orbit trim at a constant acceleration of 0.55 g. This capability offers alternately:

- a change of apoapsis only from 100 R_J to 29 R_J
- a change of orbit inclination only, a decrease of 8°

The other characteristics of these motors are summarized in table E-4. The OF_2/B_2H_6 vernier subsystem has a total mass of 391.6 kg and has capability for the three course-corrections and thrust vector control during the operation of the two solid propellant motors. The total mass of propellant is 326.6 kg (720 lb) divided as following:

mass of oxidizer = 68 kg (150 lb)

mass of fuel = 258.6 kg (570 lb)

The total mass of helium pressurant gas is 2.29 kg (5.05 lb). The four propellant tanks and the two helium tanks are described in Table E-4. As

in the first solution, each of the four engines has a nominal operating thrust of 40 lbf except during TVC operation where they are throttled. Burning times are as following:

	Propellant Mass Burnt	Burning Time
course maneuvers:	290 kg	1660 sec
TVC (first motor):	23 kg	148 sec
TVC (second motor):	13.6 kg	160 sec

The total mass of the propulsion system, 1241 kg, is slightly above the limit of 1230 kg but appears in an acceptable range. Tables E-2 and E-4 offer all parameters for both solutions.

a. Design of the Solid Propellant Motors

All motors considered in the preceding solutions are identical and have the following characteristics. The charge is fully case-bonded throughout its lateral surface and without mechanical stress relief. Based on the available information, the chamber is specified to be heat-treated, 6 AP 4V, titanium alloy because of its high strength-to-weight ratio and non-magnetic properties (there is a magnetometer aboard). One of the advanced composite materials might be considered and would provide a lighter chamber. The nozzle design is an external configuration with an 80:1 expansion ratio and centered unit core. An external configuration improves motor performance with beryllium propellant and aids in sweeping the beryllium oxide from the chamber. Tape-wrapped light-weight carbon cloth surrounding a high density graphite insert and light-weight silica cloth will be used in the construction of the nozzle throat section and exit cone, respectively. Pyrolitic

graphite may be used in the throat section to minimize erosion and consequent vector misalignment and offset. Alternately, a radiating nozzle will be considered because of its potential weight reduction; recently, such a nozzle was fired successively at JPL and appears promising.

b. Design Specifications of the Vernier Subsystem

The subsystem consists in four identical thrusters one of which is gimballed in order to provide roll control and will be designed for long-term spacelife, long-time operation and multiple restart capability. Each engine utilizes the conduction cooling process to cool the chamber and a 60:1 radiation cooled nozzle skirt. The four engines are located at the maximum radius of the propulsion envelope. The subsystem is functionally a multi-start pressure regulated system using helium pressurant gas. It consists in two arrays hydraulically linked. Each array has two engines and are identical (Fig. E-6). Principal subsystem components are four propellant tanks (two for the fuel and two for the oxidizer) plus a positive expulsion screen as propellant acquisition device, pairs of normally closed/normally open (NC/NO) squib valves and four vernier engine units including throttle valves and shutoff valves.

The function of the hydraulic connection between arrays is to provide capability of uniform propellant consumption from each tank in order to reduce potential excursions of the center of gravity. A solenoid valve and a NO explosively actuated valve are included in the propellant line joining the two vernier subsystem branches. The solenoid valve is opened whenever nonuniform consumption occurs so that CG excursions are minimized. The NO pyro valve can be actuated to the closed position,

thereby hydraulically isolating each branch in the event that a branch unexpectedly develops a leakage that would jeopardize the mission. Capability for a degraded mission exists with the remaining thrusters.

The helium pressurant gas is stored in two separate tanks. Pairs of NC/NO squib valves are provided to seal the helium tanks whenever there is a long term storage (during the second-third course-correction interval and during the orbit insertion-orbit trim interval). Fig. E-7 and E-8 give a schematic of the two solutions.

A more detailed study should deal with the following problems:
- the influence of Jupiter radiation and RTG radiation on propellants properties and behavior. Their effects are presently unknown.
- the integration of the propulsion subsystem into the spacecraft including insulation of the parts to be kept within a range of acceptable temperatures and shielding for micrometeroroid protection.

B. Fluid Propulsion System

The high performances offered by new bipropellant liquid systems due to their high specific impulse ($I_s \geq 400$ sec) make them very attractive for planet orbiter missions where large velocity increments are needed. Their flexibility, precise control and multiple restart capability compensate for their complexity brought about by critical components such as valves and pressure regulators.

Fluid systems can operate in many different ways and emphasis has been placed in this study, on the various parameters that characterize their operation. In particular, both pump-fed and pressure-fed systems are considered together with the three general classes of liquid propellants:

- earth storables: in the liquid state at earth ambient temperatures and pressures.
- space storables: in the liquid state at temperatures below earth ambient but higher than liquid hydrogen.
- cryogenic or deep cryogenic: propellants using liquid hydrogen as the fuel.

The first class is mainly represented by N_2O_4/A-50 which benefits from long experience. Some propellants of the two other classes are used for launch vehicle propulsion, but none of them has been flown in space.

The study was directed toward an analytical evaluation of a fluid propulsion system satisfying the mission requirements within the limits of specified spacecraft and payload weights. Different systems are described, the large components (tanks, engine) are sized and a mass breakdown is given. For economy, the term "payload" will refer to the spacecraft without its propulsion subsystem.

The general design of the spacecraft is assumed to be separated into two parts:

- the propulsion module: tanks and the engine in a compact stage configuration
- the capsule

The orientation with respect to the sun will be referred as "sun on capsule" the propulsion module is shaded, and "sun on tanks" - the propulsion module receives the solar flux directly (Fig. E-9). All designs featured separate fuel and oxidizer tanks. No analysis was made with common bulkheads.

1. General Characterization and Specific Constraints of Fluid Propulsion Systems

In addition to various parameters to which liquid systems are sensi-

tive, some conditions of operation are specified by engine companies (Refs. 4 and 7) and can be consequently viewed as constraints.

a. Mission Environment and Thermodynamic Considerations

The basic life-time for the propulsion system is the 815 days of transfer to Jupiter plus 365 days revolving around the planet. During the Jupiter transit phase the primary energy source is the sun, and the heat sink is deep space at a temperature of absolute zero. The solar flux density varies inversely with the square of the distance from the sun and is computed as a function of time for specific transfer trajectories. Fig. E-10 gives the evaluation of the solar flux versus time. Orbiting around Jupiter on a 1.1 x 100 R_J, the spacecraft spends most of the time far from Jupiter and the thermal influence of the planet can be neglected for a first approximation. Other heat transfers may occur from the payload for all cases and between propellants if the temperature ranges of the fuel and the oxidizer are different. The only critical case is the F_2/NH_3 combination for which this problem must be carefully considered.

Liquid propellants are very sensitive to thermal environment. For cryogenic and in a certain measure, space storables, heat transfer may cause boiloff with its resulting high pressure consequence and weight penalty. In the opposite way, low space temperatures may cause the earth storables to freeze. Consequently, tank pressure, tank dry weight, propellant boiloff, insulation and coatings which are thermally sensitive parameters may penalize heavily the propulsion system weight and will require considerable attention.

b. Propellants Candidates

The propellants usually considered for future space missions are:

- cryogenic: O_2/H_2 ; F_2/H_2
- space storables: Flox*/CH_4 ; OF_2/CH_4 ; OF_2/B_2H_6 ; F_2/NH_3
- earth storables: N_2/O_4/A-50 ; CIF_5/MHF-5

* Flox is 82.5% F_2 and 17.5% O_2.

Their liquid temperature range (Fig. E-11) shows their classification from H_2 to $40^{\circ}R$ approximately, to the common space storable ($150^{\circ}R$ - $200^{\circ}R$) and up to A-50 at $550^{\circ}R$ approximately. Storability is directly related to the liquid range as a function of both temperature and pressure.

c. Specific Impulse

The rocket equation shows how dependent on the specific impulse the mass of propellant is. Theoretical vacuum specific impulses are based on complete combination of fuel and oxidizer. However practical and effective figures are in short supply and vary among rocket engine companies. Morever, the specific impulse depends on several parameters, mainly the type of engine system (pressure-fed or pump-fed), the thrust, the chamber pressure, the nozzle expansion ratio, mixture ratio; figures finally selected are considered conservative and can be considered achievable by future operating propulsion systems. Table E-5 summarizes the specific impulses for the propellant candidates and the operating conditions.

d. Mixture Ratio and Bulk Density

Mixture ratios are optimized to give the best combination efficiency, therefore, the maximum specific impulse. The bulk densities of the various propellants combinations are shown in Table E-6 for the selected mixture ratios. The cryogenics, especially O_2/H_2, are the least dense (density approximately one-half that of the space storables). The space storables show a marked increase in densities followed by earth storables. A high propellant bulk density can offer a significant payload benefit since tank size (and weight) can be reduced. With the

exception of the hydrogen fueled propellants combinations, the effect of mixture ratio on bulk density is small.

e. Material Compatibility (Tables E-7, E-8)

Fluorine, OF_2 and Flox are reactive with most metals but compatible with passivated stainless steel, certain aluminum alloys, and monel. Passivated aluminum alloys are recommended for long-time storage of N_2O_4 and ClF_5.

f. Engine

The basic engine configuration usually considered is the fixed bell nozzle for both pump-fed and pressure-fed. However, the pressure-fed systems work at low pressure and require much larger nozzles than pump-fed systems. If the envelope is exceeded by the length of a fixed bell nozzle, the extendable bell nozzle configuration must be considered (Fig. E-12). But this causes increased weight, complexity and production costs and a degradation of performance. In any case, it should be noted that performance is very sensitive to the nozzle expansion ratio (Fig. E-13) This indicates that the largest practical value of this parameter must be employed subject to the limitations imposed by the available envelope.

Contrary to the case of solid propellant motors, fluid propulsion systems operate at constant thrust. The thrust level should be compatible with the maximum acceleration the spacecraft can take and accomodate the low ΔV requirement of course-corrections. If problems are caused by this last condition, throtteable systems would be considered.

Some sort of thrust-vector-control must be provided which requires that the engine be gimballed.

Nozzle cooling techniques selection depends mainly on the total burning time. Engine companies generally recommend a specific method

for the engine they build. According to their reports, regenerative cooling is selected for all propellants except OF_2/B_2H_6, N_2O_4/A-50 and CIF_5/MFH-5 because it involves no performance losses and has an unlimited lifetime. There exists upper limits on the chamber pressure for regenerative cooling but they are well above the selected range. Ablative cooling is selected for the remaining three combinations because decomposition may occur in a regeneratively cooled system.

g. Engine Start Mode

One of the attractive features of a fluid propulsion system is the restart capability. Since a total number of six burns is required for the proposed mission, engine ignition is a very important operation and requires further investigation. For engine start modes, some propellants must be oriented over the propellant feed lines at engine ignition to insure safe and reliable engine starts. Basically, three methods are available. For the idle-mode start, the engine operates initially on either liquid or vapor. The pressurization gas is not introduced until after the engine is started and the liquid is settled.

A liquid containment device (screen) assures liquid availability for engine start. There is no positive ullage orientation before starting and the tanks are pressurized before the engine is started. The weight of a containment screen is estimated to be 3 lb per tank based on previous experiences. However, the pressurization requirements for the hydrogen system using only a containment device is so great that another start mode used in conjunction may be advantageous.

External ullaging: ullaging rockets or preferably the ACS (attitude control system) of the spacecraft are utilized to provide ullaging thrust.

They orient the ullage before gas is introduced, therefore, gas is never injected directly into liquid and liquid is assured for engine start. The associated penalty is very small.

Fig. E-14 summarizes clearly the way the three modes are operating. Although the idle-mode start is not always possible, it was assumed for this baseline analysis because of its simplicity; however, further investigation will be necessary in the future for specific propellant combinations and engine configurations and will require practical experiments.

2. Baseline Propulsion Systems

a. Preliminary Evaluation

In this section, the rocket equation is used in order to get an order of magnitude of different parameters as a guideline for the study. The propellant loading factor is defined by $\lambda = m_p/m_o$ where m_p is the mass of propellant and m_o is the initial gross mass of the spacecraft. For a constant thrust, the rocket equation gives

$$\lambda = I - e^{-\frac{\Delta V}{g I_s}} .$$

The total burning time t_b (sec) is given by

$$t_b = g\, I_s \frac{m_p}{F}$$

where F is the engine thrust (Newton). The total impulse I is defined by

$$I = F\, t_b \quad (N.sec)$$

Subsequently, the propellant loading factor can be plotted as a function of the specific impulse for different ΔV (Fig. E-14a).

For ΔV = 5 km/sec and if we assume I_s = 400 sec (it is a good representative value for a space storable propellant, mainly Flox/CH_4),

the corresponding λ is 0.725. Two conclusions can be drawn:

- if the payload is fixed to 725 kg (1600 lb) then the mass of propellant is 5590 kg (12,350 lb) and the mass of the spacecraft at launch is 7725 kg (17,030 lb).
- if the mass of the spacecraft at launch is fixed to 1955 kg (4300 lb) then the mass of propellant is 1418 kg (3120 lb) and the payload is 185 kg (408 lb).

None of these preliminary designs appear feasible and it was decided to proceed in the following way: keeping I_s = 400 sec and a mass fraction of 0.8, both the mass of the spacecraft and the payload are specified at their baseline values, 1955 kg and 725 kg respectively. Therefore, the mass of propellant allowed is 1005 kg (2220 lb), the resulting loading factor is λ = 0.515 and the maximum ΔV achievable is approximately 2.85 km/sec. The last method presents a trade-off between mass capability and ΔV available for maneuvers. The value of 2.85 km/sec exceeds the minimum value of 1.66 km/sec required to fulfill the basic mission to orbit the spacecraft around Jupiter (i.e., the three course-corrections and orbit insertion). The resulting design appears feasible and satisfactory; these values were retained as a basis for further study.

b. Characteristic

Although the variations of performance with thrust level for different nozzle expansion ratios and chamber pressures indicate that a high thrust level is preferable, the engine thrust is determined by limiting the maximum acceleration to 1 g. This maximum acceleration occurs at the end of the burning process when all the propellant is almost burnt. The constant level of thrust selected is 2000 lbf (8900 N) therefore keeping the acceleration between 0.46 g and 1g. Furthermore,

this domain of acceleration assures that the propulsion system weight is independent of the thrust-weight ratio. The selected thrust gives a 7.2 sec. (minimum) operating time for the smallest ΔV, which is quite acceptable. Using the basic assumption retained earlier - ΔV capability of 2.85 km/sec - a total burning time of 450 sec is found, a value very reasonable from the cooling techniques viewpoint. A nozzle expansion ratio of 100 for all propellant combinations and a chamber pressure P_c of 100 psia for all pressure-fed systems have been selected.

c. Description

- Fuel tank configuration: with the exception of H_2 fueled systems, the basic design utilizes four spherical tanks for all propellants, two tanks for the oxidizer and two tanks for the fuel. This configuration offers the best arrangement and yields a well-sized, compact propulsion module which can be easily integrated on the spacecraft. Tanks have reasonable dimensions and problems of long feed-lines are eliminated. Furthermore, if one tank suffered some sort of failure during the mission, the second one would provide a minimum capability to assure a kind of degraded mission. Due to the low density of H_2, a three tank configuration is preferred for H_2 fueled systems. It incorporates a single ellipsoidal H_2 tank and two spherical oxidizer tanks. Each propellant tank is individually insulated. The meteoroid shield may alternately cover each tank separately or covers the whole propulsion module.

- Pressurization system: helium pressurization systems are selected as the most applicable system for all propellants except for hydrogen tanks where heated GH_2 is used.

For cryogenic and space storable propellants, helium is stored within the oxidizer or fuel tank, whichever has the lower temperature. The appropriate tank volume is increased to include the volume of the

pressurant storage sphere. This configuration reduces the gas storage temperature, hence the weight of the bottle. Its temperature is assumed to be at the maximum liquid saturation temperature reached in the mission. The maximum helium storage pressure is 4500 psia.

For earth storable propellants, helium is stored outside at 530°R, since there is no advantage to keep the previous configuration. A proper insulation is provided by thermal protection.

All systems offer a common feature: the helium gas is heated by the engine before being injected into the propellant tanks.

- Thermal assumptions: the payload section is assumed to be maintained at 530°R (70°F) throughout the mission. A propellant tank staying in the shadow of the spacecraft will have an average temperature of approximately 160°R. It turns out that the spacecraft orientation is a very efficient means for thermal control of the propulsion system. Comparison of the temperature range of the various propellants leads to the following configurations. For the cryogenic and space storable propellants, the spacecraft will be oriented so that the tanks are shaded. Then propellant boiloff probably can be eliminated for all of them except hydrogen. For the earth storables, sun-facing tanks are desired because sun-shielded would present a definite risk of freezing.

Two other passive thermal control techniques will be considered. Insulation is simple and effective; it consists in double-aluminized mylar with tissue glass spacers and weighs 2.3 lb/ft^3. Its advantages are counterbalanced by a weight penalty. Surface finish will be of interest for the sun-on-tanks configurations. High α/ε ratios (absorptivity over emittance) are desirable, up to 2.2.

- Propellant initial conditions: all propellants are assumed to be at their normal boiling point temperature at the start of the mission,

with the exception of A-50 and MHF-5 which are assumed to liftoff at 530°R. Subcooling propellants prior to liftoff may be considered in order to increase thermal capacity if necessary. In this case, it will decrease operating pressures and insulation requirements therefore reducing the propulsion module weight.

- Propellant leak rate sensitivity: based on conservative evaluation for a Mars mission, propellant loss due to leakage is negligible, varying from an estimated 3 lb for N_2O_4 to 28 lb for H_2 for the total 1180 days of the propulsion module operating lifetime.

3. Analysis of Possible Solutions

After consideration of propellant performances and characteristics and probable developments in the future, it was decided to design the propulsion subsystem for four combinations representative of classes and feed-systems. They are:

F_2/H_2	cryogenic	pump-fed
Flox/CH_4	space storable	pump-fed
OF_2/B_2H_6	space storable	pressure-fed
N_2O_4/A-50	earth storable	pressure-fed

The first three are new (no space experience) but are highly promising and currently under intensive investigation and testing. The last one benefits from extensive experience in space.

Table E-5 summarizes several parameters for the propellants and the operating conditions. The most important are the specific impulse I_s, the mixture ratio r and the chamber pressure P_c. They are recalled below:

H_2/F_2	I_s = 460 sec	r = 12	P_c = 900 psia
$Flox/CH_4$	400 sec	5	500 psia
OF_2/B_2H_6	414 sec	3.82	100 psia
N_2O_4/A-50	305 sec	1.65	100 psia

The first three use the sun-on-payload orientation, N_2O_4/A-50 uses the sun-on-tanks orientation.

a. Specifications for Tanks and Engines

Following considerations previously stated all combinations use the four spherical tanks configuration except the F_2/H_2 system which uses an ellipsoidal hydrogen tank and two spherical fluorine tanks.

All tanks are designed with 2021 Aluminum with the following requirements:

- minimum skin thickness 0.040 inch
- maximum temperature +70°F
- tank pressure varied from 0 to 300 psi
- manhole covers in all tanks for accessibility
- allowances made for local beef-up for support attachments and discontinuities.

The ellipsoidal tank has a $\sqrt{2}$:1 dome. Figures E-15 and E-16 show typical tank configurations for spherical and ellipsoidal shapes respectively. Total tank weights as a function of tank pressure are shown in Figs. E-17 and E-18. The tank weights are independent of tank pressure up to the minimum gauge limitation at which point they become very pressure sensitive. Each tank is individually insulated.

Pressurization spheres are stored inside the propellant tanks for all systems except N_2O_4/A-50 where they are stored externally. The nozzle expansion ratio is assumed to be 100 for pump-fed systems and is restricted

to 60 for pressure-fed systems in order to hold the propulsion module to a reasonable length. All the engine parameters being selected, the dimensions and the weight of the engine can be determined. Figures E-19 and E-20 give the information for the Flox/CH_4 system.

b. Pressurization System Operation

The determination of this system, its dimensions and weight, requires some insight into its mode of operation.

- Pump-fed systems: helium pressurization furnishes the net positive suction pressure (NPSP) of 4 psi above the propellant saturation pressure for engine burn throughout expulsion. Evaluation of the helium pressurization system is based on the following assumptions: ullage and liquid is at thermal equilibrium between burns so that the total tank pressure is the sum of the partial pressures of the saturated propellant vapor and the partial pressure of the helium; helium inlet temperature is equal to propellant saturation temperature. Heated helium, which collapses after burn (since heating ends) is used.

- Pressure-fed systems: they require more details because of the significantly higher pressure used. This implies more pressurant, larger storage spheres, heavier propellant tanks and finally a heavier propulsion system. The pressurization system must supply the net positive suction pressure (NPSP) requirements, chamber pressure P_c) and pressure drops through the feed-lines and injectors (typical value 65 psia for N_2O_4/A-50). The minimum tank operating pressure is the sum of the system pressure drops plus the 100 psia chamber pressure. Helium pressurant always supplies the 100 psi chamber pressure plus any portion of the system pressure drop not provided by the propellant vapor pressure. When the sum of the propellant saturation pressure (P_v) plus 100 psi is greater

than the minimum operating pressure, P_c is then greater than 100 psi. However, when P_v plus 100 psi is less than the minimum operating pressure, additional helium is required (P_c is never less than 100 psi) to maintain the tank pressure at the minimum. Helium is stored in the conditions defined before (pressure 4500 psia, lowest temperature available). It is heated through a heat exchanger by the engine and then expanded isothermally at 350 psia. A complete analysis of the pressurization system especially for pressure-fed systems appears highly complex. Scaling methods and extrapolations were used for a first order analysis based on currently operating systems.

c. Determination of Tanks Pressure, Ullage and Insulation from Thermal Considerations

A thermodynamic analysis would consist of defining the external environment throughout the mission, developing a thermal model of the spacecraft, computing the heat transfers and temperatures as experienced during the various phases of the mission, then selecting the thermally sensitive parameters to minimize total system mass. This highly complex analysis which requires a sophisticated computer program was not included in the first order design. However, in order to take into account as many factors as possible, available information has been extrapolated to this specific Jupiter Orbiter mission and allows substantial results and conclusions. Figures E-21 and E-22 show approximated average surface temperatures as a function of time for all selected systems.

- F_2/H_2 system: the surface of the hydrogen tank reaches a steady-state temperature of 80°R approximately. Constant heating of the tank from structural heat leaks due to the sun-on-payload orientation and, in a lesser extent, by heat transfer through the insulation causes the H_2

tank pressure to take high values, up to 170 psia. Minimum gage capability is exceeded and consequently a strong weight penalty is imposed on the tank. There is a one inch thickness of insulation for the H_2 tank, but insulation cannot control significantly the pressure because heat comes from the structure. An efficient solution would be the introduction of a shadow shield between payload and propulsion module. This can reduce the pressure to an acceptable range.

Fig. E-23 presents an indication of H_2 pressure profile during the mission and shows the NPSP which is provided each time a burn occurs. The surface of the F_2 tank remains at a constant temperature of about 130°R. This is well in the range of liquid fluorine and the maximum tank pressure is only 35 psia. An insulation thickness of 0.5 in. is assumed sufficient to protect the two F_2 tanks. Table E-9 summarizes these various results and gives also the initial ullage assumed to compute the dimensions of the tanks.

- Flox/CH_4 system: it proves to be particularly well suited to the mission and space environment since the temperature of surface of both propellants tanks remains at about 140°R, well within the range of their liquid state. Therefore, pressure levels are fairly low, 40 psia for Flox and 35 psia for CH_4. This is always below the minimum gage pressure capability. Similarly to the F_2 tanks, an insulation thickness of 0.5 in. is sufficient for both propellants (Table E-9).

- OF_2/B_2H_6 system: the temperature of interest decreases from 300°R to 250°R approximately. It is in the range of liquid B_2H_6 but slightly above the range of liquid OF_2. This causes OF_2 to require a higher operating tank pressure and an insulation thickness of 1 in. (0.5 is sufficient for B_2H_6). Pressure-fed systems utilize greater pressures

than pump-fed; OF_2 tank pressure is 230 psia, B_2H_6 tank pressure is 165 psia (Table E-9).

- N_2O_4/A-50 system: the tank surface temperature constantly decreases to an approximate value of 300°R. To prevent freezing the propellants, a surface finish with a ratio $\alpha/\varepsilon = 2.2$ (the largest value found) is combined with five inches of insulation for all tanks. Subsequently pressures are acceptable, 220 psia for N_2O_4 and 190 psia for A-50 (Table E-9). In order to reduce the insulation penalty, two solutions can be considered. The first is loading the propellants subcooled at 500°R and keeping α/ε as high as 2.2, which will require a certain quantity of insulation anyway. The second solution which would prove more attactive, it consists of active propellant heating using, for example, the RTG.

d. Determination of the Design Parameters and Performances

A computer program was developed to evaluate most of the design parameters, weights of the propellants and pressurant, weights, sizes and insulation of all tanks according to the following scheme. Both the mass of the spacecraft and the payload were specified (1955 kg and 725 kg respectively). Using a mass fraction as accurate as possible from current experience, the mass of propellant is determined. The mixture ratio permits calculation of the weight of both oxidizer and fuel. Taking into account the ullage and the fact that a pressurant tank may be stored inside a propellant tank, the tank volumes are evaluated. Tank dimensions follow. A weight is then possible. The same program performs the various maneuvers and shows the ΔV performance of each system. This will be detailed and used later.

- Propellant parameters: propellant weights range from 2050 lb to 2180 lb approximately. Except for the hydrogen whose inside dimensions are 57 in. by 40.3 in. all the other tanks have approximately the same diameter of 30 in. Consequently, all the tanks weigh an average value of 60 lb except the H_2 tank which weighs 105 lb. All the insulation weights are reasonable - especially for space storable propellants - except for the N_2O_4/A-50 system which needs 64 lb. This is due to the 5 in. thickness requirement to prevent the liquids from freezing. Table E-10 defines all selected parameters.

- Pressurant system parameters: Table E-11 presents the configuration and computed values for each system based on a scaling method. The F_2/H_2 system needs only one pressurant tank stored inside the H_2 tank to pressurize the F_2 tanks, H_2 being pressurized by GH_2. The Flox/CH_4 and OF_2/B_2H_6 system offer a two pressurant tank configuration. This is to keep both CH_4 tanks and both OF_2 tanks where the pressurant is stored, identical and to allow a symmetric design.

The N_2O_4/A-50 system requires greater volume storage than the other systems due to high temperatures of helium which no longer benefits from low storage temperatures.

Pump-fed systems require respectively 16 and 14.8 lb as pressurant system total weight. The requirement is greater for pressure-fed systems and reaches 48 lb approximately.

- Engine system parameters: Table E-12 summarizes the operating conditions for both pump-fed and pressure-fed engines, their overall dimensions, and their weight. These values are obtained from diagrams like Fig. E-19 and E-20. As expected, the pressure-fed engine has a very large size of 48 in by 30 in even at a limited ratio of 60.

e. Weight Breakdown

A summary of the weights for the four systems is shown in Table E-13. These weight statements give a breakdown of all the inert weight elements, the impulse propellant (propellant used for ΔV), the total propulsion module and the payload. The summary weight items are made of the following:

- structure: a weight is allocated for tank supports, attachments and tank bulkhead insulation.
- propellant feed assembly:

  tanks

  valves and plumbing: 38 lb for all systems except 28 lb for N_2O_4/A-50.

  insulation
- pressurization system: helium, tanks, plumbing
- engine system

The sum of the above is the dry inert weight; to this must be added weight allowances for the following:

- contingency: 10% of dry inert weight
- residuals: they are liquid and vaporized propellant remaining at the end of the final burn. They are given as percentage of mass of propellant: 3.5% for cryogenic systems and 2% for all others.
- performance reserve: it is a contingency for specific impulse degradation and corresponds to 1% of total ΔV.

The inert weight is the sum of the above three allowance weights plus the dry inert weight.

- impulse propellant: propellant used for ΔV
- propulsion module: inert plus impulse propellant weights

- payload: weight of the spacecraft at launch (4300 lb) minus propulsion module.

As a consequence of the method used to determine the systems, the resulting payloads are approximately 1600 lb; there is a slight advantage for F_2/H_2 and OF_2/B_2H_6 systems and a slight penalty for the Flox/CH_4 system. This is not true for the N_2O_4/A-50 system due mainly to the high insulation weight required.

f. Comparison of Propulsion Systems Based on ΔV Performance

Each ΔV requirement being known, the computer evaluated the propellant consumed and the burning time for each maneuver successively (Table E-14).

- First course-correction: ΔV = 33 m/sec

  All systems require the same burning time of 7.2 sec which is the smallest of all burns but is readily achieved by the systems.

- Second course-correction: ΔV = 77 m/sec

- Third course-correction: ΔV = 560 m/sec

- Orbit insertion: ΔV = 1000 m/sec

  The burning times for this last maneuver range from 150 to 170 sec approximately. From the viewpoint of guidance and efficiency of the maneuver, this range is highly satisfactory and would assure a good resulting orbit.

- At this point, the basic mission of orbiting the spacecraft is fulfilled and the ΔV capability remaining is computed to compare propellant merits and to evaluate possible orbit trims.

The F_2/H_2 system offers the best capability, providing an excess ΔV of 1248 m/sec, which is just the ΔV required to bring the orbit apoapsis down from 100 R_J to 20 R_J. The Flox/CH_4 system offers approximately 100 m/sec more than the OF_2/B_2H_6 system which provides 1000 m/sec excess ΔV.

The N_2O_4/A-50 system has a very poor capability of 371 m/sec

- Then an orbit trim is operated consisting of a ΔV = 330 m/sec which brings the apoapsis down from 100 R_J to 50 R_J.

- After this trim, the remaining V capability is computed for the same reason as stated before. F_2/H_2 system shows the best result of 846 m/sec due to its high specific impulse, followed by the Flox/CH_4 system with 695 m/sec. Although it has a higher specific impulse than Flox/CH_4, the OF_2/B_2H_6 system offers less capability with 613 m/sec because of the weight penalty associated with pressure-fed systems. The N_2O_4/A-50 system shows a very poor result with 37 m/sec which is almost negligible.

g. Additional Specifications

- Fluid systems: Figures E-24, E-25, and E-26 represent fluid system schematics for earth storable, space storable and cryogenic systems respectively. These schematics are typical of the three classes and have been directly borrowed from the supporting literature (Ref. 4). Both fuel tanks are manifolded together with a common feed-line and common vent line. The oxidizer system employs common manifold also. Tanks with common liquids utilize a parallel vent system with one relief valve. Filling is made through check quick disconnect valves which can be made to seal very effectively. The pressurization plumbing features bottle, relief valve, fill system and regulation system. Helium is filled through a quick disconnect and is closed off with a squib fired valve. In the event of any over-pressurization within the bottle, a burst disc will rupture and a relief valve will open. The high pressure in the bottle is initially stepped down by regulator RG-1 to 500 psia. This pressure is then regulated to the propellant tank by two individual

regulators RG-2 and RG-3. This provides the proper pressure for each oxidizer tank and fuel tank. The heat exchanger is sized to always bring the hot side gas up to the same temperature. The hot flow is mixed with a cool flow coming through a calibrated bypass loop. The mixture will produce the desired pressurization temperature.

Earth storable and space storable fluid systems are rather similar but cryogenic systems need special features. The differences consist mainly in additional valves used to insulate completely the hydrogen tank between burns,i.e., to prevent heat inputs by fuel trapped in the feed-line. Also the hydrogen tank is pressurized by GH_2.

- F_2/H_2 and Flox/CH_4 pump-fed systems utilize regeneratively cooled engines while OF_2/B_2H_6 and N_2O_4/A-50 pressure-fed systems utilize ablatively cooled engines.

h. Requirement for a Full Capability System

In order to obtain an order of magnitude estimate of the spacecraft design based on the preliminary evaluation having a given payload of 1600 lb and a total ΔV of 5 km/sec, the following characteristic parameters were computed for a Flox/CH_4 pump-fed propulsion system.

Weight of the spacecraft at launch:	17,030 lb
Weight of the propulsion module:	15,430 lb
Weight of propellant:	12,488 lb
Inside diameter of a fuel tank:	49.3 in.
Inside diameter of an oxidizer tank:	58.1 in'
Engine thrust:	4800 lb
Overall engine length (ε = 100):	46 in.
Nozzle exit diameter:	26 in

5. Trade-Off

The poor performance offered by the N_2O_4/A-50 system and the risk of freezing during the mission leads to the conclusion that it is definitively not suited to the mission.

The F_2/H_2 system has the overall best performance exceeding the second system by 151 m/sec. However, the high pressure reached by the hydrogen tank presents some hazards and furthermore, the stated performance is believed to be too optimistic. Although they offer slightly less capability, the space storable systems are preferred because of their overall satisfactory operating conditions (especially temperature and pressure). The OF_2/B_2H_6 system offers less ΔV capability than the Flox/CH_4 and has the disadvantage of a large engine causing a penalty for the design of the spacecraft.

It is therefore concluded that the Flox/CH_4 system is the best suited to the mission and is recommended assuming its development, testing and qualification in the future prior 1980.

After orbit insertion, the remaining capability of this system can be used in two different ways:

- change of orbit apoapsis only, from 100 R_J to 22.5 R_J approximately
- change of inclination only, by 11° approximately.

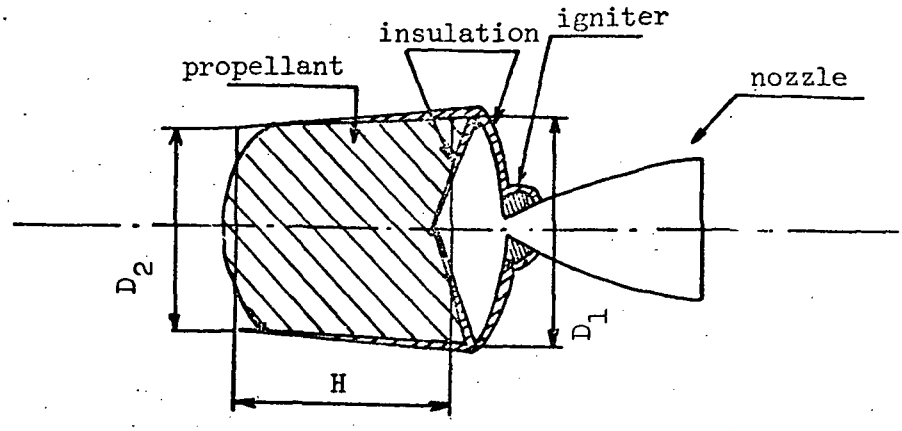

Fig. E.2 Solid Propellant Motor Schematic

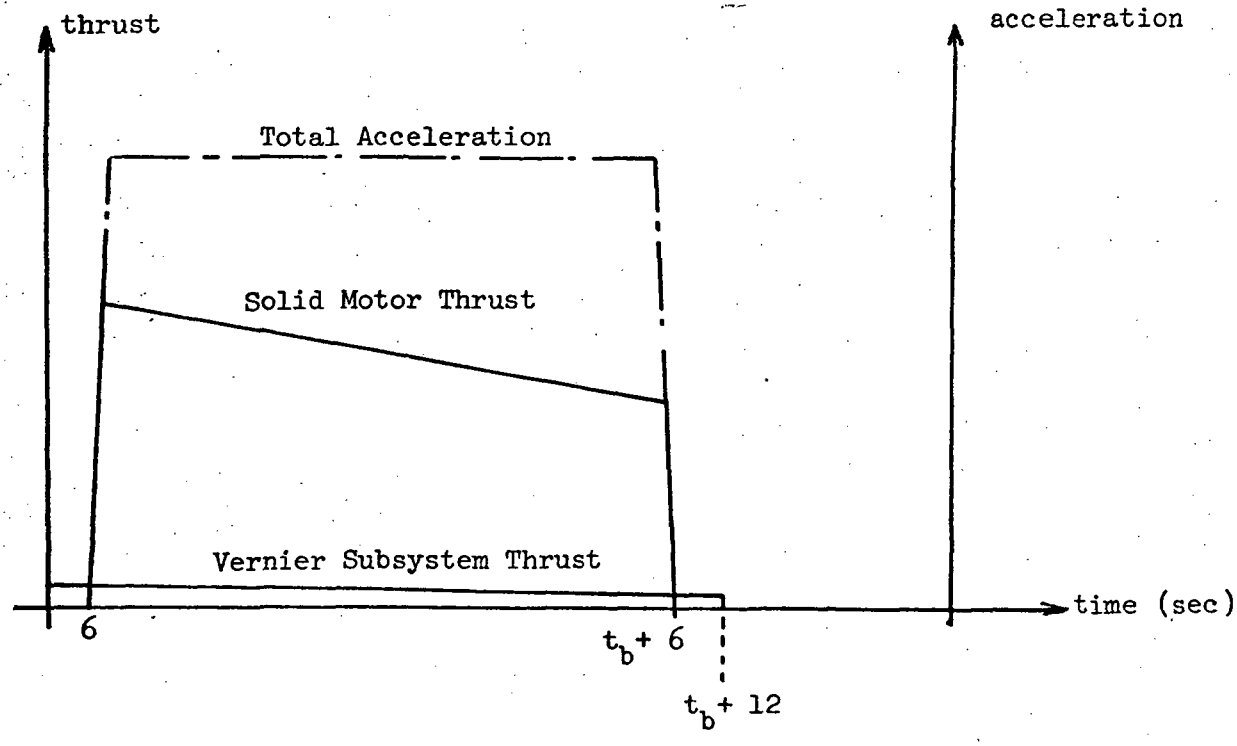

Fig. E.1 Thrust and Acceleration Profiles Schematic

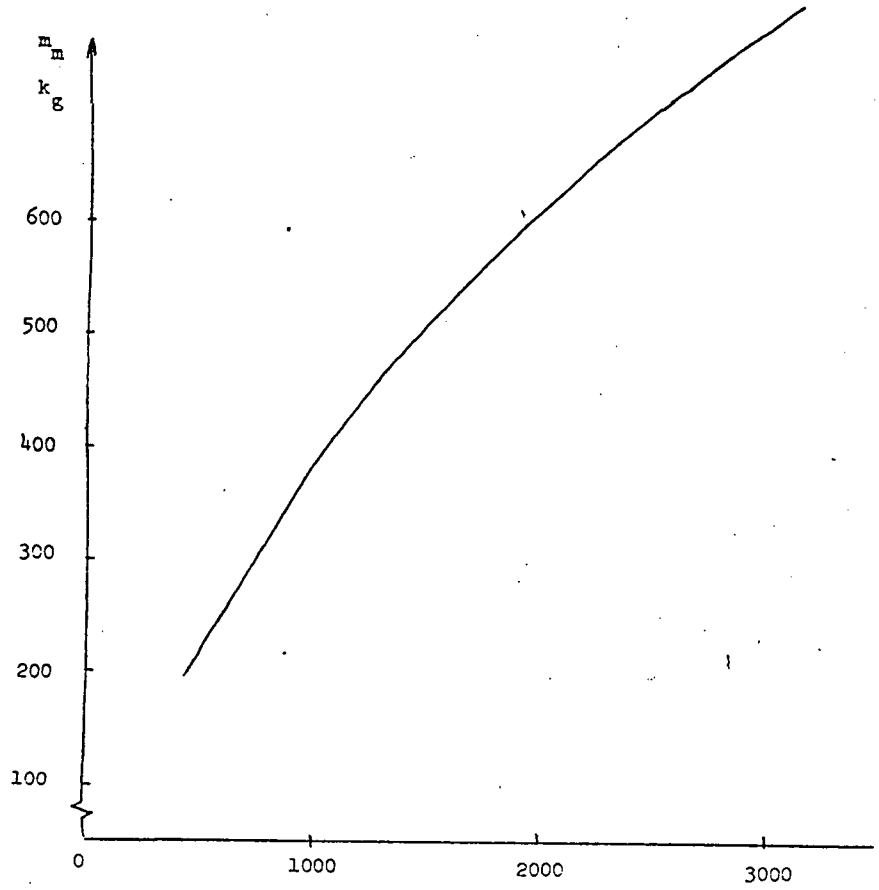

Fig. E-3 Two Motors Configurations: Mass of the Second Motor Versus ΔV Offered

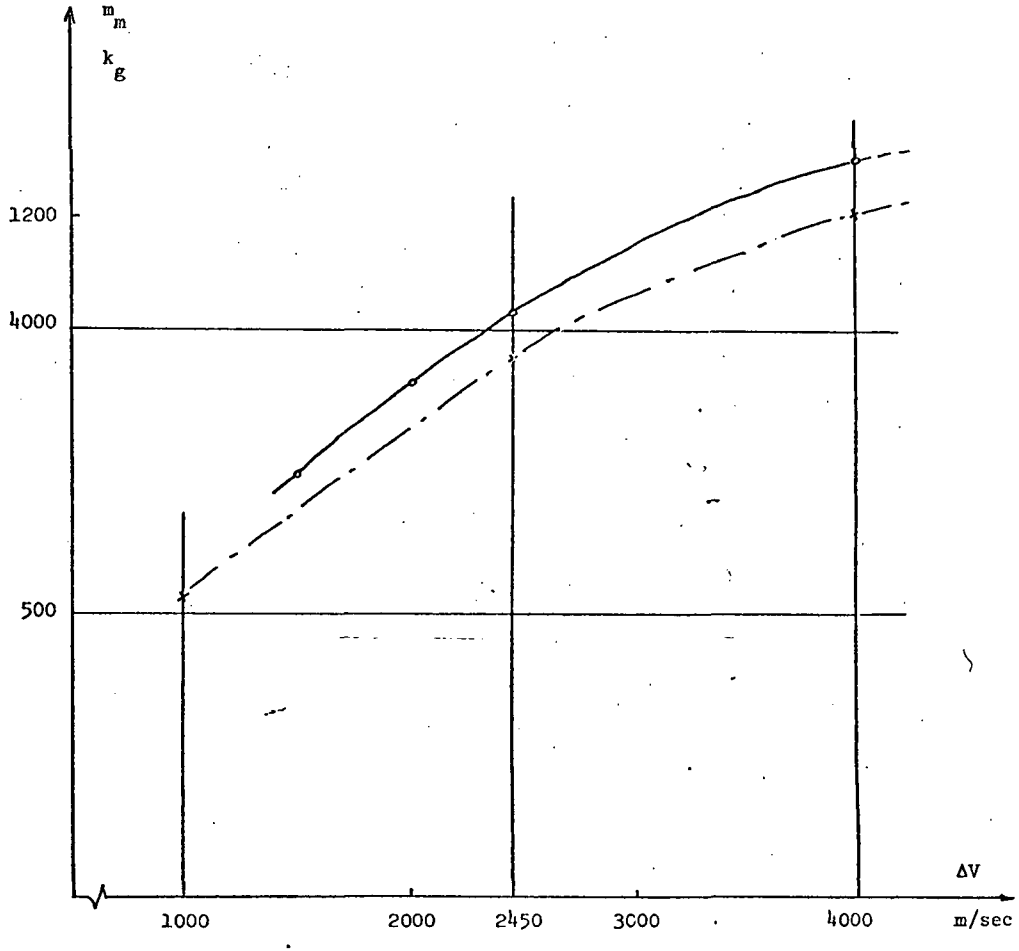

Fig. E-4 Mass of Solid Motor System vs. ΔV

x one motor configuration
o two motors configuration

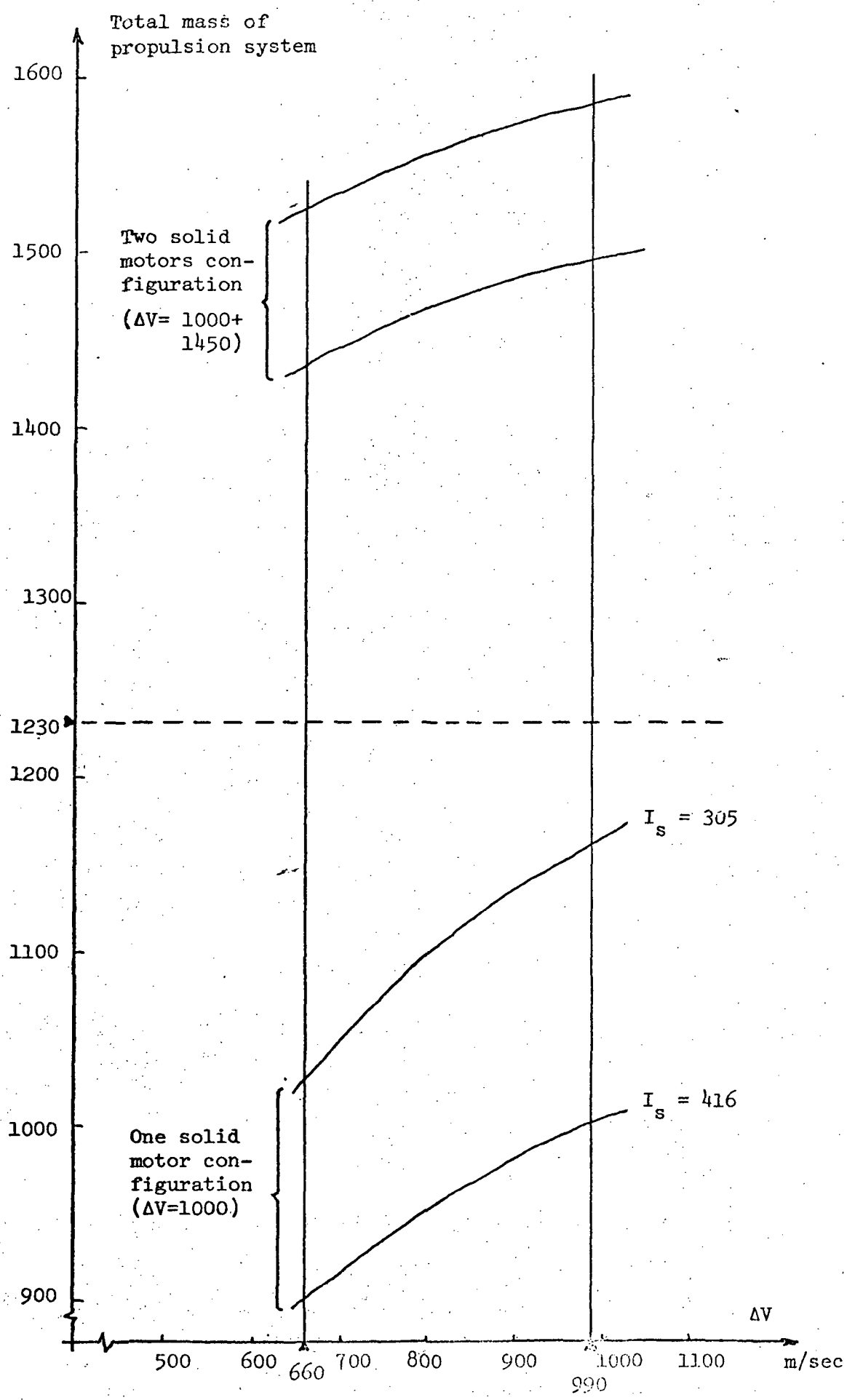

Fig. E.5 ΔV provided by the vernier subsystem vs. the total mass of the propulsion system

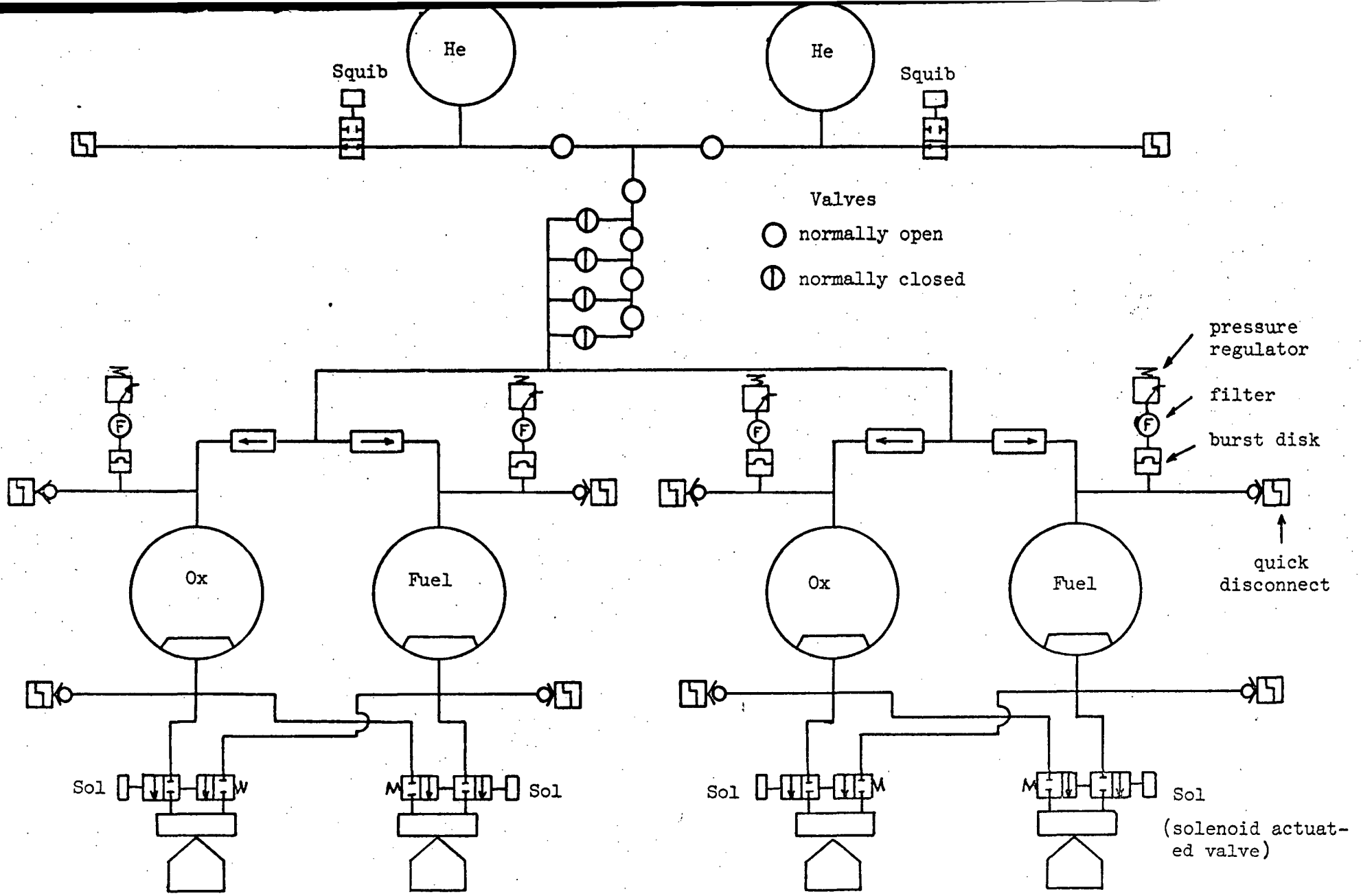

Fig. E.6 Bipropellant Vernier Subsystem Schematic

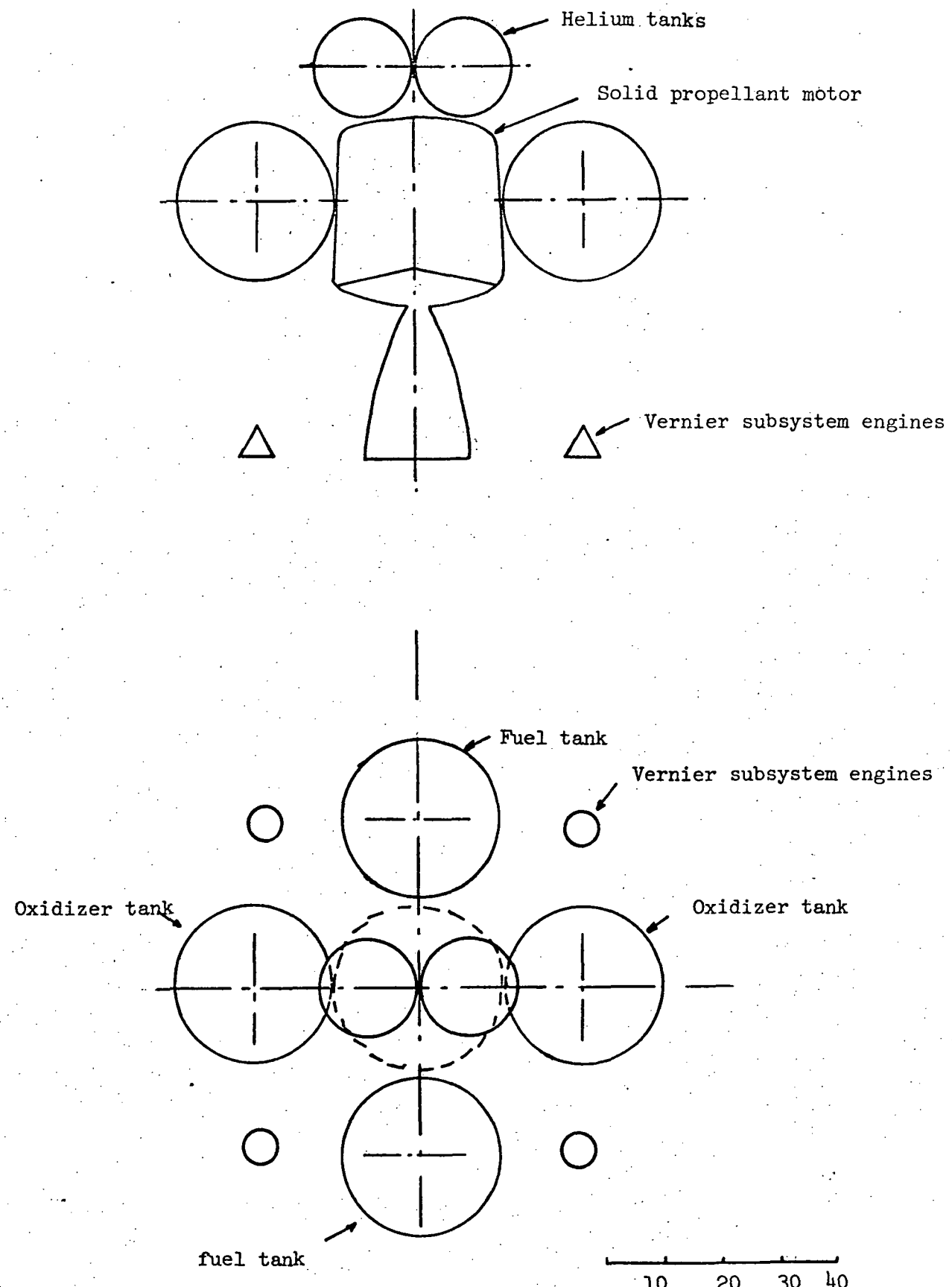

Fig. E.7 Schematic of the First Solution

One solid propellant motor: N_2O_4/A-50

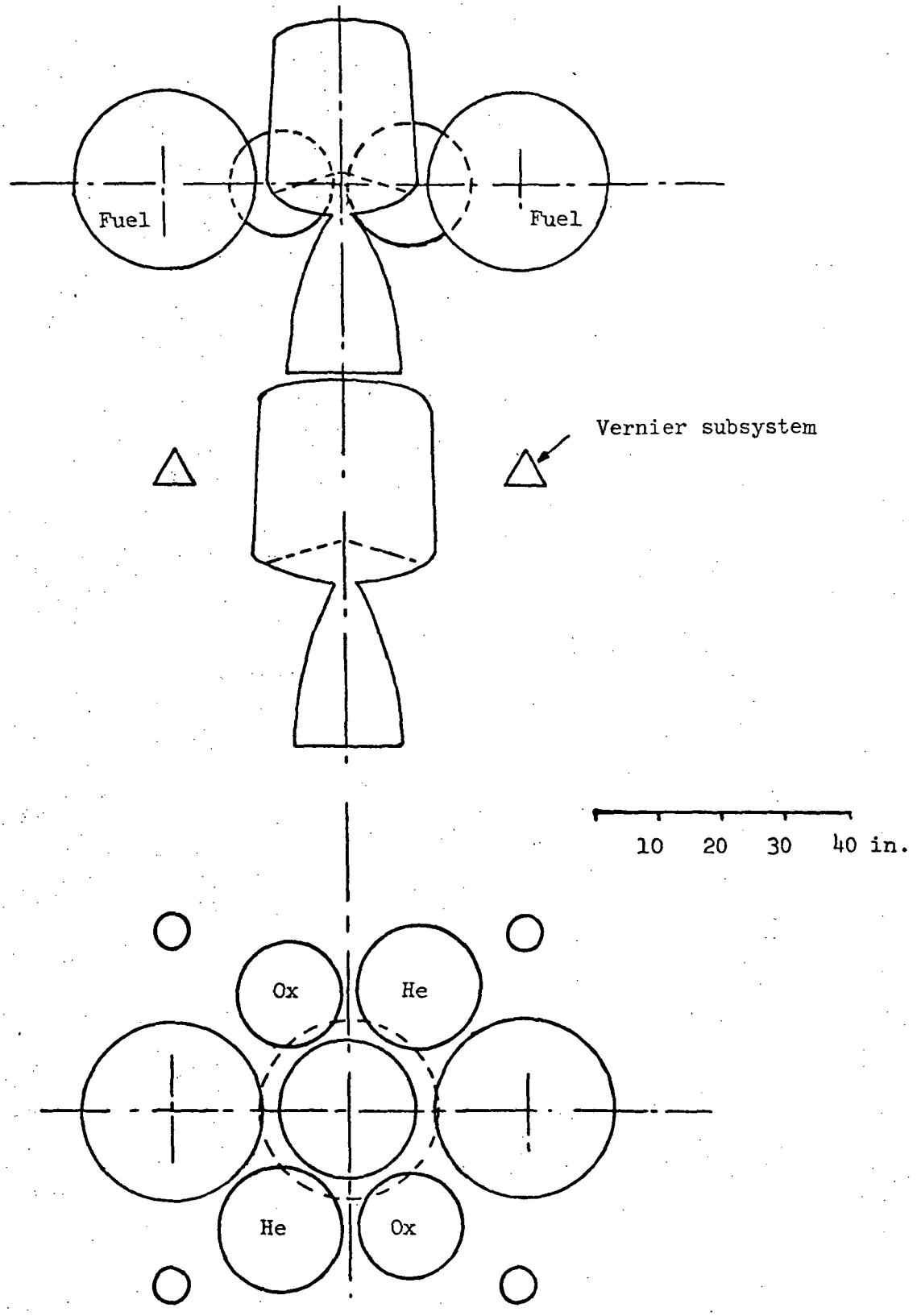

Fig. E.8 Schematic of the Second Solution

2 Solid propellant motors - OF_2/B_2H_6

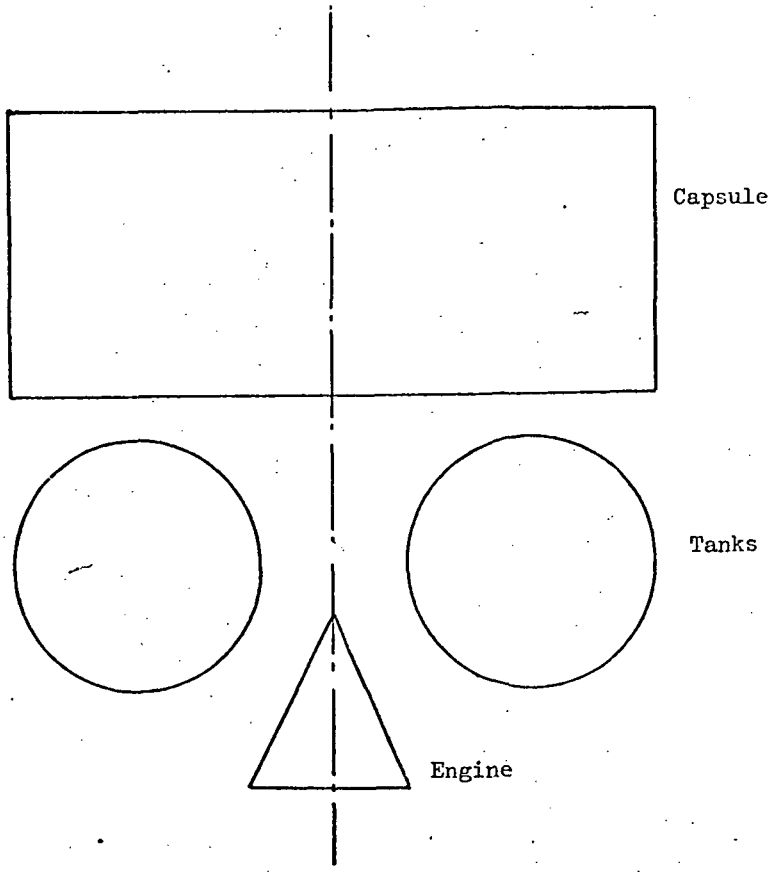

Fig. E-9 Basic Spacecraft Configuration

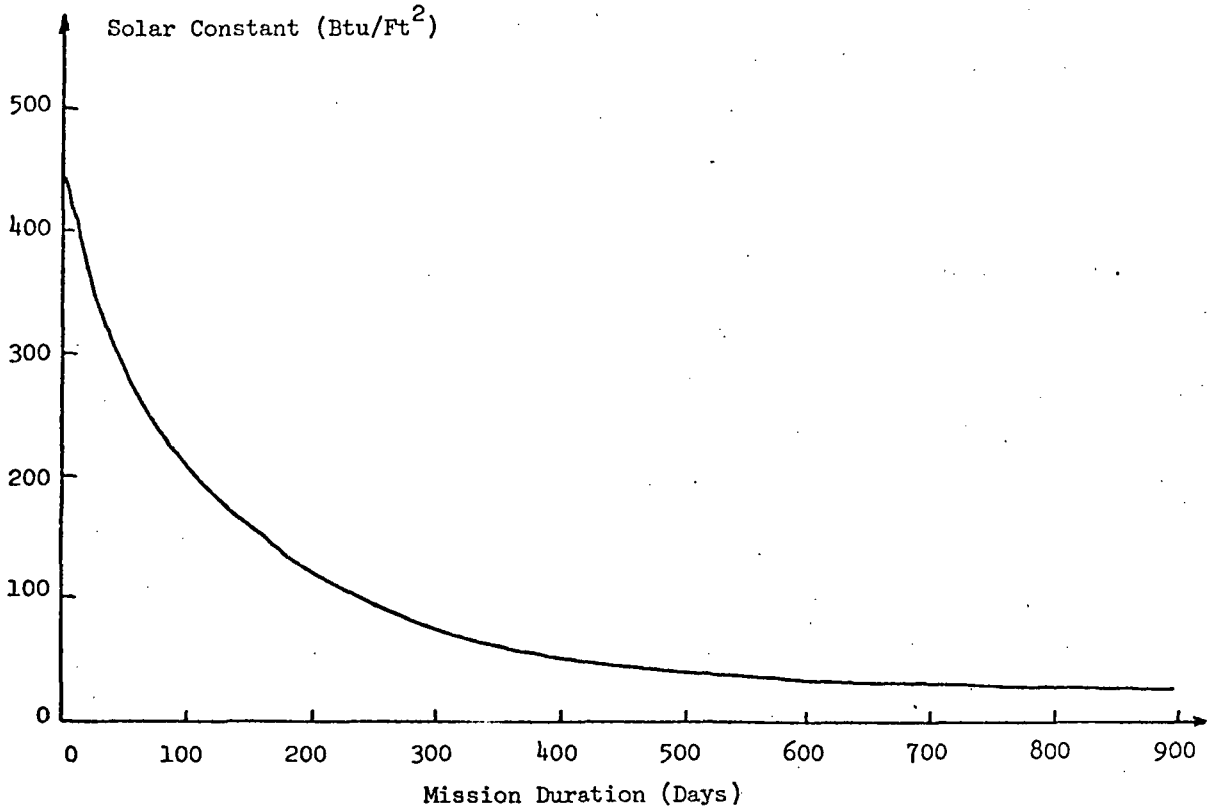

Fig. E-10 Solar Constant vs. Mission Duration

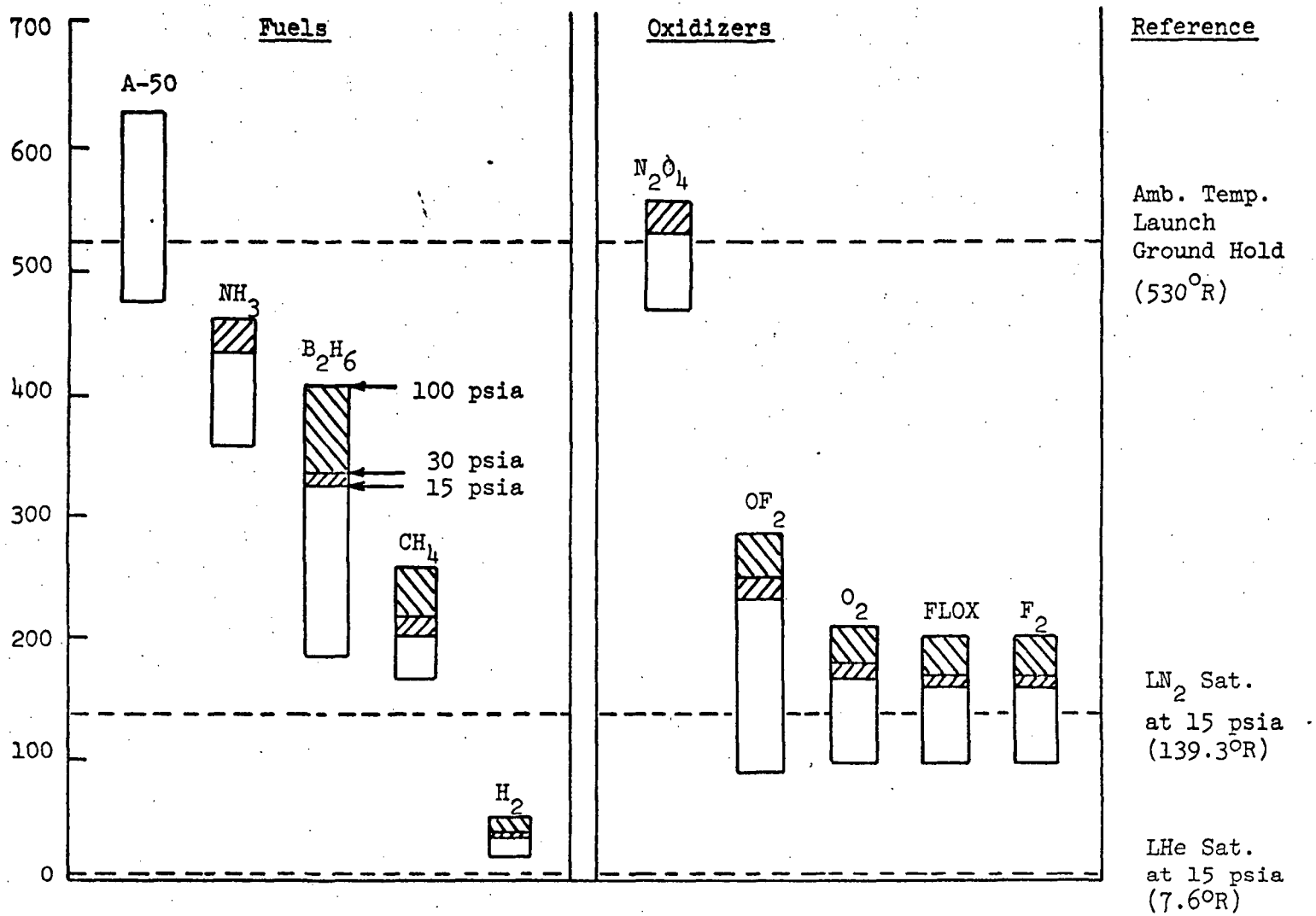

Fig. E.11 Propellant Liquid Temperature Range

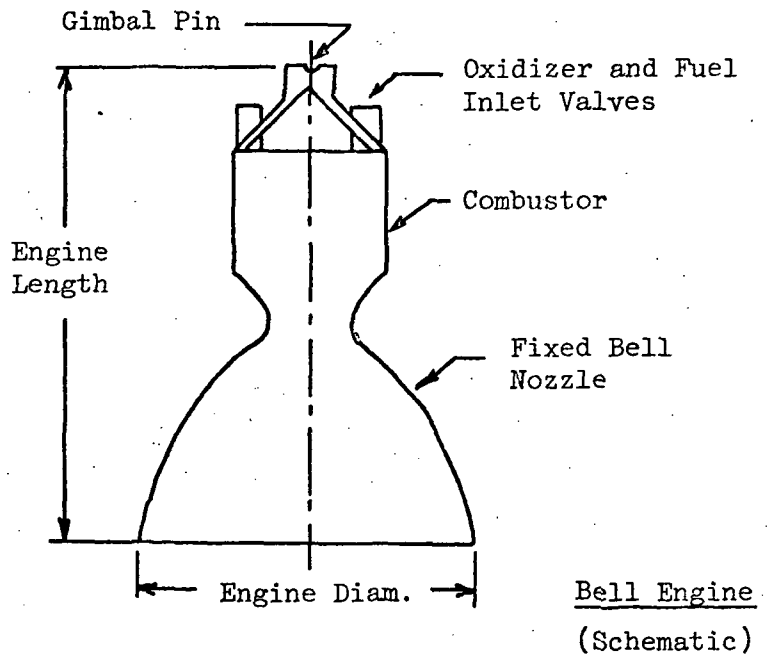

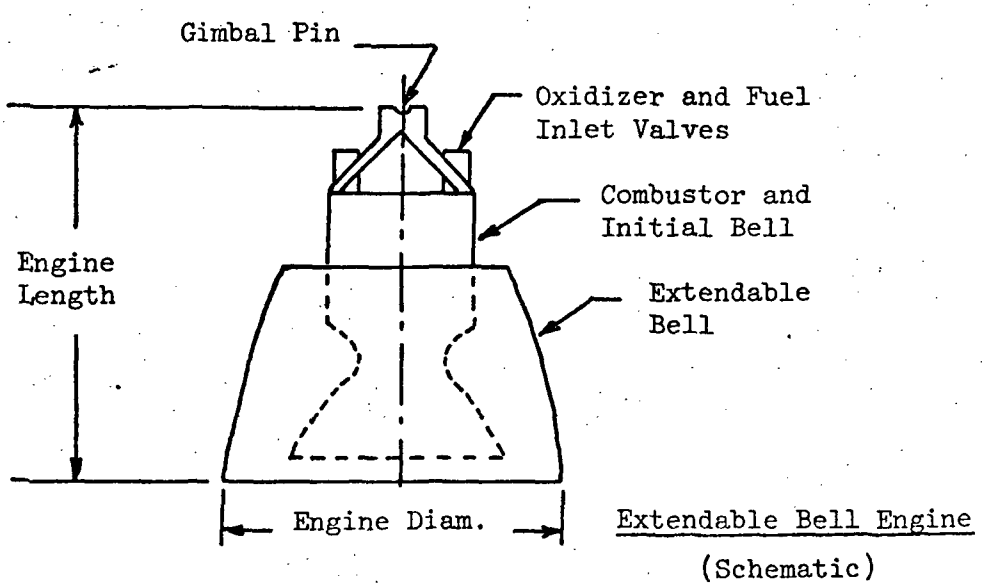

Fig. E.12 Engine Configurations

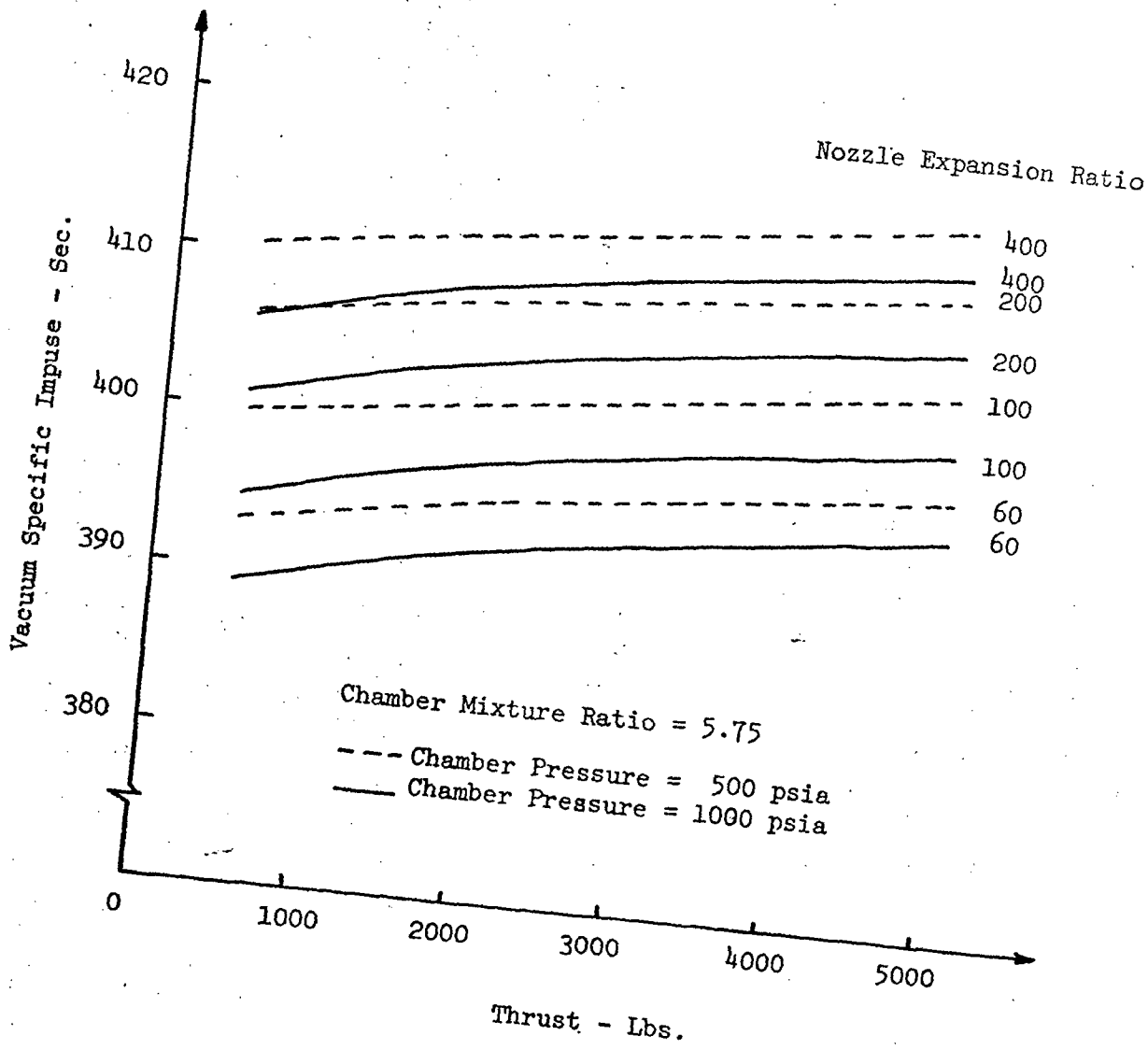

Fig. E.13 Estimated Engine Performance, Flox/Methane Propellants, Open Expander Cycle

IDLE MODE START

Pressurizing gas injection started after propellant expulsion is started. Engine starts on liquid or vapor.

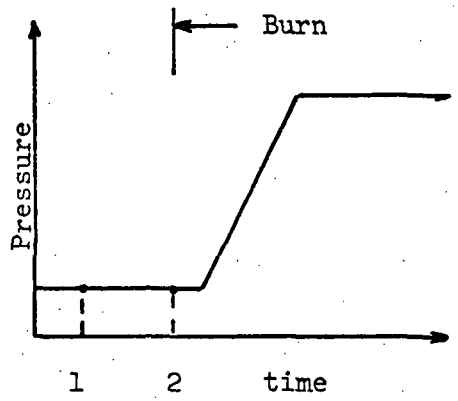

PROPELLANT CONTAINMENT SYSTEM

Tank pressure increased to operating level before expelling propellant. Engine starts on liquid.

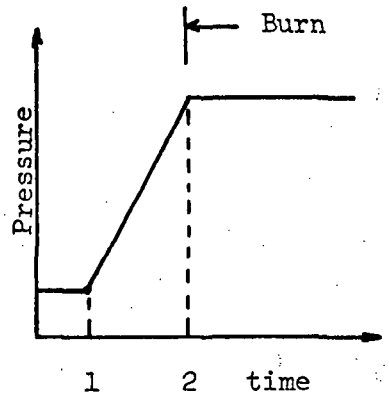

LIQUID SETTLING WITH ULLAGE ROCKET

Tank pressure increased to operating level before expelling propellant. Engine starts on liquid.

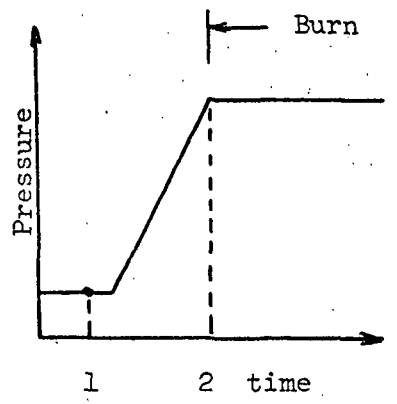

1 - initiate start sequence

2 - Engine ignition

Fig. E.14 Engine Start Mode

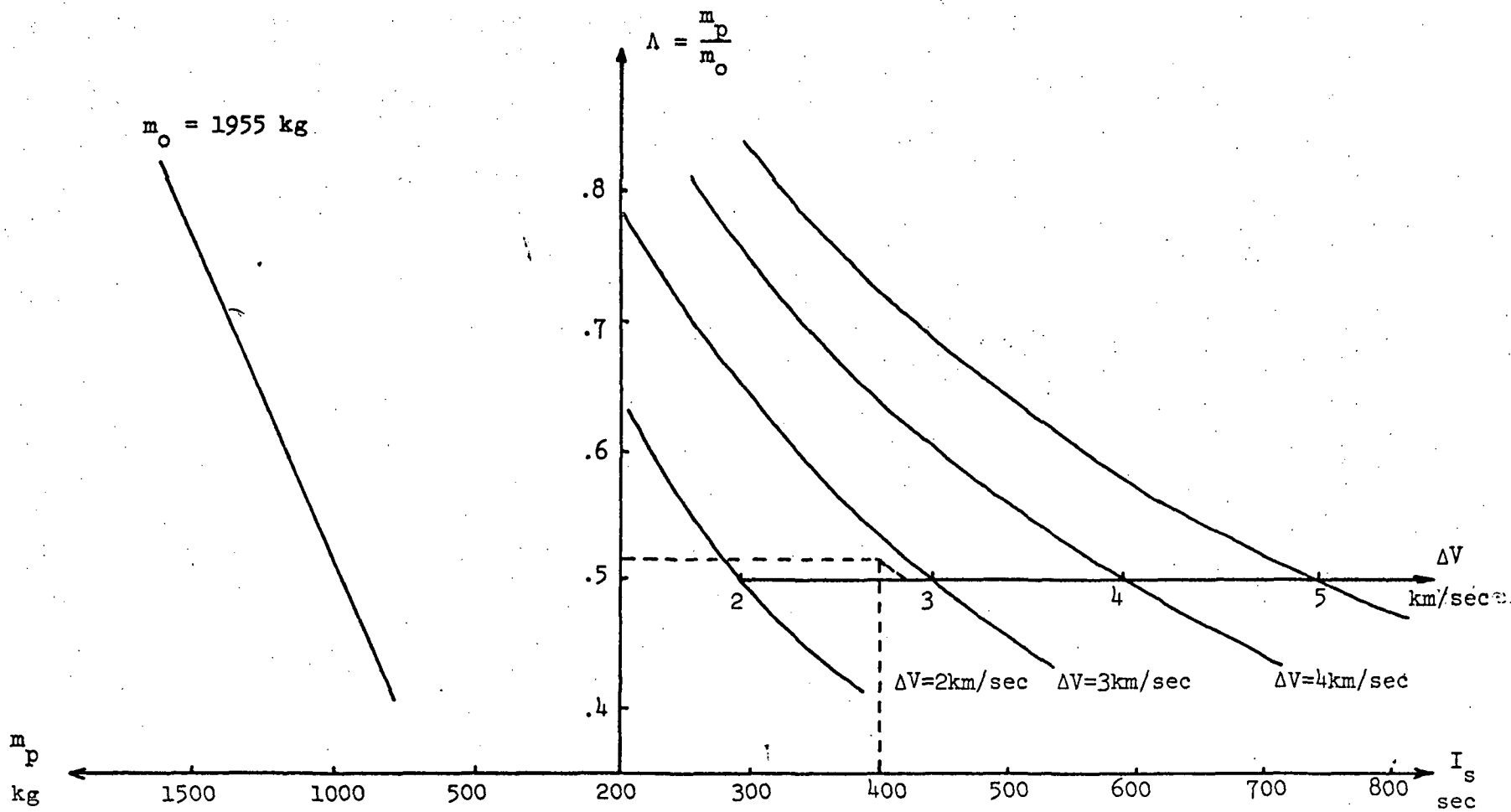

Fig. E-14a Propellant Loading Factor Vs. Specific Impulse for Different ΔV

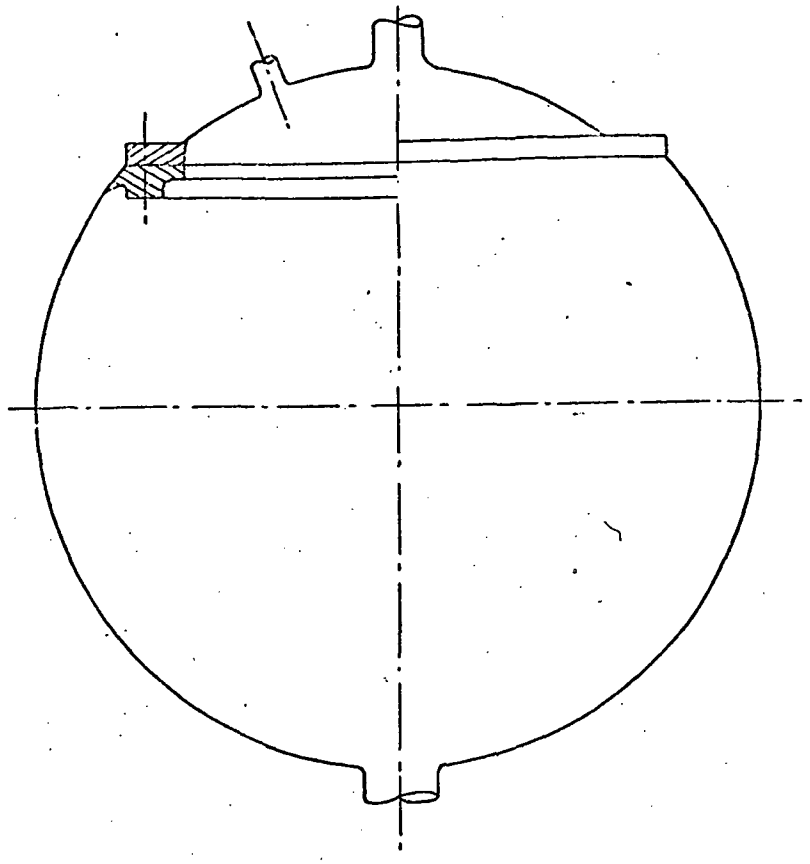

Fig. E-15 Spherical Tank Configuration

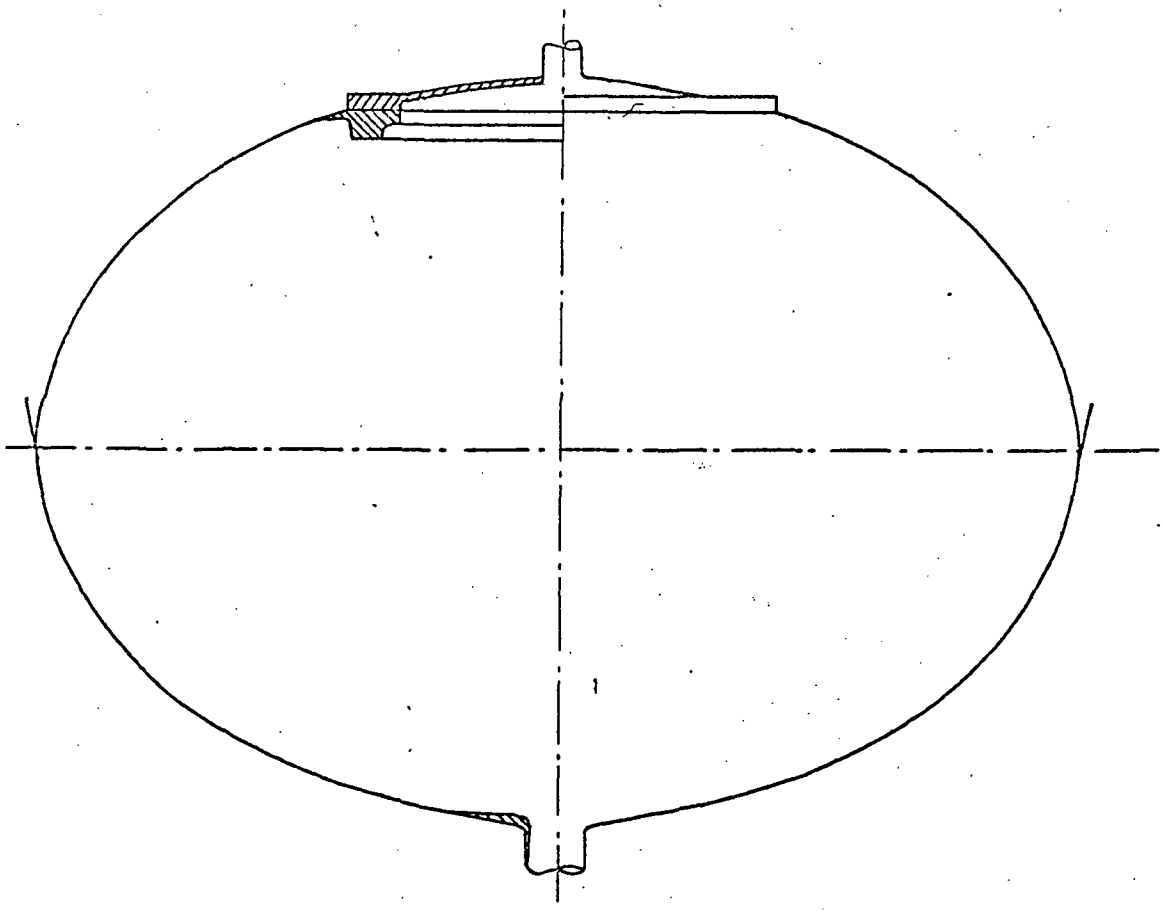

Fig. E-16 Ellipsoidal Tank Configuration

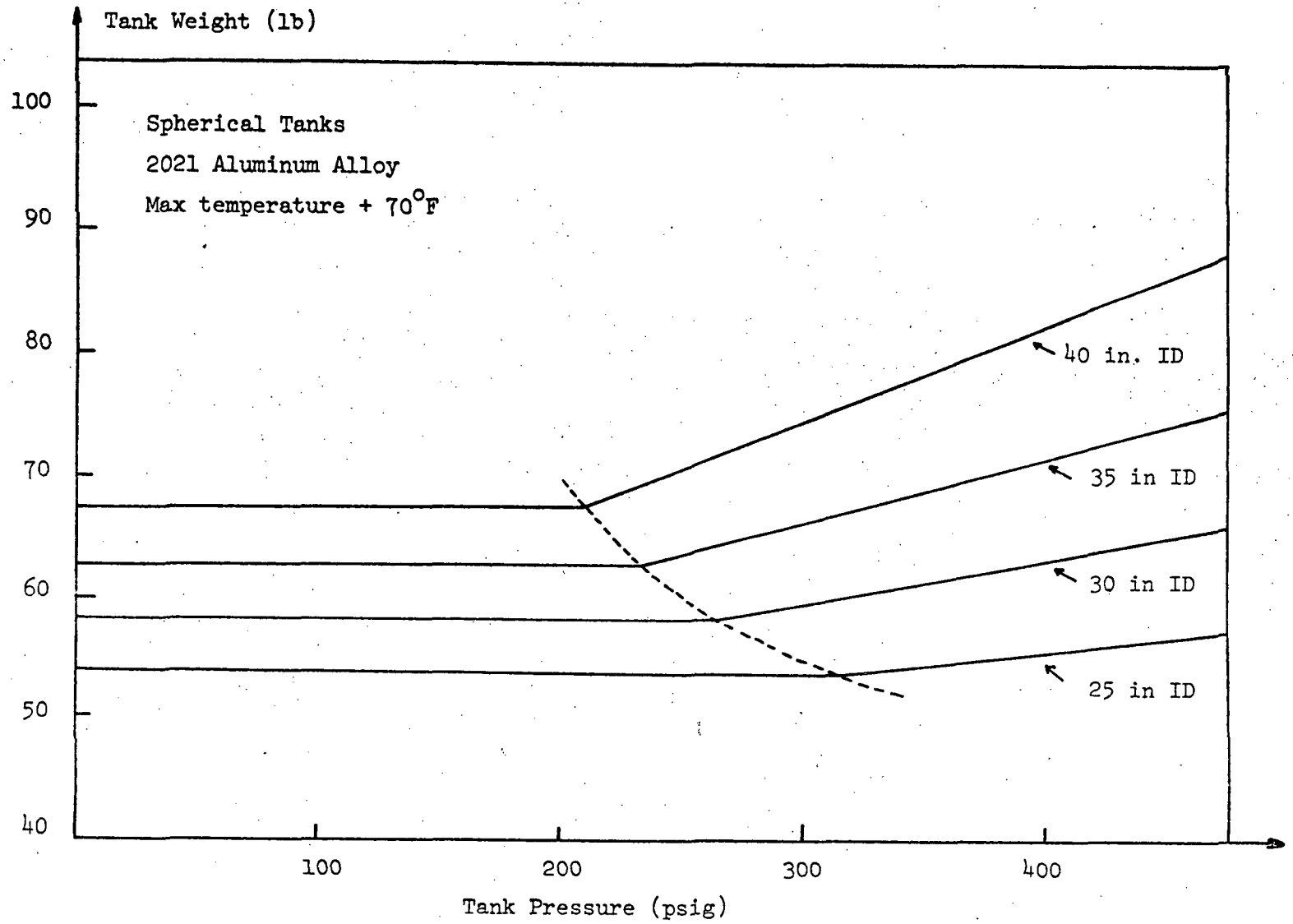

Fig. E.17 Spherical Tank Weights

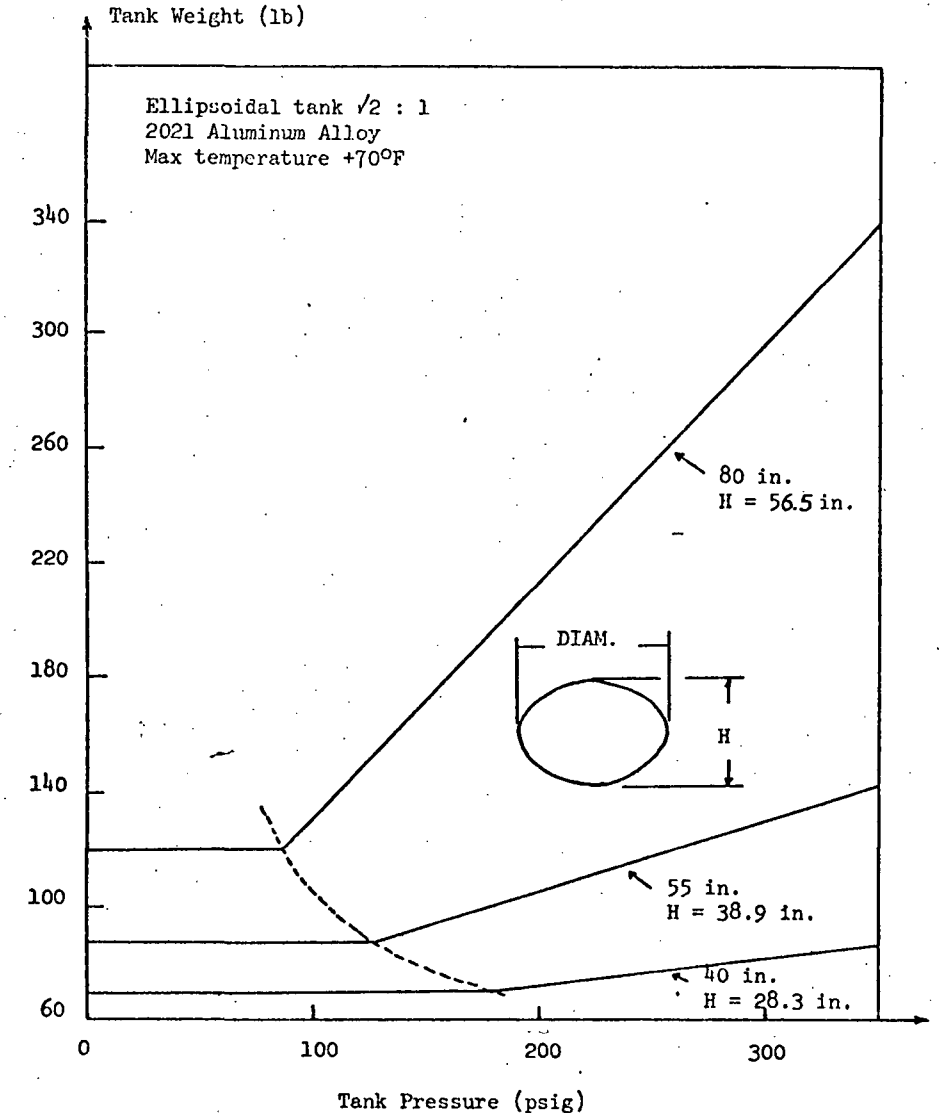

Fig. E-18 Ellipsoidal Tank Weights

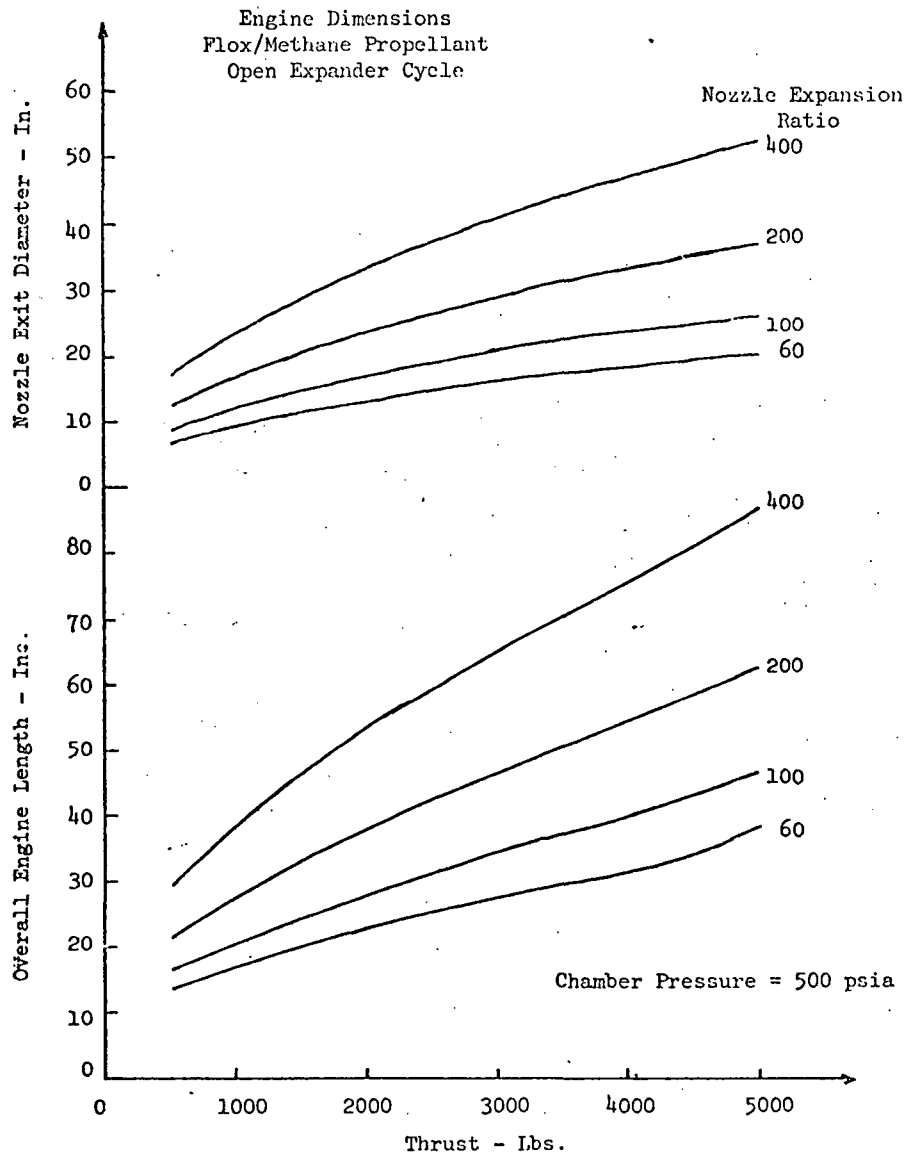

Fig. E-19 Engine Dimensions, Flox/Methane Propellants
Open Expander Cycle, Chamber Pressure = 500 psia

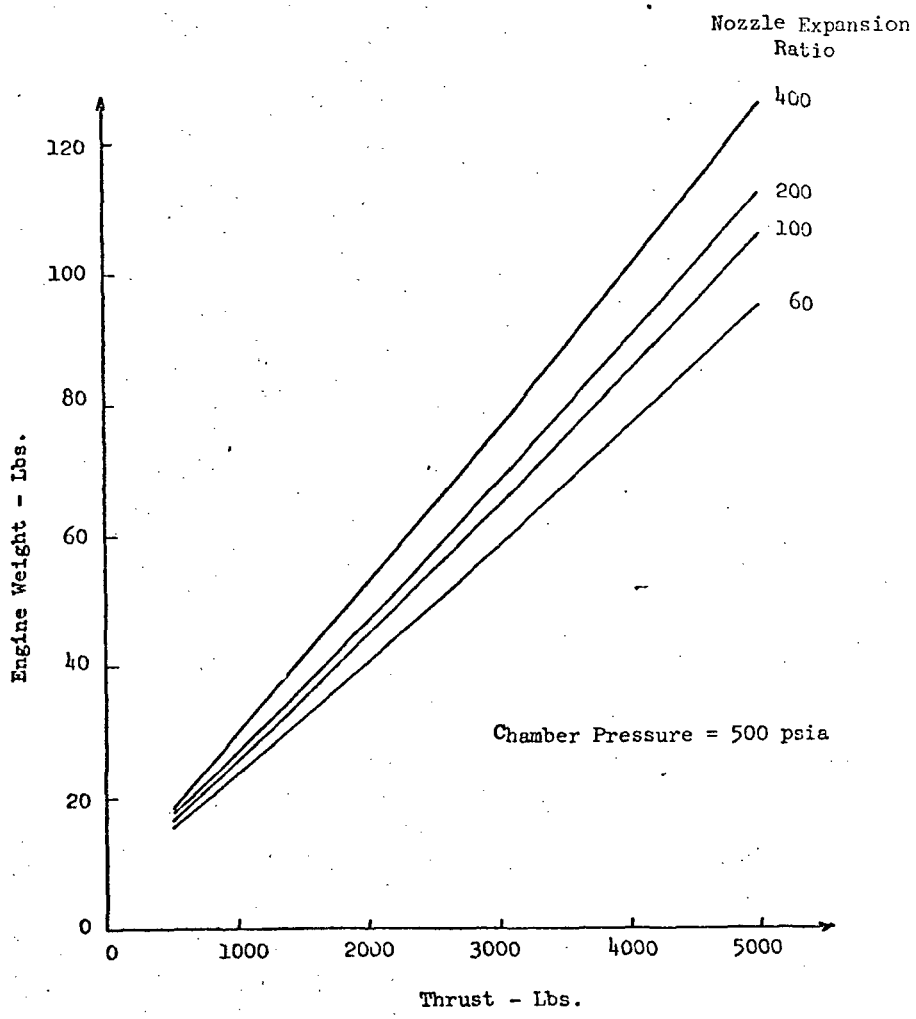

Fig. E-20 Engine Weight, Flox/Methane Propellants
Open Expander Cycle, Chamber Pressure = 500 psia

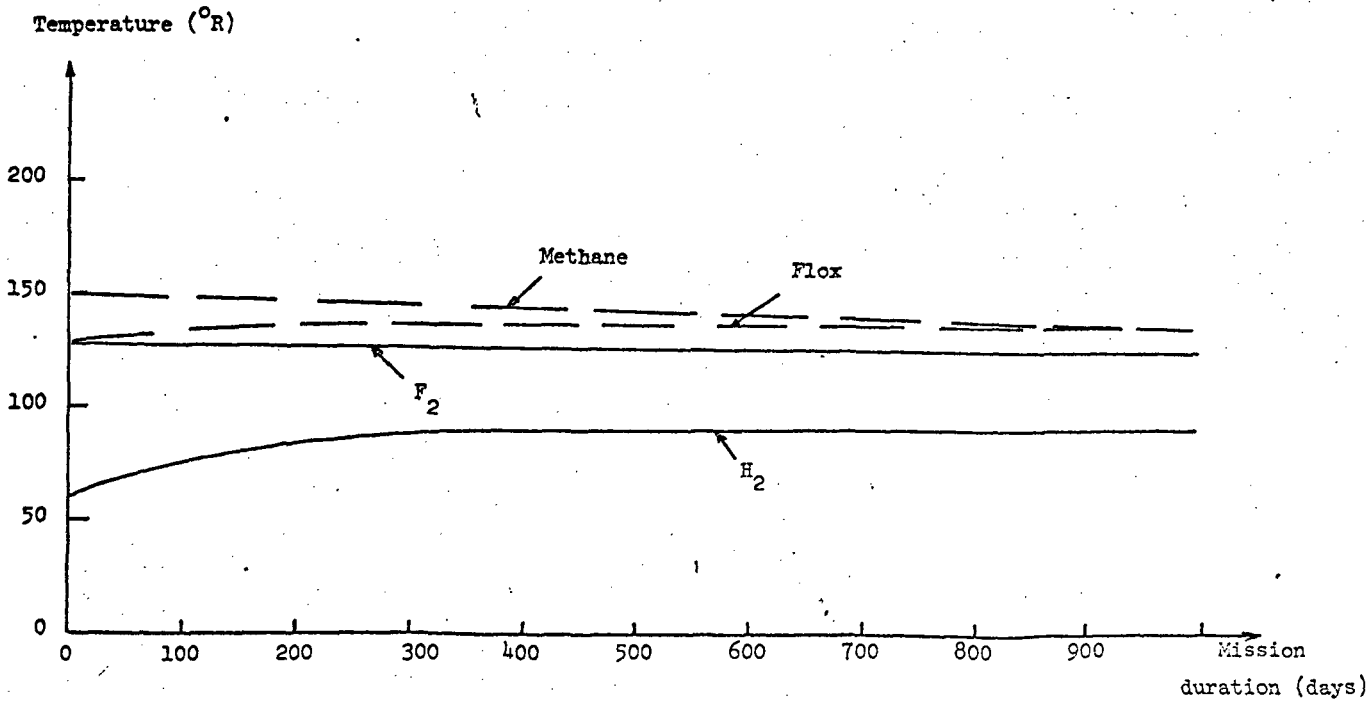

Fig. E-21 Insulation Surface Temperature for F_2/H_2 and Flox/CH_4

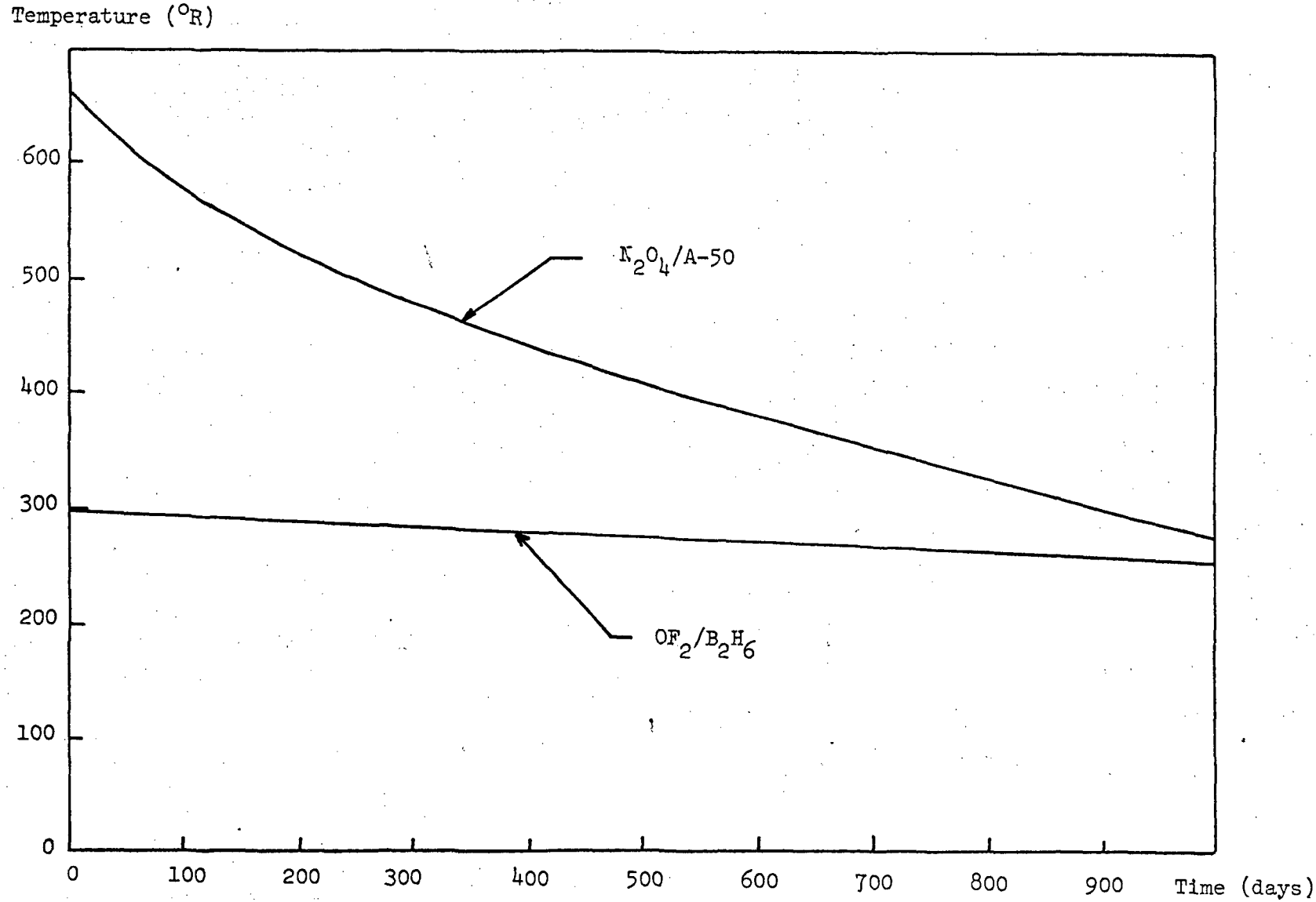

Fig. E-22 Insulation Surface Temperature vs. Time for N_2O_4/A-50 and OF_2/B_2H_6

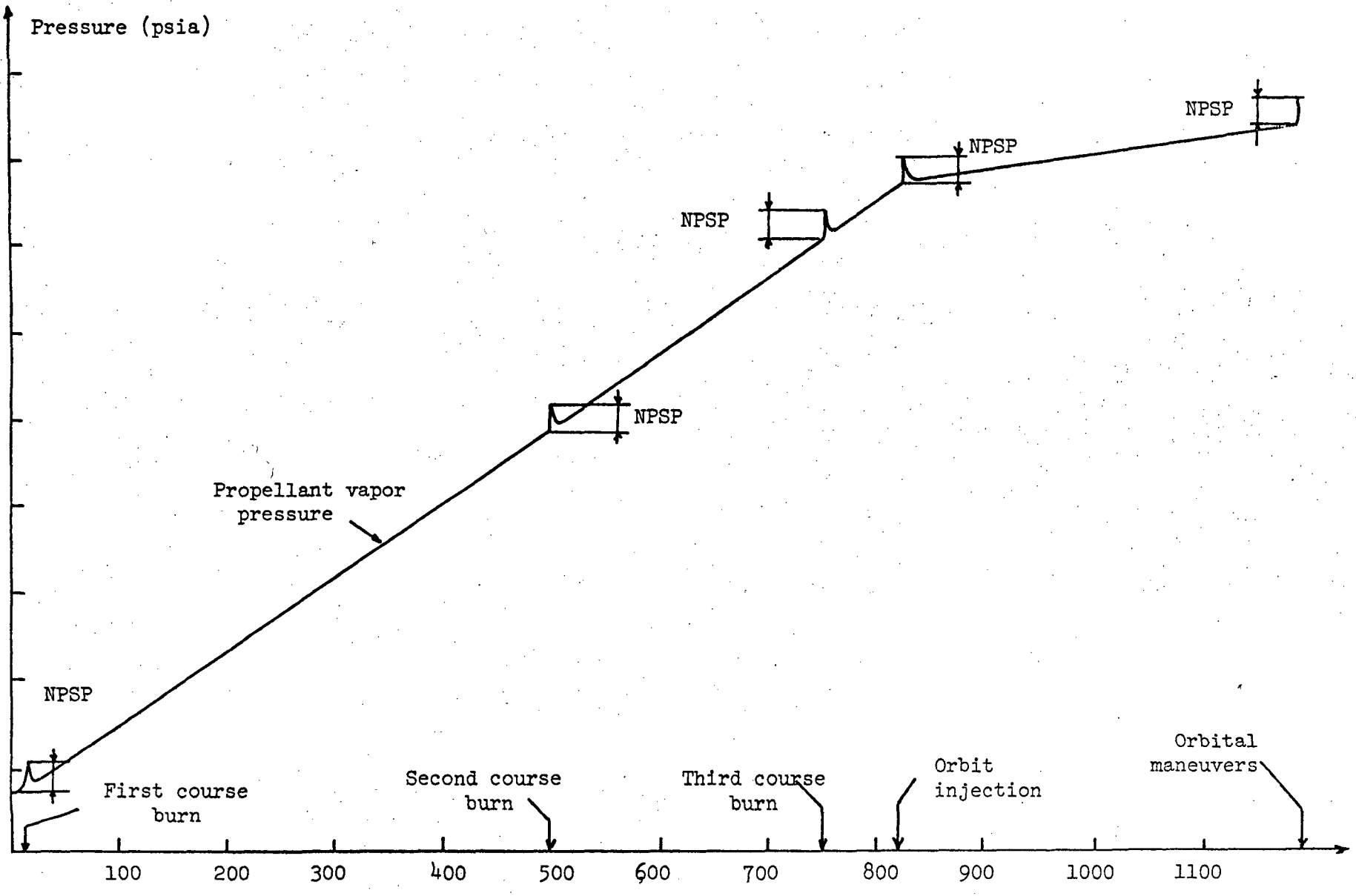

Fig. E.23 Evolution of H_2 Tank Pressure Versus Time

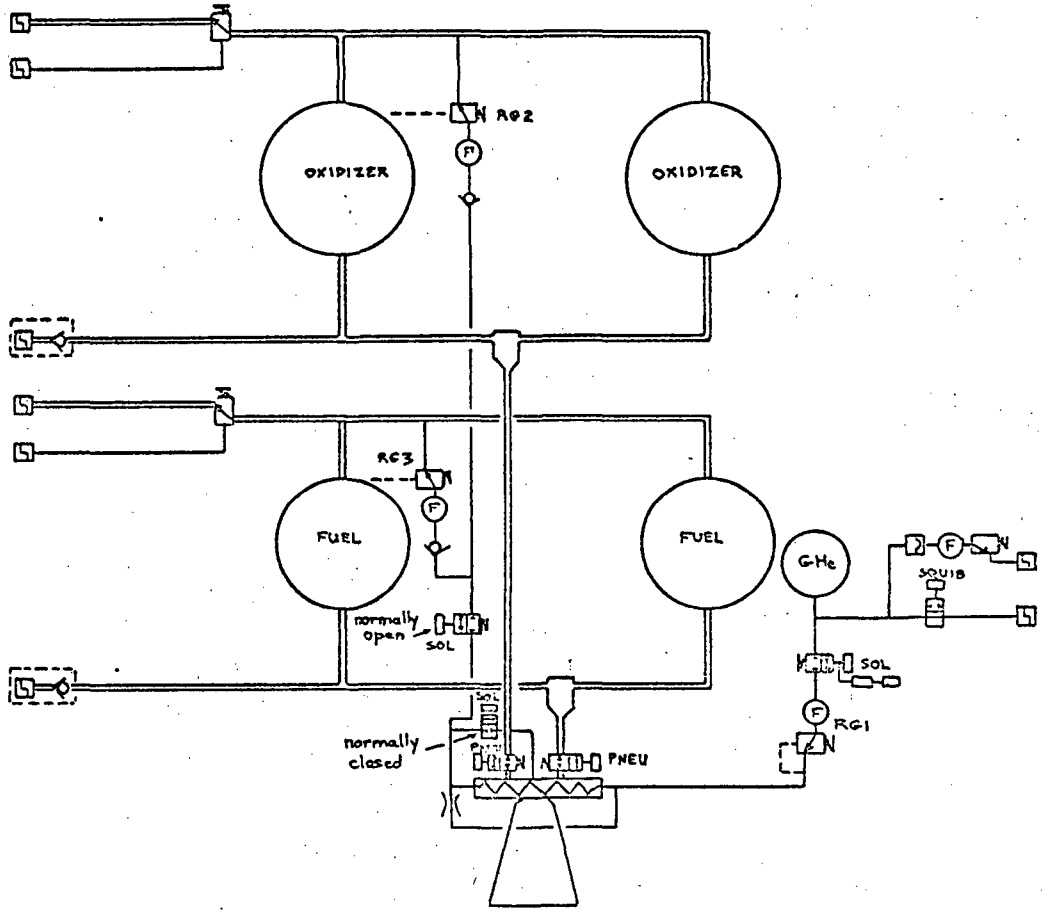

Fig. E-24 Earth-Storable Stage Fluid Systems Schematic

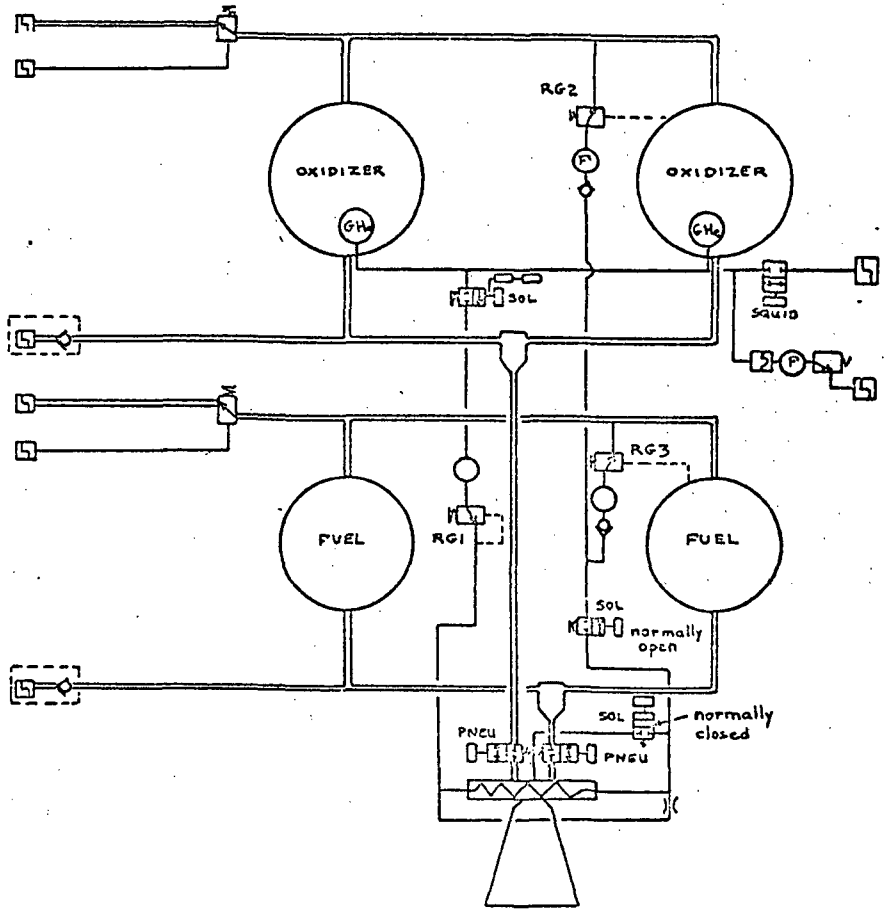

Fig. E-25 Space-Storable Stage Fluid Systems Schematic

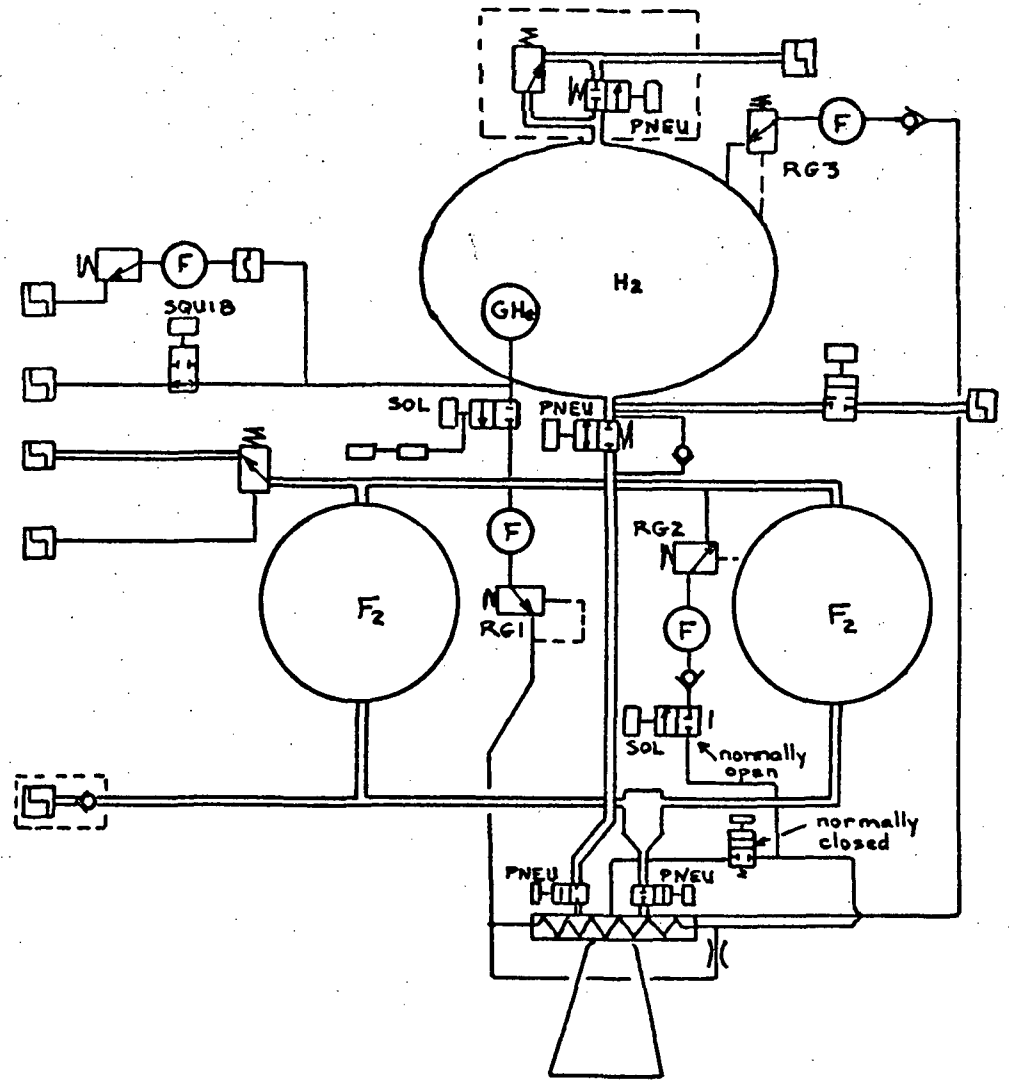

Symbols

- Quick Disconnect
- Check Valve
- Orifice
- Pressure Regulator
- Filter
- Burst Disk
- Solenoid Actuated Valve
- Normally closed pneumatically actuated valve
- Normally open squib actuated valve
- Normally closed solenoid actuated valve with a solenoid actuated detent

Fig. E.26 Cryogenic Stage Fluid Systems Schematic

TABLE E.1 Estimated Propulsion Performance Characteristics

Berylliumized solid propellant motor:	
I_s (Vac, $\varepsilon = 80$)	315 sec
Propellant burning rate	$0.2(P_c/300)^{0.3}$ in/sec
Nozzle expansion ratio	80:1
Thrust coefficient	1.88
Nozzle throat diameter	2.10 in.
Nozzle exit diameter	18.8 in.
g-dot ignition and tailoff	$\pm$ 0.2 g/sec
N_2O_4/(50% N_2H_4 + 50% UDMH) vernier subsystem	
I_s (Vac, $\varepsilon = 60$)	305 sec
Mixture ratio O/F	1.6
Bulk density	73 lb/ft^3
Instability above	100°F
Nozzle expansion ratio	60:1
OF_2/B_2H_6 vernier subsystem	
I_s (Vac, $\varepsilon = 60$)	414 sec
Mixture ratio	3.7
Bulk density	62 lb/ft^3
Instability above	-4°F
Nozzle expansion ratio	60:1

Type of Solid Motor(s)	Single Two Burn Solid Motor		Two Burn to Completion Solid Motors in Stage Configuration			
			First Engine	Second Engine	Second Engine	Second Engine
ΔV capability (m/sec)	4000	2450	1000	3000	2450	800
Acceleration Coefficient	1.95	1.35	0.75	1.6	0.95	0.55
Burning time (sec)	209	185	136	191	156	148
Maximum Thrust (lbF)	8412	5823.5	3235	5045	2996	1734
Minimum Thrust (lbF)	3665	3248	2444	2560	2039	1378
Max. chamber-pressure (psia)	1292	894	497	775	460	266
Min. chamber-pressure (psia)	563	499	375	393	313	212
Max. diameter of case (in.)	42.7	37.5	30.6	35.7	29.7	24.6
Min. diameter of case (in.)	32.0	30.6	27.7	28.2	26.0	22.7
Length of case (in.)	36.6	34.6	26.2	32	27.3	24.5
Mass of propellant (kg)	1103	865	478	704	457	294
Mass of motor (kg)	1213.4	951	526	774	502	323
Mass of the two motors in stage configuration	-	-		ΔV=1000+3000 1300 kg	ΔV=1000+2450 1028 kg	ΔV=1000+800 849 kg
Final mass of the proposed solid propellant system lb.	2669 lb	2092 lb		2860 lb	2262 lb	1875 lb

TABLE E.2 Characterization of the Solid Motor Propellant Candidates

TABLE E.3 Mass Evaluation of Vernier Subsystems

Configuration	One Solid Propellant Motor ΔV = 1000 m/sec		Two Solid Propellant Motors ΔV = 1000 + 1450 m/sec	
Vernier subsystem	N_2O_4/(50%N_2H_4 50% UDMH)	OF_2/B_2H_6	N_2O_4/(50%N_2H_4 50% UDMH)	OF_2/B_2H_6
Mass of liquid propellant for T.V.C. (kg)	31.5	23	31.5 + 31.5	23 + 23
Mass of liquid propellant for course-corrections (kg)	386	290	386	290
Mass of liquid propellant for change of apoapsis (kg)	110	90	no capability	49
Mass of hardware for vernier subsystem (kg)	105	80	90	80
Mass of vernier subsystem	632.5	483	539	465
Total mass of propulsion system (kg)	1158.5	1009	1522	1494

TABLE E.4 Component Characteristics for the Recommended Systems

Configuration: each of the oxidizer, the fuel and the Helium is stored in two identical spherical tanks.		N_2O_4/A-50	OF_2/B_2H_6
Mixture ratio O/F		1.6	3.82
Bulk density (lb/ft^3)		73	63.8
Weight of oxidizer (lb)		800	150
Weight of fuel (lb)		500	570
Weight of Helium pressurant gas (lb)		3.2	5.05
Helium tanks characteristics	tank weight (lb)	19.5	28
	tank inside diameter (in)	12.7	15.5
	tank wall thickness (in)	0.2	0.25
Oxidizer tanks characteristics	tank weight (lb)	8	1.5
	tank inside diameter (in)	25	12.5
	tank wall thickness (in)	0.025	0.01
Fuel tanks characteristics	tank weight (lb)	8	10.5
	tank inside diameter (in)	25	27
	tank wall thickness	0.025	0.03

Based on: propellant tank pressure, 230 psia - isothermal expansion - pressurant tank pressure, 3500 psia - tank safety factor 2.2 - 3% ullage - tank material, 6Al-4V annealed titanium - Design stress 130,000 psia ultimate - Maximum temperature 70°F - tank weights include 10% for tank fitting and mounting.

Reference 9

Propellants	O_2/H_2		F_2/H_2		Flox/CH_4		OF_2/CH_4	
Parameters	Ox	Fuel	Ox	Fuel	Ox	Fuel	Ox	Fuel
Heat of vaporization at N. boiling point (Btu/lb)	91.62	195.3	74.1	195.3	77	219.2	81.9	219.2
Boiling point (^oR)	162.3	36.5	153.04	36.5	154.0	201	231.4	201.1
Freezing point (^oR)	97.9	24.9	96.4	24.9	96.7	163.2	88.7	163.2
Density (lb/Ft^3)	71.29	4.42	94.3	4.42	91.2	26.46	95.7	26.46
Expansion ratio (ϵ)	100/1		100/1		100/1		100/1	
Engine type	Bell		Bell		Bell		Bell	
Feed type	Pump fed		Pump fed		Pump fed		Pump fed	
Chamber pressure (psia)	900		900		500		500	
Mixture ratio (O/F)	6		12		5		5.3	
I_s (lb-sec/lb)	444		460		400		400	
Density of mixture (lb/Ft^3)	22.6		38.5		68.7		67.7	

TABLE E.5 PART I: Propulsion System Parameters for 2000 lbf Engine Thrust

Propellants / Parameters	OF_2/B_2H_6		F_2/NH_3		N_2O_4/A-50		ClF_5/MHF-5	
	Ox	Fuel	Ox	Fuel	Ox	Fuel	Ox	Fuel
Heat of vaporization at N. boiling point (Btu/lb)	81.9	224.3	74.1	596.3	178.1	425.8	128	208
Boiling point (^{o}R)	231.4	183.8	153.1	432	471.5	478.7	466.8	652.1
Freezing point (^{o}R)	88.7	325.2	96.4	351.8	529.8	619	306.6	388.1
Density (lb/ft^3)	95.7	28.1	94.3	42.57	89.3	56.2	118.5	63
Expansion ratio (ε)	100/1		100/1		100/1		100/1	
Engine type	Extended Bell		Extended Bell		Extended Bell		Extended Bell	
Feed type	Pressure fed		Pressure fed		Pressure fed		Pressure fed	
Chamber pressure (psia)	100		100		100		100	
Mixture ratio (O/F)	3.82		3.3		1.65		2.4	
I_s (lb-sec/lb)	414		386		305		330	
Density of mixture (lb/ft^3)	63.8		73.7		74.7		94.3	

TABLE E.5 PART II: Propulsion System Parameters for 2000 lbF Engine Thrust

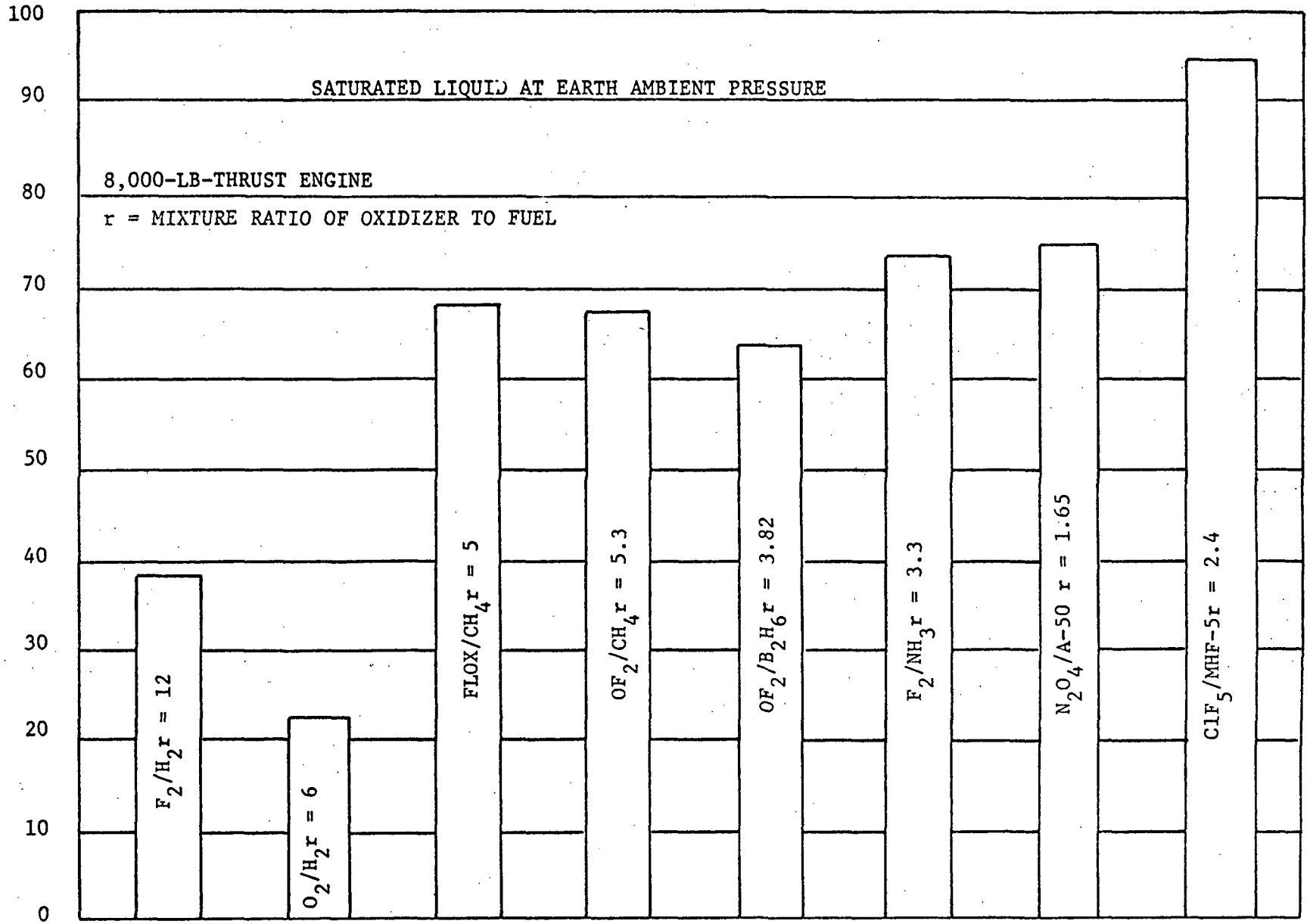

TABLE E.6 Bulk Density of Propellants

TABLE E.7

Materials Compatibility

Oxygen, O_2	Reactive with some materials. Liquid compatible with most metals, teflon, silicon compounds.
Fluorine, F_2 Flox	Reactive with most metals. Liquid compatible with passivated stainless steel, some aluminum alloys, monel, copper, bronze, brass, tin, nickel, and teflon.
Oxygen Difluoride, OF_2	Reactive with most materials. Compatible with glass, passivated stainless steel, monel, aluminum, copper, nickel, and teflon.
50% N_2H_4 50% UDMH MMH	Reactive with some materials. Compatible with most materials for short-term storage. Aluminum, glass, and polyethylene are suitable for long-term storage.
Chlorine Pentafluoride, ClF_5	Reactive with most materials. Liquid compatible with some aluminum alloys, passivated stainless steel, and carboxyl-nitroso rubber.

Other propellants used in this study pose no unusual compatibility problems.

TABLE E.8

Propellant/Materials Compatibility

		Metals							Non-Metals				
		Titanium	Mild Steel	Stainless Steel	Aluminum	Nickel	Copper	Brass	Poly-Ethylene	Asbestos	Teflon	Kel-F	Mylar
Oxidizer	Flox	no	no	340L	yes	yes	yes	yes	no	no	yes	yes	no
	F_2	↓	↓	340L	↓	↓	↓	yes	↓	↓	↓	↓	↓
	OF_2	↓	↓	yes	↓	↓	↓	yes	↓	↓	↓	↓	↓
	O_2	no	no	yes	↓	↓	yes	no	no	↓	↓	↓	↓
	N_2O_4	yes	yes	yes	yes	yes	no	no	yes	no	yes	yes	no
Fuel	B_2H_6	*	no	yes	*	yes	no	yes	yes	yes	yes	yes	yes
	H_2	yes	↓	↓	yes	yes	yes	yes	no	no	↓	↓	yes
	CH_4	*	↓	↓	yes	yes	↓	yes	yes	yes	↓	↓	yes
	NH_3	yes	↓	↓	no	no	↓	no	yes	yes	↓	↓	no
	A-50	yes	no	yes	yes	no	yes	no	yes	no	yes	yes	yes

* Insufficient data available

TABLE E.9 Design Parameters

Propellant	Maximum tank pressure (psia)	Insulation thickness (in.)	Initial Ullage (%)
F_2	35	0.5	2
H_2	170	1.0	10.5
Flox	40	0.5	2
CH_4	35	0.5	3
OF_2	230	1.0	7
B_2H_6	165	0.5	2
N_2O_4	220	5	2
A-50	190	5	6

Propulsion System	F_2/H_2	Flox/CH_4	OF_2/B_2H_6	N_2O_4/A-50
Weight of propellant (lb)	2048	2174	2072	2127
Weight of fuel (lb)	158	362	430	803
Volume of fuel tank (ft^3)	19.8	7.2	7.8	7.6
Inside diameter of fuel tank (in.)	Ellipsoidal D = 57 H = 40.3	28.8	29.5	29.2
Weight of fuel tank (lb)	105	57.5	57.5	57.5
Weight of oxydiser (lb)	1890	1812	1642	1324
Volume of oxydiser tank (ft^3)	10.2	10.1	10.5	7.6
Inside diameter of oxydiser tank (in.)	32.3	32.2	32.6	29.2
Weight of oxyd. tank (lb.)	60	60	60	57.5
Weight of insulation	18	7.8	9.2	64

TABLE E.10 Propellant Parameters

Pressurant system	F_2/H_2	Flox/CH_4	OF_2/B_2H_6	N_2O_4/A-50
Configuration	One tank inside H_2-tank	Two tanks inside the two CH_4 tanks	Two tanks inside the two OF_2 tanks	Four tanks outside the propellant tanks
Weight of helium (lb)	1.2	1,8	13	6.2
Volume of one He tank (ft^3)	0.1	0.16	1.3	0.6
Inside diameter of one tank (in.)	6.9	8.1	16.3	12.5
Weight of one He tank (lb)	0.8**	1.5**	12***	8**
Allocation for plumbing (lb)	10	10	10	10
Total weight of pressurant system (lb)	16*	14.8	47	48.2

* There is an allocation of 4 lb for GH_2 pressurization system (H_2 tank only)

** Based on titanium

*** Based on Inconel

TABLE E.11 Pressurant System Parameters

Engine System	Pump-fed	Pressure-fed
Nozzle expansion ratio	100	60
Cooling techniques	Regenerative	Ablative
Overall engine length (in.)	28	48
Nozzle exit diameter (in.)	17	30
Engine weight	45	65

Idle mode start for both engine systems

TABLE E.12 Engine System Parameters

Item	F_2/H_2	Flox/CH_4	OF_2/B_2H_6	N_2O_4/A-50
Structure	150	102	114	125
Propellant feed assembly	281	281	282	322
Pressurization system	16	15	47	48
Engine system	45	45	65	65
Contingency	50	44	51	56
Residuals	72	43	41	43
Performance reserve	17	17	17	17
Inert	631	547	617	676
Impulse propellant	2048	2174	2072	2127
Propulsion module	2679	2721	2689	2803
Payload	1621	1579	1611	1497

TABLE E.13 Weight Breakdown (in. lb.)

TABLE E.14 ΔV Performance

System	F_2/H_2		$Flox/CH_4$		OF_2/B_2H_6		N_2O_4/A-50	
W_p=Weight of propellant burnt* t_b=corresponding burning time	Wp or ΔV	t_b	W_p or ΔV	t_b	W_p or ΔV	t_b	W_p or ΔV	t_b
First course correct ΔV = 33 m/sec	31.3	7.2	36	7.2	24.8	7.2	47.2	7.2
Second course correct ΔV = 77 m/sec	72.2	16.6	82.9	16.6	80.1	16.6	108.1	16.5
Third course correct ΔV = 560 m/sec	489.9	112.7	556.2	111.2	539.2	111.6	707.7	108
Orbit insertion ΔV = 1000 m/sec	737	169.5	8.517	163.1	796	164.7	976.8	148.9
ΔV available after (m/sec)	1247.6	165	1092.4	136.6	998.9	128.7	371	43.8
Orbit trim ΔV = 330 m/sec	209.5	48.2	226.7	45.3	222.5	46.1	257	39.2
ΔV remaining (m/sec)	846.4	116.8	695.1	91.2	612.5	82.6	36.7	4.6

* W_p(lb), t_b (sec)

Appendix F: Orbiter Zeodesy

1. Introduction.

Orbiter Zeodesy is a term commonly known to many investigators as a Jupiter celestial mechanics experiment. The experiment consists of the measurement and analysis of SC orbital perturbations to describe the general gravitational potential of a celestial body. Orbital Zeodesy is the science of this gravitational analysis with respect to the planet Jupiter, orbital geodesy with respect to Earth. Artifical satellite applications to geodesy are now approximately ten years old. Zeodesy can fortunately draw on the extensive analytical theory developed for geodetic applications of satellites, but there are many significant distinctions between zeodetic and geodetic satellite applications which are considered in this chapter. These are enumerated below:

(a). Geodetic satellites generally have orbital periods of about 1½ hours (much less than the Earth's rotational period of 24 hours), the orbits are nearly circular (eccentricity $e \approx 0$), and the satellites are well within one Earth radius during the entire orbit, and are thus sensitive, in a perturbational sense, to mass anomalies in the Earth's crust. As was seen in Chapter III, however, JOSE has an initial orbital period of 45 days (much greater than Jupiter's rotational period of 10 hours), the orbit is highly eccentric ($e = 0.975$), and the SC is within one Jupiter radius of the planet for approximately one hour during the entire orbit. Thus JOSE is sensitive to planetary mass anomalies only during perijove passage.

(b). Jupiter, having a thick atmosphere and a probable solid hydrogen surface, would apparently be closer to hydrostatic equilibrium than the Earth or terrestrial planets. This would imply that the higher order harmonics of

the gravity potential are extremely small, thus permitting a solution for only the very lowest order terms. Although at first glance this may appear discouraging, it should be remembered that the absence of higher order terms in the potential implies less undesirable perturbations to the spacecraft (lowering of perijove, for example) and the reduction of errors in solving for the lower order harmonic coefficients due to the truncation of the series for the potential.

(c). Orbital perturbations of Earth satellites are generally computed from measurements by ground tracking stations. These perturbations generally take the form of mean or secular rates of change to the orbital parameters. Secular rates are directly proportional to time t, hence the orbital parameter continues to change indefinitely. Tracking station support cannot be relied upon for orbit determination of a Jupiter orbiter at the time of this writing. Thus JOSE will make use of an on-board radar system and the television system, both described in Chapter VI, to determine the osculating parameters which are periodic in nature. DSN will be relied upon only to determine gross orbital parameters when JOSE is near apoapsis.

(d). Secular rates for Earth satellites are generally greater (on the order of degrees per day) than a Jupiter orbiter of 1.1 R_J by 100 R_J (on the order of a small fraction of a degree per day) since the Jupiter orbiter is close to the planet for such an insignificant amount of time. The periodic short term perturbations during an hour or two near perijove are the most significant. Short term, periodic perturbations are those involving Sine v and Cosine v terms, where v is the true anomaly of the SC orbit.

(e). Earth geodetic analysis is especially complicated by atmospheric drag, solar radiation, and luni-solar mass effects on the SC perturbations. In many cases these effects are as significant as the Earth's gravity potential itself. A suitable atmospheric model for isolating the drag perturbations

has plagued geodesists for years. All of these secondary perturbations are shown to be negligible herein for a Jupiter orbiter, except for the very significant natural satellite perturbations, a theory for which is developed in this chapter.

Space will not permit an introduction to gravitational potential theory at this point; it is assumed that the reader is familar with the solution of Laplace's equation ($\nabla^2 V = 0$) for the gravitational potential V of a planet in spherical harmonics, where ∇^2 is the Laplacian operator. Jupiter's potential can then be expressed:

$$V = GM_J/r - GM_J/r \sum_{\ell=2}^{\infty} \sum_{m=o}^{n} (R_J/r)^{\ell} P_{\ell m}(\mathrm{Sin}\phi)(C_{\ell m}\mathrm{Cos}\ m\lambda + S_{\ell m}\mathrm{Sin}\ m\lambda) \quad \text{(F-1)}$$

or: $$V = GM_J/r - \sum_{\ell,m} V_{\ell m}$$

where: GM_J = the gravitational mass of Jupiter

R_J = Jupiter equatorial radius

$P_{\ell m}(\mathrm{Sin}\ \phi)$ = Legendre Associated Polynomial, degree ℓ, order m

ϕ = latitude

λ = longitude

GM_J/r is designated the central term, $V_{\ell m}$ the perturbation terms

$C_{\ell m}$, $S_{\ell m}$ = harmonic coefficients

All terms with m = 0 are termed zonal harmonics and are independent of λ. Thus, from eq. (F-1), the central term and two of the zonal harmonics can be written:

$$V = \frac{GM_J}{r} - \frac{GM_J R_J^2 J_2}{r^3} P_2(\mathrm{Sin}\ \phi) - \frac{GM_J R_J^4 J_4}{r^5} P_4(\mathrm{Sin}\ \phi) \quad \text{(F-2)}$$

as a close approximation to Jupiter's gravitational potential. J_2 and J_4 are used to designate C_{20} and C_{40} since J appears more commonly in the

literature for a zonal harmonic. J_2 and J_4 can be approximated by values of J and K planetary moments of inertia given by Brouwer and Clemence*:

$J_2 = 2/3\ J = 2/3(0.02206) = 0.01470$, $J_4 = -4/15(0.00253) = -0.00067$.

The third order harmonic (coefficient J_3) describes the meridianal "pear-shaped" term, and is apparently quite negligible since no value could be found in the literature for Jupiter and it is probably safe to assume that Jupiter's gravity potential is fairly symmetric with respect to its equator. The unknown C_{22} and S_{22} tesseral harmonic terms, describing the ellipticity of Jupiter's equator, can be added to eq. (F-2) to yield a closer approximation to the potential:

$$V = \frac{GM_J}{r} - \frac{GM_J R_J^2 J_2}{r^3} P_2 (\text{Sin } \phi) - \frac{GM_J R_J^4 J_4}{r^5} P_4 (\text{Sin } \phi) - \frac{GM_J R_J^2}{r^3} P_{22} (\text{Sin } \phi) (C_{22} \text{Cos } 2\lambda + S_{22} \text{ Sin } 2\lambda) \qquad \text{(F-3)}$$

These various analyses are carried out in this appendix:

Section 2 analyzes the long term, secular perturbations on 1.1 R_J by 100 R_J and 1.1 R_J by 20 R_J orbits. 1.1 R_J by 20 R_J is the most circular orbit which is feasible from a propellant sense, as seen by Figure III-18 in Chapter III. These orbits can have any general inclination i (except $i = 0^\circ$, the equatorial case), longitude of ascending node Ω, and argument of perijove ω. The derivation parallels the more general development of Kaula** of expressing a potential term $V_{\ell m}$ in terms of the orbital parameters rather than the spherical coordinates. Equation (F-2) is the appropriate equation for this analysis, since only J_2 and J_4 of the coefficients are known, and they are the dominant terms. The problem is transforming V_{20}

---

* Brouwer, D. and Clemence, G.M., "Orbits and Masses of Planets and Satellites" Ch. 3, Vol. III of The Solar System, G.P. Kuiper & B.M. Middlehurst, eds., the University of Chicago Press, 1961.

** Kaula, William M., Theory of Satellite Geodesy, Blaisdell Publishing Co., Waltham, Massachusetts, 1966.

and V_{40} from functions of spherical coordinates to functions of orbital elements for differentiation in the Lagrange equations of motion.

Section 3 uses the results of Section 2 to determine oscillations in perijove height above the planetary surface.

Section 4 derives the Lagrange equations for an equatorial orbit since the analysis of Section 2 fails for equatorial orbits. The long term, secular perturbations for equatorial 1.1 R_J by 100 R_J and 1.1 R_J by 20 R_J orbits are computed for comparison with the three non-equatorial orbits considered in Chapter III and Section 2 of this appendix. The equatorial case is of prime interest since one current science philosophy is to initially deboost into Jupiter equatorial orbit and remain orbiting equatorially for perhaps one year (8 orbits) before inclining the orbit.

Section 5 then formulates the short term periodic perturbations which will affect on-board radar range and range rate measurements. Equation (F-3) is then used, since the radar measurements are to be used to solve C_{22} and S_{22} as well as more accurate values of J_2 and J_4.

Section 6 provides the methods of solving the four harmonic coefficients from radar measurements. The radar was initially proposed for JOSE for atmospheric experiments and its potential for refined orbital determination near perijove was later realized. The radar measures range (r) and range rate ($\dot{r}$) by time delay and doppler shift respectively of a signal reflected from Jupiter's atmosphere. This study assumes a reflected signal from Jupiter; i.e., the signal is not completely attenuated, and that the depth to the reflection layer is known around Jupiter's equator. Chapter X, Conclusions, elaborates on this assumption.

Section 7 analyzes the perturbations on the SC other than Jupiter's gravity field to isolate the gravitational perturbations. The only significant non-planetary perturbations are those arising from the four Galilean

satellites, JI through JIV, and Amalthea, JV.

2. The Long Term Secular Perturbations of the General Inclined Orbit

The general expression for a potential term $V_{\ell m}$ in orbital parameters (a, e, M, i, ω, Ω) is derived and given by Kaula and others:

$$V_{\ell m} = \frac{GM_J R_J^{\ell}}{a^{\ell+1}} \sum_{p=0}^{\ell} F_{\ell mp}(i) \sum_{q=-\infty}^{\infty} G_{\ell pq}(e)\, S_{\ell mpq}(\omega, M, \Omega, \theta) \qquad \text{(F-4)}$$

where: M = the mean anomaly described initially in Appendix B, Section 1.

θ = Greenwich Sidereal Time

i, ω, Ω = orbital angles defined previously

$F_{\ell mp}(i)$ = a function of inclination i derived and tabulated by Kaula and others

$G_{\ell pq}(e)$ = a function of eccentricity e derived and tabulated by Kaula and others

$$S_{\ell mpq}(\omega, M, \Omega\ \theta) = \text{or } -\begin{cases} C_{\ell m} & \ell\text{-m even} \\ S_{\ell m} & \ell\text{-m odd} \end{cases} \text{Cos}\left[(\ell-2p)\omega + (\ell-2p+q)M + m(\Omega-\theta)\right]$$

$$\text{or } +\begin{cases} S_{\ell m} & \ell\text{-m even} \\ C_{\ell m} & \ell\text{-m odd} \end{cases} \text{Sin}\left[(\ell-2p)\omega + (\ell-2p+q)M + m(\Omega-\theta)\right]$$

The perturbational terms from eq. (F-2) are zonal (m=0) and we are interested only in the secular terms independent of M; i.e., $q = 2p - \ell$ in $S_{\ell mpq}$. Eq. (F-4) thus reduces to:

$$V_{\ell 0} = \frac{GM_J R_J^{\ell} J_{\ell}}{a^{\ell+1}} \sum_{p=0}^{\ell} F_{\ell 0p}^{(i)} G_{\ell p(2p-\ell)}(e) \begin{cases} \text{Cos} & \ell \text{ even} \\ \text{Sin} & \ell \text{ odd} \end{cases} \left[(\ell-2p)\omega\right]$$

Since $S_{\ell 0} = 0$ for all ℓ, $C_{\ell 0} = J_{\ell}$ by definition and:

$$F_{\ell 0p}(i) = \sum_{t=0}^{p} \frac{(-1)^{k+p-t}(2\ell-2t)!\ \text{Sin}^{\ell-2t} i}{t!(\ell-t)!(p-t)!(\ell-p-t)!\,2^{2\ell-2t}}$$

where: k = integer part of $\ell/2$.

$$G_{\ell p(2p-\ell)}^{(e)} = \frac{1}{(1-e^2)^{\ell-\frac{1}{2}}} \sum_{d=0}^{p'-1} \binom{\ell-1}{2d+\ell-2p'} \binom{2d+\ell-2p'}{d} \left(\frac{e}{2}\right)^{2d+\ell-2p'}$$

where: $p' = p$ for $p \leq \ell/2$

$p' = \ell - p$ for $p > \ell/2$

Thus, the V_{20} and V_{40} terms can be written:

$$V_{20} = \frac{GM_J R_J^2 J_2}{a^3} \sum_{p=0}^{2} F_{20p}(i)\, G_{2p(2p-\ell)}(e)\, \text{Cos}\left[(2-2p)\omega\right]$$

$$V_{40} = \frac{GM_J R_J^4 J_4}{a^5} \sum_{p=0}^{4} F_{40p}(i)\, G_{4p(2p-4)}(e)\, \text{Cos}\left[(4-2p)\omega\right] \qquad \text{(F-5)}$$

These terms become quite simplified as many of the F and G functions are 0.

They can be reduced to:

$$V_{20} = \frac{GM_J R_J^2 J_2}{a^3} F_{201}(i)\, G_{210}(e)$$

$$V_{40} = \frac{GM_J R_J^4 J_4}{a^5} \left[2F_{401}(i)\, G_{41(-2)}(e)\, \text{Cos}\, 2\omega + F_{402}(i)\, G_{420}(e)\right]$$

The Lagrange equations of orbital perturbations are well documented in the literature of orbital mechanics and presented below:

$$\frac{da}{dt} = \frac{2}{na} \frac{\partial F}{\partial M}$$

$$\frac{de}{dt} = \frac{(1-e^2)}{na^2 e} \frac{\partial F}{\partial M} - \frac{\sqrt{1-e^2}}{na^2 e} \frac{\partial F}{\partial \omega}$$

$$\frac{d\omega}{dt} = \frac{-\text{Cot } i}{na^2\sqrt{1-e^2}} \frac{\partial F}{\partial i} + \frac{\sqrt{1-e^2}}{na^2 e} \frac{\partial F}{\partial e}$$

$$\frac{di}{dt} = \frac{\text{Cot } i}{na^2\sqrt{1-e^2}} \frac{\partial F}{\partial \omega} - \frac{1}{na^2\sqrt{1-e^2}\ \text{Sin } i} \frac{\partial F}{\partial \Omega} \qquad \text{(F-6)}$$

$$\frac{d\Omega}{dt} = \frac{1}{na^2\sqrt{1-e^2}\ \text{Sin } i} \frac{\partial F}{\partial i}$$

$$\frac{dM}{dt} = \frac{-(1-e^2)}{na^2 e} \frac{\partial F}{\partial e} - \frac{2}{na} \frac{\partial F}{\partial a}$$

where: n = mean orbital velocity given by $\sqrt{GM_J/a^3}$

F = the force function given by $GM_J/2a - \sum_{\ell,m} V_{\ell m}$, (F-7)

$GM_J/2a$ is termed the central field force, $V_{\ell m}$ (V_{20} and V_{40} in our case) the perturbations.

The force function is qualitatively the gravitational potential minus the kinetic energy per unit mass of SC, or $GM_J/r - \sum_{\ell,m} V_{\ell m} - \frac{1}{2}V^2$, where V is the linear velocity of the SC = $\sqrt{GM_J(2/r - 1/a)}$. Thus the expression for F follows.

The task now is simply algebraic, placing (F-5) and (F-7) into (F-6) and carring out the differentiation. Appendix F1 lists the reduced equations of motion for the force function F. Numerical results are presented at the end of Section 4 in Table F-1.

3. Periodic Oscillations in Perijove

As mentioned previously, one sequence of desirable science objectives would entail: (1) inclining JOSE's orbit from equatorial to some inclined orbit (inclination i) after a year of equatorial orbiting, then (2) reducing apoapsis to some value R_a'. The ordering of (1) and (2) is significant, from a propellant point of view, since the inclination change is performed most economically at apoapsis where the SC velocity is minimum, and the greater the apojove, the smaller this minimum orbital velocity.

Thus, immediately after the inclination change to i, and the reduction to apoapsis of R_a', it is relevant to consider the periodic oscillations of the perijove altitude from its nominal height of 0.1 R_J (or 7137 km. above the atmospheric surface of Jupiter).

Perijove distance R_{per} is given by:

$$R_{per} = a(1-e)$$

Since $\frac{da}{dt} = 0$, $\frac{d}{dt} R_{per} = -a \frac{de}{dt}$

Again, restricting ourselves to the central, second, and fourth degree zonal terms of the gravity potential, Appendix F1 gives $\frac{de}{dt}$, hence:

$$\frac{d}{dt} R_{per} = \frac{15n J_4 R_J^4 e}{16a^3(1-e^2)^3} \left(\frac{-7}{2} \text{Sin}^4 i + 3 \text{Sin}^2 i \right) \text{Sin } 2\omega \qquad \text{(F-8)}$$

Although e, i, and ω are all varying with respect to time, a glance at Table F-1 at the end of Section 4 confirms two remarks allowing a simplification of eq. (F-8); i.e., (1) the time rate of change of ω is predominant over changes in e and i, and (2) the time rate of change in ω due to the V_{20} term is greater than that due to the V_{40} term. Hence, $\frac{d}{dt} R_{per}$ is considered as a function of ω only (e and i are considered constants) and $\frac{d\omega}{dt}$ is approximated by:

$$\frac{d\omega}{dt} = \frac{-3nJ_2R_J^2}{4a^2(1-e^2)^2} (1 - 5 \text{Cos}^2 i) = C_1 \quad \text{(a constant)}$$

Then, $\omega = C_1 t$; the constant of integration is zero since, at time t = 0, the orbit is being inclined from an equatorial orbit about the line of nodes, hence the initial $\omega = 0$.

Integrating Eq. (F-8) with respect to t:

$$R_{per} = C_3 + C_2 \int_o^t \text{Sin } 2\omega \, d\, t \qquad \text{(F-9)}$$

where: C_3 = constant of integration

$$C_2 = \frac{15n\, J_4 R_J^4 e}{16a^3(1-e^2)^3}\left(\frac{-7}{2}\,\mathrm{Sin}^4 i + 3\,\mathrm{Sin}^2 i\right)$$

and $$\int_o^t \mathrm{Sin}\ 2\omega dt = -\,\mathrm{Cos}\ 2\omega/2\ \frac{d\omega}{dt}$$

The constant of integration C_3 is readily evaluated by noting that $R_{per} = 1.1\ R_J$ at $t = 0$. Then, eventually:

$$R_{per} = 1.1 - \frac{5J_4 R_J^2 e\left(\frac{-7}{2}\,\mathrm{Sin}^4 i + 3\,\mathrm{Sin}^2 i\right)}{8J_2 a(1-e^2)(1-5\,\mathrm{Cos}^2 i)}\ (1 - \mathrm{Cos}\ 2\omega) \qquad \text{(F-10)}$$

where: R_J = 1 planetary radius.

Thus, R_{per} is periodic with respect to the argument of perijove ω which is continuously changing with respect to time. The amplitude of the oscillation in R_{per} is of course two times the factor before the term $(1 - \mathrm{Cos}\ 2\omega)$. As J_4 is negative, the expression $(-7/2\ \mathrm{Sin}^4 i + 3\ \mathrm{Sin}^2 i)/(1 - 5\ \mathrm{Cos}^2 i) = f(i)$ is negative for: $0 \leq i < 63.6^\circ$, and $67.8^\circ < i \leq 90^\circ$; and $(1 - \mathrm{Cos}\ 2\omega) \geq 0$; it is seen that we are considering decreases in perijove for all inclinations except: $63.6^\circ < i \leq 67.8^\circ$. Note the resonant condition at $i = 63.6^\circ$; i.e., $1 - 5\ \mathrm{Cos}^2 63.6^\circ = 0$. This is the well known natural resonance condition for orbiting Earth satellites; orbits at inclinations near 63.6° are extremely unstable. The maximum decrease in perijove occurs in eq. (F-10) when $\omega = (2n + 1)\pi/2$, $n = 0,1, \ldots$. This total maximum decrease in perijove is plotted in Figure F-1 for various reduced apojoves from 20 R_J to 100 R_J and inclinations from 10° to 90°. Also shown in the figure is the period of periapsis oscillation, the time in which ω rotates by π radians. Note that, for i such that $63.6^\circ < i \leq 67.8^\circ$, the perijove oscillates at distances greater than the initial 1.1 R_J.

Recalling that, of the three original orbits considered in Chapter III which were not in Jupiter's equatorial plane, the orbit of 1975 has an inclination of 63.8°, very close to the resonant condition. Thus it was decided to calculate the perijove oscillations for these three orbits. Noting from Figures III-13 through III-15 the initial arguments of perijove, and labeling them as ω_o so as not to confuse them with the free variable ω, the derivation employed to obtain eq. (F-10) gives:

$$R_{per} = 1.1 - \frac{5J_4R_J^2e(\frac{-7}{2}\,\mathrm{Sin}^4 i + 3\,\mathrm{Sin}^2 i)}{8J_2a(1-e^2)(1-5\,\mathrm{Cos}^2 i)}(\mathrm{Cos}\,2\omega_o - \mathrm{Cos}\,2\omega) \qquad \text{(F-11)}$$

Considering 1.1 R_J x 100 R_J dimensions for all three trajectories, and substituting the appropriate i and ω_o angles for each orbit 1975, 1980, and 1985, the minimum perijoves are:

1975: Min. R_{per} (at $\omega = 0^{\circ}$) = 1.0975 R_J

1980: Min. R_{per} (at $\omega = \pi/2$) = 1.0917 R_J

1985: Min. R_{per} (at $\omega = \pi/2$) = 1.0908 R_J

Thus it can be concluded that the danger of planetary impact from gravitational effects can be ignored unless the inclination happens to be very precisely (within a few hundredths of a degree) near the resonant inclination of 63.6°.

Note from Figure F-1 that if the mission personnel are daring, or if later in the orbital mission (after three years) the gamble is considered worth the risk, the inclination can be increased slowly above 60° allowing closer planetary viewing and atmospheric dynamic measurements as perijove oscillates closer and closer to the surface. The possibility should be considered if propellant considerations are such that inclination increases are unrestricted, and planetary quarantines are not in effect for Jupiter.

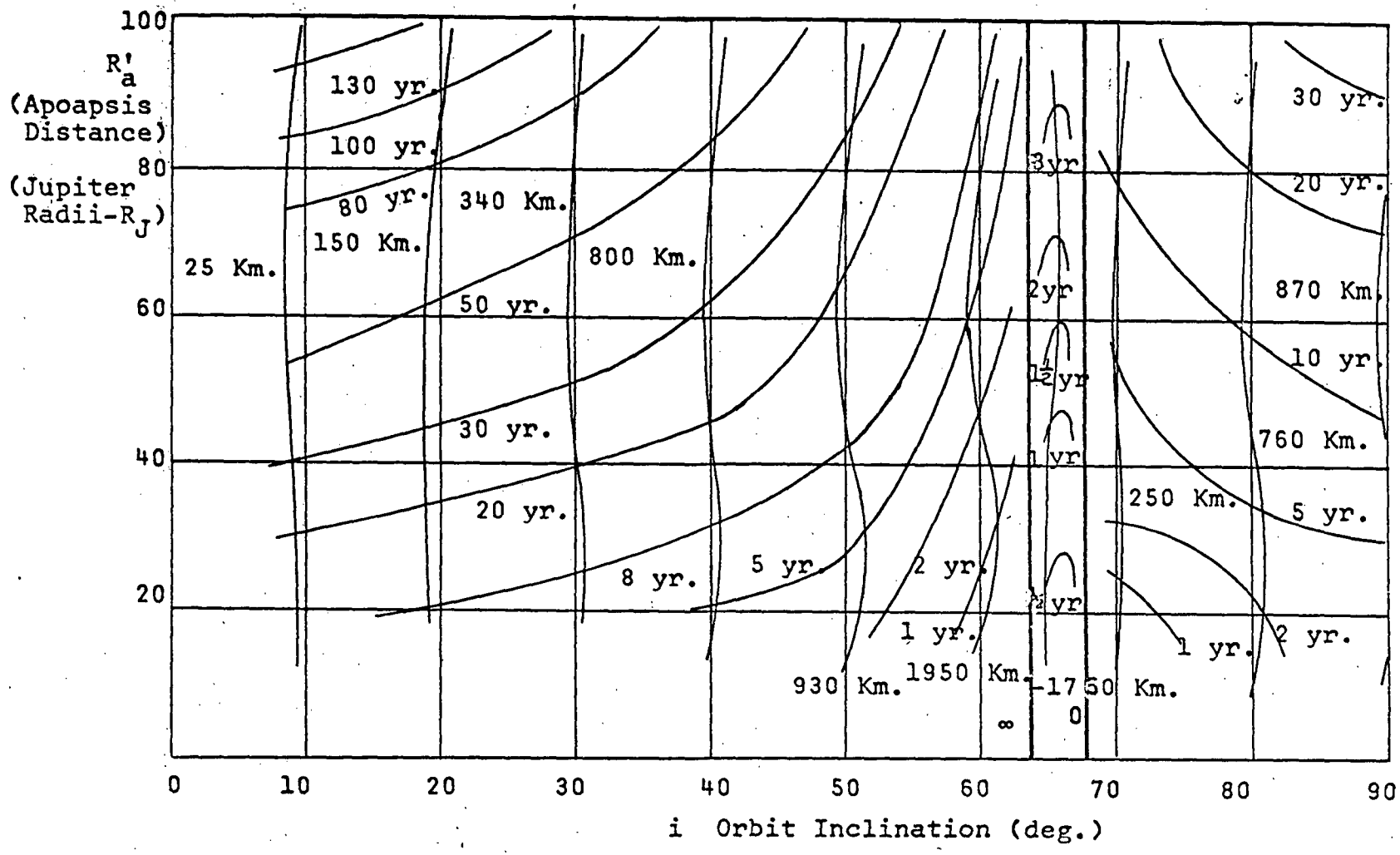

Figure F-1: Maximum Decrease in Periapsis Distance (Km.) and Period of Periapsis Oscillation in Number of Orbits and Years. From an Initial Equatorial Orbit of 1.1 x 100 R_J.

4. The Long Term Secular Perturbations of an Equatorial Orbit

A glance at the Lagrange equations (F-6) quickly convinces one that equatorial perturbations require special treatment. Investigators in the field of orbital perturbations tend to develop the equatorial case to suit their own immediate needs, usually by energy or momentum considerations. This author could not find in the literature a general treatment and derivations for Lagrange equations similar to eq. (F-6) for the equatorial case, hence Appendix F-2 presents this development performed by the Author. By way of introduction, the orbital set (a, e, M, θ) is introduced, θ being the angle measured counterclockwise from the Aries vector projection on Jupiter's equatorial plane ($\bar{X}_J$ of Chapter III) to perijove. Intuitively, it would appear that eq. (F-6) would hold if the following changes are made:

(1) Eliminate the $\frac{di}{dt}$ and $\frac{d\Omega}{dt}$ equations.

(2) In the remaining four equations, simply substitute θ for ω.

That this is indeed the case is verified in Appendix F-2.

The force function F is now expressed in terms of the orbital parameters (a, e, M, θ) in the following manner. The general perturbation term is, from eq. (F-1):

$$V_{\ell m} = \frac{GM_J R_J^{\ell}}{r^{\ell+1}} P_{\ell m}(\text{Sin } \phi)(C_{\ell m} \text{ Cos } m\lambda + S_{\ell m} \text{ Sin } m\lambda) \qquad \text{(F-12)}$$

Since we are considering the equatorial case, $\phi = 0$, and $P_{\ell m}(\text{Sin}\phi) = P_{\ell m}(0)$. From the sketch below,

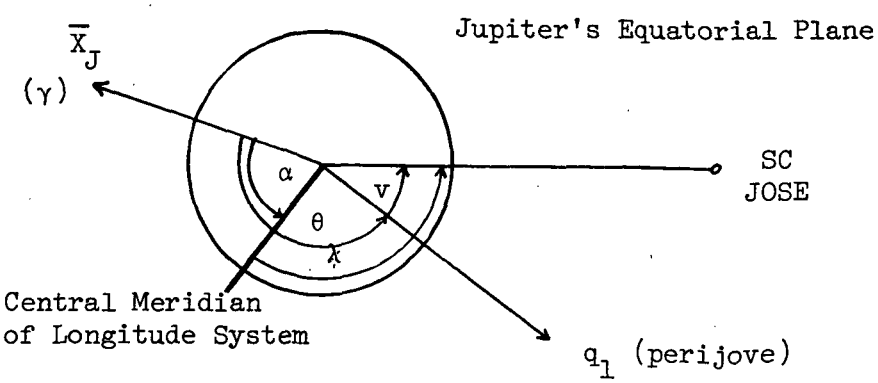

the longitude can be expresses as: $\lambda = \theta + v - \alpha$, where α is the right ascension of the central meridian in the longitude system (I or III, since the orbit is equatorial, see Chapter I, Section C). α is known, given the time t. Thus, in eq. (F-12), Cos $m\lambda$ and Sin $m\lambda$ can be expressed in terms of cosines and sines of $m(\theta-\alpha)$ and mv. The cosine and sine of mv can be expressed in terms of powers of cosines and sines of v by:

$$\text{Cos } mv = \text{Re} \sum_{s=o}^{m} \binom{m}{s} j^s \text{Cos}^{m-s} v \text{ Sin}^s v$$

$$\text{Sin } mv = \text{Re} \sum_{s=o}^{m} \binom{m}{s} j^{s-1} \text{Cos}^{m-s} v \text{ Sin}^s v$$

where: Re = real part of

$j = \sqrt{-1}$

$\binom{m}{s}$ = the binomial coefficient $m!/s!(m-s)!$

Thus, after some algebra:

$$V_{\ell m} = \frac{GM_J R_J^{\ell}}{r^{\ell+1}} P_{\ell m}(0) \text{ Re } \{[(C_{\ell m} - j S_{\ell m}) \text{Cos } m(\theta-\alpha) + (S_{\ell m} + j C_{\ell m}) \text{ Sin } m(\theta-\alpha)] \sum_{s=o}^{m} \binom{m}{s} j^s \text{Cos}^{m-s} v \text{ Sin}^s v\} \qquad \text{(F-13)}$$

Separation of trigonometric terms involing $m(\theta-\alpha)$ and v to various powers has been achieved. It is desirable to express the $\text{Cos}^{m-s} v$ and $\text{Sin}^s v$ terms as terms involving first powers of Cos v and Sin v. This is accomplished by noting:

$$\text{Sin}^s v \text{ Cos}^{m-s} v = \left[\frac{-j}{2}(e^{jv} - e^{-jv})\right]^s \left[\frac{1}{2}(e^{jv} + e^{-jv})\right]^{m-s} = \frac{(-j)^s}{2^m} \sum_{c=o}^{s} \sum_{d=o}^{m-s} \qquad \text{(F-14)}$$

$$\binom{s}{c}\binom{m-s}{d} (-1)^c \left[\text{Cos}(m-2c-2d)v + j \text{ Sin}(m-2c-2d)v\right]$$

When this is substituted into (F-13) and the multiplication within the Re brackets carried out, trigonometric terms like, for example, Cos $m(\theta-\alpha)$ times Cos$(m-2c-2d)v$ will result. There will also be Cos Sin, Sin Cos, and Sin Sin terms of the same angles. These can be nicely expressed as single trigonometric terms by noting, for any angles a and b:

$$\begin{aligned}
&\text{Cos a Cos b} = \tfrac{1}{2}\text{Cos (a+b)} + \tfrac{1}{2}\text{Cos (a-b)} \\
&\text{Sin a Sin b} = -\tfrac{1}{2}\text{Sin (a+b)} + \tfrac{1}{2}\text{Cos (a-b)} \\
&\text{Sin a Cos b} = \tfrac{1}{2}\text{Sin (a+b)} + \tfrac{1}{2}\text{Sin (a-b)} \\
&\text{Cos a Sin b} = \tfrac{1}{2}\text{Sin (a+b)} - \tfrac{1}{2}\text{Sin (a-b)}
\end{aligned} \qquad \text{(F-15)}$$

Substituting $a = m(\theta-\alpha)$ and $b = (m-2c-2d)v$ into eq. (F-15), substituting equations (F-15) and (F-14) into eq. (F-13), carrying out the multiplication, and ignoring imaginary terms, eventually:

$$V_{\ell m} = \frac{GM_J R_J^{\ell}}{r^{\ell+1}} P_{\ell m}(0) \sum_{s=o}^{m} \frac{1}{2^m} \binom{m}{s} \sum_{c=o}^{s} \sum_{d=o}^{m-s} \binom{s}{c}\binom{m-s}{d} (-1)^c \, x$$

$$\left\{ \begin{bmatrix} C_{\ell m} & \text{Cos} \\ + & \\ S_{\ell m} & \text{Sin} \end{bmatrix} \left[m(\theta-\alpha) + (m-2c-2d)v \right] \right\} \qquad \text{(F-16)}$$

where the notation $\begin{bmatrix} C_{\ell m} & \text{Cos} \\ + & \\ S_{\ell m} & \text{Sin} \end{bmatrix} [\text{angle}]$ represents $C_{\ell m}$ Cos [angle] + $S_{\ell m}$ Sin [angle].

To facilitate the differentiation which follows, let $p = c+d$. Note $s \leq m$, $c \leq s$, $d \leq m-s$. The index variable d can be eliminated, and after a little work, eq. (F-16) can be written:

$$V_{\ell m} = \frac{GM_J R_J^{\ell}}{r^{\ell+1}} P_{\ell m}(0) \sum_{p=o}^{m} \sum_{s=o}^{m} \frac{1}{2^m} \binom{m}{s} \sum_{c=o}^{s} \binom{s}{c} \binom{m-s}{p-c} (-1)^c \, x$$

$$\left\{ \begin{bmatrix} C_{\ell m} & \text{Cos} \\ + & \\ S_{\ell m} & \text{Sin} \end{bmatrix} \left[m(\theta-\alpha) + (m-2p)v \right] \right\} \qquad \text{(F-17)}$$

The v terms can now be averaged out, since we are considering only the

long term secular perturbations. The averaging is performed over the mean anomaly, M, from 0 to 2π. Thus, writing eq. (F-17) as a function of v, or $V_{\ell m}(v)$;

$$V_{\ell m}\ (\text{secular}) = 1/2\pi \int_o^{2\pi} V_{\ell m}(v)\ dM \qquad \text{(F-18)}$$

From formulas used in Subprogram TIM, Appendix B, Section 1, involving the anomalies v, E, and M, the expression:

$$dM = r^2\ dv/a^2\ \sqrt{1-e^2} \qquad \text{(F-19)}$$

can be derived. From the well known formula: $r = a(1-e^2)/(1+e\ \text{Cos}\ v)$; we have:

$$\frac{r^2}{r^{\ell+1}} = \left[\frac{1+e\ \text{Cos}\ v}{a(1-e^2)}\right]^{\ell-1} \qquad \text{(F-20)}$$

Expanding $(1+e\ \text{Cos}\ v)^{\ell-1}$ by the binomial theorem:

$$(1+e\ \text{Cos}\ v)^{\ell-1} = \sum_{b=o}^{\ell-1} \binom{\ell-1}{b} e^b\ \text{Cos}^b v = \sum_{b=o}^{\ell-1} \binom{\ell-1}{b} e^b \left[\frac{1}{2^b}(e^{jv} + e^{-jv})^b\right] = \qquad \text{(F-21)}$$

$$\sum_{b=o}^{\ell-1} \binom{\ell-1}{b}\left(\frac{e}{2}\right)^b \sum_{d=o}^{b} \binom{b}{d} e^{-jvd} e^{j(b-d)v} = \sum_{b=o}^{\ell-1} \binom{\ell-1}{b}\binom{b}{d}\left(\frac{e}{2}\right)^b \left[\text{Cos}(b-2d)v + j\text{Sin}(b-2d)v\right]$$

Substituting eq. (F-21) into (F-20), ignoring the imaginary terms, using this result with (F-19) and (F-17), and using eq. (F-15) to expand trigonometric terms which are multiplied together, eq. (F-18) becomes:

$$V_{\ell m} = \frac{GM_J R_J^{\ell}\ P_{\ell m}(0)}{2\pi a^{\ell+1}(1-e^2)^{\ell-\frac{1}{2}}} \sum_{p=0}^{m} F_{mp} \int_o^{2\pi} \sum_{b=o}^{\ell-1} \sum_{d=o}^{b} \binom{\ell-1}{b}\binom{b}{d}\left(\frac{e}{2}\right)^b \times \frac{1}{2}\left\{\begin{bmatrix} C_{\ell m}\text{Cos} \\ S_{\ell m}\text{Sin} \end{bmatrix}\right. \qquad \text{(F-22)}$$

$$\left[m(\theta-\alpha) + (m-2p+b-2d)v\right] + \left.\begin{bmatrix} C_{\ell m}\text{Cos} \\ S_{\ell m}\text{Sin} \end{bmatrix}\left[m(\theta-\alpha) + (m-2p-(b-2d))v\right]\right\}\ dv$$

where: $F_{mp} = \frac{1}{2^m} \sum_{s=o}^{m} \sum_{c=o}^{s} (-1)^c \binom{m}{s}\binom{s}{c}\binom{m-s}{p-c}$

The reward of this tedious algebra is now evident, as every item is seen to integrate to 0 except two cases: $m-2p \pm (b-2d) = 0$, or, by elimination of the index variable b in the summation, for the two cases $b = 2d \pm (m-2p)$. For these two cases, we are integrating a constant over 2π, thus the 2π in the denominator of eq. (F-22) cancels. A little more algebraic manipulation plus the remark that the symmetry of the binomial coefficients just inside the integral and double summation signs of (F-22) eventually cause the cancellation of the ½ before the trigonometric terms, and there results:

$$V_{\ell m} = \frac{GM_J R_J^{\ell} P_{\ell m}(0)}{a^{\ell+1}} \sum_{p=o}^{m} F_{mp}\, G_{\ell mp(2p-m)}^{(e)} \begin{bmatrix} C_{\ell m} \\ + \\ S_{\ell m} \end{bmatrix} \begin{matrix} \text{Cos} \\ \\ \text{Sin} \end{matrix} \left[M(\theta-\alpha)\right] \qquad \text{(F-23)}$$

where: $G_{\ell mp(2p-m)}^{(e)} = \frac{1}{(1-e^2)^{\ell-\frac{1}{2}}} \sum_{d=0}^{p'-1} \binom{\ell-1}{2d+m-2p'} \binom{2d+m-2p'}{d} \left(\frac{e}{2}\right)^{2d+m-2p'}$

$p' = p$ for $p \leq \ell/2$

$p' = \ell - p$ for $p > \ell/2$

Thus equation (F-23) is the general expression for the secular gravitational perturbation $V_{\ell m}$ for an orbiter in a planet's equatorial plane. The case considered here with eq. (F-2), m = 0, simplifies the numerical work considerably. Thus, for V_{20} and V_{40}, noting that $P_{20}(0) = -\frac{1}{2}$, $P_{40}(0) = 3/8$:

$$V_{20} = \frac{-GM_J R_J^2 J_2}{2a^3(1-e^2)^{3/2}} \quad , \quad V_{40} = \frac{3GM_J R_J^4 J_4}{8a^5(1-e^2)^{7/2}}$$

Thus, substituting these terms into the force function eq. (F-7), and substituting this force function into the equatorial Lagrange equations of eq. (F2-5), the results are listed in Appendix F3. Table F-1 thus presents

the numerical results for orbits under consideration for JOSE for equatorial and the three sample inclined trajectories of Chapter III. The equatorial case, not depending on θ for the V_{20} and V_{40} terms, is thus not dependent on the date of arrival at Jupiter.

5. The Short Term Periodic Perturbations to an Equatorial Orbit

Equation (F-3) for the potential V is now used. The force function F is then:

$$F = \frac{GM_J}{2a} + GM_J R_J^2 \left[\frac{J_2}{2r^3} - \frac{3R_J^2 J_4}{8r^5} - \frac{3}{r^3} \{ C_{22} \text{Cos } 2(\theta-\alpha+v) + S_{22} \text{ Sin } 2(\theta-\alpha+v) \} \right] \qquad \text{(F-24)}$$

and is the F to be substituted in the Lagrange equations (F2-5). Since the radar measures r (range) and $\dot{r}$ (range rate), and the true anomaly v must be solved before the orbital parameters (a, e, M, θ) are solved, there is no advantage in expressing F solely in terms of the orbital parameters. Direct differentiation of eq. (F-24) is performed, bearing in mind that, for differentiation with respect to M:

$$\frac{\partial F}{\partial M} = \frac{\partial F}{\partial r} \frac{\partial r}{\partial v} \frac{dv}{dM} + \frac{\partial F}{\partial v} \frac{dv}{dM}$$

where: $\frac{dr}{dv} = \frac{re \text{ Sin } v}{1 + e \text{ Cos } v}$, $\frac{dv}{dM} = \frac{a^2\sqrt{1-e^2}}{r^2}$

The results eventually obtained are:

$$\begin{pmatrix} da/dt \\ de/dt \\ dM/dt \\ d\theta/dt \end{pmatrix} = \begin{pmatrix} 0 \\ 0 \\ n \\ 0 \end{pmatrix} + G \begin{pmatrix} J_2 \\ J_4 \\ C_{22} \\ S_{22} \end{pmatrix} \qquad \text{(F-25)}$$

Table F-1: Secular Rates of Orbital Parameters (ω, i, Ω, M) (degrees/orbit) (e/orbit)

Elemental Rate	Contributing Gravitational Terms	1975 Orbit		1980 Orbit		1985 Orbit		Equatorial Orbit (independent of year)	
		1.1 x 100	1.1 x 20	1.1 x 100	1.1 x 20	1.1 x 100	1.1 x 20	1.1 x 100	1.1 x 20
$\frac{da}{dt}$	$GM_J/2a$	0	0	0	0	0	0	0	0
	$-V_{20}$	0	0	0	0	0	0	0	0
	$-V_{40}$	0	0	0	0	0	0	0	0
$\frac{de}{dt}$	$GM_J/2a$	0	0	0	0	0	0	0	0
	$-V_{20}$	0	0	0	0	0	0	0	0
	$-V_{40}$	-2.14×10^{-7}	-1.63×10^{-6}	5.65×10^{-7}	4.3×10^{-6}	1×10^{-6}	7.71×10^{-6}	0	0
$\frac{d\omega}{dt}$	$GM_J/2a$	0	0	0	0	0	0	$\frac{d\theta}{dt}$	
	$-V_{20}$	-.0186	-.0251	-.4910	-.6650	-.5760	-.7770	1.2400	1.6720
	$-V_{40}$	-.0120	-.0173	-.0016	-.0012	.0110	.0256	-.0154	-.0318
$\frac{di}{dt}$	$GM_J/2a$	0	0	0	0	0	0	—	—
	$-V_{20}$	0	0	0	0	0	0	—	—
	$-V_{40}$	-.000526	-.000459	.000635	.000555	.000612	.000535	—	—
$\frac{d\Omega}{dt}$	$GM_J/2a$	0	0	0	0	0	0	—	—
	$-V_{20}$	-.5460	-.7370	-.2640	-.3560	-.1470	-.1990	—	—
	$-V_{40}$	.0165	.0171	.0171	.0172	.0112	.0110	—	—
$\frac{dM}{dt}$	$GM_J/2a$	360	360	360	360	360	360	360	360
	$-V_{20}$	-.0580	-.1570	-.1200	-.3240	-.1330	-.3580	.2780	.7480
	$-V_{40}$	-.0004	-.0007	.0001	-.0008	.0010	.0021	-.0015	-.0061

where, G = a 4x4 matrix $\{g_{ij}(r, a, e, v, \theta)\}$. The individual g_{ij} are tabulated for reference in Appendix F4.

6. Gravitational Harmonics Solution by On-Board Radar

The sketch below should be consulted for reference.

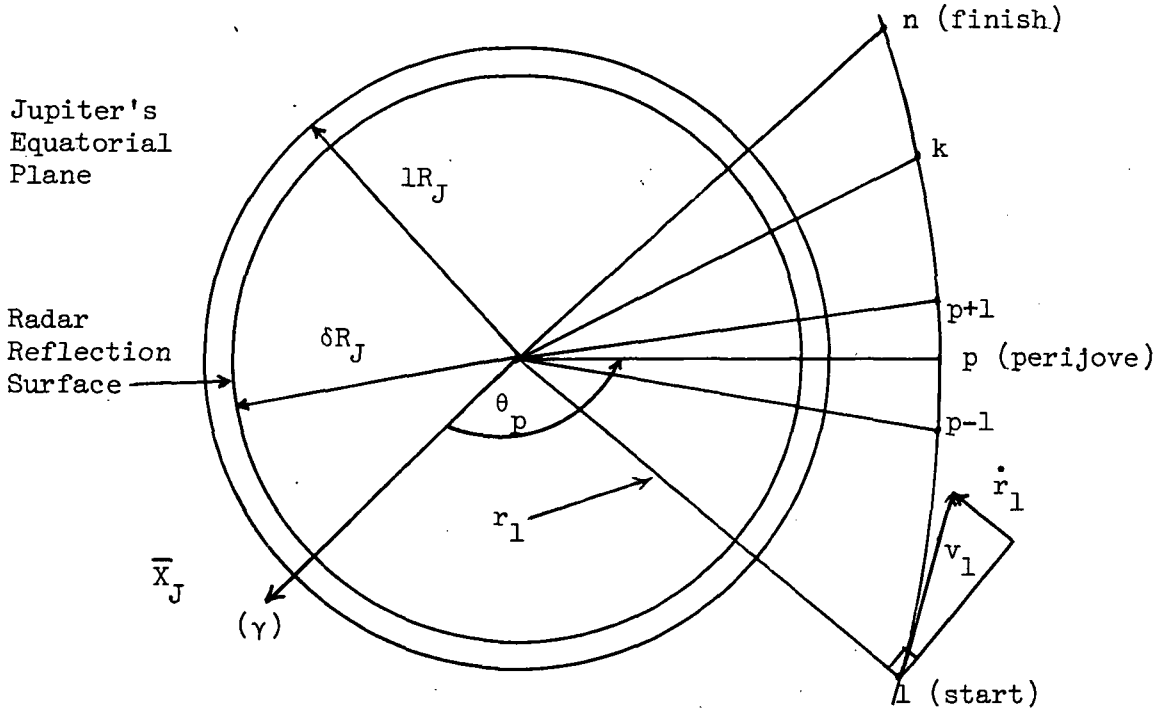

Assuming a radar reflection and a value of δR_J, the radar provides:

$$r = \delta R_J + c\Delta t$$

$$\dot{r} = c\Delta f_i / f_i$$

where: c = velocity of electromagnetic radiation through Jupiter's ionosphere

Δt = time lag of emitted and reflected signal

f_i = frequency of signal, in the X band (extremely high frequency range)

Δf_i = measured frequency shift, due to the doppler effect caused by $\dot{r}$ of the spacecraft

Rough calculations indicate that, assuming radar reflections are possible, range accuracy in the order of tens of kilometers and range rate to an accuracy

of about 20 meters per second are possible. These accuracies can possibly be improved by rigorous electronic design.

Without going into a detailed analysis of corrections necessary to the radar measurement, it suffices to enumerate them below:*

(a) Range rate $\dot{r}$ must be corrected for:

(1) ionospheric refraction effect; i.e., α/f_i must be added to Δf_i, α being a theoretically derived constant.

(2) tropospheric refraction; i.e., a correction to $\dot{r}$, $\delta\dot{r}$, must be applied. $\delta\dot{r} = -\frac{d}{dt}\int_{\delta R_J}^{R_J} \mu \, ds$

where: μ = refractive index of Jupiter's troposphere

ds = infinitestimal unit of altitude

(b) Range r must be corrected for tropospheric refraction.

(c) Other miscellaneous errors are:

(1) error in reference frequency f_i

(2) higher order ionospheric refraction effect, not accounted for by α

(3) variation of tropospheric refraction effect, not accounted for by model of μ

(4) radar failure to lock onto signal

The distance r from JOSE to Jupiter's center has been previously stated several times; i.e.,

$$r = a(1-e^2)/(1+e \text{ Cos } v) \qquad \text{(F-26)}$$

If the orbit were strictly Keplerian, i.e., the central gravity term only were present, $\dot{r}$ would be strictly a function of v only, or the SC position in the orbit of constant a and e. However, the smaller perturbation terms affect $\dot{r}$ through the periodic perturbations to a, e, and v derived in

* Kaula, William M., Theory of Satellite Geodesy, Blaisdell Publishing Co., Waltham, Mass., 1966.

Section 5. But these perturbations have been expressed explicitly in terms of the unknown harmonic coefficient in Section 5. Thus, by measuring $\dot{r}$ accurately, and providing we can solve for the osculating values of a, e, v, and θ, we can affect a solution for the coefficients. Thus an expression relating $\dot{r}$ and the harmonic coefficients is developed, which is referred to as the range rate model, which is derived from eq. (F-26) to be:

$$\dot{r} = \frac{r}{a}\frac{da}{dt} - \frac{r\left[2e+(1+e^2)\text{Cos } v\right]}{(1-e^2)(1+e\text{ Cos } v)}\frac{de}{dt} + \frac{a^2 e \text{ Sin } v\sqrt{1-e^2}}{r(1+e\text{ Cos } v)}\frac{dM}{dt} \qquad \text{(F-27)}$$

Then substituting eq. (F-25) into (F-27), and after considerable reduction, there results:

$$\bar{\dot{r}} = F\,\bar{J} + \bar{E} \qquad \text{(F-28)}$$

where: $\bar{\dot{r}}^T$ = the 1xn row vector $(\dot{r}_1, \dot{r}_2, \ldots, \dot{r}_n)$, or the vector of range rates for all positions 1 through n.

F = nx4 matrix $\{f_{ij}\}$

$\bar{J}^T$ = the 1x4 row vector $(J_2, J_4, C_{22}, S_{22})$, or the vector of unknown coefficients.

$\bar{E}^T$ = the 1xn row vector $(E_i, \ldots E_n)$ where $E_i = \dfrac{n_i . a_i . e_i \text{ Sin } v_i}{\sqrt{1 - e_i^2}}$

$$f_{il}(r_i, a_i, e_i, v_i) = \frac{3n_i a_i \text{Sin } v_i R_J^2(\text{Cos } v_i + e_i \text{Sin } v_i)}{2r_i^2\sqrt{1-e_i^2}}$$

$$f_{i2}(r_i, a_i, e_i, v_i) = \frac{-5}{4}\frac{R_J^2}{r_i^2} f_{il}$$

$$\begin{pmatrix} f_{i3} \\ f_{i4} \end{pmatrix}(r_i, a_i, e_i, v_i, \theta_i) = M \begin{pmatrix} f_{i5} \\ f_{i6} \end{pmatrix}(r_i, a_i, e_i, v_i)$$

M = 2x2 matrix $\{m_{ij}(\theta_i, v_i)\}$

$$m_{11}(\theta_i, v_i) = -m_{22}(\theta_i, v_i) = \text{Cos } 2(\theta_i - \alpha_i + v_i)$$

$$m_{12}(\theta_i, v_i) = m_{21}(\theta_i, v_i) = \text{Sin } 2\ (\theta_i - \alpha_i + v_i)$$

$$f_{i5}\ (r_i, a_i, e_i, v_i) = \frac{-9n_i a_i R_J^2 \text{Sin } v_i \left[\overline{3}e_i + \text{Cos } v_i(2+e_i^2) + 2e_i \text{Sin } v_i(1-e_i^2)\right]}{2r_i^2(1 - e_i^2)^{3/2}}$$

$$f_{i6}\ (r_i, a_i, e_i, v_i) = \frac{-3n_i a_i R_J^2 f_{i7}}{e_i r_i^2 (1-e_i^2)^{3/2}}\ (r_i, a_i, e_i, v_i)$$

$$f_{i7}(r_i, a_i, e_i, v_i) = 3e_i + 2\text{Cos } v_i(1+2e_i^2) + e_i \text{Cos}^2 v_i(2+e_i^2) - 2\left(\frac{r_i}{a_i}\right)$$
$$\left[\overline{2}e_i + (1+e_i^2)\text{Cos } v_i\right]$$

Thus, $\overline{J}$ can be solved by the methods of vector algebra, once the values of a_i, e_i, v_i, and θ_i are determined for each radar measurement. A procedure for solving these osculating parameters is now presented. Although cumbersome to describe, it's easy to implement as it utilizes formulation already presented in this report.

We adopt a system of terminology, similar to that used in geodetic surveying, to facilitate the description. We will say that the accuracy of the computed value of an orbital parameter is fifth order if that value has been determined or estimated by the least accurate method available. An order of improvement in the accuracy of the parameter results in the parameter being of fourth order accuracy. First order is the most accurate value obtainable in measuring the orbital parameters with the given instruments.

Range and range rate measurements are abbreviated hereafter as R and RR measurements respectively.

The useful radar measurement portion of the orbit will be with true anomalies v such that: $-\pi/2 \leq v \leq \pi/2$, and r is such that: $1.1\ R_J \leq r \leq 2.53\ R_J$, optimum distances for radar measurements at X band. The analysis and reduction of data is performed on Earth after the SC has passed point n and the measurements are completed. The initial fifth order values of a and e for the orbit of JOSE is determined by whatever DSN tracking may have existed before the SC arrived at point 1. These fifth order values are termed a_p and e_p.

A third very important measurement besides r and $\dot{r}$ obtained from the radar is a very precise time measurement between each consecutive pair of radar observations. The time at any point k will be termed t_k, thus the time interval between the $k+1^{st}$ and the k^{th} point is: $t_{k+1} - t_k$.

The procedure starts by determining perijove, satisfying the radar measurements: r_p = Minimum, $\dot{r}_p = 0$, where p is the perijove point. The true anomaly v_p is of course 0. The on-board television system, imaging celestial bodies such as Jupiter limb, natural satellites, and stars, is required near perijove to provide a value of θ_p. Now, using the fifth order values of a_p and e_p, the true anomaly (v_{p+1}) for the first point beyond perijove where a radar measurement is taken (p+1) can be solved:

$$\text{Cos } v_{p+1} = \frac{a_p(1-e_p^2)-r_{p+1}}{e_p r_{p+1}}$$

Chapter III solved the vectors $\bar{X}_J$, $\bar{Y}_J$, $\bar{Z}_J$ defining Jupiter's planetocentric axes. The perijove vector $\bar{r}_p$ is then:

$$\bar{r}_p = r_p(\text{Cos}\theta_p\ \bar{X}_J + \text{Sin}\ \theta_p \bar{Y}_J)$$

Also, the vector at p+1 is:

$$\bar{r}_{p+1} = r_{p+1}\ (\text{Cos}\ (\theta_p + v_{p+1})\ \bar{X}_J + \text{Sin}(\theta_p + v_{p+1})\ \bar{Y}_J) \qquad \text{(F-29)}$$

Thus, two vectors on an osculating ellipse have been established and the flight time between them is known precisely. It is recalled that this is exactly the same problem encountered in Chapter III with the interplanetary trajectories, thus, $\bar{r}_p$, $\bar{r}_{p+1}$, and $t_{p+1} - t_p$ become input for Subprogram TRAPAR of that chapter. Note that the iterations commenced in the interplanetary case for flight time convergence within a tenth of a day; in this case of the planetary orbit, convergence in the order of seconds is required. Thus, for an "average" (for lack of a more suitable word) elliptical orbit between p and p+1, TRAPAR provides as output the fourth order values of $a_p^{(1)}$, $e_p^{(1)}$, $v_p^{(1)}$, and $v_{p+1}^{(1)}$. The fourth order $\theta_p^{(1)} = \theta_p - v_p^{(1)}$, since $v_p^{(1)}$ is not necessarily 0; i.e., for the "average" ellipse between p and p+1, the point p will not in general be the perijove any longer. The values of $a_p^{(1)}$, $e_p^{(1)}$, $v_p^{(1)}$, $\theta_p^{(1)}$, r_p, and $\dot{r}_p$ are then used in equation (F-28) for i = p.

Also, values for the point p+1 are ready to be substituted into eq. (F-28). Noting that $\theta_{p+1}^{(1)} = \theta_p^{(1)} + v_{p+1}^{(1)}$; $a_p^{(1)}$, $e_p^{(1)}$, $v_{p+1}^{(1)}$, $\theta_{p+1}^{(1)}$, r_{p+1}, and $\dot{r}_{p+1}$ are substituted into eq. (F-28) for the point i = p+1.

The points p+1 and p+2 are next considered, and treated in exactly the same manner, starting with:

$$\text{Cos } v_{p+2} = \frac{a_p(1-e_p^2)-r_{p+2}}{e_p r_{p+2}}$$

Forming the vector $\bar{r}_{p+2}$ analogous to eq. (F-29), except for v_{p+2} being substituted instead of v_{p+1}, and knowing the time interval $t_{p+2} - t_{p+1}$, the "average" ellipse between p+1 and p+2 is solved. Thus, as in the case of the preceding segment from p to p+1, two additional sets of parameters (a, e, v, θ, r, $\dot{r}$) are available for points p+1 and p+2. Noting that there are two sets now for point p+1, the values can be averaged if desired.

The equation construction continues in the same manner to point n, then from p to p-1 and working backwards in time to point 1. Every point except 1 and n will have two sets of fourth order parameters which may be averaged. There are n points of the orbit, each having one equation contribution to eq. (F-28); thus a total of n equations to solve four unknowns. A least square solution is suggested if $n>4$. The greater the number of observations n,the more accurate the values of the coefficients, since fourth order orbital parameters are being used between points.

It should be mentioned at this point that:

(1) The number of additional harmonics that might be added to the theory for solution depends not only on the value of the number of observations n, but also on the accuracy obtainable in measuring r and $\dot{r}$. It is meaningless to carry additional gravitational harmonics through the involved derivations of Section 5 the effects of which on the SC orbit are less than the radar deviations in measuring r and $\dot{r}$. Rough calculations for a true anomaly $v = 20^{\circ}$ in eq. (F-28) indicates that the J_2 term contributes about 600 m/sec and J_4 about 25 m/sec to $\dot{r}$.

(2) Judicial selection of the time intervals between successive radar measurements is desirable. From refined calculations near perijove and the R and RR accuracy given above, the author deduced that a R and RR measurement should be performed within 17 seconds of each other (this switch from R to RR involves pulse switching, and other electronic manipulations on the radar). The seventeen seconds is the time in which the range r changes by 2.7 km., a figure probably already less than is capable of being measured by the radar. In other words, time intervals less than 17 seconds would provide no useful information. As the time interval is increased to one minute, for example, a greater degree of resolution in the difference between r_k and r_{k+1} allows

Subprogram TRAPAR to function more effectively. However, increasing the time interval too much;beyond five minutes, for example, means that the true anomaly v is varying by ten or more degrees which in turn implies that a and e are varying so excessively within the segment from k to k+1 that the "average" orbital parameters calculated by TRAPAR are meaningless.

The accuracy of the computed harmonic coefficients are considered fourth order, this may be the highest accuracy desired or obtainable. To refine these values, the following rigorous integration of the Lagrange equations of motion is employed (F-25). Using the fourth order values of the harmonics and noting that v varies much faster during the orbital motion than a, e, and θ, the relation between the third and fourth order values of a, e, and θ are given by:

$$a_k^{(2)} = a_p^{(1)} + \int_o^{v_k^{(1)}} \frac{da}{dt}(v)\,\frac{dt}{dv}\,dv$$

$$e_k^{(2)} = e_p^{(1)} + \int_o^{v_k^{(1)}} \frac{de}{dt}(v)\,\frac{dt}{dv}\,dv$$

$$\theta_k^{(2)} = \theta_p^{(1)} + \int_o^{v_k^{(1)}} \frac{d\theta}{dt}(v)\,\frac{dt}{dv}\,dv$$

where, as mentioned above, the only variable of the orbital parameter rates is v, and $dv/dt = dv/dM \times dM/dt = a^2\sqrt{1-e^2}/r^2 \times n$. The fourth order values $v_k^{(1)}$ cannot be improved in this manner.

The integration eventually produces:

$$a_k^{(2)} = a_p^{(1)} + h_1(a, e, v, \theta, J_2, J_4, C_{22}, S_{22})\Big|_p^k$$

$$e_k^{(2)} = e_p^{(1)} + h_2(a, e, v, \theta, J_2, J_4, C_{22}, S_{22})\Big|_p^k$$

$$\theta_k^{(2)} = \theta_p^{(1)} + h_3(a, e, v, \theta, J_2, J_4, C_{22}, S_{22})\Big|_p^k$$

where: $h_i\Big|_p^k = h_i(a_k^{(1)}, e_k^{(1)}, v_k^{(1)}, \theta_k^{(1)}, J_2, J_4, C_{22}, S_{22})$

$$- h_i(a_p^{(1)}, e_p^{(1)}, v_p^{(1)}, \theta_p^{(1)}, J_2, J_4, C_{22}, S_{22})$$

The functions h_i are given in Appendix F5.

These third order values $a_k^{(2)}$, $e_k^{(2)}$, and $\theta_k^{(2)}$, as well as the fourth order values $v_k^{(1)}$, are again used in eq. (F-28) to determine new third order values of the harmonics. The process can be repeated until first order values are obtained; however, there would probably be no improvement over the third order values if the time increments between measurements are kept to the order of a minute.

7. Non-Planetary Perturbations

To solve for the harmonics of Jupiter's gravity potential, it is necessary to subtract from $\dot{r}$ of eq. (F-28) all contributions arising from sources other than planetary gravitational sources. As mentioned previously in Section 1, Jupiter orbiters do not suffer the undesirable secondary perturbations that Earth satellites do.

Since the orbit determination (OD) scheme of Section 6 can definitely be considered a short arc method, solar and other planetary (other than Jupiter) perturbations can be neglected. Also, considering the distance of the Sun and the inverse square law for solar radiation pressure referred to in Chapter IV, as well as the fact that most of perijove passage will be occulted from the Sun, perturbations from solar radiation pressure are neglected.

Atmospheric drag is no worry whatever unless the SC reaches the resonant inclination. This can quickly be verified by noting from Section F of Chapter I that the scale height H for Jupiter is 8.3 km. In terms of the Planet's radius R_J, $1/H = 8555\ 1/R_J$ units. The density at the outer limits of Jupiter's atmosphere ($1\ R_J$) is 5.5×10^{-4} gm/cm^3 from Table I-5, Chapter I. Since the density at any altitude h is given by:

$$\rho(h) = \rho(1\ R_J)\ e^{-h/H},$$

substituting h = 0.1 R_J yields a value of around 10^{-400} gm/cm^3, and this discussion is immediately dropped.

Of the natural satellites, only the first five need be considered; i.e., JI through JV, since the other seven irregular satellites are so far from JOSE when JOSE is in the radar measuring portion of its orbit that their effects are certainly negligible. For this discussion, JI through JV will be considered to orbit in Jupiter's equatorial plane (a valid assumption; note from Table I-6, Chapter I, that JII (Europa) has the maximum inclination of merely 28.1 minutes of arc). However, for the development here, the satellites' eccentricities are kept general; it is assumed that, given any time t_k of the radar measurement at point k, the corresponding distance r_{ki} from Jupiter's center to satellite i (i = I, ..., V) is known or can be determined from ephemerides. Although the eccentricities of all five satellites are small, their radial distances r_i vary sufficiently to effect the perturbational magnitudes when compared to the accuracy of measuring $\dot{r}$ to Jupiter's surface by the radar. For instance, knowing a_i and e_i for satellite i means the distance r_i can be computed by eq. (F-26) only if v and hence the direction of perijove for each satellite is known. Additional improvements in the ephemerides of Jupiter's satellites in the 1970's prior to this orbital mission are thus in order.

Dropping the subscript k of the k^{th} observation, the perturbation function due to natural satellites I through V is given by a formula well known to investigators of the n-body problem; i.e.,

$$R = \sum_{i=1}^{5} GM_i \left(\frac{1}{\rho_i} - \frac{\bar{r} \cdot \bar{r}_i}{r_i^3} \right) \qquad \text{(F-30)}$$

where: G = the universal gravitational constant

M_i = the mass of natural satellite i (i = I, ... , V), given in Table I-7, Chapter I

ρ_i = distance between SC and satellite i

$\bar{r} = \bar{r}_k$ of Section 6

$\bar{r}_i = \bar{r}_{ki}$ defined in preceeding paragraph

Only the equatorial case of the SC is considered since only the periodic perturbations of the equatorial case have been treated. Then:

$$\rho_i = (r^2 + r_i^2 - 2rr_i \text{ Cos } \alpha)^{\frac{1}{2}}$$

$$\bar{r} \cdot \bar{r}_i = rr_i \text{ Cos } \alpha$$

where α is the equatorial angle between r and r_i. Note from Table I-6, Chapter I, that the natural satellite closest to Jupiter is JV (Amalthea) the radial distance of which is 2.54 R_J. For the orbital segment during which radar measurements are made, r is maximum at $v = -\pi/2$ and $+\pi/2$ and equals 2.53 R_J. Thus during radar R and RR, $r<r_i$, i = I, ..., V. Thus, for any term R_i of eq. (F-30):

$$R_i = \frac{GM_i}{r_i}\left[\{1 + (\frac{r}{r_i})^2 - 2(\frac{r}{r_i})\text{ Cos}\alpha\}^{-\frac{1}{2}} - \frac{r}{r_i}\text{ Cos }\alpha\right] \qquad \text{(F-31)}$$

One of the first and best known exercises encountered in the study of geodesy is the verification that the negative radical of eq. (F-31) can be expressed as an infinite series involving Legendre Polynomials and powers of r/r_i. Convergence is guaranteed by the above mentioned fact that $r<r_i$ for all i. The first power cancles the last term of eq. (F-31), thus:

$$R_i = \frac{GM_i}{r_i} \sum_{\substack{m=o \\ m\neq 1}}^{\infty} (\frac{r}{r_i})^m P_m (\text{Cos } \alpha) \qquad \text{(F-32)}$$

Now, consulting the sketch below, $\alpha = \theta_i + v_i - (\theta+v)$

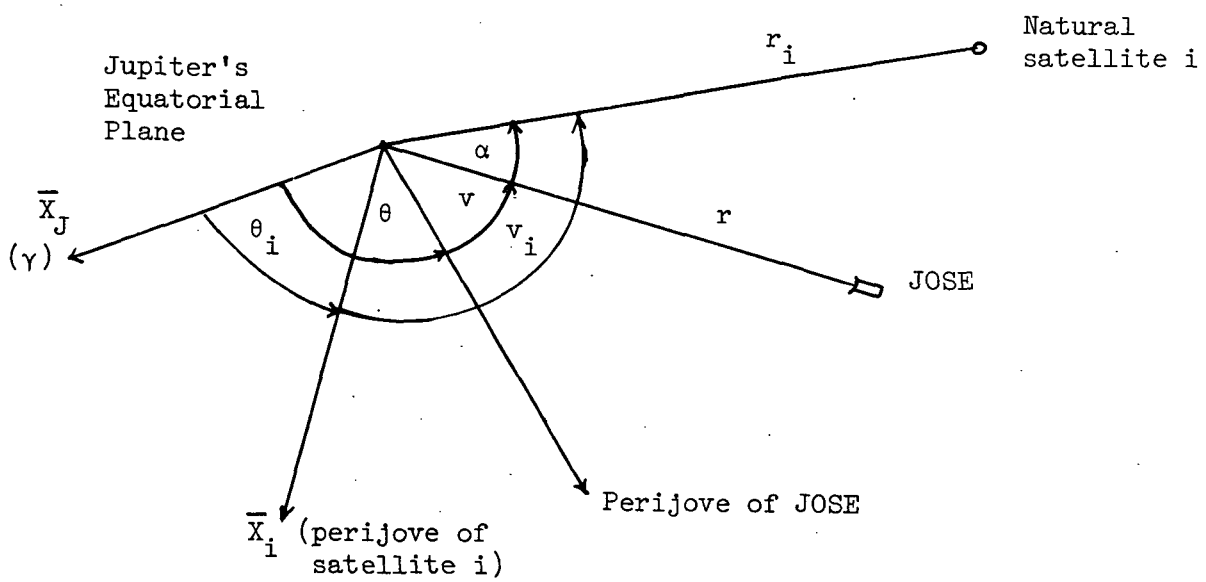

Thus, R_i can be expressed in terms of the SC's orbital parameters:

$$R_i = \frac{GM_i}{r_i}\left[1 + \sum_{m=2}^{\infty}\left[\frac{a(1-e^2)}{r_i(1+e\ \mathrm{Cos}\ v)}\right]^m P_m\left[\mathrm{Cos}(\theta_i + v_i - (\theta+v))\right]\right]$$

Substituting R_i for F in the Lagrange equations of equatorial perturbations (F2-5), then placing these orbital rates into the range rate model eq. (F-27), much reduction finally yields:

$$\dot{r}_i = \frac{GM_i\sqrt{1-e^2}}{n\,a\,r_i(1+e\ \mathrm{Cos}\ v)}\sum_{m=2}^{\infty}\left(\frac{r}{r_i}\right)^m\left[F_1(e,v)P_{m1}\left[\mathrm{Cos}(\theta_i+v_i - (\theta+v))\right] - m\,F_2(e,v)\right.$$
$$\left.P_m\left[\mathrm{Cos}(\theta_i+v_i - (\theta+v))\right]\right] \qquad \text{(F-33)}$$

where: $\dot{r}_i$ = radial velocity of JOSE due to the perturbation of the i^{th} natural satellite of Jupiter

n = mean orbital velocity of JOSE

$$F_1(e,v) = \frac{2 + e\,\mathrm{Cos}\,v - 2\,\mathrm{Cos}^2 v - e\,\mathrm{Cos}^3 v}{1 + e\,\mathrm{Cos}\,v}$$

$F_2(e,v) =$ Sin 2v

$P_{ml}(x) =$ Associated Legendre Polynomial, degree m, order l, or

$$P_{ml}(x) = (1-x^2)^{\frac{1}{2}}\, d/dx\, (P_m(x))$$

r/r_i will usually be less than ½, and the infinite series above should converge very quickly and hence can be truncated after a few terms.

It would be of interest to place some numbers in eq. (F-33) to obtain some idea of relative magnitudes. Near perijove, (for example, v = 20°) with the SC and the i^{th} satellite aligned with Jupiter's center; i.e., with $\theta_i + v_i = \theta + v$; and with a 1.1 R_J by 100 R_J SC orbit, eq. (F-33) reduces to:

$$\dot{r}_i \quad -7 \text{ m/sec} \sum_{m=2}^{\infty} m \left(\frac{r}{r_i}\right)^m \qquad \text{(F-34)}$$

Substituting α for r/r_i, it would be interesting to know the minimum α which would produce an r_i of about -1 m/sec. Eq. (F-34) can be written:

$$\dot{r}_i + 7\alpha = -7\alpha \sum_{m=1}^{\infty} m\alpha^{m-1} \qquad \text{(F-35)}$$

Noting that:

$$\sum_{m=1}^{\infty} m\alpha^{m-1} = \frac{d}{d\alpha} \sum_{m=0}^{\infty} \alpha^m = \frac{d}{d\alpha} \left(\frac{1}{1-\alpha}\right) (\text{Since } \alpha<1) = \frac{1}{(1-\alpha)^2}$$

a cubic equation results, and an α of about 0.14 is one root. For a maximum r of 2.53 R_J at $v = \pm\pi/2$, any satellite at $r_i > 2.53/\alpha = 18.1\ R_J = 1.29 \times 10^6$ km. need not be considered, since, even when it is aligned with JOSE, it would produce an $\dot{r}_i$ on JOSE of only 1 meter/sec. Note from Table I-6 of Chapter I that ironically JIV (Callisto) is at the largest distnace r_4 of the satellites of 1.884×10^6 km, just outside the range of effect on JOSE. In summary, JIV (Callisto) can be ignored, if desired, in eq. (F-36) below, and there

would certainly be portions of JIII's (Ganymede) orbit which would have no effect on JOSE (when $\theta_i+v_i-(\theta+v)$ equals 180°, for example). Generally, then, the range rate $\dot{r}'_k$, which must be subtracted from the left side of eq. (F-28) before the solution of the harmonic coefficients, is:

$$\dot{r}'_k = \sum_{i=1}^{5} \dot{r}_i \qquad \text{(F-36)}$$

where: $\dot{r}_i$ is given by Eq. (F-33).

Appendix F1

General Orbital Secular Rates of Motion Due to the

Central Gravity Term and the Second and

Fourth Degree Zonal Harmonics

Note ($i \neq 0^{\circ}$)

1. Perturbations due to the Central Term $GM_J/2a$

   (a) $\frac{dM}{dt} = n$, all others 0.

2. Perturbations due to the Second Degree Zonal Harmonic V_{20}

   (a) $\frac{da}{dt} = \frac{de}{dt} = \frac{di}{dt} = 0$

   (b) $\frac{d\omega}{dt} = \frac{-3n\ J_2 R_J^2}{4a^2(1-e^2)^2}\ (1-5\ \mathrm{Cos}^2 i)$

   (c) $\frac{d\Omega}{dt} = \frac{-3n\ J_2 R_J^2 \mathrm{Cos}\ i}{2a^2(1-e^2)^2}$

   (d) $\frac{dM}{dt} = \frac{-3n\ J_2 R_J^2}{4a^2(1-e^2)^{3/2}}\ (1-3\ \mathrm{Cos}^2 i)$

3. Perturbations due to the Fourth Degree Zonal Harmonic V_{40}

   (a) $\frac{da}{dt} = 0$

   (b) $\frac{de}{dt} = \frac{-15n\ J_4 R_J^4 e}{16a^4(1-e^2)^3}\ \left(\frac{-7}{2}\ \mathrm{Sin}^4 i + 3\ \mathrm{Sin}^2 i\right)\ \mathrm{Sin}\ 2\omega$

   (c) $\frac{d\omega}{dt} = \frac{-15n\ J_4 R_J^4}{4(1-e^2)^{9/2} a^4}\ \left[\frac{e^2 \mathrm{Sin}^2 i}{4}\ \{(7\ \mathrm{Sin}^2 i - 3)\mathrm{Cot}^2 i + \frac{7}{2}\sqrt{1-e^2}(3 - \frac{7}{2}\ \mathrm{Sin}^2 i)\}\mathrm{Cos}2\omega\right.$

   $\left. + \{(1 + \frac{3e^2}{2})(1 - \frac{7}{4}\ \mathrm{Sin}^2 i)\ \mathrm{Cos}^2 i + \frac{\sqrt{1-e^2}}{2}\ (\frac{3}{2}\ e^2 + 2)(\frac{35}{8}\ \mathrm{Sin}^4 i - 5\mathrm{Sin}^2 i + 1)\}\right]$

(d) $$\frac{di}{dt} = \frac{-15n\, J_4 R_J^4 \sin i \cos i\, e^2}{16a^4(1-e^2)^{9/2}} \left(3 - \frac{7}{2}\sin^2 i\right) \sin 2\omega$$

(e) $$\frac{d\Omega}{dt} = \frac{-15n\, J_4 R_J^4 \cos i}{4a^4(1-e^2)^{9/2}} \left[\frac{e^2}{4}(3-7\sin^2 i)\cos 2\omega + (1+\frac{3}{2}e^2)(\frac{7}{4}\sin^2 i - 1)\right]$$

(f) $$\frac{dM}{dt} = \frac{-15n\, J_4 R_J^4}{16a^4(1-e^2)^{7/2}} \left[(5-\frac{7}{2}e^2)(3-\frac{7}{2}\sin^2 i)\sin^2 i \cos 2\omega + 3e^2 \right.$$

$$\left. (\frac{35}{8}\sin^4 i - 5\sin^2 i + 1)\right]$$

Appendix F2

Derivation of the Lagrange Equations of

Orbital Motion for the Equatorial Case

The orbital set $(s_1, s_2, s_3, s_4) = (a, e, M, \theta)$ is considered.

The basic form of the Lagrange equation is commonly expressed:

$$\sum_{k=1}^{4} |s_l, s_k| \frac{ds_k}{dt} = \frac{\partial F}{\partial s_l} \qquad \text{(F2-1)}$$

where: F = the force function

$$|s_l, s_k| = \text{Lagrange's brackets} = \sum_{i=1}^{3} \left(\frac{\partial x_i}{\partial s_l}\frac{\partial \dot{x}_i}{\partial s_k} - \frac{\partial x_i}{\partial s_k}\frac{\partial \dot{x}_i}{\partial s_l}\right) \qquad \text{(F2-2)}$$

$\{x_i\}$, $\{\dot{x}_i\}$, i = 1, 2, 3 = rectangular, inertially fixed position and velocity components respectively $(\vec{X}_J \vec{Y}_J)$

(see sketch below)

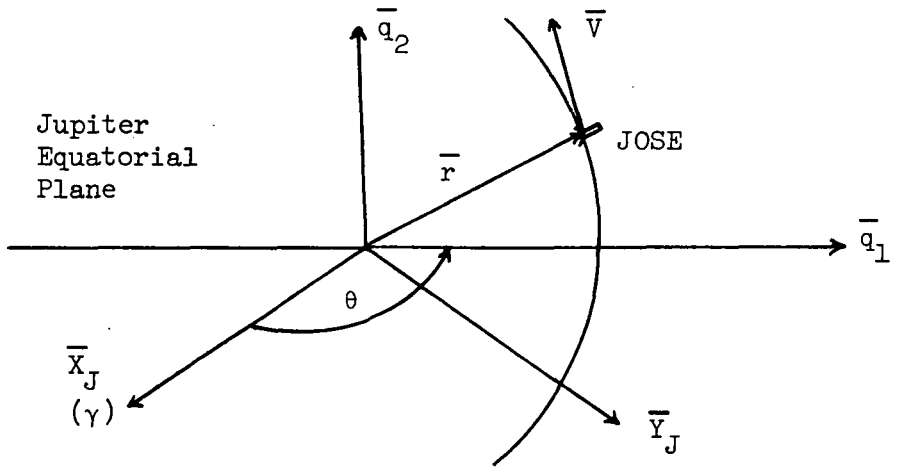

In terms of the eccentric anomaly E, semi-major axis a, eccentricity e, and mean orbital velocity n, the state vectors for JOSE in the q_i coordinate system are given by:

$$q = \begin{pmatrix} a(\text{Cos } E - e) \\ a\sqrt{1-e^2}\ \text{Sin } E \\ 0 \end{pmatrix} \qquad \dot{q} = \begin{pmatrix} -\text{ Sin } E \\ \sqrt{1-e^2}\ \text{Cos } E \\ 0 \end{pmatrix} \frac{na}{1-e\ \text{Cos } E}$$

The matrix $M_{xq} = \begin{pmatrix} \text{Cos } \theta & -\text{Sin } \theta \\ \text{Sin } \theta & \text{Cos } \theta \end{pmatrix}$ transforms the state vectors from the $\bar{q}$ coordinate system to the $\bar{X}_J\bar{Y}_J$ system, the system in which $\{x_i\}$ and $\{\dot{x}_i\}$ are defined. Thus:

$$x_1 = a(\text{Cos } E-e)\ \text{Cos } \theta - a\sqrt{1-e^2}\ \text{Sin } E\ \text{Sin } \theta$$

$$x_2 = a(\text{Cos } E-e)\ \text{Sin } \theta + a\sqrt{1-e^2}\ \text{Sin } E\ \text{Cos } \theta$$

$$x_3 = 0$$

$$\dot{x}_1 = \frac{-na\ \text{Sin } E}{(1-e\ \text{Cos } E)}\ \text{Cos } \theta - \frac{na\sqrt{1-e^2}\ \text{Cos } E}{(1-e\ \text{Cos } E)}\ \text{Sin } \theta \qquad \text{(F2-3)}$$

$$\dot{x}_2 = \frac{-na\ \text{Sin } E}{(1-e\ \text{Cos } E)}\ \text{Sin } \theta + \frac{na\sqrt{1-e^2}\ \text{Cos } E}{(1-e\ \text{Cos } E)}\ \text{Cos } \theta$$

$$\dot{x}_3 = 0$$

The Lagrange brackets are now computed. From eq. (F2-2), note that $|s_\ell, s_k| = -|s_k, s_\ell|$ and that $|s_k, s_k| = 0$. There are thus only six distinct Lagrange brackets to calculate of the total sixteen brackets. Another simplification is now valid. One of the first exercises in the study of Lagrange brackets is the verification that the Lagrange brackets are time invariant; i.e., $\frac{\partial}{\partial t}|s_\ell, s_k| = 0$ for all ℓ and k. Thus, we are free to choose $\{x_i\}$ and $\{\dot{x}_i\}$anywhere on the orbit since the resulting bracket evaluation does not depend on the orbit location of the SC. Perijove is immediately selected, since E = 0 at that position. Thus, eq. (F2-3) reduces to:

$$x_1 = a(1-e)\ \mathrm{Cos}\ \theta \qquad \dot{x}_1 = -na\sqrt{1-e^2}\ \mathrm{Sin}\ \theta/(1-e)$$
$$x_2 = a(1-e)\ \mathrm{Sin}\ \theta \qquad \dot{x}_2 = na\sqrt{1-e^2}\ \mathrm{Cos}\ \theta/(1-e) \qquad \text{(F2-4)}$$
$$x_3 = 0 \qquad \dot{x}_3 = 0$$

The remaining work for the evaluation of the brackets is simply an exercise in partial differentiation. The following points should be noted, however:

1. The partials $\partial x_i/\partial s_k$; k = 1, 2, 4; and $\partial \dot{x}_i/\partial s_k$; k = 2, 4; are no problem. However, $\partial x_i/\partial s_3 = \partial x_i/\partial M = \partial x_i/\partial E \times dE/dM$, the chain rule also applying for $\dot{x}_i$ since x_i and $\dot{x}_i$ are functions of the eccentric anomaly E. The mean anomaly M = E - e Sin E, thus dE/dM = 1/(1-e Cos E). Thus, to evaluate $\partial x_i/\partial M$, it is necessary to use the general $\{x_i\}$ and $\{\dot{x}_i\}$ given by (F2-3) so that the differentials $\partial x_i/\partial E$ can be evaluated. After multiplication by dE/dM, the perijove case can be evaluated by substituting E = 0.

2. The remaining partials; i.e., $\partial \dot{x}_i/\partial s_1$, or $\partial \dot{x}_i/\partial a$, need to be evaluated with caution since $\{\dot{x}_i\}$ are functions of a and the mean velocity n, which is itself a function of a; i.e., $n = \sqrt{GM_J/a^3}$. Thus, for example, from eq.(F2-4):

$$\frac{\partial \dot{x}_1}{\partial a} = \frac{\partial \dot{x}_1}{\partial (na)}\frac{d(na)}{da} = \frac{-\sqrt{1-e^2}\ \mathrm{Sin}\theta}{1-e}\left(n + a\frac{dn}{da}\right) = \frac{n\sqrt{1-e^2}\ \mathrm{Sin}\ \theta}{2(1-e)}$$

The six Lagrange brackets are thus solved and shown below:

$$|s_1,s_2| = -|s_2,s_1| = |a,e| = 0$$
$$|s_1,s_3| = -|s_3,s_1| = |a,M| = -na/e$$
$$|s_1,s_4| = -|s_4,s_1| = |a,\theta| = -(na/2)\sqrt{1-e^2}$$
$$|s_2,s_3| = -|s_3,s_2| = |e,M| = 0$$
$$|s_2,s_4| = -|s_4,s_2| = |e,\theta| = na^2 e/\sqrt{1-e^2}$$
$$|s_3,s_4| = -|s_4,s_3| = |M,\theta| = 0$$

Equation (D2-1) can be written in matrix notation as:

$$\begin{pmatrix} 0 & 0 & [s_1,s_3] & [s_1,s_4] \\ 0 & 0 & 0 & [s_2,s_4] \\ -[s_1,s_3] & 0 & 0 & 0 \\ -[s_1,s_4] & -[s_2,s_4] & 0 & 0 \end{pmatrix} \begin{pmatrix} ds_1/dt \\ ds_2/dt \\ ds_3/dt \\ ds_4/dt \end{pmatrix} = \begin{pmatrix} \partial F/\partial s_1 \\ \partial F/\partial s_2 \\ \partial F/\partial s_3 \\ \partial F/\partial s_4 \end{pmatrix}$$

Solving algebraically, we obtain the equatorial Lagrange equations:

$$\begin{aligned} \frac{da}{dt} &= \frac{2}{na}\frac{\partial F}{\partial M} \\ \frac{de}{dt} &= \frac{(1-e^2)}{na^2e}\frac{\partial F}{\partial M} - \frac{\sqrt{1-e^2}}{na^2e}\frac{\partial F}{\partial \theta} \\ \frac{dM}{dt} &= \frac{-2}{na}\frac{\partial F}{\partial a} - \frac{(1-e^2)}{na^2e}\frac{\partial F}{\partial e} \\ \frac{d\theta}{dt} &= \frac{\sqrt{1-e^2}}{na^2e}\frac{\partial F}{\partial e} \end{aligned} \qquad \text{(F2-5)}$$

Appendix F3

Equatorial Secular Orbital Rates of Motion Due to the Central Gravity Term and the Second and Fourth Degree Zonal Harmonics ($i = 0^{\circ}$)

1. Perturbation due to the Central Term $\frac{GM_J}{2a}$

   (a) $\frac{dm}{dt} = n$, all others 0

2. Perturbations due to the Second Degree Zonal Harmonic V_{20}

   (a) $\frac{da}{dt} = \frac{de}{dt} = 0$

   (b) $\frac{dM}{dt} = \frac{3n\, J_2 R_J^{\,2}}{2a^2(1-e^2)^{3/2}}$

   (c) $\frac{d\theta}{dt} = \frac{3nJ_2R_J^{\,2}}{2a^2(1-e^2)^2}$

3. Perturbations due to the Fourth Degree Zonal Harmonic V_{40}

   (a) $\frac{da}{dt} = \frac{de}{dt} = 0$

   (b) $\frac{dM}{dt} = \frac{9n\, J_4 R_J^{\,4}}{8a^4(1-e^2)^{7/2}}$

   (c) $\frac{d\theta}{dt} = \frac{21n\, R_J^{\,4} J_4}{8a^4(1-e^2)^4}$

Appendix F4

Elements of the Coefficient Matrix G for the

Short Term Periodic Perturbations of an Equatorial Orbit

$$g_{11} = \frac{-3GM_J R_J^2 e \text{ Sin } v}{nr^4\sqrt{1-e^2}}$$

$$g_{12} = \frac{15GM_J R_J^4 e \text{ Sin } v}{4nr^6\sqrt{1-e^2}}$$

$$g_{13} = \frac{3GM_J R_J^2}{2nr^4\sqrt{1-e^2}}\left[3e \text{ Sin } v \text{ Cos } 2(\theta-\alpha+v) + 2(1+e \text{ Cos } v) \text{ Sin } 2(\theta-\alpha+v)\right]$$

$$g_{14} = \frac{3GM_J R_J^2}{2nr^4\sqrt{1-e^2}}\left[3e \text{ Sin } v \text{ Sin } 2(\theta-\alpha+v) - 2(1+e \text{ Cos } v) \text{ Cos } 2(\theta-\alpha+v)\right]$$

$$g_{21} = \frac{-3GM_J R_J^2 \text{Sin } v\sqrt{1-e^2}}{2 n a r^4}$$

$$g_{22} = \frac{15GM_J R_J^4 \text{Sin } v\sqrt{1-e^2}}{8 n a r^6}$$

$$g_{23} = \frac{3GM_J R_J^2\sqrt{1-e^2}}{n a^2 e r^4}\{3 a e \text{ Sin } v \text{ Cos } 2(\theta-\alpha+v) + 2\left[a+ae \text{ Cos } v-r\right] \text{ Sin } 2(\theta-\alpha+v)\}$$

$$g_{24} = \frac{3GM_J R_J^2\sqrt{1-e^2}}{n a^2 e r^4}\{3 a e \text{ Sin } v \text{ Sin } 2(\theta-\alpha+v) - 2\left[a+ae \text{ Cos } v-r\right] \text{ Cos } 2(\theta-\alpha+v)\}$$

$$g_{31} = \frac{3n R_J^2 \text{Sin } v}{2r^2}$$

$$g_{32} = \frac{-15n R_J^4 \text{Sin } v}{8r^4}$$

$$g_{33} = \frac{-9n\ R_J^2 \text{Sin } v \text{ Cos } 2(\theta-\alpha+v)}{r^2}$$

$$g_{34} = \frac{-9n\ R_J^2 \text{Sin } v \text{ Sin } 2(\theta-\alpha+v)}{r^2}$$

$$g_{41} = \frac{-3n\ R_J^2(-2a + r \text{ Sin } v)}{2r^3\sqrt{1-e^2}}$$

$$g_{42} = \frac{15n\ R_J^4(-2a + r \text{ Sin } v)}{8r^5\sqrt{1-e^2}}$$

$$g_{43} = \frac{9n\ R_J^2(-2a + r \text{ Sin } v) \text{ Cos } 2(\theta-\alpha+v)}{r^3\sqrt{1-e^2}}$$

$$g_{44} = \frac{9n\ R_J^2(-2a + r \text{ Sin } v) \text{ Sin } 2(\theta-\alpha+v)}{r^3\sqrt{1 - e^2}}$$

Appendix F5

The Integral Functions h of the Periodic Orbital Rates of Motion

1. The true anomaly v is considered the only variable

2. v must be in radians

$$h_1\,(a,\ e,\ v,\ \theta,\ J_2,\ J_4,\ C_{22},\ S_{22}) = \frac{R_J^{\,2}J_2(1+e\ \mathrm{Cos}\ v)^3}{a(1-e^2)^3} - \frac{3R_J^{\,4}J_4(1+e\ \mathrm{Cos}\ v)^5}{4a^3(1-e^2)^5}$$

$$+ \frac{3R_J^{\,2}}{2a(1-e^2)^3}\left[(C_{22}\mathrm{Cos}\ 2(\theta-\alpha) + S_{22}\mathrm{Sin}\ 2(\theta-\alpha)\left(1 - \frac{3e^2}{4} + 3e\ \mathrm{Cos}\ v + (3e^2-2)\ \mathrm{Cos}^2 v\right.\right.$$

$$+ e(e^2-6)\mathrm{Cos}^3 v - 6e^2\mathrm{Cos}^4 v - 2e^3\mathrm{Cos}^5 v) + (C_{22}\mathrm{Sin}2(\theta-\alpha) - S_{22}\mathrm{Cos}\ 2(\theta-\alpha))$$

$$\left.\left(2e(3+e^2)\ \mathrm{Sin}\ v + \left(1 + \frac{3}{2}e^2\right)\mathrm{Sin}\ 2v + \frac{3e^2}{4}\mathrm{Sin}\ 4v - 2e\ (3+2e^2)\ \mathrm{Sin}^3 v\right.\right.$$

$$\left.\left. + 2e^3\mathrm{Sin}^5 v\right)\right]$$

$$h_2(a,\ e,\ v,\ \theta,\ J_2,\ J_4,\ C_{22},\ S_{22}) = \frac{R_J^{\,2}J_2(1+e\ \mathrm{Cos}\ v)^3}{ea^2(1-e^2)^2} - \frac{3R_J^{\,4}J_4(1+e\ \mathrm{Cos}\ v)^5}{8ea^4(1-e^2)^4}$$

$$+ \frac{3R_J^{\,2}}{a^3e(1-e^2)^2}\left[(C_{22}\mathrm{Cos}\ 2(\theta-\alpha) + S_{22}\mathrm{Sin}\ 2(\theta-\alpha))\left(\frac{-3ae^2}{4} + 3ae\ \mathrm{Cos}\ v - ae^2\mathrm{Cos}\ 2v\right.\right.$$

$$+ 3ae^2\mathrm{Cos}^2 v - \frac{ae}{3}(14+e^2)\mathrm{Cos}^3 v - 6ae^2\mathrm{Cos}^4 v - 2ae^3\ \mathrm{Cos}^5 v)$$

$$+ (C_{22}\ \mathrm{Sin}\ 2(\theta-\alpha) - S_{22}\ \mathrm{Cos}\ 2(\theta-\alpha))\left(4ae(1+e^2)\ \mathrm{Sin}\ v + \frac{5}{2}ae^2\ \mathrm{Sin}\ 2v\right.$$

$$\left.\left. + \frac{3}{4}ae^2\ \mathrm{Sin}\ 4v - \frac{2}{3}ae\ (7 + 8\ e^2)\ \mathrm{Sin}^3 v + 2\ ae^3\ \mathrm{Sin}^5 v\right)\right]$$

$$h_3(a,\ e,\ v,\ \theta,\ J_2,\ J_4,\ C_{22},\ S_{22}) = \frac{3R_J^{\,2}J_2}{2a^2(1-e^2)}\left[\frac{2(v + e\ \mathrm{Sin}\ v)}{1-e^2} + \mathrm{Cos}\ v\right]$$

$$- \frac{5R_J^{\,4}J_4}{4a^4(1-e^2)^3}\left[\frac{3}{1-e^2}\left\{v(1+\frac{3}{2}e^2) + e(3+e^2)\ \mathrm{Sin}\ v + \frac{3e^2}{4}\mathrm{Sin}\ 2v - \frac{e^3}{3}\mathrm{Sin}^3 v\right\}\right.$$

$$\left. - \frac{(1+e\ \mathrm{Cos}v)^3}{2e}\right] + \frac{9R_J^{\,2}}{a^2(1-e^2)^2}\left[(C_{22}\ \mathrm{Cos}\ 2(\theta-\alpha) + S_{22}\ \mathrm{Sin}\ 2(\theta-\alpha)(\ (1-e^2)\ \mathrm{Cos}\ v\right.$$

$$- 2e\ \mathrm{Sin}\ v - \mathrm{Sin}\ 2v - \frac{2}{3}(1-e^2)\ \mathrm{Cos}^3 v + \frac{4e}{3}\mathrm{Sin}^3 v)$$

$$\left. - (C_{22}\mathrm{Sin}\ 2(\theta-\alpha) - S_{22}\ \mathrm{Cos}\ 2(\theta-\alpha))(\mathrm{Cos}\ 2v + \frac{4e}{3}\mathrm{Cos}^3 v + \frac{2}{3}(1-e^2)\mathrm{Sin}^3 v)\right]$$

Appendix G: Determination of Downlink Power-Gain Product

1. Required Power-Gain Product

Following a system suggested in a JPL TOPS in house report, Table G-1 was used to determine the required product for both the S and X band transmitter power-antenna gain product. The calculations were made under the following assumptions:

RX antenna: 210 ft. dish, 72.2 db gain at X band, 62.0 db at S band

RX system noise temperature: $30^{\circ}K$

Signal power to noise density ratio required, E_t/N_o equals 3 db. This ratio is required for a convolutionally encoded, sequentially decoded phase modulated system for acceptable error probabilities (10^{-3}/bit)

Galactic noise insignificant

Distance to Jupiter: 6.4×10^8 Km

2. Item Definition

Space Loss:

$$L_s = 10 \log_{10} \frac{(16\pi^2 R^2)}{\lambda^2} \text{ db} \qquad \text{(G-1)}$$

Antenna Gain:

$$G = 10 \log_{10} \frac{4\pi A}{\lambda^2} \text{ db} \qquad \text{(G-2)}$$

where A is the effective aperature of the antenna.

RX noise spectral density:

$$N_o = 10 \log_{10} (KT) + 30 \text{ dbm/hz} \qquad \text{(G-3)}$$

where K is Boltzmann's const., 1.4×10^{-23}, T is the RX noise temp. ($^{\circ}K$), and the factor 30 is needed to convert from dbw to dbm. Zero dbm is one mw.

3. Downlink Antenna Design

The gain figures for both downlink antennas having been determined, it remains to determine the physical dimensions. An untapered filled

Table G-1: Determination of Power-Gain Product

Item	X Band DB.	X Band Adverse Tol. DB	S Band DB.	S Band Adverse Tol. DB
Xmtng. ckt. losses	.5	.2	.7	.2
" ant. point loss	0.0	.3	0.0	.3
Space loss	287.0	--	275.5	--
Pol. loss	0.0	.1	0.0	.1
Rx ant gain	72.2	1.6	62.0	.4
Rx ant point loss	0.0	.2	0.0	.1
Rx ckt loss	0.0	0.0	0.0	0.0
Net ckt loss	215.3	2.4	214.4	1.1
Data rate 120 kbps	50.8	--		
Data rate 10 kbps			40.0	--
E_t/N_o required	3.0	.5	3.0	.5
Total loss	269.1	2.9	257.4	1.6
Rx noise sp. dens.	183.8dbm/hz	.6	183.8	.6
Power-gain prod.	85.3 dbm	3.5	73.6	2.2
Allowance for xmtr pwr and ant gain variations	2.0	2.0	1.4	1.4
Total adverse tol.	3.5	--	2.2	--
	90.8 dbm	5.5	77.2 dbm	3.6

aperture gives the maximum aperture efficiency on the order of eighty percent. Such an aperture is generated by an array of halfwave dipoles spaced a halfwave apart and fed in phase. If an allowance is made for conductive, fabrication error and miscellaneous losses, a reasonable estimate for the efficiency of a square dipole array is seventy five percent. Application of (G-2) and the required downlink antenna gains of 40.8 and 29.1 db for the X and S band systems respectively, gives the required physical size of both antennas. The actual physical area of these antennas is then 1.6 m^2. Each dipole element occupies an area approximately $\lambda^2/4$ or $3.06 \times 10^{-4} m^2$ and $42 \times 10^{-4} m^2$ for X and S band respectively. Rounding off to whole numbers of dipole elements, each antenna becomes a square matrix of 73 x 73 or 20 x 20 dipole elements for X and S band respectively. This is a total of 5329 elements for the X band antenna and 400 for the S band antenna. Fabrication of the dipole elements themselves present no problem. It can be done by any one of several techniques including etching as printed circuit boards are made, or vacuum deposition of a thick metal film on an insulating substrate. The problem with this system is feeding the dipole elements in phase. Actual detailed design of this feed system must await actual hardware design and fabrication efforts. The right general direction is easy to see, however.

The dipole elements can be placed effectively in parallel by locating them along a parallel open conductor transmission line at intervals of one half wavelength. A convenient method for this would be to deposit stripline transmission lines on the substrate at the same time as the dipole elements in such a way that the lines were perpendicular to the dipole elements and passed through the center feed points where connection

to the dipole elements could be made. In the case of the X band antenna there would then be seventy three such striplines each with seventy three dipoles connected along it. The problem with this is that the phase of alternate dipole elements must be reversed, because points a half wavelength apart on a transmission line are out of phase by one hundred eighty degrees. In addition, seventy three dipoles in parallel present a very low impedance to an RF source. It is therefore more practical to place the transmission line elsewhere than on the front surface of the antenna. If the lines are placed inside the insulating substrate, or perhaps on the opposite side of the metal reflecting plane from the dipoles, there is room either to "twist" the line a half turn between elements, or to twist the lines which must now feed the dipole elements through the substrate and/or the reflector on alternate dipoles. A scheme which seems most practical is shown in Fig. G-1. Note that a thin insulating layer is applied to the entire surface of the reflector, then the transmission lines are laid on that layer. The thick supporting insulator is on top of that with the dipole elements deposited on its top surface. Holes are then drilled through the thick substrate and the feed points of the dipole elements down to the transmission lines. Alternate elements reverse their phase by "twisting" the feed holes. These holes are then made conducting by the deposition of metal film on their inside surfaces. The problem of low impedances caused by multiple parallel dipoles can be solved by feeding in smaller sections and using baluns and quarter wave impedance matching transformers to place these sections in an equivalent series-parallel arrangement. In this way at no point does the impedance become so low that conductive losses become objectionable.

An additional problem is presented in that the optimum spacing of

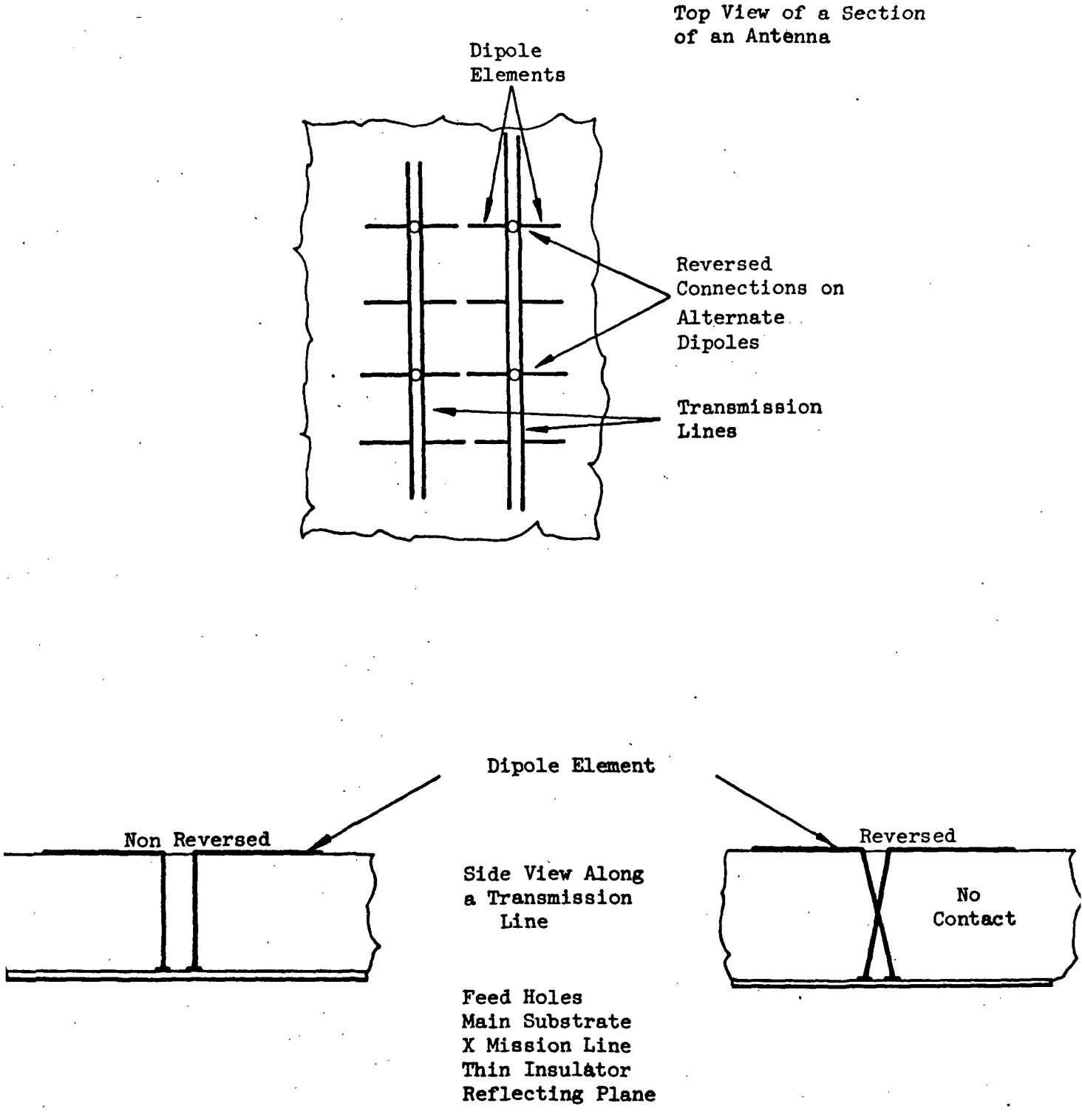

Figure G-1: Diagram of Antenna

dipole elements on the surface of the substrate is a half wavelength in free space, whereas the optimum spacing along the transmission line is a half wavelength in the substrate material. It is therfore desirable to keep the dielectric constant of the substrate material as close to one as possible. This can be done by using some sort of foam material which is mostly empty space and therefore has a low effective dielectric constant. The physical spacing of the dipole elements from antenna pattern considerations can be adjusted a slight amount to conform to the residual propagation velocity difference between a foam substance and free space.